



**HAL**  
open science

# Ultrafast spectroscopic characterization of dye-sensitized H<sub>2</sub>-evolving photocathodes: towards optimized devices

Sebastian Johannes Bold

► **To cite this version:**

Sebastian Johannes Bold. Ultrafast spectroscopic characterization of dye-sensitized H<sub>2</sub>-evolving photocathodes: towards optimized devices. Theoretical and/or physical chemistry. Université Grenoble Alpes [2020-..]; Friedrich-Schiller-Universität (Iéna, Allemagne), 2021. English. NNT : 2021GRALV052 . tel-03605040

**HAL Id: tel-03605040**

**<https://theses.hal.science/tel-03605040>**

Submitted on 10 Mar 2022

**HAL** is a multi-disciplinary open access archive for the deposit and dissemination of scientific research documents, whether they are published or not. The documents may come from teaching and research institutions in France or abroad, or from public or private research centers.

L'archive ouverte pluridisciplinaire **HAL**, est destinée au dépôt et à la diffusion de documents scientifiques de niveau recherche, publiés ou non, émanant des établissements d'enseignement et de recherche français ou étrangers, des laboratoires publics ou privés.



## THÈSE

Pour obtenir le grade de

### DOCTEUR DE L'UNIVERSITÉ GRENOBLE ALPES

Spécialité : Chimie Physique Moléculaire et Structurale

Arrêté ministériel : 25 mai 2016

Présentée par

### Sebastian Johannes BOLD

Thèse dirigée par **Murielle CHAVAROT-KERLIDOU**  
et codirigée par **Benjamin Dietzek**, Friedrich-Schiller-Universität  
Jena

préparée au sein du **Laboratoire Laboratoire de Chimie et  
Biologie des Métaux**  
dans l'**École Doctorale Chimie et Sciences du Vivant**

### Caractérisation spectroscopique ultra-rapide de photocathodes pour la production d'hydrogène : vers des systèmes moléculaires optimisés

### Ultrafast spectroscopic characterization of dye- sensitized H<sub>2</sub>-evolving photocathodes: towards optimized devices

Thèse soutenue publiquement le **1 décembre 2021**,  
devant le jury composé de :

**Madame Murielle CHAVAROT-KERLIDOU**

CHARGE DE RECHERCHE HDR, CNRS délégation Alpes, Directrice de thèse

**Madame Inke SIEWERT**

PROFESSEUR, Georg-August-Universität Göttingen, Rapporteuse

**Madame Mary PRYCE**

DOCTEUR EN SCIENCES, Dublin City University, Rapporteuse

**Monsieur Benjamin DIETZEK**

PROFESSEUR, Friedrich-Schiller-Universität Jena, Directeur de thèse

**Madame Stefanie GRÄFE**

PROFESSEUR, Friedrich-Schiller-Universität Jena, Examinatrice

**Monsieur Felix SCHACHER**

PROFESSEUR, Friedrich-Schiller-Universität Jena, Président

**Monsieur Vincent ARTERO**

INGENIEUR HDR, CEA Centre de Grenoble, Examineur

**Monsieur Renaud DEMADRILLE**

INGENIEUR HDR, CEA Centre de Grenoble, Examineur





FRIEDRICH-SCHILLER-  
UNIVERSITÄT  
JENA

**UGA**  
Université  
Grenoble Alpes

## CUMULATIVE THESIS

To obtain the degree of

**DOCTEUR of the UNIVERSITE GRENOBLE ALPES &  
DOCTOR RERUM NATURALIUM (Dr. rer. nat.) of the  
FRIEDRICH-SCHILLER-UNIVERSITÄT JENA**

**prepared in the framework of a cotutelle between  
the *Université Grenoble Alpes (UGA)* and the  
*Friedrich-Schiller-Universität Jena (FSU)***

Specialty: **Physical Chemistry**

Arrêté ministériel : 25<sup>th</sup> May 2016

Presented by **M. Sc. Sebastian BOLD**

born 14<sup>th</sup> May 1991 in Bergisch Gladbach

Thesis directed by **Benjamin DIETZEK** and  
**Murielle CHAVAROT-KERLIDOU**

prepared in the laboratories **Chimie et Biologie des Métaux** (CEA  
Grenoble) and **Molecular Photonics** (Institute of Physical  
Chemistry, Friedrich-Schiller-Universität Jena)

at the **Doctoral Schools Chimie & Sciences du Vivant (UGA)** and  
the **Faculty of Chemistry and Earth Sciences (FSU)**

**ULTRAFAST SPECTROSCOPIC  
CHARACTERIZATION OF DYE-  
DENSITIZED H<sub>2</sub>-EVOLVING  
PHOTOCATHODES: TOWARDS  
OPTIMIZED DEVICES**





FRIEDRICH-SCHILLER-  
UNIVERSITÄT  
JENA

**UGA**  
Université  
Grenoble Alpes

Thesis reviewed by:

1. **Prof. Dr. Inke SIEWERT**
2. **Dr. Mary PRYCE**

Thesis defended publicly on **1<sup>st</sup> December 2021**,  
Before the jury composed of:

**Prof. Dr. Felix SCHACHER**

Professor, FSU, Jury president

**Prof. Dr. Stefanie GRÄFE**

Professor, FSU, Jury member

**Prof. Dr. Benjamin DIETZEK**

Professor, FSU, Jury member

**Dr. Murielle CHAVAROT-KERLIDOU**

Chargée de recherche CNRS, UGA, Jury member

**Dr. Vincent ARTERO**

Research director at CEA, UGA, Jury member

**Dr. Renaud DEMADRILLE**

Senior researcher at CEA, UGA, Jury member

**Prof. Dr. Inke SIEWERT**

Professor, Georg-August-Universität Göttingen, Reviewer



Supported by:



Université  
franco-allemande  
Deutsch-Französische  
Hochschule

# Table of contents

Table of contents .....	III
Publication authorship declaration .....	V
List of Abbreviations .....	VII
List of Figures .....	IX
1 Introduction.....	11
2 Dye-sensitized H <sub>2</sub> -evolving Photocathodes: State of the Art.....	15
2.1 General considerations and design.....	15
2.2 Components of dye-sensitized photocathodes for proton reduction.....	18
2.2.1 Photosensitizers.....	18
2.2.2 Hydrogen evolution reaction (HER) catalysts.....	22
2.2.3 Dye-catalyst assemblies.....	26
2.2.4 Semiconductors .....	28
2.3 Photocathode architecture and performance .....	31
2.3.1 Catalysts in solution .....	31
2.3.2 Co-grafting .....	32
2.3.3 Dye-catalyst assemblies.....	32
2.4 Stability issues.....	38
2.5 Kinetic issues.....	39
3 Spectroscopy in solution.....	43
3.1.1 Spectroscopic techniques .....	43
3.2 Photophysics of push-pull organic dyes.....	45
3.3 Photophysics of dye-catalyst assemblies in solution .....	50
3.3.1 <b>T1-Co</b> .....	51
3.3.2 <b>T2R</b> dyads .....	56
3.3.3 <b>T2-Co</b> .....	57
3.3.4 Conclusion and Outlook .....	58

3.4	Experimental Section .....	60
3.4.1	Synthesis of T2 and T2-Co .....	60
3.4.2	Transient absorption spectroscopy.....	60
4	Dye-sensitized photocathodes .....	62
4.1	Ruthenium-cobalt dyad <b>RuCo</b> .....	63
4.1.1	Activity and stability .....	65
4.1.2	Time-resolved spectroscopy on dye-sensitized NiO films .....	66
4.1.3	Summary and Outlook.....	80
4.1.4	Experimental section .....	80
4.2	Organic covalent dye-catalyst assemblies .....	88
4.2.1	(Photo-)electrochemistry and hydrogen production activity .....	90
4.2.2	Operando and post-operando characterization .....	92
4.2.3	TA-SEC .....	94
4.2.4	Summary and Outlook.....	97
4.3	Comparing <b>RuCo</b> to <b>T2R-Cat1</b> .....	99
5	Summary .....	101
6	Zusammenfassung .....	107
7	Résumé .....	113
	Bibliography .....	119
	Appendix.....	146
	Included publications .....	146
	<b>Publication 1</b> - Electron transfer in a covalent dye–cobalt catalyst assembly – a transient absorption spectroelectrochemistry perspective. ....	146
	<b>Publication 2</b> - Investigating Light-Induced Processes in Covalent Dye-Catalyst Assemblies for Hydrogen Production. ....	161
	<b>Publication 3</b> - Spectroscopic investigations provide a rational for the hydrogen-evolving activity of dye-sensitized photocathodes based on a cobalt tetraazamacrocyclic catalyst.....	289
	Acknowledgements .....	282
	Declaration of Originality .....	284
	Complete List of Publications.....	285

Articles in peer-reviewed journals.....	285
Conference contributions .....	286
Talks.....	286
Poster presentations .....	286
Curriculum Vitae.....	288

## Publication authorship declaration

I agree to the writing of the dissertation as publication-based, i.e. cumulative, and confirm the information given on the following pages. I will submit a correspondingly justified endorsement, stating the doctoral candidate's scientific share of the publications used, to the Council of the Faculty of Chemical and Geosciences in parallel.

Ich bin mit der Abfassung der Dissertation als publikationsbasiert, d.h. kumulativ, einverstanden und bestätige die auf den folgenden Seiten gegebenen Angaben. Eine entsprechend begründete Befürwortung mit Angabe des wissenschaftlichen Anteils des Doktoranden/der Doktorandin an den verwendeten Publikationen werde ich parallel an den Rat der Fakultät der Chemisch-Geowissenschaftlichen Fakultät der Friedrich-Schiller-Universität Jena richten.

J'accepte que la rédaction de la thèse soit sur articles, c'est à dire qu'elle soit cumulative, et je confirme les informations données dans les pages suivantes. Un avenant dûment justifié, indiquant la part scientifique du candidat au doctorat dans les publications utilisées, sera envoyé parallèlement au Conseil de la Faculté de chimie et de géosciences de l'université Friedrich Schiller, Iéna.

Dr. Murielle Chavarot-Kerlidou .....

Prof. Dr. Benjamin Dietzek .....

**Declaration on own shares in publications and secondary publication rights for a cumulative dissertation**

For all manuscripts used in this cumulative dissertation, the necessary reprint permissions for the secondary publication have been obtained from the publishers. The co-authors of the manuscripts used in this cumulative dissertation have been informed about their use, about the other doctoral students' own contributions as co-authors to the publications as well as about the reprint permissions for a cumulative dissertation and agree to this.

**Erklärung zu Eigenanteilen an Publikationen und Zweitpublikationsrechten bei einer kumulativen Dissertation**

Für alle in dieser kumulativen Dissertation verwendeten Manuskripte liegen die notwendigen Genehmigungen der Verlage („Reprint permissions“) für die Zweitpublikation vor. Die Koautoren der in dieser kumulativen Dissertation verwendeten Manuskripte sind sowohl über deren Nutzung, über die in den folgenden Seiten angegebenen Eigenanteile der weiteren Doktoranden/Doktorandinnen als Koautoren an den Publikationen und über die Zweitpublikationsrechte bei einer kumulativen Dissertation informiert und stimmen dem zu.

**Déclaration sur les actions propres dans les publications et les droits de publication secondaire en cas de thèse cumulative**

Pour tous les manuscrits utilisés dans cette thèse cumulative, les autorisations de réimpression nécessaires pour la publication secondaire ont été obtenues auprès des éditeurs. Les co-auteurs des manuscrits utilisés dans cette thèse cumulative ont été informés de leur utilisation, des contributions des autres doctorants en tant que co-auteurs des publications ainsi que des autorisations de réimpression pour une thèse cumulative.

Sebastian Bold

Jena,

## List of Abbreviations

ACN	acetonitrile
bpy	2,2'-bipyridine
CPDT	cyclopentadithiophene
CR	charge recombination
CSS	charge-separated state
DMF	dimethyl formamide
DSPC	dye-sensitized photocathode
DSPEC	dye-sensitized photoelectrochemical cell
DSSC	dye-sensitized solar cell
ESA	excited state absorption
ET	electron transfer
FTO	fluorine-doped tin oxide
GSB	ground state bleach
HER	hydrogen evolution reaction
HI	hole injection
ICT	intramolecular charge transfer
ISC	intersystem crossing
ITO	indium-doped tin oxide
MeOH	methanol
MLCT	metal-to-ligand charge transfer
NDI	naphthalene diimide
OCP	open-circuit potential
PMI / PDI	perylene monoimide / perylene diimide
PS	photosensitizer
RHE	relative hydrogen electrode



SC	semiconductor
SE	stimulated emission
SEC	spectroelectrochemistry
SED	sacrificial electron donor
TA	transient absorption
TOF	turnover frequency
TON	turnover number
TPA	triphenylamine
VB	valence band

## List of Figures

Figure 1.1 Schematic outline of this thesis' structure. ....	12
Figure 2.1: Schematic representation of a tandem DSPEC for full water splitting ....	16
Figure 2.2: Core structures of PS used in DS-photocathodes .....	19
Figure 2.3: Catalysts for HER.....	23
Figure 2.4: General catalytic mechanism for hydrogen evolution by cobalt diimine dioxime complexes .....	25
Figure 2.5: Dye-catalyst assemblies reported in the literature for proton reduction in DSPEC. ....	27
Figure 2.6: Schematic representation of energy levels in a DSPEC for hydrogen evolution.....	29
Figure 2.7: Different photocathode architectures used in DSPECs for proton reduction. ....	31
Figure 2.8: Schematic representation of the light-induced processes in DSPEC photocathodes .....	40
Figure 3.1: Left: Schematic depiction of a TA experiment .....	44
Figure 3.2: Chemical structures of organic push-pull dyes, containing TPA donor and cyanovinyl-based acceptor units, investigated by TA spectroscopy in the literature. ....	45
Figure 3.3: Compounds whose photophysics were studied in solution and their UV-Vis absorption spectra .....	47
Figure 3.4: Results of TA spectroscopy of organic push-pull dyes in solution.....	49
Figure 3.5: Scheme of the electrochemical and principal light-induced processes taking place during the TA-SEC measurements on <b>T1-Co</b> .....	52
Figure 3.6: fs-TA-SEC data of <b>T1-Co</b> in DMF at various applied potentials.....	54
Figure 3.7: Results of TA spectroscopy of <b>T2</b> and <b>T2-Co</b> in solution.....	58
Figure 3.8: Deactivation pathways of the singlet excited ICT state of the dye-catalyst dyads.....	59
Figure 4.1: Chemical structures of the dye <b>Ru</b> and the dyad <b>RuCo</b> and their UV-Vis absorption spectra in ACN.....	64
Figure 4.2: Cell for TA-SEC measurements on films in the assembled and disassembled state. ....	68
Figure 4.3: fs-TA-SEC (top left) and ns-TASEC (top right) data of NiO films sensitized with <b>Ru</b> at OCP and two applied potentials (0.74 and -1.15 V vs. $Fc^{+/0}$ ).....	70
Figure 4.4: Schematic representation of different HI and CR kinetics caused by differing localization of the excited electron ( $NiO Ru^*$ ) and the excess electron in the CSS ( $NiO^+ Ru$ ). ....	73

Figure 4.5: Potential dependence of the NiO band electronics and its influence on HI and CR kinetics.....	74
Figure 4.6: Decay-associated spectra obtained by a three-exponential fit of the TA-SEC data of NiO films sensitized with <b>RuCo</b> .....	75
Figure 4.7 - Synthesis of <b>Ru</b> and <b>RuCo</b> .....	81
Figure 4.8: Scheme showing the light-induced processes in a NiO films sensitized with <b>RuCo</b> at an applied potential of -0.74 V vs. $\text{Fc}^{+/0}$ .....	86
Figure 4.9: Chemical structures of the organic dye-catalyst dyads studied in this work and their UV-Vis absorption spectra in DMF ( <b>T1</b> dyads) and MeOH ( <b>T2R</b> dyads). .....	89
Figure 4.10: Results of the photoelectrochemical measurements of the organic dye-catalyst dyads .....	91
Figure 4.11: In-operando characterization of NiO films sensitized with <b>T2R-Cat1</b> ....	93
Figure 4.12: Results of TA-SEC measurements of NiO films sensitized with <b>T2R-Cat1</b> and <b>T2R</b> .....	96
Figure 5.1. Schematic representation of the principal characterization techniques used in this work on the DSPCs.....	102

# 1 Introduction

As fossil fuel reserves dwindle and global warming increases, caused by the intensive use of fossil fuels as primary energy source, the worldwide energy demand keeps rising due to an ever-increasing human population. This situation forces humanity to use alternative, carbon emission-free and renewable energy sources such as solar, wind, tidal and geothermal energy. Solar energy in particular has an immense potential in terms of available energy to be gained.<sup>1</sup> So far, the use of solar energy is tantamount to generation of electricity by photovoltaic cells to be fed into the electrical grid or stored in batteries. However, fuels will still be needed in the future for specific purposes such as mobility where high energy densities are required, as in the case of freight trucks and air travel. Fuels are also an attractive option to move stored energy from areas with high solar influx, where the use of solar energy is more productive, to those without strong solar irradiation; or to compensate the intermittent nature of solar energy. Fuels that are produced with solar energy receive the name “solar fuels”. Currently, the most technologically mature solution to produce such fuels is to combine photovoltaics with electrolyzers, so that the electricity generated by the photovoltaics is used on site to drive the redox reaction that produces the desired fuel, e.g. to reduce protons in water to produce molecular hydrogen. However, this system requires several distinct components and on large scale, the balance-of-system costs can be substantial.<sup>2</sup> An alternative is to directly convert the energy of the sunlight into chemical energy by photocatalytic processes. The inspiration for this approach comes from the photosynthetic system found in a number of organisms in nature, which uses sunlight to drive various redox reactions, most prominently reductive reactions on carbon dioxide to produce sugars.<sup>3</sup> Certain cyanobacteria are even able to reduce protons to molecular hydrogen.<sup>4</sup> The photosynthetic system faces the difficult task of generating a charge-separated state (CSS) that is long-lived enough to drive the reaction, and has therefore evolved to a complex machinery comprised of two photosystems (PSI and PSII) with various charge shuttles and enzymes to catalyse the redox reactions. This inspired the field of artificial photosynthesis, which mimics the concept of natural photosynthesis, but tries to reduce the complexity such that the individual parts of the system are ideally easily and cheaply synthesized: the photosystems are replaced by molecular dyes for efficient light absorption, the enzymes by bio-inspired molecular catalysts, and the redox shuttles by a variety of approaches to shuttle electrons.

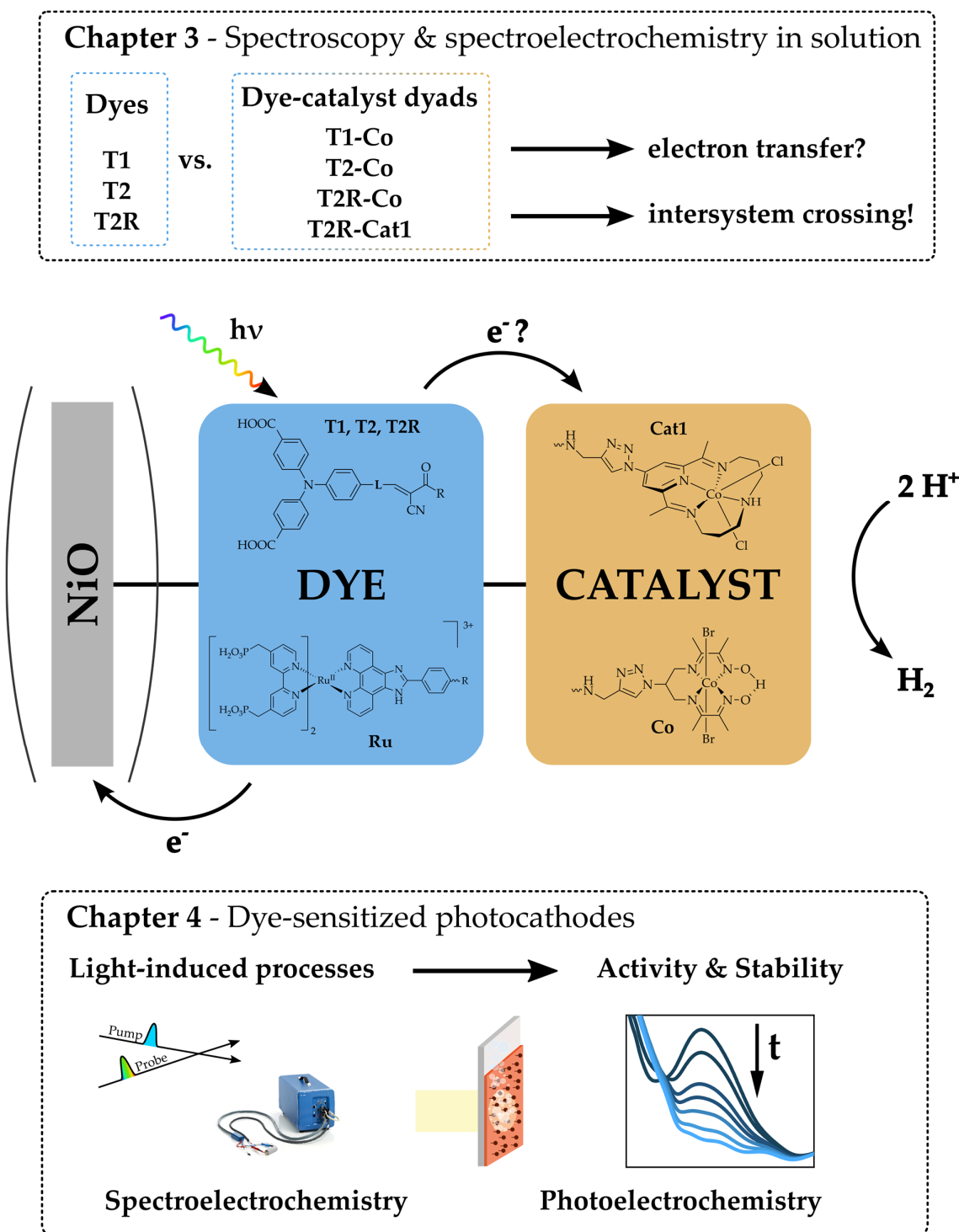


Figure 1.1 Schematic outline of this thesis' structure. In the centre, the studied systems are presented. In chapter 3, the photophysics of the organic dyes and some of their dye-catalyst dyads are investigated in solution using TA spectroscopy and spectroelectrochemistry. In chapter 4, NiO photocathodes sensitized with the dyads are investigated in terms of their activity for hydrogen production, stability under operando conditions and the light-induced processes as a function of applied potential. The latter was also performed for a Ru-Co dyad.

One is to immobilize the components on semiconductor (SC) particles and suspend those in solution, which is a very low-cost, but also less mature technology.<sup>5</sup> Furthermore, both half reactions, in the case of water splitting proton reduction and water oxidation, have to be carried out on the same particle, which can lead to difficulties. A more sophisticated approach is to separate the two reactions into two separate half cells with a photocathode and a photoanode, consisting of SC films sensitized with a dye and catalyst. The resulting system is called a dye-sensitized photoelectrochemical cell (DSPEC).<sup>3</sup> In a tandem cell with both photoanode and photocathode, the current of the worse performing half-cell is the limiting factor for the overall performance. To date, the photoanodes greatly outperform the photocathodes, generating the need for an improvement in dye-sensitized photocathodes (DSPC).<sup>6-8</sup> To do this, it is important to obtain insights into the bottleneck processes in the photocathode to be able to address them. Spectroscopic techniques, especially time-resolved techniques, can help to give a mechanistic understanding of the light-induced processes in the DSPCs.<sup>9,10</sup> Arguably the most important technique is transient absorption (TA) spectroscopy, which has the advantage of giving both kinetic as well as spectral information, allowing to identify intermediates and the kinetics of their formation and decay. However, to date the number of studies on DSPCs for proton reduction is limited, and usually not performed under conditions that are close to the operando conditions of the photoelectrochemical cell. The work in this thesis is situated in the context of the work performed in the “SolHyCat” group at the Laboratory of Chemistry and Biology of Metals, CEA Grenoble, on the construction of DSPCs for proton reduction on a molecular basis, notably covalent dye-catalyst assemblies; and the work in the group of Molecular Photonics at the Friedrich-Schiller University Jena, on the investigation of the light-induced processes in such molecular dyes and dyads. The aim of this thesis, as outlined in Figure 1.1, was to unite the expertise of both groups to

- a) construct dye-sensitized NiO photocathodes with a series of newly synthesized covalent dye-catalyst assemblies featuring an organic dye and a cobalt catalyst, and assess their activity in photoelectrochemical proton reduction
- b) to determine possible degradation mechanisms that reduce the activity and lifetime of the photocathodes
- c) to investigate the light-induced processes in the assemblies in solution and on NiO, especially the electron transfer (ET) from the dye to the catalyst unit. Especially important, the established TA spectroscopy should be combined with electrochemistry to perform transient absorption spectroelectrochemistry (TA-SEC) experiments in solution and on film, allowing to measure the light-

induced processes at different oxidation states of the catalyst and close to the operando conditions.

The goal of these studies was to identify the best-performing system and its bottlenecks to then rationally improve upon the molecular design for a higher performance of the photocathodes.

In the second chapter, I will present the state of the art of DSPCs in terms of activity and stability. The third chapter will deal with the photophysics in solution of the organic dyes and dye-catalyst assemblies synthesized in our lab, with one dyad studied by TA-SEC. The fourth chapter presents the results on the NiO photocathodes sensitized with the organic dye-catalyst assemblies, including their activity, post- and in-operando characterization and TA-SEC measurements. In addition, TA-SEC measurements of NiO photocathodes sensitized with a ruthenium-cobalt covalent assembly are presented.

## 2 Dye-sensitized H<sub>2</sub>-evolving Photocathodes: State of the Art

### 2.1 General considerations and design

Using sunlight to drive water splitting is attractive due to the abundance of sunlight and the relatively low energy necessary. Thermodynamically, 1.23 V is the standard potential for water splitting,<sup>11</sup> and 1.23 eV, the energy needed to be inserted into a chemical bond,<sup>12</sup> corresponds to a photon with a wavelength of ca. 1000 nm. Most of the sunlight spectrum consists of photons of higher energy which – based on thermodynamic considerations – should make for an easy water splitting with sunlight. However, much of the initial excitation energy is lost in relaxation processes in the photosensitizer (PS) as well as in the charge transfer to the catalyst, on top of the overpotential needed by the catalyst to drive the redox reaction. At the same time, a certain energy difference of the CSSs is needed to prevent recombination and ensure a fast downhill charge transfer cascade to the catalyst. In consequence, two PS are needed to provide sufficient driving force for water splitting through their combined excitation energy, analogous to the natural photosynthetic system which contains two photosystems. Therefore, the molecular components of molecular devices for water-splitting must be optimized to reduce these energy losses.

While the goal is full water splitting, the two half reactions are often realized and studied separately. In the following, only systems for proton reduction will be discussed. Inspired by natural photosynthesis, researchers have tried to reduce the complexity of the natural photosynthetic apparatus by identifying its key components and then synthesizing in the laboratory molecules that perform their functions: In general, in all photocatalytic systems there is a PS which absorbs light and then transfers an electron to a catalyst. Once the catalyst is fully charged, it reduces protons from the surrounding solution to molecular hydrogen. In addition, there must be an electron donor to regenerate the oxidized PS. While in full water splitting, these electrons come ultimately from the oxidation of water, when studying the proton reduction separately a different source is required.



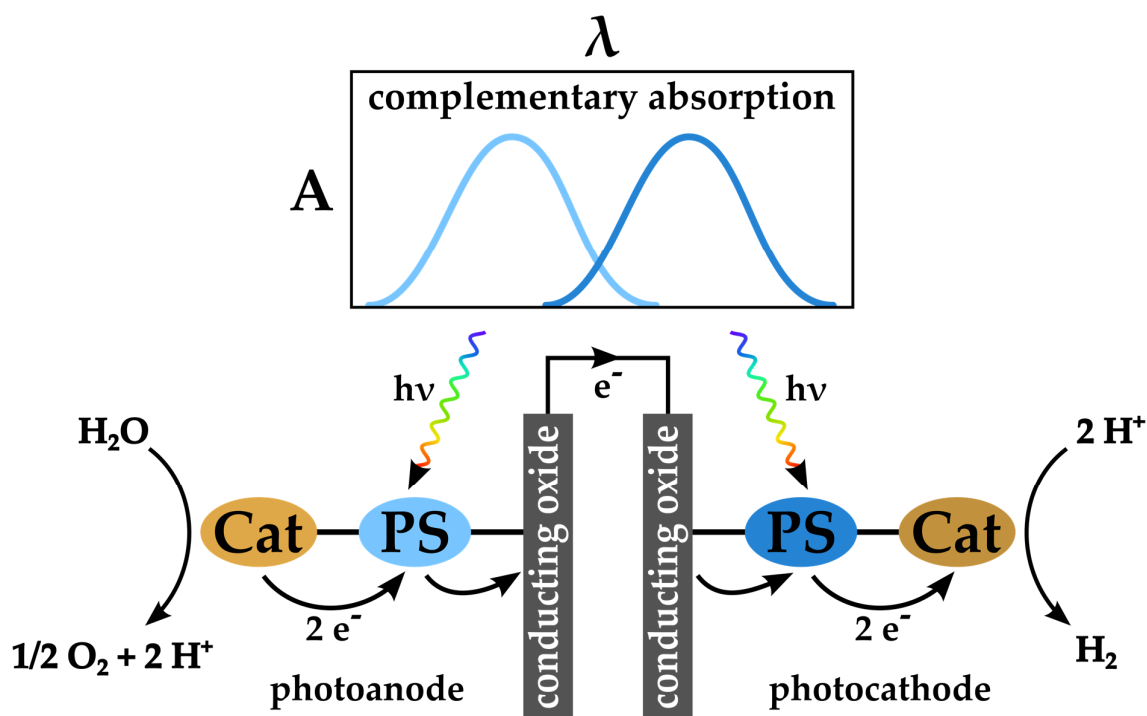


Figure 2.1: Schematic representation of a tandem DSPEC for full water splitting, in this case with dye-catalyst supramolecular assemblies.

The arguably easiest way to achieve photocatalytic proton reduction is in fully homogeneous systems, where PS and catalyst are dissolved in solution.<sup>13–17</sup> In addition, it is necessary to add a sacrificial electron donor (SED) which is ultimately the source of the electron needed for the reduction. While homogeneous photocatalysis is easy to achieve and often gives high turnover numbers (TON), the use of the SED, usually an organic molecule such as triethylamine or ascorbic acid, is prohibitive for commercial application. It can however serve to quickly identify promising candidates for application in other techniques.

Full water splitting can be achieved by dye-sensitized SC nanoparticles that perform both proton reduction and water oxidation. While this is a cheap method of achieving full water splitting, so far the achieved conversion efficiencies remain low. Their use is also hampered by the fact that hydrogen and oxygen evolve in the same solution and must afterwards be separated, which is a technical challenge.

To overcome these drawbacks, DSPEC have been proposed, based on the design of dye-sensitized solar cells (DSSC). Here, the two redox reactions (proton reduction and water oxidation) are separated into two half cells, each of which performs only one of the two reactions. Each half cell consists of a SC film on a conductive substrate which is connected to the electrical circuit. The SC film is sensitized with a PS that absorbs

light and injects charge into the SC from its excited state. The contrary charge is then transferred to a catalyst, which may be immobilized on the film or the PS and which then performs the redox reaction (Figure 2.1). By connecting two such photoelectrodes, a photocathode for proton reduction and a photoanode for water oxidation, via a diaphragm and an external circuit, a tandem DSPEC can be built for full water splitting. In the ideal case, this is achieved without applying a potential bias across the two half cells, but applying an additional bias may be necessary to drive water splitting for ineffective systems. This way, the production of hydrogen and oxygen is spatially separated and both electrodes can be optimized for the respective reaction. Some key properties of the DSPEC are essential for high currents:

1) *Efficient light absorption by the PS.* Preferably, the whole visible light spectrum should be used by the PS to maximize sunlight absorption. In addition, high extinction coefficients are beneficial to increase light absorption. In a tandem cell where light passes through two photoelectrodes, the absorption spectra of the two PS should ideally be complementary so each uses a different part of the solar spectrum.<sup>8,18</sup>

2) *Fast and long-lived charge separation.* Charge separation must occur faster than the deactivation of the PS excited state. More importantly, the created CSSs must be long-lived, since charge transfer to the catalyst may be slow and catalysis operates on very long timescales compared to typical excited state processes. In addition to this, the redox reactions in question are multi-electron reactions that require multiple charges to be transferred to the catalyst before the reaction can occur. During this time, the charges already transferred must remain on the catalyst.

3) *Fast catalysis at low overpotential.* To reduce the CSS lifetime requirements and increase currents, the reaction taking place on the catalyst should be fast. A low overpotential ensures that also low-energy photons can be used to drive the reaction.

Today, hydrogen-producing DSPEC have been published and bias-free water splitting has been achieved. However, the first systems based on first-row transition metal catalysts were published less than ten years ago and thus DSPEC are still an immature technology that suffers from low activity and are far from the currents needed for commercialization. This is especially true for the photocathodes which lag behind the photoanodes, with photocurrent densities typically lower than 100  $\mu\text{A}\cdot\text{cm}^{-2}$  (Table 2.1) compared to typically hundreds of  $\mu\text{A}\cdot\text{cm}^{-2}$  for photoanodes.<sup>19</sup> Therefore, work still must be done to understand and address the issues facing the development of more performant DSPCs.

The major problems so far seem to be the often-slow ET kinetics to the catalyst, which in combination with generally fast charge recombination (CR) lead to a low amount of long-lived, catalytically active catalysts. In addition, long-term stability under operando conditions is still an issue, as the photocurrent generated by most photocathodes quickly diminishes. These issues will be discussed in more detail in the respective sections: section 2.2 deals with the different components of DSPEC such as the PS (section 2.2.1), catalysts (section 2.2.2) and PS-catalyst dyads (section 2.2.3) as well as the SC materials (section 2.2.4); section 2.4 presents the stability issues affecting DSPEC performance; and section 2.5 discusses the light-induced processes in DSPEC.

## 2.2 Components of dye-sensitized photocathodes for proton reduction

### 2.2.1 Photosensitizers

PS are essential in DSPEC as they perform the absorption of incoming photons and are the site where the first CSS is formed. They are the only component that is always anchored to the SC film *via* anchoring groups. The necessary thermodynamic requirement a PS must fulfil to ensure a functional photocathode for solar fuel (or hydrogen) production is the position of the redox energy levels (e.g., its HOMO and LUMO): The reduction potential of the HOMO must be positive of that of the SC valence band (VB) to ensure fast hole injection (HI) after excitation of the PS, and the reduction potential of the LUMO must be negative of that of the catalyst to enable ET to the catalyst to form the catalytically active state.

Furthermore, PS used in DSPECs should possess certain properties to maximize activity: First, the extinction coefficients should be high in the visible region to maximize light absorption by the photocathode, with typical extinction coefficients of  $> 10,000 \text{ M}^{-1}\text{cm}^{-1}$ .<sup>20</sup> Related to this is the spectral distribution of absorption: Panchromatic dyes that absorb across the whole solar spectrum are desired to use the maximum possible amount of incoming sunlight.<sup>21,22</sup> The challenge lies in pushing the dye absorption to the red part of the spectrum while maintaining high extinction coefficients as well as the needed energy levels for catalysis. This is especially important for tandem DSPECs with two photoelectrodes, where the absorption of the two PS must be tuned to absorb different parts of the sunlight if a single light source is to be used.<sup>23</sup>

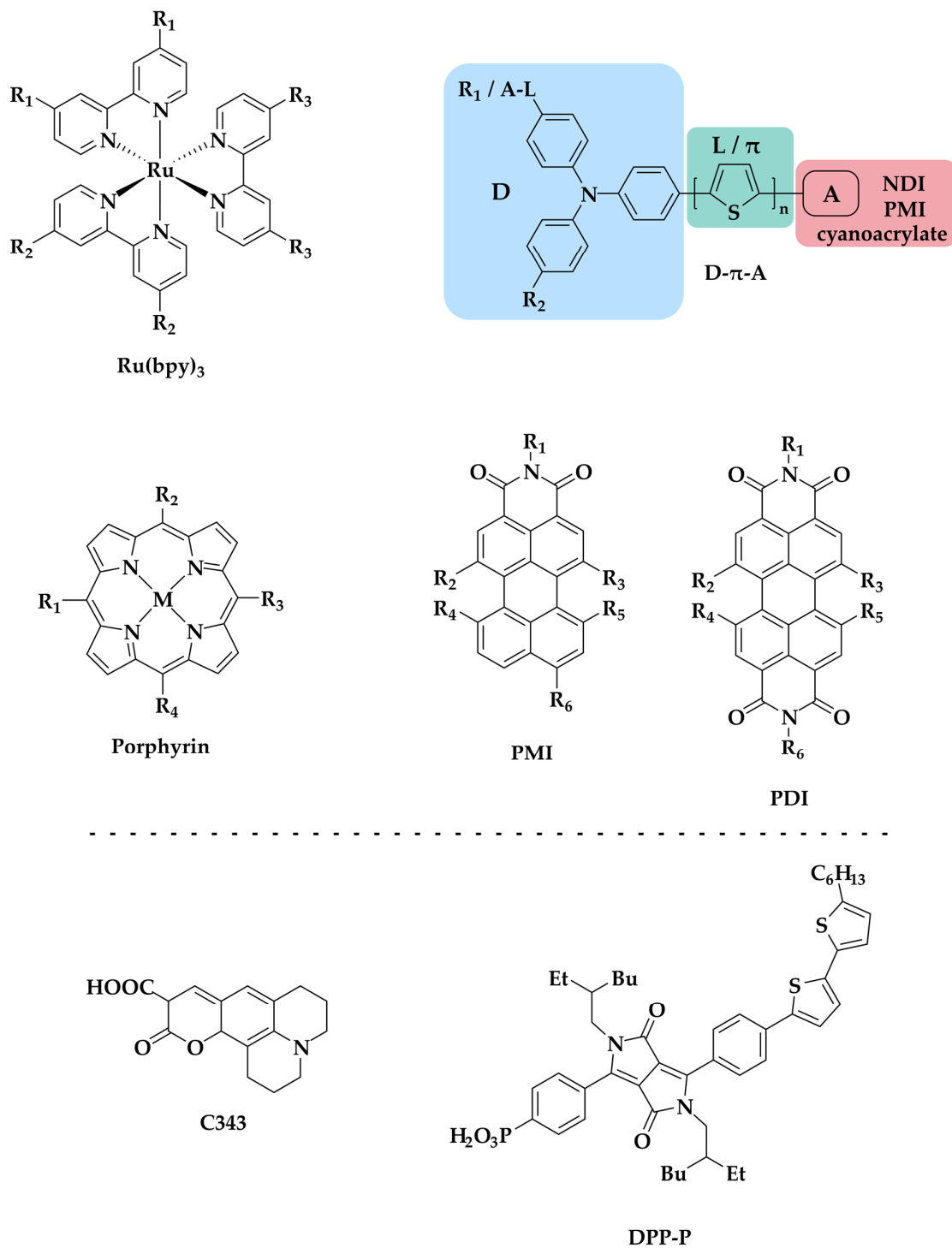


Figure 2.2: Core structures of PS used in DS-photocathodes : Tris(bipyridine)ruthenium (**Ru(bpy)<sub>3</sub>**), push-pull organic dyes (**D-π-A**), porphyrins, perylene monoimides (**PMI**) and perylene diimides (**PDI**), as well as coumarin **C343** and the isoindigo dye **DPP-P**. Rests (R) are varied, with at least one being an anchoring group.

Push-pull dyes are a popular choice since the frontier orbitals can be designed to optimize the light-induced processes: the HOMO is localized close to the anchoring groups to ensure fast HI, and the LUMO is localized far away from the anchoring groups to overcome fast CR in dye-sensitized SC,<sup>24,25</sup> especially the widely used NiO. Additionally, in dye-catalyst assemblies this can be useful to localize the LUMO close to the catalyst unit to ensure fast ET.<sup>26</sup>

An important parameter for long-term performance is the stability of the dye under the relatively harsh - aqueous and reductive - operando conditions used in photoelectrochemical experiments. Related to this is the stability of the anchorage to the SC film, as a common problem in DSPCs is the hydrolysis of the anchoring group in aqueous media which leads to desorption of the PS from the SC surface.<sup>3,24,27-29</sup> The choice of an adequate anchoring group for the PS in a given DSPC system can increase its stability markedly.<sup>3</sup> Typical anchoring groups are carboxylic acid or phosphonic acid groups that form esters on metal oxide surfaces.<sup>3,30-32</sup> These esters can be hydrolysed in the aqueous electrolyte, resulting in desorption of the anchored PS. The hydrolysis reaction kinetics depend on the pH of the electrolyte, with phosphonic acids being reported to be more stable in acidic aqueous conditions.<sup>33</sup> There have been efforts to apply different anchoring groups to overcome this issue.<sup>34</sup> Lastly, if the DSPC systems are to be transferred to commercial application, the cost of the PS and the rarity of the used materials will play an important role, as expensive molecular components can be prohibitive for large-scale applications.<sup>35</sup>

The two most common types of PS are metal complexes and organic dyes. The most widely used metal complexes are Ruthenium polypyridyl complexes due to their relatively high extinction coefficients in the visible region, well-understood photophysics and long excited state lifetimes as well as good chemical stability.<sup>36</sup> The simplest and by far most used in DSPC is tris(bipyridine)ruthenium (**Ru(bpy)<sub>3</sub>**), where one or more of the bipyridine (bpy) ligands are functionalized with anchoring groups (Figure 2.2).<sup>7,37,38</sup> Ru polypyridyl complexes with  $\pi$ -extended ligands replacing usually one of the bpy have been described in studies on photocatalytic hydrogen evolution in homogeneous solution,<sup>39-44</sup> but so far have not been used in DSPC. In these systems, the LUMO is usually localized on the extended ligand, providing a higher distance between the charges in the CSS after HI, which is hoped to reduce deleterious CR.<sup>45</sup> Extended ligands have also been used to introduce a catalytic moiety by coordinating metal ions at the far end to create photocatalytically active dyads.<sup>39-44,46-49</sup> Despite their attractive features as PS, Ru complexes have a major drawback in the rarity and therefore price of Ru, which can hinder the potential commercialization of Ru-based

systems. Additionally, their extinction coefficients are typically not as high as those of the best organic PS. Nevertheless, they remain attractive in order to provide a fundamental understanding of the light-induced processes occurring at the electrode-electrolyte interface.

The use of organic PS can partly eliminate these issues, as they are typically cheaper to synthesize and can offer very good and tuneable photophysical properties, especially high extinction coefficients. A wide variety of organic PS has been integrated in functional DSPC, including triarylamine-based push-pull dyes (**D- $\pi$ -A**),<sup>6,8,24,27,50,51</sup> perylene mono- and diimides (**PMI/PDI**),<sup>52,53</sup> coumarin 343 (**C343**)<sup>54</sup> and isoindigo dyes (**DPP-P**, Figure 2.2).<sup>28,53</sup>

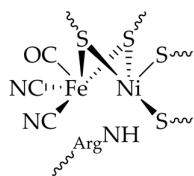
Push-pull dyes consist of an electron-rich donor and an electron-poor acceptor part which are typically linked with by a conjugated linker. These systems offer several advantages: As discussed earlier, the deliberate localization of the HOMO and LUMO can easily be achieved to optimize the light-induced processes. For this purpose, the anchoring groups are placed at the electron-rich part of the molecule where the HOMO is located; in the push-pull dyes used in DSPC, in most cases this is the triarylamine moiety. Localization of the HOMO close to the anchoring groups, and therefore to the SC surface, ensures fast HI after excitation of the PS. Conversely, the LUMO is preferably located on the distant end of the PS molecule to slow down CR once HI has occurred. The LUMO is located at the electron-acceptor group, which is either a cyanoacrylate or a PDI/ naphthalene diimide (NDI) group. The conjugated linker that connects the two groups is usually a (oligo-)thiophene. The choice of the three components that make up the push-pull affects the photophysical properties, most importantly the extinction coefficient and absorption maxima position, and can therefore be used to tune the dye to the specific needs of the DSPC.<sup>20</sup> Further elements can be added to the dye structure to fulfil additional tasks, as is the case of **BH4**, based on a tetrathiophene bridge and PMI acceptor: Here, long alkyl chains were introduced on the bridge to form a hydrophobic layer on the film surface in order to protect the anchoring group from hydrolysis and thus to increase the stability of the photocathode.<sup>24</sup>

## 2.2.2 Hydrogen evolution reaction (HER) catalysts

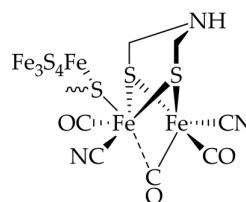
Catalysts are needed to reduce the activation energy of the proton reduction and thus drive the reaction as closely as possible to the thermodynamic potential. The discussion here will focus on those HER catalysts that have been integrated into DSPC to limit the scope of this section. However, the majority of the studies concerning the catalytic activity and mechanism were carried out in solution. Ideally, the overpotential for a redox reaction at a catalyst is zero, and the reaction is completely reversible without hysteresis. Desirable properties of HER catalysts are a high turnover frequency (TOF), produced by fast reaction kinetics, and a high stability under operando conditions, e.g. in aqueous conditions with applied potential and under irradiation. The combination of these two properties leads to high TON. From a mechanistic point of view, the catalyst must be able to consecutively accept and store two electrons since proton reduction is a two-electron process. The reduction potential of both the intermediate and final, catalytically active species must lie between the reduction potential of the reduced dye and that of protons to ensure a downhill ET cascade. Additionally, the catalyst must be stable in all of the oxidation states involved in the catalytic cycle. With a future application of the DSPEC technology in mind, rare and expensive metals such as platinum<sup>55</sup> and palladium must be avoided to reduce costs. Therefore, research has focused on using Earth-abundant elements as the catalytic centres in HER catalysts such as the first-row transition metals Co, Ni and Fe.

In nature, evolution has produced highly performing HER catalysts in the hydrogenase enzymes, most notably the [NiFe]- and [FeFe]-hydrogenases (Figure 2.3). These contain a bimetallic catalytic centre with CN<sup>-</sup> and CO ligands, while iron-sulphur clusters ensure ET to the catalytic site, and nearby amino acids work as proton relays.<sup>56</sup> Hydrogenases display very high TOF at mild reaction conditions, reaching rates of up to 10,000 s<sup>-1</sup>, which make them an attractive choice of HER catalyst.<sup>57</sup> However, they are also very labile and are especially sensitive to oxygen; they therefore need to be protected or kept in ideal working conditions.<sup>58,59</sup> This, in combination with their bulkiness which prevents high surface coverage of the enzyme,<sup>57</sup> complicate their use as catalysts in DSPC, and at the moment there is no example of a hydrogenase-based DSPC in the literature.

## Hydrogenase active sites

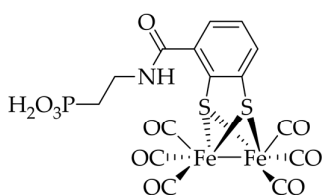


[FeNi]

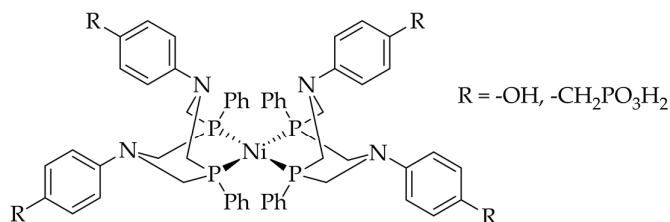


[FeFe]

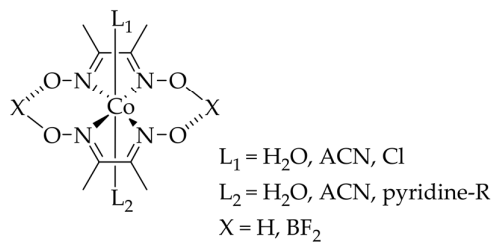
## DSPEC HER catalysts



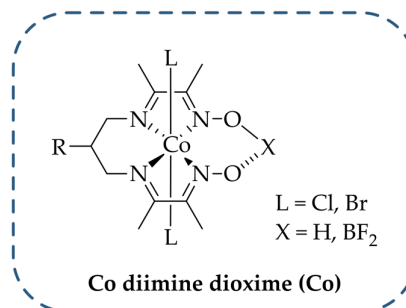
[Fe-Fe]



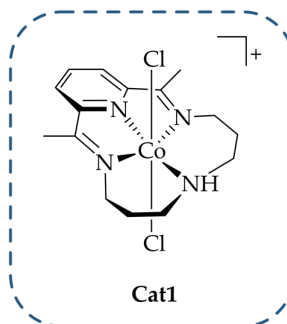
NiP



cobaloxime



Co diimine dioxime (Co)



Cat1

This work

Figure 2.3: Catalysts for HER: the active sites of [FeFe]- and [NiFe]-hydrogenases (top) and HER catalysts used in DSPEC until now (bottom).



Rather, so-called bioinspired HER catalysts have been developed that mimic essential features of hydrogenases to attain high TOF, but are less bulky, have higher long-term stability and can be synthesized in the laboratory. Some of those catalysts directly use the active site of hydrogenases such as catalyst [Fe-Fe] (Figure 2.3).<sup>54,60,61</sup> Most mimic only the functions of certain groups in the enzymes while using completely different molecular structures. A good example of this approach is the molecular Ni catalyst developed by DuBois in which amine groups on the ligands serve as proton relays, and which achieved a TOF of > 100,000 s<sup>-1</sup>.<sup>62</sup> In consequence, this catalyst has been a popular choice to develop functional DSPC.<sup>28,38,52,53,63,64</sup>

The second popular class of molecular HER catalysts in DSPC are Co catalysts. The most widely used ones are “cobaloximes”, bis-(dimethylglyoximato)cobalt, that were first reported for proton reduction in 1983<sup>65</sup> and rediscovered in the 2000s for electro- and photoelectrochemical proton reduction due to low synthetic requirements, high TON and low overpotentials of < 100 mV.<sup>66-71</sup> They consist of a cobalt metal centre coordinated to two dimethylglyoxime ligands in a planar geometry, and, depending on the oxidation state, up to two axial ligands. Protons are coordinated at the oxygen atoms of the oxime bridge, which can therefore possibly function as a proton relay.<sup>72</sup> Although cobaloximes show high performance in organic media with TON of > 50,000 (during 7 hours of electrolysis for a TOF of  $\approx 2$  s<sup>-1</sup>),<sup>17</sup> they are limited in their usefulness for water splitting by their lability in aqueous acidic conditions due to demetallation. To mitigate this, the two dimethylglyoxime ligands were connected via an alkyl chain to give a single ligand that is less easily displaced due to the chelate effect, improving stability considerably.<sup>17,73,74</sup> The resulting complexes are called Co diimine-dioximes and will be called **Co** throughout this thesis. In addition, the alkyl chain offers an opportunity to functionalize the catalyst, for example to tether it to an electrode<sup>17,75,76</sup> or a PS.<sup>26,77</sup> On cobaloximes, such functionalization is usually carried out by axial coordination of pyridines.<sup>47,78-80</sup> While this provides an easy way for functionalization, it is also very labile, especially since cobaloximes undergo ligand exchange during the catalytic cycle.<sup>17,81</sup>

In the catalytic mechanism (Figure 2.4), the Co<sup>III</sup> precatalyst is reduced to the Co<sup>II</sup> state (Co<sup>II</sup>L) by a first reduction step to enter the catalytic cycle. From this state, the Co<sup>II</sup> hydride (Co<sup>II</sup>HLH) is formed through two proton-coupled ET steps via a Co<sup>I</sup> state with a protonated oxime bridge (Co<sup>I</sup>LH). Co<sup>II</sup>HLH then produces hydrogen either through external protonation or through an intramolecular mechanism to end up in the Co<sup>II</sup>L state ready to initialise catalysis again.<sup>17</sup> The protonation of the oxime bridge allows to lower the overpotential required for catalysis to occur and is proposed to facilitate

hydrogen formation through an intramolecular protonation step. During catalysis, the axial halide ligands are displaced by solvent molecules, typically water or ACN. While the Co<sup>II</sup> state still possesses two axial ligands, in the Co<sup>I</sup> state one ligand is lost to form a pentacoordinated complex on which the hydride can form.

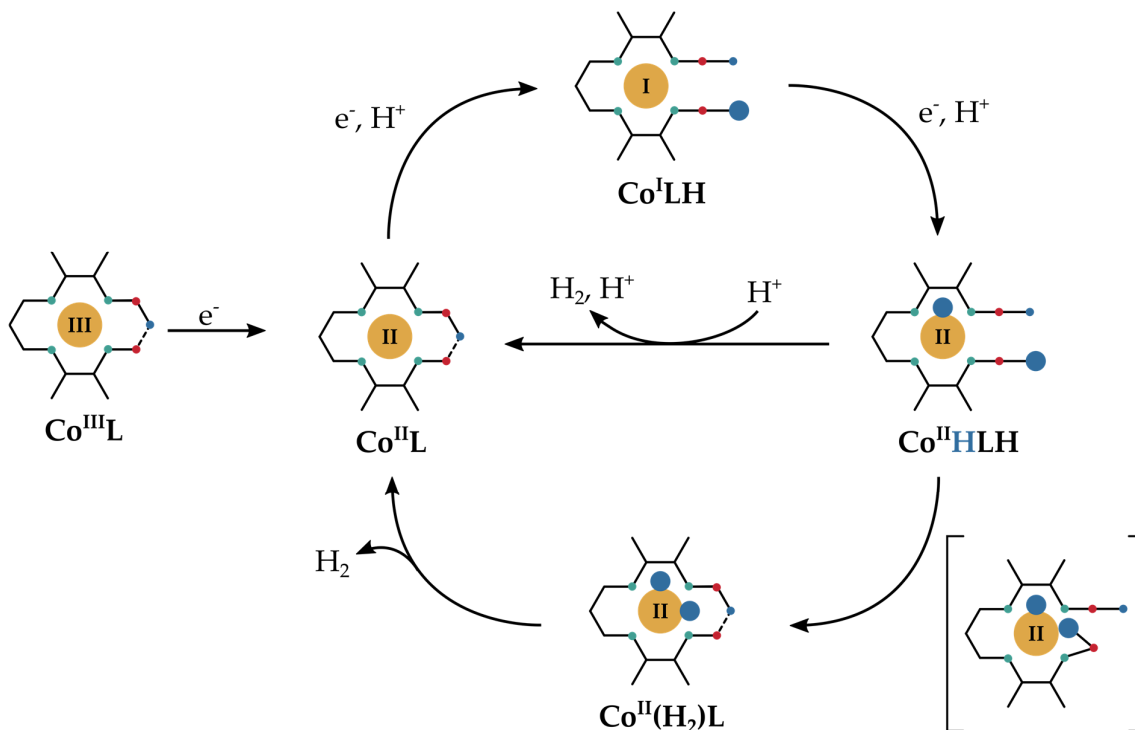


Figure 2.4: General catalytic mechanism for hydrogen evolution by cobalt diimine dioxime complexes starting from the Co<sup>III</sup>L pre-catalyst on the left side. The structure in brackets is the transition state for the intramolecular elimination of molecular hydrogen, in which a proton bound to an oxime oxygen atom comes near the Co center.

Despite the increased stability achieved with the tetradentate ligand, cobalt diimine dioximes still suffer from decomposition in aqueous reductive conditions, creating a particulate state that is also active for proton reduction.<sup>82</sup> Therefore, research should focus on more robust catalysts for hydrogen evolution. One such class are cobalt complexes using polypyridyl and aminopyridyl ligands which have been reported to be active in fully aqueous conditions.<sup>56</sup> In particular, the complex [Co<sup>III</sup>(CR)<sub>2</sub>]<sup>+</sup> (**Cat1**) (CR = 2,12-dimethyl-3,7,11,17-tetra-azabicyclo(11.3.1)-heptadeca- 1(17),2,11,13,15-pentaene, X = Cl, Br) based on a tetraaza-macrocyclic ligand has shown very good HER performance in homogeneous photocatalytic conditions.<sup>13–15,83</sup> It has achieved TON of > 1000 in homogeneous photocatalytic conditions, outperforming Co by a factor of 70.<sup>83</sup> This has been ascribed to its greater stability granted by the macrocyclic ligand which prevents hydrolysis and decomplexation. The catalytic cycle of this

catalyst has not been fully cleared up until now, partly due to the difficulty imposed by the non-redox-innocence of the ligand: While the Co<sup>III/II</sup> reduction clearly occurs on the metal centre, the formal Co<sup>II/I</sup> and Co<sup>I/0</sup> couples are partly or fully ligand-based reductions.<sup>84</sup> Electrocatalytic hydrogen evolution in aqueous solution was observed at potentials slightly negative of the Co<sup>II/I</sup> couple, suggesting the formal Co<sup>I</sup> state initiates catalysis.<sup>85</sup> In spite of its activity in homogeneous photocatalysis, hydrogen evolution with **Cat1** in DSPC has so far not been reported in the literature, and it has never been immobilized on electrodes.

### 2.2.3 Dye-catalyst assemblies

In an effort to improve upon the results obtained with co-grafted DSPC, PS have been coupled to catalysts to yield supramolecular dye-catalyst assemblies anchored on the SC film via anchoring groups on the PS unit (Figure 2.5), which could have several advantages. Firstly, the PS-catalyst distance can be precisely controlled by the choice of linker and is possibly much closer than in co-grafted systems where the distribution on the SC surface is random. Furthermore, in addition to the PS-catalyst distance, the choice of the linker group can also influence the ET kinetics in the assembly, possibly granting faster forward ET and slower CR. Slower CR can also be achieved by the fact that the catalyst is located farther away from the SC surface instead of directly anchored on it. Lastly, the surface coverage of active molecules could be increased since there is a single molecule grafted on the surface which contains both PS and catalyst, as opposed to co-grafted systems where both components occupy space on the SC surface.

In many of the assemblies, the catalyst is grafted to the PS via complexation of the PS as a ligand to the metal centre of the catalyst. This approach was used to create dyads with a Ru polypyridyl PS and a Pt or Pd catalyst, where one ligand is coordinated to both the Ru and the Pt/Pd metal centre (**Ru-Pd** and **Ru-Pt**).<sup>46</sup> In these assemblies, the excited electron relaxes to a state where it is localized on the extended ligand, from where it can more easily transfer to the catalytically active unit.<sup>86</sup>

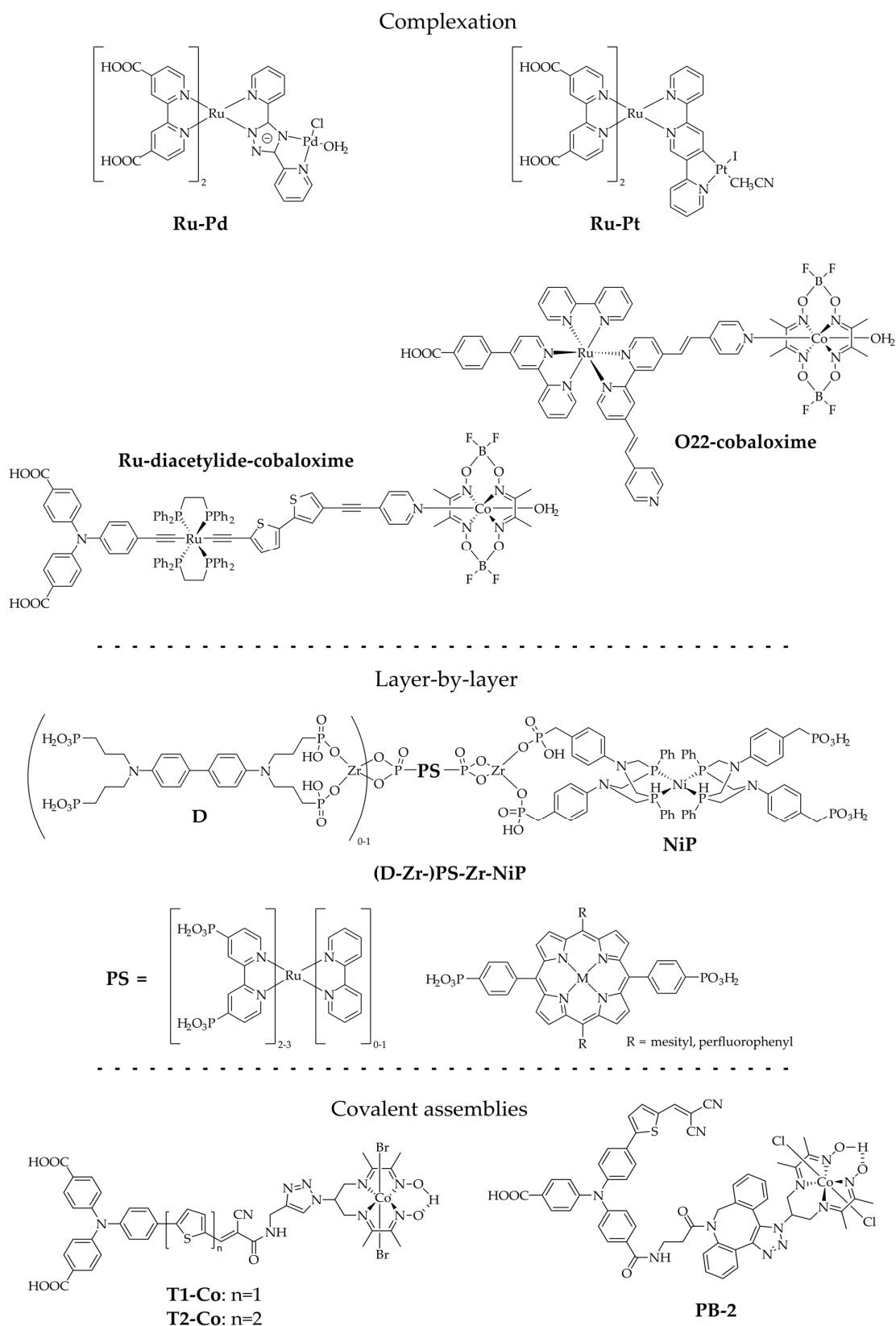


Figure 2.5: Dye-catalyst assemblies reported in the literature for proton reduction in DSPC.

Complexation was also popular for coupling cobaloxime HER catalysts to PS containing a pyridine group that displaced one of the axial ligands on the Co complex, as in the case of **O22-cobaloxime**<sup>80</sup> and **Ru-acetylide-cobaloxime**.<sup>79</sup> However, these assemblies suffer from stability issues since under operation, ligand exchange takes place that removes the catalyst from the PS unit.<sup>47</sup> To mitigate this, replacing the cobaloxime catalyst by the Co diimine-dioxime one opened up the possibility of covalent linkage at the alkyl chain, which was exploited to create dyads with organic push-pull dyads via triazole linkers created by click chemistry (**T1-Co**,<sup>26</sup> **T2-Co**<sup>87</sup> and **PB-2**<sup>77</sup>).

Finally, in a variation of the complexation approach, a layer-by-layer strategy was employed to construct dye-catalyst (**PS-Zr-NiP**)<sup>63,64</sup> and donor-dye-catalyst (**D-Zr-PS-Zr-NiP**)<sup>38</sup> assemblies (or monolayers) using Zr<sup>IV</sup>-phosphonate bridges to connect the different units. The catalyst of choice in these assemblies was **NiP**. This approach has the advantage of a very easy assembly by sequential immersion of the SC film into solutions of the different units.<sup>63</sup> In general, the assemblies created by complexation are much easier in terms of synthesis and offer high modularity for optimization of the systems, while covalent linkage typically yields a more stable assembly.

## 2.2.4 Semiconductors

SC films play an important role in the design of the photocathode as they provide the support of the PS and HER catalyst, are the immediate electron donor upon excitation of the PS and provide the contact to the external circuit. As such, there are demanding requirements placed on the SC material to ensure high activity of the overall DSPC.

A necessary requirement for a functional DSPC is the position of the VB potential of the SC material. It must be more negative than the reduction potential of the excited dye for HI to occur ( $\Delta G_{inj} < 0$ ). The precise match between the SC VB potential and the dye excited state reduction potential can be more easily fine-tuned by structural modifications on the dye. However, the reduction potential of the reduced dye must remain negative enough that ET to the catalyst is possible to drive proton reduction. SC materials for DSPC must also possess a high charge carrier mobility for injected charges to quickly move away from the surface and reach the back contact instead of recombining. Unfortunately, hole mobility in p-type SC is generally much slower than electron mobility in n-type SCs: in the case of NiO, the hole diffusion coefficient can be several orders of magnitude lower than the electron diffusion coefficient in TiO<sub>2</sub>.<sup>88-90</sup> This is caused by the localization of holes in oxygen 2p orbitals, which raises the energy

barrier that needs to be overcome for migration through the material.<sup>91-94</sup> The low hole mobility prevents injected holes from quickly moving away from the film surface, making it more likely for them to recombine. In the future, if very active molecular components are developed, the conductivity of p-type SC could become a hard limit for the achievable photocurrent. Furthermore, the SC surface must be reactive toward the anchoring groups of the molecular components of the DSPC. In metal oxides, typically surface OH groups react with either carboxylic acid or phosphonic acid groups to form the respective ester and thus covalently graft the molecules to the film surface.

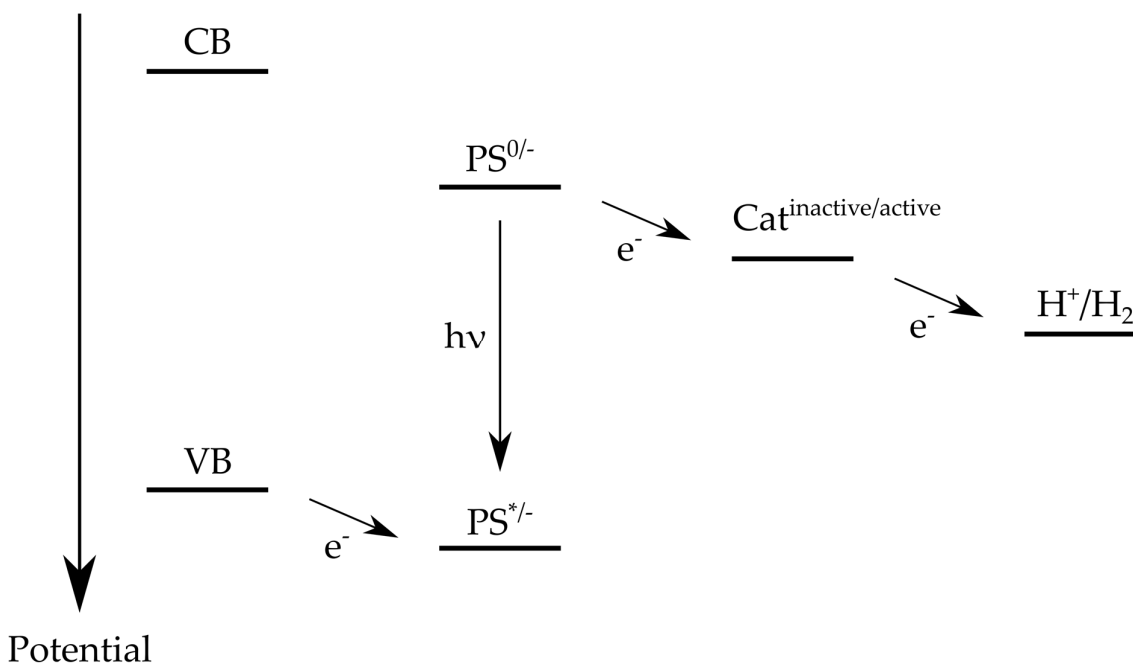


Figure 2.6: Schematic representation of energy levels in a DSPC for hydrogen evolution, including the VB and conduction band of the SC, the ground state and excited state redox potential for dye reduction, the redox potential of the catalyst to reduce it to its active state and the redox potential for proton reduction.

To increase the area of the electrode-electrolyte interface and the loading of the active molecular species and therefore increase the photocurrent flowing through the photocathode, the SC films must possess a large surface area. This is achieved by preparing porous films via a range of techniques: from sol-gel processes,<sup>95-97</sup> often using polymer-templated precursors,<sup>89,90,98-101</sup> in which the SC is formed in an annealing process directly on the conducting substrate, to the use of a suspension of preformed SC nanoparticles that is deposited on the substrate by spraying, screen printing or doctor-blading.<sup>102,103</sup> Especially polymer-templated films give high porosity due to the mesoporous structure. Other preparation techniques include chemical vapour

deposition,<sup>104</sup> electrodeposition<sup>105</sup> and hydrothermal synthesis.<sup>106</sup> However, a high porosity can also hinder charge transport to the back contact and facilitate undesired recombination of injected charges. For future commercial application, the cost and ease of large-scale fabrication is also an issue. Finally, the SC must be stable under operando conditions and be resistant to photocorrosion, because of which wide bandgap SC are chosen (NiO: 3.6-4.0 eV).<sup>22</sup> This also ensures high transparency in the visible region to optimize absorption by the PS.

The currently most widely used p-type SC material for DSPC is NiO due to its ease of fabrication, good thermal and chemical stability,<sup>22</sup> and good transparency in the visible region.<sup>95</sup> However, it also has several severe drawbacks that has prompted research into alternative materials, so far with mixed success: In addition to the low hole mobility already discussed, a severe issue is the abundance of trap states in the bandgap, mostly produced by defects on the film surface.<sup>107,108</sup> These trap states are the cause of very fast CR after HI, which severely limits the activity of the DSPC since most of the energy of absorbed photons is lost (see section 4.1.2 ). While this can be mitigated by applying a negative potential, the goal of DSPC research is bias-free water splitting, where the potential generated by the photoanode is likely not negative enough to fully fill the trap states with electrons, especially at non-equilibrium with high photocurrents.

Alternative SC materials that have been used in DSPC have been the delafossites CuCrO<sub>2</sub>,<sup>28,53</sup> and CuGaO<sub>2</sub>,<sup>6</sup> CuFe<sub>2</sub>O<sub>4</sub>,<sup>109</sup> LaFeO<sub>3</sub>,<sup>110</sup> and indium-doped tin oxide (ITO).<sup>38,64</sup> ITO is an attractive material due to its properties, however, indium is scarce and must be avoided for large-scale application.<sup>91</sup> CuGaO<sub>2</sub> showed higher photocurrent and more positive photocurrent onset potential.<sup>6</sup> CuCrO<sub>2</sub> also showed higher photocurrents than NiO.<sup>28,53</sup> CuFe<sub>2</sub>O<sub>4</sub> and LaFeO<sub>3</sub> both are small-bandgap SC that absorb visible light and drive proton reduction under irradiation when functionalized with a catalyst;<sup>111</sup> the photocurrent for both was also enhanced when additionally sensitized with a PS.<sup>109,110</sup> In spite of these efforts, so far no highly better p-type SC material than NiO has been developed.

## 2.3 Photocathode architecture and performance

DSPCs have been realized in essentially three different architectures of increasing complexity. While the PS is always grafted to the SC film surface to ensure fast HI, the catalyst is introduced in the system in different ways (Figure 2.7). It is either simply dissolved in the electrolyte solution, co-grafted on the SC film surface alongside the PS or attached to the PS in the supramolecular assemblies shown in section 2.2.3. The different architectures have advantages and disadvantages that will be presented, together with their photoelectrochemical performances.

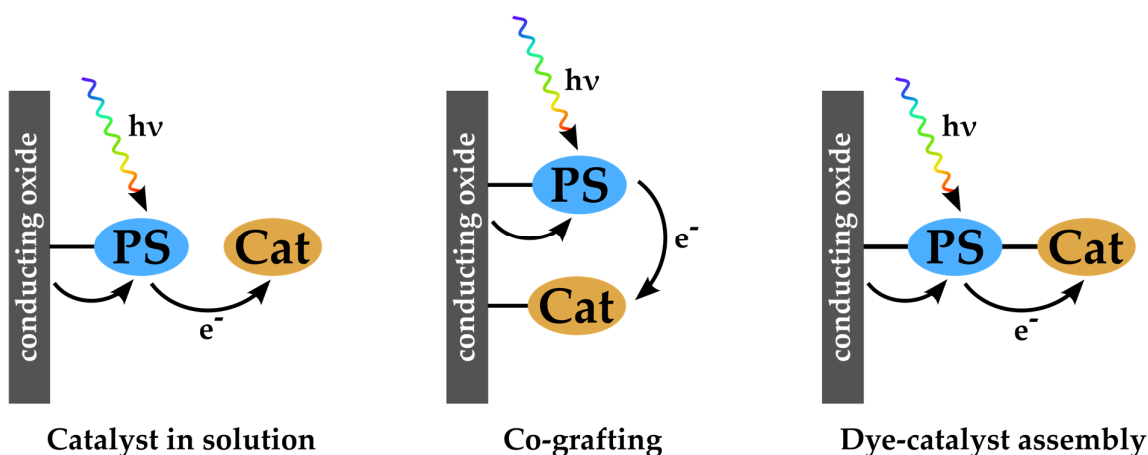


Figure 2.7: Different photocathode architectures used in DSPCs for proton reduction.

### 2.3.1 Catalysts in solution

The synthetically easiest way to prepare photocathodes for proton reduction is to simply dissolve the catalyst in the electrolyte solution, which is directly inspired by the working principle of p-DSSCs, in which the dissolved redox mediator oxidises the anchored, reduced PS. This approach avoids having to introduce anchoring groups on the catalyst and makes it possible to quickly screen several catalysts for optimal performance with a given dye-sensitized SC film.<sup>112</sup> Indeed, the simplicity of this approach caused it to be used in the first ever example of a DSPC for hydrogen evolution in 2012.<sup>50</sup> In this study, the organic dye P1 was anchored on NiO and a cobaloxime catalyst dissolved in solution, which under irradiation produced 320 nmol·cm<sup>-2</sup> H<sub>2</sub>.<sup>50</sup> However, in this approach the catalyst must diffuse to the SC surface for ET to occur from the reduced state of the dye to the catalyst. The downside of this approach is thus that ET is inherently diffusion limited, meaning that if the lifetime of



the reduced state of the dye is not sufficiently long-lived, the ET yield decreases. Furthermore, since proton reduction is a multi-electron process, singly-reduced (non-active) catalysts can diffuse away from the SC film surface before being reduced again, spending time in solution in this state, which can potentially lead to unwanted side reactions. In spite of this, the “catalyst in solution” approach has been successfully used showing high photocurrents with good production of hydrogen (up to 1150 nmol H<sub>2</sub>·cm<sup>-2</sup>),<sup>52</sup> where the system using NiP<sup>52</sup> outperformed cobaloximes (Table 2.1).<sup>50-52</sup> Due to the high amount of catalyst necessary in solution, TON per catalyst are small (< 2) for all systems built with this approach.

### 2.3.2 Co-grafting

In order to eliminate the need for catalyst diffusion and to increase spatial proximity between the PS and the catalyst, researchers started to co-graft the catalyst on the film surface together with the PS. This was hoped to accelerate ET to the catalyst to therefore achieve higher photocurrents and hydrogen production. However, it is necessary to functionalize the catalysts with anchoring groups: NiP, for example, was functionalized with phosphonate groups, while cobaloximes were coordinated to pyridines anchored via phosphonic acid<sup>8</sup> or carboxylic acid groups.<sup>6,7</sup> Furthermore, the grafting of catalyst on the surface necessarily reduces the maximum amount of PS that can be grafted on the film surface, and degraded catalysts cannot be replaced by intact ones from the solution. Co-grafting the catalyst also does not allow precise control of the PS-catalyst distance, as their distribution on the film surface is random.

For this approach, NiP<sup>28,53</sup> and cobaloximes<sup>6-8,87</sup> remained the most popular catalysts and a system using NiP and DPP-P on CuCrO<sub>2</sub> showed the highest performance with 376 nmol H<sub>2</sub>·cm<sup>-2</sup> and a TON of 126 (Table 2.1).<sup>28</sup> In general, total amounts of hydrogen produced with this approach were lower compared to dissolving the catalyst in solution, but TON were higher due to the much lower amount of catalyst used, ranging from 3 to 126, where reported.<sup>6,28,53,54</sup>

### 2.3.3 Dye-catalyst assemblies

In order to precisely control the PS-catalyst distance and to achieve fast ET, PS have been coupled to catalysts to yield supramolecular dye-catalyst assemblies either by complexation or by covalent linkage, as described in section 2.2.3. The increased control over the final system comes at the cost of much higher synthetic difficulty in the preparation of these assemblies. In terms of performance, these systems so far are

comparable to the co-grafted systems: the best-performing system **RuP<sub>2</sub>-Zr-NiP** achieved 700 nmol H<sub>2</sub>·cm<sup>-2</sup> and TON of 20,<sup>64</sup> while especially those systems based on organic sensitizers with cobalt catalysts showed very little activity (TON < 1, Table 2.1).<sup>26,77,87</sup> In terms of amount of hydrogen produced, the layer-by-layer strategy with **Ru(bpy)<sub>3</sub>** and **NiP** yielded the best results;<sup>38,64</sup> however, these were achieved in ITO as opposed to the usually used NiO which might influence the performance. In fact, the **RuP<sub>3</sub>-Zr-NiP** system anchored on NiO performed poorly.<sup>63</sup> TON-wise, **Ru-Pd** and **Ru-Pt** performed best,<sup>46</sup> but these consist of two rare metal centers that would economically be unviable in large-scale application. In summary, none of the photocathode architectures published thus far clearly outperforms the others. Therefore, they are all still viable routes of investigation. In theory, supramolecular assemblies have the highest promise since the final architecture can be precisely controlled; however, it is not clear if the possibly thus gained increase in activity makes up for the increased difficulty in their preparation. In commercial systems, this would depend on the cost of synthesis compared to the amount of hydrogen produced and other factors that involve costs, such as the area needed for the mounted systems. In addition, the wide parameter space in terms of pH, SC material, applied potential etc. makes it very difficult to compare the results achieved by different systems and identify critical parameters.

Table 2.1: Key figures of DSPCs for proton reduction published in the literature.

Architecture	Photosensitizer	Catalyst	pH	Electrode material	Applied potential / V	Current density / $\mu\text{A cm}^{-2}$	Time / h	H <sub>2</sub> / nmol (H <sub>2</sub> / nmol cm <sup>-2</sup> )	F.E. / %	TON <sub>Cat</sub>	Reference	
Catalyst solution	<b>D-<math>\pi</math>-A (P1)</b>	Cobaloxime	7	NiO	-0.4 vs. Ag/AgCl + 0.21 vs. RHE	-10	0.1	322 (322 <sup>a</sup> )	n.r.	2	L. Sun et al. 2012 <sup>50</sup>	
	<b>Ru(bpy)<sub>3</sub></b>	Cobaloxime	0.1 M [Bu <sub>4</sub> N]ClO <sub>4</sub> in ACN		-0.45 V vs. Ag/AgNO <sub>3</sub> -0.15 vs. SCE	1.3		n.r.	n.r.	n.r.	M-N. Collomb et al 2015 <sup>112</sup>	
		<b>Cat1</b>				1.2						
		<b>[Rh(dmbpy)<sub>2</sub>Cl<sub>2</sub>]<sup>+</sup></b>				32						
			<b>[Rh(dtBubpy)<sub>2</sub>Cl<sub>2</sub>]<sup>+</sup></b>				80					
	<b>D-<math>\pi</math>-A (BH4)</b>	<b>Mo<sub>3</sub>S<sub>4</sub></b>		0	NiO	0 (NHE)	183 ± 36	16.6	n.r.	49 ± 11	n.r.	Y. Wu et al. 2016 <sup>24</sup>
	<b>PMI</b>	Cobaloxime		1	NiO	-0.4 vs. Ag/AgCl	-225	2	124 <sup>a</sup> (326)	60 ± 10	<1 <sup>1</sup>	M. Wasielewski et al. 2017 <sup>52</sup>
<b>PMI</b>	<b>NiP</b>		1	NiO	-0.4 vs. Ag/AgCl	-140	2	437 <sup>a</sup> (1150)	98 ± 4	1.5		

	<b>D-<math>\pi</math>-A (T1)</b>	Cobaloxime	4.5	NiO	-0.4 vs. Ag/AgCl + 0.05 vs. RHE	-6	6	40 (12)	3	<1 <sup>1</sup>	M. Chavarot-Kerlidou et al. 2019 <sup>51</sup>
Co-grafting	<b>Ru(bpy)<sub>3</sub></b>	cobaloxime	7	NiO	-0.4 vs. Ag/AgCl +0.2 vs. RHE	-13		n.r.	n.r.	n.r.	L. Sun et al. 2014 <sup>7</sup>
	<b>D-<math>\pi</math>-A (P1)</b>	cobaloxime	7	NiO	-0.2 vs. Ag/AgCl +0.41 vs. RHE	-35	1.5	290 (290 <sup>a</sup> )	68	n.r.	L. Sun et al. 2015 <sup>8</sup>
	<b>C343</b>	<b>[Fe-Fe]</b>	4.5	NiO	-0.3 vs. Ag/AgCl +0.17 vs. RHE	< -10	0.3	12.4 (12.4 <sup>1</sup> )	50	$\leq 3$	L.Hammarström et al. 2016 <sup>54</sup>
	<b>D-<math>\pi</math>-A (RBG-174)</b>	<b>Co</b>	5.5	NiO	-0.4 vs. Ag/AgCl +0.14 vs. RHE	-8	2	n.r.	9.3 $\pm$ 1.5	n.r.	V. Artero et al. 2018 <sup>27</sup>
	<b>DPP-P</b>	<b>NiP</b>	3	CuCrO <sub>2</sub>	0 (RHE)	-15.1	2	94 $\pm$ 10 (376 $\pm$ 40) <sup>1</sup>	34 $\pm$ 8	126 $\pm$ 13	E. Reisner et al. 2018 <sup>28</sup>
				NiO	0 vs. RHE	-5.8	2	35 $\pm$ 2	31 $\pm$ 8	n.r.	
	<b>D-<math>\pi</math>-A (RBG-174)</b>	cobaloxime	7	CuGaO <sub>2</sub>	0.41 (RHE)	-45	2	555	74	82	V. Artero et al. 2019 <sup>6</sup>

			7	NiO	0.14 (RHE)	-12	2	540 ± 80	80 ± 8	14 (after 1 h)	
			5.5	NiO	-0.4 vs. Ag/AgCl 0.14 vs RHE	-12	2	300	70	n.r.	
	<b>PMI (PMI-P)</b>	<b>NiP</b>	3	IO-CuCrO <sub>2</sub>	0 vs. RHE	-25	2	54 ± 3 (215 ± 10)	41 ± 8	48 ± 2	E. Reisner et al. 2019 <sup>53</sup>
	<b>DPP-P</b>	<b>NiP</b>	3	IO-CuCrO <sub>2</sub>	0 vs. RHE	-18	2	40 ± 6 (160 ± 24)	40 ± 14	36 ± 5	
Supramolecular assembly	<b>O22-cobaloxime</b>		7	NiO	-0.2 vs. NHE + 0.2 vs. RHE	-15	2.5	290 (290 <sup>a</sup> )	45	n.r.	Y. Wu et al. 2013 <sup>80</sup>
	<b>T1-Co</b>		5.5	NiO	-0.4 vs. Ag/AgCl + 0.14 vs. RHE	-15	2	37 ± 6 (26 ± 10)	9 ± 1	<1 <sup>a</sup>	V.Artero et al. 2016 <sup>26</sup>
	<b>T2-Co</b>		5.5	NiO	-0.4 vs. Ag/AgCl + 0.14 vs. RHE	-11	2	16 ± 5	13 ± 1	n.r.	V.Artero et al. 2018 <sup>87</sup>
	<b>PB-2</b>		4.8	NiO	0 vs. Ag/AgCl + 0.48 vs. RHE	-10	0.3	2.5	n.r.	0.05	H. Tian et al. 2017 <sup>77</sup>
	<b>Ru-Pt</b>		3	NiO	-0.2 vs. Ag/AgCl	-33 ± 7	1	198 (250)	59	47	E. A. Gibson et al. 2019 <sup>46</sup>

					+0.18 vs. RHE						
	<b>Ru-Pd</b>		3	NiO	-0.2 vs. Ag/AgCl +0.18 vs. RHE	-36 ± 2	1	324 (410)	89	46	
	<b>Ru-acetylide-cobaloxime</b>		4.5	NiO	-0.4 vs. Ag/AgCl +0.07 vs. RHE	-3.2	4.5	109 (33 <sup>a</sup> )	27	2.5	C. Olivier et al. 2019 <sup>79</sup>
	<b>PS-Zr-NiP (RuP3-Zr-NiP)</b>		3	NiO	+0.3 vs. RHE	-7	2	6 ± 1	9 ± 2	≈1 <sup>a</sup>	E. Reisner et al. 2016 <sup>63</sup>
	<b>D-Zr-PS-Zr-NiP (Dianiline-Zr-RuP<sub>2</sub>-Zr-NiP)</b>		5.1	io-ITO	-0.25 vs. NHE	-56	4	>1000	53 ± 5	>15 <sup>a</sup>	T. J. Meyer et al. 2016 <sup>38</sup>
	<b>PS-Zr-NiP (RuP<sub>2</sub>-Zr-NiP)</b>		5	Doped NiO/ioITO	-0,25 NHE	-40	2	700 ± 80 (700 ± 80) <sup>a</sup>	86 ± 3	20 <sup>a</sup>	T. J. Meyer et al. 2017 <sup>64</sup>

## 2.4 Stability issues

During operation, most DSPCs reported so far lose their activity over the course of minutes to hours. This can be traced to several processes caused by the operando conditions, including the aqueous electrolyte at usually acidic pH, the applied reductive potential and the irradiation with visible light.

The issue most often described is desorption of grafted molecules from the SC film surface.<sup>27–29</sup> This is a consequence of the hydrolysis of the anchoring groups, which are usually surface carboxylic or phosphonic esters formed between the respective acid on the PS/catalyst and OH groups on the film surface. In operation, the aqueous electrolyte solution can hydrolyse the esters and thus cause leaching of the formerly grafted molecules into the solution. To eliminate this degradation channel, the use of different anchoring groups that are more resistant to hydrolysis such as silatrane and siloxane groups have been proposed.<sup>3,34</sup> The pH of the electrolyte solution must also be taken into account, as different esters are most stable at different pH values. However, so far no anchoring group has been discovered that withstands the acidic pH required for high catalytic turnover frequencies and thus for high currents. A promising approach are the use of protecting layers that cover the anchoring groups. One type are thin metal oxide layers that are deposited after sensitization, typically prepared by atomic layer deposition since it is a low-temperature technique that does not destroy the grafted molecules.<sup>3</sup> The metal oxide used for this so far has been Al<sub>2</sub>O<sub>3</sub>, however, in the only study on DSPC photocathodes it was used in, it did not lead to an obvious improvement in stability of the systems.<sup>52</sup> A different approach was used by Wu et al., who functionalized their organic push-pull PS (**BH4**) with long alkyl chains on the bridge to form a hydrophobic protection layer which blocked the aqueous electrolyte from reaching the anchoring groups and thus prevented hydrolysis. This strategy had remarkable success, as their photocathode showed stable photocurrents for 16 hours in acidic electrolyte.<sup>24</sup> This enabled them to even use a pH 0 electrolyte, which gave ≈6 times higher photocurrents than using pH 5, which is in a range more typically used in DSPC.

The second issue is the degradation or modification of the molecular components during operation. The photoreductive conditions during photoelectrochemical experiments can lead to damage to the molecular structures such as bond cleavage. This issue has been somewhat overlooked so far and has only been studied in detail for one photocathode using a PDI PS and a cobalt diimine dioxime catalyst.<sup>27</sup> Related to this is pure photodamage, for example structural rearrangements such as

isomerizations at double bonds.<sup>113</sup> Typically, the PS used in DSPC come from the more mature field of DSSC, but photodegradation is expected to be more severe in DSPC than in DSSC as the catalysis is much slower than the one-ET to the electrolyte taking place in DSSC, which leads to an accumulation of negative charges on the film surface. This accumulation can lead to faster damage to photoactive systems.<sup>114</sup> To eliminate this issue, molecular structures must be devised that are stable under photoreductive conditions, and especially stable in their reduced state. To protect the PS, fast ET to the catalyst is desired to reduce the time the PS spends in its reduced state. So far, there have not been any efforts directed especially at making more stable PS for DSPC. A stability issue that concerns the catalysts used in DSPC is their hydrolysis and demetallation. For example, cobaloximes are very stable in electrocatalysis in organic media, but have been found to quickly hydrolyse and demetalate in aqueous conditions.<sup>17</sup> This might partially be caused by the absorbance of visible light most catalysts show and which can lead to undesired side reactions, especially in lower oxidation states. A solution to this issue is to use macrocyclic, chelating ligands that do not decoordinate as easily, making the catalyst more resistant to hydrolysis. Alternatively, polypyridinic Co complexes, in which low oxidation states are better stabilized, can be used.<sup>115</sup> If possible, the catalyst itself should also show low absorbance of visible light.

In summary, there are several stability issues plaguing DSPC and that prevent their long-term activity. However, so far little effort has been undertaken to study the degradation processes in detail, which could be achieved using a variety of in- and post-operando spectroscopic techniques. This information could then be used to rationally design more stable systems.

## 2.5 Kinetic issues

As sunlight is the energy source used for water splitting in DSPEC, light-induced processes and their kinetics are an essential part of DSPEC research. Figure 2.8 shows the light-induced processes that take place in a photocathode upon excitation with light. Initially, a photon is absorbed by the PS to raise it to the excited state. From there, the excited dye can inject a hole into the VB of the SC ( $k_{\text{HI,red}}$ ) to yield the primary CSS, with the negative charge localized on the PS. From this state, thermally activated ET can then occur to the catalyst ( $k_{\text{ET,red}}$ ) to yield the secondary CSS. The hole injected into the SC can diffuse away from the film surface to eventually end up at the back contact ( $k_{\text{diff}}$ ). Since the excited state is quenched by an ET to the excited PS, this pathway occurs via reductive quenching. There is also the possibility of an oxidative quenching



pathway, in which the excited state is quenched by ET from the PS to the catalyst ( $k_{\text{ET,ox}}$ ) to give the primary CSS with an electron on the catalyst and a hole on the PS. The oxidised PS is then regenerated by HI into the SC ( $k_{\text{HI,ox}}$ ) to end up in the same secondary CSS as in the reductive quenching pathway.

In parallel to these desired “forward” processes, detrimental processes occur in which the excitation energy is lost. In general, these processes become a problem if the forward process from the respective state is not significantly faster than the detrimental process. First, the excited PS can return to the ground state before charge separation can occur ( $k_{\text{D}}$ ). This is only an issue if the PS has a very short excited state lifetime on the picosecond to a few nanosecond timescale while HI or ET is slow. The more important issue is CR from the several CSS involved in the light-induced processes ( $k_{\text{rec}}$ ) since CR often occurs on timescales that are similar or faster than the forward reactions. This especially affects DSPEC since the targeted redox reactions are multi-electron processes and the CSS therefore must be long-lived enough to enable multiple successive charge transfers.

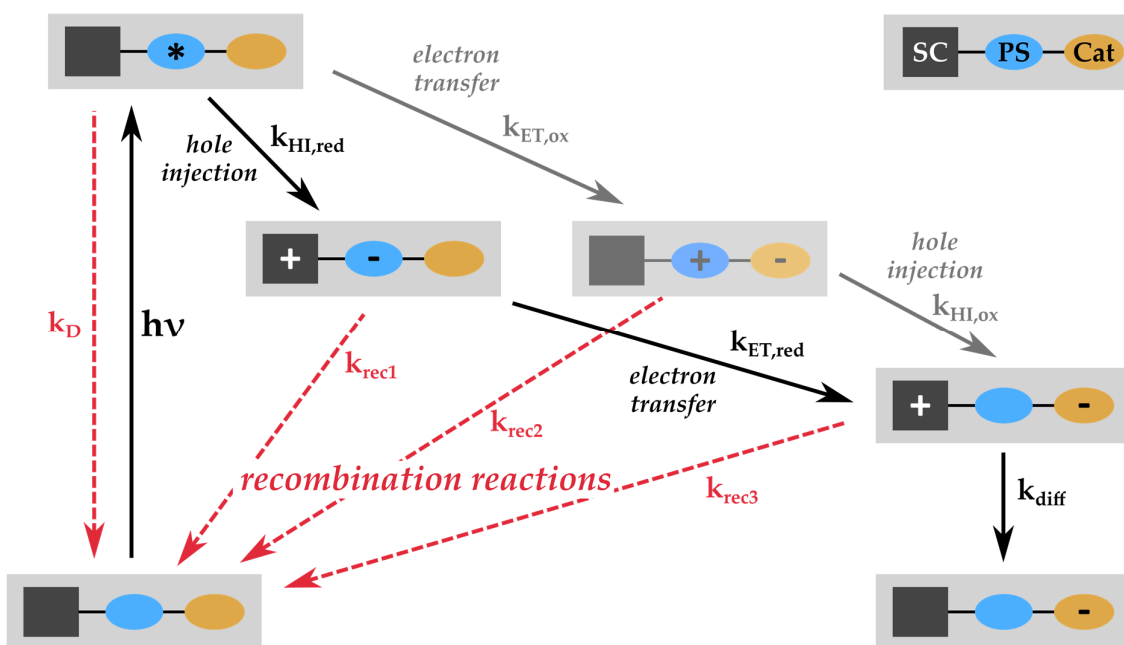


Figure 2.8: Schematic representation of the light-induced processes in DSPEC photocathodes, here shown with a dye-catalyst supramolecular assembly.

The study of the intramolecular and interfacial processes and their kinetics is therefore of utmost importance in DSPEC research. Ideally, this should be done under operando conditions since the light-induced processes could depend on the surrounding electrolyte solution and especially the applied potential. To perform these measurements, in this thesis the relatively new technique of TA-SEC, i.e. TA spectroscopy at an applied potential, was used to study NiO films sensitized with dye-catalyst assemblies. To this end, a dedicated spectroelectrochemical cell was designed and built. Complementary to these experiments, traditional TA spectroscopy was also measured of the molecular dyads in solution.



## 3 Spectroscopy in solution

*Parts of this chapter have been published in the following articles:*

**Publication 1** - Bold, S., Zedler, L., Zhang, Y., Massin, J., Artero, V., Chavarot-Kerlidou, M., & Dietzek, B. Electron transfer in a covalent dye–cobalt catalyst assembly – a transient absorption spectroelectrochemistry perspective. *Chemical Communications*, **2018**, 54(75), 10594–10597.

**Publication 2** – Bold, S., Straistari, T., Muñoz-García, A. B., Pavone, M., Artero, V., Chavarot-Kerlidou, M., & Dietzek, B. Investigating Light-Induced Processes in Covalent Dye-Catalyst Assemblies for Hydrogen Production. *Catalysts*, **2020**, 10(11), 1340.

The easiest way to study the excited state behaviour of a given compound is in solution, and this is usually the starting point for every investigation. In this chapter, characterization of the photophysical properties of a series of organic push-pull dyes and dye-catalyst assemblies in solution will be discussed. The synthesis of the compounds was performed by Quentin Vacher, Julien Massin and Emmanouil Giannoudis. Since in DSPEC, absorption of a photon by the PS is the first step in a cascade of processes that ultimately ends with catalysis, it is of paramount importance to investigate the excited state processes taking place in a dye or dye-catalyst assembly. In particular, ET processes are fundamental, which is why a study of their kinetics and the detection of the formed states is critical. Measurements in solution provide the easiest and fastest way to study these processes.

Section 3.2 deals with the excited state photophysics of a series of push-pull dyes in solution. In section 3.3, the dye-catalyst dyads based on those dyes are investigated. The focus will be on the deactivation processes from the thermalized singlet excited state, including internal conversion, intersystem crossing (ISC), energy transfer and ET.

### 3.1.1 Spectroscopic techniques

To gain a full understanding of the performance of DSPEC systems, it is indispensable to study the light-induced processes taking place, if possible at operando conditions. To achieve this, a variety of spectroscopic techniques are available, from basic steady-state such as absorption and emission spectroscopy to more advanced time-resolved

techniques. The technique that will be crucial in this thesis is TA spectroscopy, a pump-probe technique that yields time-resolved spectral information. This allows to identify the transient species involved in the light-induced processes as well as the kinetics of the processes that lead to their formation and decay. In TA spectroscopy, a laser pump pulse excites the sample and after a time delay, a probe pulse is used to measure the absorbance of the sample (Figure 3.1). By varying the pump-probe delay, the temporal evolution of the spectral response and therefore of the excited state can be recorded. The pump pulse is usually intense, spectrally narrow and tuned to a defined wavelength to excite a selected transition in the sample. The probe pulse is typically weak and, if possible, spectrally broad to enable studying a wide spectral window. The spectra that are measured are differential spectra where the reference absorbance without excitation is subtracted from the absorbance at time  $t$  after excitation.

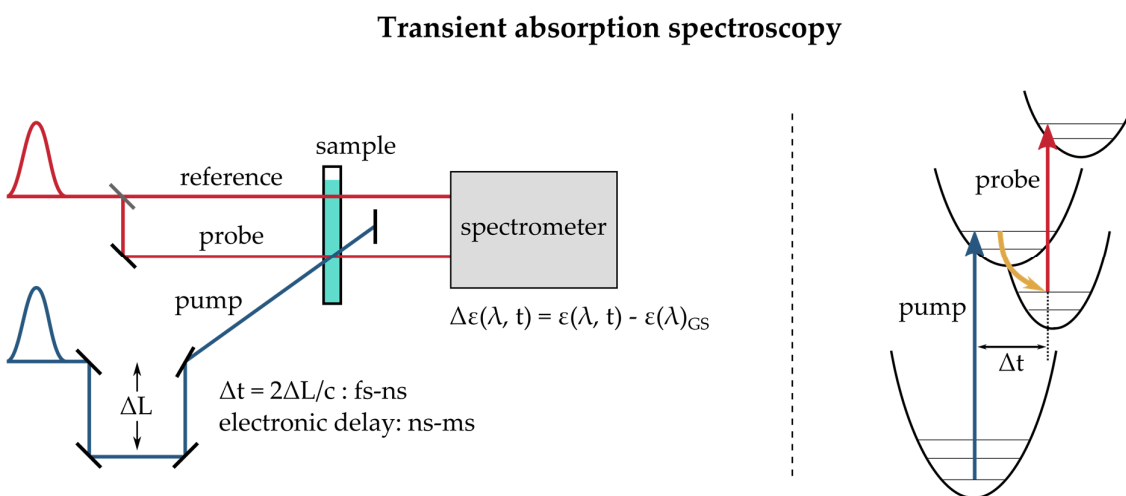


Figure 3.1: Left: Schematic depiction of a TA experiment. The sample is excited by the pump pulse and its absorbance is measured by the probe pulse after the time delay  $\Delta t$ . Differential spectra are obtained by subtracting the absorption spectrum in the ground state from the absorption spectrum at  $\Delta t$ . The time delay is produced by a mechanical delay stage for ultrafast measurements ( $< 10$  ns) and by an electronic delay for longer timescales (ns-ms). Right: Schematic depiction of the processes taking place in a TA experiment.

A complementary technique are time-resolved emission measurements using a streak camera or time-correlated single photon counting. These techniques allow to measure the temporal, and in the case of the streak camera spectral, evolution of emission after excitation by a pump pulse. This technique can be used to substantiate results from TA measurements and yield information on the contributions from emissive states.

## 3.2 Photophysics of push-pull organic dyes

### 3.2.1.1 Organic push-pull (D- $\pi$ -A) dyes in the literature

Due to the large number of published D- $\pi$ -A compounds, I will focus on those based on a triphenylamine (TPA) donor and a cyanovinyl-based acceptor group (Figure 3.2), to which the organic dyes studied in this thesis belong. In general, these dyes show two main absorption bands: one band in the UV caused by a transition localized on the TPA moiety and an intramolecular charge transfer (ICT) band in the visible part of the spectrum ( $\epsilon = 29,000$  to  $58,000 \text{ M}^{-1}\text{cm}^{-1}$ ).<sup>25,116–121</sup> Upon excitation of the latter, electron density is shifted from the TPA part, where the HOMO is localized, to the cyanovinyl acceptor part, where the LUMO is localized. The absorption, but especially the emission from the ICT state shows a strong solvatochromic effect due to the stabilization of the charge-transfer state in polar solvents.<sup>116,122,123</sup> While the excited state lifetimes observed are in the range of 450 ps to 3.4 ns in non-polar solvents (hexane, toluene and tetrahydrofuran),<sup>116,120,123–125</sup> in polar solvents such as acetonitrile (ACN) they are much lower, in the range of 3 ps to 1.2 ns.<sup>25,116,117,119,124</sup>

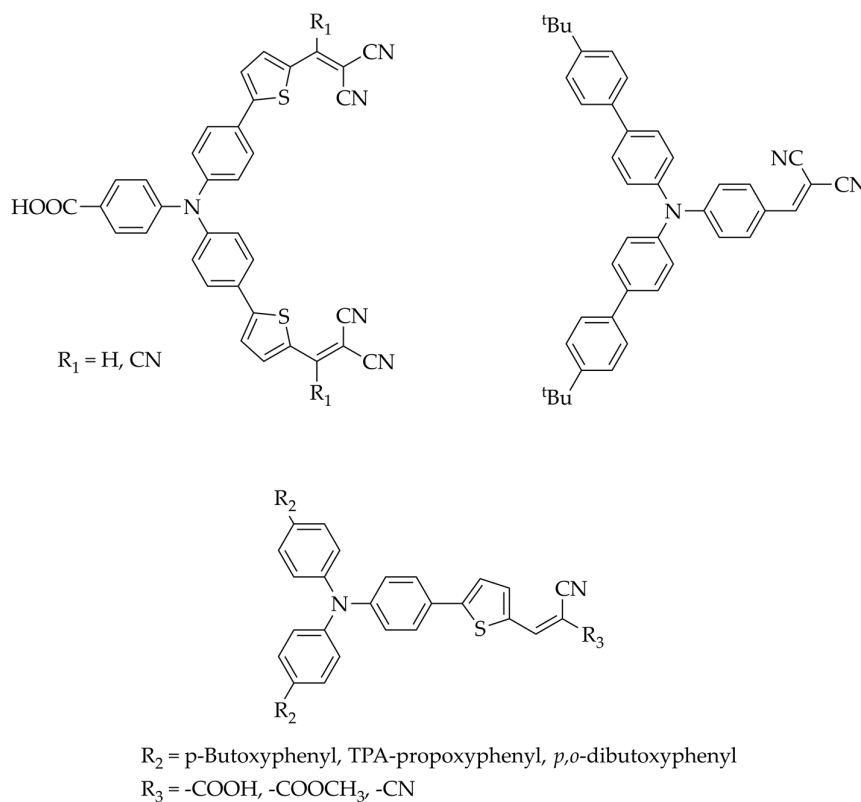


Figure 3.2: Chemical structures of organic push-pull dyes, containing TPA donor and cyanovinyl-based acceptor units, investigated by TA spectroscopy in the literature.

The general excited-state processes published in literature are a cascade of relaxation processes, including solvent rearrangement and molecular motions such as flattening, that lead from the initially excited Franck-Condon state to a thermalized ICT state (sometimes called the  $S_1$ ), from which return to the ground state occurs.<sup>116,117,119,122,123</sup> These results are at first sight not promising for photocatalytic applications due to the short excited state lifetime in polar solvents, which creates the need for fast excited state quenching processes in the final assembly.

### 3.2.1.2 Organic push-pull (D- $\pi$ -A) dyes in this thesis

The organic dyes investigated in this thesis are push-pull organic dyes consisting of a TPA donor and a cyanoacrylate acceptor part (Figure 3.3), connected by a bridge varying in length and rigidity from a single thiophene (**T1**) over a dithiophene (**T2**) to the rigid cyclopentadithiophene (CPDT, **T2R**). In **T2R**, the linker additionally possesses alkyl chains that were introduced with the intent of reducing dye aggregation on the sensitized film surface and of creating a hydrophobic blocking layer that protects the anchoring groups from hydrolysis under operando conditions.<sup>24</sup> Furthermore, the acceptor group can be prepared as a cyanoacrylamide group with an alkyne group to further attach the catalyst via copper-catalyzed azide-alkyne cycloaddition. In addition, upon excitation, these push-pull dyes should exhibit ICT that localizes the hole (the HOMO) on the TPA, close to the anchoring groups, to accelerate HI and the electron (the LUMO) on the cyanoacrylate group close to the catalyst for fast ET to the latter.

In terms of their photophysics, the three dyes show very similar behaviour. In UV-Vis absorption spectra (Figure 3.3), they all show two main bands: localized at 355 nm, the  $\pi$ - $\pi^*$  transition localized on the TPA, and whose position and intensity are independent of the linker. At longer wavelengths, there is a band produced by the ICT from the TPA donor to the cyanoacrylate acceptor group, which is the HOMO-LUMO transition. The spectral position and intensity of this band depends on the linker, experiencing a bathochromic and hypochromic shift upon changing the single thiophene linker in **T1** for bithiophene linkers, with the effect much more pronounced for the rigid CPDT linker in **T2R**. The bathochromic shift is a result of a smaller HOMO-LUMO gap, suggesting that the linker takes part in one or both of the two frontier orbitals. DFT calculations in literature performed on an analogue of **T2R** show that it is indeed the HOMO which is more strongly localized on the bridge than in an analogue of **T1**.<sup>126</sup>

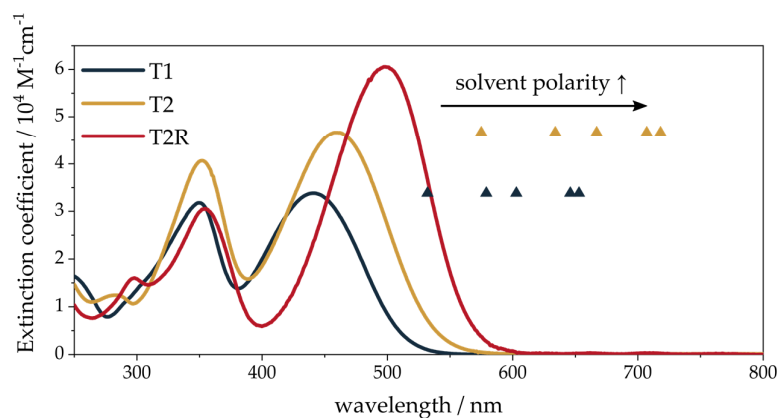
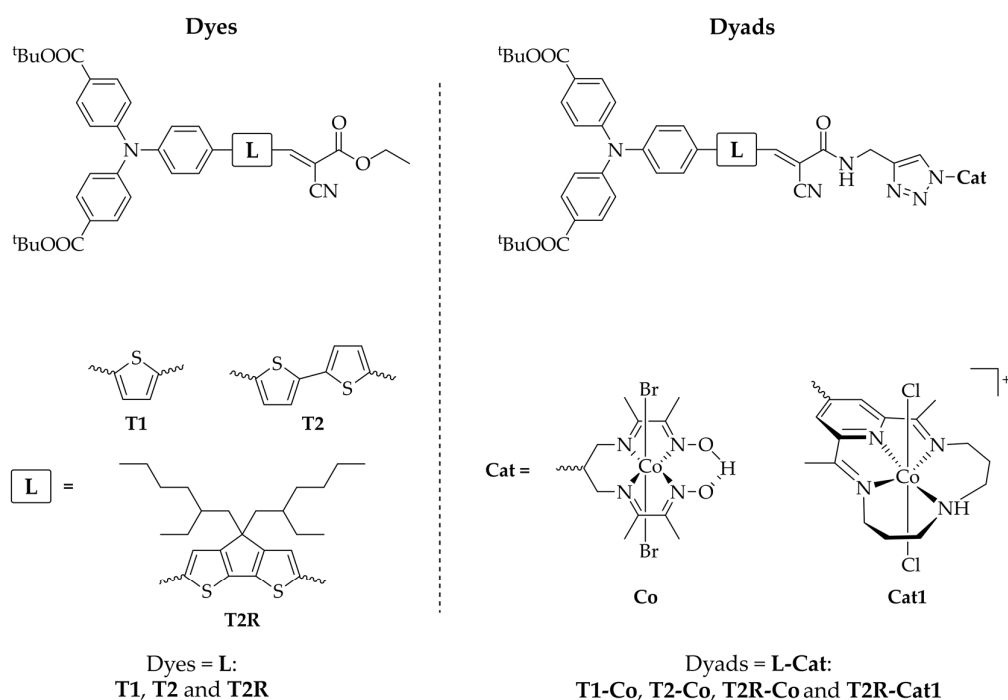


Figure 3.3: Compounds whose photophysics were studied in solution and their UV-Vis absorption spectra (solid lines) and emission maxima (triangles) in various solvents of increasing polarity (Toluene < Chloroform < Dichloromethane < Dimethylformamide < ACN).

This is further corroborated by electrochemical measurements, which show a strong negative shift of the redox potential of the dye oxidation upon introducing the CPDT linker (ca. 230 mV negative shift for **T2R** compared to **T1**) while the dye reduction potential is much less affected by this change (ca. 50 mV negative shift). Since the dye oxidation is equivalent to removal of an electron from the HOMO and dye reduction to the addition of an electron to the LUMO, these measurements also suggest that the principal change is in the HOMO position which is raised by the electron-rich CPDT linker. This leads to more negative oxidation potentials and a smaller HOMO-LUMO gap. The **T2** dye represents an intermediate case.<sup>127</sup>



All dyes fluoresce with quantum yields of  $\Phi = 0.2-0.25$  in ACN. The emission shows a solvatochromic behaviour (Figure 3.3), caused by a stabilization of the excited CSS in polar solvents which leads to a bathochromic shift in emission. The CSS has been proposed to lead to a twisted geometry with increased charge separation and localization which enhances the solvatochromic effect.<sup>116</sup> While the absolute values of the Stokes shift itself are slightly higher in the **T2** systems in all solvent polarities, the dependence on solvent polarity is, within the experimental error, identical.

The similarity in photophysical behaviour of the organic push-pull dyes also holds true in the fs-TA experiments. The light-induced processes in the dyes can be separated into two major parts (Figure 3.4): first, a relaxation to the thermalized singlet excited ICT state and then a decay to the ground state from this state. In general, the TA spectra of the dyes in polar solvents such as ACN and DMF show three major bands: a ground state bleach (GSB) at the position of the ground-state absorption band, a broad excited state absorption (ESA) at longer wavelengths and a stimulated emission (SE) band at the position of the fluorescence band. For the dyes containing longer linkers, these bands are all red-shifted in comparison to **T1**. Furthermore, the broad ESA band overlaps with the other bands, which leads especially to a further red-shift of the apparent SE band. In the first few ps, all dyes show a relaxation of the initially excited state to the thermalized  $S_1$  state, reflected by a concomitant hypsochromic shift of ESA and bathochromic shift of SE. This relaxation process is attributed to a mixture of solvent rearrangement around the dipole formed in the ICT state and molecular motions such as rotation and flattening, as previously observed in the literature.<sup>116,117,119,122,123</sup> While the spectral response to this process is identical, the kinetics vary between dyes and especially depending on the solvent. In ACN, these relaxation processes are very fast, occurring within the first few ps. **T1** and **T2** show a biphasic process with time constants of  $t_1 = 0.2$  ps and  $t_2 = 0.9$  ps (**T1**), 1.7 ps (**T2**), while **T2R** shows a monophasic process with  $t_1 = 1$  ps. The higher time constant for the slow process in **T2** might be due to the involvement of a rotation around the bond connecting the two thiophenes in this cooling process, a motion only possible in **T2**. The influence of the solvent is much more pronounced: for **T1**, switching the solvent to dimethyl formamide (DMF) increased the time constants for cooling to  $t_1 = 0.7$  ps and  $t_2 = 2.6$  ps, while using methanol (MeOH) lead to a biphasic process with  $t_1 = 1.3$  ps and  $t_2 = 11$  ps for **T2R**. This can be explained by their higher viscosity compared to ACN (0.37 cp, DMF: 0.92 cp, MeOH: 0.55 cp), retarding relaxation processes that involve major molecular motion. In the case of MeOH, an additional factor could be the formation of hydrogen bonds.

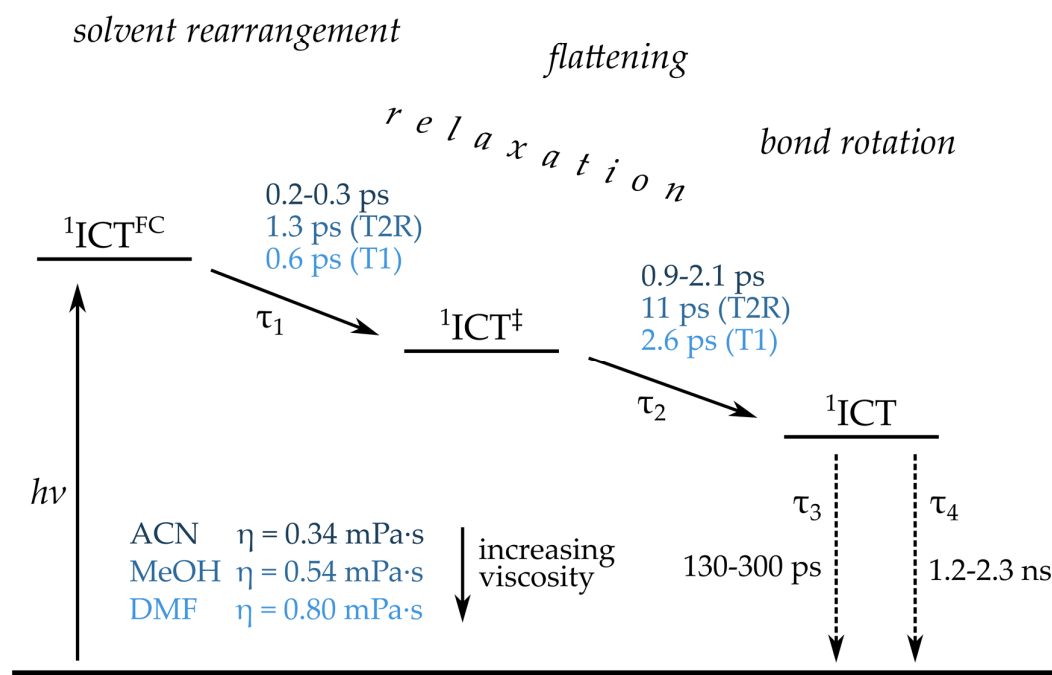
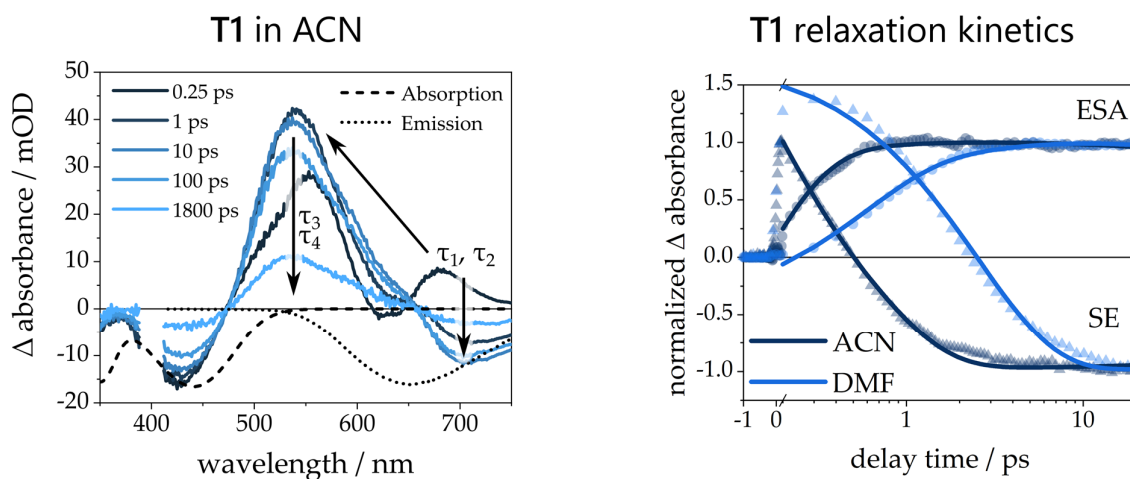


Figure 3.4: Results of TA spectroscopy of organic push-pull dyes in solution. Top: TA spectra of **T1** in ACN and kinetic traces of the ESA ( $\lambda = 535$  nm in ACN, 550 nm in DMF) and SE ( $\lambda = 705$  nm) at early delay times in ACN and DMF that shows the influence of solvent viscosity on the relaxation kinetics. Bottom: Jablonski scheme showing the excited state processes taking place in the organic push-pull dyes **T1**, **T2** and **T2R**.

After the relaxation cascade is complete, the dyes are in the thermalized singlet excited ICT state, from which they decay back to the ground state in either monophasic (**T2R**) or biphasic fashion (**T1**, **T2**) on a sub-ns to ns timescale. This fast excited state decay has been suggested to occur due to a twisted geometry with increased charge

separation and localization in the  $S_1$  state, which was proposed to approximate the  $S_1$  and  $S_0$  potential energy surfaces, leading to a fast internal conversion and thus to a fast excited state decay and low emission quantum yield.<sup>116</sup> This was supported by an observation on a TPA-cyanoacrylate dye, in which the  $S_0$  and  $S_1$  state were essentially degenerate at  $90^\circ$  and  $270^\circ$  rotation around the double bond, providing a low-barrier mechanism for internal conversion to the ground state.<sup>113</sup> In **T1** and **T2**, this might be the reason for the biphasic decays which could result from different rotational conformers. The faster excited state decay for **T2** might be due to the lower HOMO-LUMO gap or to the additional (rotational) degrees of freedom introduced by the longer linker.

### 3.3 Photophysics of dye-catalyst assemblies in solution

In the photophysics of dye-catalyst dyads, the most interesting question is the kinetics of ET and CR. They are important to determine the yield of CSS and its lifetime. This ET can occur either via an oxidative quenching, i.e. from the excited dye to the catalyst, or via a thermal ET, i.e. from the reduced dye (generated by a reductive quenching of the excited PS by an external electron donor) to the catalyst. Depending on the kinetics of the processes involved, dyads can undergo one of the two or possibly a mixture of both mechanisms.

In this thesis, covalent dye-catalyst assemblies based on the dyes **T1**, **T2** and **T2R** covalently linked to the cobalt HER catalysts **Co** and **Cat1** via copper-catalysed azide-alkyne cycloaddition ("click chemistry") were investigated (Figure 3.3). The idea behind these dye-catalyst assemblies is to provide a directionality of the ET away from the electrode surface when grafted, and to fix the two units in a spatially close conformation to ensure fast and efficient ET from the excited or reduced dye to the catalyst. To investigate whether this goal was achieved, the resulting dyads were studied by TA spectroscopy and spectroelectrochemistry.

Electrochemical measurements showed that there is no ground state interaction between the dye and catalyst unit in any of the dyads, which is corroborated by their UV-Vis spectra. Three reduction processes were observed for **Cat1** of which two are positive of the dye reduction potentials and are therefore accessible by ET from the reduced dye. The first two reductions, to the  $Co^{II}$  and  $Co^I$  state, are localized on the metal-organic centre while the third process is ligand-based.<sup>83,85,128,129</sup> Concerning the dyes, the reduction potential is unaffected by the introduction of the CPDT linker, but the oxidation potential decreases by ca. 220 mV, equivalent to a HOMO shift to higher

energy, due to the electron-rich dithiophene unit. Steady-state spectroscopy and electrochemical measurements showed that i) HI from the excited state of the dyes to NiO and ii) ET from either the excited or reduced dye to the catalyst up to its Co<sup>I</sup> state is thermodynamically possible.

Emission spectroscopy indicated an interaction in the excited state in the form of emission quenching in the **T1** and **T2R** dyads which reduced the emission quantum yield by 68 to 92 %. Thus, the covalent assemblies with the cobalt catalysts seem to enable non-radiative decay pathways for the emissive state. The nature and kinetics of these non-radiative pathways were the focus of the TA spectroscopic experiments performed on the dyads in solution.

Upon excitation, the initial behaviour of all dyads studied is identical to that of the respective dyes up until the formation of the thermalized singlet excited ICT state, irrespective of the catalyst unit. In short, the initially excited Franck-Condon state relaxes on the sub-ps to ps timescale in a relaxation cascade to the thermalized singlet excited state via solvent rearrangement and molecular motions such as rotation and flattening. The spectral shape of the TA spectra and their evolution during the relaxation process is identical to that of the respective dyes. After the initial relaxation, the deactivation pathways taking place from the thermalized singlet excited state are however quite distinct between the different dyads and in comparison to the respective dyes.

### 3.3.1 **T1-Co**

The original dyad **T1-Co** shows a spectrally identical, but faster excited state deactivation in the TA experiments compared to the dye **T1**. This suggests that the same deactivation process takes place in the dyad but is accelerated. Since the dyads were constructed to enable fast ET from the dye to the catalyst, we would like to know whether the excited state deactivation involves such an ET process. Observation of the spectral signature of the reduced catalyst together with the signature of the oxidized dye unit would enable an unequivocal assignment of the deactivation to ET. Steady-state UV-Vis spectroelectrochemical experiments were carried out to reveal the spectral features of the respective units in their oxidised and reduced state: in **T1-Co**, upon reduction of the initially present Co<sup>III</sup> state of the catalyst to the Co<sup>II</sup> state, the catalyst shows only a low-intensity absorption at 512 nm (Figure 3.5). At the same wavelength, the oxidised dye shows a strong bleach of its ICT absorption, which would hide the Co<sup>II</sup> band in case of ET. However, the Co<sup>I</sup> state shows a much stronger absorption at 600-800 nm, which does not overlap with the bleach of the oxidised dye

and should therefore be observable in TA spectroscopy if ET takes place upon excitation of a dyad already in the  $\text{Co}^{\text{II}}$  oxidation state.

Thus, to study whether the faster excited state decay of **T1-Co** is due to ET, TA spectroscopy was performed in a spectroelectrochemical cell at various applied potentials: at the open-circuit potential (OCP, e.g., without an applied potential, where the Co catalyst is in its initial  $\text{Co}^{\text{III}}$  state), and at potentials sufficiently negative to reduce the cobalt catalyst to its  $\text{Co}^{\text{II}}$  and  $\text{Co}^{\text{I}}$  state. It was hypothesized that under these conditions, the existence of ET could be unequivocally confirmed or ruled out, either by the appearance of the  $\text{Co}^{\text{I}}$  state after excitation of the  $\text{Co}^{\text{II}}$  state of the dyad, or by a marked difference in excited state decay kinetics, especially in comparison to the reference  $\text{Co}^{\text{I}}$  state. Figure 3.5 shows the principal possible processes during the TA-SEC measurement of **T1-Co**. Of special interest were the measurements at the  $\text{Co}^{\text{II}}$  state, which should provide the possibility of observing the  $\text{Co}^{\text{I}}$  state after ET, and at the  $\text{Co}^{\text{I}}$  state which served as reference since ET is not thermodynamically possible in this state.

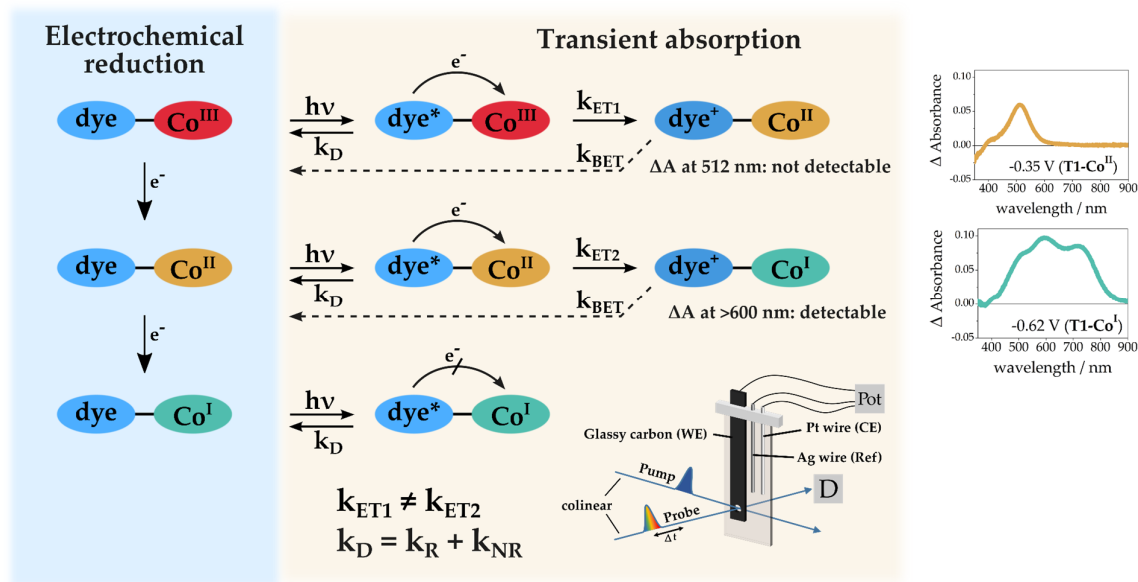


Figure 3.5: Scheme of the electrochemical and principal light-induced processes taking place during the TA-SEC measurements on **T1-Co** and the differential absorption spectra of the **T1-Co<sup>II</sup>** and **T1-Co<sup>I</sup>** species obtained by UV-Vis spectroelectrochemistry.  $k$  are rate constants for the different processes, with  $k_D$  = decay to the ground state,  $k_R$  = radiative decay,  $k_{NR}$  = non-radiative decay,  $k_{ET}$  = ET,  $k_{BET}$  = back ET. Bottom right: Schematic representation of the spectroelectrochemical cell used in this experiment.

More in general, this setup allows to study excited state processes and especially ET kinetics at a variety of oxidation states of the donor and/or acceptor in a dyad, or indeed a multicomponent system. This is very valuable in the field of multielectronic redox catalysis where multiple ET steps are required: While the first ET step, which is the only one accessible by traditional TA spectroscopy, might occur rapidly due to a high driving force or favourable orientation/geometry, this is not necessarily the case for subsequent ET steps. These might be severely slowed down or inactivated by lower driving force, structural rearrangements taking place upon the preceding ET step or other influences. TA-SEC makes it possible to study each ET step separately, arguably most importantly the final step that leads to the formation of the catalytically active species, in this case the  $\text{Co}^{\text{I}}$  state. To date, this has been used to study a reduced copper PS<sup>130</sup> and two dye-catalyst assemblies, a Ru-Rh<sup>42</sup> and a Ir-polyoxometalate dyad.<sup>131</sup>

The setup, which was designed by Dr. Linda Zedler, consists of a three-electrode setup in a 1 mm cuvette (scheme in Figure 3.5). The working electrode was a glassy carbon electrode with 0.4 mm thickness and a drilled hole with 1 mm diameter through which the pump and probe beam were focused colinearly. This electrode design enables a high local concentration of reduced species at the focal point of the pump and probe beams, taking advantage of the highly resistant glassy carbon material while achieving optimal light transmission despite its opacity. The counter electrode was a Pt wire and the pseudo-reference electrode a Ag wire.

During the experiment, the sample was reduced in a chronoamperometric measurement before starting the TA measurement. During the measurement, the potential was continuously applied to ensure a constant high concentration of reduced species in the sample space.

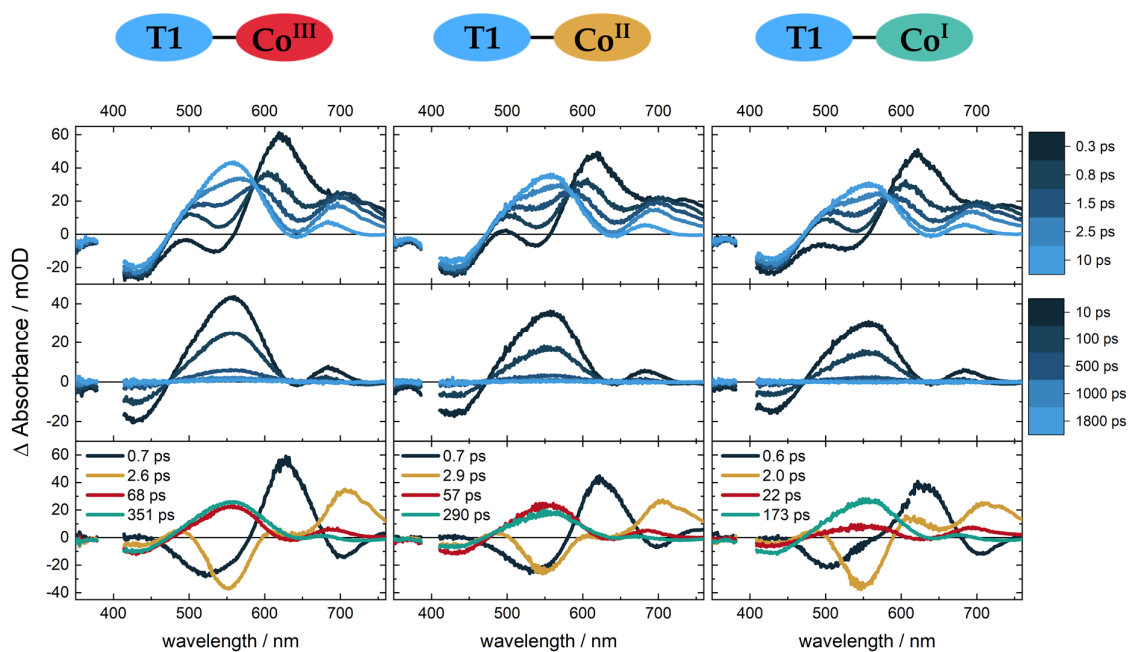


Figure 3.6: fs-TA-SEC data of **T1-Co** in DMF at various applied potentials: OCP (left), Co(II) (middle) and Co(I) (right) reductive potential. The upper graphs show the spectra at early delay times while the middle ones show late delay times. The bottom graphs show the decay-associated spectra (DAS) obtained by a four-component parallel exponential fit.

In the experiment, it was observed that the oxidation state of the catalyst had little to no influence on the excited state kinetics (Figure 3.6). Importantly, there was no spectral or kinetic indication which would point to ET to the cobalt catalyst: i) the Co<sup>I</sup> spectral signature was not observed when exciting the sample in the Co<sup>II</sup> state, the spectral shape was in fact identical at all applied potentials; and ii) the excited state decay kinetics were not faster for the measurements with thermodynamically possible ET in comparison to the reference measurement at Co<sup>I</sup>, where it was not. In fact, a counter-intuitive faster excited state decay was observed at more negative potentials, which might be due to a Coulombic repulsion between electron density at the cobalt catalyst and the electron localized on the dye acceptor group, leading to a destabilization of the ICT state and therefore to its faster decay. Thus, it could be concluded that ET does not take place in the excited state of **T1-Co** and that the faster excited state decay must stem from a different pathway. An alternative explanation for the increase in the non-radiative rate could be an increased density of vibrational modes upon addition of the cobalt moiety. Dexter energy transfer from the excited donor chromophore to short-lived cobalt-centred dd-states might also play a role.

Therefore, it must be deduced that the ET that enables hydrogen production in photoelectrochemical experiments with **T1-Co** takes place on a much slower timescale

than its rather short excited state lifetime. Therefore, it seems likely that instead of an oxidative quenching pathway, which we failed to observe in our TA-SEC experiment, a reductive quenching pathway is indeed active. Here, the excited state is first quenched by HI into NiO, which is typically ultrafast (see section 4.1.2.3), and subsequently ET from the reduced dye to the catalyst takes place.

This hypothesis is supported by observations made by Aukauloo and coworkers who studied a series of dye-catalyst dyads with Ru polypyridyl complexes connected to various acceptor moieties by triazole bridges prepared by “click” chemistry. In their studies, the ruthenium excited state was usually quenched very quickly by an external SED or acceptor, followed by a thermally activated intramolecular ET to the acceptor unit.<sup>132–136</sup> The ET was observed on the ns- $\mu$ s timescale, with the fastest occurring in  $< 20$  ns in a **Ru(bpy)<sub>3</sub>-NDI** assembly<sup>134</sup> and the slowest with a characteristic time constant of 31  $\mu$ s in a **Ru(bpy)<sub>3</sub>-Ni(cyclam)** assembly.<sup>133</sup> These results suggest that indeed the CSS generated by HI on the NiO surface might have to be stable for up to tens of  $\mu$ s for ET to the catalytic center to occur, and thus much longer than the 1.7 ns and 350 ps lifetimes of the excited state of **T1** and **T1-Co**, respectively.

It also highlights that the triazole bridge might be synthetically appealing, but not ideal in terms of the excited state photophysics and ultimately the performance of these dyads. Further evidence for this comes from studies with triazole-bridged donor-acceptor assemblies without SED, e.g. looking at excited state ET. ET in triazole-bridged dyads was reported to occur on a wide range of timescales, ranging from ultrafast ET on the timescale of ps<sup>137–142</sup> to slower ET in ns-ms<sup>139–141,143,144</sup> to dyads where ET is not observed, even though it is thermodynamically possible.<sup>145–147</sup> Similarly, the CR rates drastically differed between systems, from the ps time scale<sup>137,141,142</sup> to hundreds of ns.<sup>138,143,148</sup> An interesting behaviour was observed in a Zn porphyrin-NDI dyad, where ET efficiency depended on whether the donor or acceptor part of the molecule was excited. Excitation of the acceptor lead to a high yield of CSS through fast ET ( $< 10$  ps), while excitation of the donor Zn porphyrin lead to a low yield because of slower ET ( $t_{ET} = 9$  ns) combined with the deactivating ISC to the triplet state on the Zn porphyrin.<sup>141</sup> One study also found an influence of the connectivity of the donor and acceptor moieties on the triazole, e.g. which part was connected to a carbon or a nitrogen atom on the triazole ring.<sup>148</sup> In general, it seems that ET through the triazole is rather slow in most assemblies; many of the fast ET rates can be ascribed to through-space ET made possible by flexible linkers, e.g. in studies in polymers functionalized with Ru dyes.<sup>149–152</sup>



### 3.3.2 T2R dyads

The study of the dyads based on the **T2R** revealed yet another influence of the cobalt moieties on the excited state behaviour of the dye unit. In this case, both dyads, based on **Co** and **Cat1**, were studied by fs-TA spectroscopy in MeOH. Interestingly, both dyads show identical excited state behaviour, except for a somewhat more pronounced emission quenching in **T2R-Cat1**. There is no SE band at any point in time. Due to the solvent, the initial relaxation process is slow and finished only after some tens of ps. Following the thermalization and unlike all the other compounds, a very long-lived signal forms in about 120 ps. Spectrally, it consists of GSB at 350 and around 490 nm and a broad ESA band above 510 nm with two maxima at 590 and 725 nm. This spectrum is ascribed to the triplet state of the **T2R** dye likely localized on the CPDT bridge, formed by ISC from the thermalized singlet ICT state (Figure 3.8). The extinction coefficients of oligothiophene triplet states observed in literature are in the same order of magnitude as that of **T2R**, in line with the observed similar intensity of the long-lived band compared to the GSB.<sup>153</sup> Although the triplet absorption of pure oligothiophenes is found at higher energies than those observed in our dyads for the triplet state band, the bithiophene structure in **T2R** is part of an extended conjugated charge-transfer system which can have a strong effect on the excited state energies. ET to the Co catalysts is discarded on the basis of i) the identical spectral shape for both **Co** and **Cat1** dyads, where the two catalysts would give a different spectral response upon reduction by ET, and ii) the similar intensity of the double band to the other dye-based bands, while extinction coefficients of the optical transitions on the cobalt complexes are much lower than those of the dye (factor > 10).

The fast ISC is explained by the rigid CPDT linker containing two thiophene units. Bi- and oligothiophenes are known to undergo fast ISC on the same time scale as observed here and could potentially show similar behaviour when used as a linker in **T2R**.<sup>153-155</sup> The extremely fast ISC rates for bithiophene are explained in the literature by the high spin-orbit coupling factor of sulfur<sup>156</sup> and a very small energy difference of the S<sub>1</sub> and T<sub>2</sub> state.<sup>154</sup> Since the fast ISC only takes place in the dyads and not in the **T2R** dye, an interaction of the CPDT linker with the cobalt complexes is likely responsible for the fast ISC. Literature on ISC induced by cobalt in binary systems is scarce and the observed effect attributed to the paramagnetic nature of Co<sup>II</sup> ions which cannot be the explanation for our diamagnetic Co<sup>III</sup> complex.<sup>157,158</sup> Instead, alternative pathways must be considered involving higher energy states on the cobalt complexes. In addition, the rigidity of the CPDT linker likely plays a role in the ISC since for **T2-Co**, only a very small yield of triplet state was detected.

In the literature, there are some other examples of heavy-atom free triplet sensitizers that operate by radical pair ISC, which is much slower than that observed in our systems,<sup>159-162</sup> or through the use of spin convertors, most prominently fullerenes.<sup>163-165</sup> In our case, the Co complex could act as a spin convertor after ET since ISC has been observed to occur on a ps time scale in the ground state of Co complexes<sup>166</sup> and < 1 ps in the excited state,<sup>167</sup> and thus could be much faster than the ISC rates observed here. If the ISC and back CT to the dye are much faster than the CT to the complex, the latter would be the gating process and there would be no accumulation of the CT state with the electron localized on the Co complex, explaining why this species was not observed in the experiment.

### 3.3.3 T2-Co

The **T2-Co** dyad shows quite a different excited state behaviour than **T1-Co**. Where **T1-Co** showed a much faster decay of the thermalized singlet ICT state than **T1**, this process is barely accelerated in **T2-Co** compared to its dye **T2** to occur with an average time constant of 500 ps. The spectral shape is identical to that of **T2** with a GSB centred at 455 nm and ESA at 620 nm, while the SE could not be observed in either **T2** or **T2-Co** since it is bathochromically shifted out of the spectral window of our setup. As in the case of the **T1** systems, the excited state decay processes are of the same nature but are slightly accelerated in the dyad. It is not clear why there seems to be a lesser acceleration of excited state decay by interaction with the cobalt catalyst than in **T1-Co**. From DFT calculations on similar dyes, the LUMO does not seem to be more strongly located on the linker, e.g. away from the cobalt catalyst, than in **T1**.<sup>127</sup> A possible explanation can be offered when inspecting the spectrum at long delay times. In **T2-Co**, after 9 ns the signal has not completely decayed to zero, instead, there still is some GSB and ESA. The spectral shape of the ESA is broader than the initial one, extending farther into the red. In comparison to **T2**, this contribution can already be observed at earlier delay times. In analogy to the results for the **T2R** dyads (see section 3.3.2), this signal is attributed to the triplet state of the **T2** dye formed by cobalt-induced ISC. Since the triplet state is more long-lived than the singlet state, the convoluted signal of the two states can result in a net slower signal decay than in **T1-Co**.

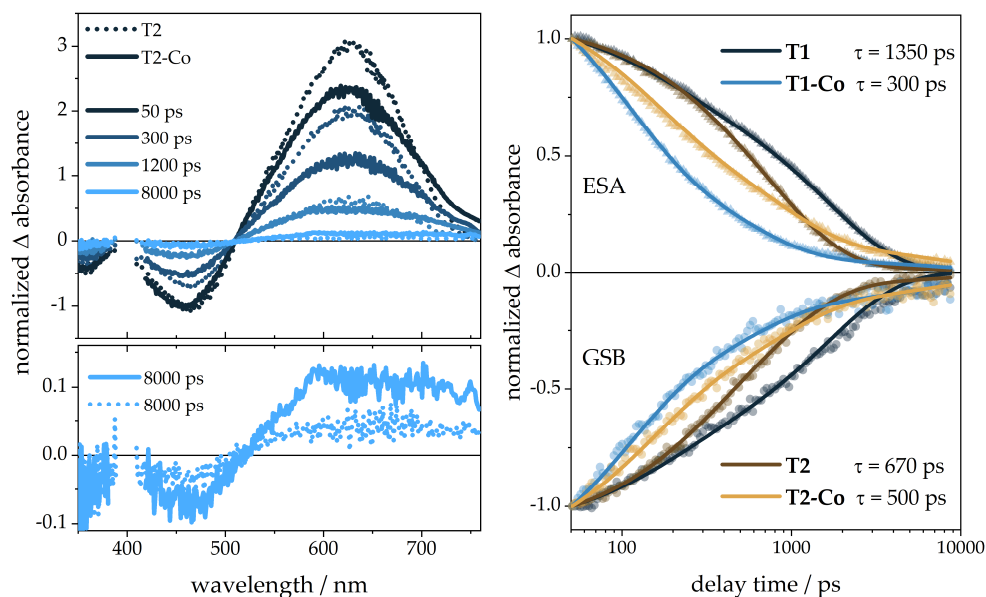


Figure 3.7: Results of TA spectroscopy of **T2** and **T2-Co** in solution. a) TA data of **T2** and **T2-Co** in ACN after the initial relaxation cascade, normalized to the GSB after 50 ps. b) Kinetic traces of **T1**, **T1-Co**, **T2** and **T2-Co** in ACN from 50 ps to 9 ns with the average lifetimes calculated from the biphasic decay at the maxima of the ESA ( $\lambda = 430$  nm for **T1** and **T1-Co**, 455 nm for **T2** and **T2-Co**) and GSB ( $\lambda = 535$  nm for **T1**, 550 nm for **T1-Co**, 620 nm for **T2** and 625 nm for **T2-Co**).

### 3.3.4 Conclusion and Outlook

Comparing the data from the different experiments on the excited state behaviour of the organic dyes and dyads in solution, several insights can be gained.

First, all dyes and dyads show identical initial ultrafast cooling processes to a thermalized singlet excited state whose kinetics are affected by solvent viscosity. Deactivation from this state is similar in the different dyes with a direct decay to the ground state on the sub-ns to ns timescale, but occurs in very different fashion for the different dyads:

1. **T1-Co** shows faster deactivation than the **T1** dye due to interactions with Co dd states or additional vibrational modes.
2. The **T2R** dyads undergo fast ISC to yield a long-lived triplet state, likely through interaction of the rigid CPDT linker and higher Co states.
3. **T2-Co** shows only slightly faster decay than **T2** and forms the excited triplet state in low yield.

The choice of linker in the design of the push-pull dye thus determined the nature and kinetics of the decay process from the singlet ICT state.

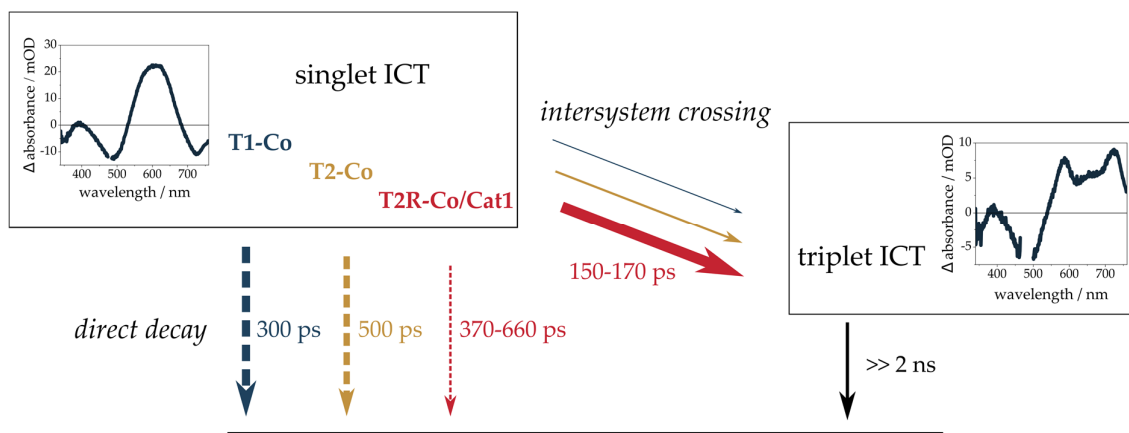


Figure 3.8: Deactivation pathways of the singlet excited ICT state of the dye-catalyst dyads via direct decay and ISC to the triplet ICT state. The width of the arrows indicates the amplitude of the processes. The spectra depicted are the TA spectra of the thermalized singlet ICT state (recorded of **T2R** in MeOH) and of the triplet ICT state (**T2R-Cat1** in MeOH).

ET from the excited state to the catalytic centre (**Co** or **Cat1**) was not observed in any of the dyads, despite its thermodynamic feasibility. This is likely due to a slow ET process competing with the fast excited state deactivation observed for these organic dyes and dyads. Thus, it seems that in DSPC, the oxidative quenching pathway is not active in these dyads, but rather a reductive quenching pathway where the electron is transferred from the reduced dye to the catalyst.

This work is one of few examples of TA-SEC measurements in solution on donor-acceptor dyads and the only one so far using an organic dye as photoactive unit and electron donor. Furthermore, it was the first time these measurements were performed on a dyad containing a cobalt catalyst active for proton reduction as acceptor. This enabled us to probe the second ET step that leads to the catalytically active state of the catalyst without using a SED or a chemical reductant which could interfere in the photophysical measurements. In general, this technique opens up the possibility of probing light-induced processes at different oxidation states which is important in the context of systems designed for photo-induced multi-electron catalysis such as proton reduction and water oxidation.

The results obtained for **T1-Co** in the TA-SEC experiments show clearly that emission quenching alone is not sufficient evidence for photoinduced ET. It is necessary to

additionally observe the spectral signature of the charge-transfer state or an influence of the oxidation state on the decay kinetics. The latter observation is now made possible by TA-SEC measurements without the need for a chemical reductant.

In general, the results show that the interaction of the donor and acceptor units, in this case the Co complexes, in molecular dyads can lead to unexpected results: Firstly, to a fast ground state decay that outcompetes ET. More interestingly, a fast ISC on the sub-ns timescale occurs in the **T2R** dyads. Such a fast, cobalt-induced ISC has so far not been observed in the literature, as it is likely a product of the interaction of the Co cobalt complex with the rigid CPDT linker containing two thiophene rings, where the triplet state is localized and which are known themselves to undergo ISC to the triplet state.<sup>153,154</sup> This shows that all the possible excited-state interactions, in addition to the desired ones, must be taken into account when designing donor-acceptor dyads. However, the unexpectedly obtained fast ISC shows a possible new architecture for organic triplet sensitizers by using tethered Co complexes instead of heavy atoms or other spin convertors.

Furthermore, our results challenge the use of triazole bridges as linkers for donor-acceptor dyads designed for light-induced charge-transfer, since ET cannot compete with the other deactivation processes. Therefore, a different linker design should be considered to achieve fast ET.

## 3.4 Experimental Section

### 3.4.1 Synthesis of T2 and T2-Co

**T2-Co.** The synthesis of **T2-Co** has been published and can be found in *Windle, C. D., Massin, J., Chavarot-Kerlidou, M., Artero, V. Dalton Transactions, 2018, 10509-10516.*

**T2.** The reference dye **T2** was synthesized according to the same protocol as **T2-Co**, using ethyl 2-cyanoacetate instead of propargyl cyanoacetamide during the Knoevenagel reaction.

### 3.4.2 Transient absorption spectroscopy

*Transient absorption measurements of T1, T2, T1-Co and T2-Co.* A custom-built setup was utilized to acquire fs-TA data. The TA setup is described in detail in *R. Siebert, D. Akimov, M. Schmitt, A. Winter, U. S. Schubert, B. Dietzek, J. Popp, ChemPhysChem, 2009, 10, 910-919.* A white-light supercontinuum probe pulse at 1 kHz repetition rate was

used to analyze the excited state dynamics. The supercontinuum was generated by focusing a minor part of the output of the Ti:Sapphire amplifier into a CaF<sub>2</sub> plate mounted on a rotating stage. After generation of the white light continuum, it is split into a probe and reference beam. Using a concave mirror with 500 nm focal length, the probe pulse was focused onto the sample by a concave mirror of 500 mm focal length. The spectra of probe and reference were detected by a Czerny-Turner spectrograph of 150 mm focal length (SP2150, Princeton Instruments) equipped with a diode array detector (Pascher Instruments AB, Sweden). The pump pulses used were of 403 nm wavelength and a pulse duration of approximately 100 fs. The repetition rate of the pump pulses was reduced to 0.5 kHz by a mechanical chopper and the polarization adjusted to the magic angle of 54.7° by a Berek compensator and a polarizer. The time delay is generated by reflecting the probe beam on a pair of mirrors mounted on a movable delay line and therefore adjusting the path length of the probe beam.

The data was analyzed using a customized data analysis software (Pascher Instruments AB, Sweden). First, the data was corrected for the chirp and subsequently, a sum of exponential functions was fitted to the data. The pulse overlap region of ±200 fs was removed from the data to exclude the coherent artefacts present in this temporal region.

The TA measurements were carried out in ACN in a standard 1 mm cuvette ( $OD_{400\text{nm}} = 0.3$ ).

## 4 Dye-sensitized photocathodes

*Parts of this chapter have been published in the following articles:*

**Publication 3** - Bold, S., Massin, J., Giannoudis, E., Koepe, M., Artero, V., Dietzek, B., & Chavarot-Kerlidou, M., Spectroscopic investigations provide a rational for the hydrogen-evolving activity of dye-sensitized photocathodes based on a cobalt tetraazamacrocyclic catalyst. *ACS Catalysis*, **2021**, 11, 6, 3662–3678.

Publication 4 – Giannoudis, E., Bold, S., Müller, C., Schwab, A., Bruhnke, J., Queyriaux, N., Gablin, C., Leonard, D., Saint-Pierre, C., Gasparutto, D., Aldakov, D., Kupfer, S., Artero, V., Dietzek, B., & Chavarot-Kerlidou, M, Hydrogen Production at a NiO Photocathode Based on a Ruthenium Dye–Cobalt Diimine Dioxime Catalyst Assembly: Insights from Advanced Spectroscopy and Post-operando Characterization. *ACS Applied Materials & Interfaces*, **2021**, 13, 42, 49802-49815.

This chapter will deal with all results obtained for the NiO photocathodes sensitized with dye-catalyst assemblies. The first part contains the TA-SEC experiments of a Ru-Co dyad, while the second part deals with the full characterization of a series of organic assemblies.

NiO films sensitized with dye-catalyst assemblies as photocathodes for hydrogen evolution in DSPC are very complex systems. The choice of the molecular components (nature of the dye, the catalyst and the structure of the linker), the preparation of the NiO film and other experimental parameters such as applied potential, light intensity and pH during the photoelectrochemical tests all affect the performance of the photocathodes, i.e. their stability and their activity, governed by the light-induced processes and the performance of the individual dye and catalyst units under the selected experimental conditions. It is therefore mandatory to use a wide variety of experimental techniques to obtain a full picture of the system, if possible under operando conditions in order to identify its bottlenecks or weak points. These insights can then be used to rationally improve the identified weak points in the molecular assembly. There are a wide range of analytical techniques that can be used to study different aspects of the systems.

To determine the activity of the DSPC for hydrogen production, standardized conditions for the photoelectrochemical experiments were established at the beginning of the work to enable an accurate determination and comparison of the results. To account for the varying performance of different individual films, all photoelectrochemical measurements were performed at least in triplicate to obtain an average value and estimate the error. In addition, the grafting density of the dyads on the film surface was measured by UV-Vis spectroscopy of desorbed solution for each film individually which enabled an accurate measurement of the TON achieved, and therefore enabled a comparison of the intrinsic activity of different dyads. The amount of produced hydrogen was quantified both in the headspace by gas chromatography and in solution with a microelectrode hydrogen probe.

To investigate the stability of the system, UV-Vis spectroscopy and inductively coupled plasma mass spectrometry (ICP-MS) were used to quantify the dye and cobalt concentration on the film pre- and post-operando. Of special importance to study both the stability and the light-induced processes in the assemblies were spectroelectrochemical techniques, i.e. spectroscopic measurements while applying a potential, as they allow to study the systems' behaviour at the operando potential of the photoelectrochemical experiments, which can differ drastically from the case without an applied potential. In particular, in this work the kinetics of the degradation processes of the dye unit were studied by time-resolved UV-Vis SEC under operando conditions. In addition, the light-induced processes were investigated by time-resolved emission spectroscopy and TA-SEC on sensitized NiO films. The latter technique allowed to study the influence of the applied potential on the interfacial processes (HI and CR) due to the influence on the NiO as well the influence of the different oxidation states of the catalyst, and to observe the ET process from the reduced dye to the cobalt catalyst unit as well as their respective lifetimes.

## 4.1 Ruthenium-cobalt dyad **RuCo**

The first dyad studied in this work consisted of a Ru(bpy)<sub>2</sub>-imidazophenanthroline complex as PS unit, coupled via CuAAC click chemistry to a diimine-dioxime cobalt catalyst (Figure 4.1). A critical point of the imadazophenanthroline ligand is the protonation state on the imidazole part which can alter the photophysical properties.<sup>168,169</sup> Under the photoelectrochemical conditions studied (pH = 5.5), one nitrogen atom on the imidazole is protonated, as indicated in Figure 4.1.



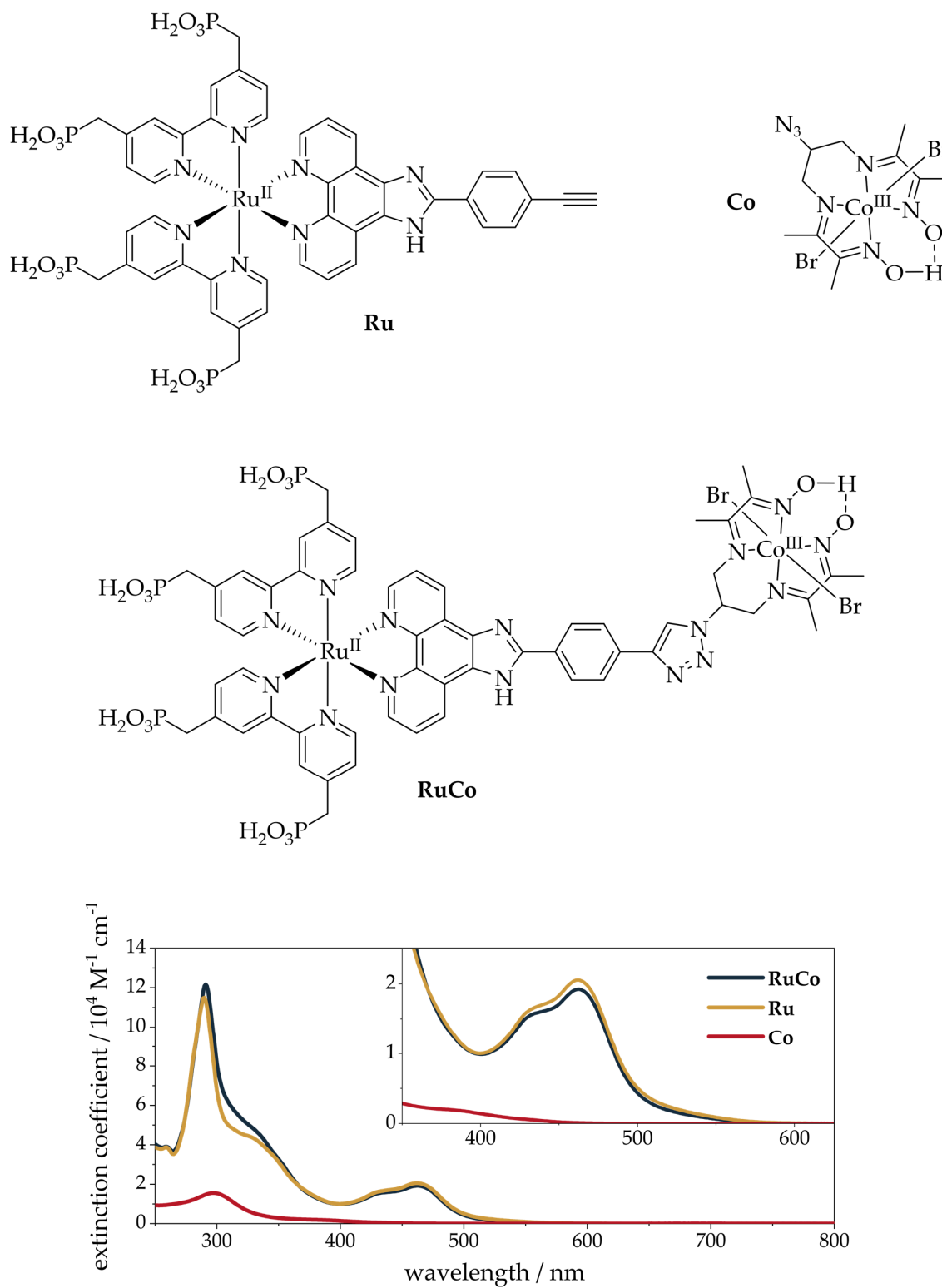


Figure 4.1: Chemical structures of the dye **Ru** and the dyad **RuCo** and their UV-Vis absorption spectra in ACN. The inset shows a close-up of the metal-to-ligand charge transfer (MLCT) band.

### 4.1.1 Activity and stability

*The results in this paragraph were obtained by Emmanouil Giannoudis at CEA Grenoble and are taken from his doctoral thesis.*

**Ru** and **RuCo** show grafting densities of  $5.2 \pm 0.8$  nmol/cm<sup>2</sup>. At -0.4 V vs. Ag/AgCl applied potential and under 1 sun equivalent irradiation in the visible region (400-800 nm), RuCo showed photocurrent densities of  $58 \pm 11$   $\mu\text{A}\cdot\text{cm}^{-2}$ , while the use of an AM 1.5 filter increased this value to  $84 \pm 7$   $\mu\text{A}\cdot\text{cm}^{-2}$  due to the strong absorption band in the UV of the Ru complex. 98 % of the initial photocurrent was lost during the first two hours of photoelectrochemical measurements due to desorption from the NiO surface and degradation of the cobalt catalyst. After two hours under photoelectrochemical conditions with visible light (-0.4 V vs. Ag/AgCl applied potential, 2-(N-morpholino)ethanesulfonic acid buffer solution with pH = 5.5), hydrogen was produced with TON of  $5 \pm 1$  ( $28 \pm 2$  nmol·cm<sup>-2</sup> H<sub>2</sub>) with a low Faradaic efficiency of 25%. While the amount of produced hydrogen doubled with the use of the AM 1.5 filter (TON =  $13 \pm 2$ ,  $60 \pm 9$  nmol·cm<sup>-2</sup> H<sub>2</sub>), the Faradaic efficiency stayed identical. The low value of the Faradaic efficiency was ascribed to side reaction on the cobalt diimine-dioxime catalyst. Short measurements of 30 minutes duration showed a much higher F.E. of 72% and almost identical TON as after two hours, meaning most of the hydrogen is produced in the initial minutes. This means that the intrinsic Faradaic efficiency of the assembly is high, but decreases quickly due to side reactions and degradation of the catalyst. MALDI-ToF MS measurements showed that demetallation due to the cleavage of the C-N bonds of the diimine-dioxime ligand was the primary degradation process. In addition, 80% of the initially present dyads were lost from the NiO surface due to desorption during the first two hours under photoelectrochemical conditions.

The obtained TON values for this assembly are very low compared to those obtained with the same catalyst under homogeneous photocatalytic conditions (300 TON)<sup>170</sup> or in electrocatalytic conditions when anchored on carbon nanotubes (7000 TON).<sup>76</sup> This suggests that the assembly suffers from performance-limiting issues which, in addition to the stability issues, might be kinetic issues, i.e. the catalyst does not receive electrons at a rate necessary for fast catalysis. To investigate this, TA-SEC experiments were performed.

### 4.1.2 Time-resolved spectroscopy on dye-sensitized NiO films

When studying PS for solar energy applications, the photophysics in solution are only the first step to obtain a general idea of the excited state processes in the molecule. For application in DSPEC, the second, very important step is to investigate the photophysics of the complete dye-sensitized film as this is the active system. When immobilizing PS on p-type SCs such as NiO, additional pathways are opened up in the excited state such as HI into the VB of the SC and the following CR as well as intermolecular interactions on the surface that can lead to excimer formation and fast excited state decay.<sup>52,171</sup> Typically kinetics of interfacial processes on metal oxide films are non-exponential, often stretching across timescales of several orders of magnitude. This applies to HI and even more so to CR (see below). In practice, these processes can be fitted either with multiexponential fits, where it must be made clear that the individual time constants obtained do not reflect separate processes, or by using a stretched exponential fit. This stretching of the timescales observed for interfacial processes can also lead to an overlapping of different processes, complicating data analysis. This can lead to uncertain assignment of HI kinetics as they often occur at the same time as other ultrafast processes such as thermal relaxation of excited states. Furthermore, sometimes the analysis is even more challenging to similar spectral signatures of excited and reduced/oxidised dyes.

It must be pointed out that a large part of the literature on excited state processes in dye-sensitized NiO films comes from the field of DSSC due to its longer history and higher maturity. Consequently, there are few studies on films with a grafted catalyst, as catalysts are not needed in DSSC due to the more easily achievable one-electron redox reaction taking place between the PS and the redox mediator. Therefore, only the reduced PS needs to be produced, and efforts were directed only to produce a very long-lived reduced dye state after excitation. To this end, some dyads were introduced containing dedicated electron acceptor units, that did however not pose the additional challenge of having to be a catalyst.

#### 4.1.2.1 TA-SEC setup

The principal technique to gain insights on the light-induced processes in dyad-sensitized photocathodes used in this work was TA-SEC. For this purpose, a spectroelectrochemical cell was designed that fulfilled the requirements of these challenging experiments:

First, the precise application of a potential to the photocathode had to be ensured to be able to accurately reproduce the applied potential during the photoelectrochemical experiments. An implicit consequence of the applied potential is the investigation of the light-induced processes at different oxidation states of the catalyst unit. In addition, we needed to investigate the ET kinetics in the absence of catalysis to accumulate the  $\text{Co}^{\text{I}}$  state in order to detect it. Therefore, the measurements must be carried out in the absence of water, using dry organic solvent. To perform these experiments, the cell had to be able to house a three-electrode setup with a reference electrode and an auxiliary electrode. In addition, the cell must allow to measure under inert conditions for the duration of the TA experiment, e.g. several hours, principally to prevent water and oxygen from entering the cell, which could react with the reduced state of the catalyst, thus preventing its detection. Also, the dye-sensitized NiO film must be fixed in plane to avoid a loss of focus, while being able to move it in plane to avoid photodamage from the pump beam which was identified as a major issue especially for the organic dye-catalyst assemblies. This was exacerbated by the low concentration of sample molecule on the film surface combined with light scattering on the NiO film, which together demanded long exposure time to obtain a good signal-to-noise ratio. In addition, the film must be electrically contacted to be connected to the potentiostat. The final challenge was to limit the path length of the laser beams through the cell to a few millimetres which was important for the detection of ultrafast kinetics such as HI in the fs-TA-SEC experiment. A long path length leads to a loss of temporal evolution due to the chirp caused by dispersion in the electrolyte solution.

The setup used in the TA-SEC experiments in solution (section 3.3.1) did not fulfil all of these criteria: the use of the leakless Ag/AgCl reference electrode, as opposed to a pseudo-reference Ag wire used in the measurements in solution, demanded a wider cell due to its higher diameter (2 mm). In addition, in the setup for solution the film could not be fixed in plane which prohibited movement to avoid photodamage. Therefore, a spectroelectrochemical cell was designed, largely based on the design of a photoelectrochemical cell by Zahner Elektrik<sup>172</sup> but adapted to fs-TA measurements.

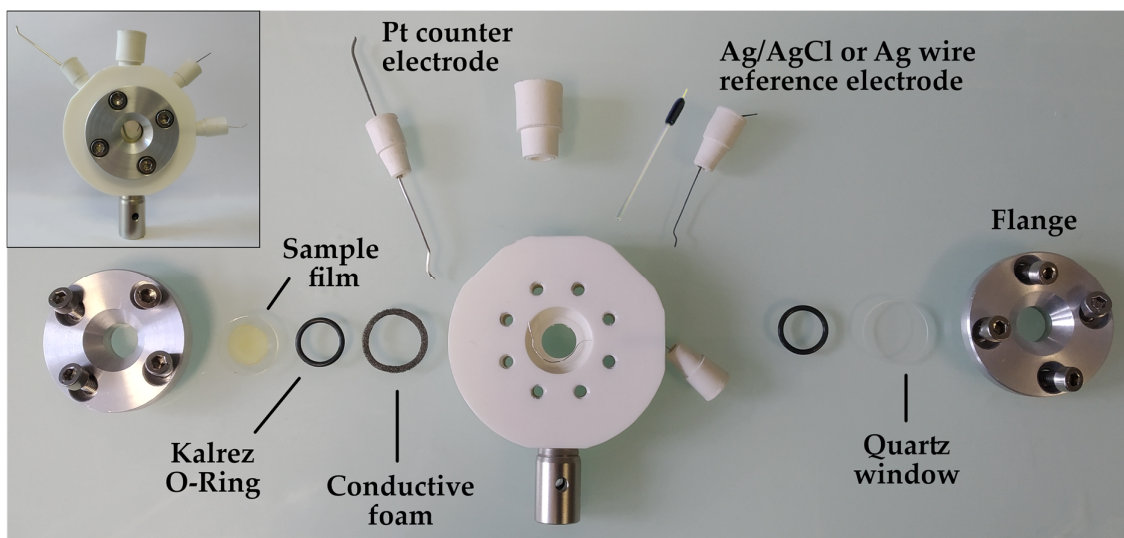


Figure 4.2: Cell for TA-SEC measurements on films in the assembled and disassembled state.

The general design consisted of a cell body with two transparent windows pressed to it with flanges and sealed with rubber O-rings (Figure 4.2). One of the windows is a glass substrate with a transparent conducting oxide coating (fluorine-doped tin oxide (FTO) or ITO) on which the sample film is deposited prior to the experiment. The films were prepared by spin-coating a precursor solution of  $\text{NiCl}_2$  and the F108 block copolymer in ethanol/water on ITO-coated glass slides (Solems, FTO coating for the photoelectrochemical experiments) and sintering at  $450^\circ\text{C}$ , followed by sensitization with the molecular components. This film is contacted via a conducting foam to a wire connected to the potentiostat. The reference and auxiliary electrodes are passed through rubber stoppers and a channel into the cuvette created by the cell body and the glass windows. The final path length through the assembled cell is 5-6 mm. For the cell body, a polymer was chosen since metal could not be used as it is a conductor, and the design would have been more difficult to achieve with a cell made of glass. The polymer had to be resistant to the electrolyte used and hard enough to resist the pressure of the flanges. Polytetrafluoroethylene is ideal in terms of chemical inertness, however it is much too soft and was deformed during use. The polymer finally chosen was polypropylene which is more resistant to pressure but limits the choice of solvent. It is however stable in contact with ACN, which was used as the electrolyte solvent.

In a typical experiment, the cell was assembled in a glovebox under inert conditions. Once closed, it was tight for the duration of a TA experiment. Oxygen and water levels in the cell were not measured to prove this, but no influence of passed time on the lifetime of the CSSs was observed. Then, TA spectra were recorded at different applied potentials, i.e. during a chronoamperometric measurement, while moving the film in

plane to avoid photodamage. This was achieved by mounting the cell on a yz-stage. The potential of the reference electrode was calibrated versus the ferrocene<sup>+0</sup> couple.

#### 4.1.2.2 TA-SEC results on **RuCo**-sensitized NiO films

Prior to the measurements, the sensitized films were washed with water to adjust the protonation state of the imidazole group. Then, TA spectra were recorded of **Ru**- and **RuCo**-sensitized NiO films without any applied potential (open circuit potential (OCP)), at -0.74 V and -1.15 V vs. Fc<sup>+0</sup>. -0.74 V vs. Fc<sup>+0</sup> corresponds to -0.4 V vs. Ag/AgCl, the potential employed in the photoelectrochemical experiments (e.g., the operando potential), and is sufficiently reductive to reduce the Co centre to its Co<sup>II</sup> state. -1.15 V vs. Fc<sup>+0</sup> served as a control measurement since the Co centre is at its Co<sup>I</sup> state at this potential, making ET from the reduced or excited dye thermodynamically impossible. The kinetics and the spectral shape were very similar for **Ru** and **RuCo**, except for some spectral broadening for the latter, and therefore the results for the two compounds will be discussed together. At the end of the discussion, a focus will be laid on the ET process in the dyad.

TA spectra of NiO films sensitized with **Ru** and **RuCo** at early times show a spectrum with GSB at 480 nm and ESA around 590 nm, corresponding to the triplet metal-to-ligand charge transfer (<sup>3</sup>MLCT) state (Figure 4.3). At OCP, this spectrum decays almost completely within 7 ns ns except for a weak positive band centred at 520 nm. At negative applied potentials, however, it develops into a long-lived spectrum with positive bands at 540 and 480 nm, completely losing the GSB. The band at 540 nm is characteristic for the one-electron reduced Ru dye (dash-dot line in Figure 4.3), while the band at 480 nm is tentatively assigned to oxidized Ni centres produced by HI,<sup>173,174</sup> leading to the assignment of this spectrum to the primary CSS produced by HI from the excited dye into the NiO film (formal NiO<sup>+</sup>|Ru<sup>I</sup>). From a three-component exponential fit to the experimental data, the time constant for HI is determined to be 45 to 70 ps, becoming faster and more pronounced at more negative applied potential.



Since at more negative applied potentials the initial signal at 480 nm (GSB) is weaker while the signal at 540 nm (reduced Ru dye) is stronger, we postulate an additional ultrafast ( $< 2$  ps) HI process that rises in amplitude at more negative applied potentials. For **RuCo**, the ultrafast HI process has higher amplitude than for **Ru**, reflected in a higher initial ratio of signal at 540 nm to 480 nm. HI is followed by CR, which is strongly affected by the applied potential, increasing from a time constant of tens of picoseconds at OCP to  $> 7$  ns at negative applied potentials, leading to a long-lived CSS. At OCP, the fast CR following the fast HI leads to the overall much faster decay of  $^3\text{MLCT}$  signal than in solution. In parallel, there is a process with a characteristic time constant of  $\tau_2 = 950$  to  $1470$  ps which shows the spectral signature of a decay of  $^3\text{MLCT}$  to the ground state (concerted loss of GSB and ESA). This decay might be produced by an accelerated direct decay of excited molecules that have not undergone HI and thus remain in the  $^3\text{MLCT}$  state, due to self-quenching of tightly packed compounds on the NiO surface.<sup>175</sup> Alternatively, a combination of HI and CR can lead to the same spectral result. The lower amplitude and slower rate for this component at more negative applied potentials supports this assignment: HI is faster, decreasing the amount of long-lived  $^3\text{MLCT}$  states, and CR is slowed down by the lower number of holes on the NiO surface. Most importantly, the TA spectra of **RuCo** in the time window up to 7 ns do not show any spectral indication of charge transfer to the cobalt catalyst unit. Such a charge transfer would be observable as an increasing absorption band between 550 and 750 nm, produced by the  $\text{Co}^{\text{I}}$  state in the case of **RuCo** at  $-0.74$  V vs.  $\text{Fc}^{+/0}$ , which is not present in the TA spectra.

Since thermally activated ET in triazole-bridged dyads has been shown to occur on the ns- $\mu\text{s}$  time scale,<sup>132,133,135,136,176</sup> we performed TA experiments under identical conditions in the ns- $\mu\text{s}$  time scale. The TA spectra in this time range are spectrally identical to the last spectra recorded in the fs-TASEC experiment and decay without any spectral changes, with 15% of the initial signal still left after 45  $\mu\text{s}$  (Figure 4.3). The decay occurs in a non-exponential fashion as typical for CR reactions in molecularly functionalized NiO photoelectrodes<sup>52,107,108,177</sup> and could be approximated with a three-component exponential fit which yields similar lifetimes under all experimental conditions ( $\tau_1 \approx 86$  ns,  $\tau_2 \approx 1.4$   $\mu\text{s}$ ,  $\tau_3 \approx 14$   $\mu\text{s}$ , Table 4.1), with an average lifetime of  $\tau_{\text{ave}} = 3.6$  to  $5.2$   $\mu\text{s}$ . In these experiments, an additional band was observed at 390 nm which in the fs-TA-SEC experiment was blocked by the pump scatter, and which was also observed in UV-Vis SEC measurements upon one-electron reduction of **Ru**. Since this band is produced by the one-electron reduced bpy ligand, it seems that the excess electron is partly localized on the anchoring bpy ligands, possibly through thermally activated interligand ET from the extended ligand. This partial localization on the anchoring ligand could lead



to faster CR due to the spatial proximity to the NiO surface (Figure 4.4), as previously discussed for related ruthenium complexes.<sup>45</sup>

Table 4.1: Obtained time constants by fitting the TA-SEC data of Ru- and RuCo-sensitized NiO films at OCP and different applied potentials with multiexponential fits.

	Applied potential/ V vs. Fc <sup>+0</sup>	fs-TASEC				ns-TASEC						
		$\tau_0$	$\tau_1$ / ps	$\tau_2$ / ps	$\tau_3$	$\tau_1$ / $\mu$ s	$\tau_2$ / $\mu$ s	$\tau_3$ / $\mu$ s	Normalized integral DAS		$\tau_{ave}$ / $\mu$ s	
<b>Ru</b>	OCP	< 2 ps	67	1070	> 7 ns							
	-0.74		52	735		0.1	1.6	15	1	0.97	0.48	3.6
	-1.15		31	655		0.1	1.5	16	1	1.18	0.93	5.2
<b>RuCo</b>	OCP	< 2 ps	67	950	> 7 ns							
	-0.74		69	1360		0.1	1.2	13	1	0.77	0.66	3.9
	-1.15		45	1470		0.1	1.2	13	1	0.85	0.77	4.3

Overall, by applying a reductive potential, the lifetime of the CSS was increased from hundreds of picoseconds to up to 15  $\mu$ s, an increase of up to 5 orders of magnitude. However, in spite of the long-lived CSS, no direct evidence for ET to the cobalt catalyst could be observed: within the experimental signal to noise, the spectral signature of the Co<sup>I</sup> state did not appear in the TA spectra of **RuCo**-sensitized NiO films at -0.74 V vs. Fc<sup>+0</sup>, and the decay kinetics of the reduced Ru complex were not accelerated in comparison to **Ru**-sensitized films. On the basis of the ratio of the extinction coefficients of the reduced dye and the Co<sup>I</sup> state from the UV-Vis SEC experiment, and an experimental noise of 0.52 mOD, the limit of detection at a signal-to-noise ratio of 2:1 is at 12% efficiency for the ET in the ns-TASEC experiment, meaning that less than 12% of the reduced state of the Ru dye undergoes ET.

#### 4.1.2.3 Influence of the applied potential on the interfacial processes – hole injection

From the TA-SEC data it becomes apparent that the applied potential influences the kinetics of the interfacial charge-transfer processes, e.g. HI and CR, as observed before.<sup>107,108</sup> HI in **Ru(Co)**-sensitized NiO films occurs in a biphasic fashion with an ultrafast ( $\tau_0 < 2$  ps) and a slower component that takes place in tens of picoseconds ( $\tau_1 = 30$  to 70 ps). This is in line with the published literature, where HI in dye-sensitized NiO films was observed in some cases in < 1 ps to some ps,<sup>45,46,52,54,61,77,107,125,178–192</sup> while

some PS have slower HI that takes place in some tens of ps.<sup>36,45,77,107,183,193</sup> These slower HI kinetics are usually observed for Ru complexes, while organic dyes almost exclusively show ultrafast HI. There are very few examples where HI was very slow (250 ns),<sup>194</sup> did not occur at all<sup>175</sup> or only from the oxidised PS after oxidative quenching with an electron acceptor.<sup>195</sup> A good example for multiexponential HI is that of **Ru(bpy)<sub>3</sub>** by Dillon and coworkers, who used a four-component multiexponential fit for HI with time constants of 2.8, 39, 280 ps and 10 ns.

The amplitude of the ultrafast HI component increases at more negative potentials which translates to a lower GSB signal and a higher signal of the reduced Ru at 540 nm at the beginning of the experiment. The slower component increases both in rate and in amplitude at more negative potentials. The biphasic HI kinetics might be caused by a different localization of the excited electron: if the electron is primarily located on the anchoring bpy ligand, the excess charge density slows down HI into NiO, while localization on the extended ligand presents no impediment and thus leads to fast HI, as observed before for Ru(bpy)<sub>3</sub>.<sup>36</sup> In this case, the slower component might be an inter-ligand ET from the bpy to the imidazophenanthroline ligand that gatekeeps the fast HI.

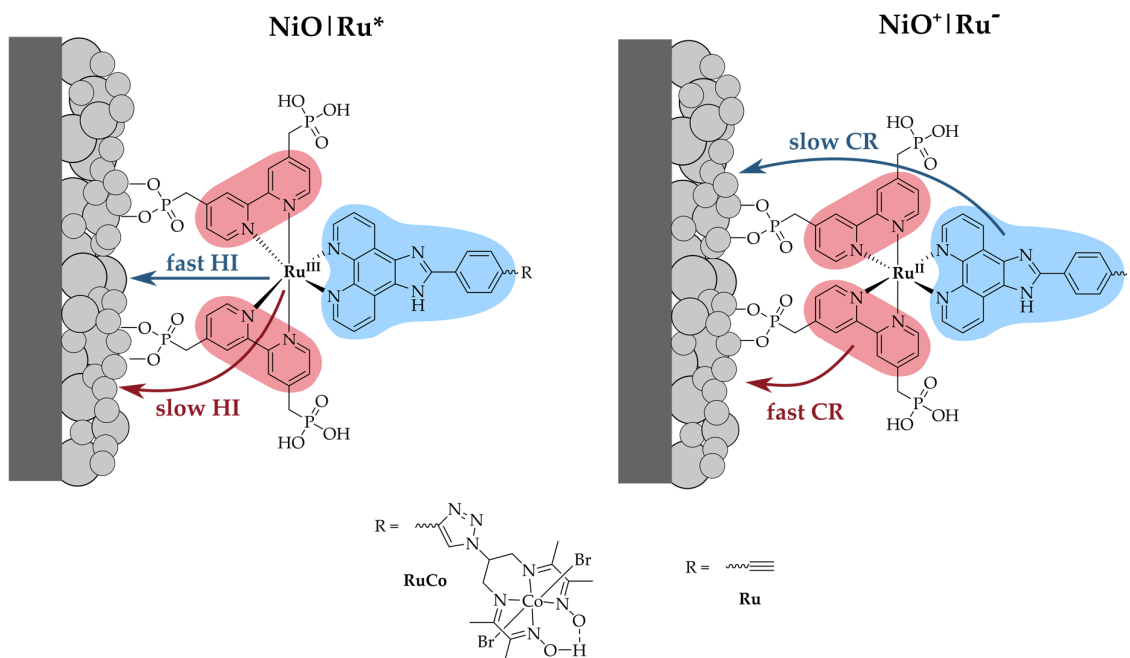


Figure 4.4: Schematic representation of different HI and CR kinetics caused by differing localization of the excited electron ( $\text{NiO} | \text{Ru}^*$ ) and the excess electron in the CSS ( $\text{NiO}^+ | \text{Ru}^-$ ). The red colour indicates a localization on the anchoring bpy ligands and the blue colour a localization on the extended imidazophenanthroline ligand.

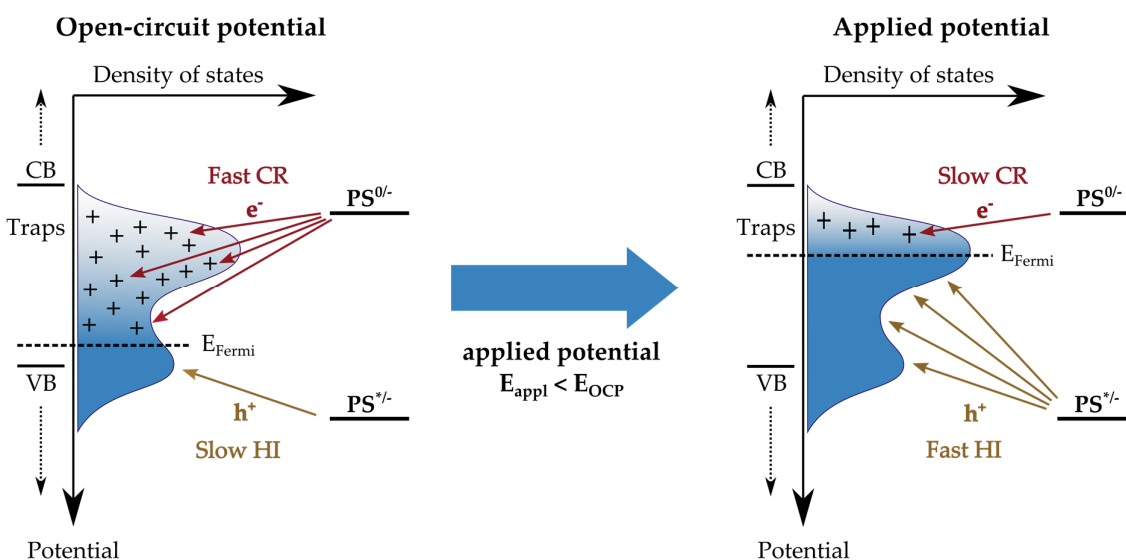


Figure 4.5: Potential dependence of the NiO band electronics and its influence on HI and CR kinetics.

It might also be caused by different local environments on the NiO and predominantly electron- or hole-filled surfaces as suggested by Dillon and co-workers for a Ru(bpy)<sub>3</sub> complex grafted on NiO,<sup>107</sup> and the time constants observed here fit well with those obtained in their study. (2.8 and 39 ps). To obtain a good fit for their TA-SEC data, the authors proposed a model consisting of predominantly electron filled and predominantly electron depleted surface sites. This, in a band picture, corresponds to empty and filled intragap states between the NiO valence and conduction bands. In a chemical picture, these sites/trap states are essentially Ni<sup>2+</sup> atoms that can be oxidized to Ni<sup>3+</sup>. Applying a negative potential to the NiO film reduces these Ni sites to Ni<sup>2+</sup>, thus filling the intragap states and producing an electron-filled surface. This model explains the influence of the applied potential on the HI kinetics: the NiO film as prepared – equivalent to the OCP measurements – presents a primarily electron-depleted surface, corresponding to unfilled trap states or Ni<sup>3+</sup> atoms at defect sites, respectively (Figure 4.5). As the surface electrons are those that will transfer to the excited Ru complex during HI, a low concentration of surface electrons leads to slow HI; in a band/energy picture the electrons in the NiO have low driving force for HI resulting in slow HI. Applying a reductive potential reduces the Ni atoms to Ni<sup>2+</sup>, filling the trap states with electrons, thereby raising the Fermi level and producing an electron-filled surface. This leads to a higher driving force for HI, resulting in faster kinetics and especially higher amplitude ultrafast HI. It was also observed that for **RuCo**, especially at more negative potentials, the ratio of the amplitude of the ultrafast to the slow HI component is higher compared to **Ru**. This could be caused by an

influence of the triazole linker on the ligand energy levels, if the presence of the triazole leads to a faster localization of the excited electron on the extended ligand.

#### 4.1.2.4 Influence of the applied potential on the interfacial processes – charge recombination

The second interfacial process influenced by the applied potential is CR of  $\text{NiO}^+|\text{Ru}^{\text{I}}(\text{Co})$ . From the fit of the fs-TA-SEC data, the amplitude of the CR component increases at more reductive potential. Since the time constant of this component is  $> 7$  ns, this increase in amplitude means that more CSS is present at the end of the 7 ns time window of the experiment as a result of slower CR kinetics, in line with the higher signal of the reduced dye. The lower signal at OCP means that the formed CSS already decays in under 7 ns, and the failure of a build-up of signal of the reduced dye at 540 nm shows that CR takes place on the same time scale as HI. This also shows in the decay-associated spectra of the slow HI component which is positive at  $> 500$  nm at OCP, while at reductive potentials it is negative. This difference is caused by the convolution of HI and CR spectral features, as the differential DAS show: subtracting the HI DAS at more reductive potentials which show much slower CR reveals the spectral signature of CR in the first DAS at OCP (Figure 4.6). This means that at OCP, CR occurs on the same time scale as HI, namely tens of picoseconds.

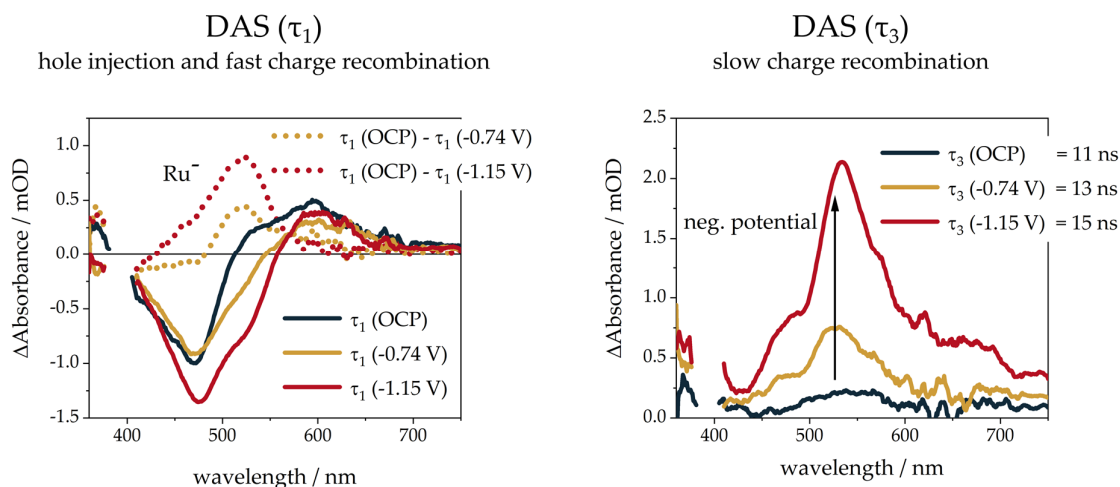


Figure 4.6: Decay-associated spectra obtained by a three-exponential fit of the TA-SEC data of NiO films sensitized with **RuCo**. Left: DAS of  $\tau_1$  at different applied potentials (solid), associated with HI and fast CR. The dotted lines show the differential spectra of the DAS at negative applied potentials subtracted from OCP which reveals the contribution of fast CR at OCP. Right: DAS of  $\tau_3$ , associated with CR.

This behaviour was also observed in the literature on dye-sensitized NiO films: as for HI, CR occurs in a highly non-exponential fashion, stretching over timescales of several orders of magnitude. In most of the studied dye-sensitized NiO films, CR occurs on a sub-ns timescale with time constants of tens to hundreds of ps.<sup>36,45,46,52,77,101,107,125,178–193</sup> Indeed, CR can be so fast that no signal of the reduced PS is observed which can also complicate the assignment of the HI process. However, the generally faster excited state decay than that observed for the PS in solution, due to this fast HI and CR, can be a hint for the existence of both, even if the reduced PS is not observed. Despite this fast recombination and due to the highly non-exponential behaviour of CR on NiO films, there is often some reduced dye still observed on the ns- $\mu$ s timescale.<sup>36,45,52,54,61,101,177,180–184,186,188,190,191,193,194,196–199</sup> However, this is usually only a small amount (< 10 %) of initially present CSS, but in some cases more efficient retardation of CR has been achieved. The most successful strategy to extend the lifetime of the CSS was installing a secondary electron acceptor such as NDI or PMI on the dye to which ET occurs after HI.<sup>101,181,190</sup> A certain degree of success was also achieved by introducing electron-withdrawing trifluoromethyl groups on the ligands of a **Ru(bpy)<sub>3</sub>** complex<sup>193</sup> or longer linkers between the Ru centre and the anchoring groups.<sup>188</sup> Some studies only present data recorded on the ns- $\mu$ s time scale, which does not allow to determine the yield of CSS since the fast CR on the sub-ns timescale cannot be observed. Due to the higher pump power used in ns-TA setups, even small amounts of CSS can still be observed, and so the slow CR part of a multiexponential (fast) decay could mistakenly be assumed to be the only CR process taking place in a system, leading to an overestimation of CSS average lifetime.

For **RuCo**-sensitized NiO films at more negative applied potentials, the fast CR channel is increasingly deactivated, leading to a build-up of CSS that lives for up to 15  $\mu$ s compared to hundreds of picoseconds at OCP, an increase of up to five orders of magnitude. To explain this strong increase in lifetime, the reason for the fast CR at OCP must be determined and the mechanism by which the application of a negative potential eliminates it. A first hint as to the reason for the fast CR came from a study using a series of PMI dyes with increasing driving force for recombination. Instead of a Marcus inverted behaviour as expected for the large driving forces calculated for CR with holes in the NiO VB, a Marcus normal behaviour was observed.<sup>186</sup> This led to the idea that CR actually takes place with intragap trap states, for which the driving force for CR should be lower and lie in the Marcus normal region. Further insight comes from the few studies that employed TA-SEC. The first study to use this technique did not investigate the exact role of NiO, but did observe potential-dependent kinetics of CR for a PMI-oligothiophene-TPA push-pull dye, with lifetimes increasing from ca.

2  $\mu\text{s}$  at -0.15 V vs.  $\text{Fc}^{+/0}$  to a biphasic decay with 50-100  $\mu\text{s}$  and ms lifetime at -0.9 V vs  $\text{Fc}^{+/0}$ .<sup>199</sup> A similar long-lived CSS was observed for a polymer consisting of a  $\text{Ru}(\text{bpy})_3$  PS and a Re catalyst for  $\text{CO}_2$  reduction, immobilized on NiO and at an applied potential of -0.5 V vs. NHE: the reduced  $\text{Ru}(\text{bpy})_3$  polymer alone showed a lifetime of 18  $\mu\text{s}$  (from a Kohlrausch-Williams-Watts stretched exponential fit), while with the Re catalyst this was reduced to 6  $\mu\text{s}$  due to ET to the catalyst, the reduced state of which recombined in 1.7 ms.<sup>200</sup>

Another study looked more closely at the origin of this dependence in NiO films sensitized with Ru-NMI in a potential range of -0.54 to 0.36 V vs  $\text{Fc}^{+/0}$ : D'Amario and coworkers observed a biexponential decay of the reduced dye species, with a fast decay with a potential-independent lifetime of ca. 15 ns whose amplitude increased at positive potential and a slow decay whose rate increased at more positive potential (lifetime decreased from 500 ns to 700 ns), with a high dispersion of rates.<sup>108</sup> Based on these observations, the authors proposed that CR takes place via two pathways: the fast decay would be due to CR with the injected hole in the valence, while the slow decay results from CR with the injected hole after its relaxation into the intragap trap states. A somewhat different explanation was proposed by Dillon and coworkers in what is to date the only TA-SEC study on dye-sensitized NiO films that investigated the ultrafast processes in a fs-TA setup.<sup>107</sup> They observed faster HI at more negative applied potential, until the multiexponential HI kinetics became biexponential at very negative applied potential with 2.8 and 39 ps time constants, and the yield of reduced dye increased from 0% at 0.4 V to 91% at -0.4 V vs. Ag/AgCl. This was ascribed to a retardation of CR. To obtain a good fit for their data, the authors proposed the model presented in section 4.1.2.3, consisting of predominantly electron-filled and predominantly electron-depleted surface sites. Applying a negative potential to the NiO film reduces these Ni sites to  $\text{Ni}^{2+}$ , thus filling the intragap states and producing an electron-filled surface (Figure 4.5). This, in turn, leads to slower CR: from their model, the authors obtained a ratio between the fast and slow CR times on the sub-ns data, which increased from 1:1 at 0.4 V to 1:13,000 at -0.4 V vs. Ag/AgCl. In a ns-TA SEC experiment, it was reflected in a rise of the characteristic time constant for CR from 430 ns at -0.2 V to 750 ns at -0.6 V vs. Ag/AgCl. Note that these experiments were performed with **Ru(bpy)<sub>3</sub>** as sensitizer, which in another study at OCP was found to not inject holes from its excited state due to the localization of the LUMO at the anchoring ligand,<sup>36</sup> which should also accelerate CR from the reduced dye.

The lifetime obtained for the CSS in **Ru(Co)**-sensitized NiO films is thus longer than that observed for Ru(bpy)<sub>3</sub> at applied potential,<sup>107</sup> in which the electron is located unfavourably close to the NiO surface, but much shorter than that of the Ru(bpy)<sub>2</sub>bpy-NDI complex, which possessed the additional electron acceptor NDI.<sup>108</sup> On this timescale, the influence of the increasingly negative potential when going from -0.74 V to -1.15 V vs. Fc<sup>+0</sup> seems to be weak as it only leads to a 10-40 % increase in lifetime. In the fs-TA-SEC experiment, however, the signal of the CSS increased two-fold when going to -1.15 V vs. Fc<sup>+0</sup>, suggesting that the overall yield of long-lived CSS is still significantly enhanced at more negative potential.

#### 4.1.2.5 Electron transfer

Arguably the most important process for the use of the dyad in light-driven proton reduction is the ET process from the excited or reduced dye to the catalyst unit. In **RuCo**-sensitized NiO films, no evidence for such a process could be observed in the TA-SEC experiments. Firstly, there was no direct spectral evidence of the formation of the Co<sup>II</sup> species (in the OCP measurement) or the Co<sup>I</sup> species (in the measurement at -0.74 V vs. Fc<sup>+0</sup>) that would form upon such an ET process. Secondly, the decay kinetics of the CSS on the Ru dye are not accelerated in **RuCo** in comparison to **Ru**, which would be a sign for a competing process such as ET. However, from photoelectrochemical experiments it is known that to some degree, ET must occur since hydrogen is produced. Since the TON after 30 minutes is only 11, it stands to reason that the ET to the catalyst might be very inefficient. Thus, the amount of Co<sup>I</sup> formed might simply lie below the limit of detection of the TA setup. Considering a signal-to-noise ratio of 2:1 as detectable, the ET efficiency was estimated to be below 12 % on the ns- $\mu$ s timescale. In light of the low TON achieved, a much lower efficiency seems plausible.

Similar observations have been made in the literature: in a dyad especially relevant to the Ru complexes studied in this thesis, i.e. based on a Ru(bpy)<sub>2</sub>ip PS and a copper diimine-dioxime complex as acceptor linked by a triazole group, no ET could be unequivocally observed.<sup>145</sup> In the dyad, the excited state lifetime of the PS was reduced compared to the PS alone (380 ns vs. 1.1  $\mu$ s), but the CSS could not be detected. In addition to the issues known for triazole linkers in such donor-acceptor dyads (see section 3.3.1), a study by Mulfort and co-workers suggests that indeed the combination of a Ru complex donor with a Co complex acceptor might be the issue: they could not observe ET in either of two such assemblies, whether they were linked by a methylene

spacer or the Co was coordinated to an extended tetrapyrrophenazine ligand of the Ru complex.<sup>48</sup> In contrast, Ru-Pt and Ru-Pd assemblies also prepared by coordinating the catalytic metal centre to extended ligands on the Ru PS have shown fast ET to the catalytic centre in the sub-ns region.<sup>39,86,201,202</sup> This could suggest that the Co complexes employed are poor acceptors for photoinduced intramolecular ET.

Due to the relative novelty of the DSPEC field, there are few studies containing time-resolved spectroscopy on dye-sensitized NiO films that contain a co-grafted catalyst<sup>54,61,177,182</sup> or dye-catalyst dyads.<sup>46,77,198,200</sup> This might be partly due to the fact that the catalysts employed typically do not have strong optical transitions, which complicates the analysis by UV-Vis TA spectroscopy. However, visible-pump mid-infrared-probe TA spectroscopy has been employed to study the CO vibrational bands of FeFe catalysts.<sup>182</sup> In combination with C343 as PS, following ultrafast HI to yield the reduced C343, fast ET to the catalyst took place in some ps.<sup>54,61</sup> The lifetime of the reduced catalyst depended on the anchoring group employed: a carboxylic acid group directly on the coordinating phenyl group led to fast CR in 2 and 30  $\mu$ s,<sup>54,61</sup> while the use of a longer linker extended the lifetime to up to 20 ms.<sup>54</sup> When this catalyst was co-grafted with the push-pull dye **E2**, ET took place from the excited state of the dye instead and this led to fast CR between dye and catalyst.<sup>182</sup>

As for dye-catalyst dyads studied on NiO, the number is also very limited.<sup>46,77,198,200</sup> The first study was on a porphyrin-Re dyad, in which HI was observed in < 30 ps and CR from the porphyrin dye in 180 ns, however only ns-TA data was recorded. ET to the catalyst was not directly observed but assumed to occur due to previous results in solution.<sup>198</sup> In Ru-Pd and Ru-Pt dyads, HI was observed within the pump pulse and CR in 30 ps, with some residual <sup>3</sup>MLCT population which decayed in 1 ns. The analysis was difficult due to overlapping signals for the CSS and residual excited state in both dyads, as well as the multiexponential decay kinetics as mentioned before.<sup>46</sup> The CSS with the reduced catalyst was not unequivocally observed. In **PB-2**, an organic dyad comprised of a push-pull dye clicked to a cobalt diimine-dioxime catalyst, fast HI in 1 and 30 ps and fast CR in 350 ps was observed, as expected for the organic dye.<sup>77</sup> The authors proposed ET to the catalyst in 330 ps based on the faster decay kinetics of the reduced dye, but did not obtain spectral evidence of the reduced catalyst and therefore could not determine the lifetime of the reduced catalyst. In the only example where this was possible, a negative potential of -0.5 V vs. NHE was applied to the film to retard CR (see section 4.1.2.4), but only ns-TA data was recorded.<sup>200</sup> The molecular component in this case was a polymer structure containing Ru(bpy)<sub>3</sub> as PS and a Re catalyst. While the Ru-polymer alone showed CR with an average lifetime of 18  $\mu$ s



(from a stretched exponential fit), in the dye-catalyst polymer this was decreased to 6.4  $\mu\text{s}$  due to ET to the catalyst, from which CR occurred in 1.7 ms. In summary, for a mixture of several reasons – low extinction coefficients of catalyst optical transitions, fast CR on NiO films without applied potential, leading to overlapping of different processes - the observation of reduced catalyst on dye-sensitized NiO films and the determination of its lifetime remains rare in the literature.

In our case, since the formation of the reduced catalyst state could not be observed, its lifetime could not be assessed, but it is likely higher than that of the reduced Ru complex due to its longer distance from the NiO surface and lower driving force for recombination, as observed for the Ru complex with a NDI acceptor group which showed several orders of magnitude higher lifetime than the  $\text{Ru}(\text{bpy})_3$  alone.<sup>107,108</sup>

### 4.1.3 Summary and Outlook

In summary, a long-lived CSS on the Ru dye was achieved at applied potential, but ET to the cobalt catalyst was not observed which seems to be the main impediment to high activity of the dyad (Figure 4.8). This low activity, in addition to the low stability of the assembly, leads to the low TON observed in photoelectrochemical experiments. Future designs of dye-catalyst dyads should therefore aim to improve the ET kinetics (see section 4.3).

A sophisticated spectroelectrochemical cell was built that enabled TA measurements on films at applied potential under inert conditions that were stable for hours. The cell thus permitted long measurement times, important to obtain a good signal to noise ratio in dye-sensitized films which typically have low signal intensities and high noise due to scattering. It was used to perform the first-ever TA measurements at operando potential on NiO films sensitized with a dye-catalyst dyad (**RuCo**) that were functional for photoelectrochemical  $\text{H}_2$  evolution. These measurements showed that the low activity of the photocathodes was due to a slow and inefficient ET to the catalyst from the reduced Ru complex.

### 4.1.4 Experimental section

*Synthesis of Ru and RuCo.* All reagents were purchased from Sigma Aldrich or Strem and used as obtained unless otherwise stated. Reagent-grade solvents were used

without further purification. The 4,4'-bis(diethylphosphonomethyl)-2,2'-bipyridine (4,4'-(CH<sub>2</sub>PO<sub>3</sub>Et<sub>2</sub>)<sub>2</sub>-bpy) and N<sub>2</sub>,N<sub>2</sub>'-2-azidopropanediylbis(2,3-butadione-2-imine-3-oxime) ligands were custom-synthesized by the companies Oribase Pharma and Provence Technologies, respectively. The 2-(4-ethynylphenyl)-1H-imidazo[4,5-f][1,10]phenanthroline (EPIP) ligand, [Ru(4,4'-(CH<sub>2</sub>PO<sub>3</sub>Et<sub>2</sub>)<sub>2</sub>-bpy)<sub>2</sub>(EPIP)](PF<sub>6</sub>)<sub>2</sub> (**RuP<sub>4</sub><sup>OEt</sup>-EPIP**), [Cu(DO)(DOH)N<sub>3</sub>pn(OH<sub>2</sub>)](ClO<sub>4</sub>) (**CuN<sub>3</sub>**) and [Co(DO)(DOH)N<sub>3</sub>pnBr<sub>2</sub>] (**CoN<sub>3</sub>**) complexes were prepared according to previously reported procedures. <sup>1</sup>H and <sup>13</sup>C NMR spectra were recorded at 298 K on a Bruker Avance 300 MHz spectrometer and the resulting spectra are referenced to the residual solvent peak and reported in relative to tetramethylsilane reference (δ = 0 ppm). UV-vis absorption spectra were recorded either on a Shimadzu UV-1800 spectrometer or on an Agilent Cary 60 UV-vis spectrometer.

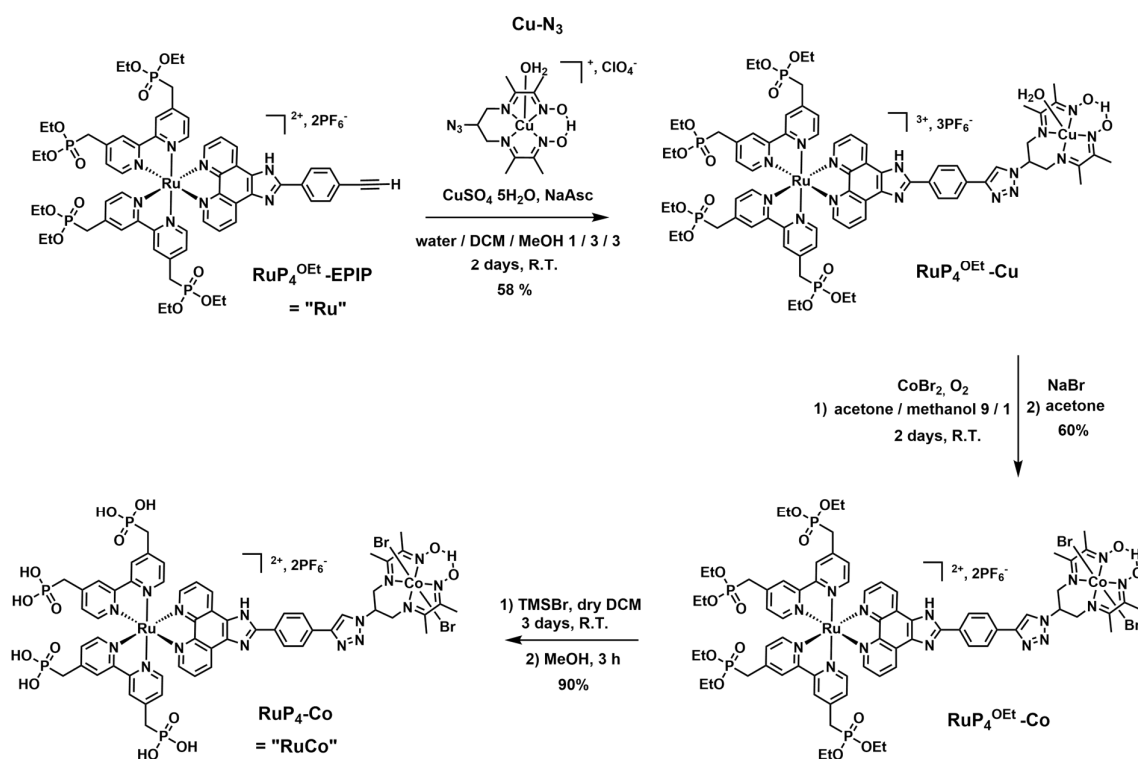


Figure 4.7 - Synthesis of Ru and RuCo

**Synthesis of RuP<sub>4</sub><sup>OEt</sup>-Cu.** In an argon-purged round bottom flask, RuP<sub>4</sub><sup>OEt</sup>-EPIP (150 mg, 0.09 mmol) and CuN<sub>3</sub> (86 mg, 0.18 mmol) were dissolved in a 15 mL of a degassed homogeneous 3:3:1 MeOH/CH<sub>2</sub>Cl<sub>2</sub>/H<sub>2</sub>O solvent mixture. Sodium ascorbate (93 mg, 0.46 mmol) and copper sulfate (11 mg, 0.05 mmol) were added under argon and the

reaction mixture was stirred at room temperature under argon in the dark over the weekend. After evaporation of the organic solvents and dropwise addition of 5ml saturated KPF<sub>6</sub> aqueous solution, the orange solution was extracted with dichloromethane and dried under vacuum. The crude product was purified by column chromatography on silica gel (MeCN/0.4 M aqueous KNO<sub>3</sub>, 80:20). The organic solvents were evaporated and the product was extracted with dichloromethane after the dropwise addition of 5 ml of saturated KPF<sub>6</sub> aqueous solution. After evaporation of dichloromethane and drying under vacuum, **RuP<sub>4</sub><sup>OEt</sup>-Cu** was isolated as a dark orange powder. Yield: 58 % (110 mg). ESI-MS: m/z 559.3 [M-H<sub>2</sub>O-3PF<sub>6</sub>]<sup>3+</sup>, 838.3 [M-H<sub>2</sub>O-3PF<sub>6</sub>]<sup>2+</sup>, 911.0 [M-H<sub>2</sub>O-2PF<sub>6</sub>]<sup>2+</sup>. HR-MS (ESI+): m/z calcd for C<sub>72</sub>H<sub>90</sub>CuN<sub>15</sub>O<sub>14</sub>P<sub>4</sub>Ru 559.1355; found 559.1356 [M-3PF<sub>6</sub>]<sup>3+</sup>. E.A.: calcd for C<sub>72</sub>H<sub>93</sub>CuN<sub>15</sub>O<sub>15</sub>P<sub>8</sub>F<sub>24</sub>Ru: C, 37.98; H, 4.12; N, 9.23; found: C, 39.01; H, 4.53; N, 8.74.

**Synthesis of RuP<sub>4</sub><sup>OEt</sup>-Co.** **RuP<sub>4</sub><sup>OEt</sup>-Cu** (110 mg, 0.05 mmol) and CoBr<sub>2</sub> hydrate (100 mg, 0.45 mmol, 9 eq) were solubilized in a mixture of acetone/methanol 9 / 1 (15 ml) and stirred under air bubbling overnight. The organic solvents were evaporated and the crude product was purified by column chromatography on silica gel using a 90:9:1 acetone/H<sub>2</sub>O/KBr (sat. aq. solution) eluent mixture. The organic solvents were evaporated and the product was extracted with dichloromethane after the dropwise addition of a saturated KPF<sub>6</sub> aqueous solution. After evaporation of dichloromethane and drying under vacuum, **RuP<sub>4</sub><sup>OEt</sup>-Co** was isolated as an orange powder. Yield: 60 % (70 mg). <sup>1</sup>H NMR (300 MHz, CD<sub>3</sub>CN): δ (ppm) 19.35 (s, 1H), 9.67 (d, J = 8.1 Hz, 1H), 9.10 (d, J = 8.73 Hz, 1H), 8.66 (d, J = 8.7, 2H), 8.53 (s, 1H), 8.43 (d, J = 14.4, 4H), 8.12 (t, J = 8.28 Hz, 2H), 7.98 (d, J = 6.8 Hz, 2H), 7.81 – 7.76 (m, 4H), 7.52 (t, J = 4.6, 2H), 7.40 (d, J = 5.6, 2H), 7.16 (d, J = 6.2, 2H), 5.89 (t, J = 11.2, 1H), 4.78 – 4.57 (m, 4H). 4.1 – 3.88 (m, 16H), 3.46 – 3.29 (m, 8H), 2.64 – 2.57 (m, 12H), 1.22 – 1.1 (m, 24H). ESI-MS: m/z 584.8 [M-Br-2PF<sub>6</sub>]<sup>3+</sup>, 916.6 [M-2PF<sub>6</sub>]<sup>2+</sup>. HR-MS (ESI+): m/z calcd for C<sub>72</sub>H<sub>90</sub>Br<sub>2</sub>CoN<sub>15</sub>O<sub>14</sub>P<sub>4</sub>Ru 916.6239; found 916.6227 [M-2PF<sub>6</sub>]<sup>2+</sup>. E.A.: calcd for C<sub>72</sub>H<sub>91</sub>Br<sub>2</sub>CoN<sub>15</sub>O<sub>14</sub>F<sub>18</sub>P<sub>7</sub>Ru: C, 38.11; H, 4.04; N, 9.26; found: C, 39.21; H, 4.44; N, 8.93.

At the end of the synthesis, we observed that **RuP<sub>4</sub><sup>OEt</sup>-Co** was isolated under a protonated imidazole (ImH<sub>2</sub><sup>+</sup>) form (see acido-basic titration Figure S2). A similar observation was made for the Ru-imidazole precursor **RuP<sub>4</sub><sup>OEt</sup>-EPIP**. For a related Ru-imidazole complex, Aukauloo and coworkers determined pKa values of 3.1 for the first protonation (ImH<sub>2</sub><sup>+</sup> ⇌ ImH) and of 8.7 for the second protonation (ImH ⇌ Im<sup>-</sup>) of the imidazole group in aqueous solution<sup>168</sup>. *This supports that **RuP<sub>4</sub><sup>OEt</sup>-Co** is under its neutral Im form under our operating photoelectrochemical conditions (pH 5.5).* However, as the imidazole-protonation state might affect intramolecular electron transfer efficiencies (either photoinduced or thermal electron transfer processes), spectroscopic data were recorded in acetonitrile solution both in the absence and in the presence of 1 equivalent of base (triethylamine) and transient absorption – spectroelectrochemical (TA-SEC) measurements were recorded on sensitized films that have been washed with distilled water beforehand.

**Synthesis of RuP<sub>4</sub>-Co.** **RuP<sub>4</sub><sup>OEt</sup>-Co** (16 mg, 0.007 mmol) was added in an oven-dried schlenk under argon and was solubilized in 2 ml of dry dichloromethane. Under argon, TMSBr (21 µl, 0.17 mmol) was added and the reaction mixture was stirred at room temperature, under argon for 3 days. After evaporation of the solvent, 5 ml of methanol was added and the solution was stirred for 3 hours. The organic solvent was evaporated and the orange powder was dried under vacuum. Yield: 90 % (13 mg). The deprotected dyad was then immediately employed for the NiO film sensitization.

The same procedure was used to prepare **RuP<sub>4</sub>-EPIP** from **RuP<sub>4</sub><sup>OEt</sup>-EPIP**.

*fs-TA spectroscopy.* A custom-built setup was utilized to acquire fs-TA data. The TA setup is described in detail elsewhere<sup>203</sup>. A white-light supercontinuum probe pulse at 1 kHz repetition rate was used to analyze the excited state dynamics. The supercontinuum was generated by focusing a minor part of the output of the Ti:Sapphire amplifier onto a CaF<sub>2</sub> plate mounted on a rotating stage and after generation, it was split into a probe and reference beam. Using a concave mirror, the probe pulse was focused onto the sample. The spectra of probe and reference were

detected by a Czerny-Turner spectrograph of 150 mm focal length (SP2150, Princeton Instruments) equipped with a diode array detector (Pascher Instruments AB, Sweden). The pump pulses used were of 400 nm wavelength and a pulse duration of approximately 100 fs. The repetition rate of the pump pulses was reduced to 0.5 kHz by a mechanical chopper and the polarization adjusted to the magic angle of  $54.7^\circ$  by a Berek compensator and a polarizer. The data was analyzed using a customized data analysis software written by Jens Uhlig (Lund University). First, the data was corrected for the chirp and subsequently, a sum of exponential functions was fitted to the data. The artifact region of  $\pm 1$  ps was removed from the data during the fitting process to exclude the coherent artefacts present in this temporal region.

*ns-TA spectroscopy.* The setup for ns transient absorption measurements was previously described<sup>204</sup>. The pump pulse was generated by a Continuum Surelite OPO Plus (pumped by a Nd:YAG laser,  $\approx 20$  ns pulse duration, 10 Hz repetition rate). The probe light was generated by a 75 W Xenon arc lamp and focussed through the sample and detected by a Hamamatsu R928 photomultiplier. The signal was amplified and processed by a commercially available detection system (Pascher Instruments AB, Sweden). The measurements were performed upon 410~nm (2.0 W) at sample (RuP4OEt-EPIP and RuP4-Co) concentrations of 15  $\mu\text{M}$  (OD at  $\lambda_{\text{exc}} \approx 0.25$ ) in acetonitrile and upon addition of 1 molar equivalent of triethylamine (TEA).

*Preparation of NiO films for spectroelectrochemistry.* NiO films were prepared using a F108 precursor solution prepared by mixing 2 g of  $\text{NiCl}_2$ , 2 g of F108 triblock copolymer in a mixture of ethanol (15 mL) and Milli-Q water (6 mL), according to our previously reported procedures<sup>87</sup>. The mixture was sonicated for 6 h, centrifuged and passed through a 45  $\mu\text{m}$  pore size polyethersulfone syringe filter. Round ITO-coated glass substrates (Solems ITO SOL 30, 1 mm thickness) were cleaned by sonication in isopropanol, distilled water and ethanol for 10 min each. The F108 precursor solution was then spin-coated on the substrates (5000 rpm, 60 s) followed by sintering in an oven in air (30 min ramp to  $450^\circ\text{C}$ , 30 min at  $450^\circ\text{C}$ ). Spin-coating and sintering was repeated for a total of four layers. The NiO films were then soaked in methanolic solutions (0.2 mM) of RuP4-EPIP and RuP4-Co at room temperature for 24 h. After sensitization, films were rinsed with methanol and dried with pressured air. To deprotonate the initially protonated species that results from the synthesis, the films were then soaked in distilled water for 5 minutes and rinsed with dry acetonitrile.

*TA-SEC measurements.* TA-SEC experiments on films were performed using a home-built spectroelectrochemical cell, designed to work in a three-electrode setup under inert conditions and to optimize time resolution in the fs measurements, with a

minimized path length (ca. 4 mm). The sensitized NiO film was used as the working electrode, a miniature leakless Ag/AgCl electrode (EDAQ) as reference electrode and a Pt wire as auxiliary electrode. The cell was assembled in a glove box and filled with 0.1 M TBABF<sub>4</sub> in ACN. Transient absorption measurements were performed at open circuit potential and different applied potentials on the same film, moving the film in the plane periodically to prevent photodegradation. Prior to each experiment, the reference electrode was calibrated using ferrocene. In the ns-TASEC experiments, the pump pulse ( $\lambda = 485$  nm) power was set to 0.2 mJ. To remove pump scatter, a 475 nm short pass and a 500 nm long pass edge filters were used for short and long wavelengths, respectively.

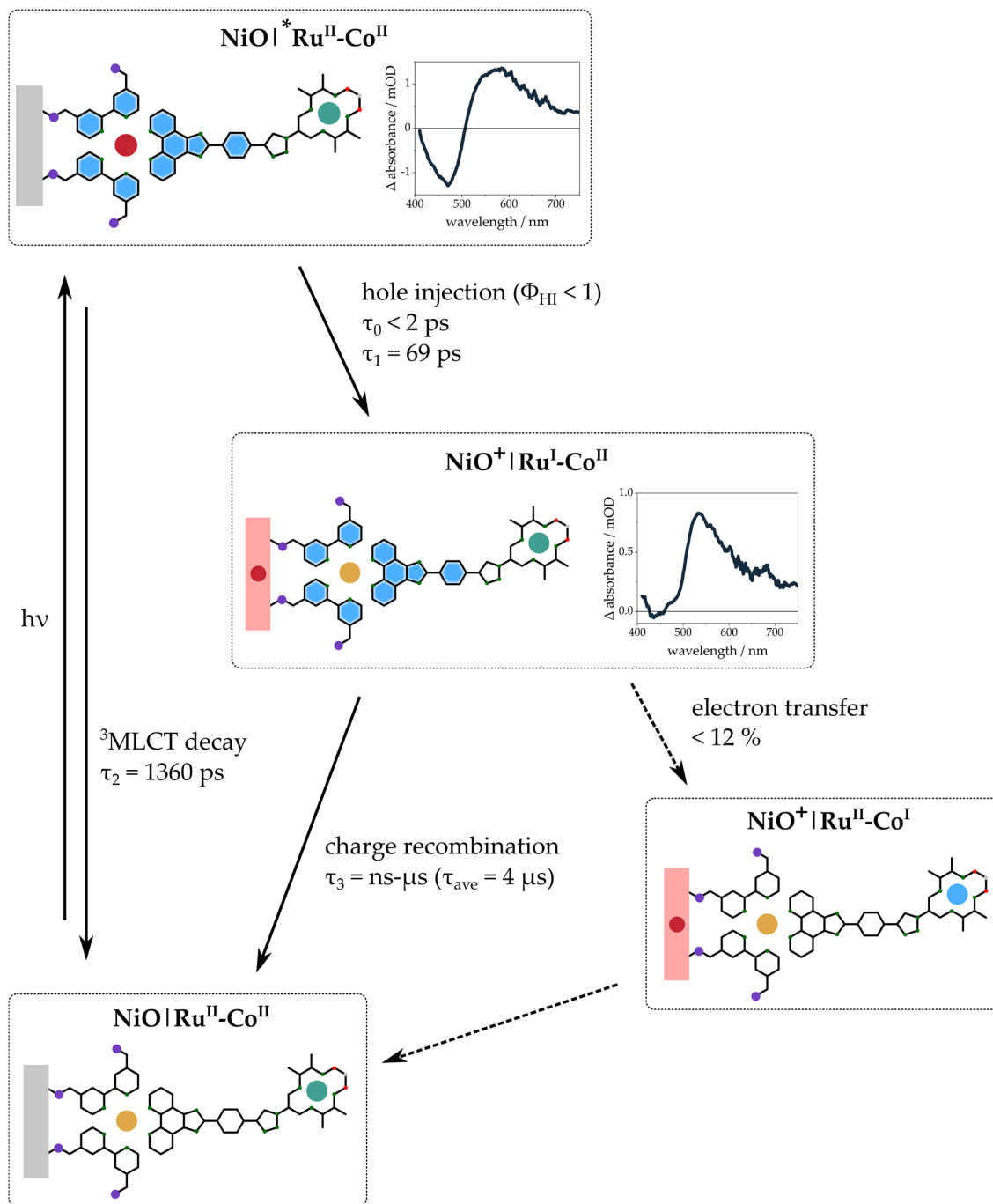


Figure 4.8: Scheme showing the light-induced processes in a NiO films sensitized with **RuCo** at an applied potential of  $-0.74 \text{ V vs. } \text{Fc}^{+/0}$ . Blue colouring indicates the localization of negative charge, e.g. an electron, while red colouring indicates the localization of positive charge, e.g. a hole.

The results confirm recent studies and thus consolidate the picture of the influence of the applied potential on the interfacial process kinetics in NiO films sensitized with Ru complexes, affirming the need to apply a potential to the NiO film to enable a long-lived charge separation due to the high amount of intragap trap states at the NiO film surface. This is prohibitive to the use of NiO as p-type SC material in DSPEC for bias-free water splitting as fast CR prevents catalytic turnover and thus decreases the DSPC activity. To overcome this, methods will have to be developed that eliminate the intragap trap states at the NiO film surface and can therefore eliminate the fast CR pathway. Instead, alternative p-type SC could also be developed that do not present such a high density of trap state. So far, the search for better-performing p-type SC materials has been difficult.

The TA-SEC results also suggest the existence of distinct slow and fast HI and CR pathways, depending on whether the excess electron density is localized on the anchoring or the extended ligand. This insight might help in the ligand design of future molecular systems by trying to localize the excess electron density even more strongly on the extended, non-anchoring ligand. This should furthermore lead to faster ET transfer to the acceptor unit.

On the issue of ET from the reduced dye to the cobalt catalyst, the results challenge the use of the triazole linker even further: despite the conjugated linker and long lifetime of the reduced donor unit, i.e. the Ru complex, no ET could be observed. This suggests that the triazole group is a poor conductor of charge, at least under the conditions present here. Therefore, future synthetic efforts should foremost be concerned with introducing a different linker structure that enables fast ET to the catalyst.



## 4.2 Organic covalent dye-catalyst assemblies

The main part of the work on DSPCs performed in this thesis was done on a series of dye-catalyst assemblies based on the organic push-pull dyes (**T1**, **T2R**) linked to cobalt catalysts (**Co**, **Cat1**) (Figure 4.9). All four combinations of the two different dyes with the two different cobalt catalysts were studied to investigate the respective influence of both building blocks on performance, under otherwise identical experimental conditions. The dyad **T1-Co** had been previously published,<sup>26</sup> but was re-examined under identical conditions to the other dyads to allow comparison to the newly synthesized dyads.

As mentioned in section 3.2, introducing the rigid CPDT linker led to a bathochromic and hypochromic shift in the absorption spectrum ( $\lambda_{\max} = 493 \text{ nm}$ ,  $\epsilon_{\max} = 57,400 \text{ M}^{-1}\cdot\text{cm}^{-1}$  in MeOH) for **T2R** in comparison to **T1**, making **T2R** the better light-absorbing unit, as observed before in the literature.<sup>126,127</sup> The alkyl side chains on the linker were intended to prevent desorption of the compounds from the NiO surface by protecting the anchoring groups from the aqueous electrolyte.<sup>24,205</sup> The catalyst **Cat1** has shown good activity and especially stability for photocatalytic proton reduction in aqueous solution.<sup>15,83,85,128,206–208</sup> The stability is conferred to the complex by its macrocyclic ligand that resists decomplexation and hydrolysis, while cobaloximes-based catalyst such as **Co** are known to decompose under aqueous photocatalytic conditions via demetallation,<sup>209</sup> hydrolysis and/or reduction of the oxime-based ligands,<sup>17,82,210,211</sup> as already observed for **RuCo**.

For these dyads, and especially for the best-performing **T2R-Cat1**, the wide range of analytical and spectroscopic techniques mentioned in the introductory paragraph were used to determine their activity, stability, degradation processes and investigate the light-induced processes. Where possible, time-resolved measurements were conducted at the operando potential to reflect the system's behaviour in operando.

The NiO photocathodes were prepared by spin-coating and sintering a F108-templated NiCl<sub>2</sub> sol-gel<sup>26,90,100</sup> to give 4-layered films with a thickness of  $880 \pm 170 \text{ nm}$  as determined by scanning electron microscopy. The films were sensitized by soaking for 24 h in methanolic solutions of the deprotected dyes and dyads. The grafting densities, determined by desorption of the molecules from the surface followed by measuring UV-Vis absorption spectra of the resulting solution, were in the range of 6 to 14 nmol·cm<sup>-2</sup>, similar to those observed in literature on other dye-sensitized NiO films.<sup>26,79,87,121</sup> As the grafting density varies between films and especially between different batches of prepared NiO, the grafting density was determined for each

prepared film individually to accurately determine the TON values of hydrogen production for each film.

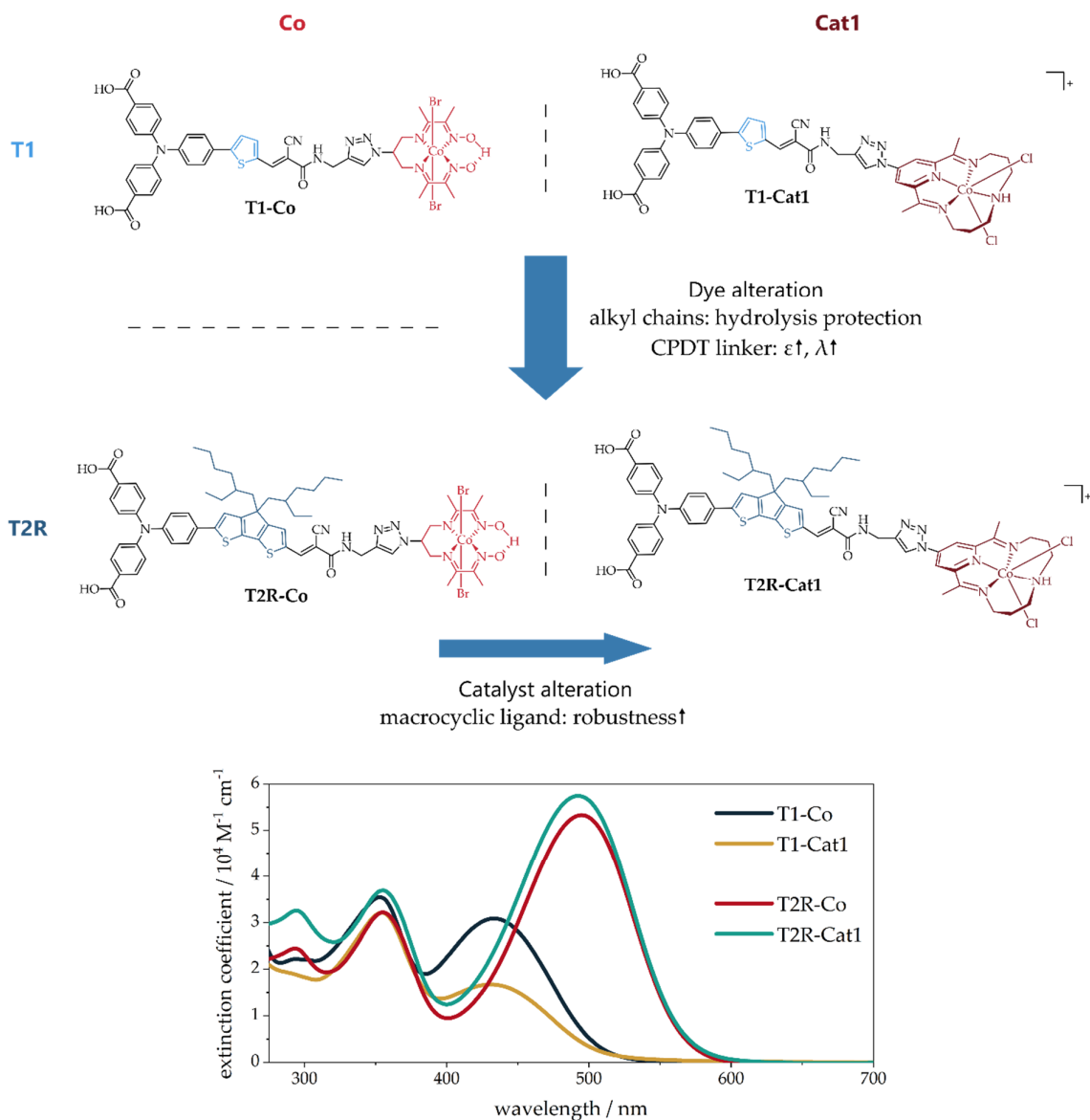


Figure 4.9: Chemical structures of the organic dye-catalyst dyads studied in this work and their UV-Vis absorption spectra in DMF (T1 dyads) and MeOH (T2R dyads).

### 4.2.1 (Photo-)electrochemistry and hydrogen production activity

In photoelectrochemical experiments in 2-(N-morpholino)ethanesulfonic acid buffer at pH 5.5, all dyads showed a photocurrent produced by irradiation with visible light. In linear scan voltammograms, photocurrent is observed below an applied potential of ca. 0.95 V vs. relative hydrogen electrode (RHE) and increases substantially below 0.5 V vs. RHE (-0.06 V vs. Ag/AgCl). All chronoamperometric measurements were carried out at -0.4 V vs. Ag/AgCl applied potential (0.14 V vs. RHE). In chronoamperometric experiments under chopped light irradiation, cathodic and anodic current spikes were detected upon turning the light on and off, respectively. This was ascribed to charge accumulation at the electrode-electrolyte interface and will be explained in the section on TA-SEC measurements. NiO films sensitized with just the dyes **T1** and **T2R** show very low photocurrents, which is enhanced ten-fold by the introduction of the **Cat1** catalyst in the dyads with up to  $-6.3 \mu\text{A}\cdot\text{cm}^{-2}$  for **T2R-Cat1**-sensitized films after 20 minutes (Figure 4.10). Interestingly, the **T1-Co** dyad initially showed by far the highest photocurrent which decayed rapidly. While it is not entirely clear why this dyad shows this behaviour, it might be a product of a fast degradation of the catalyst unit, as the hydrogen production – the activity of the system – does not correlate with the high photocurrent. To compare the intrinsic activity of the dyads, the photocurrent was normalized to the grafting density of the photocathodes: the **Cat1** and **T2R** dyads showed slower decay in photocurrent and higher overall photocurrent than their **Co** and **T1** counterparts, respectively and cumulatively: on average, the **Cat1** dyads produced 3.2 times higher current than the **Co** dyads and the **T2R** dyads 1.7 times as much as the **T1** dyads, for a total 5.4-fold increase of **T2R-Cat1** over **T1-Co**, making **T2R-Cat1** the most active dyad.

This was also true when looking at the hydrogen produced, where **T2R-Cat1** performed best both in terms of activity – the rate of hydrogen production – and stability – the duration of hydrogen production. After the first four hours of irradiation, the **Cat1** dyads achieved TON values for hydrogen production of  $13 \pm 1$  (**T1-Cat1**) and  $22 \pm 7$  (**T2R-Cat1**) and Faradaic efficiencies around 65 %. The activity of the **Co** dyads was much lower, with TON values below 2 and Faradaic efficiencies of  $\approx 10 \%$ , as observed before for dyads based on the same diimine dioxime catalysts.<sup>26,27,87</sup> Continuing irradiation for a total of 22 hours almost doubled the TON values for the **Cat1** systems, while the **Co** dyads showed no increase in produced hydrogen, meaning they had lost their activity during the first 4 hours, as also observed for **RuCo**. Thus, after 22 hours, the **Cat1** dyads produced 26 times more hydrogen than their **Co** counterparts. This is largely thanks to the high increase in Faradaic efficiency and

long-term stability of **Cat1** in aqueous medium, as already observed in solution photocatalytic studies;<sup>83</sup> and which is more generally observed for polypyridinic and aminopyridinic cobalt catalysts.<sup>83,115,212–214</sup> The low Faradaic efficiency of **Co**, on the other hand, could be a result of the various degradation processes that plague cobaloximes-based catalysts.<sup>17,82,209–211</sup>

In addition, the **T2R** dyads showed 1.7-fold higher hydrogen production than their **T1** analogues, correlating with the higher photocurrent. The individual influence of both the catalyst and dye units could thus be quantified. It becomes clear that the nature of the catalytic centre was key to the photocathode performance, much more than the exact dye structure.

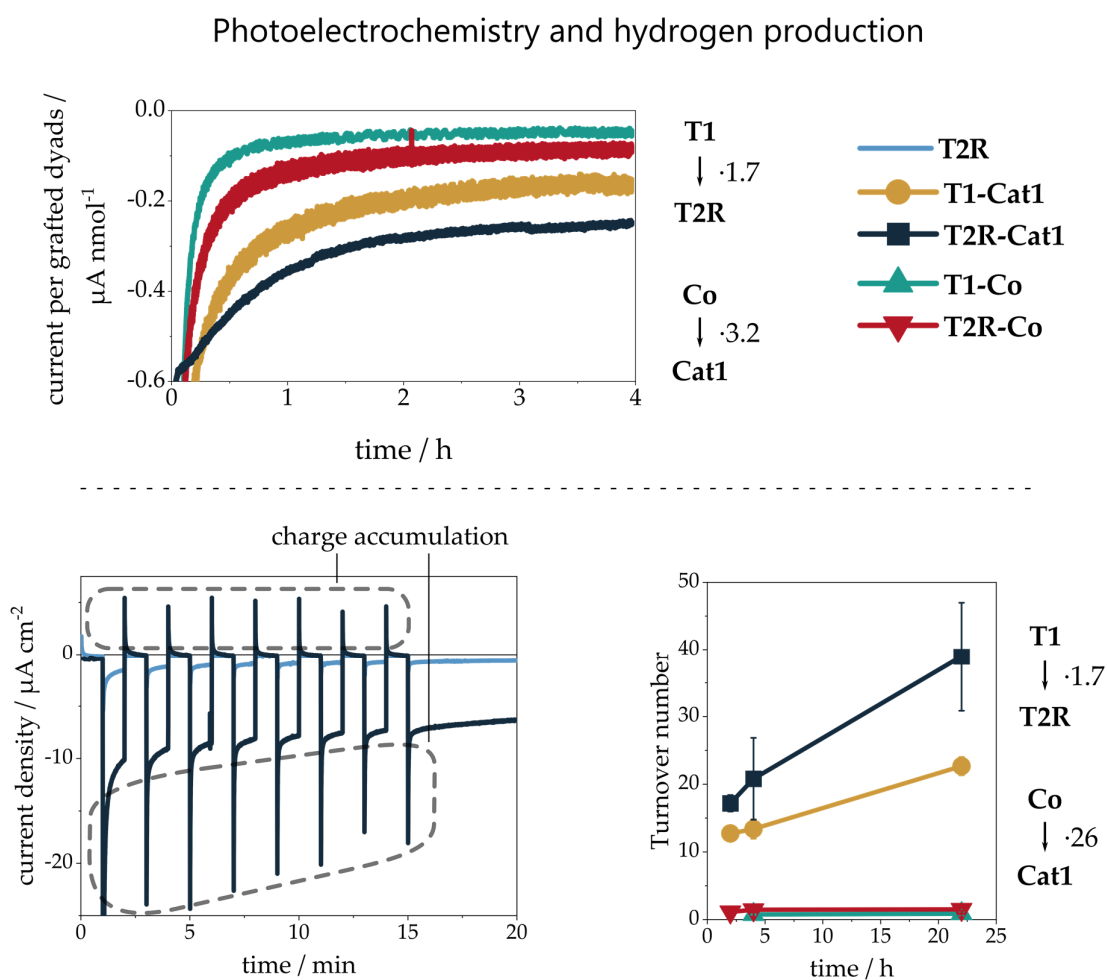


Figure 4.10: Results of the photoelectrochemical measurements of the organic dye-catalyst dyads. Top: Chronoamperometry during the first four hours of measurement, normalized to the amount of grafted dyad. Bottom left: Chronoamperometry under chopped light irradiation, showing the current spikes due to charge accumulation on the dye. Bottom right: TON of produced hydrogen over 22 hours.

## 4.2.2 Operando and post-operando characterization

To evaluate the nature and the kinetics of the deactivation processes of the photocathodes, they were studied post-operando by ICP-MS and UV-Vis spectroscopy as well as in-operando by time-resolved UV-Vis spectroelectrochemistry. Post-operando UV-Vis spectra of solutions obtained by desorption from the used films revealed that the  $\pi$ - $\pi^*$  band on the TPA was only slightly reduced in intensity, more so for **T1** than for the **T2R** systems. As a reduction in band intensity can be attributed to desorption from the film surface during operation, it seems that desorption was no major issue affecting the stability of the systems. The increased resistance of the **T2R** systems against desorption confirmed the design choice of using hydrophobic alkyl chains to protect the anchoring groups from hydrolysis by the aqueous electrolyte.<sup>24</sup> The low solubility of the organic compounds in water can be another factor improving the stability of the anchorage.

At the same time, the ICT band shows a sharp decrease in intensity while a new band appears at higher energies. Time-resolved UV-Vis SEC experiments under operando conditions (Figure 4.11) showed that i) the spectral changes take place only in photoelectrochemical conditions, i.e. with both applied potential and irradiation, and ii) that they do so with characteristic time constants of 1 and 90 min for **T2R-Cat1**, and 0.75 and 21 min for **T2R**. Irradiation alone led to a slight spectral change attributed to photoisomerization on the cyanoacrylate double bond,<sup>113</sup> while the applied potential by itself did not cause any changes. UV-Vis SEC of the **T2R** and **T1** dye in dry ACN shows an identical irreversible spectral change upon reduction of the dyes. In conclusion, the dye structure degrades in its reduced state irrespective of the surrounding solvent. The exact structure of the degradation product could not be determined, although the observations that i) the  $\pi$ - $\pi^*$  absorption of the triarylamine group is still present, and ii) a similar alteration is observed for **T1** and **T2R** under reductive conditions suggest that the degradation occurs on the acceptor group of the push-pull structures, i.e. the cyanoacrylate/cyanoacrylamide groups. Since **T2R** showed faster degradation kinetics than **T2R-Cat1**, it seems that there is an additional process competing with degradation in the dyad, which TA-SEC measurements showed was ET to the catalyst (see section 4.2.3).

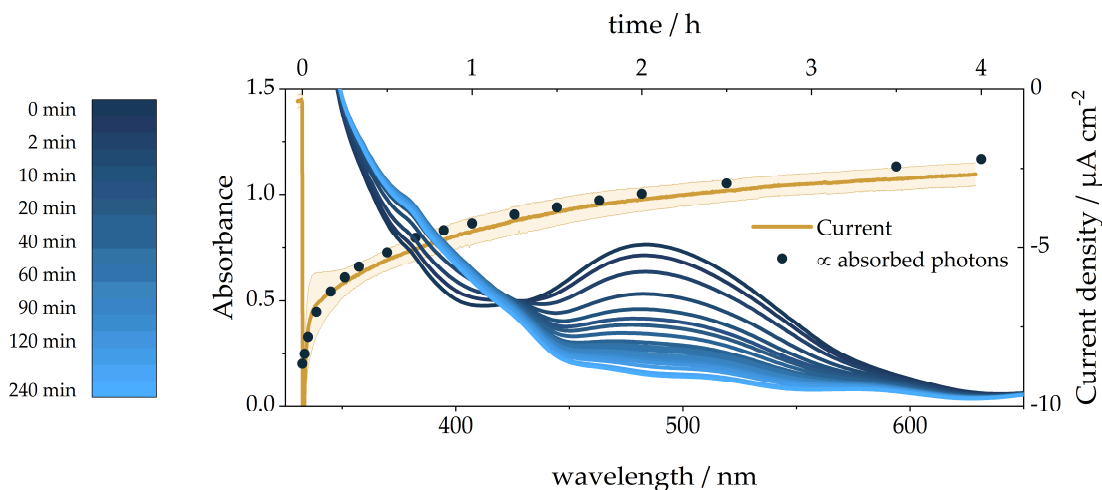


Figure 4.11: In-operando characterization of NiO films sensitized with **T2R-Cat1**: UV-Vis spectra recorded during four hours under operando conditions (blue spectra) and the average current density of four different **T2R-Cat1**-sensitized NiO films plotted against  $1-10^{-A}$ , where  $A$  is the integrated absorbance in the visible range recorded during the operando UV-Vis measurements after subtracting the NiO background.  $1-10^{-A}$  is proportional to the number of absorbed photons and was scaled to the current density at 600 s to account for the initial current spike.

In addition, post-operando ICP-MS measurements performed for **T2R-Cat1** showed that a high amount of cobalt is lost during operation (84 % after 4 hours, 93 % after 22 h), indicating a loss of the catalytic unit or demetallation. The clear correlation found between the photocurrent decrease during the 4-hour photoelectrochemical measurement, the loss of absorbance, and the loss of Co from the surface, strongly suggests that i) the dye degradation is the main deactivation process in our system and ii) it involves a bond breaking leading to the detachment of the catalytic centre from the assembly. The dyads remaining intact on the surface (16 % after 4 h) account for the H<sub>2</sub>-evolving activity still detected after 4 hours under irradiation. Assuming the correlation between the photocurrent decrease and the loss of catalytic unit holds true, the average surface concentration of intact dyads present during the first four hours of activity was estimated to be  $2.0 \pm 0.4 \text{ nmol}\cdot\text{cm}^{-2}$ , leading to a more accurate TON value of  $94 \pm 16$  per active dyad, corresponding to a TOF of  $6.5\cdot 10^{-3} \text{ s}^{-1}$  ( $0.4 \text{ min}^{-1}$ ). By contrast to other studies, where dye/catalyst desorption from the SC film is the main reported deactivation process,<sup>28,29,54,77</sup> only a low amount of dyads is released into solution.

### 4.2.3 TA-SEC

As for **RuCo**, TA-SEC measurements on dye-sensitized NiO films were also carried out with the best-performing system **T2R-Cat1** and the **T2R** dye as a reference. Again, TA spectra were recorded at OCP, the operando potential ( $-0.74$  V vs.  $\text{Fc}^{+/0} \triangleq -0.4$  V vs Ag/AgCl) where the cobalt catalyst is reduced to the  $\text{Co}^{\text{II}}$  state and a more reductive potential ( $-1.15$  V vs.  $\text{Fc}^{+/0}$ ) where it is reduced to the  $\text{Co}^{\text{I}}$  state. The latter serves as a reference measurement since ET is not thermodynamically possible from the reduced dye to the  $\text{Co}^{\text{I}}$  state of the catalyst.

As the spectral shape and initial kinetics of **T2R-Cat1** and **T2R**-sensitized films are identical, they will be discussed together. The TA spectra initially show GSB at 490 nm and ESA at  $> 550$  nm (Figure 4.12). The ESA evolves in some ps to form a band at 620 nm. At OCP, this signal decays completely within 1.6 ns together with the GSB. At negative applied potentials, it is increasingly long-lived and reaches the ns-ms scale. In addition, **T2R-Cat1**-sensitized films showed a signal at 430 nm on the ns- $\mu\text{s}$  timescale which did not decay completely in 1 ms and which was absent at all other conditions (**T2R** at all potentials and **T2R-Cat1** at  $-1.15$  V vs.  $\text{Fc}^{+/0}$ ).

Kinetic and spectral analysis of the data showed that the initially populated excited state undergoes ultrafast HI in  $< 1$  ps to form the primary CSS with an electron localized on the organic push-pull dye. On this timescale the TA spectra change from that characteristic of the vibrationally hot, excited state of the dye (GSB at around 500 nm and ESA maximum at 680 nm) to that of the reduced dye, which produces the band observed at 620 nm. This was supported by UV-Vis spectroelectrochemical measurements. Contrary to the case of **Ru(Co)**, no influence of the applied potential on the principal HI kinetics was observed since the kinetics are already ultrafast even at OCP. This can be explained by the closer spatial proximity of the HOMO to the NiO surface and the absence of retarding factors such as electron density on the anchoring ligands, as in the case of **Ru(Co)**. In general, such ultrafast HI is often observed for organic dyes on NiO.<sup>52,54,61,77,101,125,178–184,186,190–192</sup> A second process taking place in some ps spectrally shows a further decay of residual excited state of the dye, which probably occurs through a slower HI component and fast CR, since amplitude and rate decrease at more negative applied potential. The third process, and the most affected by the applied potential, is CR: the characteristic time constant for CR increases from  $\approx 150$  ps at OCP to  $\gg 2$  ns at applied potential. At  $-0.74$  V, the average lifetime of the primary CSS, obtained by a multiexponential fit of the non-exponential decay, was 28  $\mu\text{s}$  for **T2R** and 7  $\mu\text{s}$  for **T2R-Cat1**, which at  $-1.15$  V vs  $\text{Fc}^{+/0}$  increased to 131  $\mu\text{s}$  (67% relative

amplitude) and  $< 1$  ms (33 % rel. ampl.) for **T2R** and similar values for **T2R-Cat1**. It shows the same non-exponential behaviour as observed for **RuCo** and in literature.<sup>107,108</sup> The explanation for the influence of the applied potential on the CR kinetics is the same as that presented for **Ru(Co)** (section 4.1.2.4).

Most importantly, the signal observed at 430 nm is caused by the  $\text{Co}^{\text{I}}$  state of the catalyst unit, as confirmed by UV-Vis SEC measurements. The presence of this signal confirms ET from the reduced state of the dye to the catalyst to form the catalytically active state. The major part of this ET takes place in 1.6-20 ns and is thus much slower than HI. Therefore, in **T2R-Cat1**-sensitized NiO films, charging of the catalyst occurs through a reductive quenching mechanism, in which the reduced dye is formed first, and ET is thermally activated. The sub-20 ns ET time constant is quite fast compared to other examples of thermally activated ET in triazole-bridged donor-acceptor dyads in solution, which takes place on the ns- $\mu\text{s}$  timescale.<sup>132-136</sup> ET from a Ru dye to a Ni catalyst in a layer-by-layer assembly was determined to occur before 50 ns, either from the excited or reduced state of the dye.<sup>38</sup> A recent study on a Ru-Re system anchored on NiO by electropolymerization also showed ET on the ns- $\mu\text{s}$  scale ( $< 10$   $\mu\text{s}$ ), which was attributed to electron tunnelling between the components due to the presence of an electronically insulating alkyl linker,<sup>200</sup> as is also the case in **T2R-Cat1**. This casts doubts on the design of the **T2R-Cat1** dyad, since its linker contains both an insulating methylene group and a triazole group, the use of which as a linker in donor-acceptor dyads is disputed in literature (see section 4.1.2.5). This translates into a slow ET process in comparison to some examples of co-grafted systems where ET from the dye (excited or reduced state) to the catalyst was observed on the ps timescale.<sup>61,182</sup>

Assuming the faster decay of the primary CSS in **T2R-Cat1** compared to **T2R** is due to a slower ET process, this process would take place in a non-exponential fashion with an average time constant of 9  $\mu\text{s}$ . However, the ET observed is not quantitative since a significant amount of signal produced by the reduced dye remains in parallel to the signal of reduced catalyst.

The secondary CSS with the electron localized on the cobalt catalyst decays in a non-exponential fashion with a lifetime of 30  $\mu\text{s}$  (84 % rel. ampl.) and  $< 1$  ms (16% rel. ampl.). The CR from this state is therefore slower than that from the reduced dye at this potential, which can be explained with the lower driving force for recombination and the higher distance between the catalyst and the NiO surface.



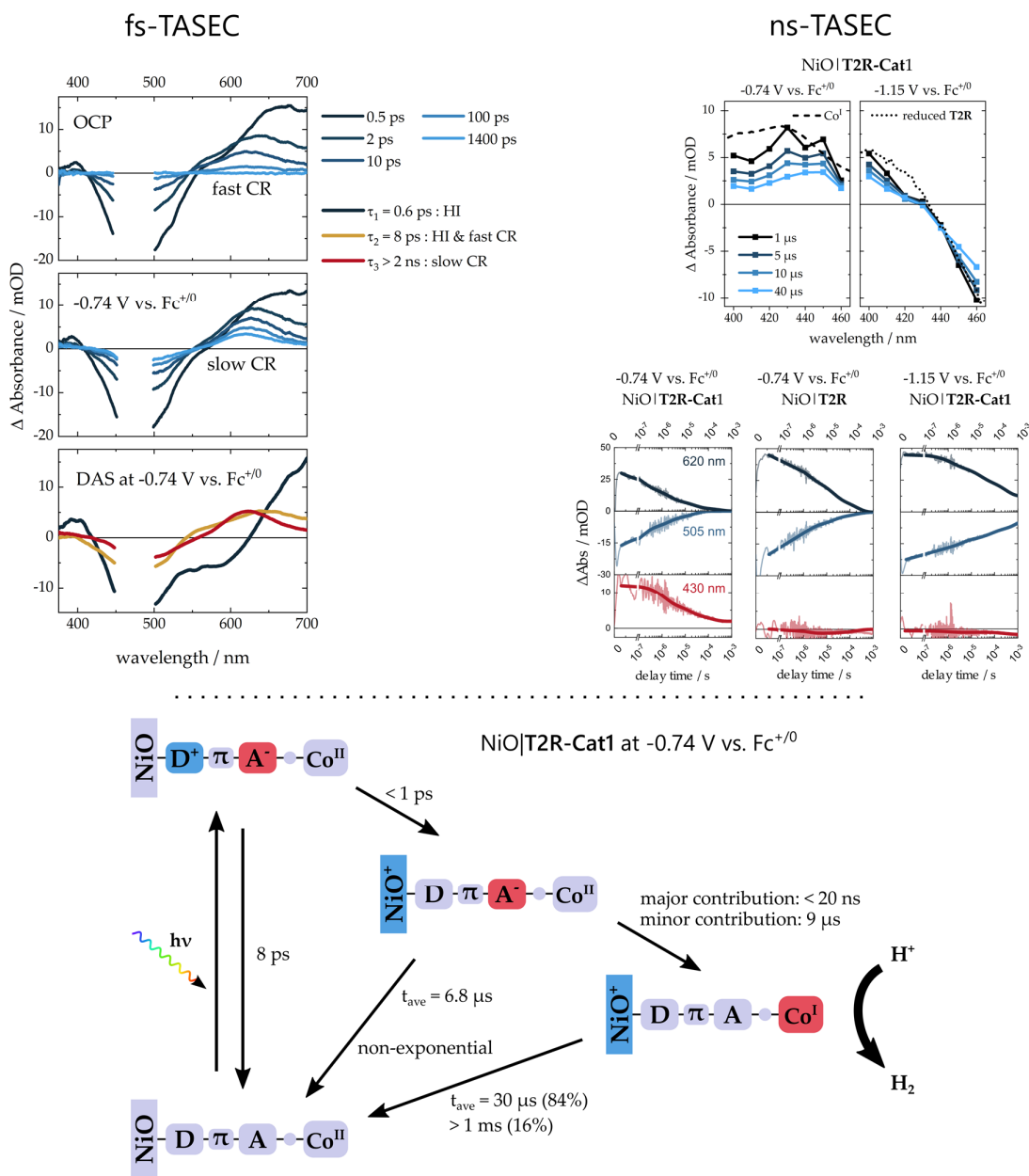


Figure 4.12: Results of TA-SEC measurements of NiO films sensitized with **T2R-Cat1** and **T2R**. Left: fs-TA-SEC spectra at OCP and -0.74 V vs.  $\text{Fc}^{+/0}$  applied potential as well as DAS at -0.74 V vs.  $\text{Fc}^{+/0}$  applied potential. Right: ns-TA-SEC spectra at -0.74 V and -1.15 V vs.  $\text{Fc}^{+/0}$  with reference spectra of the  $\text{Co}^{\text{I}}$  state of **Cat1** (dashed) and of the one-electron reduced dye (dotted). Bottom: Schematic representation of the light-induced processes taking place in a NiO|**T2RCat1** photocathode at -0.74 V vs.  $\text{Fc}^{+/0}$  applied potential.

## 4.2.4 Summary and Outlook

In summary, the use of TON as a metric for hydrogen evolution while using standardized experimental conditions to assess the performances of the dyad-sensitized photocathodes, together with in-depth post- and in-operando characterization including especially TA-SEC measurements, allowed a detailed comparison of their activity, stability and the underlying photophysical processes. A comparison of the activity metrics such as photocurrent, the amount of hydrogen produced and TON with the state of the art in the literature on DSPCs for hydrogen production is difficult as these parameters vary considerably from one study to another, preventing the establishment of a sound structure-activity relationship, which is necessary for a rational improvement of the molecular systems. By using TON as a measure of the intrinsic activity of the dye-catalyst molecules and systematically varying both the dye and catalyst unit, we were able to quantify the respective contribution of each unit to the overall hydrogen production.

In spite of the difficulty of comparison with literature values, it can be stated that the **T2R-Cat1**-sensitized photocathode favourably competes with the best-performing dye-sensitized NiO photocathodes for hydrogen production in the literature in terms of Faradaic efficiency, stability and hydrogen produced.<sup>19,28,56</sup> This is certainly the case when comparing to other dye-catalyst assemblies based on Earth-abundant materials, none of which have achieved TON or amounts of produced hydrogen close to that of **T2R-Cat1**, with typically more than ten times less. The only superior assemblies used Pd and Pt catalysts and/or Ru complexes as PS.<sup>46,80</sup>

The TA-SEC results on sensitized NiO films obtained in this thesis present a novelty as it is the first time that i) an organic dye and ii) a functional hydrogen-evolving NiO photocathode, especially using a dye-catalyst dyad, were studied using this technique. In addition, it was the first time a long-lived  $\text{Co}^{\text{I}}$  state of a cobalt HER catalyst was observed on a dye-sensitized NiO photocathode and its lifetime could be determined. Crucially, the observed lifetime of the  $\text{Co}^{\text{I}}$  state of up to  $> 1$  ms is enough to reach the timescale on which catalysis occurs, giving further support for the observed role for activity of the cobalt catalyst.

From the post- and operando characterization, two main impediments for the performance were identified:

*The degradation of the dye structure in the reduced state which leads to a loss of absorption and a loss of the catalyst unit and therefore strongly limits the stability of the assembly.* This contrasts with the existing literature, where desorption from the film surface is given as the main deactivation process.<sup>28,29,54,77</sup> To overcome this, a more robust acceptor group than the cyanoacrylate group should be introduced in the assembly that does not easily degrade, while still fulfilling the energetic requirements for ET to the catalyst.

*The low efficiency of the ET from the reduced dye to the catalyst.* This non-quantitative ET leads to an accumulation of charges on the dye that are not consumed by catalysis and thus produce the current spikes observed in the chopped light chronoamperometric experiments by charging and discharging of the electrode-electrolyte interface. This accumulation in turn leads to degradation of the dye due to its instability. Similar observations were recently made for organic SC photocathodes with a PDI acceptor polymer and an upper limit for charge accumulation was determined for stable long-term operation, above which the PDI underwent irreversible change.<sup>114</sup> In our case, the accumulated reduced state of the dye is not stable and yields over the course of 2 to 4 hours a modified assembly without the catalyst unit and with a very low light harvesting efficiency in the visible region. This process is clearly accelerated in the absence of the catalyst (**T2R** vs **T2R-Cat1** photocathode) which highlights that ET to the catalyst competes with the reduced dye alteration. A fast ET to the catalyst reduces the lifetime of the reduced dye and thereby protects it from degradation. Therefore, changing the dyad structure in a way that enables fast and quantitative ET to the catalyst will improve both the activity and the stability of the system at the same time which could lead to significantly increased hydrogen evolution.

These results also highlight the value of the TA-SEC measurements at operando potential which allow to determine the limiting processes and identify the weak points of the assembly. This is especially important since, as demonstrated here, a slow forward process can not only hinder activity of the assembly, but also compromise its long-term stability.

### 4.3 Comparing **RuCo** to **T2R-Cat1**

In the TA-SEC experiments, both **Ru(Co)** and **T2R(-Cat1)** show a potential dependence of HI and CR. In **Ru(Co)**, the HI kinetics show a stronger dependence, probably due to the generally slower HI and the different localization of the excited electron on the ligands, whereas in **T2R** HI is ultrafast at all potentials. As the time constant for HI is much lower than the excited state lifetime in all cases, it becomes obvious that the excited state lifetime of the dye does not have an impact on the system performance, but rather the lifetime of the CSS formed by HI. Here, it is interesting to observe that the organic dye **T2R** shows longer lifetimes of the CSS than **Ru**. This is probably related to the localization of the excess electron in the reduced state: while in **T2R** it is very localized on the cyanoacrylate acceptor group, in **Ru** it seems to be partially localized on the anchoring bpy ligands, whose closer proximity to the NiO surface could lead to faster CR. Therefore, the CSS lifetime of **Ru** might be improved by increasing the energy difference between the extended ligand and the bpy ligands or increasing the spatial distance, both of which could be achieved through an additional acceptor unit appended to the extended ligand. This strategy yielded very long CSS lifetimes in a Ru(bpy)<sub>2</sub>bpy-NDI complex on NiO.<sup>108</sup> Alternatively, if very fast ET to the catalyst unit can be promoted by a different linker architecture, this would serve the same purpose as the additional acceptor group.

A puzzling observation is that the CSS lifetime of **T2R**, in addition to being higher, is also *more affected* by the applied potential than **Ru** – that is,  $\frac{d(\tau)}{d(E)}$  is greater for **T2R** than for **Ru**: when increasing the negative bias from -0.74 V to -1.15 V vs Fc<sup>+0</sup>, the lifetime of the CSS of **Ru** less than doubled, while it increased more than 15-fold for **T2R**. The energy levels of the reduced dyes cannot play a role since they differ only by ca. 100 mV and are still about 500 mV negative of the most negative applied bias. Thus, despite the much shorter excited state lifetime of **T2R** in solution, the light-induced processes are more favourable than for **Ru**, including faster HI and slower CR, when immobilized on NiO.

Since ET from the reduced dye to the catalyst is a crucial process, a comparison of ET efficiency of the two dyads studied by TA-SEC is insightful. However, since both the dye and catalyst unit as well as the exact linker structure is different in the two dyads, the validity of this comparison and the assignment of the kinetic differences to certain structural motives is limited. However, since ET could not be observed spectroscopically for **RuCo** while for **T2R-Cat1** it was observed in < 20 ns, even though incomplete, there are obviously structural factors in **T2R-Cat1** that promote ET. Since

the linker is shorter and fully conjugated in **RuCo**, which should more easily promote ET in comparison to the longer and electronically isolating linker in **T2R-Cat1**, the exact linker structure does not seem to be the decisive factor here. One issue might be the localization of the excess charge: in **T2R-Cat1** it is localized on the acceptor group very close to the linker, while in **RuCo** part of the charge seems to be localized on the anchoring bpy groups far away from the linker. Another factor could be the structure of the cobalt complex and especially its ligands: while the diimine-dioxime ligand of **Co** is bound to the linker via a propyl chain, **Cat1** is connected at the pyridine unit of the macrocyclic ligand. This electron-poor unit with a conjugated  $\pi$ -system should be a much better acceptor unit than the alkyl chain of **Co**. In addition, in **Co** the reductions are exclusively metal-based, while for **Cat1** a ligand-based reduction is proposed for the formal  $\text{Co}^{\text{I}}$  state in some of the reported studies.<sup>84</sup> Therefore, the electron-accepting molecular orbital could be much bigger in **Cat1** leading to more efficient ET. To fully understand these influences, TA-SEC measurements on **T2R-Co** and **Ru-Cat1** would help to understand the exact role played by the nature of the catalyst unit in the ET process.

Another advantage of the organic systems is the higher grafting density achieved in comparison to the Ru complexes, which can be attributed to the higher steric demand of the **Ru** core compared to the planar **T2R**. The major drawback for the organic dye is its instability in the reduced state and therefore under photoelectrochemical conditions which leads to its fast degradation. However, the Ru complexes are desorbed much more easily from the NiO film surface, possibly because they are cationic which could lead to a higher solubility in water than the organic dyes which are insoluble.

In conclusion, the more favourable kinetics of the light-induced processes for **T2R**, in addition to the better light absorption properties and the use of Earth-abundant materials for its synthesis, makes **T2R** the more attractive light-harvesting unit, if the issues with the lack of stability of its reduced state can be resolved. **Cat1** is clearly a better catalyst unit in comparison to **Co** due to its higher stability in aqueous conditions, but also possibly by being a better electron acceptor for ET from the reduced dye. In the future, the dye structures should be optimized for faster and quantitative ET to the catalyst unit, which is the main impediment for high activity in the current dyads. This would further serve to protect the dyes from degradation in their reduced state.

## 5 Summary

Dye-sensitized photoelectrochemical cells represent a highly promising technology for the production of solar fuels via light-driven water splitting as an integral part of a carbon-neutral economy. In that context, the design of more performant dye-catalyst assemblies is highly demanded as they should allow to precisely control over the excited state processes, especially ET. However, detailed investigations on the light-induced processes of dyad-sensitized photocathodes under operando conditions are scarce in the literature, and few studies have addressed in depth the degradation processes in those photocathodes.

Therefore, this work aimed at providing a comprehensive understanding of the performances of hydrogen-evolving DSPC based on a series of molecular dye-catalyst assemblies varying by the nature of the dye and the catalyst, including the elucidation of the systems' weak points and bottlenecks for hydrogen production. To this end, a full characterization of the photoelectrochemistry and activity of the photocathodes was combined with the study of the excited state processes both in solution and on films to gain a full understanding of the systems and their performance-limiting factors. Especially important was the determination of the lifetime of the CSS and the kinetics of the ET to the catalyst unit. The mainly studied compounds were a series of four noble-metal free dyads which varied in the nature of the push-pull organic dye (**T1** or **T2R**) and in that of the catalyst for proton reduction (**Co** or **Cat1**). Assessing the activity of all four combinations enabled the determination of each part's contribution to the overall performance and therefore to link the molecular structure to the activity of the system. The elucidation of such a structure-activity relationship is important to be able to rationally improve the molecular structure of the dyads. The best-performing system **T2R-Cat1** was studied in detail, notably including the excited state processes at applied potential by TA-SEC and post- and in-operando measurements to determine the deactivation pathways and kinetics. In addition, NiO photocathodes sensitized with a Ruthenium-cobalt dyad were studied by TA-SEC for comparison.

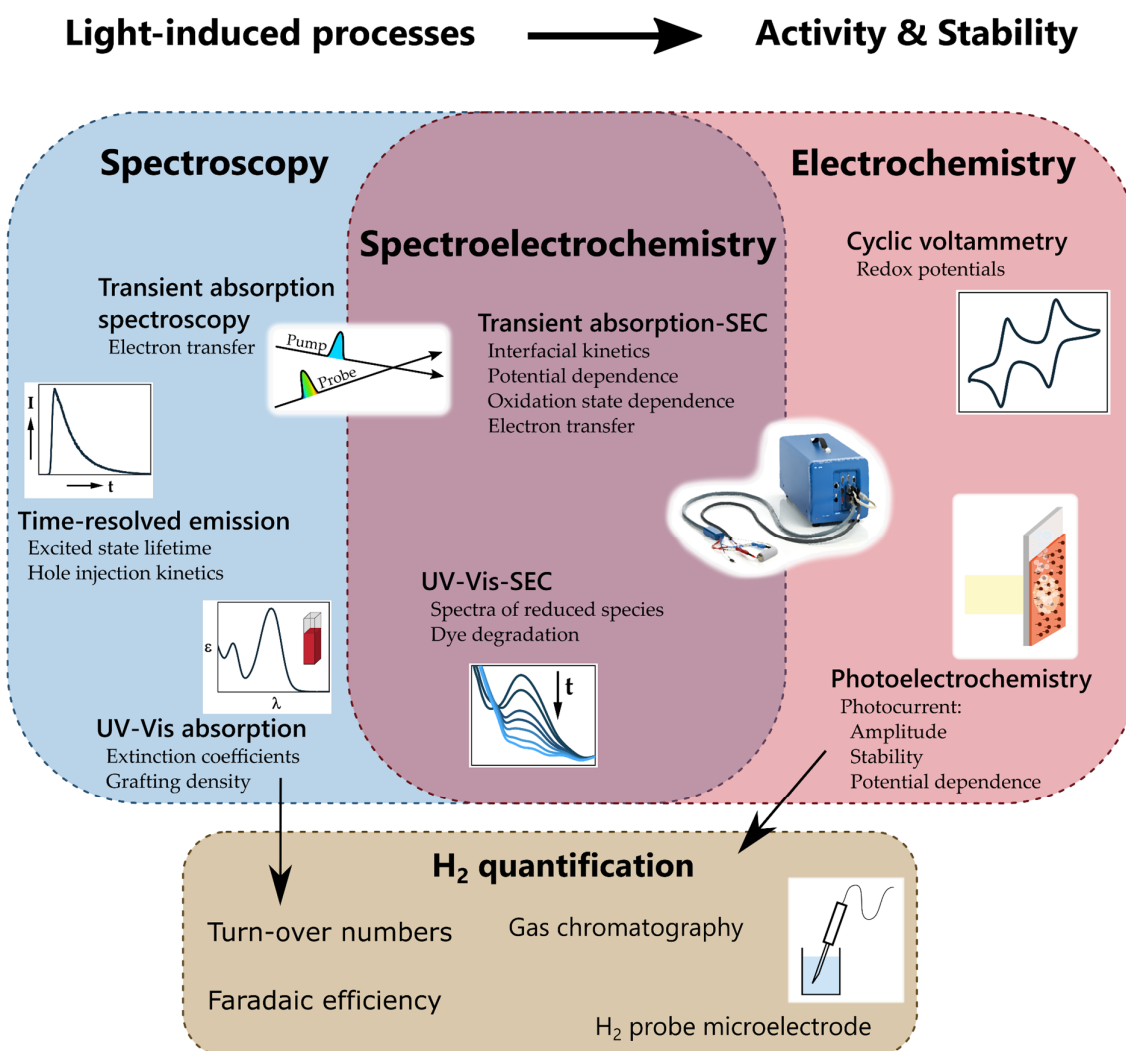


Figure 5.1. Schematic representation of the principal characterization techniques used in this work on the DSPCs.

The first important part of the work was the investigation of the photophysics of the organic dyes and dyads in solution. The dyad **T1-Co**, which had already shown promising performance in a functional H<sub>2</sub>-evolving NiO photocathode, was studied by TA spectroscopy to identify the light-induced processes and the possible ET to the catalyst. The **T1** dye underwent ultrafast relaxation to the thermally relaxed excited singlet state, from which it decayed to the ground state in the sub-ns to ns timescale. To access all oxidation states of the catalyst in the dyad, the measurements were carried out at applied potential (TA-SEC). Despite the emission quenching and reduced excited state lifetime in the dyad compared to the dye, ET in the excited state could not be observed, neither directly by a spectral contribution of the reduced cobalt complex nor indirectly by a potential dependence of the kinetics. The faster excited state decay in the dyad can be explained by an increased density of vibrational modes

upon addition of the cobalt moiety or Dexter energy transfer from the excited donor chromophore to short-lived cobalt-centered dd-states. The study showed that in photocathodes sensitized with **T1-Co**, the oxidative quenching pathway is not active, but rather a reductive quenching pathway where the electron is transferred from the reduced dye, produced by HI, to the catalyst. Furthermore, the TA-SEC technique enables the investigation of the light-induced processes at different oxidation states which is important in the context of systems designed for photo-induced multi-electron catalysis such as proton reduction and water oxidation.

Additionally, the **T2R** dye and the dyads based on it were also studied in solution by TA spectroscopy. While the initial relaxation processes were identical to the **T1** systems, the dyads showed a markedly different behaviour from **T1-Co**, undergoing fast ISC to the long-lived excited triplet state of the dye, which did not occur in the dye alone. The fast ISC was explained by an interplay of both the rigid CPDT bridge and the cobalt catalyst, possibly involving higher energy states of the cobalt complex that lie between the singlet and triplet state energy of the **T2R** dye. This study showed how the interaction of different structures in a dye-catalyst assembly can lead to unexpected excited state behaviour that must be considered when designing a dye-catalyst dyad. The fast ISC induced by the Co complex observed here might open up new possibilities in the area of organic triplet sensitizers.

As part of the work on DSPCs, NiO films sensitized with **RuCo** were studied by TA-SEC to investigate the light-induced processes in the dyad and the potential dependence of the interfacial processes such as HI and CR. There are very few examples in the literature where this technique was applied, and this work was the first time it has been applied to NiO films sensitized with a dye-catalyst dyad that were functional for photoelectrochemical H<sub>2</sub> evolution. To this end, a dedicated spectroelectrochemistry cell was designed that enabled femtosecond-TA experiments on films with a precise applied potential under inert conditions that were stable for several hours and enabled us to measure TA-SEC spectra with good signal-to-noise ratio.

The TA-SEC data showed that HI occurs in a biphasic fashion with a sub-ps and a slower time constant with tens of picoseconds. The amplitude depended on the applied potential, favouring fast HI at more negative applied potential. Likewise, CR from the reduced Ru complex was affected by the applied potential, slowing down severely at negative applied potential: while at OCP a major contribution takes place on the same timescale as HI, preventing a build-up of charge-separated species, at



negative applied potentials it occurs on the ns- $\mu$ s timescale with average lifetimes of 3.6-5.2  $\mu$ s. All the interfacial processes were found to be non-exponential. The influence of the applied potential could be explained by the reduction of Ni<sup>3+</sup> defect states to Ni<sup>2+</sup>, corresponding to the filling of intragap trap states with electrons. This transformation of an electron-depleted to an electron-rich NiO surface leads to both accelerated HI and retarded CR. Most importantly, no ET from the reduced Ru complex to the catalyst was observed, putting the efficiency of the formation of the catalytically active state to below 12%, determined by the limit of detection of the setup, in line with the low activity for hydrogen evolution. These results highlight the importance of the applied potential on the light-induced processes on sensitized NiO photocathodes and revealed the inefficient ET as a weak point of the assembly. This is in contrast to the literature where a fast recombination process from the primary CSS is invoked to explain the lack of efficiency of the photocathodes since the photophysical measurements are carried out on dry films without an applied potential. It could not be established which factor prevented ET, whether the donor or acceptor units or the triazole linker. The TA-SEC results also suggest the existence of distinct slow and fast HI and CR pathways, depending on whether the excess electron density is localized on the anchoring or the extended ligand. This insight might help in the ligand design of future molecular systems by trying to localize the excess electron density even more strongly on the extended, non-anchoring ligand. This should furthermore lead to faster ET to the acceptor unit.

The main part of the work on NiO photocathodes was performed on organic dye-catalyst dyads. Cyclic voltammetry experiments showed that there is no interaction in the ground state between the dye and catalyst unit and that the oxidation potential of **T2R** is shifted negatively in comparison to **T1** due to the electron-rich CPDT linker. UV-Vis absorption spectra showed that this linker also caused a bathochromic and hyperchromic shift in the dye which made it the better light-absorbing unit. Then, the activity of the compounds when immobilized on NiO was studied in photoelectrochemical experiments in terms of photocurrent and hydrogen produced. The photocurrent increased in the order **T1-Co** < **T2R-Co** < **T1-Cat1** < **T2R-Cat1** with a total of 5-fold increase in current from **T1-Co** to **T2R-Cat1**. The amount of hydrogen produced follows the same trend with the **Cat1** dyads being significantly more productive than the **Co** dyads due to a much higher Faradaic efficiency. The individual contribution of the dye and catalyst units could thus be established to lead to a 26-fold increase for **Cat1** in comparison to **Co** and a 1.7-fold increase for **T2R** in comparison to **T1**, highlighting the decisive role of the catalyst. A crucial factor was the stability of the assemblies, with the **Cat1** dyads showing photocurrent and hydrogen evolution

after more than four hours, when the **Co** dyads are already inactive. This confirms the previously observed higher activity and especially stability for **Cat1** in homogeneous photocatalysis, but is in contrast to the literature on DSPC where desorption from the electrode surface is usually given as the main deactivation process.

The stability was further investigated by post- and in-operando measurements. The post-operando measurements revealed that the dyad loses both its main absorption band and the cobalt during operation. Time-resolved in-operando UV-Vis spectroelectrochemical experiments under operando conditions on the best-performing **T2R-Cat1** system, in combination with reductive UV-Vis SEC in organic solvent, showed that the **T2R** dye is unstable in its reduced state and degrades over the timescale of minutes to hours under operando conditions. From the available evidence, it seems that there is a bond breaking at the acceptor cyanoacrylate group that leads to the loss of the main charge-transfer band and the cobalt catalyst. On a positive note, the dyads did not easily desorb from the NiO surface due to hydrolysis, especially those based on **T2R**, ascribed to the protective effect of the hydrophobic alkyl side chains on the CPDT linker.

The light-induced processes in **T2R-Cat1**-sensitized NiO films were investigated by TA-SEC. Fast HI on the sub-ps timescale was observed that was unaffected by the applied potential, producing the first CSS. The CR kinetics from this state depended on the applied potential as observed also for **RuCo**, increasing from ca. 150 ps without applied potential to the  $\mu\text{s}$ -ms scale at applied potentials. Most importantly, ET from the reduced dye to the catalyst was observed within 20 ns after excitation and possibly a slower component on the  $\mu\text{s}$  timescale to form the catalytically active  $\text{Co}^{\text{I}}$  state. The  $\text{Co}^{\text{I}}$  state decayed on the  $\mu\text{s}$  scale ( $\tau = 30 \mu\text{s}$ ), with 16 % left after 1 ms. This is an important finding as it puts the lifetime of the catalytically state of the catalyst in the range of the timescale of catalysis. The ET to the catalyst was however not quantitative, leading to charge accumulation on the reduced dye and therefore ultimately to its degradation. Therefore, an improved molecular design of the dyad that assures fast and quantitative ET to the catalyst should solve both the issue of low activity and reductive degradation of the dye unit. These results also highlight the value of the TA-SEC measurements at operando potential which allow to determine the limiting processes and identify the weak points of the assembly. This is especially important since, as demonstrated here, a slow forward process can not only hinder activity of the assembly, but also compromise its long-term stability.

This dissertation thus provides key insights on the light-induced processes in NiO photocathodes sensitized with dye-catalyst dyads and their dependence on the

---

applied bias, together with an assessment of the photocathode performance and the deactivation processes and their kinetics. The obtained findings of the systems' weak points, especially that of very inefficient ET from the dye to the catalyst and the reductive degradation of the organic dye units, will help to rationally design dyads with improved activity and stability.

## 6 Zusammenfassung

Farbstoffsensibilisierte photoelektrochemische Zellen stellen eine vielversprechende Technologie für die Herstellung von solaren Brennstoffen durch lichtgetriebene Wasserspaltung als integraler Bestandteil einer kohlenstoffneutralen Wirtschaft dar. In diesem Zusammenhang ist das Design von leistungsfähigeren molekularen Farbstoff-Katalysator-Systemen (Dyaden) sehr gefragt, da sie eine präzise Kontrolle über die Prozesse im angeregten Zustand, insbesondere den Elektronentransfer, ermöglichen sollten. Detaillierte Untersuchungen zu den lichtinduzierten Prozessen von dyaden-sensibilisierten Photokathoden unter operando-Bedingungen sind in der Literatur jedoch rar, und nur wenige Studien haben sich eingehend mit den Degradationsprozessen in diesen Photokathoden beschäftigt.

Daher zielte diese Arbeit darauf ab, ein umfassendes Verständnis der Leistungen von wasserstoffproduzierenden DSPC auf der Basis einer Reihe von molekularen Farbstoff-Katalysator-Dyaden zu liefern, die sich durch die Art des Farbstoffs und des Katalysators unterschieden, einschließlich der Aufklärung der Schwachstellen und Engpässe der Systeme für die Wasserstoffproduktion. Zu diesem Zweck wurde eine vollständige Charakterisierung der Photoelektrochemie und Aktivität der Photokathoden mit der Untersuchung der Prozesse im angeregten Zustand sowohl in Lösung als auch auf Filmen kombiniert, um ein vollständiges Verständnis der Systeme und ihrer leistungsbegrenzenden Faktoren zu erlangen. Besonders wichtig war die Bestimmung der Lebensdauer des ladungstrennten Zustands und der Kinetik des Elektronentransfers zur Katalysatoreinheit. Bei den hauptsächlich untersuchten Verbindungen handelte es sich um eine Serie von vier edelmetallfreien Dyaden, die sich in der Art des organischen Push-Pull-Farbstoffs (**T1** oder **T2R**) und in der des Katalysators für die Protonenreduktion (**Co** oder **Cat1**) unterschieden. Die Bewertung der Aktivität aller vier Kombinationen ermöglichte die Bestimmung des Beitrags jedes Teils zur Gesamtleistung und damit die Verknüpfung der molekularen Struktur mit der Aktivität des Systems. Die Aufklärung einer solchen Struktur-Aktivitäts-Beziehung ist wichtig, um die molekulare Struktur der Dyaden verbessern zu können. Das am besten funktionierende System **T2R-Cat1** wurde im Detail untersucht, insbesondere einschließlich der Prozesse im angeregten Zustand bei angelegtem Potential durch transiente Absorptions-Spektroelektrochemie und post- und in-operando Messungen zur Bestimmung der Deaktivierungswege und -kinetik. Darüber hinaus wurden NiO-Photokathoden, die mit einer Ruthenium-Cobalt-Dyade

sensibilisiert wurden, zum Vergleich mittels transienter Absorptions-Spektroelektrochemie untersucht.

Der erste wichtige Teil der Arbeit war die Untersuchung der Photophysik der organischen Farbstoffe und Dyaden in Lösung. Die Dyade **T1-Co**, die bereits eine vielversprechende Leistung in einer funktionellen, H<sub>2</sub>-entwickelnden NiO-Photokathode gezeigt hatte, wurde mittels TA-Spektroskopie untersucht, um die lichtinduzierten Prozesse und den möglichen Elektronentransfer zum Katalysator zu identifizieren. Der **T1**-Farbstoff durchlief eine ultraschnelle Relaxation zum thermisch relaxierten angeregten Singulett-Zustand, von dem er auf einer sub-ns bis ns Zeitskala in den Grundzustand zurückkehrte. Um alle Oxidationszustände des Katalysators in der Dyade zu erreichen, wurden die Messungen bei angelegtem Potential durchgeführt. Trotz der Emissionslöschung und der reduzierten Lebensdauer des angeregten Zustands in der Dyade im Vergleich zum Farbstoff konnte kein Elektronentransfer im angeregten Zustand beobachtet werden, weder direkt durch einen spektralen Beitrag des reduzierten Kobaltkomplexes noch indirekt durch eine Potentialabhängigkeit der Kinetik. Der schnellere Zerfall des angeregten Zustands in der Dyade kann durch eine erhöhte Dichte an Schwingungsmoden bei Zugabe des Kobaltanteils oder durch Dexter-Energietransfer vom angeregten Donor-Chromophor auf kurzlebige kobaltzentrierte dd-Zustände erklärt werden. Die Studie zeigte, dass in mit **T1-Co** sensibilisierten Photokathoden keine oxidative Löschung aktiv ist, sondern reduktive Löschung, bei dem das Elektron vom reduzierten Farbstoff, der durch Lochinjektion erzeugt wird, auf den Katalysator übertragen wird. Darüber hinaus ermöglicht die TA-SEC-Technik die Untersuchung der lichtinduzierten Prozesse bei verschiedenen Oxidationszuständen, was im Zusammenhang mit Systemen, die für die photoinduzierte Multielektronenkatalyse wie Protonenreduktion und Wasseroxidation ausgelegt sind, wichtig ist.

Zusätzlich wurden der **T2R**-Farbstoff und die darauf basierenden Dyaden auch in Lösung mittels transienter Absorptionsspektroskopie untersucht. Während die anfänglichen Relaxationsprozesse mit denen der **T1**-Systeme identisch waren, zeigten die Dyaden ein deutlich anderes Verhalten als **T1-Co**. Sie durchliefen ein schnelles Intersystem-Crossing zum langlebigen angeregten Triplett-Zustand des Farbstoffs, der im Farbstoff allein nicht auftrat. Das schnelle ISC wurde durch ein Zusammenspiel der starren Cyclopentadithiophen-Brücke mit dem Kobaltkatalysator erklärt, wobei möglicherweise höherliegende Energiezustände des Kobaltkomplexes beteiligt sind, die zwischen der Singulett- und Triplett-Zustandsenergie des **T2R**-Farbstoffs liegen. Diese Studie zeigte, wie die Wechselwirkung verschiedener Strukturen in einer

Farbstoff-Katalysator-Anordnung zu unerwartetem Verhalten bei angeregten Zuständen führen kann, das beim Design von Farbstoff-Katalysator-Dyaden berücksichtigt werden muss. Das hier beobachtete schnelle ISC, welches durch den Cobaltkomplex induziert wird, könnte neue Möglichkeiten auf dem Gebiet der organischen Triplett-Sensibilisatoren eröffnen.

Im Rahmen der Arbeiten zu farbstoffsensibilisierten Photokathoden wurden mit **RuCo** sensibilisierte NiO-Filme mittels TA-SEC untersucht, um die lichtinduzierten Prozesse in der Dyade und die Potentialabhängigkeit der Grenzflächenprozesse wie Lochinjektion und Ladungsrekombination zu untersuchen. Es gibt nur sehr wenige Beispiele in der Literatur, bei denen diese Technik angewandt wurde. In dieser Arbeit wurde sie zum ersten Mal auf mit einer Farbstoff-Katalysator-Dyade sensibilisierten NiO-Filme angewandt, die für photoelektrochemische H<sub>2</sub>-Entwicklung aktiv waren. Zu diesem Zweck wurde eine spezielle Spektroelektrochemie-Zelle entworfen, die Femtosekunden-TA-Experimente an Filmen mit einem präzisen angelegten Potential unter inerten Bedingungen ermöglichte, die für mehrere Stunden stabil waren und die Messung von TA-SEC-Spektren mit gutem Signal-Rausch-Verhältnis ermöglichten.

Die TA-SEC-Daten zeigten, dass die Lochinjektion biphasisch mit einer sub-ps und einer langsameren Zeitkonstante von einigen zehn Pikosekunden erfolgt. Die Amplitude hing vom angelegten Potential ab, wobei eine schnelle Lochinjektion bei einem negativeren angelegten Potential bevorzugt wurde. Ebenso wurde die Ladungsrekombination aus dem reduzierten Ru-Komplex durch das angelegte Potential beeinflusst und verlangsamt sich stark bei negativem angelegtem Potential: während ohne angelegtes Potential ein wesentlicher Beitrag auf der gleichen Zeitskala wie die Lochinjektion stattfindet und einen Aufbau der ladungsgetretenen Spezies verhindert, findet sie bei negativem angelegtem Potential auf der ns- $\mu$ s-Zeitskala mit durchschnittlichen Lebensdauern von 3,6 bis 5,2  $\mu$ s statt. Alle Grenzflächenprozesse erwiesen sich als nicht-exponentiell. Der Einfluss des angelegten Potentials konnte durch die Reduktion von Ni<sup>3+</sup>-Defektzuständen zu Ni<sup>2+</sup> erklärt werden, was der Füllung von Intragap-Fallenzuständen mit Elektronen entspricht. Diese Umwandlung von einer elektronenarmen zu einer elektronenreichen NiO-Oberfläche führt sowohl zu einer beschleunigten Lochinjektion als auch zu einer verzögerten Ladungsrekombination. Wichtig ist, dass kein Elektronentransfer vom reduzierten Ru-Komplex zum Katalysator beobachtet wurde, was eine Effizienz der Bildung des katalytisch aktiven Zustands von unter 12% bedeutet, bestimmt durch die Nachweisgrenze des Aufbaus. Dieses Ergebnis liegt im Einklang mit der geringen Aktivität für die Wasserstoffentwicklung. Diese Ergebnisse unterstreichen die

Bedeutung des angelegten Potentials auf die lichtinduzierten Prozesse an sensibilisierten NiO-Photokathoden und offenbarten den ineffizienten Elektronentransfer als Schwachpunkt des Aufbaus. Dies steht im Gegensatz zur Literatur, in der ein schneller Rekombinationsprozess aus dem primären ladungsgetrenten Zustand zur Erklärung der mangelnden Effizienz der Photokathoden herangezogen wird, da die photophysikalischen Messungen an trockenen Filmen ohne angelegtes Potential durchgeführt werden. Es konnte nicht festgestellt werden, welcher Faktor den Elektronentransfer verhinderte, ob die Donor- oder Akzeptoreinheiten oder die Triazol-Brücke. Die TA-SEC-Ergebnisse deuten auch auf die Existenz von unterschiedlichen langsamen und schnellen HI- und CR-Wegen hin, je nachdem, ob die überschüssige Elektronendichte auf dem verankernden oder dem verlängerten Liganden lokalisiert ist. Diese Erkenntnis könnte beim Ligandendesign zukünftiger molekularer Systeme helfen, indem versucht wird, die überschüssige Elektronendichte noch stärker auf dem verlängerten, nicht verankernden Liganden zu lokalisieren. Dies sollte außerdem zu einem schnelleren Elektronentransfer auf die Akzeptoreinheit führen.

Der Hauptteil der Arbeiten an NiO-Photokathoden wurde an organischen Farbstoff-Katalysator-Dyaden durchgeführt. Zyklische Voltammetrie-Experimente zeigten, dass es im Grundzustand keine Wechselwirkung zwischen Farbstoff und Katalysatoreinheit gibt und dass das Oxidationspotential von **T2R** im Vergleich zu **T1** aufgrund des elektronenreichen CPDT-Linkers negativ verschoben ist. UV-Vis-Absorptionsspektren zeigten, dass dieser Linker auch eine bathochrome und hyperchrome Verschiebung des Farbstoffs verursachte, was ihn zur besseren lichtabsorbierenden Einheit machte. Dann wurde die Aktivität der Verbindungen, wenn sie auf NiO immobilisiert waren, in photoelektrochemischen Experimenten in Bezug auf den Photostrom und den produzierten Wasserstoff untersucht. Der Photostrom stieg in der Reihenfolge **T1-Co** < **T2R-Co** < **T1-Cat1** < **T2R-Cat1** mit einem insgesamt 5-fachen Anstieg des Stroms von **T1-Co** zu **T2R-Cat1**. Die Menge des produzierten Wasserstoffs folgt dem gleichen Trend, wobei die **Cat1**-Dyaden aufgrund einer viel höheren faradaischen Effizienz deutlich produktiver sind als die **Co**-Dyaden. So konnte festgestellt werden, dass der individuelle Beitrag der Farbstoff- und Katalysatoreinheiten zu einer 26-fachen Steigerung für **Cat1** im Vergleich zu **Co** und zu einer 1,7-fachen Steigerung für **T2R** im Vergleich zu **T1** führt, was die entscheidende Rolle des Katalysators unterstreicht. Ein entscheidender Faktor war die Stabilität der Dyaden, wobei die **Cat1**-Dyaden noch nach mehr als vier Stunden Photostrom produzierten und Wasserstoffentwicklung zeigten, während die **Co**-Dyaden bereits inaktiv waren. Dies bestätigt die zuvor beobachtete höhere Aktivität

und vor allem Stabilität für **Cat1** in der homogenen Photokatalyse, steht aber im Gegensatz zur Literatur über DSPC, wo üblicherweise die Desorption von der Elektrodenoberfläche als Hauptdeaktivierungsprozess angegeben wird.

Die Stabilität wurde weiter durch post- und in-operando-Messungen untersucht. Die post-operando-Messungen zeigten, dass die Dyade sowohl ihre Hauptabsorptionsbande als auch das Cobalt während des Betriebs verliert. Zeitaufgelöste in-operando UV-Vis-spektroelektrochemische Experimente unter operando-Bedingungen an dem am besten funktionierenden **T2R-Cat1**-System, in Kombination mit reduktiver UV-Vis-SEC in organischem Lösungsmittel, zeigten, dass der **T2R**-Farbstoff in seinem reduzierten Zustand instabil ist und sich über die Zeitskala von Minuten bis Stunden unter operando-Bedingungen degradiert. Nach den vorliegenden Erkenntnissen scheint es zu einem Bindungsbruch an der Akzeptor-Cyanacrylatgruppe zu kommen, der zum Verlust der Haupt-Ladungstransferbande und des Cobaltkatalysators führt. Positiv zu vermerken ist, dass die Dyaden nicht leicht von der NiO-Oberfläche durch Hydrolyse desorbiert wurden, insbesondere die auf **T2R** basierenden, was auf die schützende Wirkung der hydrophoben Alkyl-Seitenketten an der CPDT-Brücke zurückzuführen ist.

Die lichtinduzierten Prozesse in **T2R-Cat1**-sensibilisierten NiO-Filmen wurden mittels TA-SEC untersucht. Es wurde eine schnelle Lochinjektion auf der sub-ps Zeitskala beobachtet, die vom angelegten Potential unbeeinflusst war und den ersten ladungstrennenden Zustand erzeugte. Die Rekombinationskinetik der Ladungen aus diesem Zustand hing vom angelegten Potential ab, wie es auch für **RuCo** beobachtet wurde, und stieg von ca. 150 ps ohne angelegtes Potential bis in den  $\mu\text{s}$ -ms-Bereich bei angelegtem Potential. Wichtig ist, dass der Elektronentransfer vom reduzierten Farbstoff zum Katalysator innerhalb von 20 ns nach der Anregung beobachtet wurde mit zusätzlich einer langsameren Komponente auf der  $\mu\text{s}$ -Zeitskala, um den katalytisch aktiven  $\text{Co}^{\text{I}}$ -Zustand zu bilden. Dieser Zustand zerfiel auf der  $\mu\text{s}$ -Skala ( $\tau = 30 \mu\text{s}$ ), wobei 16 % nach 1 ms verblieben. Dies ist ein wichtiges Ergebnis, da es die Lebensdauer des katalytisch aktiven Zustands des Katalysators in den Bereich der Zeitskala der Katalyse legt. Der Elektronentransfer zum Katalysator war jedoch nicht quantitativ, was zu einer Ladungsakkumulation auf dem reduzierten Farbstoff und damit letztlich zu dessen Abbau führte. Daher sollte ein verbessertes molekulares Design der Dyade, das einen schnellen und quantitativen Elektronentransfer zum Katalysator sicherstellt, sowohl das Problem der geringen Aktivität als auch des reduktiven Abbaus der Farbstoffeinheit lösen. Diese Ergebnisse unterstreichen auch den Wert der TA-SEC-Messungen bei operando-Potential, die es erlauben, die



limitierenden Prozesse zu bestimmen und die Schwachstellen des Systems zu identifizieren. Dies ist besonders wichtig, da, wie hier gezeigt, ein langsamer Vorwärtsprozess nicht nur die Aktivität verringern, sondern auch die Langzeitstabilität beeinträchtigen kann.

Diese Dissertation liefert somit wichtige Erkenntnisse über die lichtinduzierten Prozesse in NiO-Photokathoden, die mit Farbstoff-Katalysator-Dyaden sensibilisiert sind, und deren Abhängigkeit von der angelegten Vorspannung, zusammen mit einer Bewertung der Photokathodenleistung und der Deaktivierungsprozesse und deren Kinetik. Die gewonnenen Erkenntnisse über die Schwachstellen der Systeme, insbesondere den sehr ineffizienten Elektronentransfer vom Farbstoff zum Katalysator und den reduktiven Abbau der organischen Farbstoffeinheiten, werden helfen, Dyaden mit verbesserter Aktivität und Stabilität zu entwickeln.

## 7 Résumé

Dans le contexte de développement d'une économie neutre en carbone, les cellules photoélectrochimiques à colorant représentent une approche innovante pour la production de carburants solaires, typiquement l'hydrogène par photodissociation de l'eau. Pour cela, la conception d'assemblages colorants-catalyseurs plus performants est très demandée car ces derniers devraient permettre de contrôler précisément les processus photoinduits, en particulier le transfert d'électrons. Cependant, les investigations détaillées de ces processus sont rares dans la littérature pour les photocathodes à colorants en conditions *operando*, de même que peu d'études ont abordé en profondeur les processus de dégradation conduisant à la désactivation de ces photocathodes.

Par conséquent, ce travail visait à fournir une analyse approfondie des performances de DSPC basées sur une série d'assemblages covalents colorants-catalyseurs moléculaires, incluant l'élucidation de leurs points faibles et des verrous limitant l'activité de production d'hydrogène de ces systèmes. À cette fin, la caractérisation complète de l'activité photoélectrochimique de ces photocathodes a été combinée à l'étude des processus photoinduits en solution et sur les films afin d'obtenir une compréhension globale des systèmes et des facteurs limitant les performances. La détermination de la durée de vie de l'état de séparation de charges et de la cinétique du transfert d'électrons vers l'unité catalytique a été particulièrement importante. Les composés étudiés étaient une série de quatre dyades sans métaux nobles, variant par la nature du colorant organique push-pull (**T1** ou **T2R**) et par celle du catalyseur de réduction des protons à base de cobalt (**Co** ou **Cat1**). Cela a permis de déterminer la contribution de chaque composé à la performance globale ; en effet, l'élucidation de telle relations structure-activité est importante pour pouvoir améliorer de façon rationnelle la structure moléculaire des dyades. Le système le plus performant **T2R-Cat1** a été étudié en détail, notamment grâce à la caractérisation des processus photoinduits en présence d'un potentiel appliqué par spectroélectrochimie d'absorption transitoire (TA-SEC) et à des mesures *post- et operando* et *post-operando* qui ont permis d'identifier les phénomènes de désactivation du système et leur cinétique. En outre, des photocathodes NiO sensibilisées par une dyade ruthénium-cobalt ont aussi été étudiées par spectroélectrochimie d'absorption transitoire à des fins de comparaison.

La première partie de cette thèse a porté sur l'étude de la photophysique des colorants organiques et des dyades en solution. La dyade **T1-Co**, qui avait déjà montré des performances prometteuses dans une première photocathode de production d'hydrogène à base de NiO fonctionnelle, a été étudiée par spectroscopie d'absorption transitoire pour identifier la nature des processus photoinduits, et vérifier si un transfert d'électrons vers le catalyseur a lieu ou non. Les résultats obtenus ont montré qu'après excitation, le colorant **T1** subit une relaxation ultrarapide jusqu'à l'état excité singulet, suivi d'un retour à l'état fondamental sur une échelle de temps de la sub-ns à ns. Afin d'étudier ce mêmes processus à différents états d'oxydation du catalyseur dans la dyade, les mesures ont été effectuées en présence d'un potentiel appliqué. Malgré l'extinction de l'émission et la durée de vie réduite de l'état excité du colorant au sein de la dyade, aucun transfert d'électrons photoinduit intramoléculaire n'a pu être observé, que ce soit directement par une contribution spectrale du complexe de cobalt réduit ou indirectement via une potentielle dépendance de la cinétique. La désactivation plus rapide de l'état excité dans la dyade peut être expliquée par une densité accrue des modes vibratoires lorsque le centre catalytique est attaché ou par un transfert d'énergie de type Dexter du chromophore excité vers les états dd à courte durée de vie centrés sur le cobalt. L'étude a aussi montré que dans les photocathodes sensibilisées par **T1-Co**, la désactivation oxydante du colorant excité n'est pas active non plus, et la mécanisme passe plutôt par la voie de désactivation réductrice où l'électron est transféré du colorant réduit, généré par injection de trous dans la bande de valence de NiO, au catalyseur. En outre, la technique TA-SEC permet d'étudier les processus photoinduits à différents états d'oxydation du catalyseur, ce qui est important dans le contexte de la catalyse redox multiélectronique, comme la réduction des protons et l'oxydation de l'eau.

Le colorant **T2R** et les dyades basées sur celui-ci ont également été étudiés en solution par spectroscopie d'absorption transitoire. Alors que les processus de relaxation initiaux sont identiques à ceux des systèmes **T1**, les dyades ont montré un comportement nettement différent de celui de **T1-Co**, subissant un croisement inter-systèmes générant l'état excité triplet à longue durée de vie du colorant, qui n'est pas observé dans le colorant seul. Ceci s'explique par une interaction entre le pont cyclopentadithiophène rigide et le catalyseur au cobalt, impliquant peut-être les états d'énergie plus élevés du complexe de cobalt qui se situent entre l'énergie de l'état singulet et de l'état triplet du colorant **T2R**. Cette étude a montré comment l'interaction des différentes sous-unités dans un assemblage colorant-catalyseur peut conduire à un comportement inattendu de l'état excité du système, qui doit être pris en compte lors de la conception d'une dyade colorant-catalyseur. Le croisement inter-systèmes induit

par le complexe de Co observé ici et générant un état triplet de longue durée de vie pourrait aussi ouvrir de nouvelles possibilités dans le domaine des photosensibilisateurs organiques.

Dans le cadre des travaux sur les photocathodes à colorants, des films de NiO sensibilisés par la dyade **RuCo** ont été étudiés par la technique TA-SEC afin d'identifier les processus photoinduits interfaciaux et leur dépendance au potentiel appliqué. Il y a très peu d'exemples dans la littérature où cette technique a été appliquée, et ce travail représente à notre connaissance le premier exemple d'étude sur une photocathode de production d'hydrogène fonctionnelle à base d'une dyade colorant-catalyseur. À cette fin, une cellule de spectroélectrochimie dédiée a été conçue et a permis de mettre en œuvre des expériences d'absorption transitoire à l'échelle de la femtoseconde sur des films avec un potentiel appliqué précis, dans des conditions inertes et stables pendant plusieurs heures.

Les données TA-SEC ainsi obtenues ont montré que l'injection de trous se produit de manière biphasique avec une première constante de temps à l'échelle de la sub-ps et une seconde plus lente, de l'ordre d'une dizaine de picosecondes. L'amplitude dépend du potentiel appliqué, favorisant une injection rapide du trou à un potentiel appliqué plus négatif. De même, la recombinaison de charge entre le complexe de Ru réduit et le NiO est fortement affectée par le potentiel appliqué. En effet, alors qu'en absence de potentiel, la recombinaison a lieu majoritairement en même temps que l'injection de trous, empêchant l'accumulation de l'état de séparation de charge, à des potentiels appliqués négatifs, elle se produit à l'échelle de temps de la ns à la  $\mu$ s avec des durées de vie moyennes de 3,6-5,2  $\mu$ s. L'influence du potentiel appliqué pourrait s'expliquer par la réduction des défauts  $\text{Ni}^{3+}$  en  $\text{Ni}^{2+}$ , correspondant au remplissage des états de piégés intra bandgap avec des électrons. Cette transformation d'une surface de NiO appauvrie en électrons en une surface de NiO riche en électrons entraîne à la fois une injection accélérée des trous et une recombinaison retardée des charges. Plus important encore, aucun transfert d'électrons du complexe de Ru réduit vers le catalyseur n'a pu être observé, mettant ainsi l'efficacité de la formation de l'état catalytiquement actif en dessous de 12 % (déterminée par la limite de détection de la méthode), en ligne avec la faible activité de production d'hydrogène de la photocathode sensibilisée avec **RuCo**. Ces résultats soulignent l'importance du potentiel appliqué sur les processus photoinduits sur les photocathodes NiO à colorants et ont révélé le manque d'efficacité du transfert d'électrons au catalyseur comme point faible de l'assemblage. Cela contraste avec la littérature où un processus

de recombinaison rapide de l'état de séparation de charges primaire est le plus souvent invoqué pour expliquer le manque d'efficacité des photocathodes puisque les mesures photophysiques sont effectuées sur des films secs sans potentiel appliqué. Il n'a pas été possible d'établir précisément quel facteur limitait le transfert d'électrons, que ce soit les unités donneuse ou acceptrice ou le lien triazole. Les résultats de la TA-SEC suggèrent également que l'existence de voies lentes et rapides distinctes pour l'injection de trou et la recombinaison de charges puissent s'expliquer par la localisation de l'excès de densité électronique sur les différents ligands du complexe de Ru. Cette observation pourrait aider à la conception des futurs systèmes moléculaires en essayant de localiser l'excès de densité électronique plus fortement sur le ligand étendu, à l'opposé de la surface. Cela devrait en outre permettre de favoriser le transfert d'électrons vers l'unité acceptrice.

La majeure partie du travail sur les photocathodes de NiO a été réalisée sur les dyades à base de colorants push-pull organiques. Les expériences de voltampérométrie cyclique ont montré qu'il n'y a pas d'interaction à l'état fondamental entre le colorant et l'unité catalytique et que le potentiel d'oxydation du **T2R** est décalé négativement par rapport au **T1** en raison du lieu CPDT riche en électrons. Les spectres d'absorption UV-Vis ont montré que ce motif est également à l'origine d'un déplacement bathochrome et hyperchrome de l'absorption du colorant dans le visible. Ensuite, l'activité des composés immobilisés sur NiO a été étudiée par des mesures photoélectrochimiques couplées à la quantification de l'hydrogène produit. Les photocourants mesurés augmentent selon l'ordre suivant : **T1-Co** < **T2R-Co** < **T1-Cat1** < **T2R-Cat1**, avec au final un photocourant 5 fois plus important pour **T2R-Cat1** par rapport à **T1-Co**. La quantité d'hydrogène produite suit la même tendance, les dyades **Cat1** étant nettement plus productives que les dyades **Co** en raison d'un rendement faradique beaucoup plus élevé. La contribution individuelle des unités de colorants et de catalyseurs a ainsi pu être établie pour conduire à une multiplication de l'activité par 26 pour **Cat1** par rapport à **Co** et par 1,7 pour **T2R** par rapport à **T1**, ce qui souligne le rôle décisif du catalyseur. Un facteur crucial était la stabilité des assemblages, les dyades **Cat1** produisant toujours de l'hydrogène après plus de quatre heures, alors que les dyades **Co** sont déjà inactives. Cela confirme les observations précédemment faites en photocatalyse homogène, mais contraste avec la littérature sur les DSPC où la désorption de la surface de l'électrode est généralement donnée comme le principal processus de désactivation.

La stabilité a été étudiée plus en détail par des mesures operando et post-operando. Ces dernières ont révélé que la dyade a perdu à la fois sa bande d'absorption principale

dans le visible et le cobalt après 4 heures d'activité. Des expériences spectrochimiques UV-Vis en conditions operando sur le système le plus performant **T2R-Cat1** ont montré que le colorant **T2R** est instable à l'état réduit et se dégrade en quelques minutes à quelques heures dans les conditions d'opération. Il semblerait qu'il y ait une rupture de liaison au niveau du groupe cyanoacrylate accepteur qui entraîne la perte de la bande de transfert de charge principale et du catalyseur de cobalt. Une observation positive, par contre, est que ces dyades ne se sont pas facilement désorbées de la surface de NiO, en particulier celles basées sur le **T2R**, en raison de l'effet protecteur des chaînes latérales alkyles hydrophobes sur le motif CPDT.

Les processus photoinduits sur les films de NiO sensibilisés par **T2R-Cat1** ont été étudiés par TA-SEC. Une injection de trou ultra-rapide a lieu à l'échelle de temps de la sub-ps, produisant l'état de séparation de charge primaire, et ce processus n'est pas affecté par le potentiel appliqué. La cinétique de recombinaison de charges à partir de cet état dépend par contre fortement du potentiel appliqué, comme précédemment observé pour **RuCo**, passant d'environ 150 ps en absence de potentiel à l'échelle de la  $\mu$ s à la ms lorsque des potentiels cathodiques sont appliqués. Plus important encore, le transfert d'électrons du colorant réduit vers le catalyseur a été observé dans les 20 ns suivant l'excitation, et peut-être aussi via une composante plus lente sur l'échelle de la  $\mu$ s, pour former l'état  $\text{Co}^I$  catalytiquement actif. Cet état se désactive par recombinaison à l'échelle de la  $\mu$ s ( $\tau = 30 \mu$ s), 16 % étant toujours présent après 1 ms. Il s'agit d'une observation fondamentale car elle situe la durée de vie de ce dérivé réduit du catalyseur dans l'échelle de temps de la catalyse. Le transfert d'électrons vers le catalyseur n'est cependant pas quantitatif, ce qui conduit à une accumulation de charge sur le colorant réduit et donc finalement à sa dégradation. Par conséquent, une conception moléculaire optimisée de la dyade devra permettre d'assurer un transfert d'électrons rapide et quantitatif vers le catalyseur pour résoudre à la fois le problème de la faible activité et de la dégradation réductrice de l'unité colorante. Ces résultats mettent également en avant l'importance des mesures TA-SEC au potentiel operando pour déterminer les processus cinétiquement limitants et identifier les points faibles de l'assemblage. Ceci est particulièrement important car, comme démontré ici, un processus lent peut non seulement entraver l'activité de l'assemblage, mais aussi compromettre sa stabilité à long terme.

Cette thèse fournit donc des informations clés sur les processus photoinduits au sein de photocathodes de NiO sensibilisées par des dyades colorants-catalyseurs et sur leur dépendance vis-à-vis du bias appliqué, ainsi qu'une évaluation des performances de ces photocathodes et l'identification des processus de désactivation et de leur

---

cinétique. Les résultats marquants obtenus sur les verrous de ces systèmes, notamment le manque d'efficacité du transfert d'électrons du colorant vers le catalyseur et la dégradation réductrice des colorants organiques, aideront à concevoir de manière rationnelle des dyades ayant une activité et une stabilité optimisées.

## Bibliography

- (1) Perez, R.; Perez, M. A Fundamental Look At Supply Side Energy Reserves For The Planet. *The International Energy Agency SHC programme Solar Update* **2015**, 62 (April 2009), 4–6.
- (2) Grimm, A.; de Jong, W. A.; Kramer, G. J. Renewable Hydrogen Production: A Techno-Economic Comparison of Photoelectrochemical Cells and Photovoltaic-Electrolysis. *International Journal of Hydrogen Energy* **2020**, 45 (43), 22545–22555. <https://doi.org/10.1016/j.ijhydene.2020.06.092>.
- (3) Brennaman, M. K.; Dillon, R. J.; Alibabaei, L.; Gish, M. K.; Dares, C. J.; Ashford, D. L.; House, R. L.; Meyer, G. J.; Papanikolas, J. M.; Meyer, T. J. Finding the Way to Solar Fuels with Dye-Sensitized Photoelectrosynthesis Cells. *Journal of the American Chemical Society* **2016**, 138 (40), 13085–13102. <https://doi.org/10.1021/jacs.6b06466>.
- (4) McTavish, H. Hydrogen Evolution by Direct Electron Transfer from Photosystem I to Hydrogenases. *Journal of Biochemistry* **1998**, 123 (4), 644–649. <https://doi.org/10.1093/oxfordjournals.jbchem.a021986>.
- (5) McKone, J. R.; Lewis, N. S.; Gray, H. B. Will Solar-Driven Water-Splitting Devices See the Light of Day? *Chemistry of Materials* **2014**, 26 (1), 407–414. <https://doi.org/10.1021/cm4021518>.
- (6) Windle, C. D.; Kumagai, H.; Higashi, M.; Brisse, R.; Bold, S.; Joussetme, B.; Chavarot-Kerlidou, M.; Maeda, K.; Abe, R.; Ishitani, O.; Artero, V. Earth-Abundant Molecular Z-Scheme Photoelectrochemical Cell for Overall Water-Splitting. *Journal of the American Chemical Society* **2019**, 141 (24), 9593–9602. <https://doi.org/10.1021/jacs.9b02521>.
- (7) Fan, K.; Li, F.; Wang, L.; Daniel, Q.; Gabrielsson, E.; Sun, L. Pt-Free Tandem Molecular Photoelectrochemical Cells for Water Splitting Driven by Visible Light. *Phys. Chem. Chem. Phys.* **2014**, 16 (46), 25234–25240. <https://doi.org/10.1039/C4CP04489D>.
- (8) Li, F.; Fan, K.; Xu, B.; Gabrielsson, E.; Daniel, Q.; Li, L.; Sun, L. Organic Dye-Sensitized Tandem Photoelectrochemical Cell for Light Driven Total Water Splitting. *Journal of the American Chemical Society* **2015**, 137 (28), 9153–9159. <https://doi.org/10.1021/jacs.5b04856>.



- (9) Ponceca, C. S.; Chábera, P.; Uhlig, J.; Persson, P.; Sundström, V. Ultrafast Electron Dynamics in Solar Energy Conversion. *Chem. Rev.* **2017**, *117*, 10940–11024. <https://doi.org/10.1021/acs.chemrev.6b00807>.
- (10) Hammarström, L. Accumulative Charge Separation for Solar Fuels Production: Coupling Light-Induced Single Electron Transfer to Multielectron Catalysis. *Accounts of Chemical Research* **2015**, *48* (3), 840–850. <https://doi.org/10.1021/ar500386x>.
- (11) Nocera, D. G. The Artificial Leaf. *Accounts of Chemical Research* **2012**, *45* (5), 767–776. <https://doi.org/10.1021/ar2003013>.
- (12) Lewis, N. S.; Nocera, D. G. Powering the Planet: Chemical Challenges in Solar Energy Utilization. *Proceedings of the National Academy of Sciences* **2006**, *103* (43), 15729–15735. <https://doi.org/10.1073/pnas.0603395103>.
- (13) Hogue, R. W.; Schott, O.; Hanan, G. S.; Brooker, S. A Smorgasbord of 17 Cobalt Complexes Active for Photocatalytic Hydrogen Evolution. *Chemistry - A European Journal* **2018**, *24* (39), 9820–9832. <https://doi.org/10.1002/chem.201800396>.
- (14) Gueret, R.; Castillo, C. E.; Rebarz, M.; Thomas, F.; Sliwa, M.; Chauvin, J.; Dautreppe, B.; Pécaut, J.; Fortage, J.; Collomb, M.-N. Cobalt(II) Pentaaza-Macrocyclic Schiff Base Complex as Catalyst for Light-Driven Hydrogen Evolution in Water: Electrochemical Generation and Theoretical Investigation of the One-Electron Reduced Species. *Inorganic Chemistry* **2019**, *58* (14), 9043–9056. <https://doi.org/10.1021/acs.inorgchem.9b00447>.
- (15) Gueret, R.; Poulard, L.; Oshinowo, M.; Chauvin, J.; Dahmane, M.; Dupeyre, G.; Lainé, P. P.; Fortage, J.; Collomb, M.-N. Challenging the [Ru(Bpy)<sub>3</sub>]<sup>2+</sup> Photosensitizer with a Triazatriangulenium Robust Organic Dye for Visible-Light-Driven Hydrogen Production in Water. *ACS Catalysis* **2018**, *8* (5), 3792–3802. <https://doi.org/10.1021/acscatal.7b04000>.
- (16) Panagiotopoulos, A.; Ladomenou, K.; Sun, D.; Artero, V.; Coutsolelos, A. G. Photochemical Hydrogen Production and Cobaloximes: The Influence of the Cobalt Axial N-Ligand on the System Stability. *Dalton Transactions* **2016**, *45* (15), 6732–6738. <https://doi.org/10.1039/C5DT04502A>.
- (17) Kaeffer, N.; Chavarot-Kerlidou, M.; Artero, V. Hydrogen Evolution Catalyzed by Cobalt Diimine-Dioxime Complexes. *Accounts of Chemical Research* **2015**, *48* (5), 1286–1295. <https://doi.org/10.1021/acs.accounts.5b00058>.

- (18) Yu, Z.; Li, F.; Sun, L. Recent Advances in Dye-Sensitized Photoelectrochemical Cells for Solar Hydrogen Production Based on Molecular Components. *Energy Environ. Sci.* **2015**, *8* (3), 760–775. <https://doi.org/10.1039/C4EE03565H>.
- (19) Xu, P.; McCool, N. S.; Mallouk, T. E. Water Splitting Dye-Sensitized Solar Cells. *Nano Today* **2017**, *14*, 42–58. <https://doi.org/10.1016/j.nantod.2017.04.009>.
- (20) Decavoli, C.; Boldrini, C. L.; Manfredi, N.; Abboto, A. Molecular Organic Sensitizers for Photoelectrochemical Water Splitting. *European Journal of Inorganic Chemistry* **2020**, *2020* (11–12), 978–999. <https://doi.org/10.1002/ejic.202000026>.
- (21) Hagfeldt, A.; Boschloo, G.; Sun, L.; Kloo, L.; Pettersson, H. Dye-Sensitized Solar Cells. *Chemical Reviews* **2010**, *110* (11), 6595–6663. <https://doi.org/10.1021/cr900356p>.
- (22) Odobel, F.; le Pleux, L.; Pellegrin, Y.; Blart, E. New Photovoltaic Devices Based on the Sensitization of P-Type Semiconductors: Challenges and Opportunities. *Accounts of Chemical Research* **2010**, *43* (8), 1063–1071. <https://doi.org/10.1021/ar900275b>.
- (23) Sherman, B. D.; Sheridan, M. v.; Wee, K. R.; Marquard, S. L.; Wang, D.; Alibabaei, L.; Ashford, D. L.; Meyer, T. J. A Dye-Sensitized Photoelectrochemical Tandem Cell for Light Driven Hydrogen Production from Water. *Journal of the American Chemical Society* **2016**, *138* (51), 16745–16753. <https://doi.org/10.1021/jacs.6b10699>.
- (24) Click, K. A.; Beauchamp, D. R.; Huang, Z.; Chen, W.; Wu, Y. Membrane-Inspired Acidically Stable Dye-Sensitized Photocathode for Solar Fuel Production. *Journal of the American Chemical Society* **2016**, *138* (4), 1174–1179. <https://doi.org/10.1021/jacs.5b07723>.
- (25) Qin, P.; Wiberg, J.; Gibson, E. A.; Linder, M.; Li, L.; Brinck, T.; Hagfeldt, A.; Albinsson, B.; Sun, L. Synthesis and Mechanistic Studies of Organic Chromophores with Different Energy Levels for P-Type Dye-Sensitized Solar Cells. *The Journal of Physical Chemistry C* **2010**, *114* (10), 4738–4748. <https://doi.org/10.1021/jp911091n>.
- (26) Kaeffer, N.; Massin, J.; Lebrun, C.; Renault, O.; Chavarot-Kerlidou, M.; Artero, V. Covalent Design for Dye-Sensitized H<sub>2</sub> -Evolving Photocathodes Based on a Cobalt Diimine–Dioxime Catalyst. *Journal of the American Chemical Society* **2016**, *138* (38), 12308–12311. <https://doi.org/10.1021/jacs.6b05865>.

- (27) Kaeffer, N.; Windle, C. D.; Brisse, R.; Gablin, C.; Leonard, D.; Jusselme, B.; Chavarot-Kerlidou, M.; Artero, V. Insights into the Mechanism and Aging of a Noble-Metal Free H<sub>2</sub>-Evolving Dye-Sensitized Photocathode. *Chemical Science* **2018**, *9* (32), 6721–6738. <https://doi.org/10.1039/C8SC00899J>.
- (28) Creissen, C. E.; Warnan, J.; Reisner, E. Solar H<sub>2</sub> Generation in Water with a CuCrO<sub>2</sub> Photocathode Modified with an Organic Dye and Molecular Ni Catalyt. *Chemical Science* **2018**, *9* (6), 1439–1447. <https://doi.org/10.1039/C7SC04476C>.
- (29) Sahara, G.; Kumagai, H.; Maeda, K.; Kaeffer, N.; Artero, V.; Higashi, M.; Abe, R.; Ishitani, O. Photoelectrochemical Reduction of CO<sub>2</sub> Coupled to Water Oxidation Using a Photocathode with a Ru(II)–Re(I) Complex Photocatalyst and a CoOx /TaON Photoanode. *Journal of the American Chemical Society* **2016**, *138* (42), 14152–14158. <https://doi.org/10.1021/jacs.6b09212>.
- (30) Guerrero, G.; Alauzun, J. G.; Granier, M.; Laurencin, D.; Mutin, P. H. Phosphonate Coupling Molecules for the Control of Surface/Interface Properties and the Synthesis of Nanomaterials. *Dalton Transactions* **2013**, *42* (35), 12569. <https://doi.org/10.1039/c3dt51193f>.
- (31) Pellegrin, Y.; le Pleux, L.; Blart, E.; Renaud, A.; Chavillon, B.; Szuwarski, N.; Boujtita, M.; Cario, L.; Jobic, S.; Jacquemin, D.; Odobel, F. Ruthenium Polypyridine Complexes as Sensitizers in NiO Based P-Type Dye-Sensitized Solar Cells: Effects of the Anchoring Groups. *Journal of Photochemistry and Photobiology A: Chemistry* **2011**, *219* (2–3), 235–242. <https://doi.org/10.1016/j.jphotochem.2011.02.025>.
- (32) Farré, Y.; Maschietto, F.; Föhlinger, J.; Wykes, M.; Planchat, A.; Pellegrin, Y.; Blart, E.; Ciofini, I.; Hammarström, L.; Odobel, F. A Comparative Investigation of the Role of the Anchoring Group on Perylene Monoimide Dyes in NiO-Based Dye-Sensitized Solar Cells. *ChemSusChem* **2020**, *13* (7), 1844–1855. <https://doi.org/10.1002/cssc.201903182>.
- (33) Hanson, K.; Brennaman, M. K.; Luo, H.; Glasson, C. R. K.; Concepcion, J. J.; Song, W.; Meyer, T. J. Photostability of Phosphonate-Derivatized, Ru II Polypyridyl Complexes on Metal Oxide Surfaces. *ACS Applied Materials & Interfaces* **2012**, *4* (3), 1462–1469. <https://doi.org/10.1021/am201717x>.
- (34) Materna, K. L.; Lalaoui, N.; Laureanti, J. A.; Walsh, A. P.; Rimgard, B. P.; Lomoth, R.; Thapper, A.; Ott, S.; Shaw, W. J.; Tian, H.; Hammarström, L. Using Surface Amide Couplings to Assemble Photocathodes for Solar Fuel

- Production Applications. *ACS Applied Materials & Interfaces* **2020**, acsami.9b19003. <https://doi.org/10.1021/acsami.9b19003>.
- (35) Zhang, B.; Sun, L. Artificial Photosynthesis: Opportunities and Challenges of Molecular Catalysts. *Chemical Society Reviews* **2019**, *48* (7), 2216–2264. <https://doi.org/10.1039/C8CS00897C>.
- (36) Bräutigam, M.; Kübel, J.; Schulz, M.; Vos, J. G.; Dietzek, B. Hole Injection Dynamics from Two Structurally Related Ru–Bipyridine Complexes into NiOx Is Determined by the Substitution Pattern of the Ligands. *Physical Chemistry Chemical Physics* **2015**, *17* (12), 7823–7830. <https://doi.org/10.1039/C4CP05663A>.
- (37) Youngblood, W. J.; Lee, S. A.; Kobayashi, Y.; Hernandez-pagan, E. A.; Hoertz, P. G.; Moore, T. A.; Moore, A. L.; Gust, D.; Mallouk, T. E.; Cell, D. P. Photoassisted Overall Water Splitting in a Visible Light-Absorbing Dye-Sensitized Photoelectrochemical Cell. *J. Am. Chem. Soc.* **2009**, *131*, 926–927. <https://doi.org/10.1021/ja809108y>.
- (38) Shan, B.; Das, A. K.; Marquard, S.; Farnum, B. H.; Wang, D.; Bullock, R. M.; Meyer, T. J. Photogeneration of Hydrogen from Water by a Robust Dye-Sensitized Photocathode. *Energy & Environmental Science* **2016**, *9* (12), 3693–3697. <https://doi.org/10.1039/C6EE02903E>.
- (39) Kowacs, T.; Pan, Q.; Lang, P.; O'Reilly, L.; Rau, S.; Browne, W. R.; Pryce, M. T.; Huijser, A.; Vos, J. G. Supramolecular Bimetallic Assemblies for Photocatalytic Hydrogen Generation from Water. *Faraday Discussions* **2015**, *185*, 143–170. <https://doi.org/10.1039/c5fd00068h>.
- (40) Tschierlei, S.; Karnahl, M.; Presselt, M.; Dietzek, B.; Guthmuller, J.; González, L.; Schmitt, M.; Rau, S.; Popp, J. Photochemical Fate: The First Step Determines Efficiency of H<sub>2</sub> Formation with a Supramolecular Photocatalyst. *Angewandte Chemie International Edition* **2010**, *49* (23), 3981–3984. <https://doi.org/10.1002/anie.200906595>.
- (41) Rau, S.; Schäfer, B.; Gleich, D.; Anders, E.; Rudolph, M.; Friedrich, M.; Görls, H.; Henry, W.; Vos, J. G. A Supramolecular Photocatalyst for the Production of Hydrogen and the Selective Hydrogenation of Tolane. *Angewandte Chemie - International Edition* **2006**, *45* (37), 6215–6218. <https://doi.org/10.1002/anie.200600543>.
- (42) Zedler, L.; Mengele, A. K.; Ziems, K. M.; Zhang, Y.; Wächtler, M.; Gräfe, S.; Pascher, T.; Rau, S.; Kupfer, S.; Dietzek, B. Unraveling the Light-Activated Reaction Mechanism in a Catalytically Competent Key Intermediate of a Multifunctional Molecular Catalyst for Artificial Photosynthesis. *Angewandte*

- Chemie International Edition* **2019**, *58* (37), 13140–13148.  
<https://doi.org/10.1002/anie.201907247>.
- (43) Pfeffer, M. G.; Zedler, L.; Kupfer, S.; Paul, M.; Schwalbe, M.; Peuntinger, K.; Guldi, D. M.; Guthmuller, J.; Popp, J.; Gräfe, S.; Dietzek, B.; Rau, S. Tuning of Photocatalytic Activity by Creating a Tridentate Coordination Sphere for Palladium. *Dalton transactions (Cambridge, England : 2003)* **2014**, *43* (30), 11676–11686. <https://doi.org/10.1039/c4dt01034e>.
- (44) Karnahl, M.; Kuhnt, C.; Ma, F.; Yartsev, A.; Schmitt, M.; Dietzek, B.; Rau, S.; Popp, J. Tuning of Photocatalytic Hydrogen Production and Photoinduced Intramolecular Electron Transfer Rates by Regioselective Bridging Ligand Substitution. *ChemPhysChem* **2011**, *12* (11), 2101–2109.  
<https://doi.org/10.1002/cphc.201100245>.
- (45) Queyriaux, N.; Wahyuono, R. A.; Fize, J.; Gablin, C.; Wächtler, M.; Martinez, E.; Léonard, D.; Dietzek, B.; Artero, V.; Chavarot-Kerlidou, M. Aqueous Photocurrent Measurements Correlated to Ultrafast Electron Transfer Dynamics at Ruthenium Tris Diimine Sensitized NiO Photocathodes. *The Journal of Physical Chemistry C* **2017**, *121* (11), 5891–5904.  
<https://doi.org/10.1021/acs.jpcc.6b12536>.
- (46) Pöldme, N.; O'Reilly, L.; Fletcher, I.; Portoles, J.; Sazanovich, I. v; Towrie, M.; Long, C.; Vos, J. G.; Pryce, M. T.; Gibson, E. A. Photoelectrocatalytic H<sub>2</sub> Evolution from Integrated Photocatalysts Adsorbed on NiO. *Chemical Science* **2019**, *10* (1), 99–112. <https://doi.org/10.1039/C8SC02575D>.
- (47) Li, C.; Wang, M.; Pan, J.; Zhang, P.; Zhang, R.; Sun, L. Photochemical Hydrogen Production Catalyzed by Polypyridyl Ruthenium – Cobaloxime Heterobinuclear Complexes with Different Bridges. *Journal of Organometallic Chemistry* **2009**, *694* (17), 2814–2819.  
<https://doi.org/10.1016/j.jorganchem.2009.04.041>.
- (48) Kohler, L.; Mulfort, K. L. Photoinduced Electron Transfer Kinetics of Linked Ru-Co Photocatalyst Dyads. *Journal of Photochemistry and Photobiology A: Chemistry* **2019**, *373* (November 2018), 59–65.  
<https://doi.org/10.1016/j.jphotochem.2018.12.025>.
- (49) Fihri, A.; Artero, V.; Razavet, M.; Baffert, C.; Leibl, W.; Fontecave, M. Cobaloxime-Based Photocatalytic Devices for Hydrogen Production. *Angewandte Chemie* **2008**, *120* (3), 574–577.  
<https://doi.org/10.1002/ange.200702953>.

- (50) Li, L.; Duan, L.; Wen, F.; Li, C.; Wang, M.; Hagfeldt, A.; Sun, L. Visible Light Driven Hydrogen Production from a Photo-Active Cathode Based on a Molecular Catalyst and Organic Dye-Sensitized p-Type Nanostructured NiO. *Chemical Communications* **2012**, 48 (7), 988–990. <https://doi.org/10.1039/C2CC16101J>.
- (51) Massin, J.; Bräutigam, M.; Bold, S.; Wächtler, M.; Pavone, M.; Muñoz-García, A. B.; Dietzek, B.; Artero, V.; Chavarot-Kerlidou, M. Investigating Light-Driven Hole Injection and Hydrogen Evolution Catalysis at Dye-Sensitized NiO Photocathodes: A Combined Experimental–Theoretical Study. *The Journal of Physical Chemistry C* **2019**, 123 (28), 17176–17184. <https://doi.org/10.1021/acs.jpcc.9b04715>.
- (52) Kamire, R. J.; Majewski, M. B.; Hoffeditz, W. L.; Phelan, B. T.; Farha, O. K.; Hupp, J. T.; Wasielewski, M. R. Photodriven Hydrogen Evolution by Molecular Catalysts Using Al<sub>2</sub>O<sub>3</sub>-Protected Perylene-3,4-Dicarboximide on NiO Electrodes. *Chemical Science* **2017**, 8 (1), 541–549. <https://doi.org/10.1039/C6SC02477G>.
- (53) Creissen, C. E.; Warnan, J.; Antón-García, D.; Farré, Y.; Odobel, F.; Reisner, E. Inverse Opal CuCrO<sub>2</sub> Photocathodes for H<sub>2</sub> Production Using Organic Dyes and a Molecular Ni Catalyst. *ACS Catalysis* **2019**, 9 (10), 9530–9538. <https://doi.org/10.1021/acscatal.9b02984>.
- (54) Antila, L. J.; Ghamgosar, P.; Maji, S.; Tian, H.; Ott, S.; Hammarström, L. Dynamics and Photochemical H<sub>2</sub> Evolution of Dye–NiO Photocathodes with a Biomimetic FeFe-Catalyst. *ACS Energy Letters* **2016**, 1 (6), 1106–1111. <https://doi.org/10.1021/acsenergylett.6b00506>.
- (55) Gordon, R. B.; Bertram, M.; Graedel, T. E. Metal Stocks and Sustainability. *Proceedings of the National Academy of Sciences* **2006**, 103 (5), 1209–1214. <https://doi.org/10.1073/pnas.0509498103>.
- (56) Dalle, K. E.; Warnan, J.; Leung, J. J.; Reuillard, B.; Karmel, I. S.; Reisner, E. Electro- and Solar-Driven Fuel Synthesis with First Row Transition Metal Complexes. *Chemical Reviews* **2019**, 119 (4), 2752–2875. <https://doi.org/10.1021/acs.chemrev.8b00392>.
- (57) Jeuken, L. J. C. *Biophotoelectrochemistry: From Bioelectrochemistry to Biophotovoltaics*; Jeuken, L. J. C., Ed.; Advances in Biochemical Engineering/Biotechnology; Springer International Publishing: Cham, 2016; Vol. 158. <https://doi.org/10.1007/978-3-319-50667-8>.

- (58) Oughli, A. A.; Conzuelo, F.; Winkler, M.; Happe, T.; Lubitz, W.; Schuhmann, W.; Rüdiger, O.; Plumeré, N. A Redox Hydrogel Protects the O<sub>2</sub>-Sensitive [FeFe]-Hydrogenase from *Chlamydomonas Reinhardtii* from Oxidative Damage. *Angewandte Chemie - International Edition* **2015**, *54* (42), 12329–12333. <https://doi.org/10.1002/anie.201502776>.
- (59) Plumeré, N.; Rüdiger, O.; Oughli, A. A.; Williams, R.; Vivekananthan, J.; Pöller, S.; Schuhmann, W.; Lubitz, W. A Redox Hydrogel Protects Hydrogenase from High-Potential Deactivation and Oxygen Damage. *Nature Chemistry* **2014**, *6* (9), 822–827. <https://doi.org/10.1038/nchem.2022>.
- (60) Gatty, M. G.; Pullen, S.; Sheibani, E.; Tian, H.; Ott, S.; Hammarström, L. Direct Evidence of Catalyst Reduction on Dye and Catalyst Co-Sensitized NiO Photocathodes by Mid-Infrared Transient Absorption Spectroscopy. *Chemical Science* **2018**, *9* (22), 4983–4991. <https://doi.org/10.1039/C8SC00990B>.
- (61) Brown, A. M.; Antila, L. J.; Mirmohades, M.; Pullen, S.; Ott, S.; Hammarström, L. Ultrafast Electron Transfer between Dye and Catalyst on a Mesoporous NiO Surface. *Journal of the American Chemical Society* **2016**, *138* (26), 8060–8063. <https://doi.org/10.1021/jacs.6b03889>.
- (62) Helm, M. L.; Stewart, M. P.; Bullock, R. M.; DuBois, M. R.; DuBois, D. L. A Synthetic Nickel Electrocatalyst with a Turnover Frequency Above 100,000 S<sup>-1</sup> for H<sub>2</sub> Production. *Science* **2011**, *333* (August), 863–867. <https://doi.org/10.5040/9780755621101.0007>.
- (63) Gross, M. A.; Creissen, C. E.; Orchard, K. L.; Reisner, E. Photoelectrochemical Hydrogen Production in Water Using a Layer-by-Layer Assembly of a Ru Dye and Ni Catalyst on NiO. *Chemical Science* **2016**, *7* (8), 5537–5546. <https://doi.org/10.1039/c6sc00715e>.
- (64) Shan, B.; Sherman, B. D.; Klug, C. M.; Nayak, A.; Marquard, S. L.; Liu, Q.; Bullock, R. M.; Meyer, T. J. Modulating Hole Transport in Multilayered Photocathodes with Derivatized P-Type Nickel Oxide and Molecular Assemblies for Solar-Driven Water Splitting. *The Journal of Physical Chemistry Letters* **2017**, *8* (18), 4374–4379. <https://doi.org/10.1021/acs.jpcclett.7b01911>.
- (65) Hawecker, J.; Lehn, J.-M.; Zissel, R. Efficient Homogeneous Photochemical Hydrogen Generation and Water Reduction Mediated by Cobaloxime or Macrocyclic Cobalt Complexes. *Nouveau Journal de Chimie* **1983**, *7* (5), 271–277.
- (66) Dempsey, J. L.; Brunschwig, B. S.; Winkler, J. R.; Gray, H. B. Hydrogen Evolution Catalyzed by Cobaloximes. *Accounts of Chemical Research* **2009**, *42* (12), 1995–2004. <https://doi.org/10.1021/ar900253e>.

- (67) Baffert, C.; Artero, V.; Fontecave, M. Cobaloximes as Functional Models for Hydrogenases. 2. Proton Electroreduction Catalyzed by Difluoroborylbis(Dimethylglyoximate)Cobalt(II) Complexes in Organic Media. *Inorganic Chemistry* **2007**, *46* (5), 1817–1824. <https://doi.org/10.1021/ic061625m>.
- (68) Eckenhoff, W. T.; McNamara, W. R.; Du, P.; Eisenberg, R. Cobalt Complexes as Artificial Hydrogenases for the Reductive Side of Water Splitting. *Biochimica et Biophysica Acta (BBA) - Bioenergetics* **2013**, *1827* (8–9), 958–973. <https://doi.org/10.1016/j.bbabi.2013.05.003>.
- (69) Hu, X.; Brunschwig, B. S.; Peters, J. C. Electrocatalytic Hydrogen Evolution at Low Overpotentials by Cobalt Macrocyclic Glyoxime and Tetraimine Complexes. *Journal of the American Chemical Society* **2007**, *129* (29), 8988–8998. <https://doi.org/10.1021/ja067876b>.
- (70) Hu, X.; Cossairt, B. M.; Brunschwig, B. S.; Lewis, N. S.; Peters, J. C. Electrocatalytic Hydrogen Evolution by Cobalt Difluoroboryl-Diglyoximate Complexes. *Chemical Communications* **2005**, *1* (37), 4723. <https://doi.org/10.1039/b509188h>.
- (71) Razavet, M.; Artero, V.; Fontecave, M. Proton Electroreduction Catalyzed by Cobaloximes: Functional Models for Hydrogenases. *Inorganic Chemistry* **2005**, *44* (13), 4786–4795. <https://doi.org/10.1021/ic050167z>.
- (72) Bhattacharjee, A.; Andreiadis, E. S.; Chavarot-Kerlidou, M.; Fontecave, M.; Field, M. J.; Artero, V. A Computational Study of the Mechanism of Hydrogen Evolution by Cobalt(Diimine-Dioxime) Catalysts. *Chemistry - A European Journal* **2013**, *19* (45), 15166–15174. <https://doi.org/10.1002/chem.201301860>.
- (73) Artero, V.; Chavarot-Kerlidou, M.; Fontecave, M. Splitting Water with Cobalt. *Angewandte Chemie International Edition* **2011**, *50* (32), 7238–7266. <https://doi.org/10.1002/anie.201007987>.
- (74) Seeber, R.; Parker, W. O.; Marzilli, P. A.; Marzilli, L. G. Electrochemical Synthesis of Costa-Type Cobalt Complexes. *Organometallics* **1989**, *8* (10), 2377–2381. <https://doi.org/10.1021/om00112a018>.
- (75) Rosser, T. E.; Reisner, E. Understanding Immobilized Molecular Catalysts for Fuel-Forming Reactions through UV/Vis Spectroelectrochemistry. *ACS Catalysis* **2017**, *7* (5), 3131–3141. <https://doi.org/10.1021/acscatal.7b00326>.
- (76) Andreiadis, E. S.; Jacques, P.-A.; Tran, P. D.; Leyris, A.; Chavarot-Kerlidou, M.; Jusselme, B.; Matheron, M.; Pécaut, J.; Palacin, S.; Fontecave, M.; Artero, V. Molecular Engineering of a Cobalt-Based Electrocatalytic Nanomaterial for H<sub>2</sub>



- Evolution under Fully Aqueous Conditions. *Nature Chemistry* **2013**, *5* (1), 48–53. <https://doi.org/10.1038/nchem.1481>.
- (77) Pati, P. B.; Zhang, L.; Philippe, B.; Fernández-Terán, R.; Ahmadi, S.; Tian, L.; Rensmo, H.; Hammarström, L.; Tian, H. Insights into the Mechanism of a Covalently Linked Organic Dye–Cobaloxime Catalyst System for Dye-Sensitized Solar Fuel Devices. *ChemSusChem* **2017**, *10* (11), 2480–2495. <https://doi.org/10.1002/cssc.201700285>.
- (78) Reynal, A.; Willkomm, J.; Muresan, N. M.; Lakadamyali, F.; Planells, M.; Reisner, E.; Durrant, J. R. Distance Dependent Charge Separation and Recombination in Semiconductor/Molecular Catalyst Systems for Water Splitting. *Chem. Commun.* **2014**, *50* (84), 12768–12771. <https://doi.org/10.1039/C4CC05143B>.
- (79) Lyu, S.; Massin, J.; Pavone, M.; Muñoz-García, A. B.; Labrugère, C.; Toupance, T.; Chavarot-Kerlidou, M.; Artero, V.; Olivier, C. H<sub>2</sub>-Evolving Dye-Sensitized Photocathode Based on a Ruthenium–Diacetylide/Cobaloxime Supramolecular Assembly. *ACS Applied Energy Materials* **2019**, *2* (7), 4971–4980. <https://doi.org/10.1021/acsaem.9b00652>.
- (80) Ji, Z.; He, M.; Huang, Z.; Ozkan, U.; Wu, Y. Photostable P-Type Dye-Sensitized Photoelectrochemical Cells for Water Reduction. *Journal of the American Chemical Society* **2013**, *135* (32), 11696–11699. <https://doi.org/10.1021/ja404525e>.
- (81) McCormick, T. M.; Han, Z.; Weinberg, D. J.; Brennessel, W. W.; Holland, P. L.; Eisenberg, R. Impact of Ligand Exchange in Hydrogen Production from Cobaloxime-Containing Photocatalytic Systems. *Inorganic Chemistry* **2011**, *50* (21), 10660–10666. <https://doi.org/10.1021/ic2010166>.
- (82) Kaeffer, N.; Morozan, A.; Fize, J.; Martinez, E.; Guetaz, L.; Artero, V. The Dark Side of Molecular Catalysis: Diimine–Dioxime Cobalt Complexes Are Not the Actual Hydrogen Evolution Electrocatalyst in Acidic Aqueous Solutions. *ACS Catalysis* **2016**, *6* (6), 3727–3737. <https://doi.org/10.1021/acscatal.6b00378>.
- (83) Varma, S.; Castillo, C. E.; Stoll, T.; Fortage, J.; Blackman, A. G.; Molton, F.; Deronzier, A.; Collomb, M.-N. Efficient Photocatalytic Hydrogen Production in Water Using a Cobalt(III) Tetraaza-Macrocyclic Catalyst: Electrochemical Generation of the Low-Valent Co(I) Species and Its Reactivity toward Proton Reduction. *Physical Chemistry Chemical Physics* **2013**, *15* (40), 17544. <https://doi.org/10.1039/c3cp52641k>.
- (84) Gueret, R.; Castillo, C. E.; Rebarz, M.; Thomas, F.; Hargrove, A.-A.; Pécaut, J.; Sliwa, M.; Fortage, J.; Collomb, M.-N. Cobalt(III) Tetraaza-Macrocyclic

- Complexes as Efficient Catalyst for Photoinduced Hydrogen Production in Water: Theoretical Investigation of the Electronic Structure of the Reduced Species and Mechanistic Insight. *Journal of Photochemistry and Photobiology B: Biology* **2015**, *152*, 82–94. <https://doi.org/10.1016/j.jphotobiol.2015.04.010>.
- (85) Grau, S.; Schilling, M.; Moonshiram, D.; Benet-Buchholz, J.; Lubner, S.; Llobet, A.; Gimbert-Suriñach, C. Electrochemically and Photochemically Induced Hydrogen Evolution Catalysis with Cobalt Tetraazamacrocycles Occurs Through Different Pathways. *ChemSusChem* **2020**, *13* (10), 2745–2752. <https://doi.org/10.1002/cssc.202000283>.
- (86) Tschierlei, S.; Presselt, M.; Kuhnt, C.; Yartsev, A.; Pascher, T.; Sundström, V.; Karnahl, M.; Schwalbe, M.; Schäfer, B.; Rau, S.; Schmitt, M.; Dietzek, B.; Popp, J. Photophysics of an Intramolecular Hydrogen-Evolving Ru-Pd Photocatalyst. *Chemistry - A European Journal* **2009**, *15* (31), 7678–7688. <https://doi.org/10.1002/chem.200900457>.
- (87) Windle, C. D.; Massin, J.; Chavarot-Kerlidou, M.; Artero, V. A Protocol for Quantifying Hydrogen Evolution by Dye-Sensitized Molecular Photocathodes and Its Implementation for Evaluating a New Covalent Architecture Based on an Optimized Dye-Catalyst Dyad. *Dalton Transactions* **2018**, *47* (31), 10509–10516. <https://doi.org/10.1039/C8DT01210E>.
- (88) Watson, D. F.; Meyer, G. J. Electron Injection At Dye-Sensitized Semiconductor Electrodes. *Annu. Rev. Phys. Chem* **2005**, *56*, 119–156. <https://doi.org/10.1146/annurev.physchem.56.092503.141142>.
- (89) Mori, S.; Fukuda, S.; Sumikura, S.; Takeda, Y.; Tamaki, Y.; Suzuki, E.; Abe, T. Charge-Transfer Processes in Dye-Sensitized NiO Solar Cells. *The Journal of Physical Chemistry C* **2008**, *112* (41), 16134–16139. <https://doi.org/10.1021/jp803919b>.
- (90) Li, N.; Gibson, E. A.; Qin, P.; Boschloo, G.; Gorlov, M.; Hagfeldt, A.; Sun, L. Double-Layered NiO Photocathodes for p-Type DSSCs with Record IPCE. *Advanced Materials* **2010**, *22* (15), 1759–1762. <https://doi.org/10.1002/adma.200903151>.
- (91) Wrede, S.; Tian, H. Towards Sustainable and Efficient P-Type Metal Oxide Semiconductor Materials in Dye-Sensitised Photocathodes for Solar Energy Conversion. *Physical Chemistry Chemical Physics* **2020**, *19*. <https://doi.org/10.1039/D0CP01363C>.
- (92) Banerjee, A. N.; Chattopadhyay, K. K. Recent Developments in the Emerging Field of Crystalline P-Type Transparent Conducting Oxide Thin Films. *Progress*

- in Crystal Growth and Characterization of Materials* **2005**, 50 (1–3), 52–105.  
<https://doi.org/10.1016/j.pcrysgrow.2005.10.001>.
- (93) Kawazoe, H.; Yanagi, H.; Ueda, K.; Hosono, H. Transparent p-Type Conducting Oxides: Design and Fabrication of p-n Heterojunctions. *MRS Bulletin* **2000**, 25 (8), 28–36. <https://doi.org/10.1557/mrs2000.148>.
- (94) Yim, K.; Youn, Y.; Lee, M.; Yoo, D.; Lee, J.; Cho, S. H.; Han, S. Computational Discovery of P-Type Transparent Oxide Semiconductors Using Hydrogen Descriptor. *npj Computational Materials* **2018**, 4 (1), 17.  
<https://doi.org/10.1038/s41524-018-0073-z>.
- (95) Zhu, H.; Hagfeldt, A.; Boschloo, G. Photoelectrochemistry of Mesoporous NiO Electrodes in Iodide/Triiodide Electrolytes. *The Journal of Physical Chemistry C* **2007**, 111 (47), 17455–17458. <https://doi.org/10.1021/jp077134k>.
- (96) Qin, P.; Zhu, H.; Edvinsson, T.; Boschloo, G.; Hagfeldt, A.; Sun, L. Design of an Organic Chromophore for P-Type Dye-Sensitized Solar Cells. *Journal of the American Chemical Society* **2008**, 130 (27), 8570–8571.  
<https://doi.org/10.1021/ja8001474>.
- (97) Qin, P.; Linder, M.; Brinck, T.; Boschloo, G.; Hagfeldt, A.; Sun, L. High Incident Photon-to-Current Conversion Efficiency of p-Type Dye-Sensitized Solar Cells Based on NiO and Organic Chromophores. *Advanced Materials* **2009**, 21 (29), 2993–2996. <https://doi.org/10.1002/adma.200802461>.
- (98) Bräutigam, M.; Weyell, P.; Rudolph, T.; Dellith, J.; Kriek, S.; Schmalz, H.; Schacher, F. H.; Dietzek, B. Porous NiOx Nanostructures Templated by Polystyrene-Block-Poly(2-Vinylpyridine) Diblock Copolymer Micelles. *Journal of Materials Chemistry A* **2014**, 2 (17), 6158. <https://doi.org/10.1039/c3ta14890d>.
- (99) Nakasa, A.; Usami, H.; Sumikura, S.; Hasegawa, S.; Koyama, T.; Suzuki, E. A High Voltage Dye-Sensitized Solar Cell Using a Nanoporous NiO Photocathode. *Chemistry Letters* **2005**, 34 (4), 500–501.  
<https://doi.org/10.1246/cl.2005.500>.
- (100) Sumikura, S.; Mori, S.; Shimizu, S.; Usami, H.; Suzuki, E. Syntheses of NiO Nanoporous Films Using Nonionic Triblock Co-Polymer Templates and Their Application to Photo-Cathodes of p-Type Dye-Sensitized Solar Cells. *Journal of Photochemistry and Photobiology A: Chemistry* **2008**, 199 (1), 1–7.  
<https://doi.org/10.1016/j.jphotochem.2008.04.007>.
- (101) le Pleux, L.; Smeigh, A. L.; Gibson, E.; Pellegrin, Y.; Blart, E.; Boschloo, G.; Hagfeldt, A.; Hammarström, L.; Odobel, F. Synthesis, Photophysical and

- Photovoltaic Investigations of Acceptor-Functionalized Perylene Monoimide Dyes for Nickel Oxide p-Type Dye-Sensitized Solar Cells. *Energy and Environmental Science* **2011**, 4 (6), 2075–2084. <https://doi.org/10.1039/c1ee01148k>.
- (102) Click, K. A.; Beauchamp, D. R.; Garrett, B. R.; Huang, Z.; Hadad, C. M.; Wu, Y. A Double-Acceptor as a Superior Organic Dye Design for p-Type DSSCs: High Photocurrents and the Observed Light Soaking Effect. *Phys. Chem. Chem. Phys.* **2014**, 16 (47), 26103–26111. <https://doi.org/10.1039/C4CP04010D>.
- (103) Gibson, E. a; Awais, M.; Dini, D.; Dowling, D. P.; Pryce, M. T.; Vos, J. G.; Boschloo, G.; Hagfeldt, A. Dye Sensitised Solar Cells with Nickel Oxide Photocathodes Prepared via Scalable Microwave Sintering. *Physical Chemistry Chemical Physics* **2013**, 15 (7), 2411. <https://doi.org/10.1039/c2cp43592f>.
- (104) Velevska, J.; Ristova, M. Electrochromic Properties of NiOx Prepared by Low Vacuum Evaporation. *Solar Energy Materials and Solar Cells* **2002**, 73 (2), 131–139. [https://doi.org/10.1016/S0927-0248\(01\)00118-0](https://doi.org/10.1016/S0927-0248(01)00118-0).
- (105) Vera, F.; Schrebler, R.; Muñoz, E.; Suarez, C.; Cury, P.; Gómez, H.; Córdova, R.; Marotti, R. E.; Dalchiele, E. A. Preparation and Characterization of Eosin B- and Erythrosin J-Sensitized Nanostructured NiO Thin Film Photocathodes. *Thin Solid Films* **2005**, 490 (2), 182–188. <https://doi.org/10.1016/j.tsf.2005.04.052>.
- (106) Lepleux, L.; Chavillon, B.; Pellegrin, Y.; Blart, E.; Cario, L.; Jobic, S.; Odobel, F. Simple and Reproducible Procedure to Prepare Self-Nanostructured NiO Films for the Fabrication of P-Type Dye-Sensitized Solar Cells. *Inorganic Chemistry* **2009**, 48 (17), 8245–8250. <https://doi.org/10.1021/ic900866g>.
- (107) Dillon, R. J.; Alibabaei, L.; Meyer, T. J.; Papanikolas, J. M. Enabling Efficient Creation of Long-Lived Charge-Separation on Dye-Sensitized NiO Photocathodes. *ACS Applied Materials & Interfaces* **2017**, 9 (32), 26786–26796. <https://doi.org/10.1021/acsami.7b05856>.
- (108) D'Amario, L.; Antila, L. J.; Pettersson Rimgard, B.; Boschloo, G.; Hammarström, L. Kinetic Evidence of Two Pathways for Charge Recombination in NiO-Based Dye-Sensitized Solar Cells. *The Journal of Physical Chemistry Letters* **2015**, 6 (5), 779–783. <https://doi.org/10.1021/acs.jpcllett.5b00048>.
- (109) Li, X.; Liu, A.; Chu, D.; Zhang, C.; Du, Y.; Huang, J.; Yang, P. High Performance of Manganese Porphyrin Sensitized P-Type CuFe<sub>2</sub>O<sub>4</sub> Photocathode for Solar Water Splitting to Produce Hydrogen in a Tandem Photoelectrochemical Cell. *Catalysts* **2018**, 8 (3), 108. <https://doi.org/10.3390/catal8030108>.

- (110) Li, F.; Xu, R.; Nie, C.; Wu, X.; Zhang, P.; Duan, L.; Sun, L. Dye-Sensitized LaFeO<sub>3</sub> Photocathode for Solar-Driven H<sub>2</sub> Generation. *Chemical Communications* **2019**, *55* (86), 12940–12943. <https://doi.org/10.1039/C9CC06781G>.
- (111) Tapia, C.; Bellet-Amalric, E.; Aldakov, D.; Boudoire, F.; Sivula, K.; Cagnon, L.; Artero, V. Achieving Visible Light-Driven Hydrogen Evolution at Positive Bias with a Hybrid Copper–Iron Oxide|TiO<sub>2</sub>–Cobaloxime Photocathode. *Green Chemistry* **2020**, *22* (10), 3141–3149. <https://doi.org/10.1039/D0GC00979B>.
- (112) Castillo, C. E.; Gennari, M.; Stoll, T.; Fortage, J.; Deronzier, A.; Collomb, M.-N.; Sandroni, M.; L egalit e, F.; Blart, E.; Pellegrin, Y.; Delacote, C.; Boujtita, M.; Odobel, F.; Rannou, P.; Sadki, S. Visible Light-Driven Electron Transfer from a Dye-Sensitized p-Type NiO Photocathode to a Molecular Catalyst in Solution: Toward NiO-Based Photoelectrochemical Devices for Solar Hydrogen Production. *The Journal of Physical Chemistry C* **2015**, *119* (11), 5806–5818. <https://doi.org/10.1021/jp511469f>.
- (113) Zietz, B.; Gabrielsson, E.; Johansson, V.; El-Zohry, A. M.; Sun, L.; Kloo, L. Photoisomerization of the Cyanoacrylic Acid Acceptor Group – a Potential Problem for Organic Dyes in Solar Cells. *Physical Chemistry Chemical Physics* **2014**, *16* (6), 2251. <https://doi.org/10.1039/c3cp54048k>.
- (114) Yao, L.; Guijarro, N.; Boudoire, F.; Liu, Y.; Rahmanudin, A.; Wells, R. A.; Sekar, A.; Cho, H.-H.; Yum, J.-H.; le Formal, F.; Sivula, K. Establishing Stability in Organic Semiconductor Photocathodes for Solar Hydrogen Production. *Journal of the American Chemical Society* **2020**, *142* (17), 7795–7802. <https://doi.org/10.1021/jacs.0c00126>.
- (115) Queyriaux, N.; Jane, R. T.; Massin, J.; Artero, V.; Chavarot-Kerlidou, M. Recent Developments in Hydrogen Evolving Molecular Cobalt(II)-Polypyridyl Catalysts. *Coordination Chemistry Reviews* **2015**, *304–305*, 3–19. <https://doi.org/10.1016/j.ccr.2015.03.014>.
- (116) Ishow, E.; Guillot, R.; Buntinx, G.; Poizat, O. Photoinduced Intramolecular Charge-Transfer Dynamics of a Red-Emitting Dicyanovinyl-Based Triarylamine Dye in Solution. *Journal of Photochemistry and Photobiology A: Chemistry* **2012**, *234*, 27–36. <https://doi.org/10.1016/j.jphotochem.2011.12.018>.
- (117) Flender, O.; Scholz, M.; Klein, J. R.; Oum, K.; Lenzer, T. Excited-State Relaxation of the Solar Cell Dye D49 in Organic Solvents and on Mesoporous Al<sub>2</sub>O<sub>3</sub> and TiO<sub>2</sub> Thin Films. *Physical Chemistry Chemical Physics* **2016**, *18* (37), 26010–26019. <https://doi.org/10.1039/C6CP05167G>.

- (118) Oum, K.; Flender, O.; Lohse, P. W.; Scholz, M.; Hagfeldt, A.; Boschloo, G.; Lenzer, T. Electron and Hole Transfer Dynamics of a Triarylamine-Based Dye with Peripheral Hole Acceptors on TiO<sub>2</sub> in the Absence and Presence of Solvent. *Physical Chemistry Chemical Physics* **2014**, *16* (17), 8019. <https://doi.org/10.1039/c3cp55298e>.
- (119) Oum, K.; Lohse, P. W.; Klein, J. R.; Flender, O.; Scholz, M.; Hagfeldt, A.; Boschloo, G.; Lenzer, T. Photoinduced Ultrafast Dynamics of the Triphenylamine-Based Organic Sensitizer D35 on TiO<sub>2</sub>, ZrO<sub>2</sub> and in Acetonitrile. *Physical Chemistry Chemical Physics* **2013**, *15* (11), 3906. <https://doi.org/10.1039/c3cp44095h>.
- (120) Labrunie, A.; Gorenflot, J.; Babics, M.; Alévêque, O.; Dabos-Seignon, S.; Balawi, A. H.; Kan, Z.; Wohlfahrt, M.; Levillain, E.; Hudhomme, P.; Beaujuge, P. M.; Laquai, F.; Cabanetos, C.; Blanchard, P. Triphenylamine-Based Push–Pull  $\sigma$ -C 60 Dyad As Photoactive Molecular Material for Single-Component Organic Solar Cells: Synthesis, Characterizations, and Photophysical Properties. *Chemistry of Materials* **2018**, *30* (10), 3474–3485. <https://doi.org/10.1021/acs.chemmater.8b01117>.
- (121) Massin, J.; Bräutigam, M.; Kaeffer, N.; Queyriaux, N.; Field, M. J.; Schacher, F. H.; Chavarot-Kerlidou, M.; Dietzek, B.; Artero, V. Dye-Sensitized PS- b -P2VP-Templated Nickel Oxide Films for Photoelectrochemical Applications. *Interface Focus* **2015**, *5*.
- (122) Ishow, E.; Clavier, G.; Miomandre, F.; Rebarz, M.; Buntinx, G.; Poizat, O. Comprehensive Investigation of the Excited-State Dynamics of Push–Pull Triphenylamine Dyes as Models for Photonic Applications. *Physical Chemistry Chemical Physics* **2013**, *15* (33), 13922. <https://doi.org/10.1039/c3cp51480c>.
- (123) Zhu, H.; Wang, X.; Ma, R.; Kuang, Z.; Guo, Q.; Xia, A. Intramolecular Charge Transfer and Solvation of Photoactive Molecules with Conjugated Push–Pull Structures. *ChemPhysChem* **2016**, *17* (20), 3245–3251. <https://doi.org/10.1002/cphc.201600674>.
- (124) Zhang, L.; Boschloo, G.; Hammarström, L.; Tian, H. Solid State P-Type Dye-Sensitized Solar Cells: Concept, Experiment and Mechanism. *Physical Chemistry Chemical Physics* **2016**, *18* (7), 5080–5085. <https://doi.org/10.1039/C5CP05247E>.
- (125) Black, F. A.; Clark, C. A.; Summers, G. H.; Clark, I. P.; Towrie, M.; Penfold, T.; George, M. W.; Gibson, E. A. Investigating Interfacial Electron Transfer in Dye-Sensitized NiO Using Vibrational Spectroscopy. *Physical Chemistry Chemical Physics* **2017**, *19* (11), 7877–7885. <https://doi.org/10.1039/C6CP05712H>.

- (126) Yen, Y.-S.; Chen, W.-T.; Hsu, C.-Y.; Chou, H.-H.; Lin, J. T.; Yeh, M.-C. P. Arylamine-Based Dyes for p-Type Dye-Sensitized Solar Cells. *Organic Letters* **2011**, *13* (18), 4930–4933. <https://doi.org/10.1021/ol202014x>.
- (127) Li, R.; Liu, J.; Cai, N.; Zhang, M.; Wang, P. Synchronously Reduced Surface States, Charge Recombination, and Light Absorption Length for High-Performance Organic Dye-Sensitized Solar Cells. *The Journal of Physical Chemistry B* **2010**, *114* (13), 4461–4464. <https://doi.org/10.1021/jp101222s>.
- (128) Leung, C.; Chen, Y.; Yu, H.; Yiu, S.; Ko, C.; Lau, T.-C. Electro- and Photocatalytic Hydrogen Generation in Acetonitrile and Aqueous Solutions by a Cobalt Macrocyclic Schiff-Base Complex. *International Journal of Hydrogen Energy* **2011**, *36* (18), 11640–11645. <https://doi.org/10.1016/j.ijhydene.2011.06.062>.
- (129) Lacy, D. C.; McCrory, C. C. L.; Peters, J. C. Studies of Cobalt-Mediated Electrocatalytic CO<sub>2</sub> Reduction Using a Redox-Active Ligand. *Inorganic Chemistry* **2014**, *53* (10), 4980–4988. <https://doi.org/10.1021/ic403122j>.
- (130) Zhang, Y.; Zedler, L.; Karnahl, M.; Dietzek, B. Excited-State Dynamics of Heteroleptic Copper(I) Photosensitizers and Their Electrochemically Reduced Forms Containing a Dipyridophenazine Moiety – a Spectroelectrochemical Transient Absorption Study. *Physical Chemistry Chemical Physics* **2019**, *21* (20), 10716–10725. <https://doi.org/10.1039/C9CP00412B>.
- (131) Luo, Y.; Maloul, S.; Wächtler, M.; Winter, A.; Schubert, U. S.; Streb, C.; Dietzek, B. Is Electron Ping-Pong Limiting the Catalytic Hydrogen Evolution Activity in Covalent Photosensitizer–Polyoxometalate Dyads? *Chemical Communications* **2020**, *56* (72), 10485–10488. <https://doi.org/10.1039/D0CC04509H>.
- (132) Sheth, S.; Baron, A.; Herrero, C.; Vauzeilles, B.; Aukauloo, A.; Leibl, W. Light-Induced Tryptophan Radical Generation in a Click Modular Assembly of a Sensitiser-Tryptophan Residue. *Photochemical & Photobiological Sciences* **2013**, *12* (6), 1074. <https://doi.org/10.1039/c3pp50021g>.
- (133) Herrero, C.; Quaranta, A.; el Ghachtouli, S.; Vauzeilles, B.; Leibl, W.; Aukauloo, A. Carbon Dioxide Reduction via Light Activation of a Ruthenium-Ni(Cyclam) Complex. *Physical Chemistry Chemical Physics* **2014**, *16* (24), 12067–12072. <https://doi.org/10.1039/c3cp54946a>.
- (134) Baron, A.; Herrero, C.; Quaranta, A.; Charlot, M.-F.; Leibl, W.; Vauzeilles, B.; Aukauloo, A. Efficient Electron Transfer through a Triazole Link in Ruthenium(II) Polypyridine Type Complexes. *Chemical Communications* **2011**, *47* (39), 11011. <https://doi.org/10.1039/c1cc13683f>.

- (135) Herrero, C.; Batchelor, L.; Baron, A.; el Ghachtouli, S.; Sheth, S.; Guillot, R.; Vauzeilles, B.; Sircoglou, M.; Mallah, T.; Leibl, W.; Aukauloo, A. Click Chemistry as a Convenient Tool for the Incorporation of a Ruthenium Chromophore and a Nickel-Salen Monomer into a Visible-Light-Active Assembly. *European Journal of Inorganic Chemistry* **2013**, 2013 (4), 494–499. <https://doi.org/10.1002/ejic.201201161>.
- (136) Herrero, C.; Quaranta, A.; Sircoglou, M.; Sénéchal-David, K.; Baron, A.; Marín, I. M.; Buron, C.; Baltaze, J.-P.; Leibl, W.; Aukauloo, A.; Banse, F. Successive Light-Induced Two Electron Transfers in a Ru–Fe Supramolecular Assembly: From Ru–Fe(II)–OH<sub>2</sub> to Ru–Fe(IV)–Oxo. *Chemical Science* **2015**, 6 (4), 2323–2327. <https://doi.org/10.1039/C5SC00024F>.
- (137) Ngo, T. H.; Zieba, D.; Webre, W. A.; Lim, G. N.; Karr, P. A.; Kord, S.; Jin, S.; Ariga, K.; Galli, M.; Goldup, S.; Hill, J. P.; D'Souza, F. Engaging Copper(III) Corrole as an Electron Acceptor: Photoinduced Charge Separation in Zinc Porphyrin-Copper Corrole Donor-Acceptor Conjugates. *Chemistry - A European Journal* **2016**, 22 (4), 1301–1312. <https://doi.org/10.1002/chem.201503490>.
- (138) Villegas, C.; Delgado, J. L.; Bouit, P. A.; Grimm, B.; Seitz, W.; Martín, N.; Guldi, D. M. Powering Reductive Charge Shift Reactions - Linking Fullerenes of Different Electron Acceptor Strength to Secure an Energy Gradient. *Chemical Science* **2011**, 2 (9), 1677–1681. <https://doi.org/10.1039/c1sc00331c>.
- (139) Odobel, F.; Séverac, M.; Pellegrin, Y.; Blart, E.; Fosse, C.; Cannizzo, C.; Mayer, C. R.; Elliott, K. J.; Harriman, A. Coupled Sensitizer-Catalyst Dyads: Electron-Transfer Reactions in a Perylene-Polyoxometalate Conjugate. *Chemistry - A European Journal* **2009**, 15 (13), 3130–3138. <https://doi.org/10.1002/chem.200801880>.
- (140) Harriman, A.; Elliott, K. J.; Alamiry, M. A. H.; Pleux, L. le; Séverac, M.; Pellegrin, Y.; Blart, E.; Fosse, C.; Cannizzo, C.; Mayer, C. R.; Odobel, F. Intramolecular Electron Transfer Reactions Observed for Dawson-Type Polyoxometalates Covalently Linked to Porphyrin Residues. *The Journal of Physical Chemistry C* **2009**, 113 (14), 5834–5842. <https://doi.org/10.1021/jp900643m>.
- (141) Natali, M.; Ravaglia, M.; Scandola, F.; Boixel, J.; Pellegrin, Y.; Blart, E.; Odobel, F. Long-Range Charge Separation in a Ferrocene–(Zinc Porphyrin)–Naphthalenediimide Triad. Asymmetric Role of 1,2,3-Triazole Linkers. *The Journal of Physical Chemistry C* **2013**, 117 (38), 19334–19345. <https://doi.org/10.1021/jp406405k>.



- (142) Nikolaou, V.; Plass, F.; Planchat, A.; Charisiadis, A.; Charalambidis, G.; Angaridis, P. A.; Kahnt, A.; Odobel, F.; Coutsolelos, A. G. Effect of the Triazole Ring in Zinc Porphyrin-Fullerene Dyads on the Charge Transfer Processes in NiO-Based Devices. *Physical Chemistry Chemical Physics* **2018**, *20* (37), 24477–24489. <https://doi.org/10.1039/C8CP04060E>.
- (143) Mohanraj, J.; Barbieri, A.; Armaroli, N.; Vizueté, M.; Langa, F.; Delavaux-Nicot, B.; Vartanian, M.; Iehl, J.; Hahn, U.; Nierengarten, J. F. Efficient Photoinduced Energy and Electron Transfer in ZnII–Porphyrin/Fullerene Dyads with Interchromophoric Distances up to 2.6 Nm and No Wire-like Connectivity. *Chemistry - A European Journal* **2017**, *23* (57), 14200–14212. <https://doi.org/10.1002/chem.201701668>.
- (144) Nantalaksakul, A.; Mueller, A.; Klaikherd, A.; Bardeen, C. J.; Thayumanavan, S. Dendritic and Linear Macromolecular Architectures for Photovoltaics: A Photoinduced Charge Transfer Investigation. *Journal of the American Chemical Society* **2009**, *131* (7), 2727–2738. <https://doi.org/10.1021/ja809194u>.
- (145) Queyriaux, N.; Andreiadis, E. S.; Torelli, S.; Pecaut, J.; Veldkamp, B. S.; Margulies, E. A.; Wasielewski, M. R.; Chavarot-Kerlidou, M.; Artero, V. CuAAC-Based Assembly and Characterization of a Ruthenium–Copper Dyad Containing a Diimine–Dioxime Ligand Framework. *Faraday Discussions* **2017**, *198*, 251–261. <https://doi.org/10.1039/C6FD00204H>.
- (146) Shetti, V. S.; Ravikanth, M. Synthesis of Triazole-Bridged Unsymmetrical Porphyrin Dyads and Porphyrin-Ferrocene Conjugates. *European Journal of Organic Chemistry* **2010**, *2010* (3), 494–508. <https://doi.org/10.1002/ejoc.200901070>.
- (147) Pla, S.; Martín-Gomis, L.; Ohkubo, K.; Fukuzumi, S.; Fernández-Lázaro, F.; Sastre-Santos, Á. Macrocyclic Dyads Based on C 60 and Perylenediimides Connected by Click Chemistry. *Asian Journal of Organic Chemistry* **2014**, *3* (2), 185–197. <https://doi.org/10.1002/ajoc.201300235>.
- (148) de Miguel, G.; Wielopolski, M.; Schuster, D. I.; Fazio, M. A.; Lee, O. P.; Haley, C. K.; Ortiz, A. L.; Echegoyen, L.; Clark, T.; Guldi, D. M. Triazole Bridges as Versatile Linkers in Electron Donor–Acceptor Conjugates. *Journal of the American Chemical Society* **2011**, *133* (33), 13036–13054. <https://doi.org/10.1021/ja202485s>.
- (149) Wang, L.; Puodziukynaite, E.; Grumstrup, E. M.; Brown, A. C.; Keinan, S.; Schanze, K. S.; Reynolds, J. R.; Papanikolas, J. M. Ultrafast Formation of a Long-Lived Charge-Separated State in a Ru-Loaded Poly(3-Hexylthiophene)

- Light-Harvesting Polymer. *The Journal of Physical Chemistry Letters* **2013**, *4* (14), 2269–2273. <https://doi.org/10.1021/jz401089v>.
- (150) Morseth, Z. A.; Pho, T. v.; Gilligan, A. T.; Dillon, R. J.; Schanze, K. S.; Reynolds, J. R.; Papanikolas, J. M. Role of Macromolecular Structure in the Ultrafast Energy and Electron Transfer Dynamics of a Light-Harvesting Polymer. *Journal of Physical Chemistry B* **2016**, *120* (32), 7937–7948. <https://doi.org/10.1021/acs.jpcc.6b05589>.
- (151) Shi, H.; Du, L.; Xiong, W.; Dai, M.; Chan, W. K.; Phillips, D. L. Study of Electronic Interactions and Photo-Induced Electron Transfer Dynamics in a Metalloconjugated Polymer-Single-Walled Carbon Nanotube Hybrid by Ultrafast Transient Absorption Spectroscopy. *Journal of Materials Chemistry A* **2017**, *5* (35), 18527–18534. <https://doi.org/10.1039/c7ta02753b>.
- (152) Wang, L.; Puodziukynaite, E.; Vary, R. P.; Grumstrup, E. M.; Walczak, R. M.; Zolotar'skaya, O. Y.; Schanze, K. S.; Reynolds, J. R.; Papanikolas, J. M. Competition between Ultrafast Energy Flow and Electron Transfer in a Ru(II)-Loaded Polyfluorene Light-Harvesting Polymer. *The Journal of Physical Chemistry Letters* **2012**, *3* (17), 2453–2457. <https://doi.org/10.1021/jz300979j>.
- (153) Grebner, D.; Helbig, M.; Rentsch, S. Size-Dependent Properties of Oligothiophenes by Picosecond Time-Resolved Spectroscopy. *The Journal of Physical Chemistry* **1995**, *99* (46), 16991–16998. <https://doi.org/10.1021/j100046a027>.
- (154) Rentsch, S.; Yang, J. P.; Paa, W.; Birckner, E.; Schiedt, J.; Weinkauff, R. Size Dependence of Triplet and Singlet States of  $\alpha$ -Oligothiophenes. *Physical Chemistry Chemical Physics* **1999**, *1* (8), 1707–1714. <https://doi.org/10.1039/a808617f>.
- (155) Paa, W.; Yang, J. P.; Helbig, M.; Hein, J.; Rentsch, S. Femtosecond Time-Resolved Measurements of Terthiophene: Fast Singlet-Triplet Intersystem Crossing. *Chemical Physics Letters* **1998**, *292* (4–6), 607–614. [https://doi.org/10.1016/S0009-2614\(98\)00694-0](https://doi.org/10.1016/S0009-2614(98)00694-0).
- (156) Janssen, R. A. J.; Smilowitz, L.; Sariciftci, N. S.; Moses, D. Triplet-state Photoexcitations of Oligothiophene Films and Solutions. *The Journal of Chemical Physics* **1994**, *101* (3), 1787–1798. <https://doi.org/10.1063/1.467757>.
- (157) Volchkov, V. v.; Ivanov, V. L.; Uzhinov, B. M. Induced Intersystem Crossing at the Fluorescence Quenching of Laser Dye 7-Amino-1,3-Naphthalenedisulfonic Acid by Paramagnetic Metal Ions. *Journal of Fluorescence* **2010**, *20* (1), 299–303. <https://doi.org/10.1007/s10895-009-0555-y>.

- (158) Takashima, H.; Kawahara, H.; Kitano, M.; Shibata, S.; Murakami, H.; Tsukahara, K. Metal Ion-Dependent Fluorescent Dynamics of Photoexcited Zinc - Porphyrin and Zinc - Myoglobin Modified with Ethylenediaminetetraacetic Acid. *Journal of Physical Chemistry B* **2008**, *112* (48), 15493–15502. <https://doi.org/10.1021/jp807692w>.
- (159) Ji, S.; Zhao, J.; Donato, M. di; Xing, Y. H.; Mahmood, Z.; Taddei, M.; Rehmat, N.; Bussotti, L.; Doria, S.; Guan, Q.; Huo, Y. Color-Tunable Delayed Fluorescence and Efficient Spin-orbit Charge Transfer Intersystem Crossing in Compact Carbazole-Anthracene-BODIPY Triads Employing the Sequential Electron Transfer Approach. *Journal of Physical Chemistry C* **2020**, *124* (11), 5944–5957. <https://doi.org/10.1021/acs.jpcc.9b11687>.
- (160) Weiss, E. A.; Ratner, M. A.; Wasielewski, M. R. Direct Measurement of Singlet-Triplet Splitting within Rodlike Photogenerated Radical Ion Pairs Using Magnetic Field Effects: Estimation of the Electronic Coupling for Charge Recombination. *Journal of Physical Chemistry A* **2003**, *107* (19), 3639–3647. <https://doi.org/10.1021/jp0224315>.
- (161) Dance, Z. E. X.; Mi, Q.; McCamant, D. W.; Ahrens, M. J.; Ratner, M. A.; Wasielewski, M. R. Time-Resolved EPR Studies of Photogenerated Radical Ion Pairs Separated by p-Phenylene Oligomers and of Triplet States Resulting from Charge Recombination. *Journal of Physical Chemistry B* **2006**, *110* (50), 25163–25173. <https://doi.org/10.1021/jp063690n>.
- (162) Colvin, M. T.; Ricks, A. B.; Scott, A. M.; Co, D. T.; Wasielewski, M. R. Intersystem Crossing Involving Strongly Spin Exchange-Coupled Radical Ion Pairs in Donor-Bridge-Acceptor Molecules. *Journal of Physical Chemistry A* **2012**, *116* (8), 1923–1930. <https://doi.org/10.1021/jp212546w>.
- (163) Wu, W.; Zhao, J.; Sun, J.; Guo, S. Light-Harvesting Fullerene Dyads as Organic Triplet Photosensitizers for Triplet-Triplet Annihilation Upconversions. *Journal of Organic Chemistry* **2012**, *77* (12), 5305–5312. <https://doi.org/10.1021/jo300613g>.
- (164) Huang, L.; Cui, X.; Therrien, B.; Zhao, J. Energy-Funneling-Based Broadband Visible-Light-Absorbing Bodipy-C<sub>60</sub> Triads and Tetrads as Dual Functional Heavy-Atom-Free Organic Triplet Photosensitizers for Photocatalytic Organic Reactions. *Chemistry - A European Journal* **2013**, *19* (51), 17472–17482. <https://doi.org/10.1002/chem.201302492>.
- (165) Huang, D.; Zhao, J.; Wu, W.; Yi, X.; Yang, P.; Ma, J. Visible-Light-Harvesting Triphenylamine Ethynyl C<sub>60</sub>-BODIPY Dyads as Heavy-Atom-Free Organic Triplet Photosensitizers for Triplet-Triplet Annihilation Upconversion. *Asian*

- Journal of Organic Chemistry* **2012**, *1* (3), 264–273.  
<https://doi.org/10.1002/ajoc.201200062>.
- (166) Marroux, H. J. B.; Curchod, B. F. E.; Faradji, C. A.; Shuttleworth, T. A.; Sparkes, H. A.; Pringle, P. G.; Orr-Ewing, A. J. Spin Changes Accompany Ultrafast Structural Interconversion in the Ground State of a Cobalt Nitrosyl Complex. *Angewandte Chemie - International Edition* **2017**, *56* (44), 13713–13716.  
<https://doi.org/10.1002/anie.201707508>.
- (167) McCusker, J. K.; Walda, K. N.; Magde, D.; Hendrickson, D. N. Picosecond Excited-State Dynamics in Octahedral Cobalt(III) Complexes: Intersystem Crossing versus Internal Conversion. *Inorganic Chemistry* **1993**, *32* (4), 394–399.  
<https://doi.org/10.1021/ic00056a010>.
- (168) Quaranta, A.; Lachaud, F.; Herrero, C.; Guillot, R.; Charlot, M. F.; Leibl, W.; Aukauloo, A. Influence of the Protonic State of an Imidazole-Containing Ligand on the Electrochemical and Photophysical Properties of a Ruthenium(II)-Polypyridine- Type Complex. *Chemistry - A European Journal* **2007**, *13* (29), 8201–8211. <https://doi.org/10.1002/chem.200700185>.
- (169) Reichardt, C.; Pinto, M.; Wächtler, M.; Stephenson, M.; Kupfer, S.; Sainuddin, T.; Guthmuller, J.; McFarland, S. a.; Dietzek, B. Photophysics of Ru(II) Dyads Derived from Pyrenyl-Substituted Imidazo[4,5- f ][1,10]Phenanthroline Ligands. *J. Phys. Chem. A* **2015**, *119* (17), 3986–3994.  
<https://doi.org/10.1021/acs.jpca.5b01737>.
- (170) Zhang, P.; Jacques, P.-A.; Chavarot-Kerlidou, M.; Wang, M.; Sun, L.; Fontecave, M.; Artero, V. Phosphine Coordination to a Cobalt Diimine–Dioxime Catalyst Increases Stability during Light-Driven H<sub>2</sub> Production. *Inorganic Chemistry* **2012**, *51* (4), 2115–2120. <https://doi.org/10.1021/ic2019132>.
- (171) Bahng, H.; Hagfeldt, A.; Moser, J. Lateral Intermolecular Electronic Interactions of Diketopyrrolopyrrole D- $\pi$ -A Solar Dye Sensitizers Adsorbed on Mesoporous Alumina. *The Journal of Physical Chemistry C* **2018**, *122* (34), 19348–19358. <https://doi.org/10.1021/acs.jpcc.8b04815>.
- (172) Zahner PEC-Cells PECC-1/PECC-2  
<http://zahner.de/products/photoelectrochemistry/pec-cells.html> (accessed 2020-10-28).
- (173) Adler, D.; Feinleib, J. Electrical and Optical Properties of Narrow-Band Materials. *Physical Review B* **1970**, *2* (8), 3112–3134.  
<https://doi.org/10.1103/PhysRevB.2.3112>.

- (174) Boschloo, G.; Hagfeldt, A. Spectroelectrochemistry of Nanostructured NiO. *Journal of Physical Chemistry B* **2001**, *105* (15), 3039–3044. <https://doi.org/10.1021/jp003499s>.
- (175) Föhlinger, J.; Maji, S.; Brown, A.; Mijangos, E.; Ott, S.; Hammarström, L. Self-Quenching and Slow Hole Injection May Limit the Efficiency in NiO-Based Dye-Sensitized Solar Cells. *Journal of Physical Chemistry C* **2018**, *122* (25), 13902–13910. <https://doi.org/10.1021/acs.jpcc.8b01016>.
- (176) Tebo, A. G.; Quaranta, A.; Herrero, C.; Pecoraro, V. L.; Aukauloo, A. Intramolecular Photogeneration of a Tyrosine Radical in a Designed Protein. *ChemPhotoChem* **2017**, *1* (3), 89–92. <https://doi.org/10.1002/cptc.201600044>.
- (177) Gardner, J. M.; Beyler, M.; Karnahl, M.; Tschierlei, S.; Ott, S.; Hammarström, L. Light-Driven Electron Transfer between a Photosensitizer and a Proton-Reducing Catalyst Co-Adsorbed to NiO. *Journal of the American Chemical Society* **2012**, *134* (47), 19322–19325. <https://doi.org/10.1021/ja3082268>.
- (178) Morandeira, A.; Boschloo, G.; Hagfeldt, A.; Hammarström, L. Photoinduced Ultrafast Dynamics of Coumarin 343 Sensitized P-Type-Nanostructured NiO Films. *The Journal of Physical Chemistry B* **2005**, *109* (41), 19403–19410. <https://doi.org/10.1021/jp053230e>.
- (179) Morandeira, A.; Boschloo, G.; Hagfeldt, A.; Hammarström, L. Coumarin 343-NiO Films as Nanostructured Photocathodes in Dye-Sensitized Solar Cells: Ultrafast Electron Transfer, Effect of the I<sup>3</sup>/I<sup>-</sup> Redox Couple and Mechanism of Photocurrent Generation. *Journal of Physical Chemistry C* **2008**, *112* (25), 9530–9537. <https://doi.org/10.1021/jp800760q>.
- (180) Yu, Y.; Click, K. A.; Polen, S. M.; He, M.; Hadad, C. M.; Wu, Y. Electron Transfer Kinetics of a Series of Bilayer Triphenylamine-Oligothiophene-Perylenemonoimide Sensitizers for Dye-Sensitized NiO. *Journal of Physical Chemistry C* **2017**, *121* (38), 20720–20728. <https://doi.org/10.1021/acs.jpcc.7b07859>.
- (181) Morandeira, A.; Fortage, J.; Edvinsson, T.; Pleux, L. le; Blart, E.; Boschloo, G.; Hagfeldt, A.; Hammarström, L.; Odobel, F. Improved Photon-to-Current Conversion Efficiency with a Nanoporous p-Type NiO Electrode by the Use of a Sensitizer-Acceptor Dyad. *Journal of Physical Chemistry C* **2008**, *112* (5), 1721–1728. <https://doi.org/10.1021/jp077446n>.
- (182) Gatty, M. G.; Pullen, S.; Sheibani, E.; Tian, H.; Ott, S.; Hammarström, L. Direct Evidence of Catalyst Reduction on Dye and Catalyst Co-Sensitized NiO

- Photocathodes by Mid-Infrared Transient Absorption Spectroscopy. *Chemical Science* **2018**, *9* (22), 4983–4991. <https://doi.org/10.1039/c8sc00990b>.
- (183) Sheibani, E.; Zhang, L.; Liu, P.; Xu, B.; Mijangos, E.; Boschloo, G.; Hagfeldt, A.; Hammarström, L.; Kloo, L.; Tian, H. A Study of Oligothiophene-Acceptor Dyes in p-Type Dye-Sensitized Solar Cells. *RSC Advances* **2016**, *6* (22), 18165–18177. <https://doi.org/10.1039/c5ra26310g>.
- (184) Zhang, L.; Favereau, L.; Farré, Y.; Mijangos, E.; Pellegrin, Y.; Blart, E.; Odobel, F.; Hammarström, L. Ultrafast and Slow Charge Recombination Dynamics of Diketopyrrolopyrrole-NiO Dye Sensitized Solar Cells. *Physical Chemistry Chemical Physics* **2016**, *18* (27), 18515–18527. <https://doi.org/10.1039/c6cp01762b>.
- (185) Zhang, L.; Favereau, L.; Farre, Y.; Maufroy, A.; Pellegrin, Y.; Blart, E.; Hissler, M.; Jacquemin, D.; Odobel, F.; Hammarström, L. Molecular-Structure Control of Electron Transfer Dynamics of Push-Pull Porphyrins as Sensitizers for NiO Based Dye Sensitized Solar Cells. *RSC Advances* **2016**, *6* (81), 77184–77194. <https://doi.org/10.1039/c6ra15195g>.
- (186) Smeigh, A. L.; le Pleux, L.; Fortage, J.; Pellegrin, Y.; Blart, E.; Odobel, F.; Hammarström, L. Ultrafast Recombination for NiO Sensitized with a Series of Perylene Imide Sensitizers Exhibiting Marcus Normal Behaviour. *Chemical Communications* **2012**, *48* (5), 678–680. <https://doi.org/10.1039/c1cc16144j>.
- (187) Borgström, M.; Blart, E.; Boschloo, G.; Mukhtar, E.; Hagfeldt, A.; Hammarström, L.; Odobel, F. Sensitized Hole Injection of Phosphorus Porphyrin into NiO: Toward New Photovoltaic Devices. *Journal of Physical Chemistry B* **2005**, *109* (48), 22928–22934. <https://doi.org/10.1021/jp054034a>.
- (188) Ji, Z.; Natu, G.; Huang, Z.; Kokhan, O.; Zhang, X.; Wu, Y. Synthesis, Photophysics, and Photovoltaic Studies of Ruthenium Cyclometalated Complexes as Sensitizers for p-Type NiO Dye-Sensitized Solar Cells. *Journal of Physical Chemistry C* **2012**, *116* (32), 16854–16863. <https://doi.org/10.1021/jp303909x>.
- (189) Ji, Z.; Wu, Y. Photoinduced Electron Transfer Dynamics of Cyclometalated Ruthenium (II)-Naphthalenediimide Dyad at NiO Photocathode. *Journal of Physical Chemistry C* **2013**, *117* (36), 18315–18324. <https://doi.org/10.1021/jp405659m>.
- (190) Gibson, E. A.; Smeigh, A. L.; le Pleux, L.; Fortage, J.; Boschloo, G.; Blart, E.; Pellegrin, Y.; Odobel, F.; Hagfeldt, A.; Hammarström, L. A P-Type NiO-Based Dye-Sensitized Solar Cell with an Open-Circuit Voltage of 0.35 V. *Angewandte*

- Chemie International Edition* **2009**, *48* (24), 4402–4405.  
<https://doi.org/10.1002/anie.200900423>.
- (191) Bian, Z.; Tachikawa, T.; Cui, S.-C.; Fujitsuka, M.; Majima, T. Single-Molecule Charge Transfer Dynamics in Dye-Sensitized p-Type NiO Solar Cells: Influences of Insulating Al<sub>2</sub>O<sub>3</sub> Layers. *Chemical Science* **2012**, *3* (2), 370–379.  
<https://doi.org/10.1039/C1SC00552A>.
- (192) Hao, Y.; Wood, C. J.; Clark, C. A.; Calladine, J. A.; Horvath, R.; Hanson-Heine, M. W. D.; Sun, X. Z.; Clark, I. P.; Towrie, M.; George, M. W.; Yang, X.; Sun, L.; Gibson, E. A. Can Aliphatic Anchoring Groups Be Utilised with Dyes for P-Type Dye Sensitized Solar Cells? *Dalton Transactions* **2016**, *45* (18), 7708–7719.  
<https://doi.org/10.1039/c6dt00146g>.
- (193) Han, Y.; Dillon, R. J.; Flynn, C. J.; Rountree, E. S.; Alibabaei, L.; Cahoon, J. F.; Papanikolas, J. M.; Dempsey, J. L. Interfacial Electron Transfer Yields in Dye-Sensitized NiO Photocathodes Correlated to Excited-State Dipole Orientation of Ruthenium Chromophores. *Canadian Journal of Chemistry* **2018**, *96* (9), 865–874. <https://doi.org/10.1139/cjc-2017-0359>.
- (194) Shan, B.; Nayak, A.; Brennaman, M. K.; Liu, M.; Marquard, S. L.; Eberhart, M. S.; Meyer, T. J. Controlling Vertical and Lateral Electron Migration Using a Bifunctional Chromophore Assembly in Dye-Sensitized Photoelectrosynthesis Cells. *Journal of the American Chemical Society* **2018**, *140* (20), 6493–6500.  
<https://doi.org/10.1021/jacs.8b03453>.
- (195) Shan, B.; Nayak, A.; N. Sampaio, R.; Eberhart, M. S.; Troian-Gautier, L.; Brennaman, M. K.; Meyer, G. J.; Meyer, T. J. Direct Photoactivation of a Nickel-Based, Water-Reduction Photocathode by a Highly Conjugated Supramolecular Chromophore. *Energy & Environmental Science* **2018**, *11* (2), 447–455. <https://doi.org/10.1039/C7EE03115G>.
- (196) Freys, J. C.; Gardner, J. M.; D'Amario, L.; Brown, A. M.; Hammarström, L. Ru-Based Donor–Acceptor Photosensitizer That Retards Charge Recombination in a p-Type Dye-Sensitized Solar Cell. *Dalton Transactions* **2012**, *41* (42), 13105–13111. <https://doi.org/10.1039/c2dt30829k>.
- (197) Nattestad, A.; Mozer, A. J.; Fischer, M. K. R.; Cheng, Y. B.; Mishra, A.; Bäuerle, P.; Bach, U. Highly Efficient Photocathodes for Dye-Sensitized Tandem Solar Cells. *Nature Materials* **2010**, *9* (1), 31–35. <https://doi.org/10.1038/nmat2588>.
- (198) Kou, Y.; Nakatani, S.; Sunagawa, G.; Tachikawa, Y.; Masui, D.; Shimada, T.; Takagi, S.; Tryk, D. A.; Nabetani, Y.; Tachibana, H.; Inoue, H. Visible Light-Induced Reduction of Carbon Dioxide Sensitized by a Porphyrin-Rhenium

- Dyad Metal Complex on p-Type Semiconducting NiO as the Reduction Terminal End of an Artificial Photosynthetic System. *Journal of Catalysis* **2014**, *310*, 57–66. <https://doi.org/10.1016/j.jcat.2013.03.025>.
- (199) Daeneke, T.; Yu, Z.; Lee, G. P.; Fu, D.; Duffy, N. W.; Makuta, S.; Tachibana, Y.; Spiccia, L.; Mishra, A.; Bäuerle, P.; Bach, U. Dominating Energy Losses in NiO P-Type Dye-Sensitized Solar Cells. *Advanced Energy Materials* **2015**, *5* (4). <https://doi.org/10.1002/aenm.201401387>.
- (200) Li, T. T.; Shan, B.; Meyer, T. J. Stable Molecular Photocathode for Solar-Driven CO<sub>2</sub> Reduction in Aqueous Solutions. *ACS Energy Letters* **2019**, *4* (3), 629–636. <https://doi.org/10.1021/acsenergylett.8b02512>.
- (201) Karnahl, M.; Kuhnt, C.; Heinemann, F. W.; Schmitt, M.; Rau, S.; Popp, J.; Dietzek, B. Synthesis and Photophysics of a Novel Photocatalyst for Hydrogen Production Based on a Tetrapyridoacridine Bridging Ligand. *Chemical Physics* **2012**, *393* (1), 65–73. <https://doi.org/10.1016/j.chemphys.2011.11.027>.
- (202) Pfeffer, M. G.; Kowacs, T.; Wächtler, M.; Guthmuller, J.; Dietzek, B.; Vos, J. G.; Rau, S. Optimization of Hydrogen-Evolving Photochemical Molecular Devices. *Angewandte Chemie - International Edition* **2015**, 6627–6631. <https://doi.org/10.1002/anie.201409442>.
- (203) Siebert, R.; Akimov, D.; Schmitt, M.; Winter, A.; Schubert, U. S.; Dietzek, B.; Popp, J. Spectroscopic Investigation of the Ultrafast Photoinduced Dynamics in ??-Conjugated Terpyridines. *ChemPhysChem* **2009**, *10* (6), 910–919. <https://doi.org/10.1002/cphc.200800847>.
- (204) Sittig, M.; Schmidt, B.; Görls, H.; Bocklitz, T.; Wächtler, M.; Zechel, S.; Hager, M. D.; Dietzek, B. Fluorescence Upconversion by Triplet–Triplet Annihilation in All-Organic Poly(Methacrylate)-Terpolymers. *Physical Chemistry Chemical Physics* **2020**, *22* (7), 4072–4079. <https://doi.org/10.1039/D0CP00232A>.
- (205) Yu, Y.; Click, K. A.; Chien, S.-C.; Sun, J.; Curtze, A.; Lin, L.-C.; Wu, Y. Decoupling PH Dependence of Flat Band Potential in Aqueous Dye-Sensitized Electrodes. *The Journal of Physical Chemistry C* **2019**, *123* (14), 8681–8687. <https://doi.org/10.1021/acs.jpcc.9b00710>.
- (206) Nie, C.; Ni, W.; Gong, L.; Jiang, J.; Wang, J.; Wang, M. Charge Transfer Dynamics and Catalytic Performance of a Covalently Linked Hybrid Assembly Comprising a Functionalized Cobalt Tetraazamacrocyclic Catalyst and CuInS<sub>2</sub>/ZnS Quantum Dots for Photochemical Hydrogen Production. *Journal of Materials Chemistry A* **2019**, *7* (48), 27432–27440. <https://doi.org/10.1039/C9TA10479H>.



- (207) Sandroni, M.; Gueret, R.; Wegner, K. D.; Reiss, P.; Fortage, J.; Aldakov, D.; Collomb, M.-N. Cadmium-Free CuInS<sub>2</sub>/ZnS Quantum Dots as Efficient and Robust Photosensitizers in Combination with a Molecular Catalyst for Visible Light-Driven H<sub>2</sub> Production in Water. *Energy & Environmental Science* **2018**, *11* (7), 1752–1761. <https://doi.org/10.1039/C8EE00120K>.
- (208) Gimbert-Suriñach, C.; Albero, J.; Stoll, T.; Fortage, J.; Collomb, M.-N.; Deronzier, A.; Palomares, E.; Llobet, A. Efficient and Limiting Reactions in Aqueous Light-Induced Hydrogen Evolution Systems Using Molecular Catalysts and Quantum Dots. *Journal of the American Chemical Society* **2014**, *136* (21), 7655–7661. <https://doi.org/10.1021/ja501489h>.
- (209) Materna, K. L.; Beiler, A. M.; Thapper, A.; Ott, S.; Tian, H.; Hammarström, L. Understanding the Performance of NiO Photocathodes with Alkyl-Derivatized Cobalt Catalysts and a Push–Pull Dye. *ACS Applied Materials & Interfaces* **2020**, *12* (28), 31372–31381. <https://doi.org/10.1021/acsami.0c05228>.
- (210) Anxolabéhère-Mallart, E.; Costentin, C.; Fournier, M.; Nowak, S.; Robert, M.; Savéant, J.-M. Boron-Capped Tris(Glyoximate) Cobalt Clathrochelate as a Precursor for the Electrodeposition of Nanoparticles Catalyzing H<sub>2</sub> Evolution in Water. *Journal of the American Chemical Society* **2012**, *134* (14), 6104–6107. <https://doi.org/10.1021/ja301134e>.
- (211) Cobo, S.; Heidkamp, J.; Jacques, P.-A.; Fize, J.; Fourmond, V.; Guetaz, L.; Jusselme, B.; Ivanova, V.; Dau, H.; Palacin, S.; Fontecave, M.; Artero, V. A Janus Cobalt-Based Catalytic Material for Electro-Splitting of Water. *Nature Materials* **2012**, *11* (9), 802–807. <https://doi.org/10.1038/nmat3385>.
- (212) Queyriaux, N.; Sun, D.; Fize, J.; Pécaut, J.; Field, M. J.; Chavarot-Kerlidou, M.; Artero, V. Electrocatalytic Hydrogen Evolution with a Cobalt Complex Bearing Pendant Proton Relays: Acid Strength and Applied Potential Govern Mechanism and Stability. *Journal of the American Chemical Society* **2020**, *142* (1), 274–282. <https://doi.org/10.1021/jacs.9b10407>.
- (213) Queyriaux, N.; Giannoudis, E.; Windle, C. D.; Roy, S.; Pécaut, J.; Coutsolelos, A. G.; Artero, V.; Chavarot-Kerlidou, M. A Noble Metal-Free Photocatalytic System Based on a Novel Cobalt Tetrapyrrolyl Catalyst for Hydrogen Production in Fully Aqueous Medium. *Sustainable Energy Fuels* **2018**, *25* (2), 553–557. <https://doi.org/10.1039/c7se00428a>.
- (214) Zee, D. Z.; Chantarojsiri, T.; Long, J. R.; Chang, C. J. Metal–Polypyridyl Catalysts for Electro- and Photochemical Reduction of Water to Hydrogen.

---

*Accounts of Chemical Research* **2015**, *48* (7), 2027–2036.  
<https://doi.org/10.1021/acs.accounts.5b00082>.

# Appendix

## Included publications

**Publication 1** - Electron transfer in a covalent dye–cobalt catalyst assembly – a transient absorption spectroelectrochemistry perspective.

Reproduced from Bold, S. et al., **2018**, *Chemical Communications*, 54(75), 10594–10597. with permission from the Royal Society of Chemistry.

©2018 the Royal Society of Chemistry

Authors	<u>SB</u>	LZ	YZ	JM	VA	MCK	BD
Synthesis				x			
Characterization	x			x			
Time-resolved spectroscopy	x	x					
Data analysis and processing	x						x
Data interpretation	x					x	x
Concept development		x	x		x	x	x
Preparation of the manuscript	x						x
Revision of the manuscript	x					x	x
Proposed publication equivalents	1.0						



ChemComm

COMMUNICATION

View Article Online  
View Journal | View IssueCite this: *Chem. Commun.*, 2018, 54, 10594Received 10th July 2018,  
Accepted 9th August 2018

DOI: 10.1039/c8cc05556d

rsc.li/chemcomm

## Electron transfer in a covalent dye–cobalt catalyst assembly – a transient absorption spectroelectrochemistry perspective†

 Sebastian Bold,<sup>abc</sup> Linda Zedler,<sup>b</sup> Ying Zhang,<sup>ab</sup> Julien Massin,<sup>id c</sup>  
 Vincent Artero,<sup>id c</sup> Murielle Chavarot-Kerlidou<sup>id \*c</sup> and Benjamin Dietzek<sup>id \*abd</sup>

**Various oxidation states of the catalytically active cobalt center in a covalent dyad were electrochemically prepared and the light-induced excited-state processes were studied. Virtually identical deactivation processes are observed, irrespective of the oxidation state of the cobalt center, varying from Co<sup>III</sup> to Co<sup>I</sup>, indicating the absence of oxidative quenching within the dye–catalyst assembly.**

Artificial photosynthetic systems efficiently combining light-harvesting and solar energy conversion to ultimately drive multi-electronic redox catalytic processes are promising candidates for solar fuels production.<sup>1,2</sup> Over the past years, various molecular dyads combining a light-harvesting unit with a catalytic center (*i.e.* dye–catalyst dyads) were investigated, with a focus on cobalt-based assemblies for photocatalytic hydrogen production from water.<sup>3–8</sup> Cobalt complexes, such as the cobaloxime family, rank among the most efficient noble-metal free molecular catalysts for sunlight-driven water splitting.<sup>9,10</sup> Recently, a key step was achieved with the reports of the first functional H<sub>2</sub>-evolving photocathodes integrating such cobalt catalysts;<sup>11,12</sup> in particular, we and others successfully designed fully covalent dye–catalyst assemblies combining the cobalt diimine dioxime catalyst<sup>13</sup> with push–pull organic dyes.<sup>14,15</sup> In such dyads, an understanding of the excited state dynamics and electron transfer mechanisms is important for rationally improving the assembly design. However, they rely on a “pre-catalyst” unit where the cobalt center is in the Co<sup>III</sup> state, not involved in the H<sub>2</sub> evolution catalytic cycle. Two successive

light-driven reduction steps are thus required in order to “fully charge” the catalyst, *i.e.* to generate the catalytically active Co<sup>I</sup> species.<sup>13</sup> Classical transient absorption measurements used to investigate excited state processes only allow to probe the first of these two steps, *i.e.* reduction from Co<sup>III</sup> to Co<sup>II</sup>, without addressing the entry point to the catalytic cycle. To overcome this limitation, we designed and built an original setup, combining the advantages of electrochemistry with transient absorption spectroscopy, to generate a specific redox state of the catalytic center as a starting point to probe relevant light-driven processes. In this study, we investigate the ultrafast excited state dynamics and intramolecular electron transfer in the photo-electrocatalytically active dyad **2**<sup>14</sup> using classical spectroscopic techniques (time-resolved emission and transient absorption) and, for the first time, by transient absorption spectroelectrochemistry (TA-SEC).

Absorption spectra of the reference dye **1**<sup>16</sup> and of the dye–catalyst assembly **2**<sup>14</sup> show a peak at 350 nm, unaffected by the catalyst, assigned to a  $\pi$ – $\pi^*$  transition localized on the triarylamine moiety (Fig. 1).<sup>17</sup> At longer wavelengths, both **1** and **2** show the expected intramolecular charge transfer (ICT) transition from the triarylamine donor to the cyanoacrylate/acrylamide acceptor moiety,<sup>14,16</sup> which is slightly shifted for **2** in comparison to **1** (432 vs. 441 nm in ACN). This might be due to a weaker electron-withdrawing effect of the amide as compared to the ester. A similar blue-shift is observed for the emission band of **2**, compared to **1**. The characteristic Co<sup>III</sup> absorption band is observed at 300 nm for **2**.<sup>14</sup> This data, together with the previously reported electrochemistry,<sup>14</sup> supports the absence of electronic coupling between the dye and the catalyst moieties in the ground state of the covalent dyad **2**.

Time-resolved emission spectroscopy of **1** and **2** was performed in ACN and DMF (Fig. 1), as well as after deprotection and grafting on ZrO<sub>2</sub> films (Fig. S1, ESI†) to provide information about possible quenching processes within the dyad. ZrO<sub>2</sub> has a wide bandgap of 5.0 eV<sup>18</sup> which prevents charge injection from the dye and therefore serves as a non-quenching substrate. From a semi-logarithmic plot, it becomes apparent that the decay is monoexponential for **1** in solution, while it is biexponential for **2** (Fig. S2, ESI†). On ZrO<sub>2</sub>, a stretched exponential function was used to account for the variation

<sup>a</sup> Institute of Physical Chemistry and Abbe Center of Photonics,

Friedrich Schiller University Jena, Helmholtzweg 4, 07743 Jena, Germany

<sup>b</sup> Department Functional Interfaces, Leibniz Institute of Photonic Technology Jena

(IPHT), Albert-Einstein-Straße 9, 07745 Jena, Germany.

E-mail: benjamin.dietzek@leibniz-ipht.de

<sup>c</sup> Laboratoire de Chimie et Biologie des Métaux, Université Grenoble Alpes,

CNRS, CEA, 17 rue des Martyrs, 38000 Grenoble, France.

E-mail: murielle.chavarot-kerlidou@cea.fr

<sup>d</sup> Center for Energy and Environmental Chemistry,

Friedrich Schiller University Jena, Philosophenweg 8, 07743 Jena, Germany

† Electronic supplementary information (ESI) available: Experimental details; UV-vis absorption, time-resolved emission and transient absorption data in ACN and in DMF; UV-vis SEC and TA-SEC data in DMF. See DOI: 10.1039/c8cc05556d

## Communication

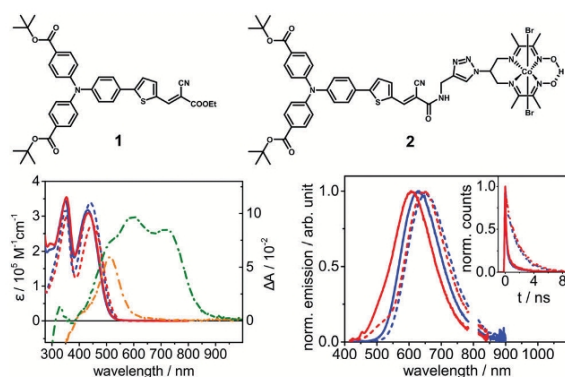


**Fig. 1** Top: Structures of **1** and **2**. Bottom: UV-vis absorption (left,  $\epsilon$ ) and normalized emission (right;  $\lambda_{\text{exc}} = 400$  nm) spectra of **1** (dashed) and **2** (solid) in ACN (blue) and DMF (red). Inset in the bottom right graph: time-resolved emission of **1** and **2** in ACN and DMF. Dashed-dot lines ( $\Delta A$ ) in the bottom left graph: UV-vis SEC differential spectra of **2** in DMF in the  $\text{Co}^{\text{II}}$  (orange) and  $\text{Co}^{\text{I}}$  (green) state.

in local binding environment of the grafted dye. The respective fitting functions were applied to the data and the resulting lifetimes are presented in Table S2 (ESI<sup>†</sup>). Emission of **1** in ACN shows the longest lifetime ( $\tau = 1745$  ps). Upon introduction of the catalyst in **2**, significant quenching is observed in both solvents and especially on  $\text{ZrO}_2$  ( $\tau = 45$  ps). This is comparable to the value obtained by Tian and coworkers when measuring a similar dye–catalyst system on  $\text{ZrO}_2$ .<sup>15</sup> In solution, a faster component around 200 ps appears with a relative amplitude of 90%, while the slower component is comparable to the lifetime of **1**. The biexponential decay seems to indicate the presence of two conformers with different decay rates. The observed quenching is also reflected in the quantum yields (Table S1, ESI<sup>†</sup>). On  $\text{ZrO}_2$ , the emission of **2** is quenched to a degree that determination of the quantum yield was not possible. Radiative ( $k_{\text{R}}$ ) and non-radiative ( $k_{\text{NR}}$ ) decay rates calculated from the emission quantum yield and lifetime show an increase in  $k_{\text{NR}}$  by an order of magnitude for **2** compared to **1** (Table S2, ESI<sup>†</sup>), leading to a dominance of non-radiative decay. On the basis of no spectral overlap between the absorption of the  $\text{Co}^{\text{III}}$  catalyst and the dye emission, this quenching might stem from an electron transfer from the excited state of the dye to the cobalt center. Indeed, oxidative quenching of the photosensitizer is thermodynamically feasible, and Tian and coworkers have assigned such a process to intramolecular oxidative quenching of a related photosensitizer by the appended cobalt catalyst, without however any spectral evidence for the reduction of the latter.<sup>15</sup>

Thus, to obtain more detailed insights into the excited-state deactivation pathways in **2**, transient absorption spectroscopy was performed on **1** and **2** in ACN (Fig. S3, ESI<sup>†</sup>). The TA spectra of **1** consist of a ground state bleach (GSB) at around 425 nm, matching with the steady-state absorption spectrum, and a stimulated emission (SE) band at 700 nm in agreement with the emission spectrum (maximum at 653 nm) recorded in ACN. These overlap with a broad excited state absorption (ESA) band with a maximum at around 530 nm, which explains the red-shift of the SE maximum compared to the emission spectra.

The dynamics of **1** will be described in detail elsewhere,<sup>19</sup> and can be summarized as follows: upon photoexcitation cooling takes place on a timescale of roughly 3 ps. Subsequently the differential absorption spectra do not change until about 50 ps after which GSB, ESA and SE decay concertedly with characteristic time constants of 132 and 1843 ps. The decay to the ground state is not complete within the experimentally accessible range of delay times. **2** shows identical behaviour in the first 3 ps in ACN as **1** (Fig. S3, ESI<sup>†</sup>) which is reflected in the spectrally very similar first two components and characteristic time constants as obtained by global fitting. Compared to **1** the amplitude of the SE band is severely reduced, which is in line with the reduced emission quantum yield of **2** as discussed above. After 3 ps, there is a much more rapid decay back to the ground state with values of 67.6 and 351 ps for  $\tau_3$  and  $\tau_4$  as well as a higher amplitude for the faster component ( $\tau_3$ ) (Table 1 and Fig. S3, ESI<sup>†</sup>). Spectrally, there is no difference between the DAS of  $\tau_3$  and  $\tau_4$  of **1** and **2**. Thus, it appears that the same decay processes act in **1** and **2**, but are accelerated in **2**.

To unequivocally attribute the observed excited state decay to intramolecular electron transfer, novel spectral features associated with the reduced cobalt center need to be observed. UV-vis spectroelectrochemistry was thus performed on **2** in DMF (Fig. S4, ESI<sup>†</sup>) in order to provide reference spectra of the different cobalt oxidation states. Differential spectra taken at  $-0.35$  V ( $\text{Co}^{\text{II}}$ ) and  $-0.65$  V ( $\text{Co}^{\text{I}}$ ) vs. Ag/AgCl are shown in Fig. 1.

For the reduction to the  $\text{Co}^{\text{II}}$  state, a positive absorption band with a maximum at 512 nm arises. Upon further reduction to the  $\text{Co}^{\text{I}}$  state, a double band with maxima at 595 and 717 nm appears, in perfect agreement with the previously reported  $\text{Co}^{\text{I}}$  signature obtained for **2** during the course of a photolysis experiment.<sup>14</sup> Finally, reduction of the dye produces a pronounced bleach of the ICT band, which overlaps with the  $\text{Co}^{\text{II}}$  absorption band, thereby hiding it. Since the same bleach is observed for the oxidized species (Fig. S4, ESI<sup>†</sup>) and as GSB in the TA measurements, it would prevent observation of the  $\text{Co}^{\text{II}}$  signature in the TA spectra if electron transfer from the excited state of the dye to the  $\text{Co}^{\text{III}}$  catalytic center occurred. However, since the  $\text{Co}^{\text{I}}$  state should be observable, a TA measurement in which the  $\text{Co}^{\text{II}}$  state is generated *in situ* by controlled potential electrolysis prior to photoexcitation, should open up the possibility of observing the occurrence of electron transfer (Fig. 2). Such a measurement would allow to study the excited state processes for **2** at the three different oxidation states of the cobalt catalyst, with the measurement taken at the final  $\text{Co}^{\text{I}}$  state serving as a reference since no electron transfer can occur. In summary, if intramolecular electron transfer occurs, one of the following should be observable: in

**Table 1** Lifetimes of components (in ps) obtained via a global four-component fit of the TA data of **1** and **2** in ACN and in DMF under different applied potentials as well as lifetimes obtained from time-resolved emission

	Solvent	$\tau_1$	$\tau_2$	$\tau_3$	$\tau_4$	$\tau_{\text{em},1}$	$\tau_{\text{em},2}$
<b>1</b>	ACN	0.2	0.9	132	1843		1745
<b>2</b>	ACN	0.3	1.1	82.6	467	199	2056
	DMF, OCP	0.7	2.6	67.7	351	231	2127
	DMF, $\text{Co}^{\text{II}}$	0.7	2.9	57.2	290		
	DMF, $\text{Co}^{\text{I}}$	0.6	2.0	22.3	173		



## Communication

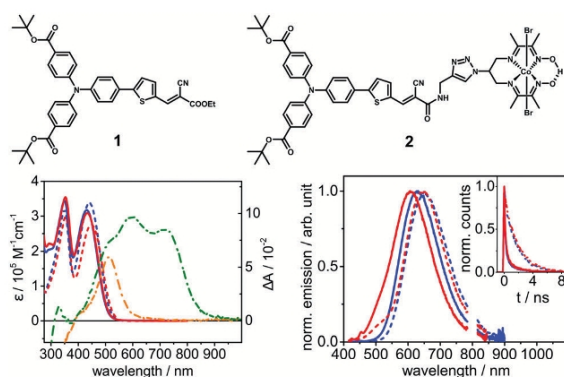


**Fig. 1** Top: Structures of **1** and **2**. Bottom: UV-vis absorption (left,  $\epsilon$ ) and normalized emission (right;  $\lambda_{\text{exc}} = 400$  nm) spectra of **1** (dashed) and **2** (solid) in ACN (blue) and DMF (red). Inset in the bottom right graph: time-resolved emission of **1** and **2** in ACN and DMF. Dashed-dot lines ( $\Delta A$ ) in the bottom left graph: UV-vis SEC differential spectra of **2** in DMF in the  $\text{Co}^{\text{II}}$  (orange) and  $\text{Co}^{\text{I}}$  (green) state.

in local binding environment of the grafted dye. The respective fitting functions were applied to the data and the resulting lifetimes are presented in Table S2 (ESI<sup>†</sup>). Emission of **1** in ACN shows the longest lifetime ( $\tau = 1745$  ps). Upon introduction of the catalyst in **2**, significant quenching is observed in both solvents and especially on  $\text{ZrO}_2$  ( $\tau = 45$  ps). This is comparable to the value obtained by Tian and coworkers when measuring a similar dye–catalyst system on  $\text{ZrO}_2$ .<sup>15</sup> In solution, a faster component around 200 ps appears with a relative amplitude of 90%, while the slower component is comparable to the lifetime of **1**. The biexponential decay seems to indicate the presence of two conformers with different decay rates. The observed quenching is also reflected in the quantum yields (Table S1, ESI<sup>†</sup>). On  $\text{ZrO}_2$ , the emission of **2** is quenched to a degree that determination of the quantum yield was not possible. Radiative ( $k_{\text{R}}$ ) and non-radiative ( $k_{\text{NR}}$ ) decay rates calculated from the emission quantum yield and lifetime show an increase in  $k_{\text{NR}}$  by an order of magnitude for **2** compared to **1** (Table S2, ESI<sup>†</sup>), leading to a dominance of non-radiative decay. On the basis of no spectral overlap between the absorption of the  $\text{Co}^{\text{III}}$  catalyst and the dye emission, this quenching might stem from an electron transfer from the excited state of the dye to the cobalt center. Indeed, oxidative quenching of the photosensitizer is thermodynamically feasible, and Tian and coworkers have assigned such a process to intramolecular oxidative quenching of a related photosensitizer by the appended cobalt catalyst, without however any spectral evidence for the reduction of the latter.<sup>15</sup>

Thus, to obtain more detailed insights into the excited-state deactivation pathways in **2**, transient absorption spectroscopy was performed on **1** and **2** in ACN (Fig. S3, ESI<sup>†</sup>). The TA spectra of **1** consist of a ground state bleach (GSB) at around 425 nm, matching with the steady-state absorption spectrum, and a stimulated emission (SE) band at 700 nm in agreement with the emission spectrum (maximum at 653 nm) recorded in ACN. These overlap with a broad excited state absorption (ESA) band with a maximum at around 530 nm, which explains the red-shift of the SE maximum compared to the emission spectra.

The dynamics of **1** will be described in detail elsewhere,<sup>19</sup> and can be summarized as follows: upon photoexcitation cooling takes place on a timescale of roughly 3 ps. Subsequently the differential absorption spectra do not change until about 50 ps after which GSB, ESA and SE decay concertedly with characteristic time constants of 132 and 1843 ps. The decay to the ground state is not complete within the experimentally accessible range of delay times. **2** shows identical behaviour in the first 3 ps in ACN as **1** (Fig. S3, ESI<sup>†</sup>) which is reflected in the spectrally very similar first two components and characteristic time constants as obtained by global fitting. Compared to **1** the amplitude of the SE band is severely reduced, which is in line with the reduced emission quantum yield of **2** as discussed above. After 3 ps, there is a much more rapid decay back to the ground state with values of 67.6 and 351 ps for  $\tau_3$  and  $\tau_4$  as well as a higher amplitude for the faster component ( $\tau_3$ ) (Table 1 and Fig. S3, ESI<sup>†</sup>). Spectrally, there is no difference between the DAS of  $\tau_3$  and  $\tau_4$  of **1** and **2**. Thus, it appears that the same decay processes act in **1** and **2**, but are accelerated in **2**.

To unequivocally attribute the observed excited state decay to intramolecular electron transfer, novel spectral features associated with the reduced cobalt center need to be observed. UV-vis spectroelectrochemistry was thus performed on **2** in DMF (Fig. S4, ESI<sup>†</sup>) in order to provide reference spectra of the different cobalt oxidation states. Differential spectra taken at  $-0.35$  V ( $\text{Co}^{\text{II}}$ ) and  $-0.65$  V ( $\text{Co}^{\text{I}}$ ) vs. Ag/AgCl are shown in Fig. 1.

For the reduction to the  $\text{Co}^{\text{II}}$  state, a positive absorption band with a maximum at 512 nm arises. Upon further reduction to the  $\text{Co}^{\text{I}}$  state, a double band with maxima at 595 and 717 nm appears, in perfect agreement with the previously reported  $\text{Co}^{\text{I}}$  signature obtained for **2** during the course of a photolysis experiment.<sup>14</sup> Finally, reduction of the dye produces a pronounced bleach of the ICT band, which overlaps with the  $\text{Co}^{\text{II}}$  absorption band, thereby hiding it. Since the same bleach is observed for the oxidized species (Fig. S4, ESI<sup>†</sup>) and as GSB in the TA measurements, it would prevent observation of the  $\text{Co}^{\text{II}}$  signature in the TA spectra if electron transfer from the excited state of the dye to the  $\text{Co}^{\text{III}}$  catalytic center occurred. However, since the  $\text{Co}^{\text{I}}$  state should be observable, a TA measurement in which the  $\text{Co}^{\text{II}}$  state is generated *in situ* by controlled potential electrolysis prior to photoexcitation, should open up the possibility of observing the occurrence of electron transfer (Fig. 2). Such a measurement would allow to study the excited state processes for **2** at the three different oxidation states of the cobalt catalyst, with the measurement taken at the final  $\text{Co}^{\text{I}}$  state serving as a reference since no electron transfer can occur. In summary, if intramolecular electron transfer occurs, one of the following should be observable: in

**Table 1** Lifetimes of components (in ps) obtained via a global four-component fit of the TA data of **1** and **2** in ACN and in DMF under different applied potentials as well as lifetimes obtained from time-resolved emission

	Solvent	$\tau_1$	$\tau_2$	$\tau_3$	$\tau_4$	$\tau_{\text{em},1}$	$\tau_{\text{em},2}$
<b>1</b>	ACN	0.2	0.9	132	1843		1745
<b>2</b>	ACN	0.3	1.1	82.6	467	199	2056
	DMF, OCP	0.7	2.6	67.7	351	231	2127
	DMF, $\text{Co}^{\text{II}}$	0.7	2.9	57.2	290		
	DMF, $\text{Co}^{\text{I}}$	0.6	2.0	22.3	173		

applied potentials (for the CV with the applied potentials, see Fig. S5, ESI†). Steady-state UV-vis spectra recorded during the TA measurements proved the stability of the sample under measurement conditions (Fig. S5, ESI†). The obtained TA spectra and DAS (Fig. 3 and Fig. S6, ESI†) are strikingly similar, whatever the oxidation state of the catalytic center in **2**. In particular, the characteristic Co<sup>I</sup> signature was not observed when exciting **2** at the Co<sup>II</sup> state (Fig. 3 middle) so direct spectral evidence for electron transfer from the dye to the catalyst unit was not obtained. Furthermore, comparison of the kinetic data obtained for **2** at the Co<sup>III</sup> or at the Co<sup>II</sup> state with the reference Co<sup>I</sup> state do not provide any indirect evidence in form of markedly different decay rates. Since the kinetic rates are not notably faster in the higher cobalt oxidation states than in the reference Co<sup>I</sup> state, electron transfer by oxidative quenching was ruled out as the emission quenching mechanism for the Co<sup>III</sup> and Co<sup>II</sup> states of the dyad. In fact, a counter-intuitive slightly faster decay is observed at more negative applied potentials (Table 1), contrary to expected slower ones in case of electron transfer. The acceleration of the decay at lower oxidation states might be due to coulombic repulsion of electron density on the cobalt with electron density in the LUMO of the dye located closely to the covalent linker. This would destabilize the charge transfer state and accelerate the decay to the ground state. Therefore, the data shows the absence of electron transfer from the excited dye to the catalyst in solution without a sacrificial electron donor (e.g., oxidative quenching). Activation of dyad **2** thus relies on two successive electron transfers to the catalytic center from the reduced state of the dye, generated by reductive quenching of its excited state by a sacrificial electron donor (photolysis experiment) or by the photoelectrode substrate, i.e. NiO (H<sub>2</sub>-evolving photocathode).<sup>14</sup> This also highlights that observing a quenching of emission in photoactive dyads is not always compelling proof for electron transfer and should be corroborated by using complementary techniques. Thus, the quenching of the emission lifetime for **2** compared to **1** must stem from other sources. A possible explanation for the increase in the non-radiative rate could be an increased density of vibrational modes upon adding the cobalt moiety. Also Dexter energy transfer from the excited donor chromophore to short-lived cobalt-centered dd-states might account for the observed rates at different applied potentials.

In conclusion, a dye–catalyst dyad was investigated with respect to the intramolecular photoinduced electron transfer processes. Various oxidation states of the catalytically active cobalt center were prepared by controlled-potential electrolysis and the light-induced processes initiated by excitation of the photoactive unit were studied. We show that virtually identical photoinduced processes are observed, irrespective of the oxidation state of the cobalt center, varying from Co<sup>III</sup> to Co<sup>I</sup>. Thus, we conclude that oxidative quenching of the initially excited chromophore is absent in the dyad investigated and “charging of the catalyst”, i.e. electron transfer from the photocenter to the cobalt center can only occur after reductive quenching of the photoactive center, e.g. by a sacrificial agent or by hole transfer to a NiO electrode. This is despite the shortening of the fluorescence decay time of the chromophore upon covalent attachment of the cobalt

center, i.e. the results point to the fact that increased luminescence quenching upon introduction of a redox-active (metal) center into the molecular framework of a photosensitizer is not always unambiguous proof for electron transfer. The experimental methodology put forward here more generally allows the investigation of excited state processes, e.g. electron transfer but also energy transfer and structural rearrangements, in different redox states of an analyte. This is especially interesting for systems designed for multielectron catalysis where multiple electron transfer steps are needed to “fully charge” a catalyst.

We thank Maria Sittig for the quantum yield data. The work was supported by the European Commission's Seventh Framework Program (FP7/2007-2013) under grant agreement no. 306398 (FP7-IDEAS-ERC, Project PhotocatH<sub>2</sub>ode), the French National Research Agency in the framework of the “Investissements d'avenir” program (IDEX UGA, ANR-15-IDEX-02 and Labex ARCANE, ANR-11-LABX-0003-01) as well as the German Science Foundation, DFG, grant no. DI1517/11-1.

## Conflicts of interest

There are no conflicts to declare.

## Notes and references

- 1 S. Berardi, S. Drouet, L. Francas, C. Gimbert-Surinach, M. Guttentag, C. Richmond, T. Stoll and A. Llobet, *Chem. Soc. Rev.*, 2014, **43**, 7501.
- 2 A. Thapper, S. Styring, G. Saracco, A. W. Rutherford, B. Robert, A. Magnuson, W. Lubitz, A. Llobet, P. Kurz, A. Holzwarth, S. Fiechter, H. de Groot, S. Campagna, A. Braun, H. Bercegol and V. Artero, *Green*, 2013, **3**, 43.
- 3 A. Fihri, V. Artero, M. Razavet, C. Baffert, W. Leibl and M. Fontecave, *Angew. Chem., Int. Ed.*, 2008, **47**, 564.
- 4 A. Fihri, V. Artero, A. Pereira and M. Fontecave, *Dalton Trans.*, 2008, 5567.
- 5 P. Zhang, M. Wang, C. Li, X. Li, J. Dong and L. Sun, *Chem. Commun.*, 2010, **46**, 8806.
- 6 M. Natali, R. Argazzi, C. Chiorboli, E. Iengo and F. Scandola, *Chem. – Eur. J.*, 2013, **19**, 9261.
- 7 G.-G. Luo, K. Fang, J.-H. Wu and J. Mo, *Chem. Commun.*, 2015, **51**, 12361.
- 8 S. Jasimuddin, T. Yamada, K. Fukujū, J. Otsuki and K. Sakai, *Chem. Commun.*, 2010, **46**, 8466.
- 9 V. Artero, M. Chavarot-Kerlidou and M. Fontecave, *Angew. Chem., Int. Ed.*, 2011, **50**, 7238.
- 10 S. Losse, J. G. Vos and S. Rau, *Coord. Chem. Rev.*, 2010, **254**, 2492.
- 11 E. A. Gibson, *Chem. Soc. Rev.*, 2017, **46**, 6194.
- 12 V. Nikolaou, A. Charisiadis, G. Charalambidis, A. G. Coutsolelos and F. Odobel, *J. Mater. Chem. A*, 2017, **5**, 21077.
- 13 N. Kaeffer, M. Chavarot-Kerlidou and V. Artero, *Acc. Chem. Res.*, 2015, **48**, 1286.
- 14 N. Kaeffer, J. Massin, C. Lebrun, O. Renault, M. Chavarot-Kerlidou and V. Artero, *J. Am. Chem. Soc.*, 2016, **138**, 12308.
- 15 P. B. Pati, L. Zhang, B. Philippe, R. Fernández-Terán, S. Ahmadi, L. Tian, H. Rensmo, L. Hammarström and H. Tian, *ChemSusChem*, 2017, **10**, 2480.
- 16 J. Massin, M. Bräutigam, N. Kaeffer, N. Queyriaux, M. J. Field, F. H. Schacher, J. Popp, M. Chavarot-Kerlidou, B. Dietzek and V. Artero, *Interface Focus*, 2015, **5**, 20140083.
- 17 E. Ishow, R. Guillot, G. Buntinx and O. Poizat, *J. Photochem. Photobiol. A*, 2012, **234**, 27.
- 18 Y. Xu and M. A. A. Schoonen, *Am. Mineral.*, 2000, **85**, 543.
- 19 J. Massin, M. Bräutigam, M. Wächter, S. Bold, A. B. Muñoz-García, M. Pavone, B. Dietzek, M. Chavarot-Kerlidou and V. Artero, manuscript in preparation.

## Supplementary Information for

### **Electron transfer in a covalent dye-cobalt catalyst assembly – a transient absorption spectroelectrochemistry perspective**

*Sebastian Bold,<sup>a,b,c,d</sup> Linda Zedler,<sup>b</sup> Ying Zhang,<sup>a,b</sup>, Julien Massin, Vincent Artero,<sup>d</sup> Murielle Charot-Kerlidou<sup>d</sup> and Benjamin Dietzek<sup>a,b,c</sup>*

a - Institute of Physical Chemistry and Abbe Center of Photonics, Friedrich Schiller University Jena, Helmholtzweg 4, 07743 Jena, Germany.

b - Department Functional Interfaces, Leibniz Institute of Photonic Technology Jena (IPHT), Albert-Einstein-Straße 9, 07745 Jena, Germany.

c - Center for Energy and Environmental Chemistry, Friedrich Schiller University Jena, Philosophenweg 8, 07743 Jena, Germany.

d - Laboratoire de Chimie et Biologie des Métaux, Université Grenoble Alpes, CNRS, CEA, 17 rue des Martyrs, 38000 Grenoble, France.



**Chemicals.**

All solvents used were of spectroscopic grade. For the transient absorption spectroelectrochemistry (TA-SEC) measurements, dimethyl formamide (DMF) was dried over a 5 Å molecular sieve prior to use. For the UV-Vis SEC measurements, Acros organics extra dry DMF was used. The synthesis of compounds **1**<sup>1</sup> and **2**<sup>2</sup> was previously reported.

*Procedure for immobilization on ZrO<sub>2</sub> films*

For the immobilization on ZrO<sub>2</sub> films, the *tert*-butyl ester groups in **1** and **2** were deprotected according to our previous studies.<sup>1,2</sup> ZrO<sub>2</sub> films were then soaked in a 0.2 mM solution of deprotected **1** or deprotected **2** in acetonitrile (ACN) for 24 hours. The films were then rinsed with ACN before measuring.

**General characterization methods and equipment.***Steady-state UV-Vis absorption spectroscopy*

Steady-state absorption spectra in solution were recorded on a Shimadzu UV-1800 spectrophotometer in 1 cm cuvettes. Absorption spectra on ZrO<sub>2</sub> films were recorded on an Agilent Cary 5000 equipped with a solid sample holder. Emission spectra were measured on a Horiba Fluorolog Spectrofluorometer in a 1 cm cuvette at 90° angle. Quantum yields were determined using an Edinburgh FLS980 emission spectrofluorometer equipped with an integrating sphere.

*Spectroelectrochemistry*

UV-Vis-SEC measurements were carried out in a three-electrode setup using a 1 mm cell equipped with a Pt mesh working electrode, a Pt wire counter electrode and a Ag/AgCl reference electrode (3M KCl). The potentiostat used was a BioLogic VSP-300. The spectra were recorded using an Agilent Cary 60 spectrometer. For the measurements, a cyclic voltammetry (CV) was run to establish the redox potentials, then potentials were applied in a Chronoamperometry and spectra recorded until equilibrium was reached before changing to the next potential. 0.1 M tetrabutylammonium tetrafluoroborate (TBABF<sub>4</sub>) in DMF was used as electrolyte solution.

*Time-resolved emission spectroscopy*

The two-dimensional (time and wavelength) emission decay profiles were measured using a Hamamatsu streak scope C4334 in photon counting mode using a time-window of 10 or 20 ns. After excitation with the frequency-doubled output of a Ti-sapphire laser (Tsunami, Newport Spectra-Physics GmbH) at  $\lambda_{\text{ex}} = 365$  nm at a pulse-to-pulse repetition rate of 400 kHz after passing a pulse selector (model 3980, Newport Spectra-Physics GmbH) the luminescence of the sample was collected

in a 90°-arrangement and spectrally dispersed using a Chromex 250IS 3 imaging spectrograph. Selected horizontal (spectral) and vertical (temporal) intervals were integrated using the HPDTA software delivered with the streak camera system. Measurements were carried out without a polarizer to decrease the acquisition time. The lifetime values were obtained from mono- or biexponential fits of the linear portion of the integrated decay profiles. The samples were prepared to yield an optical density of 0.1 at the excitation wavelength in a 1.0 cm quartz cuvette using air-equilibrated, spectroscopic grade solvents.

#### *Transient absorption spectroscopy and spectroelectrochemistry*

A custom-built setup was utilized to acquire fs-TA data. The TA setup is described in detail elsewhere.<sup>3</sup> A white-light supercontinuum probe pulse at 1 kHz repetition rate was used to analyze the excited state dynamics. The supercontinuum was generated by focusing a minor part of the output of the Ti:Sapphire amplifier into a CaF<sub>2</sub> plate mounted on a rotating stage. After generation of the white light continuum, it is split into a probe and reference beam. Using a concave mirror with 500 nm focal length, the probe pulse was focused onto the sample by a concave mirror of 500 mm focal length. The spectra of probe and reference were detected by a Czerny-Turner spectrograph of 150 mm focal length (SP2150, Princeton Instruments) equipped with a diode array detector (Pascher Instruments AB, Sweden). The pump pulses used were of 403 nm wavelength and a pulse duration of approximately 100 fs. The repetition rate of the pump pulses was reduced to 0.5 kHz by a mechanical chopper and the polarization adjusted to the magic angle of 54.7° by a Berek compensator and a polarizer.

The data was analyzed using a customized data analysis software (Pascher Instruments AB, Sweden). First, the data was corrected for the chirp and subsequently, a sum of exponential functions was fitted to the data.

The pulse overlap region of  $\pm 200$  fs was removed from the data to exclude the coherent artefacts present in this temporal region.

The TA measurements of **1** were carried out in ACN in a standard 1 mm cuvette ( $OD_{400\text{nm}} = 0.3$ ). In the TA-SEC measurements, the pump and probe beam pass collinearly through a hole drilled into a 0.4 mm thick glassy carbon working electrode (hole diameter: 1 mm). This electrode design enables a high local concentration of reduced species at the focal point of the pump and probe beams, taking advantage of the highly resistant glassy carbon material while achieving optimal light transmission despite its opacity. The setup was completed by customized electronics and control software (Pascher Instruments AB, Sweden), allowing simultaneous control of the potentiostat unit and TA setup. This enabled simultaneous measurements of TA spectra, steady-state UV-Vis spectra, current, applied potential and ensured jitter-free timing of the datasets

Transient absorption spectra of the electrochemically reduced complex were recorded at set potentials and constant current response. Steady state UV-Vis spectra were simultaneously recorded with time-resolved TA-SEC in order to assess the concentration of the reduced species within the observation. To ensure good solubility of **2**, DMF was used as the electrolyte solvent with 0.1 M TBABF<sub>4</sub> as supporting electrolyte.

**Procedure for the TA-SEC measurements.**

TA-SEC measurements were carried out as follows: After assembly of the cell with all three electrodes, the cell was purged with Argon for  $\approx 10$  min. Afterwards, the sample solution was injected into the cell and purged with Argon for another  $\approx 5$  min. At the beginning of the day, a complete CV of the sample was measured to identify the reduction potentials versus the Ag wire pseudo-reference electrode. Before each TA measurement, a CV was measured with a vertex potential slightly negative of the desired reduction to check again for the correct reductive potential and account for a possible potential drift of the pseudo-reference electrode. After disconnecting the counter electrode (CE), a chronoamperometry (CA) measurement was started and the CE reconnected after about 5 data points to observe the initial current spike and subsequent levelling off to a plateau upon reaching equilibrium. This was done for one TA scan (about 6 minutes), so in total the system had about 10 min to approach equilibrium prior to the start of the TA-SEC measurement. The CA time prior to the TA-SEC measurement was not extended to avoid degradation of the sample since pump and probe beam were already irradiating it. Then, a TA measurement was started with the potential still applied (chronoamperometry).

During the CV, CA and the TA measurement the current as well as steady-state UV-Vis spectra were recorded. The UV-Vis spectra allow to control the reduction of the sample as well as to estimate the yield of reduced species in the sample chamber.

**Table S1:** Absorption and emission maxima and emission quantum yields of compounds **1** and **2** in acetonitrile, DMF and on ZrO<sub>2</sub> excited at 400 nm (emission quantum yields: excited at 435 nm).

Sample	Solvent/ Substrate	$\lambda_{\max} (\pi-\pi^*)$ /nm	$\lambda_{\max} (\text{ICT})$ /nm	$\epsilon_{\max} (\text{ICT})$ / $\text{M}^{-1}\text{cm}^{-1}$	$\lambda_{\max, \text{em}}$ /nm	$\Phi_{\text{em}}$ [%]
<b>1</b>	ACN	350	441	33811	653	19.3
	DMF	354	448	27666	646	23.6
	ZrO <sub>2</sub>	347	444		641	6.1
<b>2</b>	ACN	349	432	31752	630	3.9
	DMF	353	433	30884	608	0.7
	ZrO <sub>2</sub>	346	439		602	

**Table S2:** Emission lifetimes obtained by fitting the time-resolved emission data of **1** and **2** in ACN, DMF and on ZrO<sub>2</sub> with a mono- or biexponential fit in solution and a stretched exponential fit for **1** on ZrO<sub>2</sub>. Also given are radiative ( $k_R$ ) and non-radiative ( $k_{NR}$ ) decay rates calculated from the emission quantum yield and emission lifetimes.

Sample	Solvent	$\tau_1$ / ps	$\tau_2$ / ps	$\tau_{\text{ave}}$ / ps	$\beta$ dispersion parameter	$\alpha$ relative amplitude	$k_R / 10^8 \text{ s}^{-1}$	$k_{NR} / 10^8 \text{ s}^{-1}$
<b>1</b>	ACN		1745				1.11	4.62
	DMF		1874				1.26	4.08
	ZrO <sub>2</sub>			1006 <sup>a</sup>	0.542			
<b>2</b>	ACN	199	2056	366 <sup>b</sup>		0.91	1.07	26.3
	DMF	231	2127	439 <sup>b</sup>		0.89	0.16	22.6
	ZrO <sub>2</sub>		45					

a: obtained from the stretched exponential fit

b: amplitude-weighted average lifetimes calculated from the lifetimes and amplitudes obtained by the biexponential fit

In case of biexponential fits, the amplitude of the first component is given by  $\alpha$ . For the calculation of the decay rates of **2**, the amplitude-weighted average lifetimes, calculated from the lifetimes and amplitudes obtained by the biexponential fit, were used. These are also given under  $\tau_{\text{ave}}$  for completeness.

The stretched exponential fit was applied using the exponential function

$$I(t) = I_0 e^{-\left(\frac{t}{\tau_c}\right)^\beta}$$

convoluted with the instrumental response function.  $\tau_c$  and  $\beta$  were used to calculate the average lifetime  $\tau_{\text{ave}}$ :

$$\tau_{\text{ave}} = \frac{\tau_c}{\beta} \int_0^\infty x^{\frac{1}{\beta}-1} e^{-x} dx$$

$\beta$  is the dispersion parameter, with  $\beta = 1$  corresponding to a monoexponential decay. For **2** on  $\text{ZrO}_2$ , the fit did not converge, and it was fitted with a monoexponential decay instead, probably due to the decay being very close to the IRF.

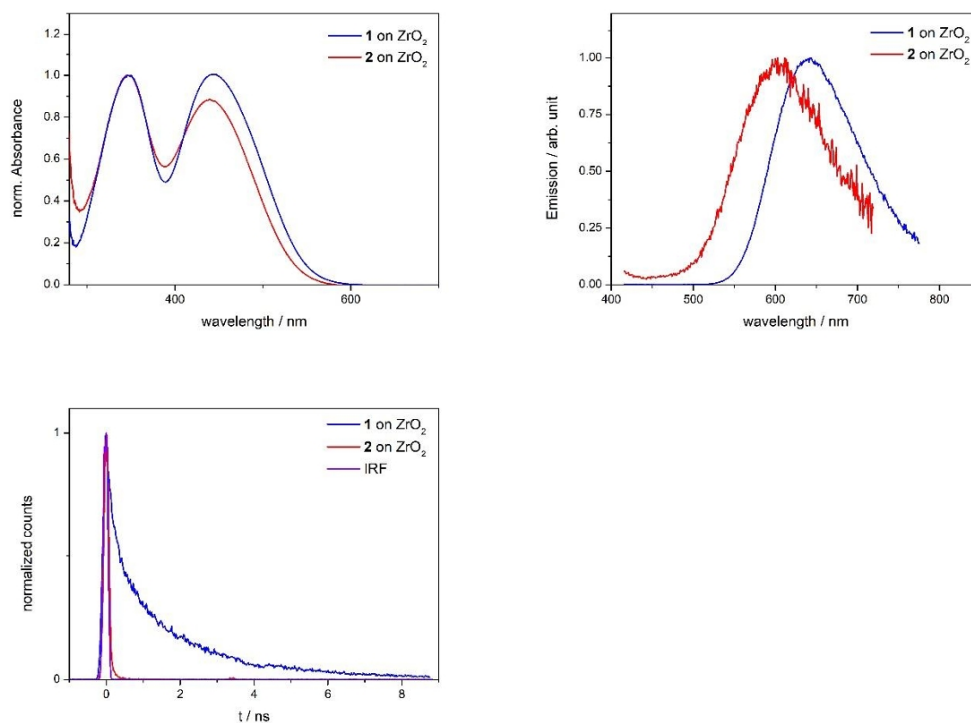


**Figure S1:** UV-Vis absorption spectra, normalized emission spectra and time-resolved emission of **1** and **2** immobilized on  $\text{ZrO}_2$  films.

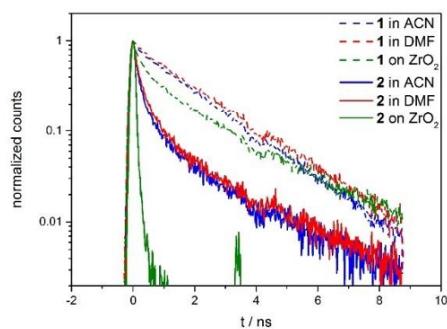


**Figure S2:** Semi-logarithmic plot of time-resolved emission data of **1** (dashed) and **2** (solid) in ACN (blue) and DMF (red) as well as on  $\text{ZrO}_2$  (green).

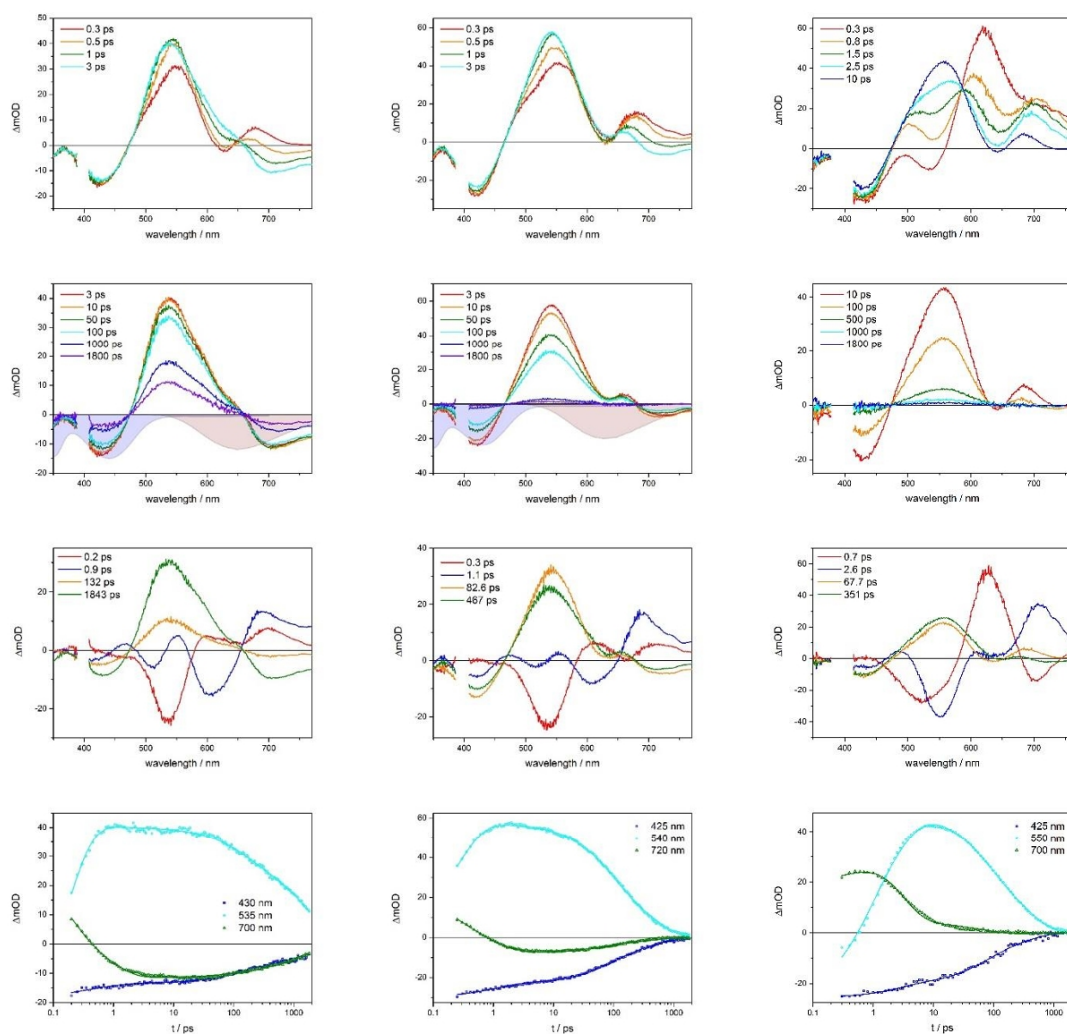


**Figure S3:** TA data of **1** (left) and **2** (middle) in ACN as well as of **2** in DMF (right). The top two graphs show the TA spectra at early (top) and late (bottom) delay times. The shaded areas depict the scaled and inverted steady-state absorption (blue) and emission (wine) spectra. The third row of graphs show the decay-associated spectra obtained with a four-component fit of the TA data. Bottom: Kinetics at the maxima of GSB (blue), ESA (cyan) and SE (green). The scatter plots show the recorded data while lines show the fit.

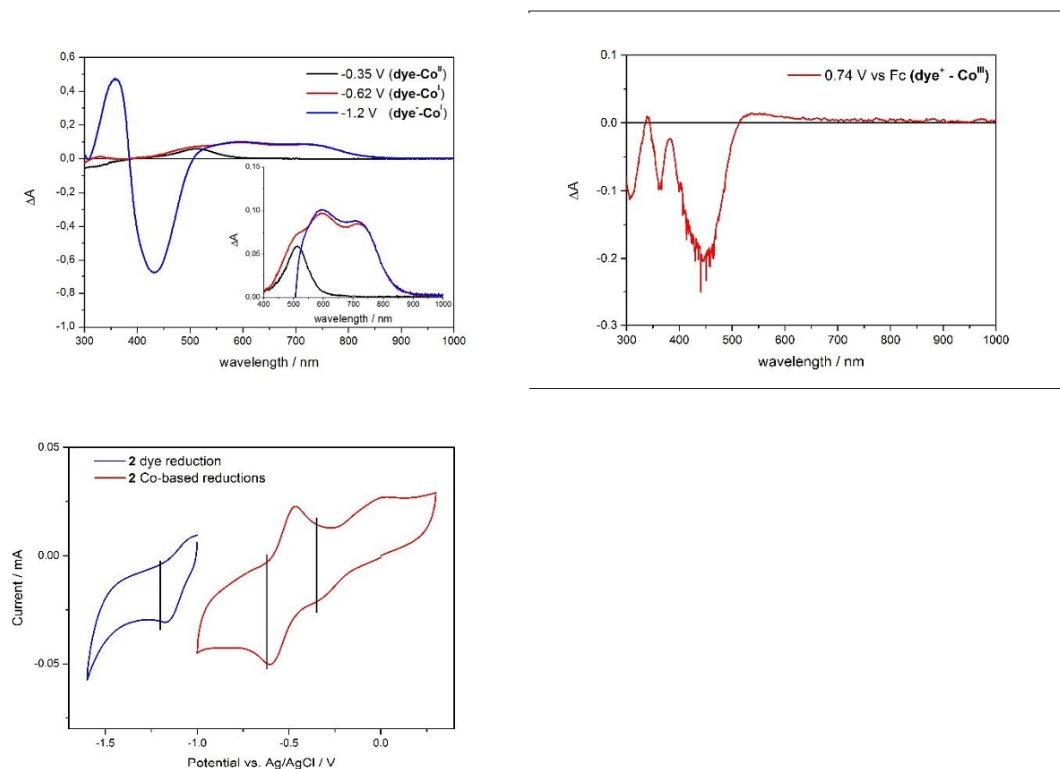


**Figure S4:** Differential steady-state UV-Vis-SEC spectra of a 0.2 mM solution of **2** in DMF (0.1 M TBABF<sub>4</sub>) at different oxidation states of the catalyst and dye. On the bottom, the respective cyclic voltammograms are shown. All potentials were measured vs. Ag/AgCl with the exception of the oxidative measurements, measured against Fc<sup>+0</sup>. The potentials applied during chronoamperometry are shown by vertical black lines.

**2** shows the rise of a positive band with a maximum at 512 nm upon reduction to the Co<sup>II</sup> state. The Co<sup>I</sup> state shows a double band at 595 and 717 nm, as previously observed in ACN.<sup>2</sup> It becomes apparent that upon reduction of the dye, the resulting bleach is much stronger than the Co<sup>II</sup> absorption band, obscuring the latter. *This is a strong indication that, in a TA spectrum, the Co<sup>II</sup> absorption band, which might be generated upon electron transfer, would be hidden beneath the GSB of the dye.*



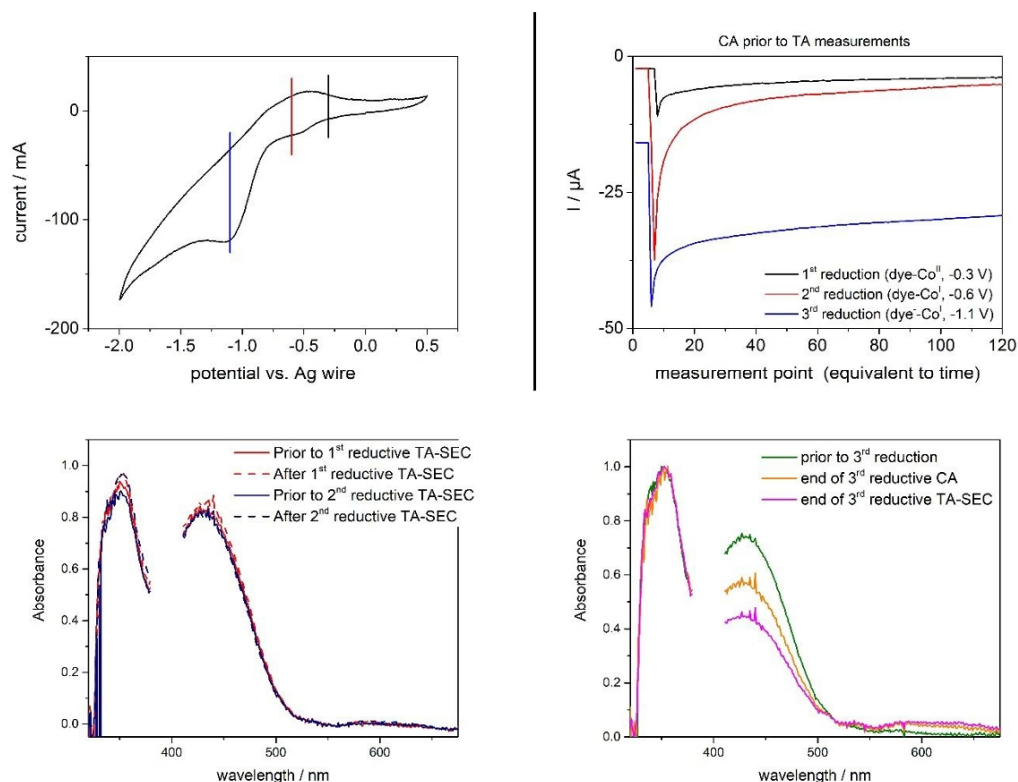


**Figure S5:** Electrochemical data (top) and steady-state UV-Vis spectra (bottom) recorded prior to and during the TA-SEC measurements. Top left: complete CV of **2** versus the pseudo-reference with the applied potentials applied for the TA measurements indicated by vertical bars. On the top right, the current vs. time of the CA run prior to the TA measurements is shown. The bottom left graph shows the steady state UV-Vis spectra of **2** prior to the CA (solid) and at the end of the TA measurement (dashed) for the first (red) and second (blue) reductive TA-SEC measurement. The reductive potentials applied for the TA measurements at these oxidation states were  $-0.3$  ( $\text{Co}^{\text{II}}$ ) and  $-0.6$  ( $\text{Co}^{\text{I}}$ ) V vs. Ag wire. No significant change in absorbance is observed in either case, proving the stability of the sample over the time range of the TA-SEC measurement. The failure to observe the expected  $\text{Co}^{\text{I}}$  double band after the second reduction (to the  $\text{Co}^{\text{I}}$  state) might be due to the low oscillator strength of this transition. To check if reduction of the sample was occurring,  $-1.1$  V vs. Ag wire was applied to reduce the dye and obtain the  $\text{dye}^{\cdot-}\text{Co}^{\text{I}}$  state. The steady-state UV-Vis spectra, normalized to the  $\pi-\pi^*$  band to enable better comparison, of this measurement are shown in the bottom right graph. Indeed, during this reduction, a clear decrease in absorption of the ICT band is observed proving the reduction of the dye. From the change in absorbance and considering the positive  $\Delta A$  for the  $\pi-\pi^*$  band upon reduction (see UV/Vis SEC), the yield of reduced sample could be estimated to be  $\approx 30\%$ . Based on the relative differential absorbance of the dye bleach at 430 nm and the  $\text{Co}^{\text{I}}$  absorption band at 600 nm from UV-Vis SEC as well as the maximum GSB at OCP in the TA measurement, in case



of quantitative electron transfer a change in absorption of  $\approx 3$  mOD at 600 nm would be expected.

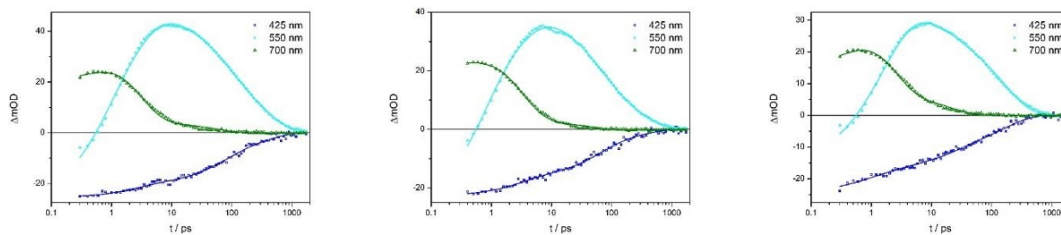


**Figure S6:** Kinetic traces of the TA measurements of **2** in DMF at OCP (left), Co<sup>II</sup> (middle) and Co<sup>I</sup> (right) at the maxima of GSB (blue), ESA (cyan) and SE (green). The scatter plots show the recorded data while lines show the fit.

1. J. Massin, M. Bräutigam, N. Kaeffer, N. Queyriaux, M. Field, F. H. Schacher, J. Popp, M. Chavarot-Kerlidou, B. Dietzek, V. Artero *Interface Focus* 2015, **5**, 20140083.
2. N. Kaeffer, J. Massin, C. Lebrun, O. Renault, M. Chavarot-Kerlidou and V. Artero, *J. Am. Chem. Soc.*, 2016, **138**, 12308–12311.
3. R. Siebert, D. Akimov, M. Schmitt, A. Winter, U. S. Schubert, B. Dietzek, J. Popp *ChemPhysChem*, 2009, **10**, 910–919.

**Publication 2** - Investigating Light-Induced Processes in Covalent Dye-Catalyst Assemblies for Hydrogen Production.



Reproduced from Bold, S. et al., **2020**, *Catalysts*, 10(11), 1340. Published by the Multidisciplinary Digital Publishing Institute (MDPI).

Authors	<u>SB</u>	TS	ABMG	MP	VA	MCK	BD
Synthesis		x					
Characterization	x	x					
Time-resolved spectroscopy	x						
Data analysis and processing	x						x
DFT calculations			x	x			
Data interpretation	x		x	x		x	x
Concept development					x	x	x
Preparation of the manuscript	x					x	x
Revision of the manuscript	x		x	x		x	x
Proposed publication equivalents	1.0						



Article

# Investigating Light-Induced Processes in Covalent Dye-Catalyst Assemblies for Hydrogen Production

Sebastian Bold<sup>1,2,3</sup> , Tatiana Straistari<sup>1</sup>, Ana B. Muñoz-García<sup>4</sup> , Michele Pavone<sup>5</sup>, Vincent Artero<sup>1</sup>, Murielle Chavarot-Kerlidou<sup>1,\*</sup> and Benjamin Dietzek<sup>2,3,6,\*</sup>

<sup>1</sup> Univ. Grenoble Alpes, CNRS, CEA IRIG, Laboratoire de Chimie et Biologie des Métaux, 17 rue des Martyrs, F-38000 Grenoble, France; sebastian.bold@uni-jena.de (S.B.); tatiana.straistari@cea.fr (T.S.); vincent.artero@cea.fr (V.A.)

<sup>2</sup> Institute of Physical Chemistry and Abbe Center of Photonics, Friedrich Schiller University Jena, Helmholtzweg 4, 07743 Jena, Germany

<sup>3</sup> Department Functional Interfaces, Leibniz Institute of Photonic Technology Jena (Leibniz-IPHT), Albert-Einstein-Straße 9, 07745 Jena, Germany

<sup>4</sup> Department of Physics “Ettore Pancini”, University of Naples Federico II, Complesso Universitario Monte Sant’Angelo Via Cintia, 80126 Naples, Italy; anabelen.munozgarcia@unina.it

<sup>5</sup> Department of Chemical Sciences, University of Naples Federico II, Complesso Universitario Monte Sant’Angelo Via Cintia, 80126 Naples, Italy; michele.pavone@gmail.com

<sup>6</sup> Center for Energy and Environmental Chemistry Jena (CEEC-Jena), Friedrich Schiller University Jena, Philosophenweg 8, 07743 Jena, Germany

\* Correspondence: murielle.chavarot-kerlidou@cea.fr (M.C.-K.); benjamin.dietzek@leibniz-ipht.de (B.D.)

Received: 17 October 2020; Accepted: 13 November 2020; Published: 18 November 2020



**Abstract:** The light-induced processes occurring in two dye-catalyst assemblies for light-driven hydrogen production were investigated by ultrafast transient absorption spectroscopy. These dyads consist of a push-pull organic dye based on a cyclopenta[1,2-b:5,4-b']dithiophene (CPDT) bridge, covalently linked to two different H<sub>2</sub>-evolving cobalt catalysts. Whatever the nature of the latter, photoinduced intramolecular electron transfer from the excited state of the dye to the catalytic center was never observed. Instead, and in sharp contrast to the reference dye, a fast intersystem crossing (ISC) populates a long-lived triplet excited state, which in turn non-radiatively decays to the ground state. This study thus shows how the interplay of different structures in a dye-catalyst assembly can lead to unexpected excited state behavior and might open up new possibilities in the area of organic triplet sensitizers. More importantly, a reductive quenching mechanism with an external electron donor must be considered to drive hydrogen production with these dye-catalyst assemblies.

**Keywords:** solar energy conversion; push-pull dye; intersystem crossing

## 1. Introduction

The conversion of solar energy into a storable fuel, such as hydrogen (H<sub>2</sub>) through sunlight-driven water splitting, is currently the subject of intensive research efforts [1,2]. In that context, photosynthesis has been a great source of inspiration for molecular chemists, leading to the development of a wide variety of H<sub>2</sub>-evolving molecular dyads [3–13], inspired by the Photosystem I-Hydrogenase couple found in some hydrogen producing photosynthetic micro-organisms [14]. Recently, the first functional H<sub>2</sub>-evolving photocathodes integrating such molecular dyads were reported in the literature [2,5,9,11,15], paving the way for solar fuels production in dye-sensitized photoelectrochemical cells. Our group contributed to the field with the design of covalent dye-catalyst assemblies based on H<sub>2</sub>-evolving cobalt catalysts [12,13,16].

Understanding the excited state dynamics and electron transfer mechanisms in these systems is key to rationally improve their design and optimize their H<sub>2</sub> evolution performances. We recently

addressed the photoinduced processes at work with our first photoelectrocatalytically active dyad, thanks to a combination of classical spectroscopic techniques and transient absorption spectroelectrochemistry [17]. In the present study, we investigate the ultrafast excited state dynamics of two novel dye-catalyst assemblies specifically designed for improved photoelectrocatalytic hydrogen production in dye-sensitized photocathodes [18]. They comprise a push-pull organic dye (T2R) covalently assembled with two different H<sub>2</sub>-evolving cobalt catalysts: either the cobalt diimine-dioxime complex Cat2 [19] or the cobalt tetraazamacrocyclic catalyst Cat1 [20–22] (Figure 1). The metal-free dye structure relies on a triphenylamine (TPA) donor group functionalized by two protected carboxylic acid groups for its future anchoring onto semiconducting oxide-based electrodes and a cyanoacrylate/cyanoacrylamide acceptor group, separated by the electron-rich cyclopenta[1,2-b:5,4-b']dithiophene (CPDT) bridge. The latter is classically employed as a building block in organic photovoltaics or for dye-sensitized solar cell applications, thanks to its increased light absorption properties in the visible region of the spectrum [23,24].

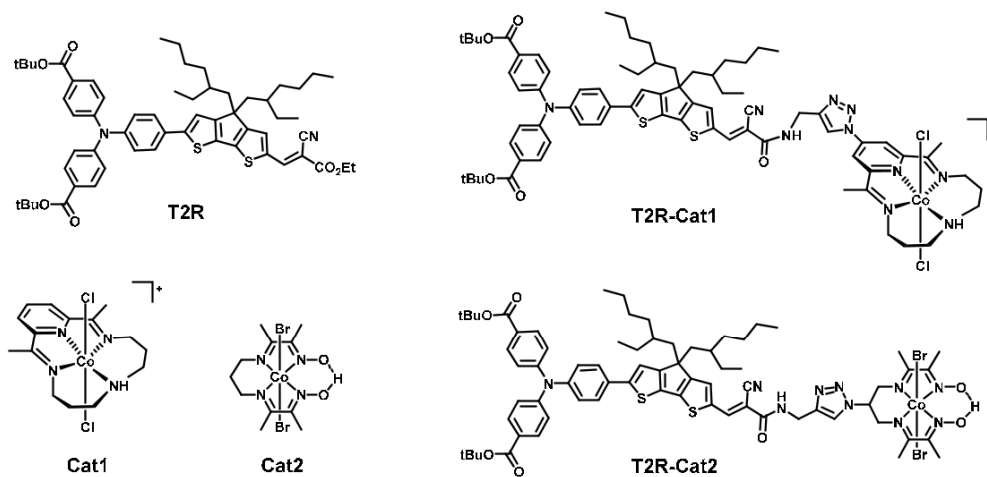


**Figure 1.** Structures of the dye T2R, catalysts Cat1 and Cat2, and dyads T2R-Cat1 and T2R-Cat2.

## 2. Results

### 2.1. Steady-State Spectroscopy and Density Functional Theory (DFT) Calculations

First insights into the light-induced processes in T2R, T2R-Cat1, and T2R-Cat2 are obtained from steady-state spectroscopy. In acetonitrile (ACN), the absorption spectra for all compounds show two main bands at 355 and around 495 nm (Figure 2). The band at 355 nm is assigned to the triphenylamine-centered transition, while the additional small band at 298 nm might be due to a localized transition on the bithiophene linker [25,26]. Below 320 nm, the dyads additionally show contribution from the respective cobalt catalysts. In the visible region, the strong band at 495 nm results from the HOMO-LUMO transition with intramolecular charge-transfer (ICT) character from the TPA donor to the cyanoacrylate acceptor. Compared to the two dyads, the ICT band of T2R is slightly red-shifted ( $\Delta E \approx 200 \text{ cm}^{-1}$ ), which might stem from the stronger electron-withdrawing character of the ester terminal group in comparison with the amide, slightly increasing the push-pull character of the dye. As previously reported [23], the presence of the rigid CPDT unit strongly enhances the light-harvesting efficiency in the visible region ( $\epsilon$  of  $60,300 \text{ M}^{-1}\cdot\text{cm}^{-1}$ ) compared to our previously-studied dyads relying on mono- or bis-thiophene units ( $\epsilon$  of  $31,800$  and  $38,600 \text{ M}^{-1}\cdot\text{cm}^{-1}$ , respectively) [12,13,17,27].

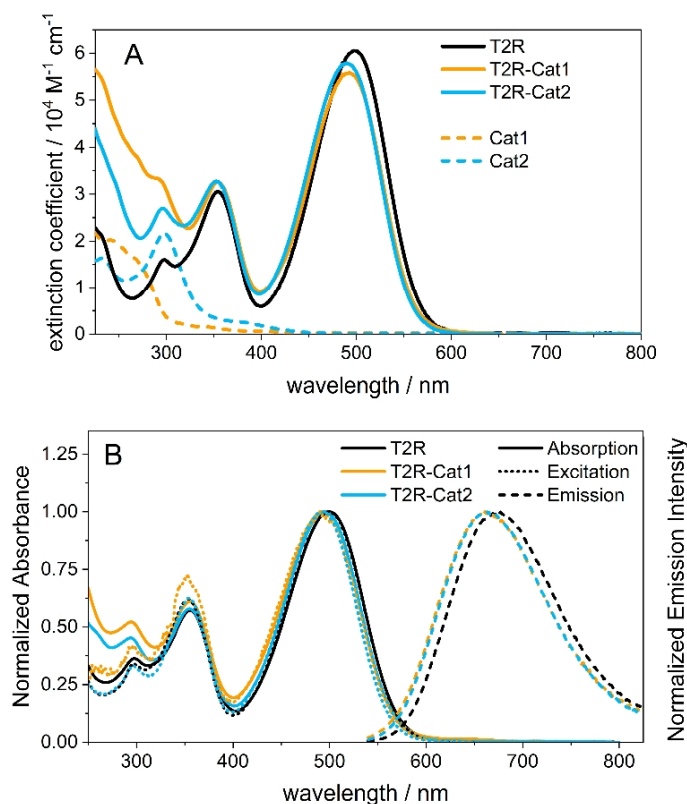


**Figure 2.** (A) UV-Vis absorption spectra of T2R, T2R-Cat1, T2R-Cat2, Cat1 and Cat2 recorded in acetonitrile. (B) Normalized absorption, emission and excitation spectra of T2R, T2R-Cat1 and T2R-Cat2 recorded in MeOH. The emission quantum yield was 0.25 (T2R), 0.02 (T2R-Cat1) and 0.08 (T2R-Cat2).

The computed time-dependent (TD)-DFT vertical transition energies confirm the experimental assignments of the optical absorption spectra. The first bright transition (i.e., with a high oscillator strength value) at 472 nm for the T2R isolated dye corresponds to the HOMO-LUMO transition (ICT). The second transition at 331 nm corresponds to the HOMO-LUMO+1 transition localized on the TPA moiety (Supplementary Figure S1). These results are in full agreement with TD-DFT calculations previously reported for a structural analog of T2R, varying only by the nature of the acceptor group (dicyanovinyl unit instead of cyanoacrylate unit) [23]. For the T2R-Cat1 complex, the absorption transition energies are very similar to T2R, with the first ICT transition at 476 nm (HOMO→LUMO+4) and the second (TPA) one at 335 nm (HOMO→LUMO+6) (Supplementary Figure S2). The same electronic structure pattern is found for the T2R-Cat2 complex.

Considering their targeted application for hydrogen production under aqueous conditions, the electronic properties of the dyads were further studied in methanol (MeOH), which is a protic solvent of higher polarity ( $E_T^N = 0.76$ ) and viscosity ( $\eta = 0.59 \text{ mPa}\cdot\text{s}^{-1}$ ) than ACN ( $E_T^N = 0.46$  and  $\eta = 0.35 \text{ mPa}\cdot\text{s}^{-1}$ ) [28,29]. The UV-Vis absorption spectra in MeOH (Supplementary Figures S2B and S3) are similar to those recorded in ACN. In particular, no significant shift of the ICT band is observed.

Upon excitation at 520 nm, the compounds show emission, which is centered at 674 nm for T2R and 662 nm for the dyads (Figure 2B). As in the absorption spectra, the dyads show identical spectra while that of T2R is red-shifted ( $\Delta E \approx 281 \text{ cm}^{-1}$ ), which again is ascribed to the different nature of the acceptor group. All compounds show a large Stokes shift of 5100–5200  $\text{cm}^{-1}$ , caused by the stabilization of the charge-transfer state in the polar solvent MeOH. While the emission quantum yield of T2R is 0.25, the dyads show much lower quantum yields, i.e., 0.02 (T2R-Cat1) and 0.08 (T2R-Cat2), corresponding



to an emission quenching of 92% (T2R-Cat1) and 68% (T2R-Cat2), respectively. The covalent assembly with the cobalt catalysts seemingly opens up non-radiative decay pathways for the emissive state, leading to this pronounced emission quenching.

The emission excitation spectra show the same bands as the absorption spectra at 355 and 395 nm, indicating that excitation in both the TPA and ICT bands leads to identical emission. For the dyads, there is a discrepancy between absorption and excitation spectra below 320 nm that is caused by the absorption band of the cobalt complexes, whose excitation does not lead to emission.

## 2.2. Transient Absorption (TA) Spectroscopy of T2R

To obtain further insights into the nature of the excited states and of the non-radiative decay induced by the covalent attachment to the catalytic center, we performed time-resolved transient absorption spectroscopy in MeOH with excitation at 480 nm. The transient absorption spectra recorded for T2R at short delay times (Figure 3A) display a ground state bleach (GSB) centered at 490 nm and at 350 nm, while an excited-state absorption (ESA) is observed above 615 nm and peaks around 690 nm. Within 50 ps, the ESA undergoes a blue-shift via a transient double band structure with maxima at 575 and 656 nm to form a broad single ESA band with a maximum at 605 nm. Simultaneously, a negative differential absorption band develops above 690 nm (Figure 3A). Once this spectral evolution is concluded, no further spectral shifts take place and an overall signal decay is observed. This decay, however, is not finished within the experimentally accessible time window of 1.6 ns.

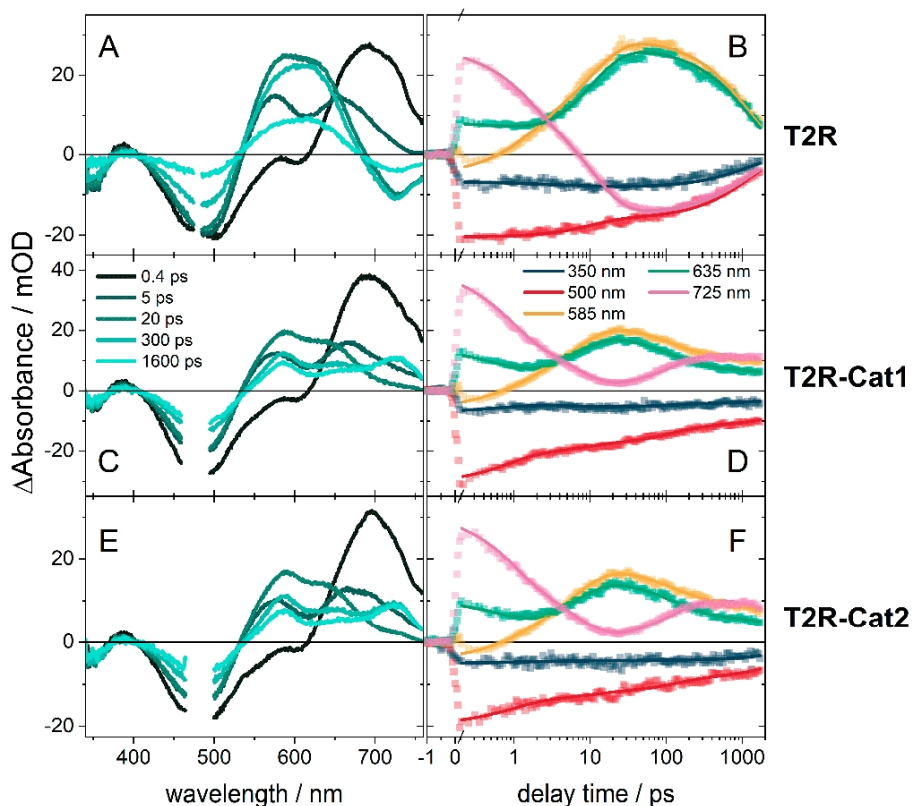


**Figure 3.** TA spectra at different pump-probe delays (A,C,E) and kinetic traces (B,D,F) of T2R (A,B), T2R-Cat1 (C,D) and T2R-Cat2 (E,F) in MeOH after excitation at 480 nm. The solid lines in the kinetic traces are fits of the experimental data to the models presented in Figure 4.

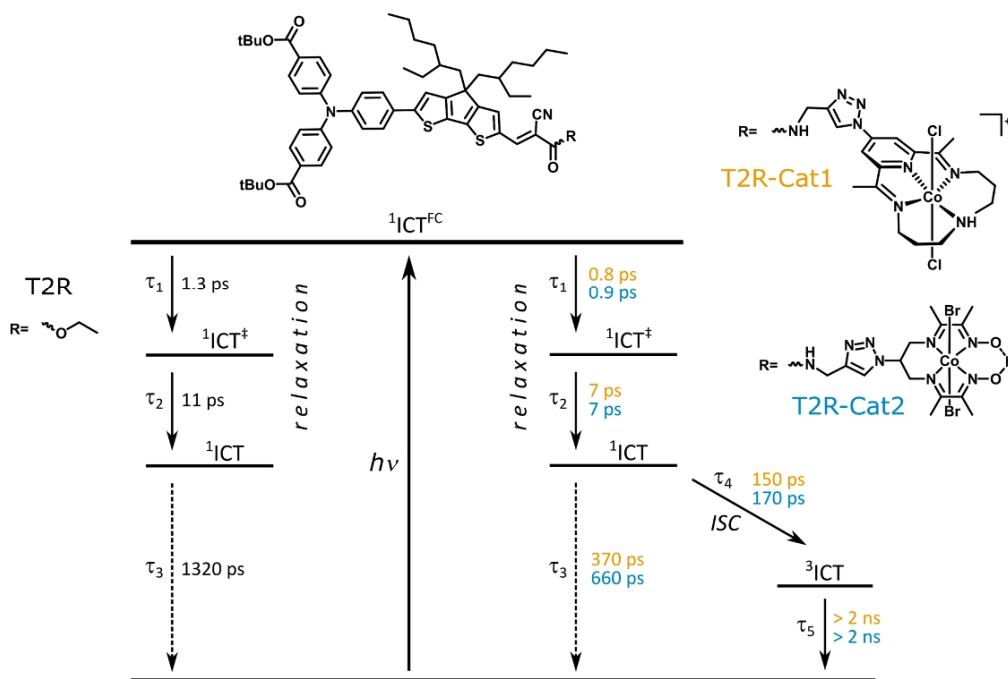


**Figure 4.** Photophysical model for the light-induced processes upon excitation at 480 nm. The pathway to the triplet state by ISC ( $\tau_4$ ) is only open for the dyads. Dashed arrows indicate radiative transitions.

The spectral evolution observed for T2R can be rationalized with a model consisting of three consecutive processes starting from the initially excited ICT state, yielding the bleach at 480 nm. The additional bleach at 350 nm is attributed to the GSB of the TPA absorption, supporting the calculations, which show this band to be a HOMO-LUMO+1 transition [23]. The negative differential absorption at  $>690$  nm is due to stimulated emission (SE). The red-shift compared to the steady-state emission measurements, where the maximum was located at 674 nm, can be explained by an overlap of the negative SE band with the positive ESA band. A sequential three-component exponential fit satisfyingly fits the data and gives characteristic time constants associated with the processes of  $\tau_1 = 1.3$ ,  $\tau_2 = 11$  and  $\tau_3 = 1320$  ps (Table 1, species-associated spectra in Figure 5).

**Table 1.** Characteristic time constants of light-induced processes upon excitation at 480 nm. The corresponding rates are given in Table S2.

	Time Constants <sup>1</sup> /ps				
	$\tau_1$	$\tau_2$	$\tau_3$	$\tau_4$	$\tau_5$
T2R	1.3	11	1320		
T2R-Cat1	0.8	7	370	150	$\gg 2$ ns
T2R-Cat2	0.9	7	660	170	$\gg 2$ ns

$$^1 \tau_n = 1/k_n.$$

Based on the spectral evolution associated with the first two processes, i.e., a blue-shift of ESA with no concurrent GSB decay, they can be assigned to relaxation of the initially populated hot state  $\text{ICT}^{\text{FC}}$  via a partly relaxed  $\text{ICT}^\ddagger$  state. The observed red-shift of the SE, from the initial dip at 600 nm to the negative band at  $>690$  nm, further supports this assignment. The exact nature of these relaxation processes is not clear in this class of push-pull dyes [30–33]. Quite generally, it is ascribed to a solvation process in response to the photoinduced intramolecular shift of electron density [33], coupled to a relaxation cascade through molecular motion such as flattening and rotation around bonds [30].

In addition, the coexistence of various conformers in solution might further complicate the assignment of the process to molecular degrees of freedom.

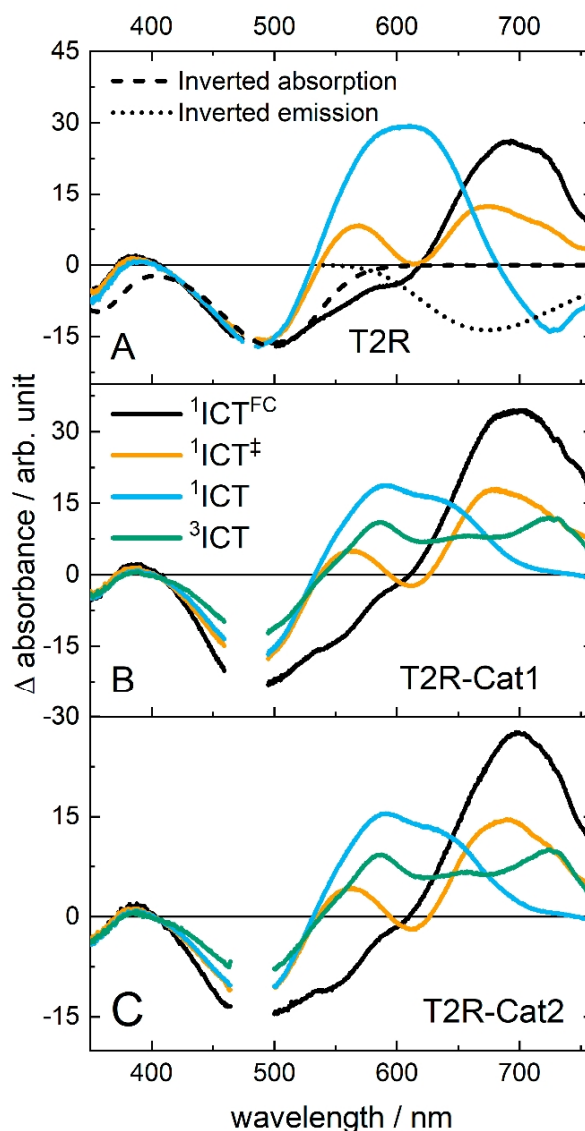


**Figure 5.** Species-associated spectra obtained by fitting the TA data of (A) T2R, (B) T2R-Cat1 and (C) T2R-Cat2 obtained at 480 nm excitation with the model shown in Figure 4. The dashed and dotted lines in the first panel show the inverted and scaled steady-state absorption and emission spectra.

To this end, we computed the DFT minimum energy structures for four conformations for the T2R dye, considering different relative positions of the CPDT system, the CN, and the CO moieties (Figure 6, Table 2). These four conformations were found to be very close in energy with energy differences in the ground state below 0.1 eV (<2.3 kcal/mol), meaning all conformers are likely present in solution. The TD-DFT vertical electronic transitions computed were scarcely affected by the different dye conformations with differences below 2 nm (Table 2). However, the molecular dynamics and the interconversion between the different conformers, not explored here, could be responsible for the complex relaxation processes in the excited state. In MeOH, the cooling processes are slowed down in comparison with measurements



performed in ACN (Supplementary Figure S4), where the cooling process could be fitted with a single component with  $\tau = 1$  ps. This can be explained by the higher viscosity of MeOH, which slows down the relaxation processes involving major molecular motion, as observed before for similar push-pull dyes [17,30]. This effect could be further increased by hydrogen bonds formed by MeOH, which ACN does not. The third process is the return to the ground state of the thermalized excited state  $^1\text{ICT}$ , reflected in a concerted decay of GSB, ESA, and SE. This excited state behavior is in line with that observed previously for a related compound with a single thiophene linker [17,34].

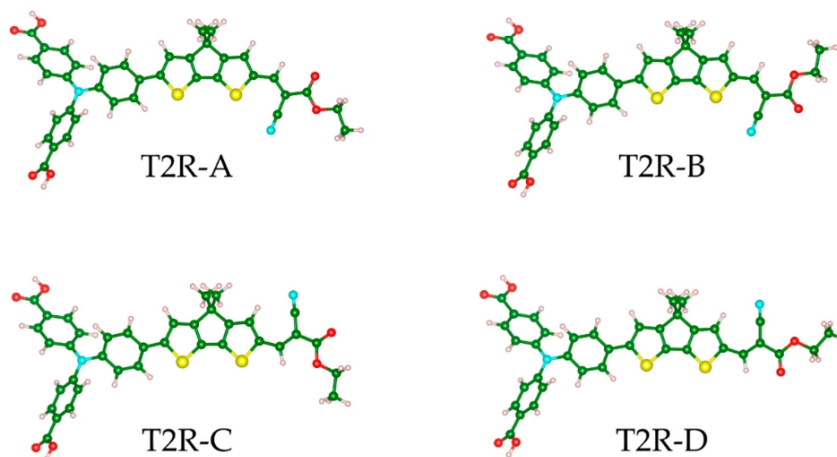


**Figure 6.** Minimum energy structures of four conformations for the T2R dye obtained by DFT calculations.

**Table 2.** Relative energies ( $\Delta E$ ) at the B3LYP level of theory, including zero-point vibrational energies within the harmonic approximation, and vertical transition energies at the CAM-B3LYP level of theory, including the acetonitrile solvent medium via the PCM, with the oscillator strengths given in parenthesis. For the labelling, refer to Figure 6.

	T2R-A	T2R-B	T2R-C	T2R-D
$\Delta E/\text{eV}$	0.014	0.107	0.084	0.0
$\lambda(\text{ICT})/\text{nm}$	473 (1.793)	472 (1.784)	471 (1.900)	472 (1.929)
$\lambda(\text{TPA})/\text{nm}$	331 (0.618)	331 (0.619)	331 (0.615)	331 (0.616)

### 2.3. Transient Absorption Spectroscopy of the Dyads

In the dyads (Figure 3B,C), the initial TA spectra are identical to those of T2R (Supplementary Figure S5a) and the processes taking place within the first 20 ps after photoexcitation are similar in timescale and spectral changes to T2R. They are therefore attributed to the relaxation of the initially excited hot singlet state of the dye moiety to the thermalized singlet excited state  $^1\text{ICT}$ . This state shows a more pronounced double band structure in the ESA than T2R, with maxima at 589 nm and 640 nm, while the absence of the negative SE band above 695 nm is in line with the reduced emission quantum yield of the dyads when compared to T2R. In contrast to T2R, an additional spectral evolution is observed within ca. 300 ps, with a decrease in intensity of the ESA and the formation of a long-lived species, characterized by a double band absorption at 590 and 725 nm. This new band persists up to the longest experimentally accessible delay times (1.6 ns), while a partial decay of the ESA band around 600 nm continues. The bleach at 500 nm shows less decay for the dyads compared to T2R (33% remaining signal for the dyads and 20% for the dye). The characteristic absorption observed at the end of the accessible time window (1.6 ns) is identical for both dyads (Supplementary Figure S5b), irrespective of the nature of the catalytic center. Furthermore, it does not match the spectra of the  $\text{Co}^{\text{II}}$  states of the catalysts, which show maxima at 595 and 512 nm for Cat1 and Cat2, respectively (Supplementary Figure S6) [17,20,35]. Additionally, the extinction coefficients of the optical transitions

on the cobalt complex are an order of magnitude lower than those of the dye, while the band observed in the TA spectrum shows a similar intensity to the other dye-based bands. These observations lead us to discard a photoinduced electron transfer process to the catalyst and formation of a charge-transfer species with the electron localized on the cobalt complex ( $\text{Co}^{\text{II}}$  state), in spite of its thermodynamic feasibility (see Supplementary Table S1). Instead, we propose that a triplet state forms by  $^1\text{ICT} \rightarrow ^3\text{ICT}$  intersystem crossing. Bi- and oligothiophenes are known to undergo fast ISC on the timescale of 50 ps to 1 ns [36,37], reminiscent of the behavior observed here for the CPDT bridge of our push-pull dye system. The extinction coefficients of the oligothiophene triplet states are also in the same order of magnitude as that of T2R ( $\approx 38,000 \text{ M}^{-1}\text{cm}^{-1}$  for the oligothiophenes,  $\approx 55,000 \text{ M}^{-1}\text{cm}^{-1}$  for T2R and T2R-based dyads) [37], in line with the observed similar intensity of the ESA band at 725 nm compared to the GSB. The triplet absorption of pure oligothiophenes is observed at higher energies (2.7 eV corresponding to 460 nm for terthiophene) [37] than those observed here. However, the CPDT structure is part of an extended conjugated charge-transfer system which can have a strong effect on the excited state energies. In addition, the long lifetime observed for this species is in full agreement with a triplet state, which generally show longer lifetimes than singlet states due to the spin-forbidden nature of the decay to the ground state. Finally, the decay of ESA signal between 540 and 690 nm observed after 300 ps is attributed to direct decay of  $^1\text{ICT}$  to the ground state, analogous to the situation in T2R.

Thus, we assume the model shown in Figure 4: following the initial relaxation processes ( $k_1$  and  $k_2$ ), the resulting singlet ICT excited state can decay directly to the ground state ( $k_3$ ) as well as, in the case of the dyads, undergo ISC to form the triplet state ( $k_4$ ), which in turn decays back to the ground state ( $k_5$ ). When fitting the TA data with this model, the direct decay ( $k_3$ ) was not fitted, probably due to the low spectral amplitude and low number of recorded points. However, from the spectral evolution after 300 ps, which shows further signal decay at 500 nm and around 600 nm, i.e., at the position of GSB and ESA of the  $^1\text{ICT}$  state, the presence of this direct decay must be deduced. We therefore eliminated the contribution of the  $^3\text{ICT}$  state from the TA spectra by subtracting the spectrum recorded at 300 ps ( $\epsilon = \epsilon(\lambda, \Delta t) - \epsilon(\lambda, 300 \text{ ps})$ ). The spectra thus obtained showed the inverted TA spectrum of the  $^1\text{ICT}$  state, validating the assignment of direct  $^1\text{ICT}$  decay to this spectral evolution (Figures S7 and S8). The decay at the maximum at 600 nm was fitted with a monoexponential decay to obtain the values for  $\tau_3$  (370 ps for T2R-Cat1 and 660 ps for T2R-Cat2), which were then fixed in the global fit to the presented model to yield the species-associated spectra and rates of the different processes (Figure 5B,C, Table 1). The obtained rate for the direct decay of the singlet excited state to the ground state is double that observed for T2R. We previously observed a similar trend for a related assembly with an organic dye and cobalt complex, where the excited state lifetime decreased from 1840 to 470 ps [17]. We proposed Dexter energy transfer to short-lived cobalt-centered states as a possible cause for the reduction in lifetime, an explanation that can equally hold true for the compounds studied here. The rate of ISC was determined to be  $k_4 = 6.5 \times 10^9 \text{ s}^{-1}$  ( $\tau_4 = 150 \text{ ps}$ ) and  $k_4 = 5.8 \times 10^9 \text{ s}^{-1}$  ( $\tau_4 = 170 \text{ ps}$ ) for T2R-Cat1 and T2R-Cat2, respectively, while the lifetime of the triplet state was  $\tau_5 \gg 2 \text{ ns}$ , reflecting the long-lived signal observed.

### 3. Discussion

The ISC rate observed in our systems is comparable to literature values for bi- and terthiophene (50–135 ps) [37,38]. The extremely fast ISC rates for bithiophene are explained in the literature by a very small energy difference of the  $S_1$  and  $T_2$  state [36]. In general, the sulfur atom plays a role in the fast ISC processes in thiophenes due to its high spin-orbit coupling factor [39]. However, as ISC is absent in T2R despite the identical dye structure as in the dyads, the bithiophene structure cannot be the sole source of the ISC and the explanations offered in the literature likely do not fully account for the fast ISC in our systems. In particular, those invoking the population of higher vibrational states in the singlet excited state do not apply in this case, as all systems show identical initial kinetics involving ultrafast relaxation to a thermalized singlet excited state that is finished before ISC is observable. The obvious difference in the dyads in comparison to the T2R is, however, the presence of the cobalt

complex. In the literature, descriptions of ISC induced by cobalt in binary systems are limited (to the best of our knowledge) to the influence of the paramagnetic nature of Co<sup>II</sup> ions [40,41]. However, the cobalt complexes in this study are diamagnetic Co<sup>III</sup> complexes. Instead, alternative pathways must be considered, most probably involving higher energy states on the cobalt complexes. In fact, there are several such states between the HOMO and LUMO energy levels of the dye, which could play a role in the observed ISC (Supplementary Figure S2). The latter was tentatively investigated by density functional calculations, unfortunately without success.

In the literature on heavy-atom free triplet sensitizers, there are examples of radical pair intersystem crossing (RP-ISC), where after charge transfer an electron changes its spin to go from the <sup>1</sup>CT state to the <sup>3</sup>CT state via hyperfine coupling, which then relaxes to a localized triplet state [42]. In our case, it would be thermodynamically feasible for the excited electron to transfer to a higher state on the cobalt and back to the dye, accompanied by a spin change. However, RP-ISC alone occurs on time scales of nanoseconds and is therefore much slower than the ISC observed in the T2R dyads [43–45]. A different approach is the use of spin convertors—most prominently fullerenes—that, after energy transfer from the chromophore to the spin convertor, undergo ISC to yield the triplet state on the spin convertor, which then by a second energy transfer step relaxes to yield the triplet state localized on the chromophore [46–48]. In our case, the Co complex could act as a spin convertor after electron transfer since ISC has been observed to occur on a ps time scale in the ground state of Co complexes [49] and <1 ps in the excited state [50], and thus could be much faster than the ISC rates observed here. If the ISC and back CT to the dye are much faster than the CT to the complex, the latter would be the gating process and there would be no accumulation of the CT state with the electron localized on the Co complex, explaining why this species was not observed in the experiment.

#### 4. Materials and Methods

Cat1 [20] and Cat2 [51] were prepared according to previously reported procedures. Detailed synthetic procedures for T2R, T2R-Cat1, and T2R-Cat2 are reported elsewhere [18]. For T2R-Cat2, the copper-catalyzed azide-alkyne cycloaddition (CuAAC) coupling we previously reported for related dyads based on push-pull dyes [12,13] was employed. The synthesis of T2R-Cat1 relies on a CuAAC coupling between 4-azido-2,6-diacetylpyridine and the alkyne derivative of T2R, followed by the template-directed synthesis of the macrocyclic catalytic center. Spectroscopic-grade solvents (Sigma Aldrich, UV-Vis grade or better) were used for all the spectroscopic characterizations.

*Steady-state UV-vis absorption spectroscopy:* Steady-state absorption spectra were recorded on a Jasco V780 spectrophotometer or a Specord S600 (Analytik Jena) in 1 cm cuvettes.

*Steady-state emission spectroscopy:* Emission spectra were measured on an Edinburgh FLS980 emission spectrofluorometer in a 1 cm cuvette at 90° angle. The solutions were prepared to have an absorbance of 0.05 at the excitation wavelength. Quantum yields were determined on the same instrument equipped with an integrating sphere, with solution at 0.1 absorbance at the excitation wavelength.

*Transient absorption spectroscopy:* The setup for femtosecond transient absorption measurements has been previously described [10]. An amplified Ti:Sapphire laser (Legend, Coherent Inc) produced the 800 nm fundamental beam which was split into two beams. One of the beams was used to pump an optical-parametric amplifier (TOPAS-C), whose output was spectrally centered at 480 nm and used as pump pulses for the pump-probe experiments. The pump pulses were typically set to 0.5 μJ per pulse. To achieve the pump-probe delay of 2 ns, the pump beam was directed over a delay line. The supercontinuum used as probe pulse was generated by passing the second beam of the fundamental 800 nm through a CaF<sub>2</sub> window, with probe intensities falling into the range of hundred nJ. The probe light was split into two beams, one of which was focused through the sample, while the other served as reference. The probe and reference beams were detected by a double-stripe diode array and converted into differential absorption signals using a commercially available detection system (Pascher Instruments AB, Lund Sweden). The recorded data were corrected for the chirp and globally fitted using a sum of three exponential. During the fitting, the pulse overlap region of ±200 fs was excluded to



avoid contributions from coherent artefacts [52]. The measurements were performed in 1 mm cuvettes on solutions prepared to have an absorbance of 0.3 at the excitation wavelength (480 nm).

**Computational details:** All the calculations were carried out with the Gaussian16 suite of quantum chemistry programs [53]. The electronic ground state and the vertical excitation energies of T2R, T2R-Cat1, and T2R-Cat2 complexes have been characterized with DFT [54] and TD-DFT [55] approaches, respectively. Structural optimizations were carried out with the B3LYP hybrid density functional [56] and the Def2TZVP [57] basis set for C, H, O, N, and S atoms, and the SDD ECP and basis for the Co atom [58]. Because the excitation energies have a strong character of intramolecular charge transfer, we recall to the CAM-B3LYP level of theory with the same basis set for all the TD-DFT calculations [59]. In all the calculations, we have included the Acetonitrile solvent medium via the polarizable continuum model (PCM) [60].

## 5. Conclusions

The photoinduced processes at work in two novel dye-catalyst assemblies designed for hydrogen production in dye-sensitized photocathodes have been investigated by steady-state and ultrafast spectroscopic techniques. Comprehensive studies on the excited state dynamics of push-pull organic dyes are not common in the literature [30–33,61–63]. Compared to metallo-organic photosensitizers such as  $\text{Ru}(\text{bpy})_3^{2+}$ , various conformers indeed coexist in solution for these structures, increasing the number of potential relaxation pathways, thus rendering the photophysical analysis much more complex. The results presented here nevertheless highlight that appending a cobalt-based catalytic unit to a push-pull organic dye strongly affects its photophysical properties. In particular, the quenching of the dye emission within the dyad is not the signature of a photoinduced intramolecular electron transfer process to the catalytic center. Instead, a new non-radiative relaxation pathway is opened, involving intersystem crossing to a long-lived triplet excited state. Although the mechanism behind that is still unclear, this opens new perspectives of application for this family of dyads as organic triplet sensitizers. This study also provides key information regarding light-driven hydrogen evolution with these dye-catalyst assemblies, i.e., an initial reductive quenching mechanism with the electron donor is required for catalysis to occur.

**Supplementary Materials:** The following are available online at <http://www.mdpi.com/2073-4344/10/11/1340/s1>. Figure S1: Frontier molecular orbitals of T2R, Figure S2: Frontier molecular orbitals of T2R-Cat1, Figure S3: UV-Vis absorption spectra of T2R, T2R-Cat1, and T2R-Cat2 in MeOH, Figure S4: TA spectra and species-associated spectra of T2R in ACN, Figure S5: Transient absorption spectra at 0.4 ps and 1600 ps time delay in MeOH, Figure S6: UV-Vis spectroelectrochemical spectra of T2R-Cat1, Figure S7: Differential TA spectra of T2R-Cat1 in MeOH of the direct decay and monoexponential fit, Figure S8: Differential TA spectra of T2R-Cat2 in MeOH of the direct decay and monoexponential fit, Table S1: Photophysical and redox properties of Cat1, Cat2, T2R, T2R-Cat1, and T2R-Cat2, Table S2: Rates and characteristic time constants of excited-state processes.

**Author Contributions:** Conceptualization, B.D. and M.C.-K.; methodology, S.B., B.D., M.P., and A.B.M.-G.; validation, S.B.; formal analysis, S.B., M.P., and A.B.M.-G.; investigation, S.B., T.S., M.P., and A.B.M.-G.; resources, B.D., M.C.-K., and V.A.; writing—original draft preparation, S.B.; writing—review and editing, M.C.-K., B.D., and S.B.; visualization, S.B.; funding acquisition, B.D., M.C.-K., and V.A. All authors have read and agreed to the published version of the manuscript.

**Funding:** This research was supported by the European Commission's Seventh Framework Program (FP7/2007–2013) under grant agreement n° 306398 (FP7-IDEAS-ERC, Project PhotocatH<sub>2</sub>ode), the French National Research Agency in the framework of the "Investissements d'avenir" program (ANR-15-IDEX-02, Labex ARCANE and CBH-EURGS, ANR-17-EURE-0003) and the Franco-German University.

**Acknowledgments:** We thank Yves Carstensen and Maria Sittig for their help in measuring the emission quantum yields. We thank Jens Uhlig for providing us with his data analysis software used for fitting the TA data.

**Conflicts of Interest:** The authors declare no conflict of interest. The funders had no role in the design of the study; in the collection, analyses, or interpretation of data; in the writing of the manuscript, or in the decision to publish the results.

## References

1. Walter, M.G.; Warren, E.L.; McKone, J.R.; Boettcher, S.W.; Mi, Q.; Santori, E.A.; Lewis, N.S. Solar Water Splitting Cells. *Chem. Rev.* **2010**, *110*, 6446–6473. [[CrossRef](#)]
2. Dalle, K.E.; Warnan, J.; Leung, J.J.; Reuillard, B.; Karmel, I.S.; Reisner, E. Electro- and Solar-Driven Fuel Synthesis with First Row Transition Metal Complexes. *Chem. Rev.* **2019**, *119*, 2752–2875. [[CrossRef](#)] [[PubMed](#)]
3. Pfeffer, M.G.; Schäfer, B.; Smolentsev, G.; Uhlig, J.; Nazarenko, E.; Guthmüller, J.; Kuhnt, C.; Wächter, M.; Dietzek, B.; Sundström, V.; et al. Palladium versus Platinum: The Metal in the Catalytic Center of a Molecular Photocatalyst Determines the Mechanism of the Hydrogen Production with Visible Light. *Angew. Chem. Int. Ed.* **2015**, *54*, 5044–5048. [[CrossRef](#)] [[PubMed](#)]
4. Dempsey, J.L.; Brunschwig, B.S.; Winkler, J.R.; Gray, H.B. Hydrogen Evolution Catalyzed by Cobaloximes. *ACC Chem. Res.* **2009**, *42*, 1995–2004. [[CrossRef](#)] [[PubMed](#)]
5. Shan, B.; Das, A.K.; Marquard, S.; Farnum, B.H.; Wang, D.; Bullock, R.M.; Meyer, T.J. Photogeneration of hydrogen from water by a robust dye-sensitized photocathode. *Energy Environ. Sci.* **2016**, *9*, 3693–3697. [[CrossRef](#)]
6. Mengele, A.K.; Kaufhold, S.; Streb, C.; Rau, S. Generation of a stable supramolecular hydrogen evolving photocatalyst by alteration of the catalytic center. *Dalton Trans.* **2016**, *45*, 6612–6618. [[CrossRef](#)]
7. Luo, G.-G.; Pan, Z.-H.; Lin, J.; Sun, D. Tethered sensitizer–catalyst noble-metal-free molecular devices for solar-driven hydrogen generation. *Dalton Trans.* **2018**, *47*, 15633–15645. [[CrossRef](#)]
8. Braumüller, M.; Schulz, M.; Sorsche, D.; Pfeffer, M.; Schaub, M.; Popp, J.; Park, B.-W.; Hagfeldt, A.; Dietzek, B.; Rau, S. Synthesis and characterization of an immobilizable photochemical molecular device for H<sub>2</sub>-generation. *Dalton Trans.* **2015**, *44*, 5577–5586. [[CrossRef](#)]
9. Pöldme, N.; O'Reilly, L.; Fletcher, I.; Portoles, J.; Sazanovich, I.V.; Towrie, M.; Long, C.; Vos, J.G.; Pryce, M.T.; Gibson, E.A. Photoelectrocatalytic H<sub>2</sub> evolution from integrated photocatalysts adsorbed on NiO. *Chem. Sci.* **2019**, *10*, 99–112. [[CrossRef](#)]
10. Karnahl, M.; Kuhnt, C.; Ma, F.; Yartsev, A.; Schmitt, M.; Dietzek, B.; Rau, S.; Popp, J. Tuning of Photocatalytic Hydrogen Production and Photoinduced Intramolecular Electron Transfer Rates by Regioselective Bridging Ligand Substitution. *ChemPhysChem* **2011**, *12*, 2101–2109. [[CrossRef](#)]
11. Shan, B.; Nayak, A.; Brennaman, M.K.; Liu, M.; Marquard, S.L.; Eberhart, M.S.; Meyer, T.J. Controlling Vertical and Lateral Electron Migration Using a Bifunctional Chromophore Assembly in Dye-Sensitized Photoelectrosynthesis Cells. *J. Am. Chem. Soc.* **2018**, *140*, 6493–6500. [[CrossRef](#)] [[PubMed](#)]
12. Windle, C.D.; Massin, J.; Chavarot-Kerlidou, M.; Artero, V. A protocol for quantifying hydrogen evolution by dye-sensitized molecular photocathodes and its implementation for evaluating a new covalent architecture based on an optimized dye-catalyst dyad. *Dalton Trans.* **2018**, *47*, 10509–10516. [[CrossRef](#)] [[PubMed](#)]
13. Kaefter, N.; Massin, J.; Lebrun, C.; Renault, O.; Chavarot-Kerlidou, M.; Artero, V. Covalent Design for Dye-Sensitized H<sub>2</sub>-Evolving Photocathodes Based on a Cobalt Diimine–Dioxime Catalyst. *J. Am. Chem. Soc.* **2016**, *138*, 12308–12311. [[CrossRef](#)] [[PubMed](#)]
14. McTavish, H. Hydrogen Evolution by Direct Electron Transfer from Photosystem I to Hydrogenases. *J. Biochem.* **1998**, *123*, 644–649. [[CrossRef](#)] [[PubMed](#)]
15. Gibson, E.A. Dye-sensitized photocathodes for H<sub>2</sub> evolution. *Chem. Soc. Rev.* **2017**, *46*, 6194–6209. [[CrossRef](#)]
16. Lyu, S.; Massin, J.; Pavone, M.; Muñoz-García, A.B.; Labrugère, C.; Toupance, T.; Chavarot-Kerlidou, M.; Artero, V.; Olivier, C. H<sub>2</sub>-Evolving Dye-Sensitized Photocathode Based on a Ruthenium–Diacetylide/Cobaloxime Supramolecular Assembly. *ACS Appl. Energy Mater.* **2019**, *2*, 4971–4980. [[CrossRef](#)]
17. Bold, S.; Zedler, L.; Zhang, Y.; Massin, J.; Artero, V.; Chavarot-Kerlidou, M.; Dietzek, B. Electron transfer in a covalent dye–cobalt catalyst assembly—a transient absorption spectroelectrochemistry perspective. *Chem. Commun.* **2018**, *54*, 10594–10597. [[CrossRef](#)]
18. Bold, S.; Massin, J.; Giannoudis, E.; Koepf, M.; Artero, V.; Dietzek, B.; Chavarot-Kerlidou, M. Spectroscopic investigations provide a rationale for the hydrogen-evolving activity of dye-sensitized photocathodes based on a cobalt tetraazamacrocyclic catalyst. **2020**. Submitted for publication.
19. Kaefter, N.; Chavarot-Kerlidou, M.; Artero, V. Hydrogen evolution catalyzed by cobalt diimine-dioxime complexes. *Acc. Chem. Res.* **2015**, *48*, 1286–1295. [[CrossRef](#)]

20. Varma, S.; Castillo, C.E.; Stoll, T.; Fortage, J.; Blackman, A.G.; Molton, F.; Deronzier, A.; Collomb, M.-N. Efficient photocatalytic hydrogen production in water using a cobalt(III) tetraaza-macrocyclic catalyst: Electrochemical generation of the low-valent Co(I) species and its reactivity toward proton reduction. *Phys. Chem. Chem. Phys.* **2013**, *15*, 17544. [[CrossRef](#)]
21. Grau, S.; Schilling, M.; Moonshiram, D.; Benet-Buchholz, J.; Lubner, S.; Llobet, A.; Gimbert-Suriñach, C. Electrochemically and Photochemically Induced Hydrogen Evolution Catalysis with Cobalt Tetraazamacrocycles Occurs Through Different Pathways. *ChemSusChem* **2020**, *13*, 2745–2752. [[CrossRef](#)] [[PubMed](#)]
22. Roy, S.; Bacchi, M.; Berggren, G.; Artero, V. A Systematic Comparative Study of Hydrogen-Evolving Molecular Catalysts in Aqueous Solutions. *ChemSusChem* **2015**, *8*, 3632–3638. [[CrossRef](#)] [[PubMed](#)]
23. Yen, Y.-S.; Chen, W.-T.; Hsu, C.-Y.; Chou, H.-H.; Lin, J.T.; Yeh, M.-C.P. Arylamine-Based Dyes for p-Type Dye-Sensitized Solar Cells. *Org. Lett.* **2011**, *13*, 4930–4933. [[CrossRef](#)]
24. Cai, Y.; Meng, L.; Gao, H.; Guo, Z.; Zheng, N.; Xie, Z.; Zhang, H.; Li, C.; Wan, X.; Chen, Y. Achieving organic solar cells with efficiency over 14% based on a non-fullerene acceptor incorporating a cyclopentathiophene unit fused backbone. *J. Mater. Chem. A* **2020**, *8*, 5194–5199. [[CrossRef](#)]
25. Fujitsuka, M.; Sato, T.; Sezaki, F.; Tanaka, K.; Watanabe, A.; Ito, O. Laser flash photolysis study on the photoinduced reactions of 3,3'-bridged bithiophenes. *J. Chem. Soc. Faraday Trans.* **1998**, *94*, 3331–3337. [[CrossRef](#)]
26. Paa, W.; Yang, J.-P.; Rentsch, S. Intersystem crossing in oligothiophenes studied by fs time-resolved spectroscopy. *Appl. Phys. B* **2000**, *71*, 443–449. [[CrossRef](#)]
27. Massin, J.; Bräutigam, M.; Kaeffer, N.; Queyriaux, N.; Field, M.J.; Schacher, F.H.; Popp, J.; Chavarot-Kerlidou, M.; Dietzek, B.; Artero, V. Dye-sensitized PS-b-P2VP-templated nickel oxide films for photoelectrochemical applications. *Interface Focus* **2015**, *5*, 20140083. [[CrossRef](#)]
28. Reichardt, C.; Welton, T. Appendix A. Properties, Purification, and Use of Organic Solvents. In *Solvents and Solvent Effects in Organic Chemistry*; Wiley-VCH Verlag GmbH & Co. KGaA: Weinheim, Germany, 2010; Volume 16, pp. 549–586. ISBN 9783527324736.
29. Montalti, M.; Credi, A.; Prodi, L.; Gandolfi, M.T. 9-Solvent Properties. In *Handbook of Photochemistry*; CRC Press (Taylor & Francis Group): Boca Raton, FL, USA, 2006; Volume 3, pp. 535–559.
30. Ishow, E.; Guillot, R.; Buntinx, G.; Poizat, O. Photoinduced intramolecular charge-transfer dynamics of a red-emitting dicyanovinyl-based triarylamine dye in solution. *J. Photochem. Photobiol. A Chem.* **2012**, *234*, 27–36. [[CrossRef](#)]
31. Ishow, E.; Clavier, G.; Miomandre, F.; Rebarz, M.; Buntinx, G.; Poizat, O. Comprehensive investigation of the excited-state dynamics of push–pull triphenylamine dyes as models for photonic applications. *Phys. Chem. Chem. Phys.* **2013**, *15*, 13922. [[CrossRef](#)]
32. Flender, O.; Scholz, M.; Klein, J.R.; Oum, K.; Lenzer, T. Excited-state relaxation of the solar cell dye D49 in organic solvents and on mesoporous Al<sub>2</sub>O<sub>3</sub> and TiO<sub>2</sub> thin films. *Phys. Chem. Chem. Phys.* **2016**, *18*, 26010–26019. [[CrossRef](#)]
33. Oum, K.; Lohse, P.W.; Klein, J.R.; Flender, O.; Scholz, M.; Hagfeldt, A.; Boschloo, G.; Lenzer, T. Photoinduced ultrafast dynamics of the triphenylamine-based organic sensitizer D35 on TiO<sub>2</sub>, ZrO<sub>2</sub> and in acetonitrile. *Phys. Chem. Chem. Phys.* **2013**, *15*, 3906. [[CrossRef](#)] [[PubMed](#)]
34. Massin, J.; Bräutigam, M.; Bold, S.; Wächtler, M.; Pavone, M.; Muñoz-García, A.B.; Dietzek, B.; Artero, V.; Chavarot-Kerlidou, M. Investigating Light-Driven Hole Injection and Hydrogen Evolution Catalysis at Dye-Sensitized NiO Photocathodes: A Combined Experimental–Theoretical Study. *J. Phys. Chem. C* **2019**, *123*, 17176–17184. [[CrossRef](#)]
35. Muresan, N.M.; Willkomm, J.; Mersch, D.; Vaynzof, Y.; Reisner, E. Immobilization of a Molecular Cobaloxime Catalyst for Hydrogen Evolution on a Mesoporous Metal Oxide Electrode. *Angew. Chem. Int. Ed.* **2012**, *51*, 12749–12753. [[CrossRef](#)] [[PubMed](#)]
36. Rentsch, S.; Yang, J.P.; Paa, W.; Birckner, E.; Schiedt, J.; Weinkauff, R. Size dependence of triplet and singlet states of  $\alpha$ -oligothiophenes. *Phys. Chem. Chem. Phys.* **1999**, *1*, 1707–1714. [[CrossRef](#)]
37. Grebner, D.; Helbig, M.; Rentsch, S. Size-Dependent Properties of Oligothiophenes by Picosecond Time-Resolved Spectroscopy. *J. Phys. Chem.* **1995**, *99*, 16991–16998. [[CrossRef](#)]
38. Paa, W.; Yang, J.P.; Helbig, M.; Hein, J.; Rentsch, S. Femtosecond time-resolved measurements of terthiophene: Fast singlet-triplet intersystem crossing. *Chem. Phys. Lett.* **1998**, *292*, 607–614. [[CrossRef](#)]
39. Janssen, R.A.J.; Smilowitz, L.; Sariciftci, N.S.; Moses, D. Triplet-state photoexcitations of oligothiophene films and solutions. *J. Chem. Phys.* **1994**, *101*, 1787–1798. [[CrossRef](#)]



40. Volchkov, V.V.; Ivanov, V.L.; Uzhinov, B.M. Induced intersystem crossing at the fluorescence quenching of laser dye 7-amino-1,3-naphthalenedisulfonic acid by paramagnetic metal ions. *J. Fluoresc.* **2010**, *20*, 299–303. [[CrossRef](#)]
41. Takashima, H.; Kawahara, H.; Kitano, M.; Shibata, S.; Murakami, H.; Tsukahara, K. Metal ion-dependent fluorescent dynamics of photoexcited zinc-porphyrin and zinc-myoglobin modified with ethylenediaminetetraacetic acid. *J. Phys. Chem. B* **2008**, *112*, 15493–15502. [[CrossRef](#)]
42. Ji, S.; Zhao, J.; Donato, M.D.; Xing, Y.H.; Mahmood, Z.; Taddei, M.; Rehmat, N.; Bussotti, L.; Doria, S.; Guan, Q.; et al. Color-tunable delayed fluorescence and efficient spin-orbit charge transfer intersystem crossing in compact carbazole-anthracene-BODIPY triads employing the sequential electron transfer approach. *J. Phys. Chem. C* **2020**, *124*, 5944–5957. [[CrossRef](#)]
43. Weiss, E.A.; Ratner, M.A.; Wasielewski, M.R. Direct measurement of singlet-triplet splitting within rodlike photogenerated radical ion pairs using magnetic field effects: Estimation of the electronic coupling for charge recombination. *J. Phys. Chem. A* **2003**, *107*, 3639–3647. [[CrossRef](#)]
44. Dance, Z.E.X.; Mi, Q.; McCamant, D.W.; Ahrens, M.J.; Ratner, M.A.; Wasielewski, M.R. Time-resolved EPR studies of photogenerated radical ion pairs separated by p-phenylene oligomers and of triplet states resulting from charge recombination. *J. Phys. Chem. B* **2006**, *110*, 25163–25173. [[CrossRef](#)] [[PubMed](#)]
45. Colvin, M.T.; Ricks, A.B.; Scott, A.M.; Co, D.T.; Wasielewski, M.R. Intersystem crossing involving strongly spin exchange-coupled radical ion pairs in donor-bridge-acceptor molecules. *J. Phys. Chem. A* **2012**, *116*, 1923–1930. [[CrossRef](#)] [[PubMed](#)]
46. Wu, W.; Zhao, J.; Sun, J.; Guo, S. Light-harvesting fullerene dyads as organic triplet photosensitizers for triplet-triplet annihilation upconversions. *J. Org. Chem.* **2012**, *77*, 5305–5312. [[CrossRef](#)]
47. Huang, L.; Cui, X.; Therrien, B.; Zhao, J. Energy-funneling-based broadband visible-light-absorbing Bodipy-C60 triads and tetrads as dual functional heavy-atom-free organic triplet photosensitizers for photocatalytic organic reactions. *Chem. A Eur. J.* **2013**, *19*, 17472–17482. [[CrossRef](#)] [[PubMed](#)]
48. Huang, D.; Zhao, J.; Wu, W.; Yi, X.; Yang, P.; Ma, J. Visible-light-harvesting triphenylamine ethynyl C60-BODIPY dyads as heavy-atom-free organic triplet photosensitizers for triplet-triplet annihilation Upconversion. *Asian J. Org. Chem.* **2012**, *1*, 264–273. [[CrossRef](#)]
49. Marroux, H.J.B.; Curchod, B.F.E.; Faradji, C.A.; Shuttleworth, T.A.; Sparkes, H.A.; Pringle, P.G.; Orr-Ewing, A.J. Spin Changes Accompany Ultrafast Structural Interconversion in the Ground State of a Cobalt Nitrosyl Complex. *Angew. Chem. Int. Ed.* **2017**, *56*, 13713–13716. [[CrossRef](#)]
50. McCusker, J.K.; Walda, K.N.; Magde, D.; Hendrickson, D.N. Picosecond Excited-State Dynamics in Octahedral Cobalt(III) Complexes: Intersystem Crossing versus Internal Conversion. *Inorg. Chem.* **1993**, *32*, 394–399. [[CrossRef](#)]
51. Jacques, P.-A.; Artero, V.; Pecaut, J.; Fontecave, M. Cobalt and nickel diimine-dioxime complexes as molecular electrocatalysts for hydrogen evolution with low overvoltages. *Proc. Natl. Acad. Sci. USA* **2009**, *106*, 20627–20632. [[CrossRef](#)]
52. Dietzek, B.; Pascher, T.; Sundström, V.; Yartsev, A. Appearance of coherent artifact signals in femtosecond transient absorption spectroscopy in dependence on detector design. *Laser Phys. Lett.* **2007**, *4*, 38–43. [[CrossRef](#)]
53. Frisch, M.J.; Trucks, G.W.; Schlegel, H.B.; Scuseria, G.E.; Robb, M.A.; Cheeseman, J.R.; Scalmani, G.; Barone, V.; Petersson, G.A.; Nakatsuji, H.; et al. *Gaussian 16, Revision A.02*; Gaussian Inc.: Wallingford, CT, USA, 2016.
54. Hohenberg, P.; Kohn, W. Inhomogeneous Electron Gas. *Phys. Rev.* **1964**, *136*, B864–B871. [[CrossRef](#)]
55. Runge, E.; Gross, E.K.U. Density-Functional Theory for Time-Dependent Systems. *Phys. Rev. Lett.* **1984**, *52*, 997–1000. [[CrossRef](#)]
56. Becke, A.D. Density-functional thermochemistry. III. The role of exact exchange. *J. Chem. Phys.* **1993**, *98*, 5648–5652. [[CrossRef](#)]
57. Weigend, F. Accurate Coulomb-fitting basis sets for H to Rn. *Phys. Chem. Chem. Phys.* **2006**, *8*, 1057–1065. [[CrossRef](#)]
58. Dolg, M.; Wedig, U.; Stoll, H.; Preuss, H. Energy-adjusted ab initio pseudopotentials for the first row transition elements. *J. Chem. Phys.* **1987**, *86*, 866–872. [[CrossRef](#)]
59. Yanai, T.; Tew, D.P.; Handy, N.C. A new hybrid exchange–correlation functional using the Coulomb-attenuating method (CAM-B3LYP). *Chem. Phys. Lett.* **2004**, *393*, 51–57. [[CrossRef](#)]

60. Tomasi, J.; Mennucci, B.; Cammi, R. Quantum Mechanical Continuum Solvation Models. *Chem. Rev.* **2005**, *105*, 2999–3094. [[CrossRef](#)]
61. Li, Y.; Hu, J.; He, G.; Zhu, H.; Wang, X.; Guo, Q.; Xia, A.; Lin, Y.; Wang, J.; Zhan, X. Influence of Thiophene Moiety on the Excited State Properties of Push–Pull Chromophores. *J. Phys. Chem. C* **2016**, *120*, 13922–13930. [[CrossRef](#)]
62. Labrunie, A.; Gorenflot, J.; Babics, M.; Alévêque, O.; Dabos-Seignon, S.; Balawi, A.H.; Kan, Z.; Wohlfahrt, M.; Levillain, E.; Hudhomme, P.; et al. Triphenylamine-Based Push–Pull  $\sigma$ -C 60 Dyad As Photoactive Molecular Material for Single-Component Organic Solar Cells: Synthesis, Characterizations, and Photophysical Properties. *Chem. Mater.* **2018**, *30*, 3474–3485. [[CrossRef](#)]
63. Oum, K.; Flender, O.; Lohse, P.W.; Scholz, M.; Hagfeldt, A.; Boschloo, G.; Lenzer, T. Electron and hole transfer dynamics of a triarylamine-based dye with peripheral hole acceptors on TiO<sub>2</sub> in the absence and presence of solvent. *Phys. Chem. Chem. Phys.* **2014**, *16*, 8019. [[CrossRef](#)]

**Publisher’s Note:** MDPI stays neutral with regard to jurisdictional claims in published maps and institutional affiliations.



© 2020 by the authors. Licensee MDPI, Basel, Switzerland. This article is an open access article distributed under the terms and conditions of the Creative Commons Attribution (CC BY) license (<http://creativecommons.org/licenses/by/4.0/>).



## Supporting Information

# Investigating light-induced processes in organic covalent dye-catalyst assemblies for hydrogen evolution

*Sebastian Bold<sup>1,2,3</sup>, Tatiana Straistari<sup>1</sup>, Ana B. Muñoz-García<sup>4</sup>, Michele Pavone<sup>5</sup>,  
Vincent Artero<sup>1</sup>, Murielle Chavarot-Kerlidou<sup>1</sup> and Benjamin Dietzek<sup>2,3,6</sup>*

<sup>1</sup> Laboratoire de Chimie et Biologie des Métaux, Université Grenoble Alpes, CNRS, CEA, 17 rue des Martyrs, 38000 Grenoble, France

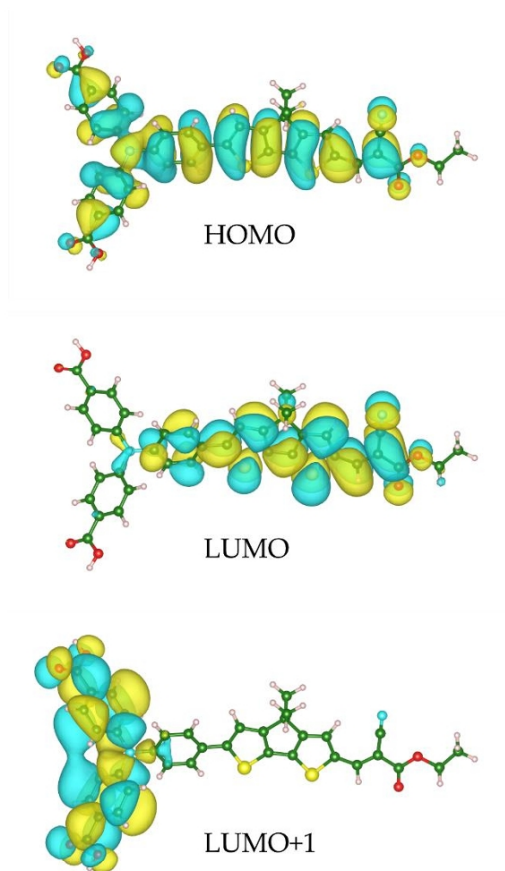
<sup>2</sup> Institute of Physical Chemistry and Abbe Center of Photonics, Friedrich Schiller University Jena, Helmholtzweg 4, 07743 Jena, Germany

<sup>3</sup> Department Functional Interfaces, Leibniz Institute of Photonic Technology Jena (Leibniz-IPHT), Albert-Einstein-Straße 9, 07745 Jena, Germany

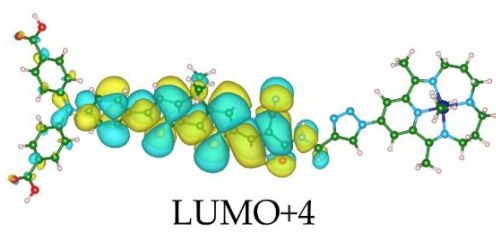
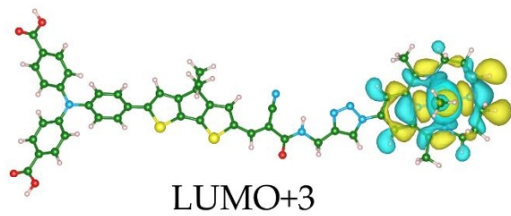
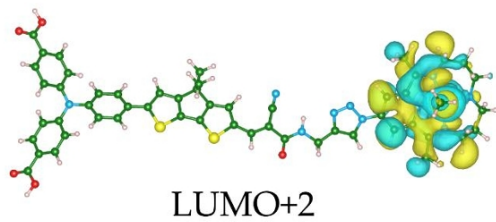
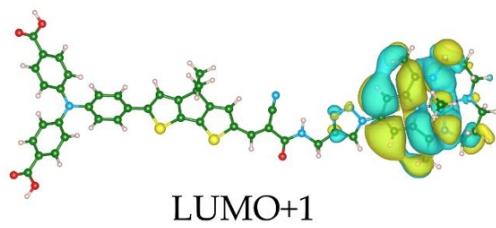
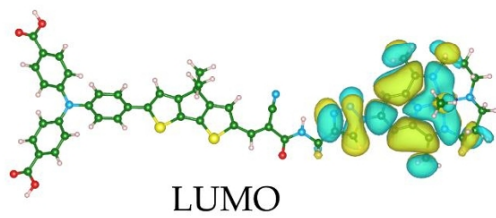
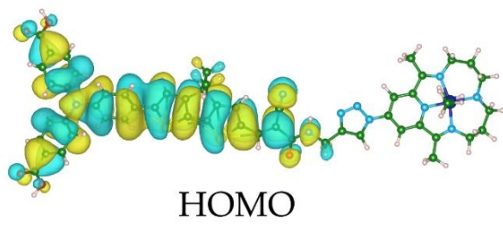
<sup>4</sup> Department of Physics “Ettore Pancini”, University of Naples Federico II, Complesso Universitario Monte Sant’Angelo Via Cintia, 80126 Naples, Italy

<sup>5</sup> Department of Chemical Sciences, University of Naples Federico II, Complesso Universitario Monte Sant’Angelo Via Cintia, 80126 Naples, Italy

<sup>6</sup> Center for Energy and Environmental Chemistry Jena (CEEC-Jena), Friedrich Schiller University Jena, Philosophenweg 8, 07743 Jena, Germany



**Figure S1.** Frontier molecular orbitals of T2R obtained by DFT calculations.



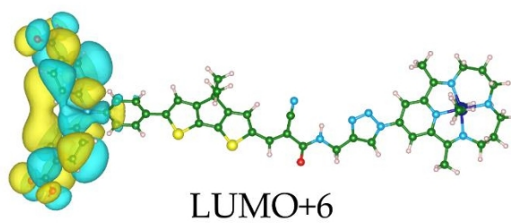
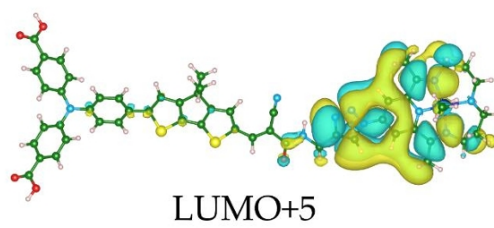


**Figure S2.** Frontier molecular orbitals of T2R-Cat1 obtained by DFT calculations.

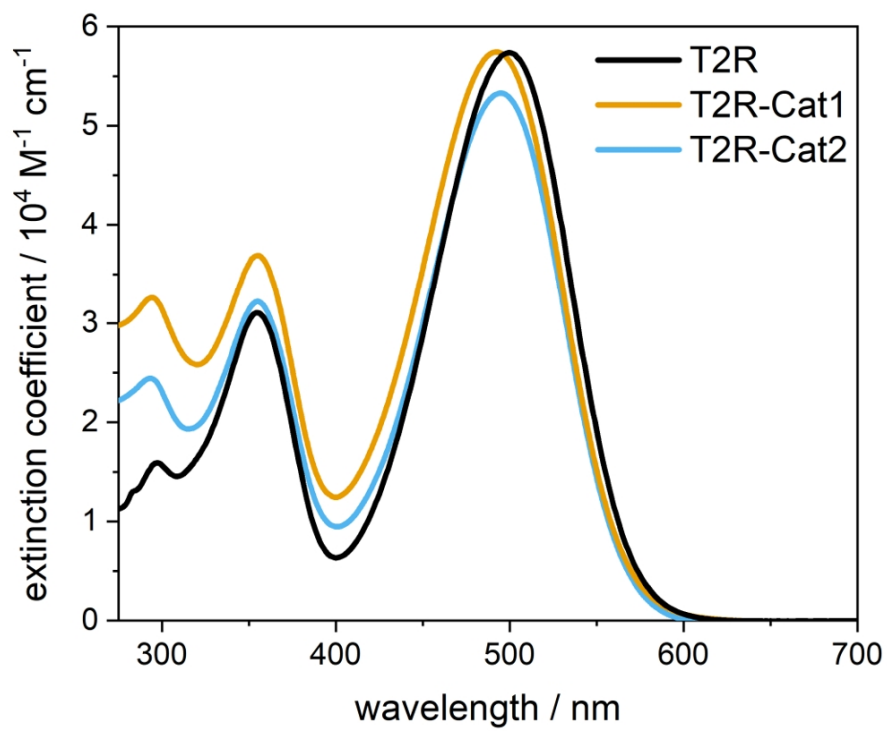


**Figure S3.** UV-Vis absorption spectra of T2R, T2R-Cat1 and T2R-Cat2 in MeOH.

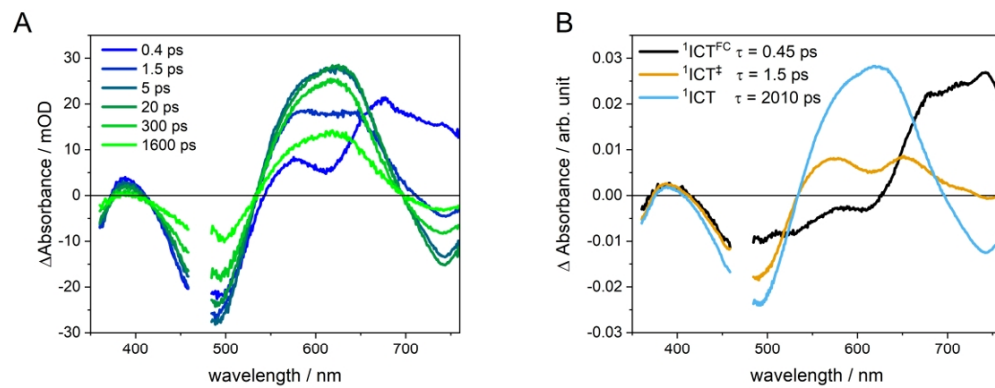


**Figure S4.** a) Transient absorption spectra of T2R in ACN, b) species-associated spectra obtained with a sequential three-component exponential fit; with the lifetimes of the species.

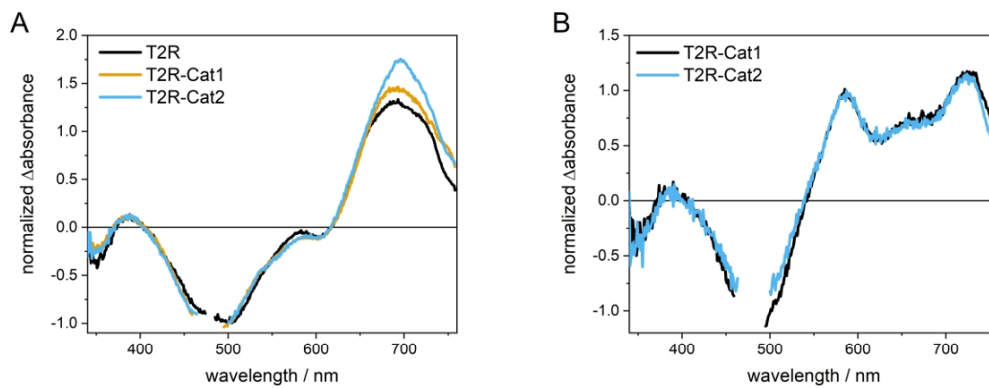


**Figure S5.** Transient absorption spectra at a) 0.4 ps and b) 1600 ps time delay in MeOH. The spectra at 0.4 ps were normalized at 500 nm and the spectra at 1600 ps were normalized at the maximum at 587 nm.

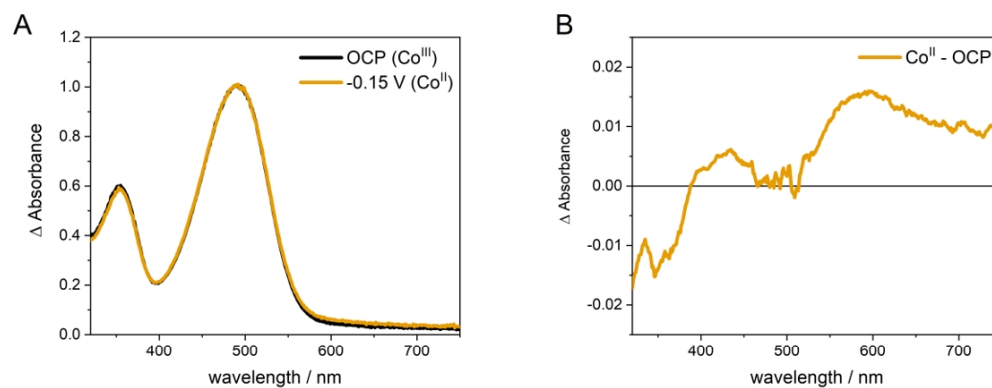


**Figure S6.** a) UV-Vis absorption spectra of T2R-Cat1 at open-circuit potential ( $\text{Co}^{\text{III}}$  state) and at -0.15 V vs. Ag wire applied potential (reduction of the cobalt complex to the  $\text{Co}^{\text{II}}$  state). b) Differential spectrum obtained by subtracting the OCP spectrum from the spectrum at -0.15 V.



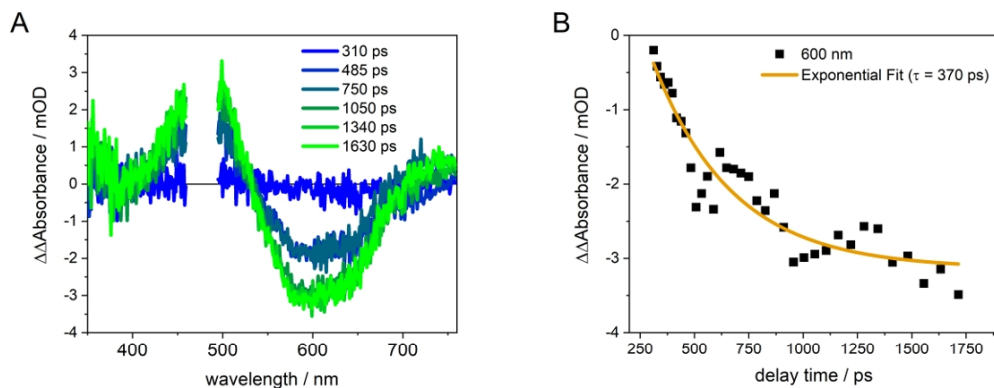


**Figure S7.** a) Differential TA spectra of T2R-Cat1 in MeOH obtained by subtracting the spectrum recorded at 300 ps time delay and b) monoexponential fit of the data thus obtained at the maximum at 600 nm. The spectrum is the inverse spectrum of the T2R  $^1$ ICT state, confirming that the observed signal decay is caused by a return to the ground state from the thermalized singlet excited state of the dye T2R.

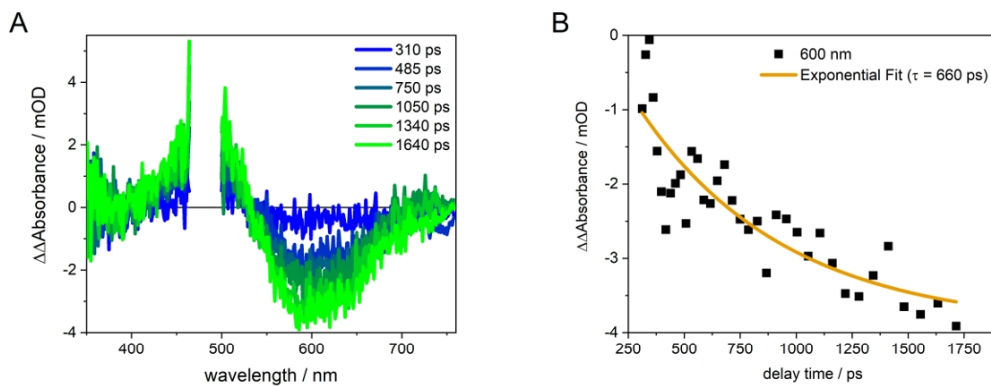


**Figure S8.** a) Differential TA spectra of T2R-Cat2 in MeOH obtained by subtracting the spectrum recorded at 300 ps time delay and b) monoexponential fit of the data thus obtained at the maximum at 600 nm. The spectrum is the inverse spectrum of the T2R <sup>1</sup>ICT state, confirming that the observed signal decay is caused by a return to the ground state from the thermalized singlet excited state of the dye T2R.

**Table S1.** Photophysical and redox properties of Cat1, Cat2, T2R, T2R-Cat1 and T2R-Cat2.

		$\lambda_{\text{Abs}}(\text{TPA})$	$\epsilon(\text{TPA}) / \text{M}^{-1}\cdot\text{cm}^{-1}$	$\lambda_{\text{Abs}}(\text{ICT})$	$\epsilon(\text{ICT}) / \text{M}^{-1}\cdot\text{cm}^{-1}$	$\lambda_{\text{Em}}$	$\Phi^{520}$	$E_{\text{ox1}}^{\text{a)}$ (Dye <sup>+0</sup> )	$E_{\text{ox2}}^{\text{a)}$ (Dye <sup>2+/+</sup> )	$E_{\text{red1}}^{\text{a)}$ (Co <sup>III/II</sup> )	$E_{\text{red2}}^{\text{a)}$ (Co <sup>II/I</sup> )	$E_{\text{red3}}^{\text{a)}$ (Dye <sup>0/-</sup> )	$E_{0-0}^{\text{b)}$	$\Delta G_1^{\text{c)}$	$\Delta G_2^{\text{d)}$
<b>Cat1</b>										-0.01	-0.51				
<b>Cat2</b>										-0.04 <sup>e)</sup>	-0.58 <sup>e)</sup>				
<b>T2R</b>	ACN	355	30570	498	60560			1.05	1.23			-1.00			
	MeOH	355	31060	498	57374	674	0.25						2.15		
<b>T2R-Cat1</b>	ACN	355	32580	493	55830			1.00	1.15	0.03	-0.40	-1.08			
	MeOH	355	36900	493	57435	660	0.02						2.17	-1.18	-0.75
<b>T2R-Cat2</b>	ACN	353	32750	490	57940			1.02	1.19	0.04	-0.45	-1.10			
	MeOH	355	32196	495	53287	663	0.08						2.17	-1.19	-0.70

a) In V vs NHE.  $1/2(E_{\text{pc}^+} + E_{\text{pc}})$  for Ered1 and Ered2;  $E_{\text{pc}}$  for Ered3. The redox potentials were converted from  $\text{Fc}^{+/0}$  to NHE, obtained from the reduction potential considering  $E^\circ(\text{Fc}^{+/0}) = 0.53$  V vs. NHE in ACN,  $E^\circ(\text{Fc}^{+/0}) = 0.57$  V vs. NHE in DMF. Unless otherwise indicated, the data was recorded in DMF.

b) 0-0 transition energy,  $E_{0-0}$ , in eV, estimated from the intercept of the normalized absorption and emission spectra.

c) The Gibbs free energy in eV for the electron transfer from the excited dye to the Co(III) catalyst was calculated according to  $\Delta G_1 = e[E(\text{Dye}^{+/*}) - E(\text{Co}^{\text{III/II}})]$ , with  $E(\text{Dye}^{+/*}) = E(\text{Dye}^{+/0}) - E(0-0)$ .

d) The Gibbs free energy in eV for the electron transfer from the reduced dye to the Co(II) catalyst was calculated according to  $\Delta G_2 = e[E(\text{Dye}^{+/*}) - E(\text{Co}^{\text{II/I}})]$ , with  $E(\text{Dye}^{+/*}) = E(\text{Dye}^{+/0}) - E(0-0)$ .

e) In ACN

**Table S2.** Rates and characteristic time constants of samples excited at 480 nm.

	Kinetic rates / s <sup>-1</sup>					Time constants <sup>1</sup> / ps				
	k <sub>1</sub>	k <sub>2</sub>	k <sub>3</sub>	k <sub>4</sub>	k <sub>5</sub>	τ <sub>1</sub>	τ <sub>2</sub>	τ <sub>3</sub>	τ <sub>4</sub>	τ <sub>5</sub>
T2R	7.6 × 10 <sup>11</sup>	8.9 × 10 <sup>10</sup>	7.6 × 10 <sup>8</sup>			1.3	11	1320		
T2R-Cat1	1.3 × 10 <sup>12</sup>	1.5 × 10 <sup>11</sup>	1.4 × 10 <sup>9</sup>	6.5 × 10 <sup>9</sup>	<< 5 × 10 <sup>8</sup>	0.8	7	370	150	>> 2 ns
T2R-Cat2	1.1 × 10 <sup>12</sup>	1.5 × 10 <sup>11</sup>	1.5 × 10 <sup>9</sup>	5.8 × 10 <sup>9</sup>	<< 5 × 10 <sup>8</sup>	0.9	7	660	170	>> 2 ns

<sup>1</sup>: τ<sub>n</sub> = 1/k<sub>n</sub>

**Publication 3** - Spectroscopic investigations provide a rational for the hydrogen-evolving activity of dye-sensitized photocathodes based on a cobalt tetraazamacrocyclic catalyst.

Reproduced with permission from *ACS Catalysis*, submitted for publication on 17.11.2020. Unpublished work ©2020 American Chemical Society.

Authors	<u>SB</u>	JM	EG	MK	VA	BD	MCK
Synthesis		x	x				
Characterization	x	x	x				
(Photo-)electrochemistry	x			x			
Time-resolved spectroscopy	x						
Data analysis and processing	x					x	x
Data interpretation	x				x	x	x
Concept development	x				x	x	x
Preparation of the manuscript	x					x	x
Revision of the manuscript	x				x	x	x
Proposed publication equivalents	1.0						

This document is confidential and is proprietary to the American Chemical Society and its authors. Do not copy or disclose without written permission. If you have received this item in error, notify the sender and delete all copies.

**Spectroscopic investigations provide a rationale for the hydrogen-evolving activity of dye-sensitized photocathodes based on a cobalt tetraazamacrocyclic catalyst**

Journal:	<i>ACS Catalysis</i>
Manuscript ID	cs-2020-05033x
Manuscript Type:	Article
Date Submitted by the Author:	17-Nov-2020
Complete List of Authors:	Bold, Sebastian; Friedrich Schiller University Jena, Institute of Physical Chemistry Massin, Julien; Aix-Marseille Université Giannoudis, Emmanouil; UMR 5249 Univ. Grenoble Alpes – CNRS – CEA, Koepp, Matthieu; CEA Grenoble, Laboratoire de Chimie et Biologie des Métaux Artero, Vincent; CEA Grenoble, iRTSV/LCBM Dietzek, Benjamin; Friedrich-Schiller-Universität Jena, Institute for Physical Chemistry Chavarot-Kerlidou, Murielle; CNRS,

SCHOLARONE™  
Manuscripts

1  
2  
3  
4 Spectroscopic investigations provide a rationale for  
5  
6  
7  
8 the hydrogen-evolving activity of dye-sensitized  
9  
10  
11  
12 photocathodes based on a cobalt  
13  
14  
15  
16 tetraazamacrocyclic catalyst  
17  
18  
19  
20

21 *Sebastian Bold,<sup>a,b,c</sup> Julien Massin,<sup>†,a</sup> Emmanouil Giannoudis,<sup>a</sup> Matthieu Koepf,<sup>a</sup> Vincent*  
22 *Artero,<sup>a</sup> Benjamin Dietzek<sup>\*b,c,d</sup> and Murielle Chavarot-Kerlidou<sup>\*a</sup>*  
23  
24  
25

26  
27 a. Univ. Grenoble Alpes, CNRS, CEA, IRIG, Laboratoire de Chimie et Biologie des Métaux,  
28  
29 17 rue des Martyrs, F-38000 Grenoble, France.  
30

31  
32 b. Institute of Physical Chemistry and Abbe Center of Photonics, Friedrich Schiller University  
33  
34 Jena, Helmholtzweg 4, 07743 Jena, Germany.  
35  
36

37  
38 c. Department Functional Interfaces, Leibniz Institute of Photonic Technology Jena (Leibniz-  
39  
40 IPHT), Albert-Einstein-Straße 9, 07745 Jena, Germany.  
41  
42

43  
44 d. Center for Energy and Environmental Chemistry Jena (CEEC Jena), Friedrich Schiller  
45  
46 University Jena, Philosophenweg 8, 07743 Jena, Germany.  
47  
48  
49  
50  
51

52 **Keywords.**

53  
54 Cobalt catalyst, solar fuels, hydrogen production, photoelectrochemical cell (PEC), dye-  
55  
56 sensitized photocathode, transient absorption spectroscopy, spectroelectrochemistry  
57  
58  
59  
60

**Abstract.**

Dye-sensitized photoelectrochemical cells (DSPECs) are a promising approach to produce solar fuels, e.g. by reduction of protons to molecular hydrogen. Here, we present functional NiO photocathodes sensitized with covalent organic dye-catalyst assemblies integrating for the first time a robust cobalt tetraazamacrocyclic complex. This catalyst proved to be decisive to improve the stability of these systems, hydrogen being produced with a 26-fold increase in turnover numbers compared to similar photocathodes based on a cobaloxime catalyst, all other conditions being strictly identical otherwise. Transient absorption spectroelectrochemical (TA-SEC) measurements for the first time observed the catalytically competent  $\text{Co}^{\text{I}}$  state in a functional dye-sensitized photocathode, with a lifetime of up to  $> 1$  ms, comparable to the timescale of catalysis. They also unveiled the lack of efficiency of the thermally activated electron transfer from the reduced dye to the catalyst, which firstly limits the photocurrent density for hydrogen production. A second consequence is the accumulation of photogenerated charges on the acceptor side of the dye, ultimately leading to its degradation, as observed in operando and post-operando characterization of the system. This study thus provides new tracks to improve the performances of hydrogen-evolving dye-sensitized photocathodes toward their integration into functional DSPECs.

**Introduction**

Storing solar energy, which by nature is intermittent, in chemical bonds, i.e. a solar fuel, is highly appealing to move from fossil fuels to renewable energies.<sup>1</sup> One promising approach to producing solar fuels relies on artificial photosynthesis, which mimics the natural photosynthetic process with synthetic components tailored to perform the desired redox reaction.<sup>2-4</sup> In that context, the production of hydrogen ( $\text{H}_2$ ) in water splitting dye-sensitized photoelectrochemical cells (DSPECs) is the subject of intensive research efforts.<sup>5,6</sup> Tandem



1  
2  
3 DSPECs combine two photoelectrodes, a photoanode driving water oxidation to oxygen and a  
4 photocathode where protons and electrons are recombined to produce H<sub>2</sub>, in that way  
5 mimicking the Z-scheme of natural photosynthesis.<sup>7-9</sup> However, the dye-sensitized  
6 photocathodes reported to date lag well behind their photoanode counterparts in terms of  
7 photocurrent density and stability and are the limiting factor in tandem DSPEC, calling for  
8 investigations to understand their limitations and to develop guidelines to improve their  
9 performances.<sup>7-9</sup>

10  
11 Recently, molecular hydrogen-evolving catalysts based on first-row transition metals (Fe, Co,  
12 Ni) have been successfully integrated in dye-sensitized photocathodes.<sup>7-27</sup> In these studies, the  
13 synthetic tunability of the catalyst most of the time governs the electrode construction strategy:  
14 (i) immobilisation of supramolecular assemblies built by axial coordination of the dye on the  
15 Co center of a cobaloxime catalyst,<sup>10,26</sup> (ii) fully covalent dye-catalyst assemblies prepared  
16 thanks to a copper-catalyzed azide-alkyne cycloaddition (CuAAC) strategy using an azido-  
17 substituted cobalt diimine-dioxime complex,<sup>14-16</sup> (iii) layer-by-layer deposition of the dye and  
18 of a nickel bis(diphosphine) catalyst (Dubois type complex) functionalized with four  
19 phosphonate groups,<sup>20-22</sup> (iv) alternatively, co-immobilisation of dyes and catalysts at the  
20 semiconductor surface,<sup>7-9,17-19,24,25</sup> simplifying the synthesis and allowing to vary the  
21 dye/catalyst ratio. In addition to this diversity in the electrode architectures, which in turn  
22 strongly affects the electron transfer kinetics to the catalytic center, H<sub>2</sub> evolution activity was  
23 assessed under a wide range of conditions (nature of the electrolyte, pH, applied potential...).

24 Altogether, this prevents direct comparison of the performances from one system to another to  
25 identify the best-performing components and to establish structure-activity relationships  
26 necessary for a rational improvement of the photocathode design.

27  
28 In this study, we present a new noble metal-free covalent dye-catalyst assembly based on push-  
29 pull organic dyes covalently linked via CuAAC “click” chemistry to the tetraazamacrocyclic  
30 cobalt complex **Cat1** as catalytic unit. The superior activity and stability of the latter, compared  
31  
32  
33  
34  
35  
36  
37  
38  
39  
40  
41  
42  
43  
44  
45  
46  
47  
48  
49  
50  
51  
52  
53  
54  
55  
56  
57  
58  
59  
60

1  
2  
3 to the cobalt diimine-dioxime catalyst, was previously reported for photocatalytic proton  
4 reduction under fully aqueous conditions.<sup>28–35</sup> In parallel, the dye structure was modified from  
5 the previously published **T1-Co**<sup>16</sup> with a cyclopenta[1,2-b:5,4-b']dithiophene (CPDT) bridge  
6 to bathochromically shift the absorption and increase the extinction coefficient in the visible  
7 region.<sup>36,37</sup> The alkyl chains introduced on the linker are intended (i) to limit dyad-dyad  
8 interactions and (ii) to prevent dyad desorption by forming a hydrophobic layer at the surface  
9 of the NiO film.<sup>38,39</sup> Photoelectrochemical activity was assessed under strictly identical  
10 conditions to our previously-reported system,<sup>16</sup> thus providing a comprehensive comparison  
11 with **T1-Co**<sup>16</sup> and highlighting the beneficial role played by the **T2R** and **Cat1** moieties on the  
12 H<sub>2</sub> production performances. In addition, in-depth operando and post-operando  
13 characterizations of the **T2R-Cat1**-sensitized photocathode allowed to identify relevant  
14 degradation processes and to determine their kinetics. Finally, the light-driven formation of the  
15 different intermediates at the surface of the NiO film, including the catalytically competent Co<sup>I</sup>  
16 state of **Cat1**, was investigated by transient absorption spectroelectrochemical (TA-SEC)<sup>40–44</sup>  
17 measurements and provided a mechanistic rationale to improve the design of these dye-sensitized  
18 photocathodes.  
19  
20  
21  
22  
23  
24  
25  
26  
27  
28  
29  
30  
31  
32  
33  
34  
35  
36  
37  
38  
39

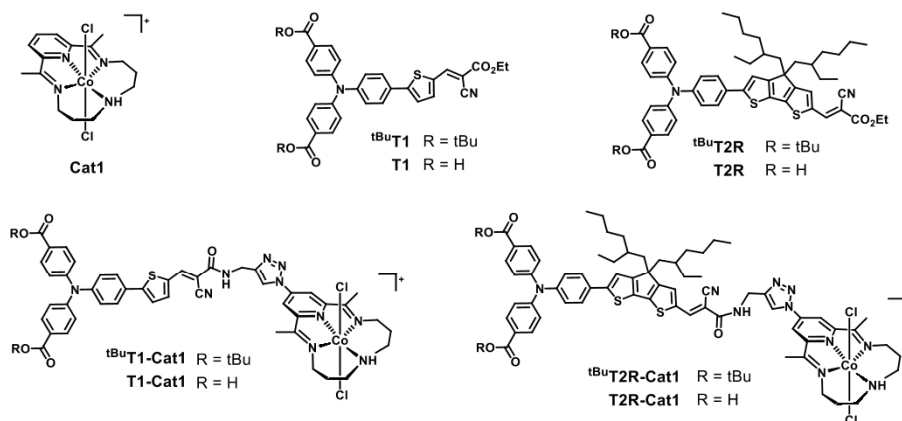
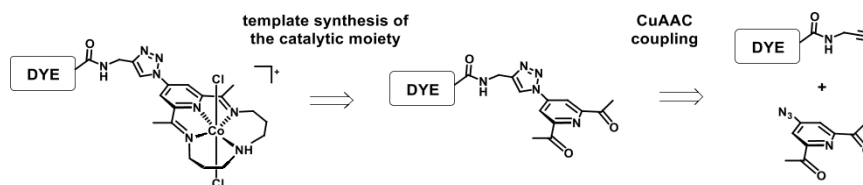


**Figure 1.** Structures of the H<sub>2</sub>-evolving catalyst **Cat1**, the dyes **T1** and **T2R**, and the dyads **T1-Cat1** and **T2R-Cat1**.

## Results

1  
2  
3 *Synthesis of the novel Cat1-based dyads.* Functionalization of **Cat1** is a challenging task, as  
4 reflected by the scarcity of procedures in the literature to prepare **Cat1** derivatives. Up to now,  
5 its catalytic performances were assessed either under electroassisted conditions<sup>29,30,45</sup> or under  
6 photocatalytic conditions in multicomponent homogenous systems.<sup>29–35</sup> The sole exception  
7 reported to date relies on a palladium-catalyzed cross-coupling introduction of a pyridine  
8 dicarboxylate anchoring group on the pyridine moiety of the ligand,<sup>28</sup> successfully allowing to  
9 assemble **Cat1** with quantum dots<sup>28</sup> or a TiO<sub>2</sub>-protected silicon photoelectrode.<sup>46</sup> On the other  
10 hand, CuAAC is a highly versatile, efficient and modular coupling reaction. It was previously  
11 employed by some of us to assemble the push-pull organic dye **T1** (Figure 1) with the H<sub>2</sub>-  
12 evolving cobalt diimine-dioxime catalyst Co(N<sup>2</sup>,N<sup>2'</sup>-propanediylbis(2,3-butandione-2-imine-3-  
13 oxime))Br<sub>2</sub> (**Co**), leading to the first functional noble metal-free NiO photocathode based on a  
14 covalent assembly.<sup>16</sup> We first decided to use the same strategy to covalently assemble **Cat1**  
15 with **T1** and with the novel **T2R** dye (Figure 1); however, all our attempts to prepare the cobalt  
16 complex **Cat1** substituted by an azido group in *para* position of the pyridine ring proved  
17 unsuccessful. An alternative route (Scheme 1) was thus developed: CuAAC coupling was first  
18 carried out between the alkyne-substituted dyes (<sup>t</sup>Bu**T1-alkyne** and <sup>t</sup>Bu**T2R-alkyne**, see SI) and  
19 the 4-azido-2,6-diacetylpyridine precursor (Scheme 1), followed by the templated synthesis of  
20 the tetraazamacrocyclic cobalt complex. This way, the targeted dyads were isolated in two steps  
21 under their *tert*-butyl ester protected forms (<sup>t</sup>Bu**T1-Cat1** and <sup>t</sup>Bu**T2R-Cat1**, Figure 1) in 50-60  
22 % overall yield. Full synthetic details and characterizations are provided in the Supporting  
23 Information.



**Scheme 1.** Synthetic strategy for the preparation of <sup>t</sup>Bu**T1-Cat1** and <sup>t</sup>Bu**T2R-Cat1**.

1  
2  
3 *Spectroscopic and electrochemical characterization in solution.* All compounds were  
4 characterized by cyclic voltammetry (Table 1, Figures 2 & S1). The cyclic voltammogram of  
5 **<sup>t</sup>BuT2R-Cat1** displays five redox events (Figure 2). On the anodic scan, two waves at +0.43 V  
6 and +0.58 V vs. Fc<sup>+0</sup> are assigned to oxidation processes occurring on the dye moiety, by  
7 comparison with the cyclic voltammogram of **<sup>t</sup>BuT2R** (Figure 2). The latter is characterized by  
8 two quasi-reversible waves at +0.48 V and +0.66 V vs. Fc<sup>+0</sup>, attributed to the oxidation of the  
9 triphenylamine (TPA) moiety and of the electron-rich CPDT bridge, respectively, as reported  
10 for related CPDT-based push-pull dyes.<sup>36,47</sup> On the cathodic scan of **<sup>t</sup>BuT2R-Cat1**, the two  
11 reversible processes observed at -0.54 V and -0.97 V vs. Fc<sup>+0</sup> are in full agreement with the  
12 two successive reversible reductions observed on the Co<sup>III</sup> catalyst **Cat1** (Figure 2) yielding the  
13 formal Co<sup>II</sup> and Co<sup>I</sup> states, respectively.<sup>30,33</sup> The reduction of the acceptor part of the dye moiety  
14 is observed at -1.62 V vs. Fc<sup>+0</sup> and shows a loss of reversibility compared to **<sup>t</sup>BuT2R**. The cyclic  
15 voltammogram of **<sup>t</sup>BuT1-Cat1** (Figure 2) displays very similar reduction processes for the  
16 catalyst (-0.53 V and -1.03 V vs. Fc<sup>+0</sup>) and dye (-1.65 V vs. Fc<sup>+0</sup>) units; the single anodic  
17 event at +0.64 V vs. Fc<sup>+0</sup> is assigned to the TPA-centered oxidation process, by comparison  
18 with the cyclic voltammogram of **T1** (Figure S1a).<sup>48,49</sup>  
19  
20  
21  
22  
23  
24  
25  
26  
27  
28  
29  
30  
31  
32  
33  
34  
35  
36  
37  
38  
39  
40  
41  
42  
43  
44  
45  
46  
47  
48  
49  
50  
51  
52  
53  
54  
55  
56  
57  
58  
59  
60

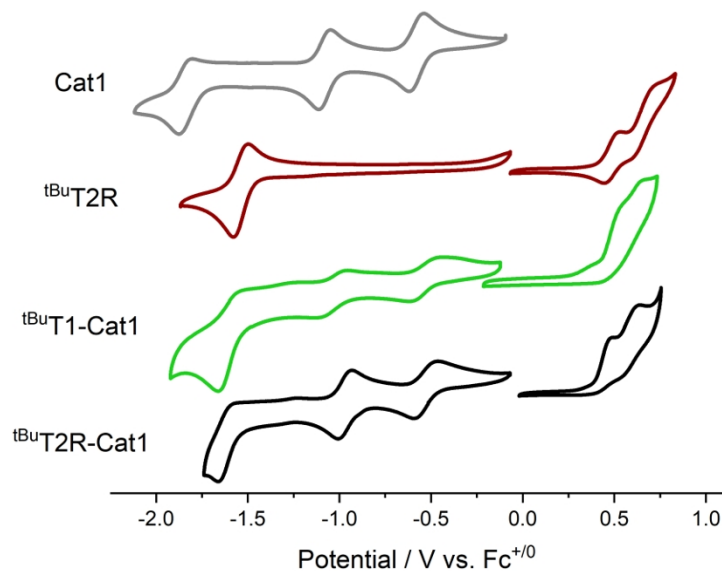


**Figure 2.** Cyclic voltammograms of **Cat1** (grey), **<sup>t</sup>BuT2R** (red), **<sup>t</sup>BuT1-Cat1** (green) and **<sup>t</sup>BuT2R-Cat1** (black). CVs were recorded at 50 mV/s scan rate in 0.1 M TBABF<sub>4</sub> in dry DMF except for the reductive scan of **T1-Cat1**, in which TBACl was used as supporting electrolyte.

**Table 1.** Electrochemical potentials ( $E_{1/2}$  in V vs. Fc<sup>+0</sup>) of investigated compounds determined by cyclic voltammetry.

Sample	$E_{\text{dye}^{+/0}}$	$E_{\text{dye}^{2+/+}}$	$E_{\text{Co}^{\text{III/II}}}$	$E_{\text{Co}^{\text{II/I}}}$	$E_{\text{Co}^{\text{I/0}}}$	$E_{\text{dye}^{0/-}}$ b)
<b>Cat1</b>	---	---	-0.58	-1.08	-1.84	---
<b><sup>t</sup>BuT1</b>	0.71	---	---	---	---	-1.52
<b><sup>t</sup>BuT2R</b>	0.48	0.66	---	---	---	-1.57
<b><sup>t</sup>BuT1-Cat1</b>	0.64 <sup>a)</sup>	---	-0.53	-1.03	---	-1.65
<b><sup>t</sup>BuT2R-Cat1</b>	0.43 <sup>a)</sup>	0.58 <sup>a)</sup>	-0.54	-0.97	---	-1.65

a) Peak potentials in the anodic scan.

b) Peak potentials in the cathodic scan.

The UV-Vis absorption spectra (Figure 3, Table S1) show two main absorption bands between 300 and 600 nm. The band at 350 nm is assigned to a  $\pi$ - $\pi^*$  transition on the TPA moiety<sup>50</sup> and its position remains unchanged for all dyads in comparison with the parent dye. At longer wavelengths, all compounds show the intramolecular charge transfer (ICT) transition from the TPA donor to the cyanoacrylate acceptor group, as typical for this class of push-pull dyes.<sup>16,36,48</sup> For the **<sup>t</sup>BuT2R** series, this absorption is red-shifted in comparison to the **<sup>t</sup>BuT1** series by ca.

0.33 eV (in ACN, Figure S2), which is attributed to the more extended conjugated system due to the CPDT linker. Furthermore, extinction coefficients for **tBuT2R** ( $57,400 \text{ M}^{-1}\text{cm}^{-1}$ ,  $\lambda_{\text{max}} = 499 \text{ nm}$ ) exceed those of **tBuT1** ( $27,700 \text{ M}^{-1}\text{cm}^{-1}$ ,  $\lambda_{\text{max}} = 448 \text{ nm}$ ).

Overall, in the covalent assemblies, the electrochemical and spectroscopic properties of the catalytic and dye units are retained, reflecting their electronic decoupling within the dyads, as previously established for **T1-Co**<sup>16</sup> and more generally frequently encountered for triazole-based dyads assembled by CuAAC coupling.<sup>51–56</sup>

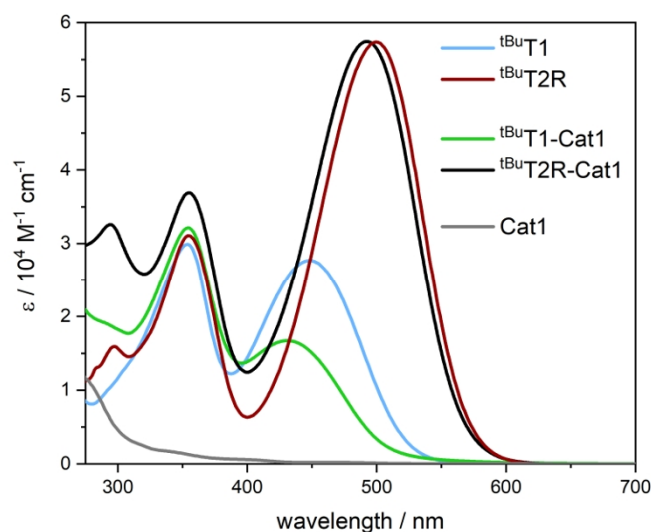


**Figure 3.** UV-Vis absorption spectra of **tBuT1** and **tBuT1-Cat1** in DMF and of **tBuT2R**, **tBuT2R-Cat1** and **Cat1** in MeOH.

*NiO film sensitization and characterization.* NiO films were prepared by spin-coating and sintering a F108 templated hydro-alcoholic NiCl<sub>2</sub> sol-gel.<sup>16,57,58</sup> The 4-layered films have a thickness of  $880 \pm 170 \text{ nm}$  as determined by SEM (Figure S3, Table S2). They were sensitized by soaking for 24 h in methanolic solutions of the deprotected dyads (or dyes).

The amount of dyad (or dye) loading was quantified by dyad (or dye) desorption in a methanolic 1M phenylphosphonic acid solution followed by UV-vis absorption measurement of the resulting solution,<sup>26,59</sup> using the molar extinction coefficient of the TPA-centered band at 350

1  
2  
3 nm (Figure S4, Table S3). Grafting densities are in the range of 6-14 nmol·cm<sup>-2</sup> (Table S4), in  
4  
5 good agreement with the literature on other dye-sensitized NiO films.<sup>14,16,26,48</sup> We observed that  
6  
7 the grafting density substantially varies from one batch of NiO films to another, preventing any  
8  
9 straightforward analysis of the loading based on the molecular structures of the dyads. This  
10  
11 supports the need to verify the grafting efficiency for each individual sample. For this, we used  
12  
13 half of each freshly-sensitized NiO film to determine the dyad (or dye) loading while the other  
14  
15 half was used for the assessment of photoelectrochemical hydrogen production. Hence, an  
16  
17 accurate quantification of the amount of dyad grafted on the considered film was obtained and  
18  
19 used to calculate the turnover number (TON) values for hydrogen production activity (see  
20  
21 below).  
22  
23  
24

25  
26 *Photoelectrochemical activity.* The photoelectrochemical activity of the dye-sensitized NiO  
27  
28 photocathodes was assessed in a three-electrode configuration setup under conditions identical  
29  
30 to our previous studies<sup>14,16,17,26</sup> using an aqueous (*N*-morpholino)ethanesulfonic acid (MES)  
31  
32 buffer solution at pH 5.5 as electrolyte; samples were irradiated with visible light at the  
33  
34 equivalent of 1 sun intensity, using a 400 nm longpass filter and an IR filter. Linear sweep  
35  
36 voltammograms (LSV) were recorded from +1.00 V to 0.00 V vs. RHE (Figure 4a). The large  
37  
38 cathodic signal observed between +1.00 and ≈+0.6 V vs. RHE is attributed to capacitive  
39  
40 charging of the NiO films.<sup>60</sup> Under irradiation, the dyad-sensitized NiO films start exhibiting  
41  
42 cathodic photocurrents at ≈ +0.95 V vs. RHE, which are stable down to ≈ +0.5 V vs. RHE  
43  
44 before increasing at more cathodic potentials. For the film sensitized with **T2R-Cat1**, the  
45  
46 photocurrent reaches 13.5 μA·cm<sup>-2</sup> at +0.14 V vs. RHE (dark current subtracted).  
47  
48  
49  
50  
51  
52  
53  
54  
55  
56  
57  
58  
59  
60

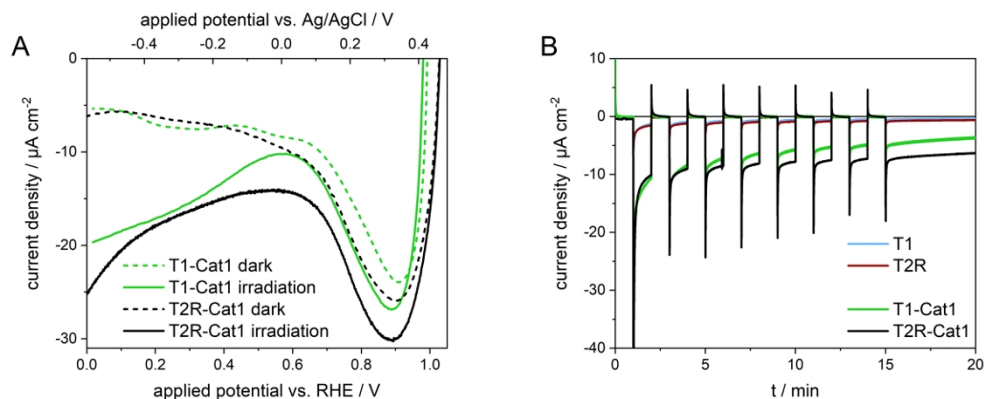


**Figure 4.** a) Linear scan voltammograms (LSV) of NiO films sensitized with the **Cat1** dyads recorded in the dark and under continuous visible light irradiation. b) Chopped-light chronoamperometric measurements recorded in aqueous 0.1 M pH 5.5 MES buffer at  $-0.4$  V vs. Ag/AgCl ( $+0.14$  V vs. RHE) on NiO films sensitized with the dyes and the **Cat1** dyads.

Chronoamperometric measurements under chopped light irradiation yielded insights into the magnitude and stability of the photocurrents measured at  $+0.14$  V vs. RHE, the potential applied for hydrogen production (Figure 4b). When light is turned on, the systems show an initial cathodic photocurrent spike; in addition, upon switching off the irradiation, a reverse anodic spike of lower intensity is observed, suggesting that some photogenerated charges are accumulated at the electrode/electrolyte interface. Importantly, almost no photocurrent is generated in the absence of the catalytic unit ( $-0.4$   $\mu\text{A}\cdot\text{cm}^{-2}$  and  $-0.6$   $\mu\text{A}\cdot\text{cm}^{-2}$  after 20 minutes for films sensitized with **T1** and **T2R**, respectively), while the presence of **Cat1** leads to a ten-fold increase of the photocurrent density ( $-3.7$  and  $-6.3$   $\mu\text{A}\cdot\text{cm}^{-2}$  for **T1-Cat1** and **T2R-Cat1**, respectively). In longer-term photoelectrochemical experiments under continuous light irradiation, all photocathodes show steady-state photocurrents (Figure 5, Figure S8), albeit with marked differences in photocurrent magnitude and stability over time.

To investigate the role of the novel catalytic unit, the photoelectrochemical activity of the previously-reported dyad containing the cobalt diimine-dioxime catalyst  $\text{Co}(\text{DO})(\text{DOH})\text{pnBr}_2$  (**T1-Co**) was reassessed, together with the activity of a novel dyad **T2R-Co** combining **T2R** with  $\text{Co}(\text{DO})(\text{DOH})\text{pnBr}_2$  (see SI for synthesis and characterisations in Table S1, Figures S1b,



S4-7). After normalisation of the photocurrent density to the amount of grafted dyad to compare the intrinsic activity of the dyads (Figure 5b), the **Cat1** and **T2R** dyads showed slower decay in photocurrent and higher overall photocurrent than their **Co** and **T1** counterparts, respectively. On average, the **Cat1** dyads produced 3.2 times higher accumulated current than the **Co** dyads and the **T2R** dyads 1.7 times as much as the **T1** dyads, for a total 5.4-fold increase of **T2R-Cat1** over **T1-Co**.

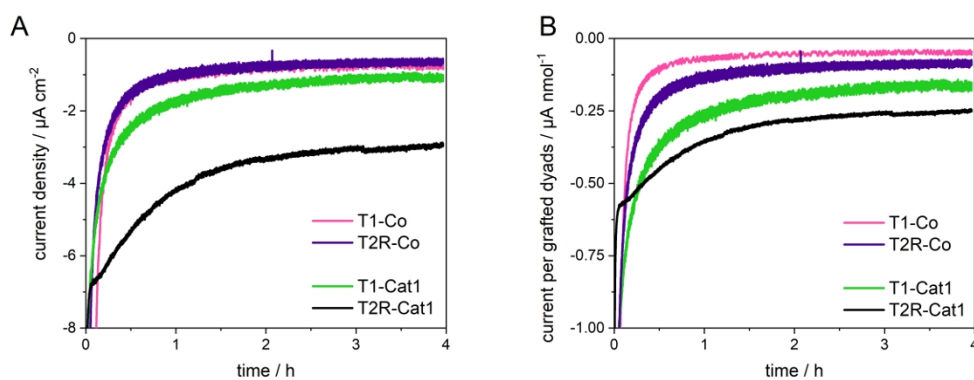


**Figure 5.** Photocurrents recorded on NiO films sensitized with the **Cat1**- and **Co**-based dyads during the first 4 hours of photoelectrochemical experiments (applied potential: +0.14 V vs. RHE). a) Absolute current density and b) current normalized to the amount of dyad grafted on the film, allowing to quantify the intrinsic activity of the dyads.

*Hydrogen-evolving activity assessment.* To confirm that the observed photocurrent originates from the reduction of protons into hydrogen, the H<sub>2</sub> evolution activity of the sensitized NiO photocathodes was assessed during long-term chronoamperometric experiments at an applied potential of +0.14 V vs. RHE and under continuous visible light irradiation. The amount of hydrogen produced was measured after 4 and 22 hours both in the headspace of the cell by gas chromatography and in the electrolyte using a micro Clark-type electrode probe following an established protocol.<sup>14</sup> Turnover numbers (TON<sub>Co</sub>) were calculated, using the dyad loading quantified for the freshly sensitized film.

**Table 2.** Figures of merit of the different dyad-sensitized photocathodes determined from chronoamperometric measurements under continuous visible-light irradiation, in aqueous MES

buffer electrolyte at pH 5.5, at an applied potential of +0.14 V vs. RHE (full set of experimental data in Table S4).

Sample	After 4 hours			After 22 hours		
	H <sub>2</sub> / (nmol·cm <sup>-2</sup> )	FE (%)	TON	H <sub>2</sub> / (nmol·cm <sup>-2</sup> )	FE (%)	TON
<b>T1-Cat1</b>	96 ± 14	65 ± 17	13 ± 1	162 ± 20	31 ± 4	23 ± 1
<b>T2R-Cat1</b>	187 ± 25	66 ± 7	21 ± 6	365 ± 122	39 ± 8	39 ± 8
<b>T1-Co</b>	11 ± 1	9 ± 1	0.7 ± 0.1	13 ± 4	3 ± 0	0.9 ± 0.3
<b>T2R-Co</b>	10 ± 2	11 ± 2	1.5 ± 0	10 ± 3	3 ± 2	1.5 ± 0.2

After 4 hours of irradiation, the **Cat1** dyads produced hydrogen with TON values of 13 ± 1 (**T1-Cat1**) and 22 ± 7 (**T2R-Cat1**) and Faradaic efficiencies around 65 % (Table 2). The activity of the **Co** dyads was much lower, with TON values below 2 and Faradaic efficiencies of ≈ 10 %, in agreement with previous reports.<sup>14,16,17</sup> Comparing the influence of the light-harvesting units, the **T2R** systems produced around twice as much hydrogen as their **T1** counterparts. Continuing irradiation for a total of 22 hours almost doubled the TON values for the **Cat1** systems, while the **Co** dyads showed no increase in produced hydrogen, meaning they had lost their activity during the first 4 hours. For all systems, the Faradaic efficiency decreased between 4 and 22 hours of irradiation (to ≈ 35 % for **Cat1** and ≈ 3 % for **Co**).

#### *Post-operando characterization*

Molecular dyads were desorbed post-operando from the NiO film in a phenylphosphonic acid methanolic solution, with the aim to quantify the amount of dyad desorbed from the NiO surface during the course of the photoelectrochemical tests as well as to identify potential structural modifications. The absorbance of the desorption solutions was measured to quantify the remaining amount of dyad still present on the surface after a 22h PEC experiment. The resulting spectra are shown in Figure 6 and Figure S9, together with the spectra recorded for the corresponding dyads desorbed from a fresh film for comparison.

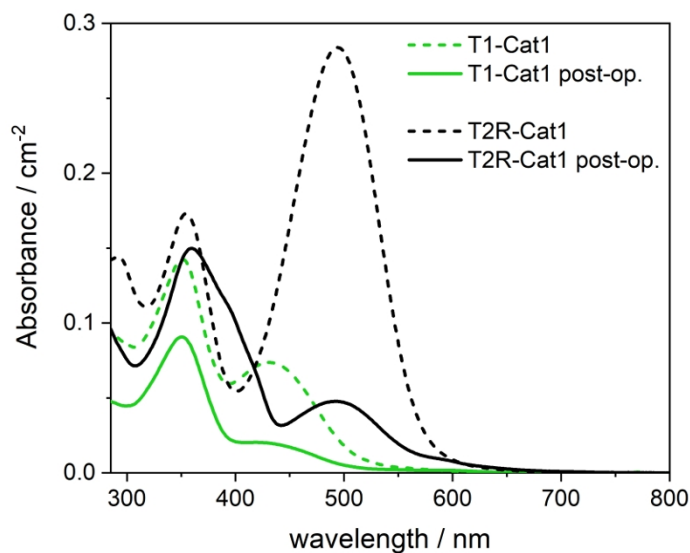


**Figure 6.** UV-Vis spectra of the **Cat1** dyads desorbed from fresh (dashed lines) and post-operando (after 22h of photoelectrochemical activity assessment, solid lines) NiO films in a 1 M phenylphosphonic acid solution in methanol, normalized to the surface area of the films.

The post-operando UV-Vis spectra show a particularly pronounced decrease in absorption for the ICT band at 435 and 495 nm for the **T1**- and **T2R**-based systems, respectively. We attribute the minor decrease in absorbance at the TPA band (355 nm) to a partial release of the dyads into the electrolyte solution during the PEC experiments. The decrease in absorbance at this position is less pronounced for **T2R-Cat1** in comparison to **T1-Cat1** (16 vs. 37 %), indicating a lesser degree of desorption which we ascribe to the protection against hydrolysis granted by the hydrophobic alkyl chains on the CPDT linker.<sup>38</sup> The strong decrease in absorbance at the ICT band, accompanied by the formation of a new band at 400 nm for **T2R-Cat1**, is likely caused by structural modification of the dye during the photoelectrochemical experiments, which expose the dye to relatively harsh conditions, *i.e.* applied reductive potential, light irradiation and aqueous buffer. We therefore decided to investigate which of these parameters is likely at the origin of the changes in dye absorption.

For this purpose, UV-Vis absorption spectra were recorded over time in a home-made cell on NiO films sensitized with **T2R-Cat1** while varying the experimental parameters, including full

1  
2  
3 operando conditions. First, spectra were recorded over one hour on a **T2R-Cat1**-sensitized NiO  
4  
5 film with the operando potential applied in the absence of irradiation (Figure S10a); under these  
6  
7 conditions, no spectral change was observed, apart from an initial jump in absorbance caused  
8  
9 by the electrochromic nature of NiO.<sup>61,62</sup> Second, when the film was submitted to visible light  
10  
11 irradiation in the absence of any applied potential (Figure S10b), small amplitude spectral  
12  
13 changes were observed that might be explained by isomerization of the cyanoacrylate double  
14  
15 bond.<sup>63</sup> By contrast, when the film was exposed both to visible light irradiation and to the  
16  
17 applied potential, *i.e. operando conditions*, fast spectral changes were observed (Figure 7a),  
18  
19 with features similar to those previously identified for the desorbed dyad in the post-operando  
20  
21 measurements (Figure 5). A kinetic analysis revealed a biexponential decay with characteristic  
22  
23 lifetimes of 6 and 90 min (Figure S11). In comparison, a **T2R**-sensitized NiO film displayed  
24  
25 faster degradation kinetics, with  $\approx 1$  and 21 min characteristic lifetimes (Figure S12-13). Thus,  
26  
27 it appears that both the applied potential and the visible light irradiation are necessary to cause  
28  
29 the dye modification observed post-operando; in addition, this process seems to be accelerated  
30  
31 when the catalyst is not present at the surface of the film.  
32  
33

34  
35 To further study this process, UV-Vis spectroelectrochemical experiments were recorded on  
36  
37 <sup>t</sup>Bu**T2R** in dry 0.1 M *n*Bu<sub>4</sub>NBF<sub>4</sub> acetonitrile solution. Under these conditions, the same  
38  
39 irreversible spectral changes were observed upon exhaustive reduction of the dye (Figure S14),  
40  
41 thus excluding any contribution from the aqueous electrolyte in the former experiments. <sup>t</sup>Bu**T1**  
42  
43 showed an identical spectral response upon reduction, suggesting the same degradation process  
44  
45 also takes place for this dye (Figure S14c).  
46  
47  
48  
49  
50  
51  
52  
53  
54  
55  
56  
57  
58  
59  
60

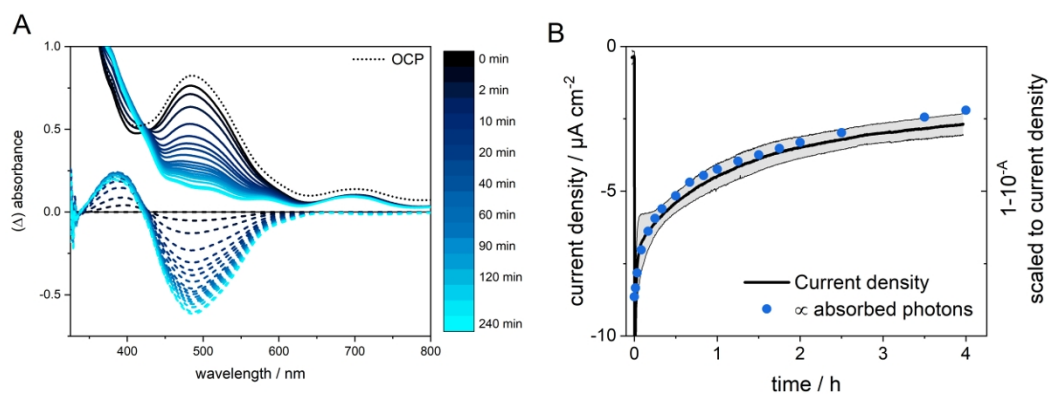


**Figure 7.** a) UV-Vis absorption monitoring of **T2R-Cat1**-sensitized NiO films under operando photoelectrochemical conditions: UV-Vis spectra (solid) and differential spectra (dashed) obtained by subtracting the spectrum obtained at applied potential before irradiation (0 min). b) Average current density of four different **T2R-Cat1**-sensitized NiO films plotted against  $1-10^{-A}$ , where  $A$  is the integrated absorbance in the visible range recorded during the operando UV-Vis measurements after subtracting the NiO background.  $1-10^{-A}$  is proportional to the number of absorbed photons and was scaled to the current density at 600 s to account for the initial current spike.

To ascertain whether the modification suffered by the dye leads to the loss of the catalytic center, *e.g.* by bond cleavage, the amount of Co present at the surface of the film was determined pre- and post-operando by ICP-MS (Table S5). After respectively 4 and 22 h of PEC activity, 84 and 93 % of the initial amount of Co was lost, which correlates very well to the loss of absorbance (84 % after 4 h). Furthermore, the photocurrent recorded on **T2R-Cat1**-sensitized NiO films correlates with the number of absorbed photons (Figure 7b), which is also tied to the absorbance. These findings suggest that the same underlying process causes both the loss of Co and of the dye absorbance, as separate, independent processes would lead to a stronger loss of photocurrent compared to either the loss of absorbance or of Co loading. Assuming therefore that the correlation between the photocurrent decrease and the loss of catalytic unit holds true, the average surface concentration of intact dyads present during the first four hours of activity was estimated to be  $2.0 \pm 0.4 \text{ nmol}\cdot\text{cm}^{-2}$ , leading to a more accurate TON value of  $94 \pm 16$  (Table S6).

### *Time-resolved spectroscopy and spectroelectrochemistry*

Since the light-induced processes in the dye-sensitized photocathodes are crucial to charge the catalyst and thus enable catalytic proton reduction, they were investigated by time-resolved spectroscopy. In a first step, time-resolved emission was measured for all compounds grafted onto NiO and ZrO<sub>2</sub> films, the latter serving as a non-quenching reference (see the Supporting Information for a detailed analysis, and Figure S15, Table S7). All systems showed a complete emission quenching within the duration of the instrumental response function (FWHM = 430 ps) on NiO, which was not observed on ZrO<sub>2</sub>. This quenching is attributed to hole injection from the excited dye into the valence band of the NiO film.<sup>64–67</sup>

To further investigate the sensitized NiO films, we turned to transient absorption (TA) spectroscopy. Since the potential applied during the photoelectrochemical measurements is sufficient to reduce the cobalt catalyst to the Co<sup>II</sup> state, we aimed to investigate the impact of the oxidation state of the cobalt catalyst on the photoinduced charge transfer kinetics. In addition, the application of a potential has been found to profoundly influence the charge recombination kinetics in NiO films sensitized with Ru-based dyes.<sup>43,44</sup> To study the influence of applied potential on the photoinduced kinetics, we performed TA-SEC experiments on NiO films sensitized either with the dyad **T2R-Cat1** or the dye **T2R** as reference. In these measurements, data was recorded at open-circuit potential (OCP), *i.e.* in the electrolyte but without any applied bias, as well as during application of two cathodic potentials to the sensitized film: first, the potential employed in the photoelectrochemical experiments (−0.74 V vs. Fc<sup>+0</sup> ≜ −0.4 V vs. Ag/AgCl), sufficient to reduce the catalyst to its Co<sup>II</sup> state; then, a more cathodic one (−1.15 V vs. Fc<sup>+0</sup>) where the catalyst is reduced to the Co<sup>I</sup> state. The latter measurement served as a reference since no electron transfer is thermodynamically possible to the catalyst in the Co<sup>I</sup> state (the third reduction process on the catalyst occurs at more negative potential than the dye reduction – see Figure 2). Dry acetonitrile was used as solvent to prevent the catalytic reaction from occurring and in this way be able to determine the lifetime of the

1  
2  
3 reduced state of the cobalt catalyst. A detailed spectroscopic analysis of the fs- and ns-TA data  
4  
5 is provided in the Supporting Information and the characteristic time constants are summarized  
6  
7 in Table S8. Since both **T2R**- and **T2R-Cat1**-sensitized NiO films showed the same behaviour  
8  
9 in the fs-TA-SEC experiment, they will be discussed together.

10  
11  
12 After laser pulse excitation and regardless of the potential applied to the electrode, the fs-TA  
13  
14 spectra of **T2R**- and **T2R-Cat1**-sensitized NiO films initially show ground-state bleach (GSB)  
15  
16 at 500 nm and excited state absorption (ESA) at > 550 nm, attributed to the vibrationally hot  
17  
18 excited state of the dye (Figure 8, Figure S16-17).<sup>68</sup> This is followed by a fast recovery of GSB  
19  
20 accompanied by a blue-shift of ESA to form a band with a maximum at 620 nm. Since the 620-  
21  
22 nm band is characteristic of the one-electron reduced dye (Figure S18), this first process is  
23  
24 assigned to hole injection, leading to the formation of the primary charge-separated state  
25  
26  $\text{NiO}^+[\text{T2R}(-\text{Cat1})]$ . Applying a three-component exponential fit to the data, a characteristic time  
27  
28 constant of  $\tau_1 < 1$  ps is obtained for this process, in line with the ultrafast hole injection observed  
29  
30 in literature for other organic dyes grafted on NiO.<sup>15,25,69-77</sup> As this class of push-pull organic  
31  
32 dyes are known to undergo a fast relaxation cascade to the relaxed ICT state on the same sub-  
33  
34 ps time scale (Figure S17),<sup>40,50,68,69,78-80</sup> it seems likely that hole injection and the relaxation  
35  
36 cascade occur simultaneously and that  $\tau_1$  therefore reflects a convolution of the two. A second  
37  
38 process, with a characteristic time constant  $\tau_2 \approx 8$  ps, can be assigned to the decay of residual  
39  
40 excited state to the ground state since the spectral change it causes is a loss of the typical features  
41  
42 of the **T2R** dye in the excited state. This excited state likely decays through hole injection  
43  
44 coupled to fast charge recombination, as the latter has been previously observed on similar  
45  
46 timescales for NiO films sensitized with organic dyes.<sup>25,72,81</sup>

47  
48 The final spectral change is a decay of the characteristic feature of the reduced dye at 620 nm  
49  
50 and of the remaining GSB and is thus assigned to charge recombination. This process shows a  
51  
52 strong dependence on the applied potential: at OCP, the signal of the primary charge-separated  
53  
54 state completely decays within the time window of 1.6 ns, while it is very long-lived when a  
55  
56  
57  
58  
59  
60

1  
2  
3 cathodic potential is applied to the film. This is also reflected in the time constant obtained from  
4  
5 the fit, which increases from  $\tau_3 = 190$  ps for **T2R** and 110 ps for **T2R-Cat1** at OCP, similar to  
6  
7 values found in literature,<sup>15,70–72,74,75,77,82–84</sup> to  $> 1$  ns at  $-0.74$  V and  $-1.15$  V vs.  $\text{Fc}^{+/0}$ . Such  
8  
9 behaviour of dye-sensitized NiO films has previously been associated with filling of intragap  
10  
11 trap states.<sup>43,44</sup> These trap states are caused by  $\text{Ni}^{3+}$  defects on the NiO surface and provide a  
12  
13 pathway for fast non-geminate charge recombination for electrons localized on the reduced dye,  
14  
15 leading to characteristic lifetimes in the picosecond range for charge recombination.<sup>43,65,66,70,85–</sup>  
16  
17  
18  
19 <sup>87</sup> Indeed, charge recombination may be so fast that no signal of the reduced dye is observed.<sup>43,65</sup>  
20  
21 Application of a cathodic potential fills these trap states, thus deactivating the charge  
22  
23 recombination channels and extending the charge-separated state lifetime. Most importantly  
24  
25 regarding the activity for hydrogen evolution, on the timescale of the femtosecond transient  
26  
27 absorption measurements ( $< 1.6$  ns) there is no spectral evidence for electron transfer from the  
28  
29 reduced dye to the catalyst in the **T2R-Cat1**-sensitized films.  
30  
31  
32  
33  
34  
35  
36  
37  
38  
39  
40  
41  
42  
43  
44  
45  
46  
47  
48  
49  
50  
51  
52  
53  
54  
55  
56  
57  
58  
59  
60



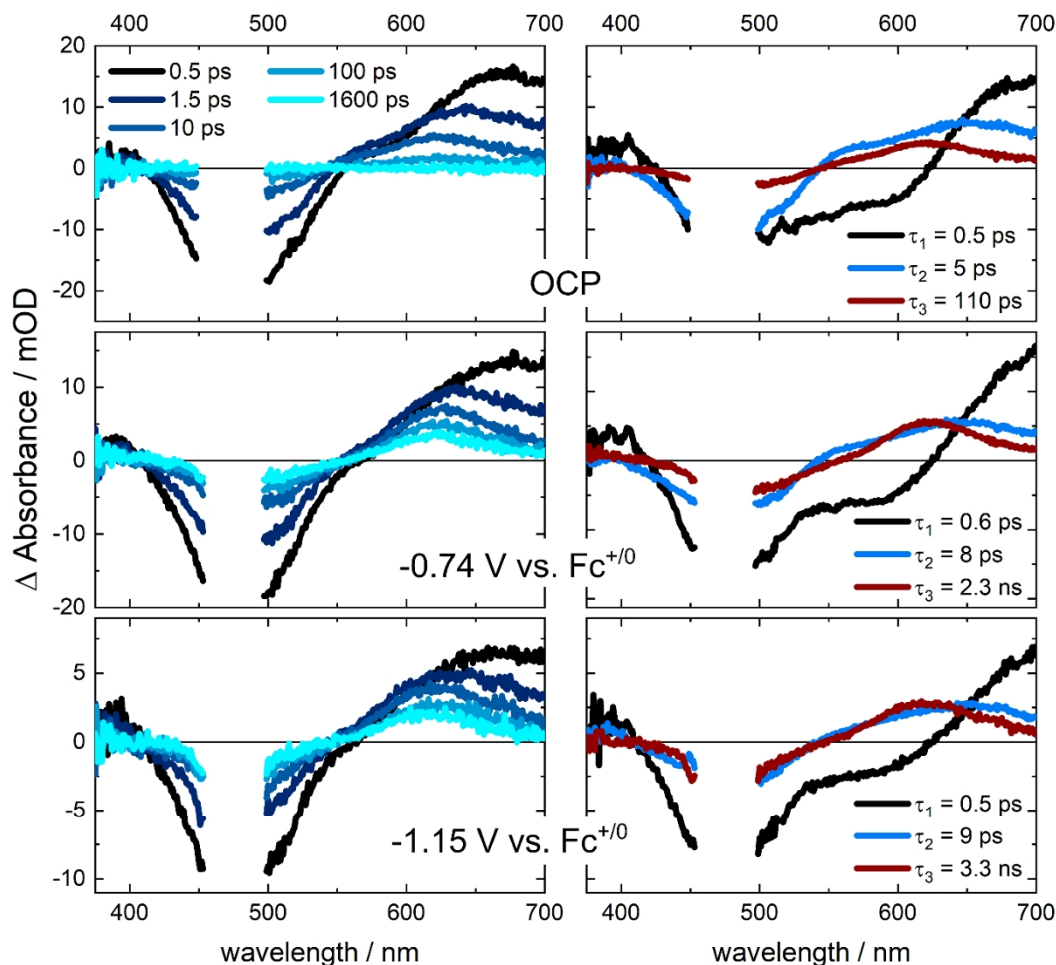
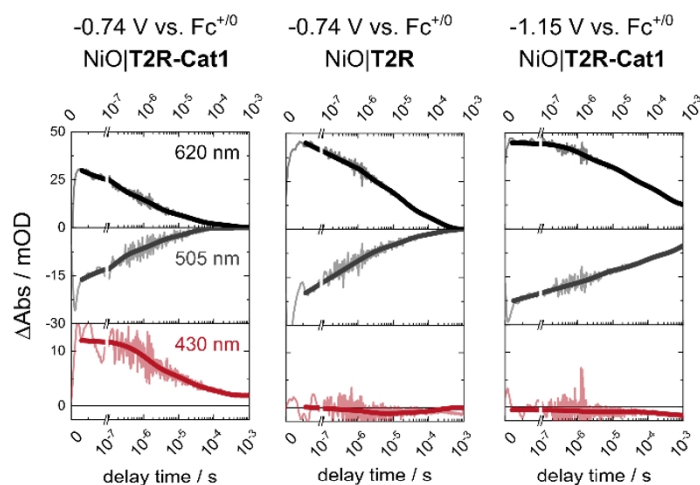


**Figure 8** Left: fs-TA-SEC spectra at different pump-probe delay times after excitation at 480 nm of **T2R-Cat1**-sensitized NiO films at OCP,  $-0.74$  V (corresponding to  $+0.14$  V vs. RHE employed for the PEC tests) and  $-1.15$  V vs.  $\text{Fc}^{+/0}$  applied potential, using  $0.1$  M  $n\text{Bu}_4\text{NBF}_4$  electrolyte in ACN. Right: Decay-associated spectra obtained with a three-component exponential fit of the respective fs-TA-SEC data.  $\tau_1$  corresponds to hole injection with associated relaxation,  $\tau_2$  to a decay of residual excited state and  $\tau_3$  to charge recombination from the charge-separated state.

To accurately determine the lifetime of the primary charge-separated state and to investigate if electron transfer to the catalytic center occurs on a longer time scale, we turned to nanosecond TA-SEC experiments (which cover the time range from 20 ns to 1 ms). Kinetic traces measured at 620 and 505 nm represent the primary charge-separated state  $\text{NiO}^+|\text{T2R}^-(\text{-Cat1})$  with the electron localized on the dye unit (Figure 9, S19). The long-lived signal decaying in a non-exponential fashion on a microsecond timescale indicates charge recombination, as observed in dye-sensitized NiO films.<sup>13,43,44,88</sup> For  $\text{NiO}|\text{T2R-Cat1}$ , the average lifetime of the primary

1  
2  
3 charge-separated state extracted from the fit at  $-0.74$  V vs.  $\text{Fc}^{+/0}$  was  $7 \mu\text{s}$ , while at  $-1.15$  V vs.  
4  
5  $\text{Fc}^{+/0}$  it increased by more than one order of magnitude to  $131 \mu\text{s}$  (27% relative decay amplitude)  
6  
7 and  $> 1$  ms (73% relative decay amplitude). **NiO|T2R** showed a similar trend with somewhat  
8  
9 longer lifetimes, especially at  $-0.74$  V vs.  $\text{Fc}^{+/0}$  ( $\tau_{\text{ave}} = 28 \mu\text{s}$ ,  $-1.15$  V vs.  $\text{Fc}^{+/0}$ :  $184 \mu\text{s}$  (67%)  
10  
11 and  $> 1$  ms (33 %), Table S8).  
12  
13  
14



15  
16  
17  
18  
19  
20  
21  
22  
23  
24  
25  
26  
27  
28  
29  
30  
31  
32  
33  
34  
35  
36  
37  
38  
39  
40  
41  
42  
43  
44  
45  
46  
47  
48  
49  
50  
51  
52  
53  
54  
55  
56  
57  
58  
59  
60  
**Figure 9.** Kinetic traces at characteristic wavelengths obtained in ns-TASEC experiments recorded on NiO films sensitized with **T2R** and **T2R-Cat1** at applied potentials of  $-0.74$  and  $-1.15$  V vs.  $\text{Fc}^{+/0}$ , using  $0.1$  M  $n\text{Bu}_4\text{NBF}_4$  electrolyte in ACN. The signals at  $620$  and  $505$  nm are characteristic of the reduced state of the **T2R** dye, while the signal at  $430$  nm is ascribed to the  $\text{Co}^{\text{I}}$  state of the catalyst.

Within the time of the pump pulse of the ns-TA-SEC experiment ( $< 20$  ns), a positive signal is formed at  $430$  nm for **T2R-Cat1** at  $-0.74$  V vs.  $\text{Fc}^{+/0}$ . Measurements at several wavelengths between  $400$  and  $460$  nm reveal a positive transient absorption band with a maximum at  $430$  nm, characteristic wavelength of the  $\text{Co}^{\text{I}}$  state of the catalyst (Figures 10, S20-21).<sup>33</sup> Furthermore, this positive signal is absent when the catalytic unit is not present at the surface of the film (**T2R** at  $-0.74$  V vs.  $\text{Fc}^{+/0}$ ), or when it is already reduced to the  $\text{Co}^{\text{I}}$  state prior to excitation (**T2R-Cat1** at  $-1.15$  V vs.  $\text{Fc}^{+/0}$ ), *i.e.* two conditions where no electron transfer is possible (Figure 9). This allowed us to unambiguously assign this spectral signature to the formation of the  $\text{Co}^{\text{I}}$  state of **Cat1** by thermally activated electron transfer from the reduced dye species.<sup>33</sup>

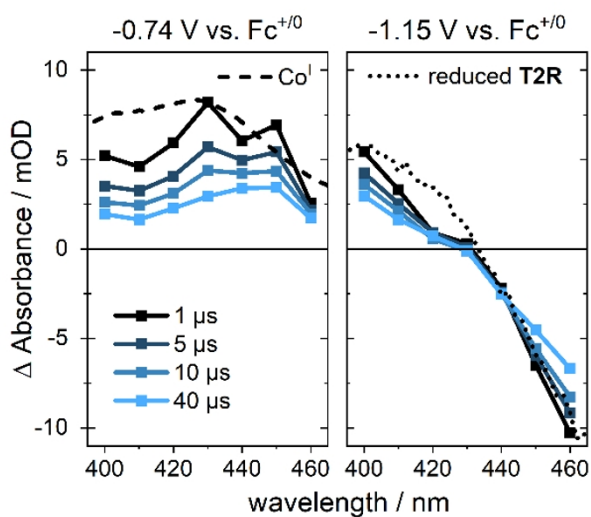


**Figure 10.** ns-TASEC spectra recorded on a NiO film sensitized with **T2R-Cat1** at  $-0.74$  V and  $-1.15$  V vs.  $\text{Fc}^{+/0}$  applied potentials at different delay times together with reference spectra obtained via UV-vis SEC of the  $\text{Co}^{\text{I}}$  state (dashed) and of the one-electron reduced **T2R** in solution (dotted).

Regarding the kinetics of the electron transfer from the reduced dye to the cobalt catalyst, its absence in the fs-TA experiments combined with the maximum signal at 430 nm being present directly after the pump pulse in the ns-TA experiment puts the characteristic time constant for this process in a time window comprised between 1.6 and 20 ns. In addition, the faster decay of the signal of the reduced dye in the dyad compared to **T2R** is likely caused by an additional, slower electron transfer process to the catalyst in the dyad. Assuming the decrease in lifetime of the reduced dye in **T2R-Cat1** in comparison to **T2R** is only due to this further process, its characteristic time constant is estimated to be 9  $\mu$ s. Once formed, the  $\text{Co}^{\text{I}}$  state undergoes much slower charge recombination than the reduced dye, with average lifetimes of 30  $\mu$ s (84 % relative decay amplitude) and  $> 1$  ms (16% relative decay amplitude).

In summary, the TA-SEC experiments revealed the following scheme (summarized in Figure 11 and S22):

- (i) after light excitation, an ultrafast hole injection process leads to the generation of the primary charge-separated state  $\text{NiO}^+|\text{T2R}^-(\text{Cat1})$ ,

- (ii) under the operando applied potential, the primary charge-separated state lifetime extends on the ns to  $\mu\text{s}$  range,
- (iii) in **T2R-Cat1**, the subsequent thermal electron transfer to the cobalt catalyst predominantly takes place within 20 ns,
- (iv) the lifetime of the catalytically competent  $\text{Co}^{\text{I}}$  state ranges from the  $\mu\text{s}$  to the ms timescale.

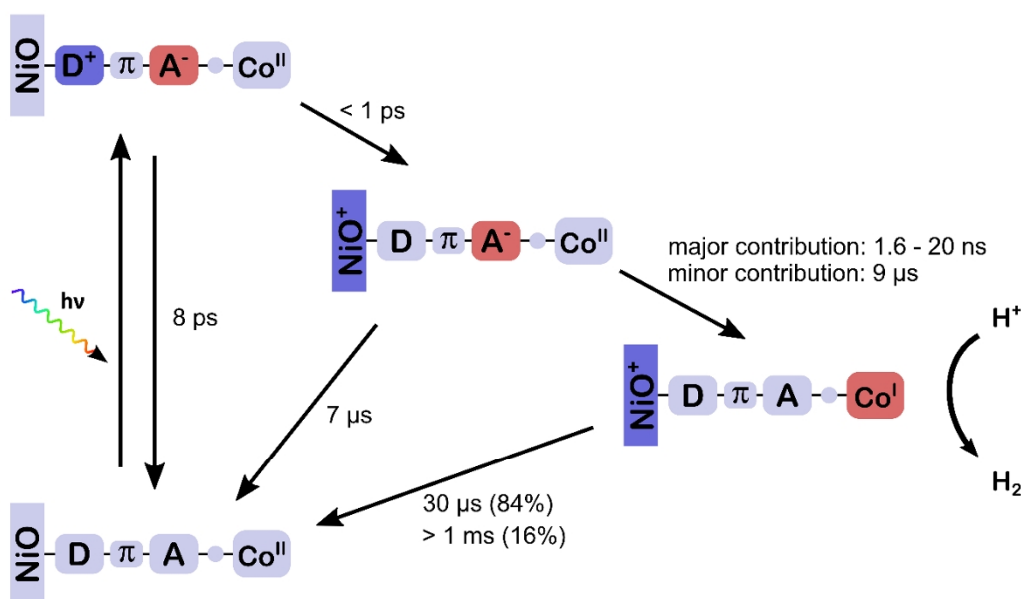


**Figure 11.** Scheme summarizing the light-induced processes in a **T2R-Cat1**-sensitized NiO film at  $-0.74$  V vs.  $\text{Fc}^{+/0}$  (corresponding to the  $+0.14$  V vs. RHE potential applied during the photoelectrochemical measurements). The times indicated are inverse first order rates. Since the charge recombination and electron transfer processes are non-exponential, the times given are averages of the inverse first order rates of a multiexponential fit (see Table S8).

## Discussion

The photocathodes introduced in this study contain the tetraazamacrocyclic cobalt catalyst **Cat1** and clearly display improved performances compared to their counterparts relying on the cobalt diimine-dioxime catalyst **Co**. Although quite similar photocurrent densities were recorded ( $\approx 10 \mu\text{A}\cdot\text{cm}^{-2}$  @  $+0.14\text{V}$  vs. RHE), significantly higher amounts of hydrogen were produced during the course of a 4 hours chronoamperometric measurement (up to  $200 \text{nmol}\cdot\text{cm}^{-2}$  for

1  
2  
3 **T2R-Cat1** versus  $10 \text{ nmol}\cdot\text{cm}^{-2}$  for **T2R-Co**), thanks to a dramatic increase in the faradaic  
4 efficiency of the process (65-70 % F.E. for **Cat1** versus 10 % F.E. for **Co**). In addition, the **Cat1**  
5 photocathodes still display some activity over 22 hours whereas the **Co** systems are fully  
6 deactivated after 4 h. TON values were calculated in order to accurately compare the efficiency  
7 of the different molecular structures while eliminating the variations in dyad loading at the  
8 surface of the NiO film. After 22 hours, 23 and 39 TONs were achieved by **T1-Cat1** and **T2R-**  
9 **Cat1** respectively, whereas TONs of 1 and 1.5 were recorded for **T1-Co** and **T2R-Co**, which  
10 represents a 26-fold increase. These results clearly highlight how the nature of the catalytic  
11 center is key for the photocathode performances, all the other parameters – *i.e.* dye structure,  
12 NiO film preparation, pH and nature of the electrolyte, light intensity, applied potential – being  
13 otherwise strictly identical. A straightforward comparison of these numerical values  
14 (photocurrent, amount of hydrogen produced, TON) with state of the art in the literature is  
15 difficult as these parameters vary considerably from one study to another, up to now preventing  
16 the determination of a sound structure-activity relationship. Nevertheless, the **T2R-Cat1**  
17 photocathode reported here favourably competes with the best-performing NiO ones, which are  
18 based on the cobaloxime CoHEC or the DuBois NiP catalyst.

19  
20  
21  
22  
23  
24  
25  
26  
27  
28  
29  
30  
31  
32  
33  
34  
35  
36  
37  
38  
39  
40 The superior hydrogen production activity observed with **Cat1** cannot be simply rationalized  
41 thermodynamically. Indeed, both **Cat1** and **Co** dyads display a significant driving force for hole  
42 injection from the dye excited state into NiO (0.6 to 0.9 eV; see Table S1) to form the reduced  
43 dye. The reduced dye itself can subsequently reduce the catalytic center to the  $\text{Co}^{\text{I}}$  state via  
44 thermally assisted electron transfer, with very close driving forces for the two catalysts (Table  
45 S1). The clear-cut difference in the photocathode performances is rather assigned to the  
46 increased stability of **Cat1** in fully aqueous medium, which previously resulted in a 70-fold  
47 higher amount of  $\text{H}_2$  produced under homogeneous photocatalytic conditions, compared to  
48 **Co**.<sup>33</sup> More generally, the robustness of polypyridinic and aminopyridinic cobalt catalysts has  
49 been recognized over the past few years<sup>33,89–92</sup> whereas cobaloximes are more prone to  
50  
51  
52  
53  
54  
55  
56  
57  
58  
59  
60

1  
2  
3 decompose under aqueous conditions of activity, via demetalation,<sup>93</sup> hydrolysis and/or  
4  
5 reduction of the oxime-based ligands,<sup>94–97</sup> if they are not constantly and rapidly supplied with  
6  
7 reductive equivalents.<sup>98</sup> The latter process might account for the low F.E. for hydrogen  
8  
9 production of the **Co** photocathodes reported here and in previous studies from our group,<sup>14,16,17</sup>  
10  
11 together with other side-reactions such as the reduction of oxygen that might diffuse in the cell  
12  
13 during the course of the experiment.<sup>14</sup>  
14  
15

16  
17 Despite having replaced **Co** by the more robust H<sub>2</sub>-evolving catalyst **Cat1**, the overall  
18  
19 performances of our photocathodes still need to be increased to reach a level of activity  
20  
21 comparable to the current photoanode state of the art, with photocurrents in the mA·cm<sup>-2</sup>  
22  
23 range.<sup>99</sup> Detailed investigations on the most efficient **T2R-Cat1**-based photocathode helped us  
24  
25 to identify two parameters currently limiting its performances:  
26  
27

28  
29 1) Operando and post-operando characterizations revealed that the **T2R** dye structure is  
30  
31 modified under reductive conditions, with the loss of the main part of its absorption in the  
32  
33 visible region as a consequence. We failed to identify the exact structure of this novel derivative,  
34  
35 although the observations that (i) the  $\pi$ - $\pi^*$  absorption of the triarylamine group is still present,  
36  
37 and (ii) a similar alteration is observed for **T1** and **T2R** under reductive conditions, indicate  
38  
39 that this modification occurs on the acceptor group of the push-pull structures, *i.e.* the  
40  
41 cyanoacrylate moiety in the case of **T2R** and the cyanoacrylamide one for **T2R-Cat1**. In  
42  
43 addition, post-operando ICP-MS measurements indicated that an important amount of Co  
44  
45 catalyst is lost during the first 4 hours of activity. The clear correlation found between the  
46  
47 photocurrent decrease, the loss of absorbance and the loss of Co from the surface, strongly  
48  
49 suggests that (i) the dye degradation is the main deactivation process in our system, rather than  
50  
51 decomposition of the catalyst, and (ii) it involves a bond breaking, leading to the detachment  
52  
53 of the whole catalytic center from the assembly. This is further supported by the recent  
54  
55 observation that **Cat1** grafted on TiO<sub>2</sub> was stable for 10 hours under photoelectrochemical  
56  
57  
58  
59  
60

1  
2  
3 conditions similar to ours (pH 4.5 acetate buffer, 1 sun visible light irradiation),<sup>46</sup> rendering a  
4 catalyst-centered degradation process very unlikely. After 4 hours of activity, the dyads still  
5 intact on the surface (retained Co loading: 16 %) account for the H<sub>2</sub>-evolving activity still  
6 detected between 4 and 22 hours. By contrast to other reported studies, where dye/catalyst  
7 desorption from the semiconductor film is the main deactivation process,<sup>15,24,25,100</sup> only a low  
8 amount of dyads is released in solution. The presence of the lateral alkyl chains on the CPDT  
9 bridge likely stabilizes the dyads on the NiO surface by forming a hydrophobic layer able to  
10 protect the carboxylate ester anchors from nucleophilic attack from water, as previously  
11 reported for another push-pull organic dye-based photocathode.<sup>38</sup> The low solubility of these  
12 dyads in aqueous medium, compared for instance to cationic ruthenium photosensitizers, might  
13 be another factor improving the stability of the sensitized NiO surface.  
14  
15  
16  
17  
18  
19  
20  
21  
22  
23  
24  
25  
26  
27

28 2) TA-SEC measurements recorded under quasi-operando conditions (same potential  
29 applied to the film as for the chronoamperometric measurements but in anhydrous acetonitrile  
30 instead of aqueous electrolyte) revealed the kinetics of the light-induced processes and provided  
31 information about the different intermediates formed at the surface of the film. First, the  
32 formation of a long-lived (> 1 ms) reduced organic dye moiety in the **T2R-Cat1** dyad was  
33 observed due to hole injection to the NiO. The charge recombination kinetics strongly depended  
34 on the applied potential, leading to a six order of magnitude increase in the lifetime of the  
35 primary charge separated state at -0.74 V vs. Fc<sup>+0</sup> with respect to OCP. While this observation,  
36 to the best of our knowledge, is unprecedented for a push-pull organic dye-sensitized  
37 photocathode, ruthenium tris-diimine dyes grafted onto NiO films showed similar  
38 behaviour.<sup>43,44</sup> Second, thermally activated electron transfer from the reduced dye to the Co<sup>II</sup>  
39 center yielding the reduced (Co<sup>I</sup>) catalyst predominantly occurred on a time window of 1.6 to  
40 20 ns, with only a small contribution taking place on longer timescales (average time constant  
41 of 9 μs). This appears to be comparable to other triazole-based dyads studied in solution, where  
42 this process has been observed on the ns-μs time scale.<sup>53,101-104</sup> A recent study on a Ru-Re  
43  
44  
45  
46  
47  
48  
49  
50  
51  
52  
53  
54  
55  
56  
57  
58  
59  
60



1  
2  
3 system anchored on NiO by electropolymerization also showed electron transfer on the ns- $\mu$ s  
4 scale ( $< 10 \mu$ s), which was attributed to electron tunnelling between the components due to the  
5 presence of an electronically insulating alkyl linker.<sup>105</sup> Electron transfer from a Ru dye to a Ni  
6 catalyst in a layer-by-layer assembly was determined to occur before 50 ns, either from the  
7 excited or reduced state of the dye.<sup>23</sup> In our dyad, this thermal electron transfer is slow, however,  
8 in comparison to some examples of co-immobilised systems where charge transfer from the  
9 dye (excited or reduced state) to the catalyst was observed on the ps timescale.<sup>81,106</sup> The  
10 resulting  $\text{Co}^{\text{I}}$  state has a lifetime reaching the ms timescale, which can be explained by a lower  
11 driving force for charge recombination together with an increased donor-acceptor distance (e.g.  
12  $\text{Co}^{\text{I}}$  to  $\text{NiO}^+$ ) compared to the primary charge separated state, in which the dye is reduced.  
13 Spectroscopic observation of the formation of the reduced catalyst at the surface of a dye-  
14 sensitized NiO film and determination of its lifetime are scarce in the literature<sup>25,105</sup> and this  
15 represents, to the best of our knowledge, the first example with a cobalt catalyst. The group of  
16 L. Hammarström previously reported a diiron catalyst reduced state with different lifetimes  
17 depending on the nature of its anchor to NiO: when grafted with a carboxylate anchoring group,  
18 this reduced state was stable on the 100  $\mu$ s timescale and no  $\text{H}_2$  was produced. Employing a  
19 phosphonate anchor, the lifetime reached the ms timescale allowing for hydrogen production.<sup>25</sup>  
20 In our case, the formation of the catalytically competent  $\text{Co}^{\text{I}}$  state appears however to be quite  
21 inefficient as an important amount of reduced dye remains present at the surface of the film on  
22 the  $\mu$ s time scale. This observation can be put directly in line with the initial photocurrent spikes  
23 observed in the photocurrent measurements (Figure 4b), which are characteristic for the  
24 accumulation of charges at the electrode/electrolyte interface; in addition, the presence of  
25 anodic spikes of lower intensity when light is switched off supports the fact that these charges  
26 are not fully consumed by catalysis.

27  
28  
29  
30  
31  
32  
33  
34  
35  
36  
37  
38  
39  
40  
41  
42  
43  
44  
45  
46  
47  
48  
49  
50  
51  
52  
53  
54  
55  
56  
57  
58  
59  
60  
Taken altogether, these data highlight that neither a low light absorption efficiency nor a  
sluggish multielectronic catalytic process limit the dye-sensitized photocathode performances.



1  
2  
3 Rather, the accumulation of photogenerated charges at the surface of the NiO film must be  
4  
5 considered as the performance-limiting factor. Similar observations were recently made for  
6  
7 organic semiconductor photocathodes with a perylene diimide (PDI) acceptor polymer: an  
8  
9 upper limit for charge accumulation was determined for stable long-term operation, above  
10  
11 which the PDI underwent irreversible change. In our case, the reduced state of the dye is not  
12  
13 stable, which causes the loss of the catalytic unit, accompanied by a strong decrease of the light  
14  
15 harvesting efficiency in the visible region. This process is clearly accelerated in the absence of  
16  
17 the catalyst (**T2R** vs. **T2R-Cat1** photocathode) highlighting that electron transfer to the catalyst  
18  
19 can compete with the reduced dye alteration. A fast electron transfer to the catalyst indeed  
20  
21 reduces the lifetime of the reduced dye and thereby protects it from degradation. This charge  
22  
23 extraction process is unfortunately not very efficient for the **T2R-Cat1** photocathode,  
24  
25 suggesting that only a small fraction of dyads is fully operative at the surface of the film,  
26  
27 possibly for conformational or topological reasons. This raises questions regarding the covalent  
28  
29 design of our dye-catalyst assemblies; indeed, the presence of a flexible methylene spacer  
30  
31 between the acceptor side of the dye and the triazole-catalyst moiety might prevent the thermal  
32  
33 electron transfer step, thus occurring only in very specific conformations of the assembly.  
34  
35 Future work should clearly focus on the design of novel photocathode architectures, integrating  
36  
37 dyes that are more robust under reductive conditions, and bridging units allowing a faster and  
38  
39 more efficient electron supply to the catalyst.  
40  
41  
42  
43  
44  
45  
46  
47  
48

## 49 **Conclusion**

50  
51 In conclusion, we successfully synthesized two novel noble metal-free covalent dye-catalyst  
52  
53 assemblies based on the robust H<sub>2</sub>-evolving tetraazamacrocyclic cobalt catalyst **Cat1**. The  
54  
55 performances of the resulting photocathodes were assessed under conditions strictly identical  
56  
57 to our previously reported dyad based on the cobalt diimine-dioxime catalyst,<sup>14,16</sup> enabling to  
58  
59 establish structure-activity relationships. Switching to **Cat1** was instrumental to increase both  
60

1  
2  
3 the activity and the stability of the systems, which could be further improved by the introduction  
4  
5 of an alkyl-substituted CPDT bridge in the push-pull structure of the dye (**T2R**). The resulting  
6  
7 **T2R-Cat1**-sensitized photocathode effectively produced hydrogen during 4 hours with 70 %  
8  
9 Faradaic efficiency and still displays some activity after 22 hours, which ranks this construction  
10  
11 within the best-performing H<sub>2</sub>-evolving dye-sensitized photocathodes reported up to  
12  
13 now<sup>24,107,108</sup> and opens perspectives toward an integration into a tandem photoelectrochemical  
14  
15 cell. In order to provide meaningful insights into the factors affecting the performances of the  
16  
17 **T2R-Cat1**-sensitized photocathode over time, we relied on a combination of operando and  
18  
19 post-operando characterization techniques. Hence, we established that the dye structure is  
20  
21 altered under reductive conditions. This non-exponential process, occurring on a minute to hour  
22  
23 timescale, is correlated to the photocurrent decrease and to the loss of Co observed during the  
24  
25 first four hours of photoelectrochemical activity. Thus, despite significant improvements,  
26  
27 stability is still hampered by the lack of robustness of the organic dye. In parallel, the electron  
28  
29 transfer dynamics at the NiO interface were investigated thanks to transient absorption  
30  
31 measurements recorded with the operando potential applied to the film. We detected the  
32  
33 formation of the catalytically competent Co<sup>I</sup> state with a lifetime of > 1 ms, sufficient to initiate  
34  
35 catalysis. This result is, to the best of our knowledge, unprecedented in the field of dye-  
36  
37 sensitized H<sub>2</sub>-evolving photocathodes.

38  
39 From these results, the major bottleneck hindering photoelectrochemical performances is the  
40  
41 low efficiency of the thermal electron transfer from the reduced dye to the catalyst; in addition  
42  
43 to limiting the photocurrent density, this leads to the accumulation of charges on the acceptor  
44  
45 part of the dye and ultimately to its degradation. This study thus provides a clear rational toward  
46  
47 the optimization of the performances of dye-sensitized photocathodes for hydrogen production  
48  
49 and we will focus our efforts on designing novel dyad assemblies and/or photocathode  
50  
51 architectures achieving faster electron transfer to the catalyst. In that context, a DFT-driven  
52  
53 approach exploiting Marcus theory to determine structures warranting higher electron transfer  
54  
55  
56  
57  
58  
59  
60

1  
2  
3 rates could be very valuable. Replacing NiO by other p-type semiconductors represents another  
4  
5 track for improvement, as recently highlighted in studies by our group and others.<sup>7,18,19</sup> Finally,  
6  
7 this work paves the way for the integration of robust cobalt polypyridinyl catalysts into  
8  
9 functional photoelectrochemical devices for solar fuels production.<sup>89,90,109</sup>  
10  
11  
12  
13  
14

### 15 **Experimental Section.**

16  
17 **Synthesis.** All reagents were purchased from Sigma Aldrich or Strem and used as obtained  
18  
19 unless otherwise stated. Reagent-grade solvents were used without further purification.  
20  
21 <sup>1</sup>H NMR experiments were carried out on Bruker Avance 300 or 500 MHz spectrometers and  
22  
23 the resulting spectra are referenced to the residual solvent peak and reported in relative to  
24  
25 tetramethylsilane reference ( $\delta = 0$  ppm). Electrospray ionization mass spectrometric (ESI-MS)  
26  
27 measurements were carried out on a Thermoquest Finnigan LCQ spectrometer. Accurate mass  
28  
29 measurements (HRMS) were recorded on a Bruker maXis mass spectrometer by the  
30  
31 "Fédération de Recherche" ICOA/CBM (FR 2708) platform. Elemental analysis was performed  
32  
33 on a Thermofisher Scientific "Flash 2000" by the "Plateforme d'analyse pour la chimie" (GDS  
34  
35 3648, Strasbourg). **tBuT1**,<sup>48</sup> its alkyne derivative **tBuT1-alkyne**,<sup>16</sup> **Cat1**<sup>33</sup> and **tBuT1-Co**<sup>16</sup> were  
36  
37 synthesized according to previously reported procedures. Detailed syntheses for the dye  
38  
39 precursors, the 4-azido-2,6-diacetylpyridine building block, **tBuT2R**, its alkyne derivative  
40  
41 **tBuT2R-alkyne** and **T2R-Co** are described in the Supporting Information.  
42  
43  
44  
45  
46  
47

48 *General procedure for the CuAAC click coupling.*<sup>14,16</sup> The alkyne-substituted dye (0.5 mmol)  
49  
50 and 4-azido-2,6-diacetylpyridine (1 equiv.) were dissolved in 20 mL of degassed CH<sub>2</sub>Cl<sub>2</sub>.  
51  
52 Sodium ascorbate (0.5 mmol) and CuSO<sub>4</sub>·5H<sub>2</sub>O (0.2 mmol) were dissolved in 10 mL of  
53  
54 degassed H<sub>2</sub>O and added to the reaction mixture. Degassed MeOH was added dropwise until a  
55  
56 single phase was obtained. The reaction mixture was stirred at room temperature for 24 hours.  
57  
58 After removal of the volatile solvents, the mixture was extracted with CH<sub>2</sub>Cl<sub>2</sub>, washed with  
59  
60

1  
2  
3 brine solution, dried over Na<sub>2</sub>SO<sub>4</sub> and filtered. The crude product was purified on silica gel  
4  
5 column to yield the diacetylpyridine-functionalized dye.  
6  
7

8 *General procedure for the template synthesis of Cat1.* The diacetylpyridine-functionalized dye  
9  
10 (0.3 mmol) was dissolved in EtOH (2 mL) and CH<sub>2</sub>Cl<sub>2</sub> (1 mL), and kept at 40 °C under argon.  
11  
12 CoCl<sub>2</sub>·6H<sub>2</sub>O (1 equiv.) and water (0.4 mL) were added and the solution was stirred at 55 °C to  
13  
14 dissolve the salt. The reaction mixture was warmed to 75 °C before addition of 3,3'-  
15  
16 diaminodipropylamine (1 equiv.) and glacial acetic acid (0.03 mL) and was then stirred at 75 °C  
17  
18 for 5 hours under argon. After cooling down to room temperature, 0.1 mL of concentrated HCl  
19  
20 was added and the reaction mixture was stirred at room temperature for 16 hours, then kept for  
21  
22 2 hours at -15 °C and centrifuged. The precipitate was washed with H<sub>2</sub>O and EtOH before  
23  
24 drying under vacuum to yield the dyad as a red solid.  
25  
26  
27  
28

29 *General procedure for the tert-butyl ester groups hydrolysis prior to film sensibilisation.*  
30  
31 Hydrolysis of the tert-butyl ester groups was carried out according to our previously reported  
32  
33 procedures,<sup>14,16,48</sup> by reacting the tert-butyl ester protected dyads (or dyes) with trifluoroacetic  
34  
35 acid (TFA) in CH<sub>2</sub>Cl<sub>2</sub> for 5 hours at room temperature.  
36  
37  
38  
39

40  
41 **NiO film preparation and sensitization.** NiO films were prepared using a F108 precursor  
42  
43 solution prepared by mixing 1 g of NiCl<sub>2</sub>, 1 g of F108 triblock copolymer in a mixture of ethanol  
44  
45 (15 mL) and Milli-Q water (6 mL), according to our previously reported procedures.<sup>14,16</sup> The  
46  
47 mixture was sonicated for 6 h, centrifuged and passed through a 45 μm pore size  
48  
49 polyethersulfone syringe filter. FTO-coated glass substrates (Solems TEC 7, sheet resistance  
50  
51 7Ω.□) for the hydrogen production experiments or round ITO-coated glass substrates (Solems  
52  
53 ITO SOL 30, 1 mm thickness) for the operando UV-Vis experiments and transient absorption  
54  
55 measurements were cleaned by sonication in isopropanol, distilled water and ethanol for 10 min  
56  
57 each, followed by ozone cleaning for 15 min. The F108 precursor solution was then spin-coated  
58  
59  
60

1  
2  
3 on the substrates (5000 rpm, 60 s) followed by sintering in an oven in air (30 min ramp to  
4  
5 450 °C, 30 min at 450 °C). Spin-coating and sintering was repeated for a total of four layers.  
6  
7 The film thickness was measured by scanning electron microscopy (SEM) with a scanning  
8  
9 electron microscope Zeiss Ultra 55 operating at 4 kV.  
10

11  
12 NiO electrodes were soaked in methanolic solutions (0.2 mM) of the different dyes and dyads  
13  
14 (acidic form) at room temperature for 24 h under orbital stirring. For the TCSPC measurements,  
15  
16 sensitizing solutions with 10 mM chenodeoxycholic acid (CDCA) added were used for  
17  
18 sensitization. After sensitization, films were then rinsed with methanol and dried with pressured  
19  
20 air. After sensitization, NiO films were cut in half. One half of the sample was used to determine  
21  
22 grafting densities pre-operando while the other half was used for photoelectrochemical  
23  
24 experiments and afterwards desorbed to determine grafting densities and possible degradation  
25  
26 post-operando.  
27  
28

29  
30 **Dyad loading quantification.** Sensitized NiO films were soaked in 1M methanolic  
31  
32 phenylphosphonic acid solution for 3 hours to desorb grafted compounds. Afterwards, UV-Vis  
33  
34 spectra of the desorption solutions were then measured and dyad (or dye) loading was  
35  
36 determined using the molar extinction coefficient at the  $\pi$ - $\pi^*$  band (Figure S3) and the film  
37  
38 surface areas. Cobalt quantification was performed by inductively coupled plasma mass  
39  
40 spectrometry (ICP-MS) using an iCAP RQ quadrupole mass instrument (Thermo Fisher  
41  
42 Scientific GmbH, Germany). The samples were prepared by soaking each film in 1 mL of aq.  
43  
44 HNO<sub>3</sub> (65% w/v) for 1 min, rinsing with 1 mL Milli-Q water, hydrolyzing again with 1 mL of  
45  
46 HNO<sub>3</sub>, rinsing with 1 mL H<sub>2</sub>O, then 2.5 mL H<sub>2</sub>O. The resulting solution (6.5 mL at 20% w/v  
47  
48 HNO<sub>3</sub>) was diluted 20 times to yield a solution at 1% w/v HNO<sub>3</sub>, which was used for the  
49  
50 measurement.  
51  
52  
53  
54  
55  
56  
57  
58  
59  
60

1  
2  
3 **Steady-state spectroscopy.** Steady-state absorption spectra were recorded on an  
4 Agilent Cary 60 or a Jasco V780 spectrophotometer in 1 cm cuvettes. All solvents used for  
5 spectroscopy were of spectroscopic grade.  
6  
7

8  
9  
10 **Time-correlated single photon counting (TCSPC) measurements.** The emission decay  
11 profiles were measured by time-correlated single photon counting (TCSPC) in a time window  
12 of 20 ns. After excitation of the sample with the frequency-doubled output of a Ti-sapphire laser  
13 (Tsunami, Newport Spectra-Physics GmbH) at  $\lambda_{\text{ex}} = 365$  nm at a pulse-to-pulse repetition rate  
14 of 400 kHz after passing a pulse selector (model 3980, Newport Spectra-Physics GmbH), the  
15 luminescence of the sample was collected in a 90°-arrangement and detected using a Becker &  
16 Hickl PMC-100-4 photon-counting module. The lifetime values were obtained from mono- or  
17 bi-exponential fits convoluted with the instrument response function (IRF). Sample solutions  
18 were prepared to yield an optical density of 0.05-0.1 at the excitation wavelength in a 1.0 cm  
19 quartz cuvette using air-equilibrated, spectroscopic grade solvents.  
20  
21  
22

23  
24  
25 **Electrochemical and photoelectrochemical experiments.** Electrochemical and  
26 photoelectrochemical experiments were recorded using either a BioLogic VSP 300,  
27 BioLogic SP 50 or Ivium CompactStat potentiostat. A three-electrode setup was used for all  
28 experiments. For electrochemical experiments, Merck SeccoSolv® dry DMF was used as  
29 solvent and the tetrabutylammonium tetrafluoroborate was recrystallized from ethanol/water  
30 prior to use. The working electrode was a glassy carbon disk electrode, the auxiliary electrode  
31 a Pt wire and the reference electrode a miniature leakless Ag/AgCl electrode (EDAQ). The  
32 supporting electrolyte was 0.1 M TBABF<sub>4</sub> in dry DMF, degassed by passing argon through the  
33 solution for 20 min before measuring. During the measurements, the argon flow was removed  
34 from the solution but left in the headspace of the cell. The scan rate during cyclic voltammetry  
35 was 50 mV·s<sup>-1</sup> and the sample concentration was 1 mM. The potential of the reference electrode  
36  
37  
38  
39  
40  
41  
42  
43  
44  
45  
46  
47  
48  
49  
50  
51  
52  
53  
54  
55  
56  
57  
58  
59  
60

1  
2  
3 was calibrated after each measurement by adding ferrocene as a reference to the solution and  
4  
5 recording the potential of the  $\text{Fc}^{+/0}$  couple.  
6

7  
8 The photoelectrochemical measurements were carried out in a home-made three-electrode cell  
9  
10 with a sensitized NiO film as working electrode, a titanium wire as auxiliary electrode and a  
11  
12 Ag/AgCl reference electrode made of a Ag/AgCl wire dipped into a 3 M aqueous KCl solution,  
13  
14 separated from the electrolyte by a Vycor® frit. The auxiliary electrode was separated from the  
15  
16 main compartment of the cell by a Vycor® frit. Irradiation was performed using a Newport 300  
17  
18 W ozone-free Xe lamp at either 280 or 130 W equipped with a water-filled Spectra-Physics  
19  
20 6123NS liquid filter to eliminate infrared radiation ( $\lambda > 800$  nm) and a 400 nm longpass filter  
21  
22 (Spectra-Physics 59472). The power density was measured using a Newport PM1918-R power-  
23  
24 meter and adjusted to  $65 \text{ mW} \cdot \text{cm}^{-2}$  (equivalent to one sun irradiation) using appropriate neutral  
25  
26 density filters. The aqueous supporting electrolyte was either 0.1 M  
27  
28 2-(N-morpholino)ethanesulfonic acid (MES)/0.1 M NaCl buffer at pH 5.5 or 0.12 M  
29  
30 Britton-Robinson buffer at pH 4.5, 5.5 or 7.0, as also stated in the respective data description.  
31  
32 The electrolyte solution was degassed with nitrogen for 30 minutes prior to use. The amount of  
33  
34 hydrogen evolved produced during the long-term chronoamperometric measurements was  
35  
36 measured in the headspace by sampling aliquots in a Perkin Elmer Clarus 580 gas  
37  
38 chromatograph equipped with a molecular sieve 5 Å column (30 m – 0.53 mm) and a TCD  
39  
40 detector. Additionally, the amount of hydrogen dissolved in solution was determined by a  
41  
42 Unisense  $\text{H}_2$  microsensor in a needle. The zero value for the microsensor was measured in the  
43  
44 assembled cell prior to irradiation. Potentials are given as converted to potentials vs. reversible  
45  
46 hydrogen electrode (RHE) using the formula:  
47  
48  
49  
50  
51  
52

$$E_{RHE} = E_{Ag/AgCl} + 0.425 \text{ V} - E_{Fe(III)/Fe(II)} + 0.059 * pH$$

1  
2  
3 where 0.425 V is the potential of the potassium ferrocyanide Fe(III)/Fe(II) couple vs. NHE at  
4  
5 0.1M potassium phosphate buffer at pH 7<sup>110</sup> and  $E_{\text{Fe(III)/Fe(II)}}$  is the potential of the potassium  
6  
7 ferrocyanide Fe<sup>III/II</sup> couple measured vs. the Ag/AgCl reference electrode.  
8  
9

10  
11 For the photoelectrochemical degradation experiment, a home-made spectroelectrochemistry  
12  
13 cell specifically designed for measurements on transparent semiconductor films was used with  
14  
15 dye-sensitized NiO films on ITO/glass substrate (Solems, ITO SOL 30, 1 mm thickness) as  
16  
17 working electrode, Pt wire as auxiliary electrode and a miniature leakless Ag/AgCl (EDAQ) as  
18  
19 reference electrode. The supporting electrolyte was 0.1 M 2-(*N*-morpholino)ethanesulfonic acid  
20  
21 (MES)/0.1 M NaCl buffer at pH 5.5. The solution was degassed for 20 minutes prior to  
22  
23 measuring. At an applied potential of -0.35 V vs. Ag/AgCl (0.21 V vs. RHE), the film was  
24  
25 irradiated as in the photoelectrochemical experiments and UV-Vis spectra were recorded in  
26  
27 intervals.  
28  
29  
30

31  
32 **Transient absorption spectroelectrochemistry (TA-SEC) measurements.** The setup for  
33  
34 femtosecond transient absorption measurements has been previously described.<sup>111</sup> An amplified  
35  
36 Ti:Sapphire laser (Legend, Coherent Inc) produced the 800 nm fundamental beam which was  
37  
38 split into two beams. One of the beams was used to pump an optical-parametric amplifier  
39  
40 (TOPAS-C), whose output was spectrally centered at 480 nm and used as pump pulses for the  
41  
42 pump-probe experiments. The pump pulses were typically set to 0.4  $\mu\text{J}$  per pulse, which was  
43  
44 lowered to 0.2  $\mu\text{J}$  per pulse for measurements at -1.15 V vs.  $\text{Fc}^{+/0}$  to avoid photodegradation.  
45  
46 To achieve the pump-probe delay of 2 ns, the pump beam was directed over a delay line. The  
47  
48 supercontinuum used as probe pulse was generated by passing the second beam of the  
49  
50 fundamental 800 nm through a  $\text{CaF}_2$  window, with probe intensities falling into the range of  
51  
52 hundred nJ. The probe light was split into two beams, one of which was focussed through the  
53  
54 sample, while the other served as reference. A 488 nm notch filter was placed between sample  
55  
56 and detector to remove scattered pump light. The probe and reference beams were detected by  
57  
58  
59  
60



1  
2  
3 a double-stripe diode array and converted into differential absorption signals using a  
4  
5 commercially available detection system (Pascher Instruments AB, Sweden). The recorded data  
6  
7 was corrected for the chirp and globally fitted using a sum of three exponential. During the  
8  
9 fitting, the pulse overlap region of  $\pm 200$  fs was excluded to avoid contributions from coherent  
10  
11 artifacts.<sup>112</sup>

12  
13  
14 The setup for ns transient absorption measurements was previously described:<sup>113</sup> The pump  
15  
16 pulse was generated by a Continuum Surelite OPO Plus (pumped by a Nd:YAG laser,  $\approx 20$  ns  
17  
18 pulse duration, 10 Hz repetition rate). The probe light was generated by a 75 W Xenon arc lamp  
19  
20 and focussed through the sample and detected by a Hamamatsu R928 photomultiplier. The  
21  
22 signal was amplified and processed by a commercially available detection system (Pascher  
23  
24 Instruments AB, Sweden). The pump pulse energy was set to 0.13 mJ. To remove pump scatter,  
25  
26 a 475 nm short pass and a 500 nm long pass edge filters were used for short and long  
27  
28 wavelengths, respectively.

29  
30  
31  
32  
33 TA-SEC experiments were performed using a home-built spectroelectrochemical cell, designed  
34  
35 to work in a three-electrode setup under inert conditions and to optimize time resolution in the  
36  
37 fs measurements, with a minimized path length (ca. 4 mm). The sensitized NiO film was used  
38  
39 as the working electrode, a miniature leakless Ag/AgCl electrode (EDAQ) as reference  
40  
41 electrode and a Pt wire as auxiliary electrode. The cell was assembled in a glove box and filled  
42  
43 with 0.1 M TBABF<sub>4</sub> in ACN. Transient absorption measurements were performed at open  
44  
45 circuit potential and different applied potentials on the same film, moving the film in the plane  
46  
47 periodically to prevent photodegradation. Prior to each experiment, the reference electrode was  
48  
49 calibrated using ferrocene.  
50  
51  
52

53  
54 ASSOCIATED CONTENT  
55  
56  
57  
58  
59  
60

1  
2  
3 **Supporting Information.** The following files are available free of charge.  
4  
5 Detailed synthetic procedures and additional spectroscopic and photoelectrochemical data  
6  
7 (PDF).  
8  
9

#### 10 AUTHOR INFORMATION

#### 11 **Corresponding Author**

12  
13  
14  
15  
16 \* Benjamin Dietzek; E-mail: [benjamin.dietzek@leibniz-ipht.de](mailto:benjamin.dietzek@leibniz-ipht.de)

17  
18 \* Murielle Chavarot-Kerlidou; E-mail: [murielle.chavarot-kerlidou@cea.fr](mailto:murielle.chavarot-kerlidou@cea.fr)  
19  
20

#### 21 **Present Addresses**

22  
23 †Present address: Aix Marseille Univ, CNRS, Centrale Marseille, iSm2, Marseille, France.  
24  
25

#### 26 **Author Contributions**

27  
28  
29 The manuscript was written through contributions of all authors. All authors have given  
30  
31 approval to the final version of the manuscript.  
32  
33

#### 34 **Funding Sources**

35  
36  
37 This work was supported by the European Commission's Seventh Framework Program  
38  
39 (FP7/2007-2013) under grant agreement n° 306398 (FP7-IDEAS-ERC, Project  
40  
41 PhotocatH<sub>2</sub>ode), the French National Research Agency in the framework of the  
42  
43 "Investissements d'avenir" program (ANR-15-IDEX-02, Labex ARCANE and CBH-EURGS,  
44  
45 ANR-17-EURE-0003) and the Franco-German University.  
46  
47  
48

#### 49 **ACKNOWLEDGMENT**

50  
51  
52 Quentin Vacher, Tatiana Straistari and Adina Morozan are acknowledged for their help in the  
53  
54 synthesis and purification of the compounds and for the SEM measurements. Jacques Pecaut  
55  
56 and Pierre-Alain Bayle from CEA/DRF/IRIG/DIESE/SyMMES are acknowledged for the ESI-  
57  
58 MS and the 500 MHz NMR measurements, respectively. Stéphane Ravanel from  
59  
60 CEA/DRF/IRIG/DBSCI/PCV is acknowledged for the ICP-MS analysis. This work was

supported by the European Commission's Seventh Framework Program (FP7/2007-2013) under grant agreement n° 306398 (FP7-IDEAS-ERC, Project PhotocatH<sub>2</sub>ode) and the French National Research Agency in the framework of the "Investissements d'avenir" program (ANR-15-IDEX-02, Labex ARCANE and CBH-EURGS, ANR-17-EURE-0003). S.B. wants to thank the Franco-German University for the cotutelle thesis funding support. We want to thank the workshop of the IPHT Jena for their help in building the spectroscopy cell.

## REFERENCES

- (1) Nocera, D. G. Solar Fuels and Solar Chemicals Industry. *Accounts of Chemical Research* **2017**, *50* (3), 616–619. <https://doi.org/10.1021/acs.accounts.6b00615>.
- (2) Zhang, B.; Sun, L. Artificial Photosynthesis: Opportunities and Challenges of Molecular Catalysts. *Chemical Society Reviews* **2019**, *48* (7), 2216–2264. <https://doi.org/10.1039/C8CS00897C>.
- (3) House, R. L.; Iha, N. Y. M.; Coppo, R. L.; Alibabaei, L.; Sherman, B. D.; Kang, P.; Brennaman, M. K.; Hoertz, P. G.; Meyer, T. J. Artificial Photosynthesis: Where Are We Now? Where Can We Go? *Journal of Photochemistry and Photobiology C: Photochemistry Reviews* **2015**, *25*, 32–45. <https://doi.org/10.1016/j.jphotochemrev.2015.08.002>.
- (4) Berardi, S.; Drouet, S.; Francàs, L.; Gimbert-Suriñach, C.; Guttentag, M.; Richmond, C.; Stoll, T.; Llobet, A. Molecular Artificial Photosynthesis. *Chem. Soc. Rev.* **2014**, *43* (22), 7501–7519. <https://doi.org/10.1039/C3CS60405E>.
- (5) Brennaman, M. K.; Dillon, R. J.; Alibabaei, L.; Gish, M. K.; Dares, C. J.; Ashford, D. L.; House, R. L.; Meyer, G. J.; Papanikolas, J. M.; Meyer, T. J. Finding the Way to Solar Fuels with Dye-Sensitized Photoelectrosynthesis Cells. *Journal of the American Chemical Society* **2016**, *138* (40), 13085–13102. <https://doi.org/10.1021/jacs.6b06466>.
- (6) Yu, Z.; Li, F.; Sun, L. Recent Advances in Dye-Sensitized Photoelectrochemical Cells for Solar Hydrogen Production Based on Molecular Components. *Energy Environ. Sci.* **2015**, *8* (3), 760–775. <https://doi.org/10.1039/C4EE03565H>.
- (7) Windle, C. D.; Kumagai, H.; Higashi, M.; Brisse, R.; Bold, S.; Jusselme, B.; Chavarot-Kerlidou, M.; Maeda, K.; Abe, R.; Ishitani, O.; Artero, V. Earth-Abundant Molecular Z-Scheme Photoelectrochemical Cell for Overall Water-Splitting. *Journal of the American Chemical Society* **2019**, *141* (24), 9593–9602. <https://doi.org/10.1021/jacs.9b02521>.
- (8) Fan, K.; Li, F.; Wang, L.; Daniel, Q.; Gabrielsson, E.; Sun, L. Pt-Free Tandem Molecular Photoelectrochemical Cells for Water Splitting Driven by Visible Light. *Phys. Chem. Chem. Phys.* **2014**, *16* (46), 25234–25240. <https://doi.org/10.1039/C4CP04489D>.
- (9) Li, F.; Fan, K.; Xu, B.; Gabrielsson, E.; Daniel, Q.; Li, L.; Sun, L. Organic Dye-Sensitized Tandem Photoelectrochemical Cell for Light Driven Total Water Splitting. *Journal of the American Chemical Society* **2015**, *137* (28), 9153–9159. <https://doi.org/10.1021/jacs.5b04856>.

- 1  
2  
3  
4  
5  
6  
7  
8  
9  
10  
11  
12  
13  
14  
15  
16  
17  
18  
19  
20  
21  
22  
23  
24  
25  
26  
27  
28  
29  
30  
31  
32  
33  
34  
35  
36  
37  
38  
39  
40  
41  
42  
43  
44  
45  
46  
47  
48  
49  
50  
51  
52  
53  
54  
55  
56  
57  
58  
59  
60
- (10) Ji, Z.; He, M.; Huang, Z.; Ozkan, U.; Wu, Y. Photostable P-Type Dye-Sensitized Photoelectrochemical Cells for Water Reduction. *Journal of the American Chemical Society* **2013**, *135* (32), 11696–11699. <https://doi.org/10.1021/ja404525e>.
- (11) Li, L.; Duan, L.; Wen, F.; Li, C.; Wang, M.; Hagfeldt, A.; Sun, L. Visible Light Driven Hydrogen Production from a Photo-Active Cathode Based on a Molecular Catalyst and Organic Dye-Sensitized p-Type Nanostructured NiO. *Chemical Communications* **2012**, *48* (7), 988–990. <https://doi.org/10.1039/C2CC16101J>.
- (12) Meng, P.; Wang, M.; Yang, Y.; Zhang, S.; Sun, L. CdSe Quantum Dots/Molecular Cobalt Catalyst Co-Grafted Open Porous NiO Film as a Photocathode for Visible Light Driven H<sub>2</sub> Evolution from Neutral Water. *Journal of Materials Chemistry A* **2015**, *3* (37), 18852–18859. <https://doi.org/10.1039/C5TA06255A>.
- (13) Kamire, R. J.; Majewski, M. B.; Hoffeditz, W. L.; Phelan, B. T.; Farha, O. K.; Hupp, J. T.; Wasielewski, M. R. Photodriven Hydrogen Evolution by Molecular Catalysts Using Al<sub>2</sub>O<sub>3</sub> - Protected Perylene-3,4-Dicarboximide on NiO Electrodes. *Chemical Science* **2017**, *8* (1), 541–549. <https://doi.org/10.1039/C6SC02477G>.
- (14) Windle, C. D.; Massin, J.; Chavarot-Kerlidou, M.; Artero, V. A Protocol for Quantifying Hydrogen Evolution by Dye-Sensitized Molecular Photocathodes and Its Implementation for Evaluating a New Covalent Architecture Based on an Optimized Dye-Catalyst Dyad. *Dalton Transactions* **2018**, *47* (31), 10509–10516. <https://doi.org/10.1039/C8DT01210E>.
- (15) Pati, P. B.; Zhang, L.; Philippe, B.; Fernández-Terán, R.; Ahmadi, S.; Tian, L.; Rensmo, H.; Hammarström, L.; Tian, H. Insights into the Mechanism of a Covalently Linked Organic Dye–Cobaloxime Catalyst System for Dye-Sensitized Solar Fuel Devices. *ChemSusChem* **2017**, *10* (11), 2480–2495. <https://doi.org/10.1002/cssc.201700285>.
- (16) Kaeffer, N.; Massin, J.; Lebrun, C.; Renault, O.; Chavarot-Kerlidou, M.; Artero, V. Covalent Design for Dye-Sensitized H<sub>2</sub> -Evolving Photocathodes Based on a Cobalt Diimine–Dioxime Catalyst. *Journal of the American Chemical Society* **2016**, *138* (38), 12308–12311. <https://doi.org/10.1021/jacs.6b05865>.
- (17) Kaeffer, N.; Windle, C. D.; Brisse, R.; Gablin, C.; Leonard, D.; Jusselme, B.; Chavarot-Kerlidou, M.; Artero, V. Insights into the Mechanism and Aging of a Noble-Metal Free H<sub>2</sub> -Evolving Dye-Sensitized Photocathode. *Chemical Science* **2018**, *9* (32), 6721–6738. <https://doi.org/10.1039/C8SC00899J>.
- (18) Li, F.; Xu, R.; Nie, C.; Wu, X.; Zhang, P.; Duan, L.; Sun, L. Dye-Sensitized LaFeO<sub>3</sub> Photocathode for Solar-Driven H<sub>2</sub> Generation. *Chemical Communications* **2019**, *55* (86), 12940–12943. <https://doi.org/10.1039/C9CC06781G>.
- (19) Creissen, C. E.; Warnan, J.; Antón-García, D.; Farré, Y.; Odobel, F.; Reisner, E. Inverse Opal CuCrO<sub>2</sub> Photocathodes for H<sub>2</sub> Production Using Organic Dyes and a Molecular Ni Catalyst. *ACS Catalysis* **2019**, *9* (10), 9530–9538. <https://doi.org/10.1021/acscatal.9b02984>.
- (20) Wang, D.; Sheridan, M. v.; Shan, B.; Farnum, B. H.; Marquard, S. L.; Sherman, B. D.; Eberhart, M. S.; Nayak, A.; Dares, C. J.; Das, A. K.; Bullock, R. M.; Meyer, T. J. Layer-by-Layer Molecular Assemblies for Dye-Sensitized Photoelectrosynthesis Cells Prepared by Atomic Layer Deposition. *Journal of the American Chemical Society* **2017**, *139* (41), 14518–14525. <https://doi.org/10.1021/jacs.7b07216>.
- (21) Gross, M. A.; Creissen, C. E.; Orchard, K. L.; Reisner, E. Photoelectrochemical Hydrogen Production in Water Using a Layer-by-Layer Assembly of a Ru Dye and Ni Catalyst on NiO. *Chemical Science* **2016**, *7* (8), 5537–5546. <https://doi.org/10.1039/c6sc00715e>.

- 1  
2  
3 (22) Shan, B.; Sherman, B. D.; Klug, C. M.; Nayak, A.; Marquard, S. L.; Liu, Q.; Bullock, R. M.;  
4 Meyer, T. J. Modulating Hole Transport in Multilayered Photocathodes with Derivatized P-  
5 Type Nickel Oxide and Molecular Assemblies for Solar-Driven Water Splitting. *The Journal of*  
6 *Physical Chemistry Letters* **2017**, *8* (18), 4374–4379.  
7 <https://doi.org/10.1021/acs.jpcclett.7b01911>.  
8  
9 (23) Shan, B.; Das, A. K.; Marquard, S.; Farnum, B. H.; Wang, D.; Bullock, R. M.; Meyer, T. J.  
10 Photogeneration of Hydrogen from Water by a Robust Dye-Sensitized Photocathode. *Energy &*  
11 *Environmental Science* **2016**, *9* (12), 3693–3697. <https://doi.org/10.1039/C6EE02903E>.  
12  
13 (24) Creissen, C. E.; Warnan, J.; Reisner, E. Solar H<sub>2</sub> Generation in Water with a CuCrO<sub>2</sub>  
14 Photocathode Modified with an Organic Dye and Molecular Ni Catalyst. *Chemical Science*  
15 **2018**, *9* (6), 1439–1447. <https://doi.org/10.1039/C7SC04476C>.  
16  
17 (25) Antila, L. J.; Ghamgosar, P.; Maji, S.; Tian, H.; Ott, S.; Hammarström, L. Dynamics and  
18 Photochemical H<sub>2</sub> Evolution of Dye–NiO Photocathodes with a Biomimetic FeFe-Catalyst.  
19 *ACS Energy Letters* **2016**, *1* (6), 1106–1111. <https://doi.org/10.1021/acsenergylett.6b00506>.  
20  
21 (26) Lyu, S.; Massin, J.; Pavone, M.; Muñoz-García, A. B.; Labrugère, C.; Toupance, T.;  
22 Chavarot-Kerlidou, M.; Artero, V.; Olivier, C. H<sub>2</sub>-Evolving Dye-Sensitized Photocathode  
23 Based on a Ruthenium–Diacylide/Cobaloxime Supramolecular Assembly. *ACS Applied*  
24 *Energy Materials* **2019**, *2* (7), 4971–4980. <https://doi.org/10.1021/acsaem.9b00652>.  
25  
26 (27) Shan, B.; Brennaman, M. K.; Troian-Gautier, L.; Liu, Y.; Nayak, A.; Klug, C. M.; Li, T. T.;  
27 Bullock, R. M.; Meyer, T. J. A Silicon-Based Heterojunction Integrated with a Molecular  
28 Excited State in a Water-Splitting Tandem Cell. *Journal of the American Chemical Society*  
29 **2019**, *141* (26), 10390–10398. <https://doi.org/10.1021/jacs.9b04238>.  
30  
31 (28) Nie, C.; Ni, W.; Gong, L.; Jiang, J.; Wang, J.; Wang, M. Charge Transfer Dynamics and  
32 Catalytic Performance of a Covalently Linked Hybrid Assembly Comprising a Functionalized  
33 Cobalt Tetraazamacrocyclic Catalyst and CuInS<sub>2</sub>/ZnS Quantum Dots for Photochemical  
34 Hydrogen Production. *Journal of Materials Chemistry A* **2019**, *7* (48), 27432–27440.  
35 <https://doi.org/10.1039/C9TA10479H>.  
36  
37 (29) Grau, S.; Schilling, M.; Moonshiram, D.; Benet-Buchholz, J.; Lubner, S.; Llobet, A.; Gimbert-  
38 Suriñach, C. Electrochemically and Photochemically Induced Hydrogen Evolution Catalysis  
39 with Cobalt Tetraazamacrocycles Occurs Through Different Pathways. *ChemSusChem* **2020**,  
40 *13* (10), 2745–2752. <https://doi.org/10.1002/cssc.202000283>.  
41  
42 (30) Leung, C.; Chen, Y.; Yu, H.; Yiu, S.; Ko, C.; Lau, T.-C. Electro- and Photocatalytic  
43 Hydrogen Generation in Acetonitrile and Aqueous Solutions by a Cobalt Macrocyclic Schiff-  
44 Base Complex. *International Journal of Hydrogen Energy* **2011**, *36* (18), 11640–11645.  
45 <https://doi.org/10.1016/j.ijhydene.2011.06.062>.  
46  
47 (31) Gueret, R.; Poulard, L.; Oshinowo, M.; Chauvin, J.; Dahmane, M.; Dupeyre, G.; Lainé, P. P.;  
48 Fortage, J.; Collomb, M.-N. Challenging the [Ru(Bpy)<sub>3</sub>]<sup>2+</sup> Photosensitizer with a  
49 Triazatriangulenium Robust Organic Dye for Visible-Light-Driven Hydrogen Production in  
50 Water. *ACS Catalysis* **2018**, *8* (5), 3792–3802. <https://doi.org/10.1021/acscatal.7b04000>.  
51  
52 (32) Sandroni, M.; Gueret, R.; Wegner, K. D.; Reiss, P.; Fortage, J.; Aldakov, D.; Collomb, M.-N.  
53 Cadmium-Free CuInS<sub>2</sub>/ZnS Quantum Dots as Efficient and Robust Photosensitizers in  
54 Combination with a Molecular Catalyst for Visible Light-Driven H<sub>2</sub> Production in Water.  
55 *Energy & Environmental Science* **2018**, *11* (7), 1752–1761.  
56 <https://doi.org/10.1039/C8EE00120K>.  
57  
58  
59  
60

- 1  
2  
3 (33) Varma, S.; Castillo, C. E.; Stoll, T.; Fortage, J.; Blackman, A. G.; Molton, F.; Deronzier, A.;  
4 Collomb, M.-N. Efficient Photocatalytic Hydrogen Production in Water Using a Cobalt(III)  
5 Tetraaza-Macrocyclic Catalyst: Electrochemical Generation of the Low-Valent Co(I) Species  
6 and Its Reactivity toward Proton Reduction. *Physical Chemistry Chemical Physics* **2013**, *15*  
7 (40), 17544. <https://doi.org/10.1039/c3cp52641k>.  
8  
9 (34) Gimbert-Suriñach, C.; Albero, J.; Stoll, T.; Fortage, J.; Collomb, M.-N.; Deronzier, A.;  
10 Palomares, E.; Llobet, A. Efficient and Limiting Reactions in Aqueous Light-Induced  
11 Hydrogen Evolution Systems Using Molecular Catalysts and Quantum Dots. *Journal of the*  
12 *American Chemical Society* **2014**, *136* (21), 7655–7661. <https://doi.org/10.1021/ja501489h>.  
13  
14 (35) Roy, S.; Bacchi, M.; Berggren, G.; Artero, V. A Systematic Comparative Study of Hydrogen-  
15 Evolving Molecular Catalysts in Aqueous Solutions. *ChemSusChem* **2015**, *8* (21), 3632–3638.  
16 <https://doi.org/10.1002/cssc.201501002>.  
17  
18 (36) Yen, Y.-S.; Chen, W.-T.; Hsu, C.-Y.; Chou, H.-H.; Lin, J. T.; Yeh, M.-C. P. Arylamine-Based  
19 Dyes for p-Type Dye-Sensitized Solar Cells. *Organic Letters* **2011**, *13* (18), 4930–4933.  
20 <https://doi.org/10.1021/ol202014x>.  
21  
22 (37) Li, R.; Liu, J.; Cai, N.; Zhang, M.; Wang, P. Synchronously Reduced Surface States, Charge  
23 Recombination, and Light Absorption Length for High-Performance Organic Dye-Sensitized  
24 Solar Cells. *Journal of Physical Chemistry B* **2010**, *114* (13), 4461–4464.  
25 <https://doi.org/10.1021/jp101222s>.  
26  
27 (38) Click, K. A.; Beauchamp, D. R.; Huang, Z.; Chen, W.; Wu, Y. Membrane-Inspired Acidically  
28 Stable Dye-Sensitized Photocathode for Solar Fuel Production. *Journal of the American*  
29 *Chemical Society* **2016**, *138* (4), 1174–1179. <https://doi.org/10.1021/jacs.5b07723>.  
30  
31 (39) Yu, Y.; Click, K. A.; Chien, S.-C.; Sun, J.; Curtze, A.; Lin, L.-C.; Wu, Y. Decoupling PH  
32 Dependence of Flat Band Potential in Aqueous Dye-Sensitized Electrodes. *The Journal of*  
33 *Physical Chemistry C* **2019**, *123* (14), 8681–8687. <https://doi.org/10.1021/acs.jpcc.9b00710>.  
34  
35 (40) Bold, S.; Zedler, L.; Zhang, Y.; Massin, J.; Artero, V.; Chavarot-Kerlidou, M.; Dietzek, B.  
36 Electron Transfer in a Covalent Dye–Cobalt Catalyst Assembly – a Transient Absorption  
37 Spectroelectrochemistry Perspective. *Chemical Communications* **2018**, *54* (75), 10594–10597.  
38 <https://doi.org/10.1039/C8CC05556D>.  
39  
40 (41) Zedler, L.; Mengele, A. K.; Ziems, K. M.; Zhang, Y.; Wächtler, M.; Gräfe, S.; Pascher, T.;  
41 Rau, S.; Kupfer, S.; Dietzek, B. Unraveling the Light-Activated Reaction Mechanism in a  
42 Catalytically Competent Key Intermediate of a Multifunctional Molecular Catalyst for  
43 Artificial Photosynthesis. *Angewandte Chemie International Edition* **2019**, *58* (37), 13140–  
44 13148. <https://doi.org/10.1002/anie.201907247>.  
45  
46 (42) Zhang, Y.; Zedler, L.; Karnahl, M.; Dietzek, B. Excited-State Dynamics of Heteroleptic  
47 Copper(I) Photosensitizers and Their Electrochemically Reduced Forms Containing a  
48 Dipyrrophenazine Moiety – a Spectroelectrochemical Transient Absorption Study. *Physical*  
49 *Chemistry Chemical Physics* **2019**, *21* (20), 10716–10725.  
50 <https://doi.org/10.1039/C9CP00412B>.  
51  
52 (43) Dillon, R. J.; Alibabaei, L.; Meyer, T. J.; Papanikolas, J. M. Enabling Efficient Creation of  
53 Long-Lived Charge-Separation on Dye-Sensitized NiO Photocathodes. *ACS Applied Materials*  
54 *& Interfaces* **2017**, *9* (32), 26786–26796. <https://doi.org/10.1021/acsami.7b05856>.  
55  
56 (44) D’Amario, L.; Antila, L. J.; Pettersson Rimgard, B.; Boschloo, G.; Hammarström, L. Kinetic  
57 Evidence of Two Pathways for Charge Recombination in NiO-Based Dye-Sensitized Solar  
58  
59  
60

- 1  
2  
3 Cells. *The Journal of Physical Chemistry Letters* **2015**, *6* (5), 779–783.  
4 <https://doi.org/10.1021/acs.jpcclett.5b00048>.  
5  
6 (45) McCrory, C. C. L.; Uyeda, C.; Peters, J. C. Electrocatalytic Hydrogen Evolution in Acidic  
7 Water with Molecular Cobalt Tetraazamacrocycles. *Journal of the American Chemical Society*  
8 **2012**, *134* (6), 3164–3170. <https://doi.org/10.1021/ja210661k>.  
9  
10 (46) Nie, C.; Liu, C.; Gong, L.; Wang, M. Boosting the Performance of a Silicon Photocathode for  
11 Photoelectrochemical Hydrogen Production by Immobilization of a Cobalt  
12 Tetraazamacrocyclic Catalyst. *Journal of Materials Chemistry A* **2020**, *5* (45), 23566–23576.  
13 <https://doi.org/10.1039/D0TA09942B>.  
14  
15 (47) Cheng, X.; Sun, S.; Liang, M.; Shi, Y.; Sun, Z.; Xue, S. Organic Dyes Incorporating the  
16 Cyclopentadithiophene Moiety for Efficient Dye-Sensitized Solar Cells. *Dyes and Pigments*  
17 **2012**, *92* (3), 1292–1299. <https://doi.org/10.1016/j.dyepig.2011.09.019>.  
18  
19 (48) Massin, J.; Bräutigam, M.; Kaeffer, N.; Queyriaux, N.; Field, M. J.; Schacher, F. H.; Popp, J.;  
20 Chavarot-Kerlidou, M.; Dietzek, B.; Artero, V. Dye-Sensitized PS-b-P2VP-Templated Nickel  
21 Oxide Films for Photoelectrochemical Applications. *Interface Focus* **2015**, *5* (3), 20140083.  
22 <https://doi.org/10.1098/rsfs.2014.0083>.  
23  
24 (49) Ji, Z.; Natu, G.; Huang, Z.; Wu, Y. Linker Effect in Organic Donor-Acceptor Dyes for p-Type  
25 NiO Dye Sensitized Solar Cells. *Energy and Environmental Science* **2011**, *4* (8), 2818–2821.  
26 <https://doi.org/10.1039/c1ee01527c>.  
27  
28 (50) Ishow, E.; Clavier, G.; Miomandre, F.; Rebarz, M.; Buntinx, G.; Poizat, O. Comprehensive  
29 Investigation of the Excited-State Dynamics of Push–Pull Triphenylamine Dyes as Models for  
30 Photonic Applications. *Physical Chemistry Chemical Physics* **2013**, *15* (33), 13922.  
31 <https://doi.org/10.1039/c3cp51480c>.  
32  
33 (51) Zieschang, F.; Schreck, M. H.; Schmiedel, A.; Holzapfel, M.; Klein, J. H.; Walter, C.; Engels,  
34 B.; Lambert, C. Photoinduced Electron Transfer Dynamics in Triarylamine-Naphthalene  
35 Diimide Cascades. *Journal of Physical Chemistry C* **2014**, *118* (48), 27698–27714.  
36 <https://doi.org/10.1021/jp5085058>.  
37  
38 (52) de Miguel, G.; Wielopolski, M.; Schuster, D. I.; Fazio, M. A.; Lee, O. P.; Haley, C. K.; Ortiz,  
39 A. L.; Echegoyen, L.; Clark, T.; Guldi, D. M. Triazole Bridges as Versatile Linkers in Electron  
40 Donor–Acceptor Conjugates. *Journal of the American Chemical Society* **2011**, *133* (33),  
41 13036–13054. <https://doi.org/10.1021/ja202485s>.  
42  
43 (53) Sheth, S.; Baron, A.; Herrero, C.; Vauzeilles, B.; Aukauloo, A.; Leibl, W. Light-Induced  
44 Tryptophan Radical Generation in a Click Modular Assembly of a Sensitiser-Tryptophan  
45 Residue. *Photochemical & Photobiological Sciences* **2013**, *12* (6), 1074.  
46 <https://doi.org/10.1039/c3pp50021g>.  
47  
48 (54) Baron, A.; Herrero, C.; Quaranta, A.; Charlot, M.-F.; Leibl, W.; Vauzeilles, B.; Aukauloo, A.  
49 Click Chemistry on a Ruthenium Polypyridine Complex. An Efficient and Versatile Synthetic  
50 Route for the Synthesis of Photoactive Modular Assemblies. *Inorganic Chemistry* **2012**, *51*  
51 (11), 5985–5987. <https://doi.org/10.1021/ic300227j>.  
52  
53 (55) Baron, A.; Herrero, C.; Quaranta, A.; Charlot, M.-F.; Leibl, W.; Vauzeilles, B.; Aukauloo, A.  
54 Efficient Electron Transfer through a Triazole Link in Ruthenium(II) Polypyridine Type  
55 Complexes. *Chemical Communications* **2011**, *47* (39), 11011.  
56 <https://doi.org/10.1039/c1cc13683f>.  
57  
58 (56) Queyriaux, N.; Andreiadis, E. S.; Torelli, S.; Pecaut, J.; Veldkamp, B. S.; Margulies, E. A.;  
59 Wasielewski, M. R.; Chavarot-Kerlidou, M.; Artero, V. CuAAC-Based Assembly and  
60

- 1  
2  
3 Characterization of a Ruthenium–Copper Dyad Containing a Diimine–Dioxime Ligand  
4 Framework. *Faraday Discussions* **2017**, *198*, 251–261. <https://doi.org/10.1039/C6FD00204H>.  
5
- 6 (57) Li, N.; Gibson, E. A.; Qin, P.; Boschloo, G.; Gorlov, M.; Hagfeldt, A.; Sun, L. Double-  
7 Layered NiO Photocathodes for p-Type DSSCs with Record IPCE. *Advanced Materials* **2010**,  
8 *22* (15), 1759–1762. <https://doi.org/10.1002/adma.200903151>.  
9
- 10 (58) Sumikura, S.; Mori, S.; Shimizu, S.; Usami, H.; Suzuki, E. Syntheses of NiO Nanoporous  
11 Films Using Nonionic Triblock Co-Polymer Templates and Their Application to Photo-  
12 Cathodes of p-Type Dye-Sensitized Solar Cells. *Journal of Photochemistry and Photobiology*  
13 *A: Chemistry* **2008**, *199* (1), 1–7. <https://doi.org/10.1016/j.jphotochem.2008.04.007>.  
14
- 15 (59) Ameline, D.; Diring, S.; Farre, Y.; Pellegrin, Y.; Naponiello, G.; Blart, E.; Charrier, B.; Dini,  
16 D.; Jacquemin, D.; Odobel, F. Isoindigo Derivatives for Application in P-Type Dye Sensitized  
17 Solar Cells. *RSC Advances* **2015**, *5* (104), 85530–85539. <https://doi.org/10.1039/C5RA11744E>.  
18
- 19 (60) Boschloo, G.; Hagfeldt, A. Spectroelectrochemistry of Nanostructured NiO. *Journal of*  
20 *Physical Chemistry B* **2001**, *105* (15), 3039–3044. <https://doi.org/10.1021/jp003499s>.  
21
- 22 (61) Sonavane, A. C.; Inamdar, A. I.; Shinde, P. S.; Deshmukh, H. P.; Patil, R. S.; Patil, P. S.  
23 Efficient Electrochromic Nickel Oxide Thin Films by Electrodeposition. *J. Alloys Compd.*  
24 **2010**, *489* (2), 667–673. <https://doi.org/10.1016/j.jallcom.2009.09.146>.  
25
- 26 (62) Xia, X. H.; Tu, J. P.; Zhang, J.; Wang, X. L.; Zhang, W. K.; Huang, H. Electrochromic  
27 Properties of Porous NiO Thin Films Prepared by a Chemical Bath Deposition. *Sol. Energ.*  
28 *Mat. Sol. C.* **2008**, *92* (6), 628–633. <https://doi.org/10.1016/j.solmat.2008.01.009>.  
29
- 30 (63) Zietz, B.; Gabrielsson, E.; Johansson, V.; El-Zohry, A. M.; Sun, L.; Kloo, L.  
31 Photoisomerization of the Cyanoacrylic Acid Acceptor Group – a Potential Problem for  
32 Organic Dyes in Solar Cells. *Physical Chemistry Chemical Physics* **2014**, *16* (6), 2251.  
33 <https://doi.org/10.1039/c3cp54048k>.  
34
- 35 (64) Queyriaux, N.; Wahyuono, R. A.; Fize, J.; Gablin, C.; Wächtler, M.; Martinez, E.; Léonard,  
36 D.; Dietzek, B.; Artero, V.; Chavarot-Kerlidou, M. Aqueous Photocurrent Measurements  
37 Correlated to Ultrafast Electron Transfer Dynamics at Ruthenium Tris Diimine Sensitized NiO  
38 Photocathodes. *The Journal of Physical Chemistry C* **2017**, *121* (11), 5891–5904.  
39 <https://doi.org/10.1021/acs.jpcc.6b12536>.  
40
- 41 (65) Bräutigam, M.; Kübel, J.; Schulz, M.; Vos, J. G.; Dietzek, B. Hole Injection Dynamics from  
42 Two Structurally Related Ru–Bipyridine Complexes into NiOx Is Determined by the  
43 Substitution Pattern of the Ligands. *Physical Chemistry Chemical Physics* **2015**, *17* (12), 7823–  
44 7830. <https://doi.org/10.1039/C4CP05663A>.  
45
- 46 (66) Han, Y.; Dillon, R. J.; Flynn, C. J.; Rountree, E. S.; Alibabaei, L.; Cahoon, J. F.; Papanikolas,  
47 J. M.; Dempsey, J. L. Interfacial Electron Transfer Yields in Dye-Sensitized NiO  
48 Photocathodes Correlated to Excited-State Dipole Orientation of Ruthenium Chromophores.  
49 *Canadian Journal of Chemistry* **2018**, *96* (9), 865–874. <https://doi.org/10.1139/cjc-2017-0359>.  
50
- 51 (67) Kou, Y.; Nakatani, S.; Sunagawa, G.; Tachikawa, Y.; Masui, D.; Shimada, T.; Takagi, S.;  
52 Tryk, D. A.; Nabetani, Y.; Tachibana, H.; Inoue, H. Visible Light-Induced Reduction of  
53 Carbon Dioxide Sensitized by a Porphyrin-Rhenium Dyad Metal Complex on p-Type  
54 Semiconducting NiO as the Reduction Terminal End of an Artificial Photosynthetic System.  
55 *Journal of Catalysis* **2014**, *310*, 57–66. <https://doi.org/10.1016/j.jcat.2013.03.025>.  
56
- 57 (68) Bold, S.; Straistari, T.; Muñoz-García, A. B.; Pavone, M.; Artero, V.; Chavarot-Kerlidou, M.;  
58 Dietzek, B. Investigating Light-Induced Processes in Covalent Dye-Catalyst Assemblies for  
59 Hydrogen Production. *Catalysts* **2020**, *Accepted f.*  
60



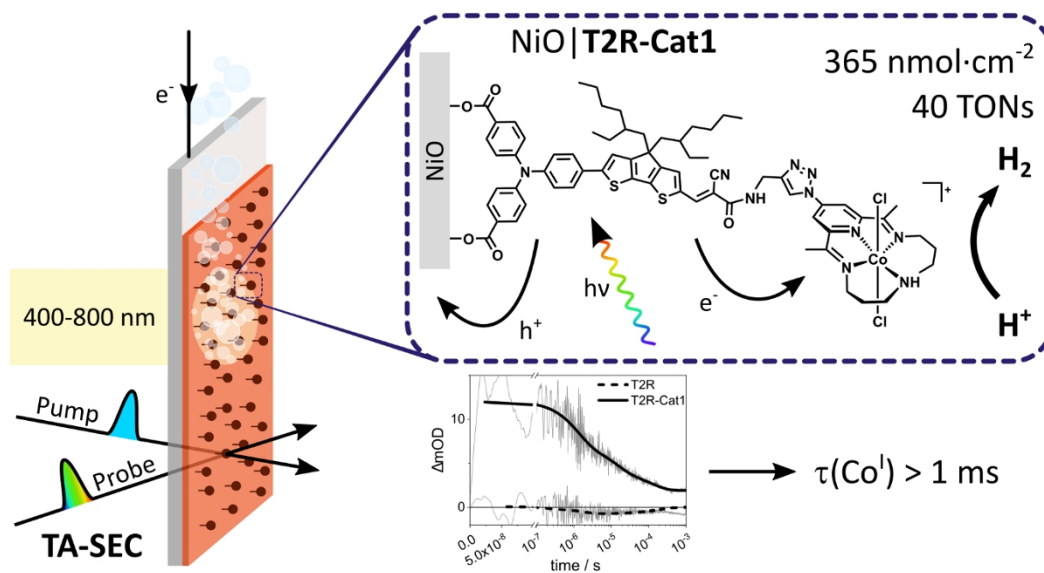
- 1  
2  
3 (69) Massin, J.; Bräutigam, M.; Bold, S.; Wächtler, M.; Pavone, M.; Muñoz-García, A. B.;  
4 Dietzek, B.; Artero, V.; Chavarot-Kerlidou, M. Investigating Light-Driven Hole Injection and  
5 Hydrogen Evolution Catalysis at Dye-Sensitized NiO Photocathodes: A Combined  
6 Experimental–Theoretical Study. *The Journal of Physical Chemistry C* **2019**, *123* (28), 17176–  
7 17184. <https://doi.org/10.1021/acs.jpcc.9b04715>.  
8  
9 (70) Black, F. A.; Clark, C. A.; Summers, G. H.; Clark, I. P.; Towrie, M.; Penfold, T.; George, M.  
10 W.; Gibson, E. A. Investigating Interfacial Electron Transfer in Dye-Sensitized NiO Using  
11 Vibrational Spectroscopy. *Physical Chemistry Chemical Physics* **2017**, *19* (11), 7877–7885.  
12 <https://doi.org/10.1039/C6CP05712H>.  
13  
14 (71) Morandeira, A.; Boschloo, G.; Hagfeldt, A.; Hammarström, L. Coumarin 343-NiO Films as  
15 Nanostructured Photocathodes in Dye-Sensitized Solar Cells: Ultrafast Electron Transfer,  
16 Effect of the I3/I<sup>-</sup> Redox Couple and Mechanism of Photocurrent Generation. *Journal of*  
17 *Physical Chemistry C* **2008**, *112* (25), 9530–9537. <https://doi.org/10.1021/jp800760q>.  
18  
19 (72) Morandeira, A.; Boschloo, G.; Hagfeldt, A.; Hammarström, L. Photoinduced Ultrafast  
20 Dynamics of Coumarin 343 Sensitized P-Type-Nanostructured NiO Films. *The Journal of*  
21 *Physical Chemistry B* **2005**, *109* (41), 19403–19410. <https://doi.org/10.1021/jp053230e>.  
22  
23 (73) Sheibani, E.; Zhang, L.; Liu, P.; Xu, B.; Mijangos, E.; Boschloo, G.; Hagfeldt, A.;  
24 Hammarström, L.; Kloo, L.; Tian, H. A Study of Oligothiophene–Acceptor Dyes in p-Type  
25 Dye-Sensitized Solar Cells. *RSC Advances* **2016**, *6* (22), 18165–18177.  
26 <https://doi.org/10.1039/C5RA26310G>.  
27  
28 (74) Smeigh, A. L.; le Pleux, L.; Fortage, J.; Pellegrin, Y.; Blart, E.; Odobel, F.; Hammarström, L.  
29 Ultrafast Recombination for NiO Sensitized with a Series of Perylene Imide Sensitizers  
30 Exhibiting Marcus Normal Behaviour. *Chemical Communications* **2012**, *48* (5), 678–680.  
31 <https://doi.org/10.1039/c1cc16144j>.  
32  
33 (75) Gibson, E. A.; Smeigh, A. L.; le Pleux, L.; Fortage, J.; Boschloo, G.; Blart, E.; Pellegrin, Y.;  
34 Odobel, F.; Hagfeldt, A.; Hammarström, L. A P-Type NiO-Based Dye-Sensitized Solar Cell  
35 with an Open-Circuit Voltage of 0.35 V. *Angewandte Chemie International Edition* **2009**, *48*  
36 (24), 4402–4405. <https://doi.org/10.1002/anie.200900423>.  
37  
38 (76) le Pleux, L.; Smeigh, A. L.; Gibson, E.; Pellegrin, Y.; Blart, E.; Boschloo, G.; Hagfeldt, A.;  
39 Hammarström, L.; Odobel, F. Synthesis, Photophysical and Photovoltaic Investigations of  
40 Acceptor-Functionalized Perylene Monoimide Dyes for Nickel Oxide p-Type Dye-Sensitized  
41 Solar Cells. *Energy and Environmental Science* **2011**, *4* (6), 2075–2084.  
42 <https://doi.org/10.1039/c1ee01148k>.  
43  
44 (77) Yu, Y.; Click, K. A.; Polen, S. M.; He, M.; Hadad, C. M.; Wu, Y. Electron Transfer Kinetics  
45 of a Series of Bilayer Triphenylamine-Oligothiophene-Perylenemonoimide Sensitizers for Dye-  
46 Sensitized NiO. *Journal of Physical Chemistry C* **2017**, *121* (38), 20720–20728.  
47 <https://doi.org/10.1021/acs.jpcc.7b07859>.  
48  
49 (78) Flender, O.; Scholz, M.; Klein, J. R.; Oum, K.; Lenzer, T. Excited-State Relaxation of the  
50 Solar Cell Dye D49 in Organic Solvents and on Mesoporous Al<sub>2</sub>O<sub>3</sub> and TiO<sub>2</sub> Thin Films.  
51 *Physical Chemistry Chemical Physics* **2016**, *18* (37), 26010–26019.  
52 <https://doi.org/10.1039/C6CP05167G>.  
53  
54 (79) Zhu, H.; Wang, X.; Ma, R.; Kuang, Z.; Guo, Q.; Xia, A. Intramolecular Charge Transfer and  
55 Solvation of Photoactive Molecules with Conjugated Push–Pull Structures. *ChemPhysChem*  
56 **2016**, *17* (20), 3245–3251. <https://doi.org/10.1002/cphc.201600674>.  
57  
58  
59  
60

- 1  
2  
3 (80) Ishow, E.; Guillot, R.; Buntinx, G.; Poizat, O. Photoinduced Intramolecular Charge-Transfer  
4 Dynamics of a Red-Emitting Dicyanovinyl-Based Triarylamine Dye in Solution. *Journal of*  
5 *Photochemistry and Photobiology A: Chemistry* **2012**, *234*, 27–36.  
6 <https://doi.org/10.1016/j.jphotochem.2011.12.018>.  
7  
8 (81) Gatty, M. G.; Pullen, S.; Sheibani, E.; Tian, H.; Ott, S.; Hammarström, L. Direct Evidence of  
9 Catalyst Reduction on Dye and Catalyst Co-Sensitized NiO Photocathodes by Mid-Infrared  
10 Transient Absorption Spectroscopy. *Chemical Science* **2018**, *9* (22), 4983–4991.  
11 <https://doi.org/10.1039/C8SC00990B>.  
12  
13 (82) Morandeira, A.; Fortage, J.; Edvinsson, T.; Pleux, L. le; Blart, E.; Boschloo, G.; Hagfeldt, A.;  
14 Hammarström, L.; Odobel, F. Improved Photon-to-Current Conversion Efficiency with a  
15 Nanoporous p-Type NiO Electrode by the Use of a Sensitizer-Acceptor Dyad. *Journal of*  
16 *Physical Chemistry C* **2008**, *112* (5), 1721–1728. <https://doi.org/10.1021/jp077446n>.  
17  
18 (83) Gatty, M. G.; Pullen, S.; Sheibani, E.; Tian, H.; Ott, S.; Hammarström, L. Direct Evidence of  
19 Catalyst Reduction on Dye and Catalyst Co-Sensitized NiO Photocathodes by Mid-Infrared  
20 Transient Absorption Spectroscopy. *Chemical Science* **2018**, *9* (22), 4983–4991.  
21 <https://doi.org/10.1039/c8sc00990b>.  
22  
23 (84) Sheibani, E.; Zhang, L.; Liu, P.; Xu, B.; Mijangos, E.; Boschloo, G.; Hagfeldt, A.;  
24 Hammarström, L.; Kloob, L.; Tian, H. A Study of Oligothiophene-Acceptor Dyes in p-Type  
25 Dye-Sensitized Solar Cells. *RSC Advances* **2016**, *6* (22), 18165–18177.  
26 <https://doi.org/10.1039/c5ra26310g>.  
27  
28 (85) Qin, P.; Wiberg, J.; Gibson, E. A.; Linder, M.; Li, L.; Brinck, T.; Hagfeldt, A.; Albinsson, B.;  
29 Sun, L. Synthesis and Mechanistic Studies of Organic Chromophores with Different Energy  
30 Levels for P-Type Dye-Sensitized Solar Cells. *The Journal of Physical Chemistry C* **2010**, *114*  
31 (10), 4738–4748. <https://doi.org/10.1021/jp911091n>.  
32  
33 (86) Pöldme, N.; O'Reilly, L.; Fletcher, I.; Portoles, J.; Sazanovich, I. v; Towrie, M.; Long, C.;  
34 Vos, J. G.; Pryce, M. T.; Gibson, E. A. Photoelectrocatalytic H<sub>2</sub> Evolution from Integrated  
35 Photocatalysts Adsorbed on NiO. *Chemical Science* **2019**, *10* (1), 99–112.  
36 <https://doi.org/10.1039/C8SC02575D>.  
37  
38 (87) Smeigh, A. L.; Pleux, L. le; Fortage, J.; Pellegrin, Y.; Blart, E.; Odobel, F.; Hammarström, L.  
39 Ultrafast Recombination for NiO Sensitized with a Series of Perylene Imide Sensitizers  
40 Exhibiting Marcus Normal Behaviour. *Chem. Commun.* **2012**, *48* (5), 678–680.  
41 <https://doi.org/10.1039/C1CC16144J>.  
42  
43 (88) Gardner, J. M.; Beyler, M.; Karnahl, M.; Tschierlei, S.; Ott, S.; Hammarström, L. Light-  
44 Driven Electron Transfer between a Photosensitizer and a Proton-Reducing Catalyst Co-  
45 Adsorbed to NiO. *Journal of the American Chemical Society* **2012**, *134* (47), 19322–19325.  
46 <https://doi.org/10.1021/ja3082268>.  
47  
48 (89) Queyriaux, N.; Sun, D.; Fize, J.; Pécaut, J.; Field, M. J.; Chavarot-Kerlidou, M.; Artero, V.  
49 Electrocatalytic Hydrogen Evolution with a Cobalt Complex Bearing Pendant Proton Relays:  
50 Acid Strength and Applied Potential Govern Mechanism and Stability. *Journal of the American*  
51 *Chemical Society* **2020**, *142* (1), 274–282. <https://doi.org/10.1021/jacs.9b10407>.  
52  
53 (90) Queyriaux, N.; Jane, R. T.; Massin, J.; Artero, V.; Chavarot-Kerlidou, M. Recent  
54 Developments in Hydrogen Evolving Molecular Cobalt(II)-Polypyridyl Catalysts.  
55 *Coordination Chemistry Reviews* **2015**, *304–305*, 3–19.  
56 <https://doi.org/10.1016/j.ccr.2015.03.014>.  
57  
58  
59  
60

- 1  
2  
3 (91) Queyriaux, N.; Giannoudis, E.; Windle, C. D.; Roy, S.; Pécaut, J.; Coutsolelos, A. G.; Artero,  
4 V.; Chavarot-Kerlidou, M. A Noble Metal-Free Photocatalytic System Based on a Novel  
5 Cobalt Tetrapyrrolyl Catalyst for Hydrogen Production in Fully Aqueous Medium. *Sustainable*  
6 *Energy Fuels* **2018**, *25* (2), 553–557. <https://doi.org/10.1039/c7se00428a>.  
7  
8 (92) Zee, D. Z.; Chantarojsiri, T.; Long, J. R.; Chang, C. J. Metal–Polypyridyl Catalysts for  
9 Electro- and Photochemical Reduction of Water to Hydrogen. *Accounts of Chemical Research*  
10 **2015**, *48* (7), 2027–2036. <https://doi.org/10.1021/acs.accounts.5b00082>.  
11  
12 (93) Materna, K. L.; Beiler, A. M.; Thapper, A.; Ott, S.; Tian, H.; Hammarström, L.  
13 Understanding the Performance of NiO Photocathodes with Alkyl-Derivatized Cobalt Catalysts  
14 and a Push–Pull Dye. *ACS Applied Materials & Interfaces* **2020**, *12* (28), 31372–31381.  
15 <https://doi.org/10.1021/acsami.0c05228>.  
16  
17 (94) Kaeffer, N.; Chavarot-Kerlidou, M.; Artero, V. Hydrogen Evolution Catalyzed by Cobalt  
18 Diimine-Dioxime Complexes. *Accounts of Chemical Research* **2015**, *48* (5), 1286–1295.  
19 <https://doi.org/10.1021/acs.accounts.5b00058>.  
20  
21 (95) Kaeffer, N.; Morozan, A.; Fize, J.; Martinez, E.; Guetaz, L.; Artero, V. The Dark Side of  
22 Molecular Catalysis: Diimine–Dioxime Cobalt Complexes Are Not the Actual Hydrogen  
23 Evolution Electrocatalyst in Acidic Aqueous Solutions. *ACS Catalysis* **2016**, *6* (6), 3727–3737.  
24 <https://doi.org/10.1021/acscatal.6b00378>.  
25  
26 (96) Anxolabéhère-Mallart, E.; Costentin, C.; Fournier, M.; Nowak, S.; Robert, M.; Savéant, J.-M.  
27 Boron-Capped Tris(Glyoximate) Cobalt Clathrochelate as a Precursor for the Electrodeposition  
28 of Nanoparticles Catalyzing H<sub>2</sub> Evolution in Water. *Journal of the American Chemical Society*  
29 **2012**, *134* (14), 6104–6107. <https://doi.org/10.1021/ja301134e>.  
30  
31 (97) Cobo, S.; Heidkamp, J.; Jacques, P.-A.; Fize, J.; Fourmond, V.; Guetaz, L.; Jusselme, B.;  
32 Ivanova, V.; Dau, H.; Palacin, S.; Fontecave, M.; Artero, V. A Janus Cobalt-Based Catalytic  
33 Material for Electro-Splitting of Water. *Nature Materials* **2012**, *11* (9), 802–807.  
34 <https://doi.org/10.1038/nmat3385>.  
35  
36 (98) Andreiadis, E. S.; Jacques, P. A.; Tran, P. D.; Leyris, A.; Chavarot-Kerlidou, M.; Jusselme,  
37 B.; Matheron, M.; Pécaut, J.; Palacin, S.; Fontecave, M.; Artero, V. Molecular Engineering of a  
38 Cobalt-Based Electrocatalytic Nanomaterial for H<sub>2</sub> Evolution under Fully Aqueous  
39 Conditions. *Nature Chemistry* **2013**, *5* (1), 48–53. <https://doi.org/10.1038/nchem.1481>.  
40  
41 (99) Lee, D. K.; Lee, D.; Lumley, M. A.; Choi, K. S. Progress on Ternary Oxide-Based  
42 Photoanodes for Use in Photoelectrochemical Cells for Solar Water Splitting. *Chemical Society*  
43 *Reviews* **2019**, *48* (7), 2126–2157. <https://doi.org/10.1039/c8cs00761f>.  
44  
45 (100) Sahara, G.; Kumagai, H.; Maeda, K.; Kaeffer, N.; Artero, V.; Higashi, M.; Abe, R.; Ishitani,  
46 O. Photoelectrochemical Reduction of CO<sub>2</sub> Coupled to Water Oxidation Using a Photocathode  
47 with a Ru(II)–Re(I) Complex Photocatalyst and a CoOx /TaON Photoanode. *Journal of the*  
48 *American Chemical Society* **2016**, *138* (42), 14152–14158.  
49 <https://doi.org/10.1021/jacs.6b09212>.  
50  
51 (101) Tebo, A. G.; Quaranta, A.; Herrero, C.; Pecoraro, V. L.; Aukauloo, A. Intramolecular  
52 Photogeneration of a Tyrosine Radical in a Designed Protein. *ChemPhotoChem* **2017**, *1* (3),  
53 89–92. <https://doi.org/10.1002/cptc.201600044>.  
54  
55 (102) Herrero, C.; Quaranta, A.; el Ghachtouli, S.; Vauzeilles, B.; Leibl, W.; Aukauloo, A. Carbon  
56 Dioxide Reduction via Light Activation of a Ruthenium–Ni(Cyclam) Complex. *Physical*  
57 *Chemistry Chemical Physics* **2014**, *16* (24), 12067–12072. <https://doi.org/10.1039/c3cp54946a>.  
58  
59  
60

- 1  
2  
3 (103) Herrero, C.; Quaranta, A.; Sircoglou, M.; Sénéchal-David, K.; Baron, A.; Marín, I. M.;  
4 Buron, C.; Baltaze, J.-P.; Leibl, W.; Aukauloo, A.; Banse, F. Successive Light-Induced Two  
5 Electron Transfers in a Ru–Fe Supramolecular Assembly: From Ru–Fe(II)–OH<sub>2</sub> to Ru–  
6 Fe(IV)–Oxo. *Chemical Science* **2015**, *6* (4), 2323–2327. <https://doi.org/10.1039/C5SC00024F>.  
7
- 8 (104) Herrero, C.; Batchelor, L.; Baron, A.; el Ghachtouli, S.; Sheth, S.; Guillot, R.; Vauzeilles, B.;  
9 Sircoglou, M.; Mallah, T.; Leibl, W.; Aukauloo, A. Click Chemistry as a Convenient Tool for  
10 the Incorporation of a Ruthenium Chromophore and a Nickel-Salen Monomer into a Visible-  
11 Light-Active Assembly. *European Journal of Inorganic Chemistry* **2013**, *2013* (4), 494–499.  
12 <https://doi.org/10.1002/ejic.201201161>.  
13
- 14 (105) Li, T. T.; Shan, B.; Meyer, T. J. Stable Molecular Photocathode for Solar-Driven CO<sub>2</sub>  
15 Reduction in Aqueous Solutions. *ACS Energy Letters* **2019**, *4* (3), 629–636.  
16 <https://doi.org/10.1021/acsenerylett.8b02512>.  
17
- 18 (106) Brown, A. M.; Antila, L. J.; Mirmohades, M.; Pullen, S.; Ott, S.; Hammarström, L. Ultrafast  
19 Electron Transfer Between Dye and Catalyst on a Mesoporous NiO Surface. *Journal of the*  
20 *American Chemical Society* **2016**, *138* (26), 8060–8063. <https://doi.org/10.1021/jacs.6b03889>.  
21
- 22 (107) Dalle, K. E.; Warnan, J.; Leung, J. J.; Reuillard, B.; Karmel, I. S.; Reisner, E. Electro- and  
23 Solar-Driven Fuel Synthesis with First Row Transition Metal Complexes. *Chemical Reviews*  
24 **2019**, *119* (4), 2752–2875. <https://doi.org/10.1021/acs.chemrev.8b00392>.  
25
- 26 (108) Xu, P.; McCool, N. S.; Mallouk, T. E. Water Splitting Dye-Sensitized Solar Cells. *Nano*  
27 *Today* **2017**, *14*, 42–58. <https://doi.org/10.1016/j.nantod.2017.04.009>.  
28
- 29 (109) Tong, L.; Duan, L.; Zhou, A.; Thummel, R. P. First-Row Transition Metal Polypyridine  
30 Complexes That Catalyze Proton to Hydrogen Reduction. *Coordination Chemistry Reviews*  
31 **2020**, *402*, 213079. <https://doi.org/10.1016/j.ccr.2019.213079>.  
32
- 33 (110) O'Reilly, J. E. Oxidation-Reduction Potential of the Ferro-Ferricyanide System in Buffer  
34 Solutions. *Biochimica et Biophysica Acta (BBA) - Bioenergetics* **1973**, *292* (3), 509–515.  
35 [https://doi.org/10.1016/0005-2728\(73\)90001-7](https://doi.org/10.1016/0005-2728(73)90001-7).  
36
- 37 (111) Karnahl, M.; Kuhnt, C.; Ma, F.; Yartsev, A.; Schmitt, M.; Dietzek, B.; Rau, S.; Popp, J.  
38 Tuning of Photocatalytic Hydrogen Production and Photoinduced Intramolecular Electron  
39 Transfer Rates by Regioselective Bridging Ligand Substitution. *ChemPhysChem* **2011**, *12* (11),  
40 2101–2109. <https://doi.org/10.1002/cphc.201100245>.  
41
- 42 (112) Dietzek, B.; Pascher, T.; Sundström, V.; Yartsev, A. Appearance of Coherent Artifact Signals  
43 in Femtosecond Transient Absorption Spectroscopy in Dependence on Detector Design. *Laser*  
44 *Physics Letters* **2007**, *4* (1), 38–43. <https://doi.org/10.1002/lapl.200610070>.  
45
- 46 (113) Sittig, M.; Schmidt, B.; Görls, H.; Bocklitz, T.; Wächtler, M.; Zechel, S.; Hager, M. D.;  
47 Dietzek, B. Fluorescence Upconversion by Triplet–Triplet Annihilation in All-Organic  
48 Poly(Methacrylate)-Terpolymers. *Physical Chemistry Chemical Physics* **2020**, *22* (7), 4072–  
49 4079. <https://doi.org/10.1039/D0CP00232A>.  
50  
51  
52  
53  
54  
55  
56  
57  
58  
59  
60

Table of content (TOC) figure:



Supplementary Information for

Spectroscopic investigations provide a rationale for the hydrogen-evolving activity of dye-sensitized photocathodes based on a cobalt tetraazamacrocyclic catalyst

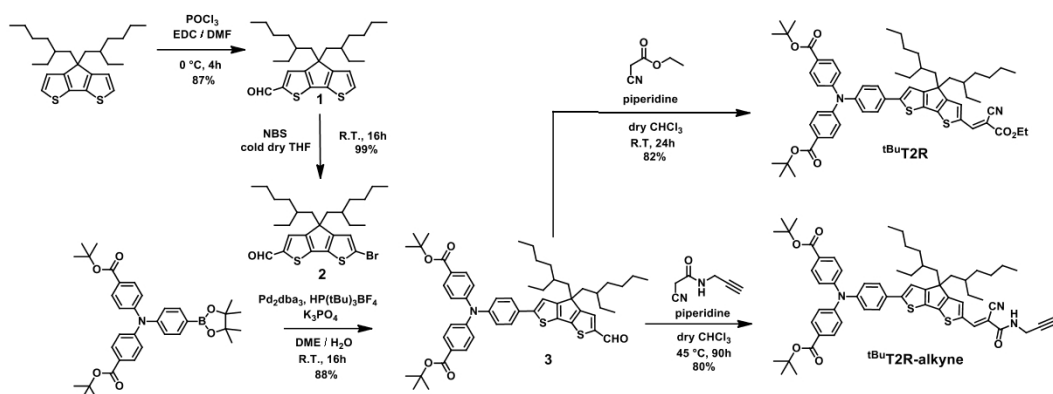
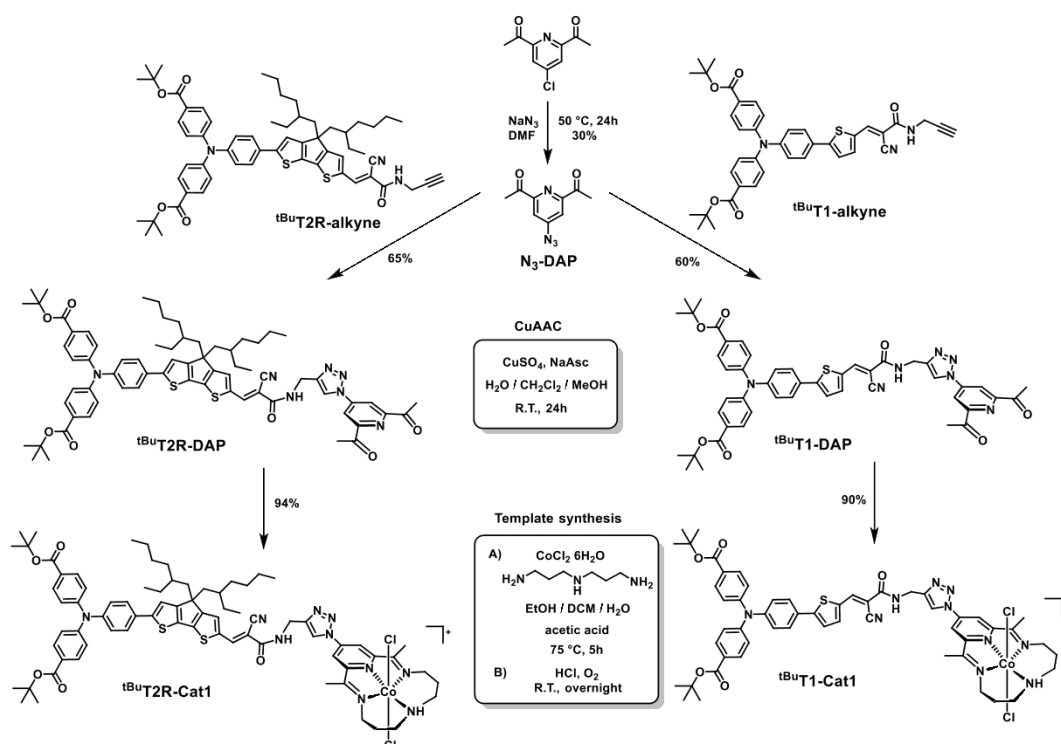
Sebastian Bold,<sup>a,b,c</sup> Julien Massin,<sup>a</sup> Emmanouil Giannoudis,<sup>a</sup> Matthieu Koepf,<sup>a</sup> Vincent Artero,<sup>a</sup> Benjamin Dietzek<sup>b,c,d</sup> and Murielle Chavarot-Kerlidou<sup>a</sup>

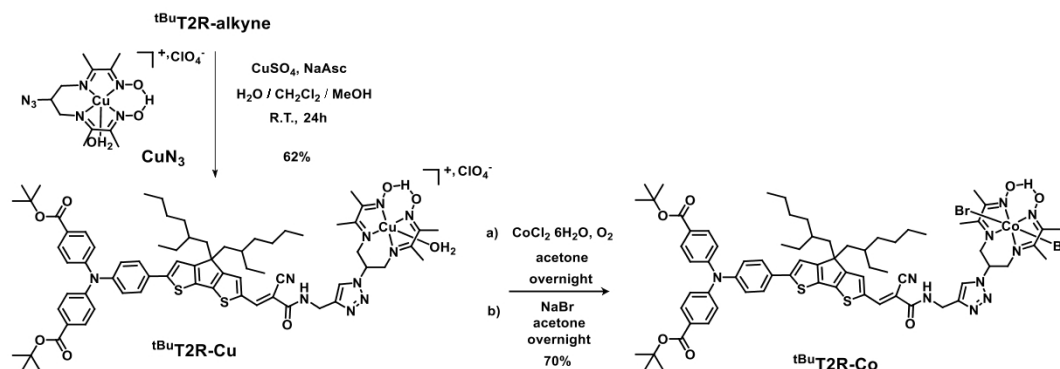
a. Univ. Grenoble Alpes, CNRS, CEA, IRIG, Laboratoire de Chimie et Biologie des Métaux, 17 rue des Martyrs, F-38000 Grenoble, France.

b. Institute of Physical Chemistry and Abbe Center of Photonics, Friedrich Schiller University Jena, Helmholtzweg 4, 07743 Jena, Germany.

c. Department Functional Interfaces, Leibniz Institute of Photonic Technology Jena (IPHT), Albert-Einstein-Straße 9, 07745 Jena, Germany.

d. Center for Energy and Environmental Chemistry (CEEC Jena), Friedrich Schiller University Jena, Philosophenweg 8, 07743 Jena, Germany.

Scheme S1. Synthetic route to **tBuT2R** and **tBuT2R-alkyne**.Scheme S2. Synthetic route to **tBuT1-Cat1** and **tBuT2R-Cat1**.



**Scheme S3.** Synthetic route to **tBuT2R-Co**.

**4,4-bis(2-ethylhexyl)-4H-cyclopenta[2,1-b:3,4-b']dithiophene-2-carbaldehyde (1).** To a cold solution of commercially available 4,4-bis(2-ethylhexyl)-4H-cyclopenta[2,1-b:3,4-b']dithiophene (5 g, 12.4 mmol) and *N,N*-dimethylformamide (1.2 equiv., 1.09 g, 14.9 mmol) in 1,2-dichloroethane (32 mL) was added at 0 °C phosphorus chloride oxide (1.2 equiv., 2.29 g, 14.9 mmol) under argon and the reaction solution was stirred at 0 °C for 4 hours. The color turned to yellow and a saturated sodium acetate aqueous solution (66 mL) was added. The mixture was stirred at room temperature for 2 hours. The crude product was extracted with  $\text{CH}_2\text{Cl}_2$ , and the organic layer was washed with brine solution and water, dried over sodium sulfate and filtered. After removal of the solvent under reduced pressure, the residue was purified on silica gel column using 30%  $\text{CH}_2\text{Cl}_2$  in petroleum ether as eluent to give a yellow oil (4.65 g, 10.8 mmol, 87%).  $^1\text{H}$  NMR (300 MHz,  $\text{CDCl}_3$ ):  $\delta$  in ppm 9.82 (s, 1H), 7.56 (s(br), 1H), 7.37 (d,  $J = 4.9$  Hz, 1H), 6.99 (m, 1H), 2-1.85 (m, 4H), 0.99-0.82 (m, 16H), 0.80-0.73 (m, 6H), 0.61-0.57 (m, 8H);  $^{13}\text{C}$  NMR (75 MHz,  $\text{CDCl}_3$ ):  $\delta$  in ppm 182.6, 162.0, 157.7, 148.0, 142.8, 135.9, 130.9, 129.2, 122.5, 53.7, 43.1, 35.1, 34.0, 28.5, 27.3, 22.7, 14.0, 10.5. HRMS (ESI<sup>+</sup>): calcd for  $\text{C}_{26}\text{H}_{39}\text{OS}_2$  ( $[\text{M}+\text{H}]^+$ ):  $m/z$  431.2437; found 431.2446. E.A.: calcd for  $\text{C}_{26}\text{H}_{38}\text{OS}_2$ : C, 72.50; H, 8.89; found: C, 72.68; H, 9.05.

**6-bromo-4,4-bis(2-ethylhexyl)-4H-cyclopenta[2,1-b:3,4-b']dithiophene-2-carbaldehyde (2).** **1** (2.58 g, 5.99 mmol) and NBS (1.1 equiv., 1.17 g, 6.59 mmol) were mixed in dry THF (165 mL) at 0°C under argon, and stirred at room temperature for 16 hours. The color turned to orange. The mixture was quenched with water (170 mL), extracted with  $\text{CHCl}_3$  (3 x 150 mL), washed with brine solution (150 mL), dried over  $\text{Na}_2\text{SO}_4$ , and filtered. The crude product was purified on silica gel column using  $\text{CHCl}_3$  as eluent and dried under vacuum to give a greenish oil (3.17 g, 5.99 mmol, 99%).  $^1\text{H}$  NMR (300 MHz,  $\text{CDCl}_3$ ):  $\delta$  in ppm 9.83 (s, 1H), 7.55 (s, 1H), 7.02 (s, 1H), 1.97-1.81 (m, 4H), 0.99-0.89 (m, 16H), 0.81-0.73 (m, 6H), 0.65-0.58 (m, 8H);  $^{13}\text{C}$  NMR (75 MHz,  $\text{CDCl}_3$ ):  $\delta$  in ppm 182.5, 160.7, 156.8, 146.9, 143.3, 136.3, 130.6, 125.6, 54.6, 43.0, 35.2, 34.1, 28.5, 27.3, 24.9,



22.7, 14.0, 10.6. HR-MS (ESI+): calcd for C<sub>26</sub>H<sub>38</sub>BrOS<sub>2</sub> ([M+H]<sup>+</sup>): *m/z* 509.1542; found 509.1548. E.A.: calcd for C<sub>26</sub>H<sub>37</sub>BrOS<sub>2</sub>: C, 61.28; H, 7.32; found: C, 61.37; H, 7.45.

***Tert*-butyl-4,4'-((4-(6-formyl-4,4-bis(2-ethylhexyl)-4H-cyclopenta[2,1-b:3,4-b'] dithiophen-2-yl)phenyl)azanediyl)dibenzoate (3).** *Tert*-butyl 4,4'-((4-(4,4,5,5-tetramethyl-1,3,2-dioxaborolan-2-yl)phenyl)azanediyl)dibenzoate<sup>1</sup> (1.34 g, 2.34 mmol), **2** (1 equiv., 1.19 g, 2.34 mmol), Pd<sub>2</sub>dba<sub>3</sub> (0.05 equiv., 73 mg, 0.11 mmol) and HP(tBu)<sub>3</sub>BF<sub>4</sub> (0.1 equiv., 73 mg, 0.23 mmol) were dissolved in dry DME (23 mL) under argon. K<sub>3</sub>PO<sub>4</sub> (6 mL, 1 M) was added and the reaction mixture was stirred at room temperature for 16 hours. The color turned rapidly to orange. After pouring in 200 mL H<sub>2</sub>O, the mixture was extracted with CHCl<sub>3</sub> (3 x 200 mL), washed with brine solution (200 mL), dried with anhydrous Na<sub>2</sub>SO<sub>4</sub>, filtered and the solvent was evaporated. The crude product was purified on silica gel column using 10% CHCl<sub>3</sub> in toluene as eluent and was dried under vacuum to give an orange solid (1.80 g, 2.06 mmol, 88%). <sup>1</sup>H NMR (300 MHz, CDCl<sub>3</sub>): δ in ppm 9.84 (s, 1H), 7.89 (d, *J* = 8.4 Hz, 4H), 7.53 (m, 3H), 7.16-7.10 (m, 7H), 2.01-1.89 (m, 4H), 1.59 (s, 18H), 0.99-0.94 (m, 16H), 0.77-0.60 (m, 14H); <sup>13</sup>C NMR (75 MHz, CDCl<sub>3</sub>): δ in ppm 206.8, 182.4, 165.3, 163.1, 157.2, 150.3, 148.2, 146.1, 143.0, 135.1, 130.9, 130.6, 126.7, 125.9, 122.9, 118.3, 80.8, 54.1, 43.2, 35.3, 34.1, 32.1, 28.4, 27.4, 22.8, 14.0, 10.6. HRMS (ESI+): calcd for C<sub>54</sub>H<sub>68</sub>NO<sub>5</sub>S<sub>2</sub> ([M+H]<sup>+</sup>): *m/z* 874.4533; found 874.4538. E.A.: calcd for C<sub>54</sub>H<sub>67</sub>NO<sub>5</sub>S<sub>2</sub> + 0.3 H<sub>2</sub>O: C, 73.73; H, 7.75; N, 1.59; found: C, 73.68; H, 7.85; N, 1.59.

**<sup>t</sup>BuT2R. 3** (200 mg, 0.23 mmol) and ethyl 2-cyanoacetate (1.2 equiv., 31 mg, 0.27 mmol) were mixed in CHCl<sub>3</sub> (12 mL). Piperidine (5 equiv., 98 mg, 1.15 mmol) was added and the reaction mixture was stirred at room temperature for 24 hours. The color turned to red. The reaction was quenched by addition of HCl 1M (100 mL). The mixture was extracted with CHCl<sub>3</sub> (3 x 70 mL), washed with brine solution (70 mL), dried over Na<sub>2</sub>SO<sub>4</sub>, filtered and the solvent was evaporated. The crude product was purified over silica gel column using 20% CHCl<sub>3</sub> in toluene as eluent to give **<sup>t</sup>BuT2R** as a red powder (180 mg, 0.19 mmol, 82%). This compound was further purified to eliminate some remaining aldehyde precursor using 7% of ethyl acetate in hexane as eluent. <sup>1</sup>H NMR (300 MHz, CDCl<sub>3</sub>): δ in ppm 8.27 (s, 1H), 7.89 (d, *J* = 8.7 Hz, 4H), 7.60-7.51 (m, 3H), 7.18 (s, 1H), 7.14-7.10 (m, 6H), 4.35 (q, *J* = 7.2 Hz, 2H), 1.95 (s(br), 4H), 1.59 (s, 18H), 1.38 (t, *J* = 7.0 Hz, 3H), 1.00-0.92 (m, 16H), 0.76-0.59 (m, 14H). <sup>13</sup>C NMR (75 MHz, CDCl<sub>3</sub>): δ in ppm 165.3, 163.7, 150.3, 146.3, 130.9, 130.6, 126.9, 126.7, 125.9, 125.8, 123.0, 80.9, 77.3, 62.2, 54.2, 43.1, 35.3, 34.1, 28.6, 28.5, 28.3, 27.4, 27.3, 22.8, 14.3, 14.1, 10.7. HR-MS (ESI+): calcd for C<sub>59</sub>H<sub>73</sub>N<sub>2</sub>O<sub>6</sub>S<sub>2</sub> ([M+H]<sup>+</sup>): *m/z* 969.4905, found 969.4906. E.A.: calcd for C<sub>59</sub>H<sub>72</sub>N<sub>2</sub>O<sub>6</sub>S<sub>2</sub>: C, 73.11; H, 7.49; N, 2.89; found: C, 72.88; H, 7.58; N, 2.88.

**<sup>t</sup>BuT2R-alkyne. 3** (481 mg, 0.55 mmol) and 2-cyano-*N*-(prop-2-yn-1-yl)acetamide (3 equiv., 202 mg, 1.65 mmol) were mixed in dry CHCl<sub>3</sub> (30 mL). Piperidine (5 equiv., 234 mg, 2.75 mmol) was added and the reaction mixture was stirred at 45 °C for 90 hours. The color turned to red. The reaction was quenched by HCl 1M (250 mL) and extracted with CH<sub>2</sub>Cl<sub>2</sub> (3 x 150 mL), washed with brine solution (100 mL), dried over Na<sub>2</sub>SO<sub>4</sub> and filtered. The crude product was purified on silica gel column using CH<sub>2</sub>Cl<sub>2</sub> as eluent and dried under vacuum to give **<sup>t</sup>BuT2R-alkyne** as a red powder (427 mg, 0.44 mmol, 80%). <sup>1</sup>H NMR (300 MHz, CDCl<sub>3</sub>): δ in ppm 8.36 (s, 1H), 7.89 (d, J = 8.6 Hz, 4H), 7.57-7.51 (m, 3H), 7.18-7.10 (m, 7H), 6.35 (s(br), 1H), 4.20 (s(br), 2H), 2.30 (s, 1H), 2.00-1.87 (m, 4H), 1.53 (s, 18H), 0.99-0.93 (m, 16H), 0.77-0.59 (m, 14H). <sup>13</sup>C NMR (75 MHz, CDCl<sub>3</sub>): δ in ppm 165.5, 163.6, 161.4, 158.1, 150.5, 149.1, 148.9, 146.4, 145.7, 136.2, 135.2, 131.0, 130.9, 126.9, 126.0, 123.1, 118.4, 94.9, 81.0, 78.9, 72.4, 54.4, 43.4, 35.6, 34.4, 30.2, 28.7, 27.5, 22.9, 14.1, 10.8. HR-MS (ESI+): calcd for C<sub>60</sub>H<sub>72</sub>N<sub>3</sub>O<sub>5</sub>S<sub>2</sub> ([M+H]<sup>+</sup>): m/z 978.4908; found 978.4906. E.A.: calcd for C<sub>60</sub>H<sub>71</sub>N<sub>3</sub>O<sub>5</sub>S<sub>2</sub>: C, 73.66; H, 7.31; N, 4.29; found: C, 73.52; H, 7.40; N, 4.29.

**4-azido-2,6-diacetylpyridine (N<sub>3</sub>-DAP**; synthesis adapted from a previously reported procedure.<sup>2</sup> 4-chloro-2,6-diacetylpyridine<sup>3</sup> (250 mg, 1.25 mmol) and NaN<sub>3</sub> (20 equiv., 1.62 g, 25 mmol) were mixed in DMF (4 mL) and then heated to 50 °C. After 24 hours, the DMF was evaporated under reduced pressure. The crude product was purified on silica gel column using 50% pentane in CH<sub>2</sub>Cl<sub>2</sub> as eluent to give a white solid (75 mg, 0.4 mmol, 30%). <sup>1</sup>H NMR (300 MHz, CDCl<sub>3</sub>): δ in ppm 7.83 (s, 2H), 2.78 (s, 6H); <sup>13</sup>C NMR (75 MHz, CDCl<sub>3</sub>): δ in ppm 198.6, 154.5, 151.5, 114.7, 25.6; ESI-MS: m/z 227.0 ([M+Na]<sup>+</sup>), 205.0 ([M+H]<sup>+</sup>).

**<sup>t</sup>BuT1-diacetylpyridine: <sup>t</sup>BuT1-alkyne** (500 mg, 0.58 mmol) and **N<sub>3</sub>-DAP** (1 equiv., 118 mg, 0.58 mmol) were dissolved in 20.8 mL of degassed CH<sub>2</sub>Cl<sub>2</sub>. Sodium ascorbate (101 mg, 0.52 mmol) and CuSO<sub>4</sub>·5H<sub>2</sub>O (43 mg, 0.17 mmol) were dissolved in 10.4 mL of degassed H<sub>2</sub>O and then added to the reaction mixture. 34.6 mL of degassed MeOH were added until a single phase was obtained. The reaction mixture was stirred at room temperature for 18 hours. After removal of the volatile solvents, the mixture was extracted with CH<sub>2</sub>Cl<sub>2</sub> (3 x 75 mL), washed with brine solution (75 mL), dried over Na<sub>2</sub>SO<sub>4</sub> and filtered. The crude product was purified on silica gel column using CH<sub>2</sub>Cl<sub>2</sub>/AcOEt (7:3) as eluent and dried under vacuum to give a red solid (390 mg, 0.45 mmol, 60%). <sup>1</sup>H NMR (300 MHz, CDCl<sub>3</sub>): δ in ppm 8.61 (s, 2H), 8.39 (s, 1H), 8.28 (s, 1H), 7.90 (d, J = 8.5 Hz, 4H), 7.71 (d, J = 3.7 Hz, 1H), 7.60 (d, J = 8.5 Hz, 2H), 7.35 (d, J = 4.2 Hz, 1H), 7.15-7.09 (m, 6H), 6.92 (s(br), 1H), 4.79 (d, J = 5.8 Hz, 2H), 2.84 (s, 6H), 1.59 (s, 18H). HR-MS (ESI+): calcd for C<sub>48</sub>H<sub>46</sub>N<sub>7</sub>O<sub>7</sub>S ([M+H]<sup>+</sup>): m/z 864.3174; found: 864.3173. E.A.: calcd for C<sub>48</sub>H<sub>45</sub>N<sub>7</sub>O<sub>7</sub>S + 1 H<sub>2</sub>O: C, 65.37 ; H, 5.37; N, 11.12; found: C, 65.35 ; H, 5.31; N, 10.99.

**<sup>t</sup>BuT1-Cat1.** <sup>t</sup>BuT1- diacetylpyridine (50 mg, 0.058 mmol) was dissolved in EtOH (1 mL) and CH<sub>2</sub>Cl<sub>2</sub> (0.5 mL), and kept at 40 °C under argon. CoCl<sub>2</sub>·6H<sub>2</sub>O (1 equiv., 14 mg, 0.058 mmol) and water (0.56 mL) were added and the mixture was stirred at 55 °C to dissolve the salt. The reaction mixture was warmed at 75 °C and 3,3'-diaminodipropylamine (1 equiv., 8 μL, 0.058 mmol) and glacial acetic acid (5 μL) were added. The solution was stirred at 75 °C for 5 hours under argon. After cooling down to room temperature, 10 μL of concentrated HCl was added and the mixture was stirred at room temperature for 16 hours. After evaporation of the solvents, precipitation was carried out with addition of cold saturated aqueous solution of KCl. The red precipitate was purified on silica gel using CH<sub>2</sub>Cl<sub>2</sub>/AcOEt (6:4) then acetone/H<sub>2</sub>O/saturated aqueous KCl (90:9:1) as eluents to yield <sup>t</sup>BuT1-Cat1 as a red solid (45 mg, 0.040 mmol, 70%). <sup>1</sup>H NMR (300 MHz, (CD<sub>3</sub>)<sub>3</sub>CO) δ in ppm 9.25 (s, 2H), 9.11 (s, 1H), 8.46 (s, 1H), 8.25 (s(br), 1H), 7.93 (d, J = 7.9 Hz, 4H), 7.82 (d, J = 8.3 Hz, 2H), 7.67 (s(br), 1H), 7.28-7.18 (m, 6H), 6.30 (s(br), 1H), 4.82 (s(br), 2H), 4.40 (d, J = 16.0 Hz, 2H), 3.78-3.68 (m, 2H), 3.50-3.40 (m, 2H), 3.36-3.31 (m, 2H), 3.18 (s, 6H), 2.43 (s(br), 2H), 2.31.2.28 (m, 2H), 1.58 (s, 18H). HR-MS (ESI+): calcd for C<sub>54</sub>H<sub>58</sub>CoN<sub>10</sub>O<sub>5</sub>SCl<sub>2</sub> ([M-Cl]<sup>+</sup>): *m/z* 1087.3016, found 1087.3014. E.A.: calcd for C<sub>54</sub>H<sub>58</sub>CoN<sub>10</sub>O<sub>5</sub>SCl<sub>3</sub> + 5 KCl + H<sub>2</sub>O: C, 42.80; H, 3.99; N, 9.24; found: C, 42.83; H, 4.60; N, 7.73.

**<sup>t</sup>BuT2R-diacetylpyridine.** <sup>t</sup>BuT2R-alkyne (570 mg, 0.58 mmol) and N<sub>3</sub>-DAP (1 equiv., 118 mg, 0.58 mmol) were dissolved in 20.8 mL of degassed CH<sub>2</sub>Cl<sub>2</sub>. Sodium ascorbate (101 mg, 0.52 mmol) and CuSO<sub>4</sub>·5H<sub>2</sub>O (43 mg, 0.17 mmol) were dissolved in 10.4 mL of degassed H<sub>2</sub>O and then added to the reaction mixture. 34.6 mL of degassed MeOH was added until a single phase was obtained. The reaction mixture was stirred at room temperature for 18 hours. After removal of the volatile solvents, the mixture was extracted with CH<sub>2</sub>Cl<sub>2</sub> (3 x 75 mL), washed with brine solution (75 mL), dried over Na<sub>2</sub>SO<sub>4</sub> and filtered. The crude product was purified on silica gel column using CH<sub>2</sub>Cl<sub>2</sub>/AcOEt (7:3) as eluent and dried under vacuum to give a red solid (447 mg, 0.38 mmol, 65%). <sup>1</sup>H NMR (300 MHz, CDCl<sub>3</sub>): δ in ppm 8.61 (s, 2H), 8.37 (s, 1H), 8.29 (s, 1H), 7.89 (d, J = 8.0 Hz, 4H), 7.57-7.52 (m, 3H), 7.17 (s, 1H), 7.14-7.09 (m, 6H), 6.86 (s(br), 1H), 4.80 (s(br), 2H), 2.84 (s, 6H), 1.93 (s(br), 4H), 1.59 (s, 18H), 1.00-0.93 (m, 16H), 0.77-0.59 (m, 14H). <sup>13</sup>C NMR (75 MHz, CDCl<sub>3</sub>): δ in ppm 198.0, 165.4, 163.7, 158.2, 155.2, 150.5, 149.2, 149.0, 146.5, 145.5, 136.2, 135.3, 131.1, 130.9, 127.0, 126.0, 123.1, 114.4, 105.9, 81.0, 54.4, 43.4, 35.6, 34.4, 28.8, 28.4, 27.5, 25.7, 22.9, 14.1, 10.8. HR-MS (ESI+): calcd for C<sub>69</sub>H<sub>80</sub>N<sub>7</sub>O<sub>7</sub>S<sub>2</sub> ([M+H]<sup>+</sup>): *m/z* 1182.5555; found 1182.5550. E.A.: calcd for C<sub>69</sub>H<sub>79</sub>N<sub>7</sub>O<sub>7</sub>S<sub>2</sub> + 0.9 H<sub>2</sub>O: C, 69.13; H, 6.79; N, 8.18; found: C, 69.14; H, 6.76; N, 8.07.

**<sup>t</sup>BuT2R-Cat1.** <sup>t</sup>BuT2R-diacetylpyridine (424 mg, 0.36 mmol) was dissolved in EtOH (2 mL) and CH<sub>2</sub>Cl<sub>2</sub> (1 mL), and kept at 40 °C under argon. CoCl<sub>2</sub>·6H<sub>2</sub>O (1 equiv., 90 mg, 0.37 mmol) and water (0.36 mL) were added and the solution was stirred at 55 °C to dissolve the salt. The reaction mixture

was warmed to 75 °C and 3,3'-diaminodipropylamine (1 equiv., 0.05 mL, 0.37 mmol) and glacial acetic acid (0.03 mL) were added and stirred at 75 °C for 5 hours under argon. After cooling down to room temperature, 0.1 mL of concentrated HCl was added and the reaction mixture was stirred at room temperature for 16 hours, kept for 2 hours at -15 °C and centrifuged. The crude product was purified on silica gel column using CH<sub>2</sub>Cl<sub>2</sub>/AcOEt (6:4), then acetone/H<sub>2</sub>O/saturated aqueous KCl (90:9:1) as eluents and dried under vacuum to give a red solid (360 mg, 0.25 mmol, 69%). <sup>1</sup>H NMR (500 MHz, CD<sub>3</sub>CN/CDCl<sub>3</sub> (5:1)) δ in ppm 9.00 (s, 1H), 8.92 (s, 2H), 8.38 (s, 1H), 7.85 (d, J = 8.5 Hz, 4H), 7.70-7.68-7.67 (3s, 1H), 7.58 (d, J = 8.5 Hz, 2H), 7.36 (s, 1H), 7.14-7.09 (m, 6H), 5.97 (s(br), 1H), 4.76 (s(br), 2H), 3.99 (d(br), J = 16.2 Hz, 2H), 3.58 (t(br), J = 15.3 Hz, 2H), 3.33 (q, J = 12.5 Hz, 2H), 2.93 (s(br), 2H), 2.89 (s, 6H), 2.29 (d(br), J = 13.8 Hz, 2H), 2.14 (s(br), 2H), 2.02-1.98 (m, 4H), 1.56 (s, 18H), 0.98-0.92 (m, 16H), 0.75-0.58 (m, 14H). HR-MS (ESI<sup>+</sup>): calcd for C<sub>75</sub>H<sub>92</sub>CoN<sub>10</sub>O<sub>5</sub>S<sub>2</sub>Cl<sub>2</sub> ([M-Cl]<sup>+</sup>): *m/z* 1405.5397; found 1405.5405; calcd for C<sub>75</sub>H<sub>92</sub>CoN<sub>10</sub>O<sub>5</sub>S<sub>2</sub>Cl ([M-2Cl]<sup>2+</sup>): *m/z* 685.2852; found 685.2855. E.A.: calcd for C<sub>75</sub>H<sub>92</sub>CoN<sub>10</sub>O<sub>5</sub>S<sub>2</sub>Cl<sub>3</sub> + 5 KCl + 1 H<sub>2</sub>O: C, 49.12; H, 5.17; N, 7.64; found: C, 48.99; H, 5.37; N, 7.07.

**<sup>t</sup>BuT2R-Cu. 9** (600 mg, 0.61 mmol) and **15** (1 equiv., 300 mg, 0.61 mmol) were dissolved in 21.9 mL of degassed CH<sub>2</sub>Cl<sub>2</sub>. Sodium ascorbate (0.9 equiv., 109 mg, 0.55 mmol) and CuSO<sub>4</sub>·5H<sub>2</sub>O (0.3 equiv., 45 mg, 0.18 mmol) were dissolved in 11.1 mL of degassed H<sub>2</sub>O and then added to the reaction mixture. 36.9 mL of degassed MeOH was added until a single phase was obtained. The reaction mixture was stirred at room temperature for 18 hours. After removal of the volatile solvents, the mixture was extracted with CH<sub>2</sub>Cl<sub>2</sub> (3 x 75 mL), washed with brine solution (75 mL), dried over Na<sub>2</sub>SO<sub>4</sub> and filtered. The crude product was purified on silica gel column using CH<sub>2</sub>Cl<sub>2</sub> 7/3 AcOEt as eluent and dried under vacuum to give a brownish red solid (506 mg, 0.38 mmol, 62%). HRMS (ESI<sup>+</sup>): calcd for C<sub>71</sub>H<sub>89</sub>N<sub>10</sub>O<sub>7</sub>CuS<sub>2</sub> ([M-H<sub>2</sub>O-ClO<sub>4</sub>]<sup>+</sup>): *m/z* 1320.5648; found 1320.5653.

**<sup>t</sup>BuT2R-Co. <sup>t</sup>BuT2R-Cu** (474 mg, 0.33 mmol) and CoCl<sub>2</sub>·6H<sub>2</sub>O (7 equiv., 532 mg, 2.24 mmol) were solubilized in 50 ml of acetone and stirred under air bubbling using an air pump overnight. The solution was evaporated under vacuum and the solid was purified by flash chromatography on silica gel using as eluent a mixture of CH<sub>3</sub>CN and KNO<sub>3</sub> aqueous solution at 10% of the saturating solution. The organic solvents were evaporated and the solution was extracted with dichloromethane. After evaporation, the solid was solubilized in 10 ml of acetone and 3 ml of NaBr-saturated aqueous solution was added. The reaction mixture was left stirring overnight. The precipitate was filtered, rinsed with water and dried under vacuum to give a red solid (336 mg, 0.23 mmol, 70%). <sup>1</sup>H NMR (300 MHz, CDCl<sub>3</sub>): δ in ppm 19.48 (s, 1H), 8.46 (s, 1H), 8.10 (s(br), 1H), 7.98 (d, J = 8.0 Hz, 4H), 7.86 (t, 1H), 7.75 (d, 2H), 7.60 (s, 1H), 7.41 (s(br), 1H), 7.24 (m, 6H), 5.88 (t, 1H), 4.83-4.59 (m, 6H), 2.65 (s, 12H), 1.67 (s, 18H), 1.07-1.02 (m, 16H), 0.84-0.70 (m, 14H). <sup>13</sup>C NMR (75 MHz,

CDCl<sub>3</sub>):  $\delta$  in ppm 175.8, 165.4, 163.7, 162.2, 158.2, 157.1, 156.3, 150.5, 146.5, 136.1, 135.2, 131.1, 130.8, 127.0, 126.0, 123.2, 122.9, 118.3, 81.0, 55.7, 54.4, 43.4, 35.6, 34.4, 31.0, 28.8, 28.7, 28.4, 27.6, 27.4, 22.9, 18.3, 14.2, 10.8. HRMS (ESI<sup>+</sup>):  $m/z$  calcd for C<sub>71</sub>H<sub>89</sub>N<sub>10</sub>O<sub>7</sub>CoS<sub>2</sub> ([M-2Br]<sup>2+</sup>):  $m/z$  658.2839; found 658.2848. E.A.: calcd for C<sub>71</sub>H<sub>89</sub>N<sub>10</sub>O<sub>7</sub>CoS<sub>2</sub>Br<sub>2</sub> + 0.5 NaBr: C, 55.78 ; H, 5.87; N, 9.16; found: C, 55.91; H, 6.00; N, 9.07.

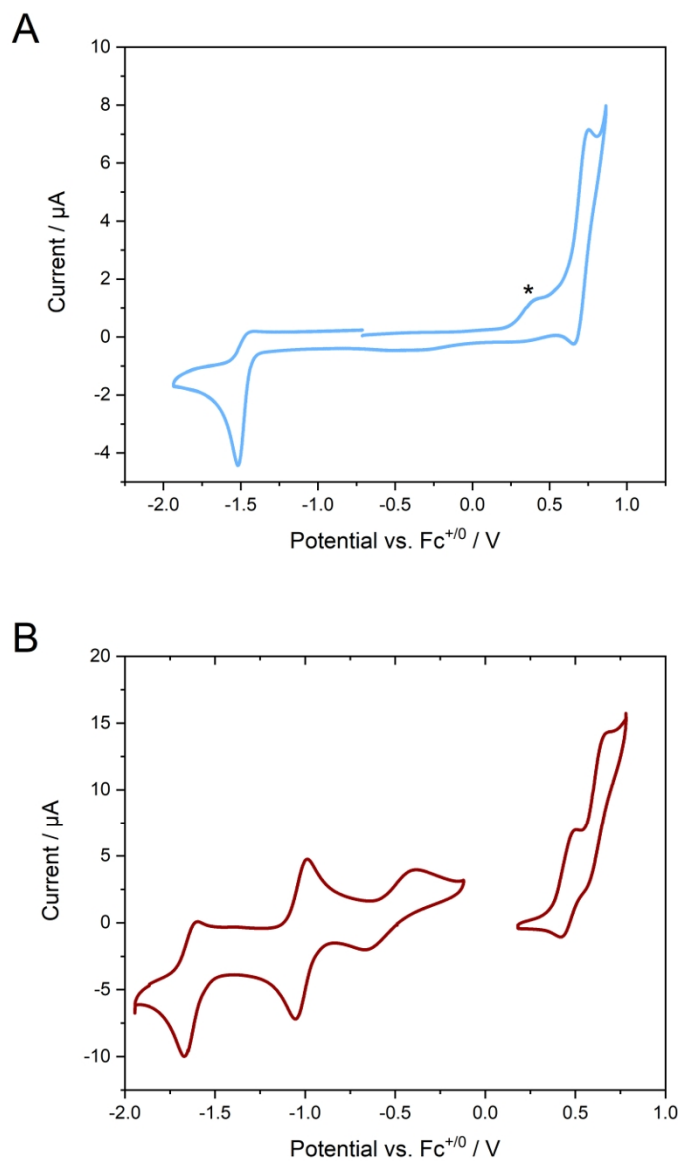


**Figure S1:** Cyclic voltammograms of A) *t*BuT1 and B) *t*BuT2R-Co. CVs were recorded at  $50 \text{ mV}\cdot\text{s}^{-1}$  scan rate in 0.1 M TBABF<sub>4</sub> in dry DMF. Measurements were carried out at a glassy carbon working electrode with a Pt wire auxiliary electrode and a Ag/AgCl reference electrode and converted to potentials vs.  $\text{Fc}^{+/0}$ .

\*The peak at 0.4 V vs.  $\text{Fc}^{+/0}$  is already present in the CV of the blank electrolyte solution without *t*BuT1.

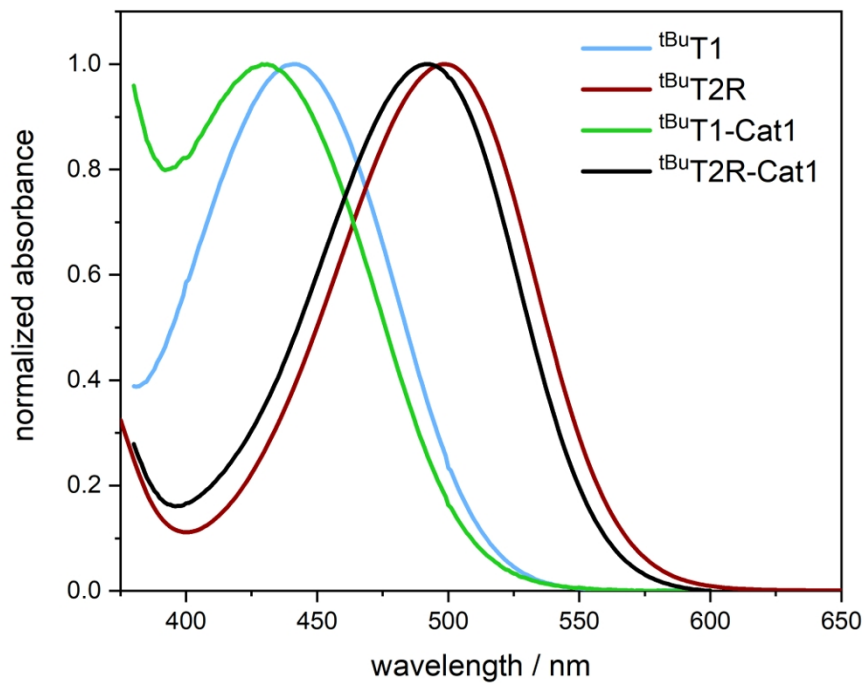


**Figure S2:** UV-Vis absorption spectra in ACN, normalized at the absorption maximum of the ICT band.

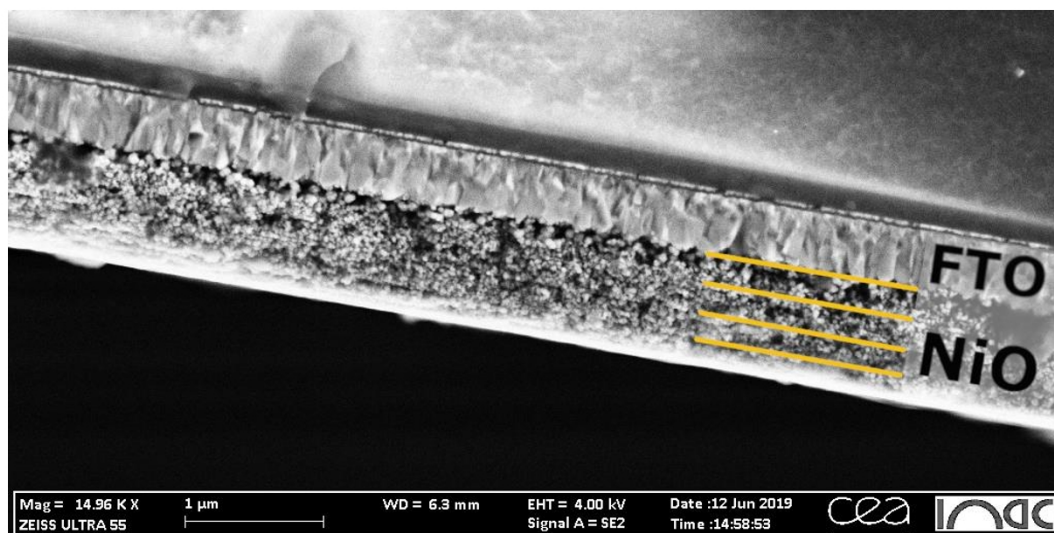


**Figure S3:** Scanning electron microscopy (SEM) image of a typical four-layer NiO film with a thickness of 847 nm. The average film thickness across three batches of NiO films was  $877 \pm 167$  nm (Table S2).



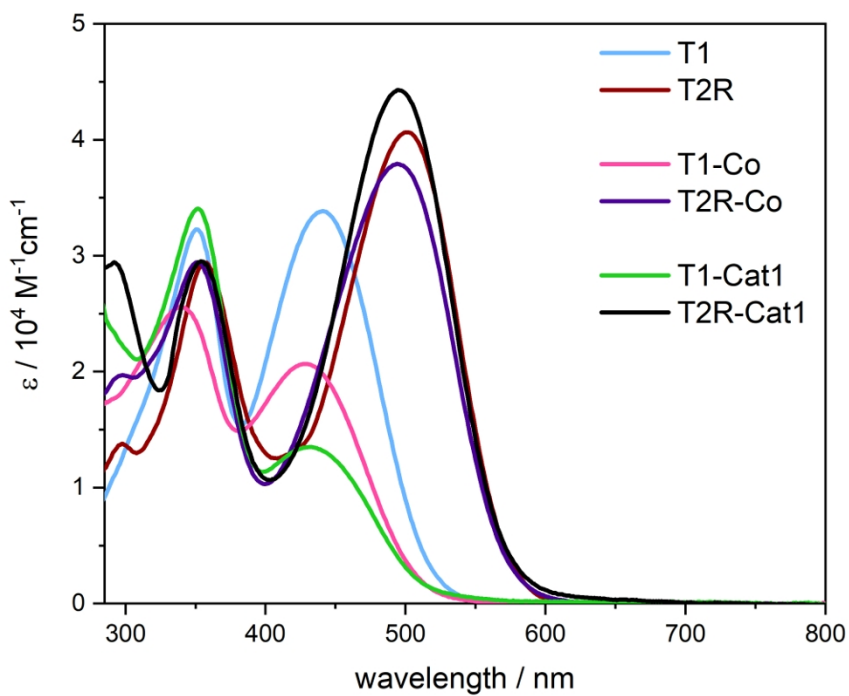


**Figure S4.** Extinction coefficients of **T1**, **T2R**, **T1-Co**, **T2R-Co** and **T2R-Cat1** in a 1M methanolic phenylphosphonic acid solution, as well as of **T1-Cat1** in a 1M DMF phenylphosphonic acid solution employed to determine the dyad and dye loadings for fresh and post-operando films.

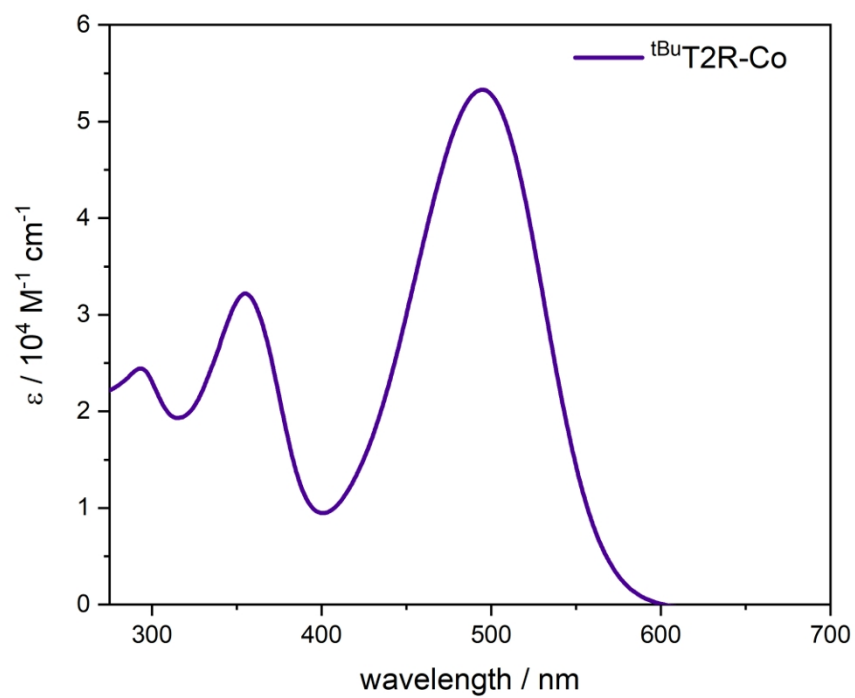


**Figure S5:** UV-Vis absorption spectrum of  $t\text{BuT2R-Co}$  in MeOH.

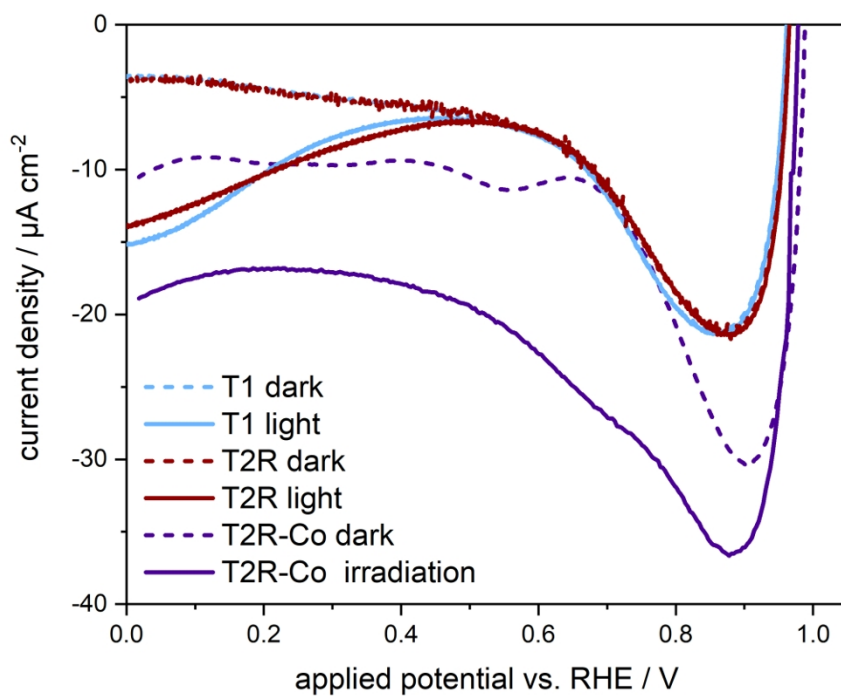


**Figure S6.** Linear scan voltammograms (LSV) of NiO films sensitized with **T1**, **T2R** and **T2R-Co** in 0.1 M MES buffer at pH 5.5 + 0.1 M NaCl aqueous buffer solutions in the dark (dashed) and under  $65 \text{ mW} \cdot \text{cm}^{-2}$  irradiation (solid).

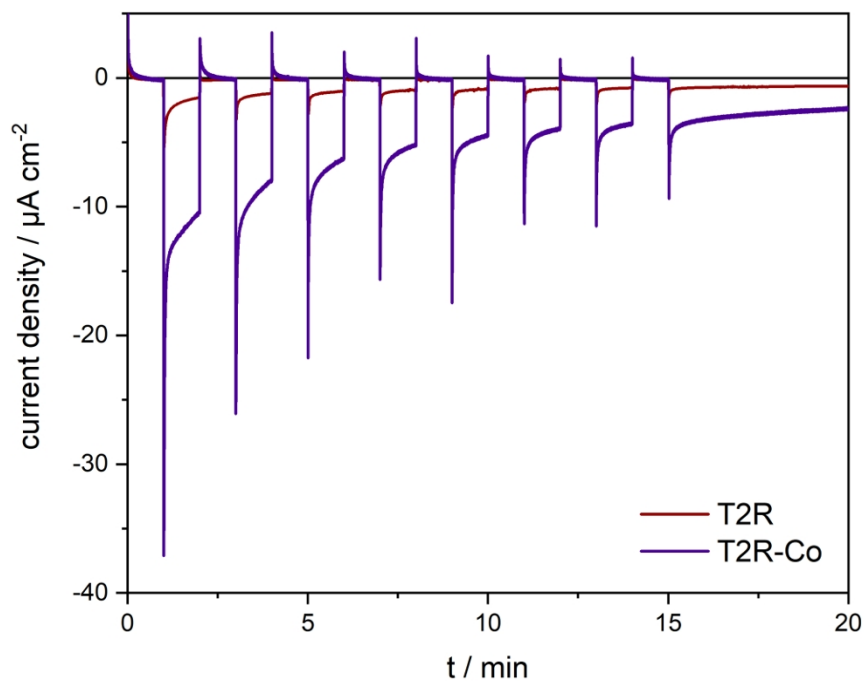


**Figure S7:** Chopped light chronoamperometry of NiO films sensitized with **T2R** (red) and the **T2R-Co** (violet) dyad in 0.1 M MES buffer at pH 5.5 + 0.1 M NaCl aqueous buffer solution. The applied potential was +0.14 V vs. RHE.

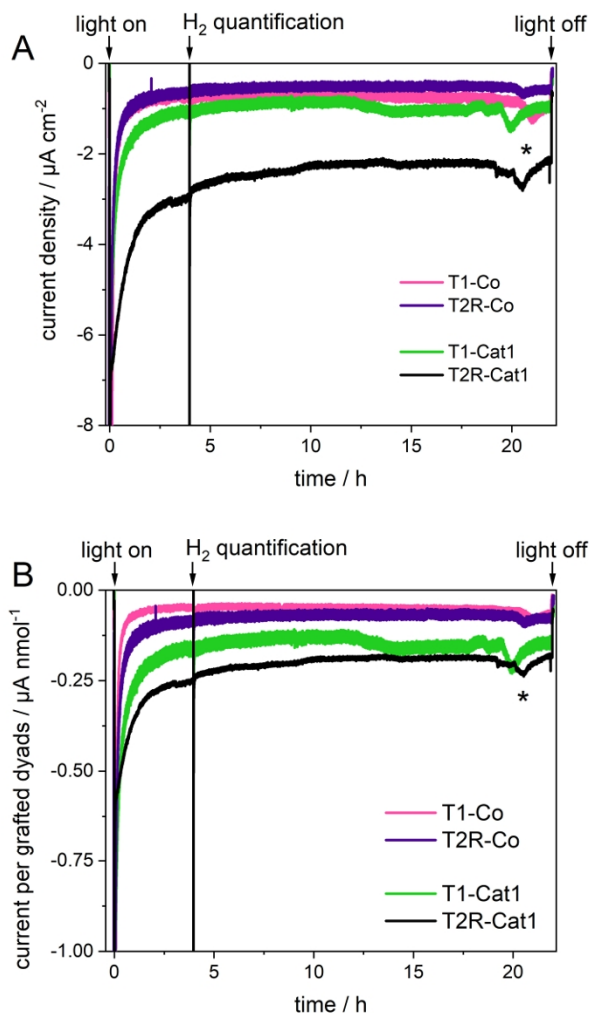


**Figure S8.** Chronoamperometric measurements under irradiation in aqueous 0.1 M pH 5.5 MES buffer at an applied potential of  $-0.4$  V vs. Ag/AgCl ( $+0.11$  V vs. RHE) of **T1-Co** (pink), **T2R-Co** (violet), **T1-Cat1** (green) and **T2R-Cat1** (black). Given are (a) current densities based on the geometric surface of the films and (b) the current normalized to the amount of grafted dyads.

The spike observed at 4 h is caused by the measurement of hydrogen produced. The spikes observed at around 20 h seem to be caused by environmental factors in the laboratory as they all appear around the same time in the morning.

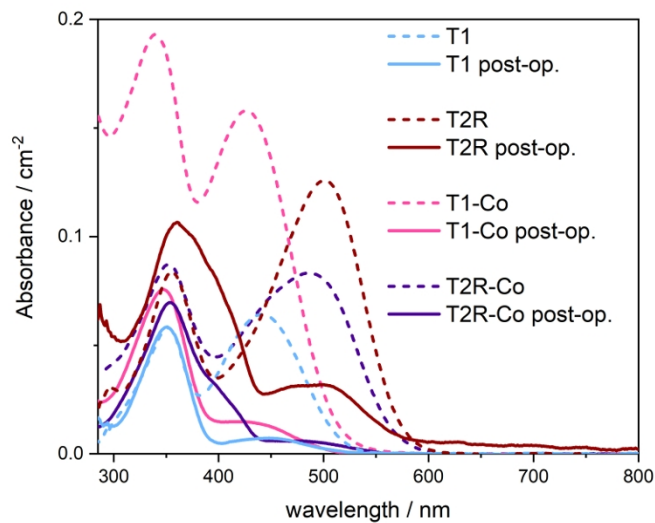


**Figure S9.** UV-Vis spectra of solutions obtained by desorbing **T1**- and **T2R**-sensitized NiO films with 1 M phenylphosphonic acid solution in methanol. Both freshly-sensitized films (dashed lines) as well as films employed for 22 hours photoelectrochemical experiments (solid lines) were desorbed.

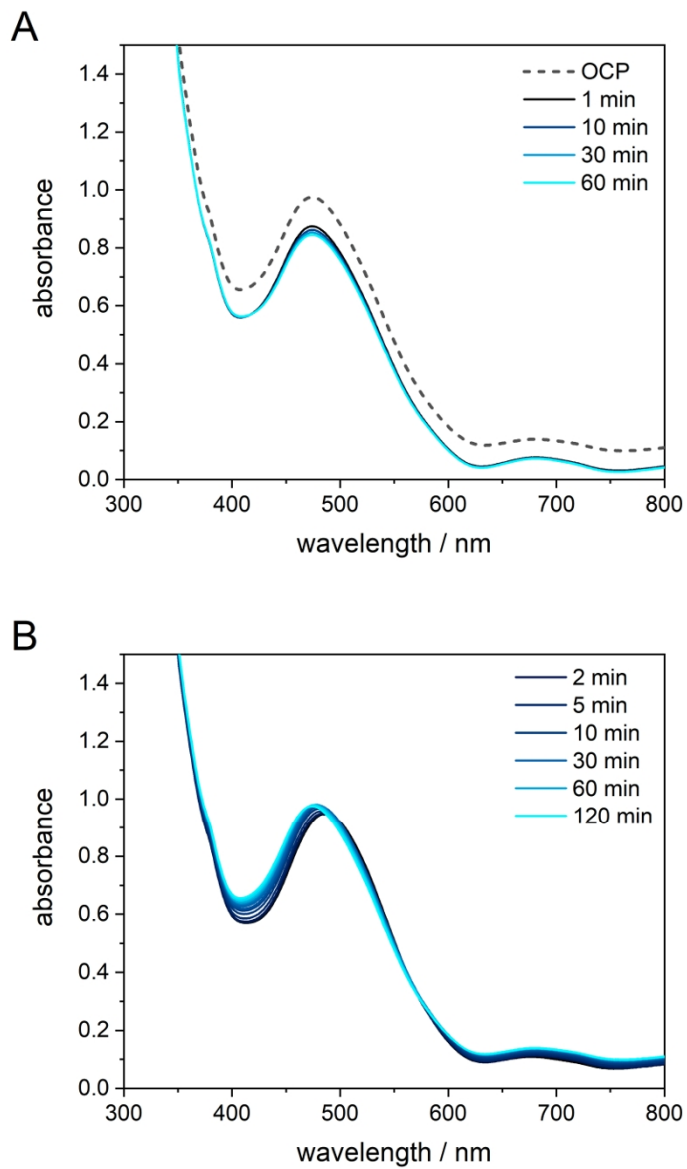


**Figure S10:** UV-Vis absorption spectra of **T2R-Cat1**-sensitized NiO films in contact with 0.1 M MES buffer at pH 5.5 while (a) applying a potential of -0.35 V vs. Ag/AgCl (+0.21 V vs. RHE) or (b) irradiating.

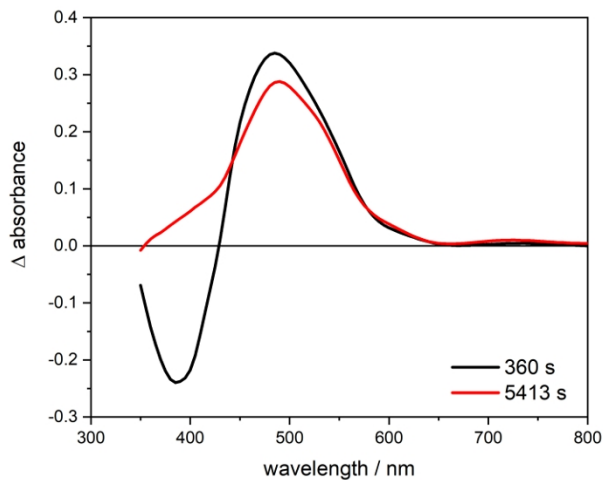


**Figure S11.** Decay-associated spectra (DAS) obtained by globally fitting the differential spectra obtained by measuring UV-Vis absorption spectra of **T2R-Cat1**-sensitized NiO films under operando photoelectrochemical conditions with a two-component exponential function of the form:

$$\Delta A(\lambda) = A_1(\lambda) * e^{-\frac{t}{\tau_1}} + A_2(\lambda) * e^{-\frac{t}{\tau_2}}$$

Where  $A_n$  are the wavelength-dependent amplitudes and  $\tau_n$  are the characteristic lifetimes of the two processes. The DAS are obtained by plotting the  $A_n(\lambda)$  as a function of  $\lambda$ .



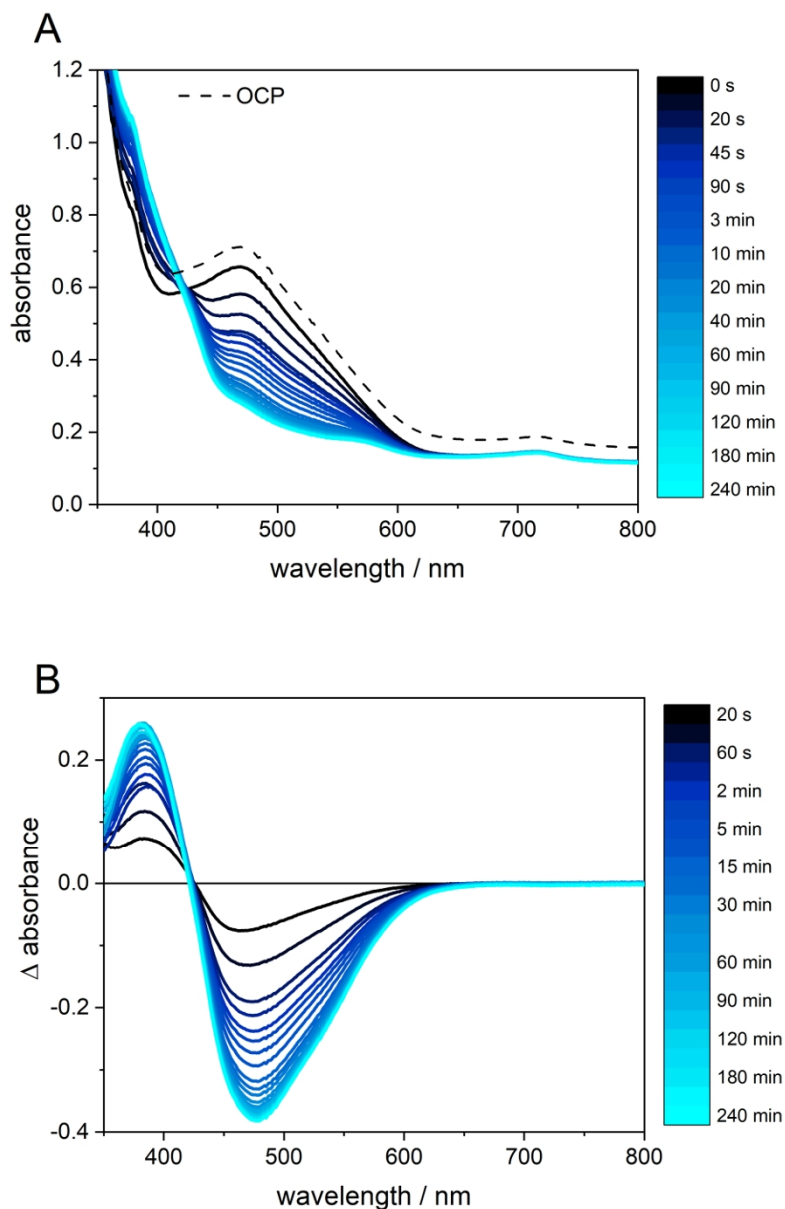


**Figure S12.** UV-vis absorption monitoring of **T2R**-sensitized NiO films under operando photoelectrochemical conditions (0.1 M MES buffer at pH 5.5 under irradiation and with an applied potential of -0.35 V vs. Ag/AgCl corresponding to +0.21 V vs. RHE). Top: UV-Vis spectra; bottom: differential spectra obtained by subtracting the spectrum obtained with applied potential before irradiation (0s).

The initial jump in absorbance upon applying a potential (between OCP and 0 s) is caused by the electrochromic nature of the NiO: Ni<sup>3+</sup> defects formed at the NiO surface show a broad absorption which disappears upon reducing these defects to Ni<sup>2+</sup> by applying a potential.<sup>4,5</sup>

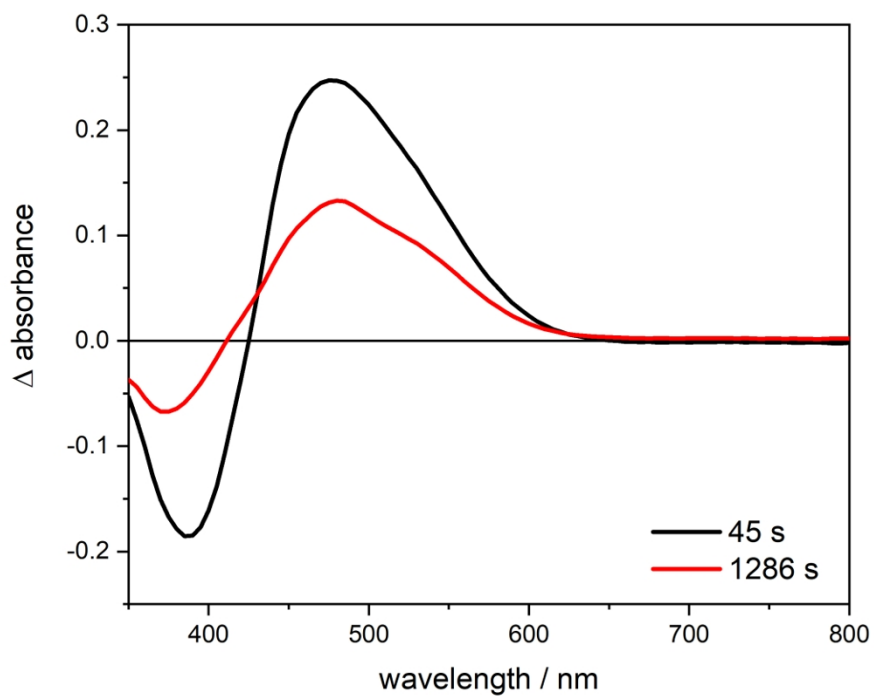


**Figure S13:** Decay-associated spectra (DAS) obtained by globally fitting the differential spectra obtained by measuring UV-Vis absorption spectra of **T2R**-sensitized NiO films under operando photoelectrochemical conditions with a two-component exponential function.

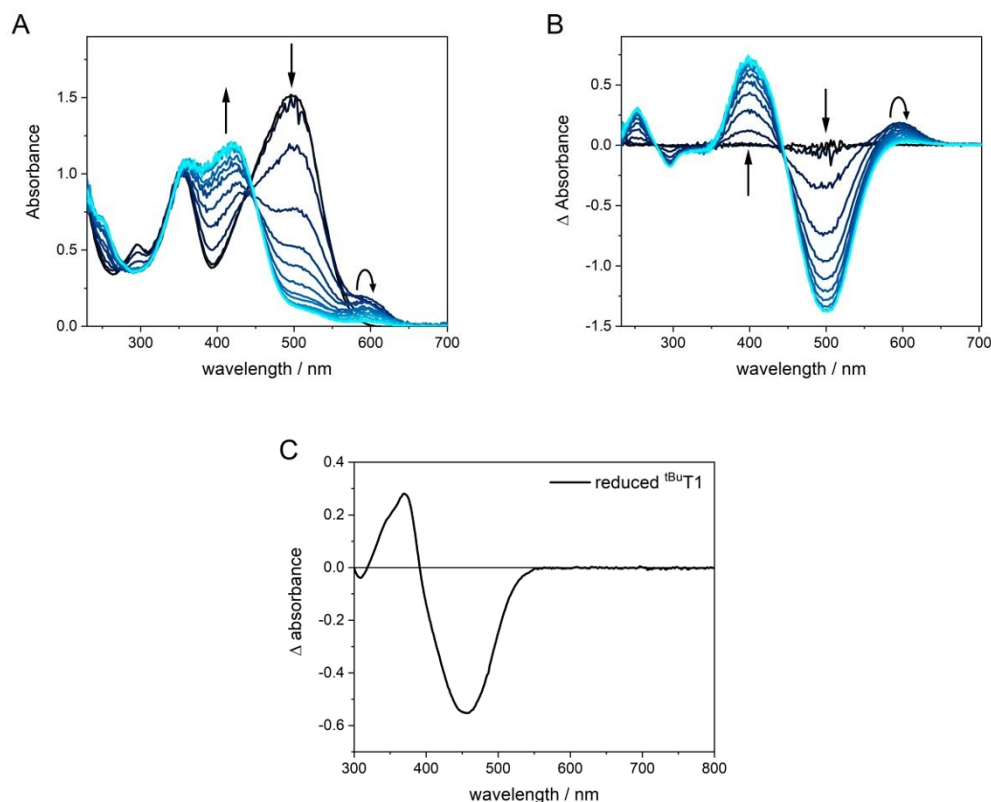


**Figure S14.** a) UV-Vis absorption spectra and b) differential spectra of **T2R** in 0.1 M TBABF<sub>4</sub> in ACN recorded while reducing the compound during a reductive LSV. c) UV-Vis absorption differential spectrum of <sup>t</sup>BuT1 while reducing the compound in a reductive chronoamperometry.

The measurement was started at a potential more positive than the dye<sup>0/-</sup> redox potential and then the potential was swepted towards more negative potentials at a rate of 10 mV/s. Spectra were taken every 7 s, corresponding to a potential difference of 70 mV between each spectra. The differential spectra were obtained by subtracting the absorption spectrum prior to reduction of the dye. The pronounced bleach at 500 nm and the positive band at 400 nm are caused by the degradation of **T2R** in its reduced state (i.e., produced by the degradation product), while the transient band at 600 nm is the band characteristic of the reduced state of the dye. Since the degradation of **T2R** in its reduced state occurs very quickly, the exact ratio of bleach to the band at 600 nm for the reduced dye itself cannot be determined by this steady state measurement.

To obtain the absorbance for the comparison with the photocurrent presented in Figure 7, several steps of data treatment were performed to determine and subtract the signal caused by the bare NiO film: using the ratio of signal at the absorption maximum at  $t = 0$  and  $t = 22$ h from the desorption of films and assuming a completed degradation process at the end of the operando UV-Vis experiment, the initial absorbance of **T2R-Cat1** on the film was determined. The absorption spectrum of **T2R-Cat1** was then normalized to this value and subtracted from the operando UV/Vis spectrum at  $t=0$  to obtain the spectrum of bare NiO. This spectrum was then subtracted from all operando UV/Vis spectra to obtain the spectra of the grafted species at each time  $t$ , which were then integrated from 400-800 nm. Finally, the values were normalized to the current at  $t = 50$  s.

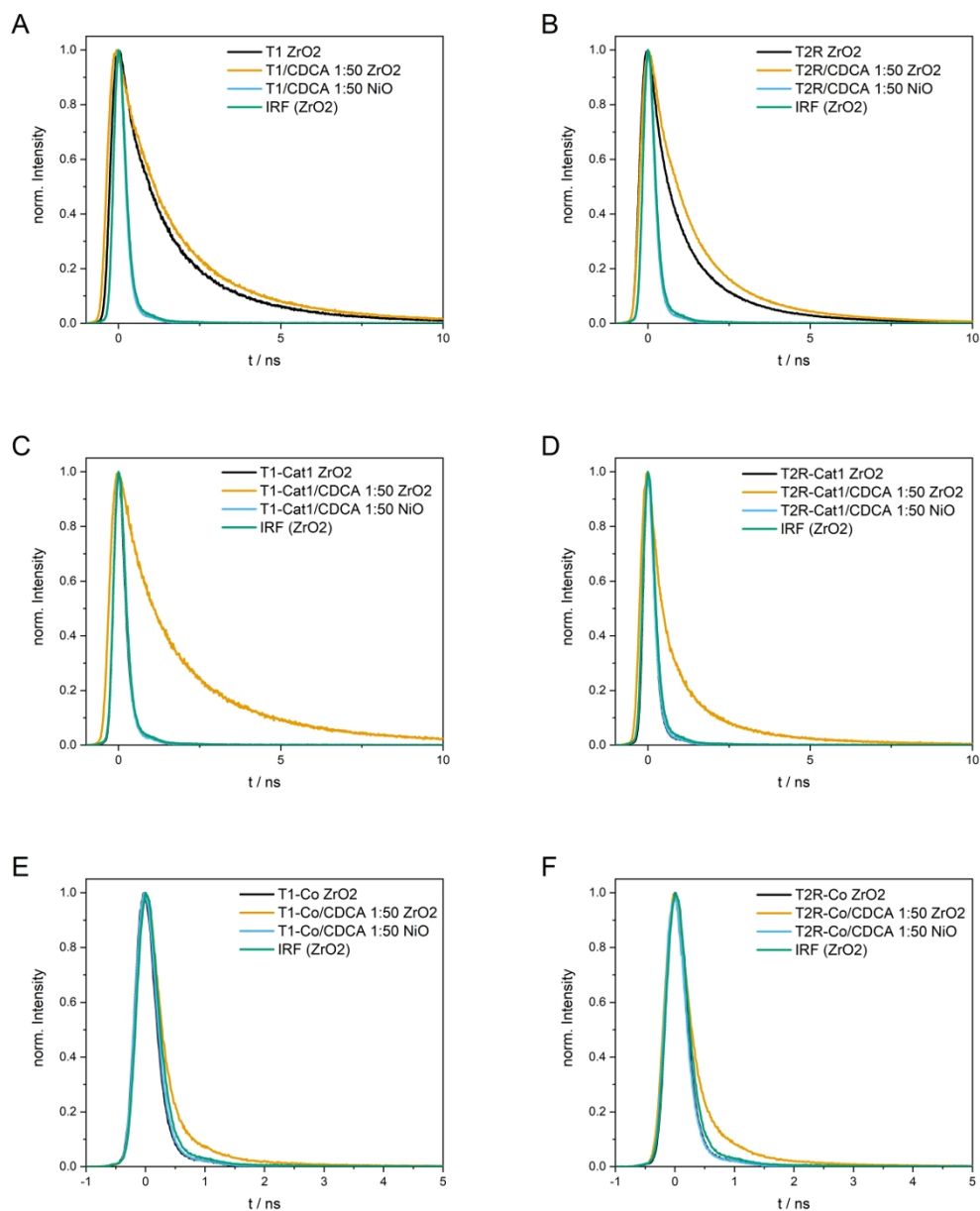


**Figure S15:** Emission decays of compounds **T1** (a), **T2R** (b), **T1-Cat1** (c), **T2R-Cat1** (d), **T1-Co** (e) and **T2R-Co** (f) on  $\text{ZrO}_2$  (black), co-sensitized with CDCA in a 1:50 ratio on  $\text{ZrO}_2$  (ochre) and on NiO (blue) as well as the instrument response function (green).

NiO and  $\text{ZrO}_2$  films were prepared by doctor-blading Solaronix nickel oxide and zirconium dioxide paste, respectively, on microscopic slides and sintering them at 450 °C for 30 min.  $\text{ZrO}_2$  is a metal oxide with a bandgap of 5 eV<sup>6</sup> into which no hole injection from the excited state of the dye is possible. Thus, sensitized  $\text{ZrO}_2$  films serve as redox inert standards to highlight the effect of dye immobilisation. The compounds were co-grafted with chenodeoxycholic acid (CDCA), a widely used co-grafting agent which prevents dye aggregation on film surfaces.<sup>7,8</sup>

The dyes grafted on ZrO<sub>2</sub> show a biexponential decay with excited state lifetimes  $\tau_1 \approx 400$  ps and  $\tau_2 \approx 2$  ns, with **T2R** having a slightly longer lifetime (Table S7). When linked to the cobalt complex in the dye-catalyst assemblies, quenching of the excited state is observed, to the point where it becomes faster than the instrumental response function of our setup (FWHM = 430 ps). Although such quenching could be related to electron transfer, we showed previously by transient absorption spectroelectrochemistry (TA-SEC) that for **T1-Co**, no electron transfer occurs in solution, suggesting other deactivation pathways such as energy transfer to cobalt states.<sup>9</sup> When co-sensitized with CDCA, the emission quenching is reduced to yield lifetimes in the hundreds of ps to ns region, indicating that the largest contribution to excited state quenching on ZrO<sub>2</sub> is due to intermolecular interactions. This effect is strongest for the **Cat1** dyads, while the **Co** dyads still display short lifetimes with the main component of around 100 ps. By contrast, NiO films co-sensitized with the dyads and CDCA show the same degree of quenching as non-co-grafted ZrO<sub>2</sub>, proving that hole injection takes place on a timescale of shorter than tens of picoseconds.

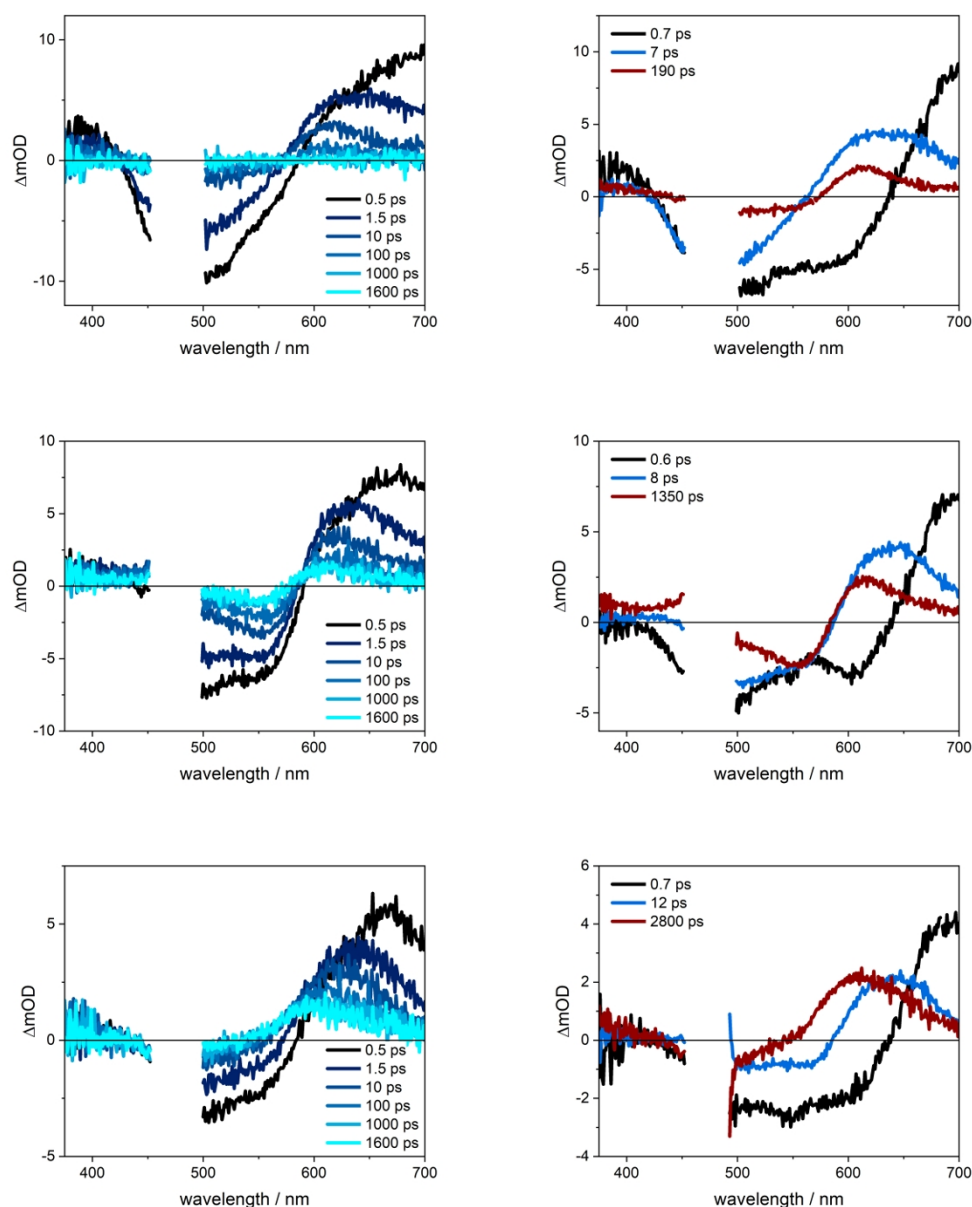


**Figure S16.** fs-TASEC data of a **T2R**-sensitized NiO film at OCP (top), -0.74 V (middle) and -1.15 V (bottom). Left: Transient absorption spectra at different pump-probe delays. Right: Decay-associated spectra obtained by sequential 3-component exponential fits.

At OCP (no applied potential), the fs-TA spectra initially show a ground-state bleach (GSB) between 425 and 575 nm and a broad excited state absorption (ESA) above 575 nm, resembling those recorded for the dye **T2R** in ACN (Figure S18). ESA above 650 nm and GSB decays in about 10 ps, leading to a transient spectrum with a maximum at 620 nm which decays in the accessible time window of 1.6 ns. In contrast to the situation in solution, where the excited-state lifetime is 2.3 ns, all excited-state processes on the film are completed within about 1 ns. In view of the favourable thermodynamics for hole injection and the very fast emission quenching observed, it seems reasonable to assume the fast excited state deactivation is due to hole injection followed by fast charge recombination. When

applying a three-component exponential fit to the data, the fastest component  $\tau_1$  (0.7 ps) shows loss of GSB and build-up of a positive band at 600 nm. This band can be assigned to the one-electron reduced state of the **T2R** dye (Figure S19), leading to the assignment of fast hole injection from the excited state of the dye to form  $\text{NiO}^+|\text{T2R}^-$ , in line with studies performed on **T1** and a related dye.<sup>10-13</sup> Note that the dye in solution shows a spectrally similar fast component without the loss of GSB, which is ascribed to thermalization of the initial excited state and can also be expected for the dye on the film. Thus, the first component on the film is most likely a mixture of hole injection and thermalization of the excited electron. The intermediate component  $\tau_2$  (7 ps) shows the spectral characteristics of deactivation of the excited state of the dye, albeit on a much faster scale than in solution. This fast deactivation can either occur via intermolecular interactions on the film surface or via hole injection coupled to fast recombination. Since the excited state decay of **T2R** on  $\text{ZrO}_2$  was only accelerated to 305 ps (Table S7), in line with literature reports of similar dyes,<sup>14,15</sup> it seems more likely that fast charge recombination is in fact responsible for the excited state decay. The decay of the  $\text{NiO}^+|\text{T2R}^-$  spectrum formed after completion of these processes, corresponding to charge recombination between the reduced dye and holes in NiO, takes place with a characteristic time constant of 188 ps, similar to that found for NiO films sensitized with the related **P1** dye.<sup>12,13</sup> When applying a reductive potential to the film, the spectral features as well as the initial kinetics remain essentially unchanged. The spectrum of the charge-separated state with the positive band at 600 nm, however, is much more long-lived than at OCP, reflected in a large increase in  $\tau_3$  as a function of applied reductive potential (1.3 and 2.8 ns at -0.74 and -1.15 V vs.  $\text{Fc}^{+/0}$ , respectively).

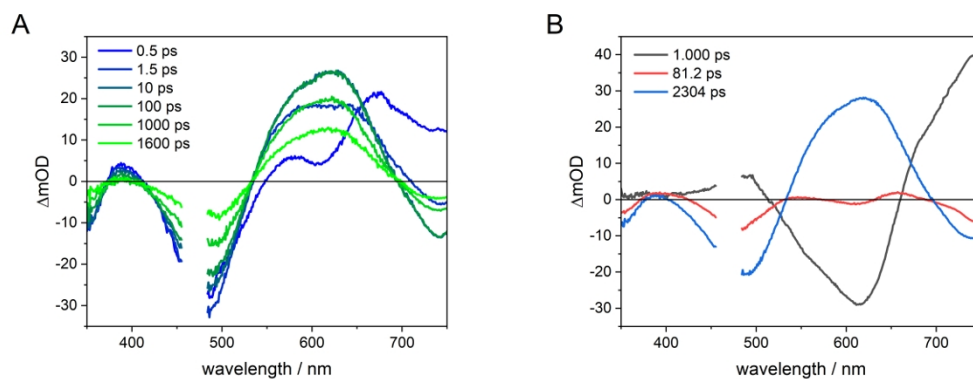


**Figure S17.** a) TA spectra of **T2R** in acetonitrile at different time delays up to 1.6 ns and b) the decay-associated spectra obtained with a sequential 3-component exponential fit.



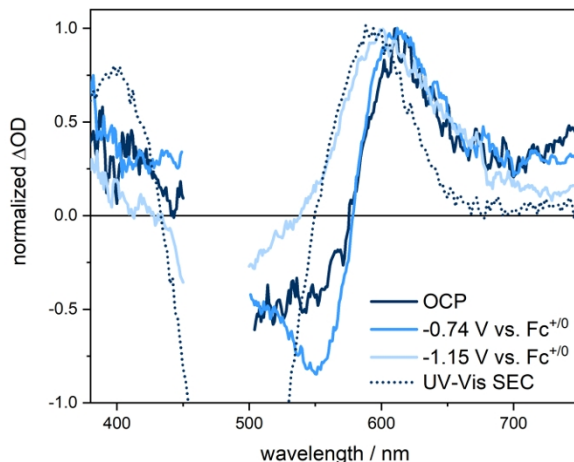


**Figure S18.** Transient absorption spectra of a **T2R**-sensitized film at OCP and at cathodic applied potentials as well as the UV-Vis absorption spectrum of the one-electron reduced dye **T2R** (from UV-Vis spectroelectrochemical measurements in solution, Figure S15).

The spectra were normalized to their absorption maximum around 600 nm. The TA-SEC spectra are the ones taken at 100 ps for the OCP and 1400 ps for the other measurements. The bleach of the charge-transfer band (at 493 nm) of **T2R** in the UV-Vis SEC experiment is more pronounced since the compound is unstable in its reduced form and undergoes a quick degradation reaction leading to loss of absorbance. This bleach therefore does not represent the spectral shape expected in the TA-SEC experiment, rather, the band at 620 nm is the characteristic band for their reduced dye that appears in the TA-SEC experiments.

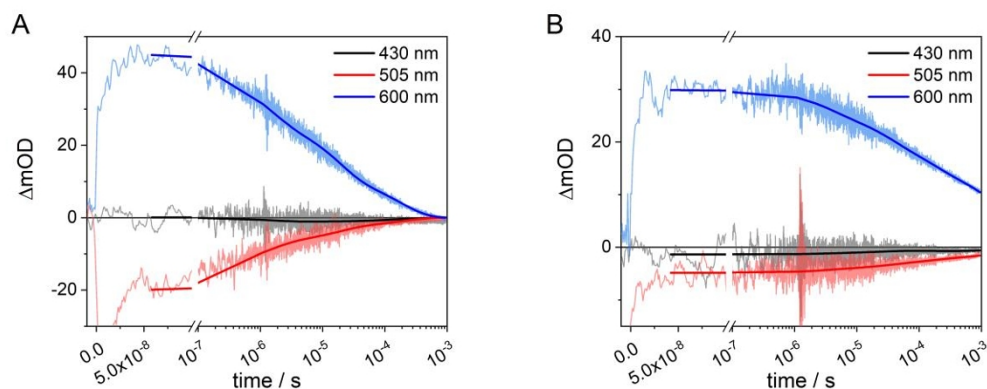


**Figure S19.** ns-TASEC data of **T2R**-sensitized films at a)  $-0.74$  V vs  $\text{Fc}^{+/0}$  and b)  $-1.15$  V vs  $\text{Fc}^{+/0}$ , at characteristic wavelengths: 430 nm (black), 505 nm (red) and 600 nm (blue).

Kinetic traces in the ns- $\mu$ s scale were measured at the characteristic wavelengths of the charge-separated state at 600 and 505 nm at identical applied potentials. A long-lived signal was observed which decayed in a non-exponential fashion, as observed before for charge recombination in dye-sensitized NiO films.<sup>16–20</sup> At  $-0.74$  V vs.  $\text{Fc}^{+/0}$ , the signal completely decays within 1 ms, while it becomes significantly longer lived at  $-1.15$  V vs.  $\text{Fc}^{+/0}$ .

The lower signal intensity at more negative applied potential is likely due to degradation of the dye in its reduced state during the experiment: As the charge-separated state has a longer lifetime at more negative applied potential, this damage is expected to be more severe, even though the duration of the experiment was reduced as much as possible to avoid this.



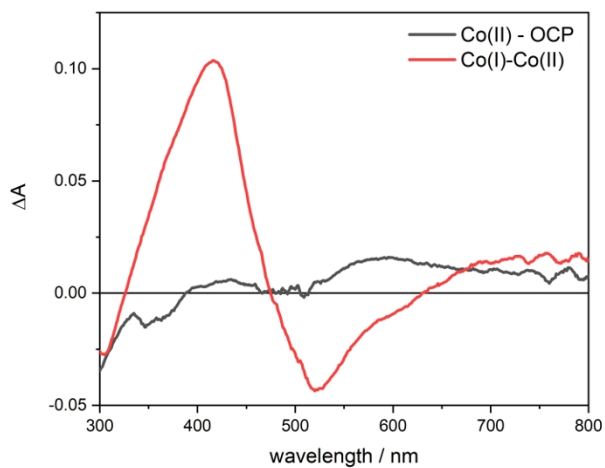


**Figure S20.** Differential UV-Vis SEC spectra of **T2R-Cat1** in 0.1M TBABF<sub>4</sub> in dry ACN upon reduction to the Co<sup>II</sup> and Co<sup>I</sup> state.

The spectra shown are the differential spectra for each reduction step, reflecting the spectral change that is expected upon photoinduced electron transfer in the TA-SEC experiments.

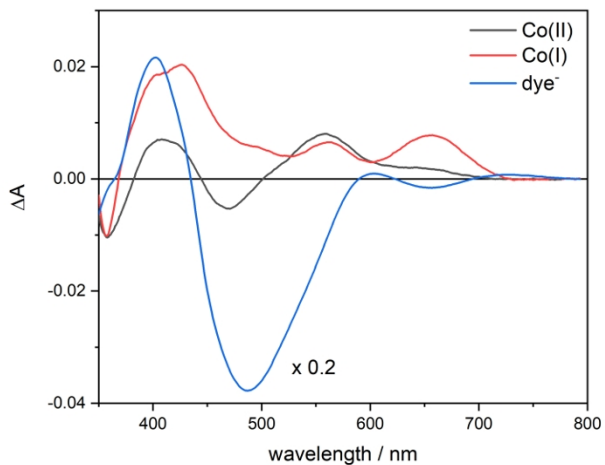


**Figure S21.** Differential UV-Vis SEC spectra of **T2R-Cat1**-sensitized NiO films in 0.1M TBABF<sub>4</sub> in dry ACN applying consecutively more reductive potentials sufficient to first reduce the cobalt catalyst to its Co<sup>II</sup> (black, -0.74 V vs Fc<sup>+0</sup>) and Co<sup>I</sup> (red, -1.15 V vs. Fc<sup>+0</sup>) state and then the dye to the one-electron reduced state (blue, -1.63 V vs. Fc<sup>+0</sup>).

The spectra shown are the differential spectra for each reduction step, reflecting the spectral change that is expected upon photoinduced electron transfer in the TA-SEC experiments. This does not hold true for reduction of the dye as the spectral response is produced by modification of the reduced dye rather than the reduced species itself.

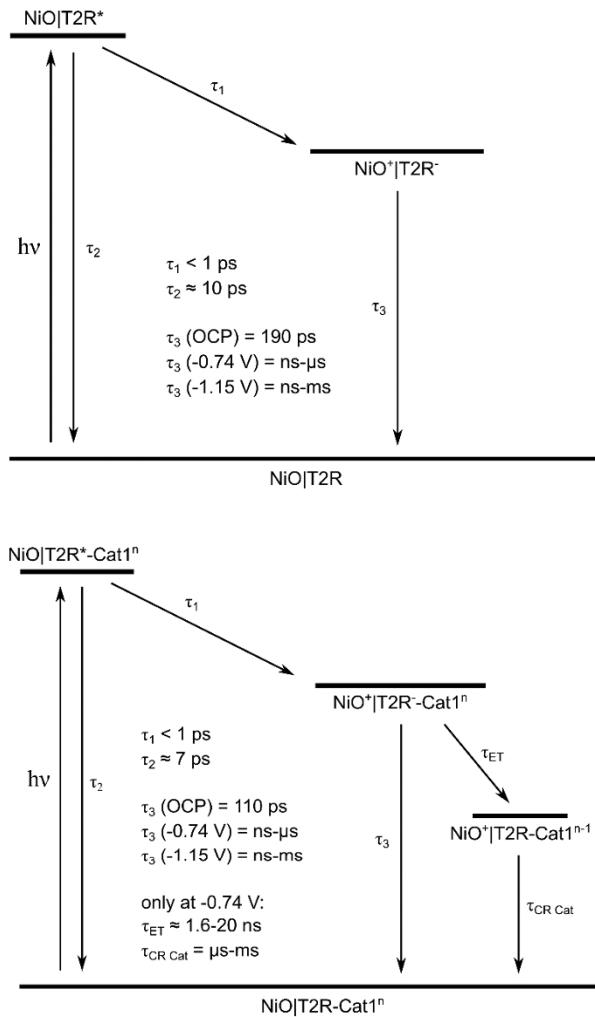


**Figure S22.** Jablonski scheme summarizing the light-induced processes in **T2R-** (top) and **T2R-Cat1-**sensitized (bottom) NiO films at different applied potentials.

**Table S1.** Photophysical and redox properties of **Cat1**, **Co**, <sup>t</sup>Bu**T1**, <sup>t</sup>Bu**T2R**, <sup>t</sup>Bu**T1-Cat1**, <sup>t</sup>Bu**T2R-Cat1** and <sup>t</sup>Bu**T2R-Co**.

	$\lambda_{Abs}$ ( $\pi-\pi^*$ ) <sup>a</sup>	$\epsilon$ ( $\pi-\pi^*$ ) / $M^{-1}\cdot cm^{-1}$	$\lambda_{Abs}$ (ICT) <sup>a</sup>	$\epsilon$ (ICT) / $M^{-1}\cdot cm^{-1}$	$\lambda_{Em}^a$	$E_{ox}^b$ (Dye <sup>0/0+</sup> )	$E_{ox}^{2b}$ (Dye <sup>2+/2+</sup> )	$E_{red}^b$ (Co <sup>III/II</sup> )	$E_{red}^{2b}$ (Co <sup>III/II</sup> )	$E_{red}^{3b}$ (Dye <sup>0/-</sup> )	$E_{0-0}^c$	$\Delta G_{inj}^d$	$\Delta G_1^e$	$\Delta G_2^f$
<b>Cat1</b>														
<b>Co</b>														
<sup>t</sup> Bu <b>T1</b>	354	29882	448	27666	649	1.25				-1.04	2.31	-0.81		
<sup>t</sup> Bu <b>T2R</b>	355	31060	499	57374	674	1.05	1.23			-1.00	2.15	-0.61		
<sup>t</sup> Bu <b>T1-Cat1</b>	354	32131	431	16707	615	1.21				-1.08	2.45	-0.91	-1.12	-0.62
<sup>t</sup> Bu <b>T2R-Cat1</b>	355	36900	493	57435	660	1.00	1.15			-1.08	2.17	-0.63	-1.09	-0.66
<sup>t</sup> Bu <b>T1-Co</b>	353	35451	433	30884	615	1.25 <sup>23</sup>				-1.07 <sup>23</sup>	2.40	-0.87	-1.09	-0.62
<sup>t</sup> Bu <b>T2R-Co</b>	355	32196	495	53287	662	1.02	1.19			-1.10	2.17	-0.61	-1.13	-0.64

a) Maximum absorption and emission wavelengths in nm recorded in DMF for all **T1** systems and in MeOH for all **T2R** systems – see Figure 2.

b) In V vs NHE.  $1/2(E_{pc} + E_{pa})$  for Ered<sub>1</sub> and Ered<sub>2</sub>;  $E_{pc}$  for Ered<sub>3</sub>; The redox potentials were converted from Fc<sup>+/0</sup> (Figure 1, S1) to NHE, obtained from the reduction potential considering  $E^\circ(Fc^{+/0}) = 0.53$  V vs. NHE in ACN;  $E^\circ(Fc^{+/0}) = 0.57$  V vs. NHE in DMF. Unless otherwise indicated, the data was recorded in DMF.

c) 0–0 transition energy,  $E_{0-0}$ , in eV, estimated from the intercept of the normalized absorption and emission spectra.

d) in eV, at pH = 5.5. The Gibbs free energy for the hole injection reaction was calculated according to  $\Delta G_{inj} = e[E_{FB}(NiO) - E(Dye^{0/-})]$ ; with  $E_{FB}(NiO) = +0.46$  V vs NHE (see below) and  $E(Dye^{0/-}) = E(Dye^{0/+}) + E_{0-0}$ .

e) The Gibbs free energy in eV for the electron transfer from the reduced dye to the Co(III) catalyst was calculated according to  $\Delta G_1 = e[E(Dye^{0/-}) - E(Co^{III/II})]$

f) The Gibbs free energy in eV for the electron transfer from the reduced dye to the Co(II) catalyst was calculated according to  $\Delta G_2 = e[E(Dye^{0/-}) - E(Co^{II/I})]$

The flat band potential of NiO at pH 5.5 was calculated according to the following formula taken from <sup>24</sup>:

$$E_{FB \text{ vs. NHE}} = 0.37 \text{ V} + 0.059 (7 - pH)$$

**Table S2.** Film thickness measured of three batches of NiO films by Scanning Electron Microscopy (SEM).

Batch	Thickness / nm
NiO9	690
NiO13	1094
NiO14	847
Average	$877 \pm 167$



**Table S3.** Extinction coefficient maxima positions and values for the  $\pi$ - $\pi^*$  and ICT bands in the studied dyes and dyads in 1M PPA solutions.

Sample	$\lambda_{\max}$ ( $\pi$ - $\pi^*$ ) / nm	$\epsilon_{\max}$ ( $\pi$ - $\pi^*$ ) / $M^{-1} cm^{-1}$	$\lambda_{\max}$ (ICT) / nm	$\epsilon_{\max}$ (ICT) / $M^{-1} cm^{-1}$	Solvent
<b>T1</b>	351	32269	441	33837	1M PPA in MeOH
<b>T2R</b>	356	29402	500	40649	1M PPA in MeOH
<b>T1-Cat2</b>	339	25605	428	20661	1M PPA in MeOH
<b>T1-Cat1</b>	352	34057	433	13505	1M PPA in DMF
<b>T2R-Cat2</b>	352	29435	494	37914	1M PPA in MeOH
<b>T2R-Cat1</b>	354	29518	495	44298	1M PPA in MeOH

**Table S4.** H<sub>2</sub> measurements during the course and at the end of the chronoamperometric measurements (MES buffer, pH 5.5, continuous visible light irradiation, applied potential: +0.14 V vs RHE)

	Time	Surface Area / cm <sup>2</sup>	Dyad loading / nmol·cm <sup>-2</sup>	H <sub>2</sub> in the headspace / nmol	H <sub>2</sub> in solution / nmol	Total amount H <sub>2</sub> / nmol	Total amount H <sub>2</sub> / nmol·cm <sup>-2</sup>	Charge passed / mC·cm <sup>-2</sup>	FE / %	TON <sup>(a)</sup>
NiO	2h	3.3		0	2.9	2.9	0.9	2.3	7.2	
	2h	3.0		0	1.2	1.2	0.4	2.7	3.0	
	average	<b>3.1 ± 0.2</b>		<b>0 ± 0</b>	<b>2.1 ± 1.2</b>	<b>2.1 ± 1.2</b>	<b>0.6 ± 0.3</b>	<b>2.5 ± 0.3</b>	<b>5.1 ± 3</b>	
	4h	2.9	6.2	18.3	19.8	38.1	13.1	10.0	25.5	2.1
NiO/T1	4h	3.1	4.9	11.1	13.4	24.6	7.9	5.2	29.0	1.6
	4h	2.7	5.5	3.6	12.4	16.1	5.9	8.9	12.8	1.1
	average	<b>2.9 ± 0.2</b>	<b>5.5 ± 0.7</b>	<b>11 ± 7.3</b>	<b>15.2 ± 4</b>	<b>26.3 ± 11.1</b>	<b>9 ± 3.8</b>	<b>8 ± 2.5</b>	<b>22 ± 9</b>	<b>1.6 ± 0.5</b>
	22h	2.9	6.2	32.6	14.4	47.0	16.2	40.4	7.8	2.6
NiO/T2R	22h	3.1	4.9	23.8	7.0	30.8	9.9	30.3	6.3	2.0
	22h	2.7	5.5	10.2	6.5	16.8	6.1	48.4	2.4	1.1
	average	<b>2.9 ± 0.2</b>	<b>5.5 ± 0.7</b>	<b>22.2 ± 11.3</b>	<b>9.3 ± 4.4</b>	<b>31.5 ± 15.2</b>	<b>10.7 ± 5.1</b>	<b>39.7 ± 9</b>	<b>5 ± 3</b>	<b>1.9 ± 0.8</b>
	4h	2.6	7.9	32.4	29.5	62.0	23.8	18.2	25.3	3.0
NiO/T1-Cat1	4h	3.0	5.4	6.1	12.0	18.1	6.0	12.1	9.6	1.1
	4h	2.9	7.7	22.6	15.0	37.6	12.8	10.5	23.5	1.7
	average	<b>2.9 ± 0.2</b>	<b>7 ± 1.4</b>	<b>20.4 ± 13.3</b>	<b>18.8 ± 9.4</b>	<b>39.2 ± 22</b>	<b>14.2 ± 9</b>	<b>13.6 ± 4.1</b>	<b>19 ± 9</b>	<b>1.9 ± 1</b>
	22h	2.6	7.9	36.9	17.7	54.6	20.9	102.7	3.9	2.7
NiO/T1-Cat1	22h	3.0	5.4	12.7	8.1	20.8	6.9	60.9	2.2	1.3
	22h	2.9	7.7	44.1	6.4	50.5	17.1	51.5	6.4	2.2
	average	<b>2.9 ± 0.2</b>	<b>7 ± 1.4</b>	<b>31.2 ± 16.5</b>	<b>10.7 ± 6.1</b>	<b>41.9 ± 18.4</b>	<b>15 ± 7.3</b>	<b>71.7 ± 27.3</b>	<b>4 ± 2</b>	<b>2.1 ± 0.7</b>
	4h	3.4	6.6	204.1	133.5	337.7	99.0	24.6	77.7	15.0
NiO/T1-Cat1	4h	3.1	8.4	205.7	127.8	333.5	107.9	29.0	71.7	12.8
	4h	3.1	6.5*	183.7	61.1	244.8	79.6	33.0	46.6	12.3
	average	<b>3.2 ± 0.2</b>	<b>7.2 ± 1.1</b>	<b>198 ± 12</b>	<b>107 ± 40</b>	<b>305 ± 52</b>	<b>96 ± 14</b>	<b>29 ± 4</b>	<b>65 ± 17</b>	<b>13.4 ± 1.4</b>
	22h	3.4	6.6	495.8	49.4	545.2	159.9	88.2	35.0	24.2

	22h	3.1	8.4	494.9	69.3	564.2	182.6	118.7	29.7	21.7
	22h	3.1	6.5 <sup>b)</sup>	403.8	35.9	439.7	143.0	101.7	27.1	22.1
	average	<b>3.2 ± 0.2</b>	<b>7.2 ± 1.1</b>	<b>465 ± 53</b>	<b>52 ± 17</b>	<b>516 ± 67</b>	<b>162 ± 20</b>	<b>103 ± 15</b>	<b>31 ± 4</b>	<b>22.7 ± 1.4</b>
NiO T2R-Cat1	4h	3.3	11.8	395.7	275.4	671.1	206.5	55.1	72.3	17.5
	4h	3.3	13.5	420.7	306.8	727.5	220.5	57.0	74.7	16.3
	4h	3.1	6.6	337.2	169.3	506.5	162.7	55.0	57.1	24.7
	4h	3.1	5.9	394.9	165.8	560.8	180.4	52.9	65.9	30.6
	4h	3.0	9.2	393.2	196.0	589.2	196.4	62.4	60.7	21.4
	4h	3.0	10.8	325.9	148.4	474.3	156.2	47.8	63.0	14.4
	average	<b>3.1 ± 0.1</b>	<b>9.6 ± 3.0</b>	<b>378 ± 38</b>	<b>210 ± 65</b>	<b>588 ± 97</b>	<b>187 ± 25</b>	<b>55 ± 5</b>	<b>66 ± 7</b>	<b>20.8 ± 6.0</b>
	22h	3.3	11.8	1017.8	75.4	1093.2	336.4	207.1	31.3	28.5
	22h	3.3	13.5	1749.3	216.5	1965.8	595.7	226.1	50.8	44.1
	22h	3.1	6.6	730.5	64.6	795.2	255.4	162.3	30.4	38.7
	22h	3.1	5.9	876.7	68.4	945.2	304.1	129.0	45.5	51.5
	22h	2.9	11.7	1017.0	123.2	1140.1	397.0	196.0	39.1	33.9
	22h	2.8	8.2	752.2	77.8	830.0	301.4	162.9	35.7	36.7
	average	<b>3.1 ± 0.2</b>	<b>9.6 ± 3.1</b>	<b>1024 ± 376</b>	<b>104 ± 59</b>	<b>1128 ± 433</b>	<b>365 ± 122</b>	<b>181 ± 36</b>	<b>39 ± 8</b>	<b>38.9 ± 8.1</b>
NiO T1-Co	4h	3.2	14.2	18.7	16.5	35.1	11.2	26.5	8.1	0.8
	4h	3.3	15.1	16.5	17.5	34.0	10.3	22.9	9.1	0.7
	average	<b>3.2 ± 0.1</b>	<b>14.7 ± 0.6</b>	<b>18 ± 2</b>	<b>17 ± 1</b>	<b>35 ± 1</b>	<b>11 ± 1</b>	<b>25 ± 3</b>	<b>9 ± 1</b>	<b>0.7 ± 0.1</b>
	22h	3.2	14.2	25.8	22.5	48.3	15.3	100.8	2.9	1.1
	22h	3.3	15.1	25.3	7.8	33.1	10.0	74.5	2.7	0.7
	average	<b>3.2 ± 0.1</b>	<b>14.7 ± 0.6</b>	<b>26 ± 0</b>	<b>15 ± 10</b>	<b>41 ± 11</b>	<b>13 ± 4</b>	<b>88 ± 19</b>	<b>3 ± 0</b>	<b>0.9 ± 0.3</b>
NiO T2R-Co	4h	3.0	7.5	20.7	12.9	33.6	11.0	17.9	11.9	1.5
	4h	3.3	6	17.1	11.4	28.5	8.6	17.4	9.6	1.4
	average	<b>3.2 ± 0.2</b>	<b>6.8 ± 1.1</b>	<b>19 ± 3</b>	<b>12 ± 1</b>	<b>31 ± 4</b>	<b>10 ± 2</b>	<b>18 ± 0</b>	<b>11 ± 2</b>	<b>1.5 ± 0</b>
	22h	3.0	7.5	37.8	0.0	37.8	12.4	52.4	4.6	1.7
	22h	3.3	6	22.5	4.4	26.8	8.1	82.0	1.9	1.4

	<b>average</b>	<b>3.2 ± 0.2</b>	<b>6.8 ± 1.1</b>	<b>30 ± 11</b>	<b>2 ± 3</b>	<b>32 ± 8</b>	<b>10 ± 3</b>	<b>67 ± 21</b>	<b>3 ± 2</b>	<b>1.5 ± 0.2</b>
--	----------------	------------------	------------------	----------------	--------------	---------------	---------------	----------------	--------------	------------------

a) The TON given for NiO films sensitized with the dyes **T1** and **T2R** are normalized to the amount of dye grafted on the film. As there is no catalyst, the TON does not reflect a catalytic process but is rather given to ease comparison with dyad-sensitized NiO films.

b) We failed to measure the dye loading of this film and therefore used the average dye loading of **T1-Cat1**-sensitized films.

**Table S5:** Co surface concentration as determined by ICP-MS for **T2R-Cat1**-sensitized films after 0, 4 and 22 h of PEC experiment. For comparison between the two techniques, the grafting densities determined of the same films by UV-Vis absorption are given.

	Grafting density / nmol·cm <sup>-2</sup>				Co loss / %
	0 h (UV-Vis)	0 h (ICP)	4 h (ICP)	22 h (ICP)	
4 h PEC experiment	9.1	6.0	1.0		84
22 h PEC experiment	11.6	13.3		1.0	93

**Table S6:** Average grafting density of active **T2R-Cat1** dyads over the first 4 hours of PEC experiments, calculated based on the integral of the photocurrent and the initial surface concentration, and turn-over numbers for the active dyads.

PEC experiment	Average active dyad surface concentration / nmol·cm <sup>-2</sup>	TON of active dyads
1	2.5	82.6
2	2.5	87.8
3	1.5	111.4
4	1.6	112.1
5	2.1	95.3
6	2.2	72.6
<b>Average</b>	<b>2.0 ± 0.4</b>	<b>93.6 ± 15.9</b>

**Table S7:** Emission lifetimes obtained by fitting the time-resolved emission data of all dyes and dyads grafted on ZrO<sub>2</sub> as well as co-grafted with chenodeoxycholic acid (CDCA) in a 1:50 ratio on ZrO<sub>2</sub> and on NiO. The data was fitted with a mono- or biexponential fit. In case of the biexponential fits,  $\alpha$  gives the amplitude of the first component.

		ZrO <sub>2</sub>		ZrO <sub>2</sub> CDCA 50:1		NiO CDCA 50:1
		t / ps	$\alpha$	t / ps	$\alpha$	t / ps
<b>T1</b>	$\tau_1$	523	0.68	790	0.68	51
	$\tau_2$	2314		2819		
<b>T2R</b>	$\tau_1$	305	0.76	555	0.72	52
	$\tau_2$	1680		2064		
<b>T1-Cat1</b>	$\tau_1$	40		756	0.73	42
	$\tau_2$			3328		
<b>T2R-Cat1</b>	$\tau_1$	37		274	0.88	43
	$\tau_2$			2013		
<b>T1-Co</b>	$\tau_1$	42		117	0.98	47
	$\tau_2$			893		
<b>T2R-Co</b>	$\tau_1$	43		47	0.97	42
	$\tau_2$			682		

**Table S8.** Characteristic time constants obtained by applying multiexponential fits of the form

$$\Delta A(\lambda, t) = \sum_1^n A_i(\lambda) * e^{-\frac{t}{\tau_i}}$$

to the fs- and ns-TASEC data (global fit for the fs-TASEC data, ns-TASEC data as indicated), where  $n$  is the number of components,  $A_i$  are the wavelength-dependent amplitudes and  $\tau_i$  are the characteristic lifetimes of the processes.

The average lifetimes were calculated of the ns-TA data using the formula:

$$\tau_{ave} = \frac{\sum A_i \tau_i}{\sum A_i}$$

Where there was a need to fit an infinite component, the relative amplitudes of the average lifetime and the infinite component is given in parentheses.

System	Applied potential vs. $Fc^{+0}$	fs-TASEC data			Wavelength	$\tau_1 / \mu s$	$\tau_2 / \mu s$	$\tau_3 / \mu s$	$\tau_4 / \mu s$	$\tau_{ave} / \mu s$
		$\tau_1 / ps$	$\tau_2 / ps$	$\tau_3 / ps$						
<b>T2R</b>	OCP	0.7	7	190						
	-0.74 V	0.6	8	1350	global	0.13	1.7	20	194	28
	-1.15 V	0.7	12	2800	global	3.5	37	383	Infinite (33 %)	184 (67 %)
<b>T2R-Cat1</b>	OCP	0.5	5	110						
	-0.74 V	0.6	8	2300	430	1.2	13	123	Infinite (16 %)	30 (84 %)
					505, 620	0.13	1.7	22	295	6.8
-1.15 V	0.5	9	3300	global	1.4	22	294	Infinite (27 %)	131 (73 %)	



**References.**

- (1) Yen, Y.-S.; Chen, W.-T.; Hsu, C.-Y.; Chou, H.-H.; Lin, J. T.; Yeh, M.-C. P. Arylamine-Based Dyes for p-Type Dye-Sensitized Solar Cells. *Organic Letters* **2011**, *13* (18), 4930–4933. <https://doi.org/10.1021/ol202014x>.
- (2) Huang, B.; Prantil, M. A.; Gustafson, T. L.; Parquette, J. R. The Effect of Global Compaction on the Local Secondary Structure of Folded Dendrimers. *Journal of the American Chemical Society* **2003**, *125* (47), 14518–14530. <https://doi.org/10.1021/ja037895a>.
- (3) Dumont, A.; Jacques, V.; Desreux, J. F. New Synthons for the Synthesis of Lanthanide Containing Macrocyclic Schiff Bases Featuring Substituents Available for Tethering. *Tetrahedron* **2000**, *56* (14), 2043–2052. [https://doi.org/10.1016/S0040-4020\(00\)00104-6](https://doi.org/10.1016/S0040-4020(00)00104-6).
- (4) Boschloo, G.; Hagfeldt, A. Spectroelectrochemistry of Nanostructured NiO. *Journal of Physical Chemistry B* **2001**, *105* (15), 3039–3044. <https://doi.org/10.1021/jp003499s>.
- (5) Xia, X. H.; Tu, J. P.; Zhang, J.; Wang, X. L.; Zhang, W. K.; Huang, H. Morphology Effect on the Electrochromic and Electrochemical Performances of NiO Thin Films. *Electrochimica Acta* **2008**, *53* (18), 5721–5724. <https://doi.org/10.1016/j.electacta.2008.03.047>.
- (6) Xu, Y.; Schoonen, M. A. A. The Absolute Energy Positions of Conduction and Valence Bands of Selected Semiconducting Minerals. *American Mineralogist* **2000**, *85* (3–4), 543–556. <https://doi.org/10.2138/am-2000-0416>.
- (7) Ito, S.; Miura, H.; Uchida, S.; Takata, M.; Sumioka, K.; Liska, P.; Comte, P.; Péchy, P.; Grätzel, M. High-Conversion-Efficiency Organic Dye-Sensitized Solar Cells with a Novel Indoline Dye. *Chemical Communications* **2008**, No. 41, 5194. <https://doi.org/10.1039/b809093a>.
- (8) Favereau, L.; Warnan, J.; Pellegrin, Y.; Blart, E.; Boujtita, M.; Jacquemin, D.; Odobel, F. Diketopyrrolopyrrole Derivatives for Efficient NiO-Based Dye-Sensitized Solar Cells. *Chemical Communications* **2013**, *49* (73), 8018. <https://doi.org/10.1039/c3cc44232b>.
- (9) Bold, S.; Zedler, L.; Zhang, Y.; Massin, J.; Artero, V.; Chavarot-Kerlidou, M.; Dietzek, B. Electron Transfer in a Covalent Dye–Cobalt Catalyst Assembly – a Transient Absorption Spectroelectrochemistry Perspective. *Chemical Communications* **2018**, *54* (75), 10594–10597. <https://doi.org/10.1039/C8CC05556D>.
- (10) Pati, P. B.; Zhang, L.; Philippe, B.; Fernández-Terán, R.; Ahmadi, S.; Tian, L.; Rensmo, H.; Hammarström, L.; Tian, H. Insights into the Mechanism of a Covalently Linked Organic Dye–Cobaloxime Catalyst System for Dye-Sensitized Solar Fuel Devices. *ChemSusChem* **2017**, *10* (11), 2480–2495. <https://doi.org/10.1002/cssc.201700285>.
- (11) Massin, J.; Bräutigam, M.; Bold, S.; Wächtler, M.; Pavone, M.; Muñoz-García, A. B.; Dietzek, B.; Artero, V.; Chavarot-Kerlidou, M. Investigating Light-Driven Hole Injection and Hydrogen Evolution Catalysis at Dye-Sensitized NiO Photocathodes: A Combined Experimental–Theoretical Study. *The Journal of Physical Chemistry C* **2019**, *123* (28), 17176–17184. <https://doi.org/10.1021/acs.jpcc.9b04715>.
- (12) Qin, P.; Wiberg, J.; Gibson, E. A.; Linder, M.; Li, L.; Brinck, T.; Hagfeldt, A.; Albinsson, B.; Sun, L. Synthesis and Mechanistic Studies of Organic Chromophores with Different Energy Levels for P-Type Dye-Sensitized Solar Cells. *The Journal of Physical Chemistry C* **2010**, *114* (10), 4738–4748. <https://doi.org/10.1021/jp911091n>.
- (13) Black, F. A.; Clark, C. A.; Summers, G. H.; Clark, I. P.; Towrie, M.; Penfold, T.; George, M. W.; Gibson, E. A. Investigating Interfacial Electron Transfer in Dye-Sensitized NiO Using Vibrational Spectroscopy.

- Physical Chemistry Chemical Physics* **2017**, *19* (11), 7877–7885.  
<https://doi.org/10.1039/C6CP05712H>.
- (14) Oum, K.; Lohse, P. W.; Klein, J. R.; Flender, O.; Scholz, M.; Hagfeldt, A.; Boschloo, G.; Lenzer, T. Photoinduced Ultrafast Dynamics of the Triphenylamine-Based Organic Sensitizer D35 on TiO<sub>2</sub>, ZrO<sub>2</sub> and in Acetonitrile. *Physical Chemistry Chemical Physics* **2013**, *15* (11), 3906.  
<https://doi.org/10.1039/c3cp44095h>.
- (15) Dryza, V.; Bieske, E. J. Does the Triphenylamine-Based D35 Dye Sensitizer Form Aggregates on Metal-Oxide Surfaces? *Journal of Photochemistry and Photobiology A: Chemistry* **2015**, *302*, 35–41.  
<https://doi.org/10.1016/j.jphotochem.2015.01.007>.
- (16) D'Amario, L.; Antila, L. J.; Pettersson Rimgard, B.; Boschloo, G.; Hammarström, L. Kinetic Evidence of Two Pathways for Charge Recombination in NiO-Based Dye-Sensitized Solar Cells. *The Journal of Physical Chemistry Letters* **2015**, *6* (5), 779–783. <https://doi.org/10.1021/acs.jpcclett.5b00048>.
- (17) Dillon, R. J.; Alibabaei, L.; Meyer, T. J.; Papanikolas, J. M. Enabling Efficient Creation of Long-Lived Charge-Separation on Dye-Sensitized NiO Photocathodes. *ACS Applied Materials & Interfaces* **2017**, *9* (32), 26786–26796. <https://doi.org/10.1021/acsmi.7b05856>.
- (18) Lindquist, R. J.; Majewski, M. B.; Hoffeditz, W. L.; Phelan, B. T.; Farha, O. K.; Hupp, J. T.; Wasielewski, M. R. Photodriven Hydrogen Evolution by Molecular Catalysts Using Al<sub>2</sub>O<sub>3</sub>-Protected Perylene-3,4-Dicarboximide on NiO Electrodes. *Chem. Sci.* **2017**, *8* (1), 541–549.  
<https://doi.org/10.1039/C6SC02477G>.
- (19) Antila, L. J.; Ghamgosar, P.; Maji, S.; Tian, H.; Ott, S.; Hammarström, L. Dynamics and Photochemical H<sub>2</sub> Evolution of Dye–NiO Photocathodes with a Biomimetic FeFe-Catalyst. *ACS Energy Letters* **2016**, *1* (6), 1106–1111. <https://doi.org/10.1021/acseenergylett.6b00506>.
- (20) Gardner, J. M.; Beyler, M.; Karnahl, M.; Tschierlei, S.; Ott, S.; Hammarström, L. Light-Driven Electron Transfer between a Photosensitizer and a Proton-Reducing Catalyst Co-Adsorbed to NiO. *Journal of the American Chemical Society* **2012**, *134* (47), 19322–19325. <https://doi.org/10.1021/ja3082268>.
- (21) Varma, S.; Castillo, C. E.; Stoll, T.; Fortage, J.; Blackman, A. G.; Molton, F.; Deronzier, A.; Collomb, M.-N. Efficient Photocatalytic Hydrogen Production in Water Using a Cobalt(III) Tetraaza-Macrocyclic Catalyst: Electrochemical Generation of the Low-Valent Co(I) Species and Its Reactivity toward Proton Reduction. *Physical Chemistry Chemical Physics* **2013**, *15* (40), 17544.  
<https://doi.org/10.1039/c3cp52641k>.
- (22) Jacques, P.-A.; Artero, V.; Pecaut, J.; Fontecave, M. Cobalt and Nickel Diimine-Dioxime Complexes as Molecular Electrocatalysts for Hydrogen Evolution with Low Overpotentials. *Proceedings of the National Academy of Sciences* **2009**, *106* (49), 20627–20632.  
<https://doi.org/10.1073/pnas.0907775106>.
- (23) Kaeffer, N.; Massin, J.; Lebrun, C.; Renault, O.; Chavarot-Kerlidou, M.; Artero, V. Covalent Design for Dye-Sensitized H<sub>2</sub>-Evolving Photocathodes Based on a Cobalt Diimine–Dioxime Catalyst. *Journal of the American Chemical Society* **2016**, *138* (38), 12308–12311. <https://doi.org/10.1021/jacs.6b05865>.
- (24) Yu, Y.; Click, K. A.; Chien, S.-C.; Sun, J.; Curtze, A.; Lin, L.-C.; Wu, Y. Decoupling pH Dependence of Flat Band Potential in Aqueous Dye-Sensitized Electrodes. *The Journal of Physical Chemistry C* **2019**, *123* (14), 8681–8687. <https://doi.org/10.1021/acs.jpcc.9b00710>.

## Acknowledgements

A doctoral thesis does not write itself – normal! During my journey, I have had the great luck to be able to count on the great help and support of many people, without whom this thesis would not have been possible.

First and foremost, I want to thank my supervisors Dr. Benjamin Dietzek and Dr. Murielle Chavarot-Kerlidou for the chance to work in their respective groups and the great collaboration. Murielle, thank you for always having an open ear, for the long (sometimes very long) scientific discussions and your support in all kinds of matters, not least French bureaucracy! Benjamin, thank you for the challenging tasks, the scientific discussions and the trust you placed in me. My thanks go also to Dr. Vincent Artero for giving me the opportunity to work in his group at CEA which was an amazing place to do science.

Very big thanks go to Dr. Ruri Wahyuono for the supervision and great co-working during my Master's thesis and beyond, and for introducing me to the field of dye-sensitized stuff. Thank you for your great patience, your unparalleled willingness to help, not to mention the delicious food. I wish you all the best for your start in Indonesia!

Equally great thanks go to Dr. Emmanouil “Manos” Giannoudis for being a great colleague, for always *echarme una mano*, for lots and lots of synthesis that I probably would have spectacularly failed at, and most of all for being a great friend. I am very happy our paths have crossed. (“Amazing!”)

A special thanks goes also to Mr. Alpaca, Dr. Mathias Micheel, for his help with various laser setups, for the great friendship and the grand Jena sports tour.

Thanks also to Dr. Nick Randell for good beer, skiing and great scientific and non-scientific discussion during coffee (did I mention beer?).

I want to thank the whole group in Jena for their help with many issues and the nice atmosphere in the group. Special thanks go to Dr. Maria Wächtler for a lot of organizational help and Dirk Müller and Dr. Denis Akimov for their help with the laser setups at IPHT. I want to thank Dr. Linda Zedler and Dr. Ying Zhang for getting me started with the spectroelectrochemical measurements that would so define my thesis. Last but not least, I want to thank soon-to-be Dr. Kilian Schneider and Dr. Yusen Luo for very successful sharing of the fs-TA lab.

I also want to thank my group in Grenoble for the very warm welcome and the great and motivating atmosphere in the lab. A special thanks goes to Dr. Matthieu Koepf for getting me started in the lab and showing me all the tricks for the

photoelectrochemical measurements, and for all the help he's given me in the past years which was way too much. Overall thanks for being the nicest person ever, and for the accordion sessions. My thanks go also to Jennifer Fize and Dr. Adina Morozan for their continuous help in the lab.

I also want to thank the workshop at IPHT for their great help in building and improving the cell for the TA-SEC measurements based on my somewhat crude first design.

I would also like to acknowledge the financial support of the Franco-German University for my cotutelle thesis.

My thanks go also to the graduate academy in Jena and the école doctorale in Grenoble for helping me with the cotutelle agreement.

Finally, I am deeply grateful to my family which has always supported me in all of my choices, my travels, my moving to Jena and my studies.

Mis últimas y más grandes gracias van para Johanna Solano. Gracias por aguantar mis a veces largas horas de laboratorio y trabajo en casa. Gracias por soportar no verme la mitad del año mientras estaba en Francia. Gracias por apoyarme siempre y darme confianza en mí mismo. Gracias por hacerme reír y relajarme cuando estaba bajo estrés. Gracias por todo. Te liebo.

## Declaration of Originality

I certify that the work presented here is, to the best of my knowledge and belief, original and the result of my own investigations, except as acknowledged, and has not been submitted, either in part or whole, for a degree at this or any other university.

### **Selbständigkeitserklärung**

Ich erkläre, dass ich die vorliegende Arbeit selbständig und nur unter Verwendung der angegebenen Hilfsmittel und Quellen angefertigt habe und dass ich nicht die gleiche oder eine in wesentlichen Teilen ähnliche Arbeit bei dieser oder einer anderen Hochschule als Dissertation eingereicht habe.

### **Déclaration d'originalité**

Je certifie que le travail présenté ici est, au meilleur de ma connaissance et de ma conviction, original et le résultat de mes propres enquêtes, sauf comme reconnu, et n'a pas été soumis, en partie ou en totalité, pour un diplôme à cette ou une autre université.

Sebastian Bold

Jena, XX.XX.2020

## Complete List of Publications

### Articles in peer-reviewed journals

1. **Bold, S.**, Zedler, L., Zhang, Y., Massin, J., Artero, V., Chavarot-Kerlidou, M., Dietzek, B. Electron transfer in a covalent dye–cobalt catalyst assembly – a transient absorption spectroelectrochemistry perspective. *Chemical Communications*, **2018**, 2(5), 10594–10597.
2. Windle, C., Kumagai, H., Higashi, M., Brisse, R., **Bold, S.**, Jusselme, B., Chavarot-Kerlidou, M., Maeda, K., Abe, R., Ishitano, O., Artero, V. Earth-Abundant Molecular Z-Scheme Photoelectrochemical Cell for Overall Water-Splitting. *Journal of the American Chemical Society*, **2019**, 141, 9593–9602.
3. Massin, J., Bräutigam, M., **Bold, S.**, Wächtler, M., Pavone, M., Muñoz-García, A. B., Dietzek, B., Artero, V., Chavarot-Kerlidou, M. Investigating Light-Driven Hole Injection and Hydrogen Evolution Catalysis at Dye-Sensitized NiO Photocathodes: A Combined Experimental-Theoretical Study. *The Journal of Physical Chemistry C*, **2019**, 123(28), 17176–17184.
4. **Bold, S.**, Straistari, T., Muñoz-García, A.B., Pavone, M., Artero, V., Chavarot-Kerlidou, M. and Dietzek, B. Investigating Light-Induced Processes in Covalent Dye-Catalyst Assemblies for Hydrogen Production, *Catalysts*, **2020**, 10(11), 1340.
5. **Bold, S.**, Massin, J., Giannoudis, E., Koepf, M., Artero, V., Dietzek, B., Chavarot-Kerlidou, M. Spectroscopic investigations provide a rational for the hydrogen-evolving activity of dye-sensitized photocathodes based on a cobalt tetraazamacrocyclic catalyst, *ACS Catalysis*, **2020**, Submitted for publication on 17.11.2020.
6. Wahyuono, R. A., Seidler, B., **Bold, S.**, Dellith, A., Dellith, J., Ahner, J., Wintergerst, P., Lowe, G., Hager, M. D., Wächtler, M., Streb, C., Schubert, U. S., Rau, S., Dietzek, B. Photocathodes Beyond NiO – Charge Transfer Dynamics in a  $\pi$ -Conjugated Polymer Functionalized with Ru Photosensitizers, *Scientific Reports*, **2020**, Submitted for publication.
7. Wahyuono, R. A., Braumüller, M., **Bold, S.**, Amthor, S., Nauroozi, D., Plentz, J., Wächtler, M., Rau, S., Dietzek, B. Localizing the initial excitation – a case study on NiO photocathodes using Ruthenium dipyrrophenazine complexes as sensitizers, *Spectrochimica Acta A*, **2020**, Submitted for publication on 7.12.2020.

## Conference contributions

### Talks

1. *3<sup>rd</sup> International Solar Fuels Conference Young meeting (ISF-3 Young), Hiroshima, November 2019*: Covalent Dye-Catalyst Assemblies for H<sub>2</sub>-Evolving Dye-Sensitized Photocathodes: Improved Performance and Transient Absorption Spectroelectrochemistry.
2. *27. Lecture Conference on Photochemistry of the GDCh, September 2020*: Activity and transient absorption spectroelectrochemistry of hydrogen-evolving dye-sensitized photocathodes. S. Bold, E. Giannoudis, V. Artero, M. Chavarot-Kerlidou, B. Dietzek.
3. *1. Catalight Young Scientist Symposium: Light Driven, November 2020*: Activity and transient absorption spectroelectrochemistry of hydrogen-evolving dye-sensitized photocathodes. S. Bold, E. Giannoudis, V. Artero, M. Chavarot-Kerlidou, B. Dietzek.

### Poster presentations

1. *3<sup>èmes</sup> Journées du GDR Solar Fuels, Paris, May-June 2018*: Synthesis and time-resolved spectroscopic characterization of covalent dye-catalyst assemblies designed for dye-sensitized solar fuel devices. S. Bold, E. Giannoudis, M. Chavarot-Kerlidou, B. Dietzek, V. Artero, Joint poster with E. Giannoudis.
2. *LightChec Summer school, Les Diablerets, July 2018*: Transient absorption spectroelectrochemistry: accessing all oxidation states of catalytic metal centers in covalent dye-catalyst dyads. S. Bold, J. Massin, M. Bräutigam, M. Wächtler, M. Chavarot-Kerlidou, B. Dietzek, V. Artero.
3. *4<sup>èmes</sup> Journées du GDR Solar Fuels, Paris, May 2019*: A new RuCo dyad for dye-sensitized hydrogen-evolving photocathodes – synthesis, photo- and spectroelectrochemical studies. E. Giannoudis, S. Bold, N. Queyriaux, L. Zedler, B. Dietzek, M. Chavarot-Kerlidou, V. Artero, Joint poster with E. Giannoudis.
4. *3<sup>rd</sup> International Solar Fuels Conference (ISF-3) / International Conference on Artificial Photosynthesis (ICARP 2019), Hiroshima, November 2019*: Covalent dye-catalyst assemblies for H<sub>2</sub>-evolving dye-sensitized photocathodes: Improved performance and transient absorption spectroelectrochemistry. S. Bold, E. Giannoudis, Julien Massin, L. Zedler, V. Artero, M. Chavarot-Kerlidou, B. Dietzek.

- 
5. 714. *Heraeus-Seminar (Resolving the Full Picture: Complementary Spectroscopic Approaches to Explore Dynamics in Physical and Chemical Systems)*, Bad Honnef, February 2020: Transient absorption spectroelectrochemistry on dye-sensitized photocathodes. S. Bold, E. Giannoudis, J. Massin, L. Zedler, V. Artero, M. Chavarot-Kerlidou, B. Dietzek, 2020



## Curriculum Vitae

### Personal information

---

Name	Sebastian Bold
Date of birth	May 14 <sup>th</sup> 1991 in Bergisch Gladbach, Germany
Nationality	German
Personal status	Not married

### Academic education

---

2017 – present	<b>Ph.D. in Chemistry</b> , “Ultrafast spectroscopic characterization of dye-sensitized H <sub>2</sub> -evolving photocathodes: towards optimized devices” Friedrich-Schiller-Universität Jena, Germany and Université Grenoble Alpes, France. Thesis in cotutelle.
2014 – 2017	<b>M.Sc. Chemistry</b> , Friedrich-Schiller-Universität Jena, Master thesis (Prof. Dr. B. Dietzek, IPC, FSU Jena): „Preparation of Au nanoparticle-doped NiO films as material for dye-sensitized photocathodes”
2013 – 2014	<b>Study abroad</b> at Universidad de Antioquia, Medellín, Colombia
2010 – 2014	<b>B.Sc. Chemistry</b> , Friedrich-Schiller-Universität Jena

### Prior to University

---

2009 – 2010	<b>Voluntary service</b> in Ecuador
2009	<b>Abitur</b> , Otto-Hahn-Gymnasium Bensberg, grade 1.3

### Teaching experience

---

2017 – present	Laboratory courses for undergraduate students of chemistry
2015 – 2016	Laboratory courses for undergraduate students of medicine

## Appendix 2

### Updated publications

**Publication 3** - Spectroscopic investigations provide a rational for the hydrogen-evolving activity of dye-sensitized photocathodes based on a cobalt tetraazamacrocyclic catalyst.

Reproduced with permission from *ACS Catalysis*, **2021**, 11, 6, 3662–3678. ©2021 American Chemical Society

Authors	<u>SB</u>	JM	EG	MK	VA	BD	MCK
Synthesis		x	x				
Characterization	x	x	x				
(Photo-)electrochemistry	x			x			
Time-resolved spectroscopy	x						
Data analysis and processing	x					x	x
Data interpretation	x				x	x	x
Concept development	x				x	x	x
Preparation of the manuscript	x					x	x
Revision of the manuscript	x				x	x	x
Proposed publication equivalents	1.0						

# Spectroscopic Investigations Provide a Rationale for the Hydrogen-Evolving Activity of Dye-Sensitized Photocathodes Based on a Cobalt Tetraazamacrocyclic Catalyst

Sebastian Bold, Julien Massin, Emmanouil Giannoudis, Matthieu Koepf, Vincent Artero, Benjamin Dietzek,\* and Murielle Chavarot-Kerlidou\*



Cite This: *ACS Catal.* 2021, 11, 3662–3678



Read Online

ACCESS |

Metrics & More

Article Recommendations

Supporting Information

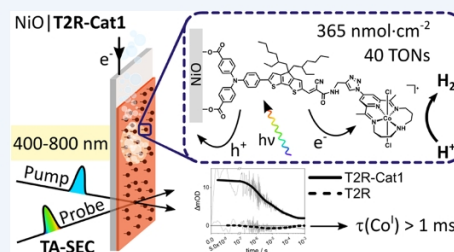
**ABSTRACT:** Dye-sensitized photoelectrochemical cells (DSPECs) are a promising approach to produce solar fuels, e.g., by reduction of protons to molecular hydrogen. Here, we present functional NiO photocathodes sensitized with covalent organic dye-catalyst assemblies integrating a robust cobalt tetraazamacrocyclic complex. This catalyst proved to be decisive in improving the stability of these systems, with hydrogen being produced with a 26-fold increase in turnover numbers compared to similar photocathodes based on a cobaloxime catalyst, all other conditions being strictly identical otherwise. Transient absorption spectroelectrochemical (TA-SEC) measurements observed the catalytically competent  $\text{Co}^{\text{I}}$  state in a functional dye-sensitized photocathode, with a lifetime of up to  $>1$  ms, comparable to the timescale of catalysis. They also unveiled the lack of efficiency of the thermally activated electron transfer from the reduced dye to the catalyst, which first limits the photocurrent density for hydrogen production. A second consequence is the accumulation of photogenerated charges on the acceptor side of the dye, ultimately leading to its degradation, as observed in operando and post operando characterizations of the system. This study thus provides tracks to improve the performances of hydrogen-evolving dye-sensitized photocathodes toward their integration into functional DSPECs.

**KEYWORDS:** cobalt catalyst, dye-sensitized, solar fuels, photoelectrocatalysis, spectroscopy

## INTRODUCTION

Storing solar energy, which by nature is intermittent, in chemical bonds, i.e., a solar fuel, is highly appealing to move from fossil fuels to renewable energies.<sup>1</sup> One promising approach to producing solar fuels relies on artificial photosynthesis, which mimics the natural photosynthetic process with synthetic components tailored to perform the desired redox reaction.<sup>2–4</sup> In that context, the production of hydrogen ( $\text{H}_2$ ) in water-splitting dye-sensitized photoelectrochemical cells (DSPECs) is the subject of intensive research efforts.<sup>5,6</sup> Tandem DSPECs combine two photoelectrodes, a photoanode driving water oxidation to oxygen and a photocathode where protons and electrons are recombined to produce  $\text{H}_2$ , in that way mimicking the Z-scheme of natural photosynthesis.<sup>7–9</sup> However, the dye-sensitized photocathodes reported to date lag well behind their photoanode counterparts in terms of photocurrent density and stability and are the limiting factors in tandem DSPEC, calling for investigations to understand their limitations and to develop guidelines to improve their performances.<sup>7–9</sup>

Recently, molecular hydrogen-evolving catalysts based on first-row transition metals (Fe, Co, Ni) have been successfully integrated in dye-sensitized photocathodes.<sup>7–27</sup> In these

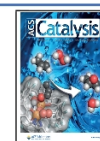


studies, the synthetic tunability of the catalyst most of the time governs the electrode construction strategy: (i) immobilization of supramolecular assemblies built by axial coordination of the dye on the Co center of a cobaloxime catalyst,<sup>10,26</sup> (ii) fully covalent dye-catalyst assemblies prepared thanks to a copper-catalyzed azide-alkyne cycloaddition (CuAAC) strategy using an azido-substituted cobalt diimine–dioxime complex,<sup>14–16</sup> (iii) layer-by-layer deposition of the dye and of a nickel bis(diphosphine) catalyst (Dubois-type complex) functionalized with four phosphonate groups,<sup>20–22</sup> and (iv) alternatively, coimmobilization of dyes and catalysts at the semiconductor surface,<sup>7–9,17–19,24,25</sup> simplifying the synthesis and allowing one to vary the dye/catalyst ratio. In addition to this diversity in the electrode architectures, which in turn strongly affects the electron-transfer kinetics to the catalytic center,  $\text{H}_2$  evolution activity

Received: November 17, 2020

Revised: January 28, 2021

Published: March 8, 2021



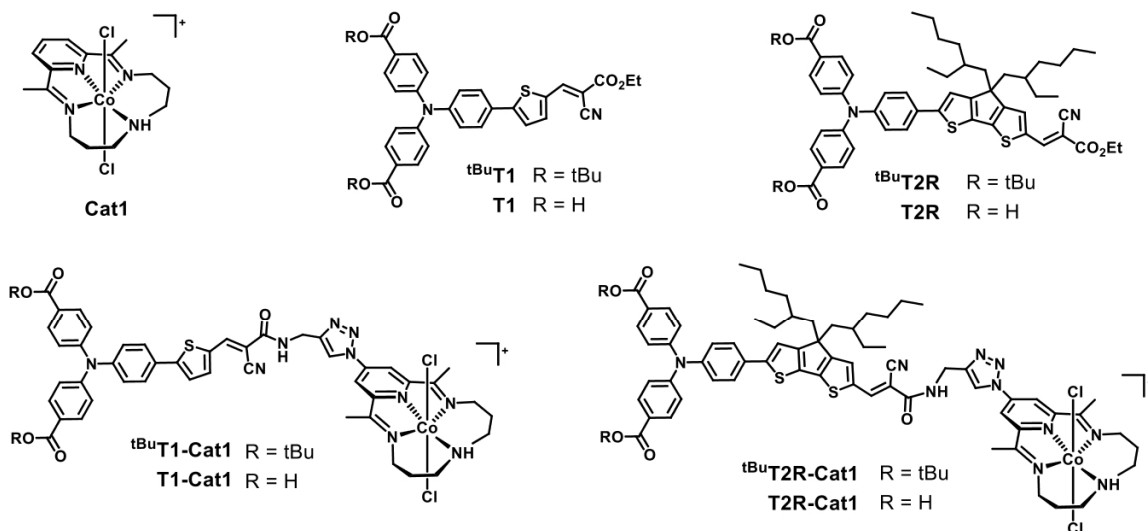
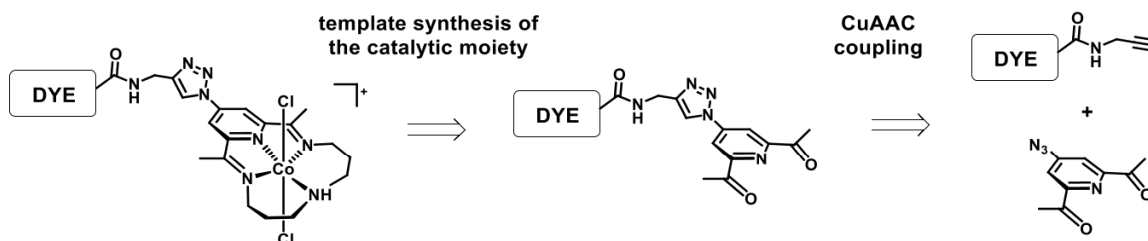


Figure 1. Structures of the H<sub>2</sub>-evolving catalyst **Cat1**, the dyes **T1** and **T2R**, and the dyads **T1-Cat1** and **T2R-Cat1**.

#### Scheme 1. Synthetic Strategy for the Preparation of **tBuT1-Cat1** and **tBuT2R-Cat1**



was assessed under a wide range of conditions (nature of the electrolyte, pH, applied potential, etc.). Altogether, this prevents direct comparison of the performances from one system to another to identify the best-performing components and to establish structure–activity relationships necessary for a rational improvement of the photocathode design.

In this study, we present a new noble-metal-free covalent dye-catalyst assembly based on push–pull organic dyes covalently linked via CuAAC “click” chemistry to the tetraazamacrocyclic cobalt complex **Cat1** as a catalytic unit. The superior activity and stability of the latter, compared to the cobalt diimine–dioxime catalyst, has been previously reported for photocatalytic proton reduction under fully aqueous conditions.<sup>28–35</sup> In parallel, the dye structure was modified from the previously published **T1-Co**<sup>16</sup> with a cyclopenta[1,2-*b*:5,4-*b'*]dithiophene (CPDT) bridge to bathochromically shift the absorption and increase the extinction coefficient in the visible region.<sup>36,37</sup> The alkyl chains introduced on the linker are intended (i) to limit dyad–dyad interactions and (ii) to prevent dyad desorption by forming a hydrophobic layer at the surface of the NiO film.<sup>38,39</sup> Photoelectrochemical activity was assessed under strictly identical conditions to our previously reported system,<sup>16</sup> thus providing a comprehensive comparison with **T1-Co**<sup>16</sup> and highlighting the beneficial role played by the **T2R** and **Cat1** moieties on the H<sub>2</sub> production performances. In addition, in-depth operando and post operando character-

izations of the **T2R-Cat1**-sensitized photocathode allowed us to identify relevant degradation processes and to determine their kinetics. Finally, the light-driven formation of the different intermediates at the surface of the NiO film, including the catalytically competent Co<sup>I</sup> state of **Cat1**, was investigated by transient absorption spectroelectrochemical (TA-SEC)<sup>40–44</sup> measurements and provided a mechanistic rationale to improve the design of these dye-sensitized photocathodes.

## RESULTS

**Synthesis of the Novel **Cat1**-Based Dyads.** Functionalization of **Cat1** is a challenging task, as reflected by the scarcity of procedures in the literature to prepare **Cat1** derivatives. To date, its catalytic performances have been assessed either under electroassisted conditions<sup>29,30,45</sup> or under photocatalytic conditions in multicomponent homogeneous systems.<sup>29–35</sup> The sole exception reported to date relies on a palladium-catalyzed cross-coupling introduction of a pyridine dicarboxylate anchoring group on the pyridine moiety of the ligand,<sup>28</sup> successfully allowing one to assemble **Cat1** with quantum dots<sup>28</sup> or a TiO<sub>2</sub>-protected silicon photoelectrode.<sup>46</sup> On the other hand, CuAAC is a highly versatile, efficient, and modular coupling reaction. It was previously employed by some of us to assemble the push–pull organic dye **T1** (Figure 1) with the H<sub>2</sub>-evolving cobalt diimine–dioxime catalyst Co(*N*<sup>2</sup>,*N*<sup>2'</sup>-propanediylbis(2,3-bu-

tandione-2-imine-3-oxime))Br<sub>2</sub> (Co), leading to the first functional noble-metal-free NiO photocathode based on a covalent assembly.<sup>16</sup> We first decided to use the same strategy to covalently assemble Cat1 with T1 and with the novel T2R dye (Figure 1); however, all of our attempts to prepare the cobalt complex Cat1 substituted by an azido group in the para position of the pyridine ring proved unsuccessful. An alternative route (Scheme 1) was thus developed: CuAAC coupling was first carried out between the alkyne-substituted dyes (<sup>t</sup>BuT1-alkyne and <sup>t</sup>BuT2R-alkyne; see the Supporting Information (S1)) and the 4-azido-2,6-diacetylpyridine precursor (Scheme 1), followed by the templated synthesis of the tetraazamacrocyclic cobalt complex. This way, the targeted dyads were isolated in two steps under their *tert*-butyl ester protected forms (<sup>t</sup>BuT1-Cat1 and <sup>t</sup>BuT2R-Cat1; Figure 1) in 50–60% overall yield. Full synthetic details and characterizations are provided in the Supporting Information.

**Spectroscopic and Electrochemical Characterization in Solution.** All compounds were characterized by cyclic voltammetry (CV; Table 1, Figures 2 and S1). The cyclic

of <sup>t</sup>BuT2R (Figure 2). The latter is characterized by two quasi-reversible waves at +0.48 and +0.66 V vs Fc<sup>+0</sup>, attributed to the oxidation of the triphenylamine (TPA) moiety and of the electron-rich CPDT bridge, respectively, as reported for related CPDT-based push–pull dyes.<sup>36,47</sup> On the cathodic scan of <sup>t</sup>BuT2R-Cat1, the two reversible processes observed at –0.54 and –0.97 V vs Fc<sup>+0</sup> are in full agreement with the two successive reversible reductions observed on the Co<sup>III</sup> catalyst Cat1 (Figure 2), yielding the formal Co<sup>II</sup> and Co<sup>I</sup> states, respectively.<sup>30,33</sup> The reduction of the acceptor part of the dye moiety is observed at –1.62 V vs Fc<sup>+0</sup> and shows a loss of reversibility compared to <sup>t</sup>BuT2R. The cyclic voltammogram of <sup>t</sup>BuT1-Cat1 (Figure 2) displays very similar reduction processes for the catalyst (–0.53 and –1.03 V vs Fc<sup>+0</sup>) and dye (–1.65 V vs Fc<sup>+0</sup>) units; the single anodic event at +0.64 V vs Fc<sup>+0</sup> is assigned to the TPA-centered oxidation process, by comparison with the cyclic voltammogram of T1 (Figure S1a).<sup>48,49</sup>

The UV–vis absorption spectra (Figure 3, Table S1) show two main absorption bands between 300 and 600 nm. The

**Table 1. Electrochemical Potentials ( $E_{1/2}$  in V vs Fc<sup>+0</sup>) of Investigated Compounds Determined by Cyclic Voltammetry**

sample	$E_{\text{dye}}^{+/0}$	$E_{\text{dye}}^{2+/+}$	$E_{\text{Co}}^{\text{III/II}}$	$E_{\text{Co}}^{\text{II/I}}$	$E_{\text{Co}}^{\text{I/0}}$	$E_{\text{dye}}^{0/-b}$
Cat1			–0.58	–1.08	–1.84	
<sup>t</sup> BuT1	0.71					–1.52
<sup>t</sup> BuT2R	0.48	0.66				–1.57
<sup>t</sup> BuT1-Cat1	0.64 <sup>a</sup>		–0.53	–1.03–0.97		–1.65
<sup>t</sup> BuT2R-Cat1	0.43 <sup>a</sup>	0.58 <sup>a</sup>	–0.54			–1.62

<sup>a</sup>Peak potentials in the anodic scan. <sup>b</sup>Peak potentials in the cathodic scan.

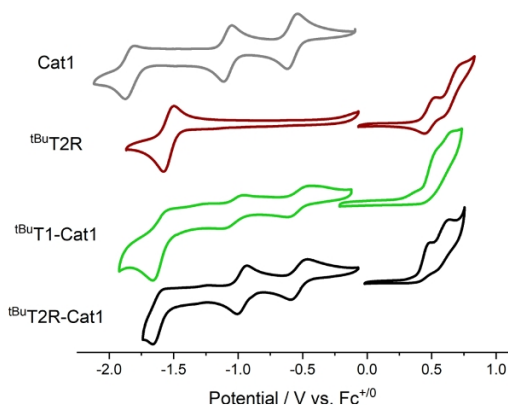


**Figure 2.** Cyclic voltammograms of Cat1 (gray), <sup>t</sup>BuT2R (red), <sup>t</sup>BuT1-Cat1 (green), and <sup>t</sup>BuT2R-Cat1 (black). CVs were recorded at 50 mV·s<sup>–1</sup> scan rate in 0.1 M TBABF<sub>4</sub> in dry dimethylformamide (DMF) except for the reductive scan of T1-Cat1, in which tetra butyl ammonium chloride (TBACl) was used as the supporting electrolyte.

voltammogram of <sup>t</sup>BuT2R-Cat1 displays five redox events (Figure 2). On the anodic scan, two waves at +0.43 and +0.58 V vs Fc<sup>+0</sup> are assigned to oxidation processes occurring on the dye moiety, by comparison with the cyclic voltammogram

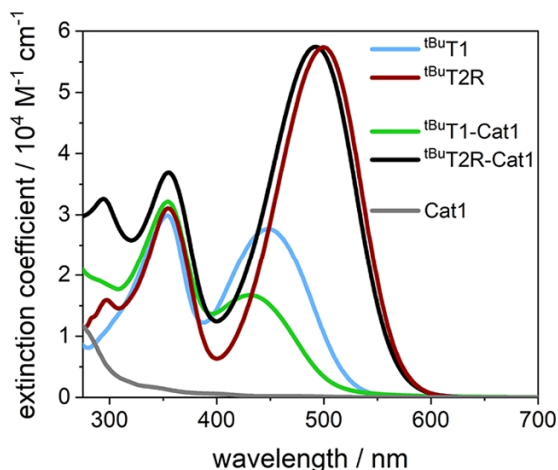


**Figure 3.** UV–vis absorption spectra of <sup>t</sup>BuT1 and <sup>t</sup>BuT1-Cat1 in DMF and of <sup>t</sup>BuT2R, <sup>t</sup>BuT2R-Cat1, and Cat1 in MeOH.

band at 350 nm is assigned to a  $\pi$ – $\pi^*$  transition on the TPA moiety,<sup>50</sup> and its position remains unchanged for all dyads in comparison with the parent dye. At longer wavelengths, all compounds show an intramolecular charge-transfer (ICT) transition from the TPA donor to the cyanoacrylate acceptor group, as is typical for this class of push–pull dyes.<sup>16,36,48</sup> For the <sup>t</sup>BuT2R series, this absorption is red-shifted in comparison to the <sup>t</sup>BuT1 series by ca. 0.33 eV (in acetonitrile (ACN), Figure S2), which is attributed to the more extended conjugated system due to the CPDT linker. Furthermore, extinction coefficients for <sup>t</sup>BuT2R (57 400 M<sup>–1</sup>·cm<sup>–1</sup>,  $\lambda_{\text{max}}$  = 499 nm) exceed those of <sup>t</sup>BuT1 (27 700 M<sup>–1</sup>·cm<sup>–1</sup>,  $\lambda_{\text{max}}$  = 448 nm).

Overall, in the covalent assemblies, the electrochemical and spectroscopic properties of the catalytic and dye units are retained, reflecting their electronic decoupling within the dyads, as previously established for T1-Co<sup>I</sup><sub>16</sub> and more generally frequently encountered for triazole-based dyads assembled by CuAAC coupling.<sup>51–56</sup>



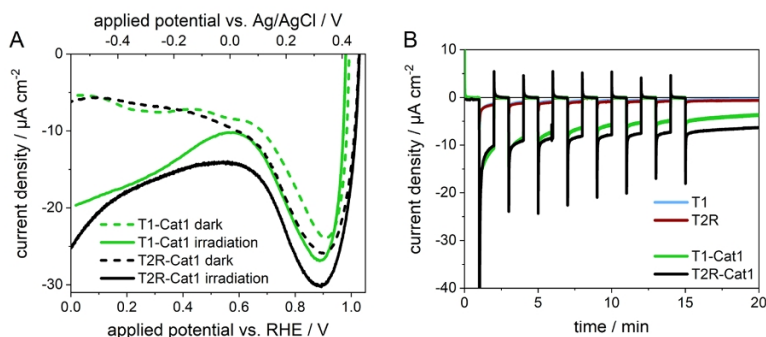


**Figure 4.** (a) Linear scan voltammograms (LSVs) of NiO films sensitized with the Cat1 dyads recorded in the dark and under continuous visible-light irradiation. (b) Chopped-light chronoamperometric measurements recorded in aqueous 0.1 M pH 5.5 MES buffer at  $-0.4$  V vs Ag/AgCl ( $+0.14$  V vs RHE) on NiO films sensitized with the dyes and the Cat1 dyads.

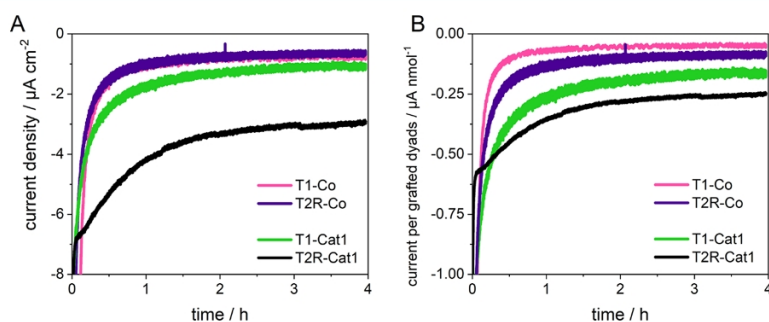


**Figure 5.** Photocurrents recorded on NiO films sensitized with the Cat1- and Co-based dyads during the first 4 h of photoelectrochemical experiments (applied potential:  $+0.14$  V vs RHE). (a) Absolute current density and (b) current normalized to the amount of dyad grafted on the film, allowing one to quantify the intrinsic activity of the dyads.

**NiO Film Sensitization and Characterization.** NiO films were prepared by spin-coating and sintering an F108 templated hydroalcoholic  $\text{NiCl}_2$  sol-gel.<sup>16,57,58</sup> The four-layered films have a thickness of  $880 \pm 170$  nm as determined by scanning electron microscopy (SEM; Figure S3, Table S2). They were sensitized by soaking for 24 h in methanolic solutions of the deprotected dyads (or dyes).

The amount of dyad (or dye) loading was quantified by dyad (or dye) desorption in a methanolic 1 M phenylphosphonic acid solution followed by UV-vis absorption measurement of the resulting solution,<sup>26,59</sup> using the molar extinction coefficient of the TPA-centered band at 350 nm (Figure S4, Table S3). Grafting densities are in the range of  $6\text{--}14$  nmol $\cdot\text{cm}^{-2}$  (Table S4), in good agreement with the literature on other dye-sensitized NiO films.<sup>14,16,26,48</sup> We observed that the grafting density substantially varies from one batch of NiO films to another, preventing any straightforward analysis of the loading based on the molecular structures of the dyads. This supports the need to verify the grafting efficiency of each individual sample. For this, we used half of each freshly sensitized NiO film to determine the dyad (or dye) loading, while the other half was used for the assessment of photoelectrochemical hydrogen production. Hence, an accurate quantification of the amount of dyad grafted on the considered film was obtained and was used to calculate the turnover number (TON) values for hydrogen production activity (see later).

**Photoelectrochemical Activity.** The photoelectrochemical activity of the dye-sensitized NiO photocathodes was assessed in a three-electrode configuration setup under conditions identical to our previous studies<sup>14,16,17,26</sup> using an aqueous (*N*-morpholino)ethanesulfonic acid (MES) buffer solution at pH 5.5 as the electrolyte; samples were irradiated with visible light at the equivalent of 1 sun intensity, using a 400 nm long-pass filter and an IR filter. Linear sweep voltammograms (LSVs) were recorded from  $+1.00$  to  $0.00$  V vs reversible hydrogen electrode (RHE; Figure 4a). The large cathodic signal observed between  $+1.00$  and  $\approx +0.6$  V vs RHE is attributed to capacitive charging of the NiO films.<sup>60</sup> Under irradiation, the dyad-sensitized NiO films start exhibiting cathodic photocurrents at  $\approx +0.95$  V vs RHE, which are stable down to  $\approx +0.5$  V vs RHE before increasing at more cathodic potentials. For the film sensitized with T2R-Cat1, the photocurrent reaches  $13.5$   $\mu\text{A}\cdot\text{cm}^{-2}$  at  $+0.14$  V vs RHE (dark current subtracted).

Chronoamperometric measurements under chopped-light irradiation yielded insights into the magnitude and stability of the photocurrents measured at  $+0.14$  V vs RHE, the potential applied for hydrogen production (Figure 4b). When light is turned on, the systems show an initial cathodic photocurrent spike; in addition, upon switching off the irradiation, a reverse anodic spike of lower intensity is observed, suggesting that some photogenerated electrons are accumulated on the dyad (see below) and not fully consumed by catalysis.<sup>10,26,61</sup> Importantly, almost no photocurrent is generated in the

**Table 2.** Figures of Merit of the Different Dyad-Sensitized Photocathodes Determined from Chronoamperometric Measurements under Continuous Visible-Light Irradiation, in Aqueous MES Buffer Electrolyte at pH 5.5, at an Applied Potential of +0.14 V vs RHE (Full Set of Experimental Data in Table S4)

sample	after 4 h			after 22 h		
	H <sub>2</sub> (nmol·cm <sup>-2</sup> )	FE (%)	TON	H <sub>2</sub> (nmol·cm <sup>-2</sup> )	FE (%)	TON
T1-Cat1	96 ± 14	65 ± 17	13 ± 1	162 ± 20	31 ± 4	23 ± 1
T2R-Cat1	187 ± 25	66 ± 7	21 ± 6	365 ± 122	39 ± 8	39 ± 8
T1-Co	11 ± 1	9 ± 1	0.7 ± 0.1	13 ± 4	3 ± 0	0.9 ± 0.3
T2R-Co	10 ± 2	11 ± 2	1.5 ± 0	10 ± 3	3 ± 2	1.5 ± 0.2

absence of the catalytic unit ( $-0.4$  and  $-0.6 \mu\text{A}\cdot\text{cm}^{-2}$  after 20 min for films sensitized with T1 and T2R, respectively), while the presence of Cat1 leads to a tenfold increase of the photocurrent density ( $-3.7$  and  $-6.3 \mu\text{A}\cdot\text{cm}^{-2}$  for T1-Cat1 and T2R-Cat1, respectively). In longer-term photoelectrochemical experiments under continuous light irradiation, all photocathodes show steady-state photocurrents (Figures 5 and S8), albeit with marked differences in photocurrent magnitude and stability over time.

To investigate the role of the novel catalytic unit, the photoelectrochemical activity of the previously reported dyad containing the cobalt diimine–dioxime catalyst Co(DO)(DOH)pnBr<sub>2</sub> (T1-Co) was reassessed, together with the activity of a novel dyad T2R-Co combining T2R with Co(DO)(DOH)pnBr<sub>2</sub> (see the SI for synthesis and characterizations in Table S1, Figures S1b and S4–S7). After normalization of the photocurrent density to the amount of grafted dyad to compare the intrinsic activity of the dyads (Figure 5b), the Cat1 and T2R dyads showed a slower decay in photocurrent and a higher overall photocurrent than their Co and T1 counterparts, respectively. On average, the Cat1 dyads produced 3.2 times higher accumulated current than the Co dyads and the T2R dyads 1.7 times as much as the T1 dyads, for a total 5.4-fold increase of T2R-Cat1 over T1-Co.

**Hydrogen-Evolving Activity Assessment.** To confirm that the observed photocurrent originates from the reduction of protons into hydrogen, the H<sub>2</sub> evolution activity of the sensitized NiO photocathodes was assessed during long-term chronoamperometric experiments at an applied potential of +0.14 V vs RHE and under continuous visible-light irradiation. The amount of hydrogen produced was measured after 4 and 22 h both in the headspace of the cell by gas chromatography and in the electrolyte using a micro-Clark-type electrode probe following an established protocol.<sup>14</sup> Turnover numbers (TON<sub>Co</sub>) were calculated, using the dyad loading quantified for the freshly sensitized film.

After 4 h of irradiation, the Cat1 dyads produced hydrogen with TON values of  $13 \pm 1$  (T1-Cat1) and  $21 \pm 6$  (T2R-Cat1) and faradaic efficiencies around 65% (Table 2). The activity of the Co dyads was much lower, with TON values below 2 and faradaic efficiencies of  $\approx 10\%$ , in agreement with previous reports.<sup>14,16,17</sup> Comparing the influence of the light-harvesting units, the T2R systems produced around twice as much hydrogen as their T1 counterparts. Continuing irradiation for a total of 22 h almost doubled the TON values for the Cat1 systems, while the Co dyads showed no increase in produced hydrogen, meaning that they had lost their activity during the first 4 h. For all systems, the faradaic efficiency decreased between 4 and 22 h of irradiation (to  $\approx 35\%$  for Cat1 and  $\approx 3\%$  for Co).

**Post Operando Characterization.** Molecular dyads were desorbed post operando from the NiO film in a phenyl-

phosphonic acid methanolic solution, with the aim to quantify the amount of dyad desorbed from the NiO surface during the course of the photoelectrochemical tests as well as to identify potential structural modifications. The absorbance of the desorption solutions was measured to quantify the remaining amount of dyad still present on the surface after a 22 h photoelectrochemical experiment. The resulting spectra are shown in Figures 6 and S9, together with the spectra recorded for the corresponding dyads desorbed from a fresh film for comparison.

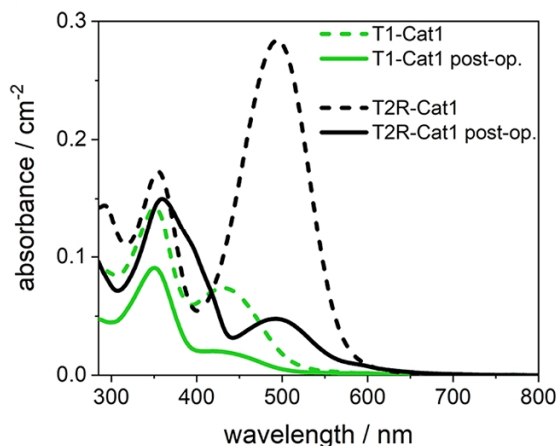


**Figure 6.** UV–vis spectra of the Cat1 dyads desorbed from fresh (dashed lines) and post operando (after 22 h of photoelectrochemical activity assessment, solid lines) NiO films in a 1 M phenylphosphonic acid solution in methanol, normalized to the surface area of the films.

The post operando UV–vis spectra show a particularly pronounced decrease in absorption for the ICT band at 435 and 495 nm for the T1- and T2R-based systems, respectively. We attribute the minor decrease in absorbance at the TPA band (355 nm) to a partial release of the dyads into the electrolyte solution during the photoelectrochemical experiments. The decrease in absorbance at this position is less pronounced for T2R-Cat1 in comparison to T1-Cat1 (16 vs 37%), indicating a lesser degree of desorption, which we ascribe to the protection against hydrolysis granted by the hydrophobic alkyl chains on the CPDT linker.<sup>38</sup> The strong decrease in absorbance at the ICT band, accompanied by the formation of a new band at 400 nm for T2R-Cat1, is likely caused by structural modification of the dye during the photoelectrochemical experiments, which exposes the dye to relatively harsh conditions, i.e., applied reductive potential, light irradiation, and aqueous buffer. We therefore decided to

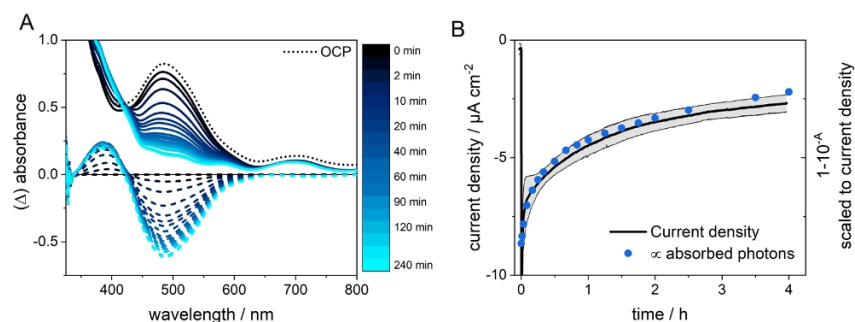


**Figure 7.** (a) UV-vis absorption monitoring of T2R-Cat1-sensitized NiO films under operando photoelectrochemical conditions: UV-vis spectra (solid) and differential spectra (dashed) obtained by subtracting the spectrum obtained at applied potential before irradiation (0 min). (b) Average current density of four different T2R-Cat1-sensitized NiO films plotted against  $1-10^{-4}$ , where  $A$  is the integrated absorbance in the visible range recorded during the operando UV-vis measurements after subtracting the NiO background. Also,  $1-10^{-4}$  is proportional to the number of absorbed photons and was scaled to the current density at 600 s to account for the initial current spike.

investigate which of these parameters is likely at the origin of the changes in dye absorption.

For this purpose, UV-vis absorption spectra were recorded over time in a home-made cell on NiO films sensitized with T2R-Cat1 while varying the experimental parameters, including full operando conditions. First, spectra were recorded over 1 h on a T2R-Cat1-sensitized NiO film with the operando potential applied in the absence of irradiation (Figure S10a); under these conditions, no spectral change was observed apart from an initial jump in absorbance caused by the electrochromic nature of NiO.<sup>62,63</sup> Second, when the film was submitted to visible-light irradiation in the absence of any applied potential (Figure S10b), small amplitude spectral changes were observed that might be explained by isomerization of the cyanoacrylate double bond.<sup>64</sup> By contrast, when the film was exposed both to visible-light irradiation and to the applied potential, i.e., operando conditions, fast spectral changes were observed (Figure 7a), with features similar to those previously identified for the desorbed dyad in the post operando measurements (Figure 6). A kinetic analysis revealed a biexponential decay with characteristic lifetimes of 6 and 90 min (Figure S11). In comparison, a T2R-sensitized NiO film displayed faster degradation kinetics, with  $\approx 1$  and 21 min characteristic lifetimes (Figures S12 and S13). Thus, it appears that both the applied potential and the visible-light irradiation are necessary to cause the dye modification observed post operando; in addition, this process seems to be accelerated when the catalyst is not present at the surface of the film.

To further study this process, UV-vis spectroelectrochemical experiments were recorded on <sup>tbu</sup>T2R in a dry 0.1 M *n*Bu<sub>4</sub>NBF<sub>4</sub> ACN solution. Under these conditions, the same irreversible spectral changes were observed upon exhaustive reduction of the dye (Figure S14), thus excluding any contribution of the aqueous electrolyte in the former experiments. <sup>tbu</sup>T1 showed an identical spectral response upon reduction, suggesting that the same degradation process also takes place for this dye (Figure S14c).

To ascertain whether the modification suffered by the dye leads to the loss of the catalytic center, e.g., by bond cleavage, the amount of Co present at the surface of the film was determined pre- and post operando by inductively coupled plasma mass spectrometry (ICP-MS; Table S5). After, respectively, 4 and 22 h of photoelectrochemical activity, 84

and 93% of the initial amount of Co was lost, which correlates very well to the loss of absorbance (84% after 4 h). Furthermore, the photocurrent recorded on T2R-Cat1-sensitized NiO films correlates with the number of absorbed photons (Figure 7b), which is also related to the absorbance. These findings suggest that the same underlying process causes the loss both of Co and of the dye absorbance, as separate, independent processes would lead to a stronger loss of photocurrent compared to the loss of either absorbance or Co loading. Assuming therefore that the correlation between the photocurrent decrease and the loss of the catalytic unit holds true, the average surface concentration of intact dyads present during the first 4 h of activity was estimated to be  $2.0 \pm 0.4 \text{ nmol}\cdot\text{cm}^{-2}$ , leading to a more accurate TON value of  $94 \pm 16$  (Table S6).

**Time-Resolved Spectroscopy and Spectroelectrochemistry.** Since the light-induced processes in the dye-sensitized photocathodes are crucial to charge the catalyst and thus enable catalytic proton reduction, they were investigated by time-resolved spectroscopy. In a first step, time-resolved emission was measured for all compounds grafted onto NiO and ZrO<sub>2</sub> films, the latter serving as a nonquenching reference (see the Supporting Information for a detailed analysis, and Figure S15, Table S7). All systems showed a complete emission quenching within the duration of the instrumental response function (full width at half-maximum (FWHM) = 430 ps) on NiO, which was not observed on ZrO<sub>2</sub>. This quenching is attributed to hole injection from the excited dye into the valence band of the NiO film.<sup>65–68</sup>

To further investigate the sensitized NiO films, we turned to transient absorption (TA) spectroscopy. We aimed to investigate the electron-transfer dynamics under conditions that are as close as possible to the operando ones, i.e., with the operando potential applied to the film, albeit in the absence of catalysis to accumulate and detect the reduced Co species, which was achieved using dry acetonitrile as a solvent. Compared to unbiased dye-sensitized NiO films, applying an external negative bias was recently shown to sharply slow down the recombination rate of reduced dye molecules with holes in the NiO film.<sup>43,44,69</sup> This phenomenon is attributed to the suppression of a detrimental nongeminate recombination pathway by populating the NiO intragap states upon applying a negative potential.<sup>43</sup> To study the influence of applied potential on the photoinduced kinetics, we performed



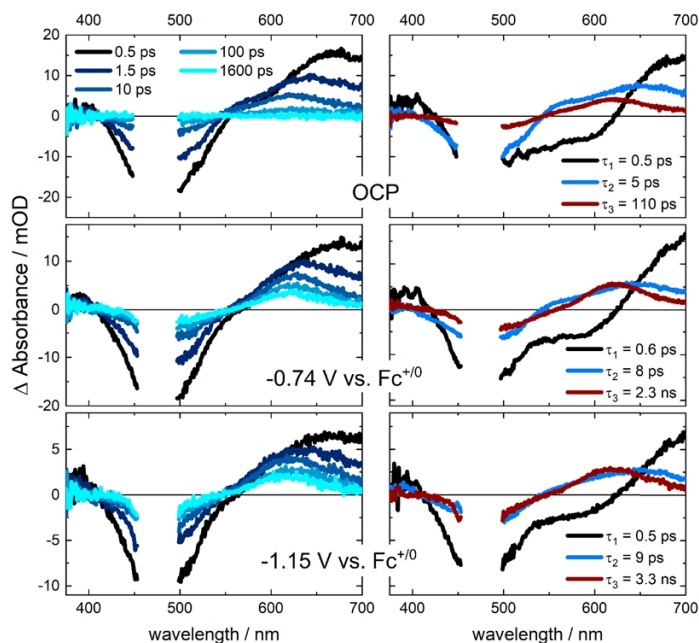


**Figure 8.** Left: fs-TA-SEC spectra at different pump-probe delay times after excitation at 480 nm of **T2R-Cat1**-sensitized NiO films at OCP,  $-0.74$  V (corresponding to  $+0.14$  V vs RHE employed for the photoelectrochemical tests) and  $-1.15$  V vs  $\text{Fc}^{+/0}$  applied potential, using a  $0.1$  M  $n\text{Bu}_4\text{NBF}_4$  electrolyte in ACN. Right: Decay-associated spectra obtained with a three-component exponential fit of the respective fs-TA-SEC data.  $\tau_1$  corresponds to hole injection with associated relaxation,  $\tau_2$  to a decay of residual excited state, and  $\tau_3$  to charge recombination from the charge-separated state.

TA-SEC experiments on NiO films sensitized either with the dyad **T2R-Cat1** or with the dye **T2R** as reference. In these measurements, data was recorded at an open-circuit potential (OCP), i.e., in the electrolyte but without any applied bias, as well as during application of two cathodic potentials to the sensitized film: first, the potential employed in the photoelectrochemical experiments ( $-0.74$  V vs  $\text{Fc}^{+/0} \triangleq -0.4$  V vs  $\text{Ag}/\text{AgCl}$ ), sufficient to reduce the catalyst to its  $\text{Co}^{\text{II}}$  state;<sup>17</sup> then, a more cathodic one ( $-1.15$  V vs  $\text{Fc}^{+/0}$ ) where the catalyst is reduced to the  $\text{Co}^{\text{I}}$  state. The latter measurement served as a reference since no electron transfer is thermodynamically possible to the catalyst in the  $\text{Co}^{\text{I}}$  state (the third reduction process on the catalyst occurs at a more negative potential than the dye reduction; see Figure 2). A detailed spectroscopic analysis of the fs- and ns-TA data is provided in the Supporting Information, and the characteristic time constants are summarized in Table S8. Since both **T2R**- and **T2R-Cat1**-sensitized NiO films showed the same behavior in the fs-TA-SEC experiment, they will be discussed together.

After laser pulse excitation and regardless of the potential applied to the electrode, the fs-TA spectra of **T2R**- and **T2R-Cat1**-sensitized NiO films initially show ground-state bleach (GSB) at 500 nm and excited-state absorption (ESA) at  $>550$  nm, attributed to the vibrationally hot excited state of the dye (Figures 8 and S16 and S17).<sup>70</sup> This is followed by a fast recovery of GSB, accompanied by a blue shift of ESA to form a band with a maximum at 620 nm. Since the 620 nm band is characteristic of the one-electron reduced dye (Figure S18), this first process is assigned to hole injection, leading to the formation of the primary charge-separated state  $\text{NiO}^+\text{T2R}^-$

(**Cat1**). Applying a three-component exponential fit to the data, a characteristic time constant of  $\tau_1 < 1$  ps is obtained for this process, in line with the ultrafast hole injection observed in the literature for other organic dyes grafted on NiO.<sup>15,25,71–79</sup> As this class of push–pull organic dyes is known to undergo a fast relaxation cascade to the relaxed ICT state on the same subpicosecond timescale (Figure S17),<sup>40,50,70,71,80–82</sup> it seems likely that hole injection and the relaxation cascade occur simultaneously and that  $\tau_1$  therefore reflects a convolution of the two. A second process, with a characteristic time constant  $\tau_2 \approx 8$  ps, can be assigned to the decay of the residual excited state to the ground state since the spectral change it causes is a loss of the typical features of the **T2R** dye in the excited state. This excited state likely decays through hole injection coupled to fast charge recombination, as the latter has been previously observed on similar timescales for NiO films sensitized with organic dyes.<sup>25,74,83</sup>

The final spectral change is a decay of the characteristic feature of the reduced dye at 620 nm and of the remaining GSB and is thus assigned to charge recombination. This process shows a strong dependence on the applied potential: at OCP, the signal of the primary charge-separated state completely decays within the time window of 1.6 ns, while it is very long-lived when a cathodic potential is applied to the film. This is also reflected in the time constant obtained from the fit, which increases from  $\tau_3 = 190$  ps for **T2R** and 110 ps for **T2R-Cat1** at OCP, similar to values found in the literature,<sup>15,72–77,79,83,84</sup> to  $>1$  ns at  $-0.74$  and  $-1.15$  V vs  $\text{Fc}^{+/0}$ . Such behavior of dye-sensitized NiO films has previously been associated with filling of intragap trap

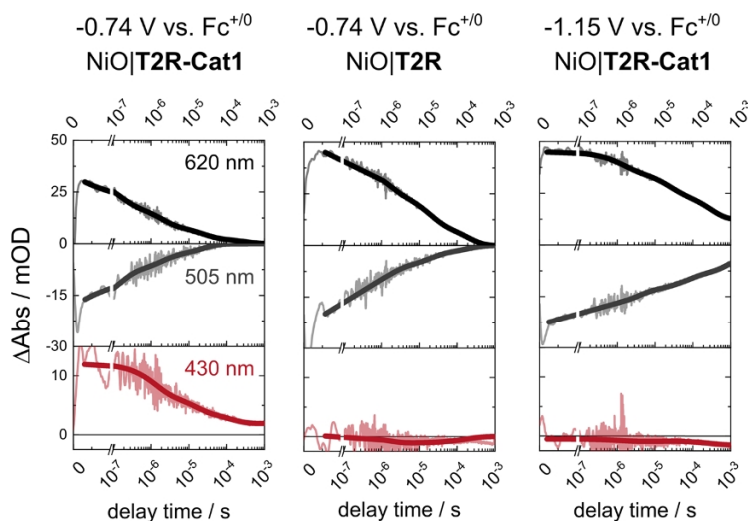


**Figure 9.** Kinetic traces at characteristic wavelengths obtained in ns-TA-SEC experiments recorded on NiO films sensitized with T2R and T2R-Cat1 at applied potentials of  $-0.74$  and  $-1.15 \text{ V vs. Fc}^{+/0}$ , using a  $0.1 \text{ M } n\text{Bu}_4\text{NBF}_4$  electrolyte in ACN. The signals at 620 and 505 nm are characteristic of the reduced state of the T2R dye, while the signal at 430 nm is ascribed to the  $\text{Co}^{\text{I}}$  state of the catalyst.

states.<sup>43,44</sup> These trap states are caused by  $\text{Ni}^{3+}$  defects on the NiO surface and provide a pathway for fast nongeminate charge recombination for electrons localized on the reduced dye, leading to characteristic lifetimes in the picosecond range for charge recombination.<sup>43,66,67,72,76,85,86</sup> Indeed, charge recombination may be so fast that no signal of the reduced dye is observed.<sup>43,66</sup> Application of a cathodic potential fills these trap states, thus deactivating the charge recombination channels and extending the charge-separated state lifetime. Most importantly regarding the activity for hydrogen evolution, on the timescale of the femtosecond transient absorption measurements ( $<1.6 \text{ ns}$ ), there is no spectral evidence for electron transfer from the reduced dye to the catalyst in the T2R-Cat1-sensitized films.

To accurately determine the lifetime of the primary charge-separated state and to investigate if electron transfer to the catalytic center occurs on a longer timescale, we turned to nanosecond TA-SEC experiments (which cover the time range from 20 ns to 1 ms). Kinetic traces measured at 620 and 505 nm represent the primary charge-separated state  $\text{NiO}^{\text{I}}\text{T2R}^{\text{I}}(-\text{Cat1})$  with the electron localized on the dye unit (Figures 9 and S19). The long-lived signal decaying in a nonexponential fashion on a microsecond timescale indicates charge recombination, as observed in dye-sensitized NiO films.<sup>13,43,44,87</sup> For NiO|T2R-Cat1, the average lifetime of the primary charge-separated state extracted from the fit at  $-0.74 \text{ V vs. Fc}^{+/0}$  was  $7 \mu\text{s}$ , while at  $-1.15 \text{ V vs. Fc}^{+/0}$ , it increased by more than one order of magnitude to  $131 \mu\text{s}$  (27% relative decay amplitude) and  $>1 \text{ ms}$  (73% relative decay amplitude). NiO|T2R showed a similar trend with somewhat longer lifetimes, especially at  $-0.74 \text{ V vs. Fc}^{+/0}$  ( $\tau_{\text{ave}} = 28 \mu\text{s}$ ,  $-1.15 \text{ V vs. Fc}^{+/0}$ :  $184 \mu\text{s}$  (67%) and  $>1 \text{ ms}$  (33%), Table S8).

Within the time of the pump pulse of the ns-TA-SEC experiment ( $<20 \text{ ns}$ ), a positive signal is formed at 430 nm for T2R-Cat1 at  $-0.74 \text{ V vs. Fc}^{+/0}$ . Measurements at several wavelengths between 400 and 460 nm reveal a positive transient absorption band with a maximum at 430 nm, characteristic wavelength of the  $\text{Co}^{\text{I}}$  state of the catalyst

(Figures 10 and S20 and S21).<sup>33</sup> Furthermore, this positive signal is absent when the catalytic unit is not present at the

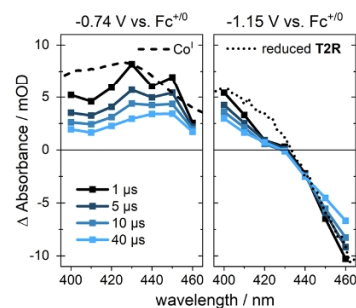


**Figure 10.** ns-TA-SEC spectra recorded on a NiO film sensitized with T2R-Cat1 at  $-0.74$  and  $-1.15 \text{ V vs. Fc}^{+/0}$  applied potentials at different delay times together with reference spectra obtained via UV-vis SEC of the  $\text{Co}^{\text{I}}$  state (dashed) and of the one-electron reduced T2R in solution (dotted).

surface of the film (T2R at  $-0.74 \text{ V vs. Fc}^{+/0}$ ) or when it is already reduced to the  $\text{Co}^{\text{I}}$  state prior to excitation (T2R-Cat1 at  $-1.15 \text{ V vs. Fc}^{+/0}$ ), i.e., two conditions where no electron transfer is possible (Figure 9). This allowed us to unambiguously assign this spectral signature to the formation of the  $\text{Co}^{\text{I}}$  state of Cat1 by thermally activated electron transfer from the reduced dye species.<sup>33</sup>

Regarding the kinetics of the electron transfer from the reduced dye to the cobalt catalyst, its absence in the fs-TA experiments combined with the maximum signal at 430 nm being present directly after the pump pulse in the ns-TA experiment puts the characteristic time constant for this process in a time window comprised between 1.6 and 20 ns. In addition, the faster decay of the signal of the reduced dye in the dyad compared to T2R is likely caused by an additional, slower electron-transfer process to the catalyst in

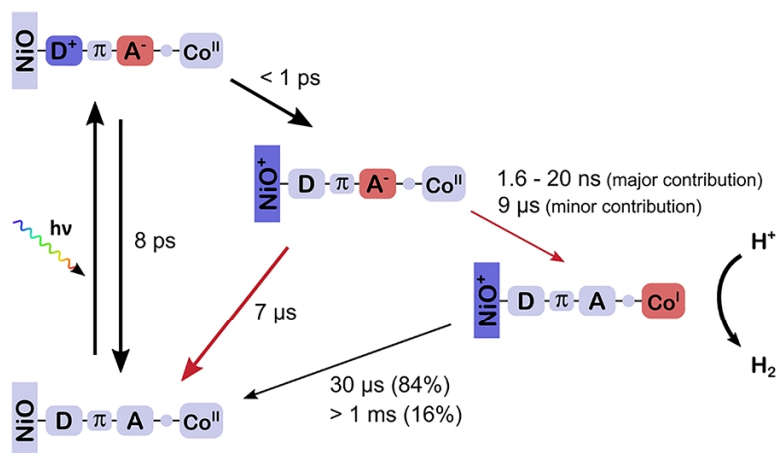


**Figure 11.** Scheme summarizing the light-induced processes in a T2R-Cat1-sensitized NiO film at  $-0.74$  V vs  $\text{Fc}^{+/0}$  (corresponding to the  $+0.14$  V vs RHE potential applied during the photoelectrochemical measurements). The times indicated are inverse first-order rates. Since the charge recombination and electron-transfer processes are nonexponential, the times given are averages of the inverse first-order rates of a multiexponential fit (see Table S8).

the dyad. Assuming that the decrease in lifetime of the reduced dye in T2R-Cat1 in comparison to T2R is only due to this further process, its characteristic time constant is estimated to be  $9 \mu\text{s}$ . Once formed, the  $\text{Co}^{\text{I}}$  state undergoes much slower charge recombination than the reduced dye, with average lifetimes of  $30 \mu\text{s}$  (84% relative decay amplitude) and  $>1$  ms (16% relative decay amplitude).

In summary, the TA-SEC experiments revealed the following scheme (summarized in Figures 11 and S22):

- after light excitation, an ultrafast hole injection process leads to the generation of the primary charge-separated state  $\text{NiO}^+\text{T2R}^-\text{Cat1}$ ;
- the subsequent thermal electron transfer to the cobalt catalyst predominantly takes place within 20 ns, and the lifetime of the catalytically competent  $\text{Co}^{\text{I}}$  state ranges from the microsecond to the millisecond timescale; and
- the yield of this thermal electron-transfer process is however far from unity, with a substantial amount of reduced dye still detectable at the surface of the film with an average lifetime of  $7 \mu\text{s}$ .

## DISCUSSION

The photocathodes introduced in this study contain the tetraazamacrocyclic cobalt catalyst Cat1 and clearly display improved performances compared to their counterparts relying on the cobalt diimine-dioxime catalyst Co. Although quite similar photocurrent densities were recorded ( $\approx 10 \mu\text{A}\cdot\text{cm}^{-2}$  @  $+0.14$  V vs RHE), significantly higher amounts of hydrogen were produced during the course of a 4 h chronoamperometric measurement (up to  $200 \text{ nmol}\cdot\text{cm}^{-2}$  for T2R-Cat1 vs  $10 \text{ nmol}\cdot\text{cm}^{-2}$  for T2R-Co), thanks to a dramatic increase in the faradaic efficiency of the process (65–70% F.E. for Cat1 vs 10% F.E. for Co). In addition, the Cat1 photocathodes still display some activity over 22 h, whereas the Co systems are fully deactivated after 4 h. TON values were calculated to accurately compare the efficiency of the different molecular structures while eliminating the variations in dyad loading at the surface of the NiO film. After 22 h, 23 and 39 TONs were achieved by T1-Cat1 and

T2R-Cat1, respectively, whereas TONs of 1 and 1.5 were recorded for T1-Co and T2R-Co, respectively, which represents a 26-fold increase. These results clearly highlight how the nature of the catalytic center is key for the photocathode performances, with all of the other parameters—i.e., dye structure, NiO film preparation, pH and nature of the electrolyte, light intensity, and applied potential—being otherwise strictly identical. A straightforward comparison of these numerical values (photocurrent, amount of hydrogen produced, TON) with state-of-the-art in the literature is difficult as these parameters vary considerably from one study to another, to date preventing the determination of a sound structure–activity relationship. Nevertheless, the T2R-Cat1 photocathode reported here favorably competes with the best-performing NiO ones, which are based on the cobaloxime CoHEC or the DuBois NiP catalyst.

The superior hydrogen production activity observed with Cat1 cannot be simply rationalized thermodynamically. Indeed, both Cat1 and Co dyads display a significant driving force for hole injection from the dye-excited state into NiO ( $0.6$ – $0.9$  eV; see Table S1) to form the reduced dye. The reduced dye itself can subsequently reduce the catalytic center to the  $\text{Co}^{\text{I}}$  state via thermally assisted electron transfer, with very close driving forces for the two catalysts (Table S1). The clearcut difference in the photocathode performances is rather assigned to the increased stability of Cat1 in a fully aqueous medium, which previously resulted in a 70-fold higher amount of  $\text{H}_2$  produced under homogeneous photocatalytic conditions, compared to Co.<sup>33</sup> More generally, the robustness of polypyridinic and aminopyridinic cobalt catalysts has been recognized over the past few years,<sup>33,88–91</sup> whereas cobaloximes are more prone to decomposing under aqueous conditions of activity, via demetalation,<sup>92</sup> hydrolysis, and/or reduction of the oxime-based ligands,<sup>93–96</sup> if they are not constantly and rapidly supplied with reductive equivalents.<sup>97</sup> The latter process might account for the low F.E. for hydrogen production of the Co photocathodes reported here and in previous studies from our group,<sup>14,16,17</sup> together with



other side reactions such as the reduction of oxygen that might diffuse in the cell during the course of the experiment.<sup>14</sup>

Despite having replaced **Co** by the more robust H<sub>2</sub>-evolving catalyst **Cat1**, the overall performances of our photocathodes still need to be increased to reach a level of activity comparable to the current photoanode state-of-the-art, with photocurrents in the mA·cm<sup>-2</sup> range.<sup>98</sup> Detailed investigations on the most efficient **T2R-Cat1**-based photocathode helped us identify two parameters currently limiting its performances.

- (1) Operando and post operando characterizations revealed that the **T2R** dye structure is modified under reductive conditions, with the loss of the main part of its absorption in the visible region as a consequence. We failed to identify the exact structure of this novel derivative, although the observations that (i) the  $\pi$ - $\pi^*$  absorption of the triarylamine group is still present and (ii) a similar alteration is observed for **T1** and **T2R** under reductive conditions indicate that this modification occurs on the acceptor group of the push-pull structures, i.e., the cyanoacrylate moiety in the case of **T2R** and the cyanoacrylamide one for **T2R-Cat1**. In addition, post operando ICP-MS measurements indicated that an important amount of Co catalyst is lost during the first 4 h of activity. The clear correlation found among the photocurrent decrease, the loss of absorbance, and the loss of Co from the surface strongly suggests that (i) dye degradation is the main deactivation process in our system, rather than decomposition of the catalyst, and (ii) it involves a bond breaking, leading to the detachment of the whole catalytic center from the assembly. This is further supported by the recent observation that **Cat1** grafted on TiO<sub>2</sub> was stable for 10 h under photoelectrochemical conditions similar to ours (pH 4.5 acetate buffer, 1 sun visible-light irradiation),<sup>46</sup> rendering a catalyst-centered degradation process very unlikely. After 4 h of activity, the dyads still intact on the surface (retained Co loading: 16%) account for the H<sub>2</sub>-evolving activity still detected between 4 and 22 h. In contrast to other reported studies, where dye/catalyst desorption from the semiconductor film is the main deactivation process,<sup>15,24,25,99</sup> only a low amount of dyads is released in solution. The presence of the lateral alkyl chains on the CPDT bridge likely stabilizes the dyads on the NiO surface by forming a hydrophobic layer able to protect the carboxylate ester anchors from nucleophilic attack from water, as previously reported for another push-pull organic dye-based photocathode.<sup>38</sup> The low solubility of these dyads in an aqueous medium, compared, for instance, to cationic ruthenium photosensitizers, might be another factor improving the stability of the sensitized NiO surface.
- (2) TA-SEC measurements recorded under quasi-operando conditions (same potential applied to the film as for the chronoamperometric measurements but in anhydrous acetonitrile instead of aqueous electrolyte) revealed the kinetics of the light-induced processes and provided information on the different intermediates formed at the surface of the film. First, the formation of a long-lived (>1 ms) reduced organic dye moiety in the **T2R-Cat1** dyad was observed due to hole injection to the NiO. The charge recombination kinetics strongly depended

on the applied potential, leading to a six order of magnitude increase in the lifetime of the primary charge-separated state at -0.74 V vs Fc<sup>+0</sup> with respect to OCP. While a similar behavior was recently reported for NiO films sensitized with a push-pull organic dye<sup>69</sup> or ruthenium tris-diimine photosensitizers,<sup>45,44,100</sup> it is, to the best of our knowledge, unprecedented for a hydrogen-evolving photocathode based on a covalent dye-catalyst assembly. It must be stated that, due to similar time constants, the excited-state relaxation of the dye as well as the hole injection and charge recombination processes overlapped temporally and could not be deconvoluted with the sum of exponential analysis performed here. In the future, more advanced tools such as the recently reported stochastic kinetics simulations<sup>101</sup> could be applied to provide a better description of these early events. Second, thermally activated electron transfer from the reduced dye to the Co<sup>II</sup> center yielding the reduced (Co<sup>I</sup>) catalyst predominantly occurred at a time window of 1.6–20 ns, with only a small contribution taking place at longer timescales (average time constant of 9  $\mu$ s). This appears to be comparable to other triazole-based dyads studied in solution, where this process has been observed on the nanosecond–microsecond timescale.<sup>53,102–105</sup> A recent study on a Ru–Re system anchored on NiO by electropolymerization also showed electron transfer on the nanosecond–microsecond scale (<10  $\mu$ s), which was attributed to electron tunneling between the components due to the presence of an electronically insulating alkyl linker.<sup>100</sup> Electron transfer from a Ru dye to a Ni catalyst in a layer-by-layer assembly was determined to occur before 50 ns, from either the excited or reduced state of the dye.<sup>23</sup> For coimmobilized systems, charge transfer from the dye (excited or reduced state) to the catalyst has been observed in as fast as a few picoseconds.<sup>25,83,92,106</sup> Direct spectroscopic observation of the reduced catalyst signature at the surface of a dye-sensitized NiO film and determination of its lifetime are however quite scarce in the literature.<sup>25,83,100,106</sup> Hammarström et al. previously reported a diiron catalyst reduced state with different lifetimes depending on the nature of its anchor to NiO: when grafted with a carboxylate anchoring group, this reduced state was stable at the 100  $\mu$ s timescale and no H<sub>2</sub> was produced. Employing a phosphonate anchor, the lifetime reached the millisecond timescale, allowing for hydrogen production.<sup>25</sup> In our dyad, in the absence of protons, the reduced Co<sup>I</sup> state also has a lifetime reaching the millisecond timescale, which can be explained by a lower driving force for charge recombination together with an increased donor–acceptor distance (e.g., Co<sup>I</sup> to NiO<sup>+</sup>) compared to the primary charge-separated state, in which the dye is reduced. The formation of this catalytically competent species appears however to be quite inefficient; an accurate quantification of the electron-transfer yield was not possible from the ns-TA-SEC experiment since the signal of the Co<sup>I</sup> species was already built up at the beginning of the experiment, yet it was far from unity as an important amount of reduced dye remained present at the surface of the film on the microsecond timescale. This observation can be put in line with the presence of

anodic discharging spikes when light is switched off in the chopped-light chronoamperometric measurements (Figure 4b), corresponding to the reoxidation of this accumulated reduced dye.

Taken together, these data highlight that neither a low light absorption efficiency nor a sluggish multielectronic catalytic process limits the dye-sensitized photocathode performances. Rather, the accumulation of photogenerated charges at the surface of the NiO film must be considered as the performance-limiting factor. Similar observations were recently made for organic semiconductor photocathodes with a perylene diimide (PDI) acceptor polymer: an upper limit for charge accumulation was determined for stable long-term operation, above which the PDI underwent irreversible change. In our case, the reduced state of the dye is not stable, which causes the loss of the catalytic unit, accompanied by a strong decrease of the light-harvesting efficiency in the visible region. This process is clearly accelerated in the absence of the catalyst (T2R vs T2R-Cat1 photocathode), highlighting that electron transfer to the catalyst can compete with the reduced dye alteration. A fast electron transfer to the catalyst indeed reduces the lifetime of the reduced dye and thereby protects it from degradation. This charge extraction process is unfortunately not very efficient for the T2R-Cat1 photocathode, suggesting that only a small fraction of dyads is fully operative at the surface of the film, possibly for conformational or topological reasons. This raises questions regarding the covalent design of our dye-catalyst assemblies; indeed, the presence of a flexible methylene spacer between the acceptor side of the dye and the triazole-catalyst moiety might prevent the thermal electron-transfer step, thus occurring only in very specific conformations of the assembly. Future work should clearly focus on the design of novel photocathode architectures, integrating dyes that are more robust under reductive conditions, and bridging units allowing a faster and more efficient electron supply to the catalyst.

## CONCLUSIONS

In conclusion, we successfully synthesized two novel noble-metal-free covalent dye-catalyst assemblies based on the robust H<sub>2</sub>-evolving tetraazamacrocyclic cobalt catalyst Cat1. The performances of the resulting photocathodes were assessed under conditions strictly identical to our previously reported dyad based on the cobalt diimine–dioxime catalyst,<sup>14,16</sup> enabling us to establish structure–activity relationships. Switching to Cat1 was instrumental to increasing both the activity and the stability of the systems, which could be further improved by the introduction of an alkyl-substituted CPDT bridge in the push–pull structure of the dye (T2R). The resulting T2R-Cat1-sensitized photocathode effectively produced hydrogen during 4 h with 70% faradaic efficiency and still displayed some activity after 22 h, which ranks this construction within the best-performing H<sub>2</sub>-evolving dye-sensitized photocathodes reported to date<sup>24,107,108</sup> and opens perspectives toward an integration into a tandem photoelectrochemical cell. To provide meaningful insights into the factors affecting the performances of the T2R-Cat1-sensitized photocathode over time, we relied on a combination of operando and post operando characterization techniques. Hence, we established that the dye structure is altered under reductive conditions. This nonexponential process, occurring on a minute to hour

timescale, is correlated to the photocurrent decrease and to the loss of Co observed during the first 4 h of photoelectrochemical activity. Thus, despite significant improvements, stability is still hampered by the lack of robustness of the organic dye. In parallel, the electron-transfer dynamics at the NiO interface were investigated thanks to transient absorption measurements recorded with the operando potential applied to the film. We detected the formation of the catalytically competent Co<sup>I</sup> state with a lifetime of >1 ms, sufficient to initiate catalysis.

From these results, one major bottleneck hindering photoelectrochemical performances is the low yield of the thermal electron transfer from the reduced dye to the catalyst; in addition to limiting the photocurrent density, this leads to the accumulation of charges on the acceptor part of the dye and ultimately to its degradation. This study thus provides a clear rationale toward the optimization of the performances of dye-sensitized photocathodes for hydrogen production, and we will focus our efforts on designing novel dyad assemblies and/or photocathode architectures achieving faster electron transfer to the catalyst. In that context, a density functional theory (DFT)-driven approach exploiting the Marcus theory to determine structures warranting higher electron-transfer rates could be very valuable. Replacing NiO by other p-type semiconductors represents another track for improvement, as recently highlighted in studies by our group and others.<sup>7,18,19</sup> Finally, this work paves the way for the integration of robust cobalt polypyridinyl catalysts into functional photoelectrochemical devices for solar fuel production.<sup>88,89,109</sup>

## EXPERIMENTAL SECTION

**Synthesis.** All reagents were purchased from Sigma-Aldrich or Strem and used as obtained unless otherwise stated. Reagent-grade solvents were used without further purification. <sup>1</sup>H NMR experiments were carried out on Bruker Avance 300 or 500 MHz spectrometers, and the resulting spectra are referenced to the residual solvent peak and reported relative to the tetramethylsilane reference ( $\delta = 0$  ppm). Electrospray ionization mass spectrometric (ESI-MS) measurements were carried out on a Thermoquest Finnigan LCQ spectrometer. Accurate mass measurements (high-resolution mass spectrometry—HRMS) were recorded on a Bruker maXis mass spectrometer by the “Fédération de Recherche” ICOA/CBM (FR 2708) platform. Elemental analysis was performed on a ThermoFisher Scientific “Flash 2000” by the “Plateforme d’analyse pour la chimie” (GDS 3648, Strasbourg). <sup>t</sup>BuTl,<sup>48</sup> its alkyne derivative <sup>t</sup>BuTl-alkyne,<sup>16</sup> Cat1,<sup>33</sup> and <sup>t</sup>BuTl-Co<sup>16</sup> were synthesized according to previously reported procedures. Detailed syntheses for the dye precursors, the 4-azido-2,6-diacetylpyridine building block, <sup>t</sup>BuT2R, its alkyne derivative <sup>t</sup>BuT2R-alkyne, and T2R-Co are described in the Supporting Information.

**General Procedure for CuAAC Click Coupling.<sup>14,16</sup>** The alkyne-substituted dye (0.5 mmol) and 4-azido-2,6-diacetylpyridine (1 equiv) were dissolved in 20 mL of degassed CH<sub>2</sub>Cl<sub>2</sub>. Sodium ascorbate (0.5 mmol) and CuSO<sub>4</sub>·5H<sub>2</sub>O (0.2 mmol) were dissolved in 10 mL of degassed H<sub>2</sub>O and added to the reaction mixture. Degassed MeOH was added dropwise until a single phase was obtained. The reaction mixture was stirred at room temperature for 24 h. After removal of the volatile solvents, the mixture was extracted with CH<sub>2</sub>Cl<sub>2</sub>, washed with brine solution, dried over Na<sub>2</sub>SO<sub>4</sub>, and filtered.



The crude product was purified on a silica gel column to yield the diacetylpyridine-functionalized dye.

**General Procedure for the Template Synthesis of Cat1.** The diacetylpyridine-functionalized dye (0.3 mmol) was dissolved in EtOH (2 mL) and CH<sub>2</sub>Cl<sub>2</sub> (1 mL) and kept at 40 °C under argon. CoCl<sub>2</sub>·6H<sub>2</sub>O (1 equiv) and water (0.4 mL) were added, and the solution was stirred at 55 °C to dissolve the salt. The reaction mixture was warmed to 75 °C before the addition of 3,3'-diaminodipropylamine (1 equiv) and glacial acetic acid (0.03 mL) and was then stirred at 75 °C for 5 h under argon. After cooling down to room temperature, 0.1 mL of concentrated HCl was added and the reaction mixture was stirred at room temperature for 16 h, kept for 2 h at −15 °C, and centrifuged. The precipitate was washed with H<sub>2</sub>O and EtOH before drying under a vacuum to yield the dyad as a red solid.

**General Procedure for the tert-Butyl Ester Groups' Hydrolysis Prior to Film Sensibilization.** Hydrolysis of the tert-butyl ester groups was carried out according to our previously reported procedures,<sup>14,16,48</sup> by reacting the tert-butyl ester protected dyads (or dyes) with trifluoroacetic acid (TFA) in CH<sub>2</sub>Cl<sub>2</sub> for 5 h at room temperature.

**NiO Film Preparation and Sensitization.** NiO films were prepared using an F108 precursor solution prepared by mixing 1 g of NiCl<sub>2</sub> and 1 g of F108 triblock copolymer in a mixture of ethanol (15 mL) and Milli-Q water (6 mL), according to our previously reported procedures.<sup>14,16</sup> The mixture was sonicated for 6 h, centrifuged, and passed through a 45 μm pore-size polyethersulfone syringe filter. Fluorine-doped tin oxide (FTO)-coated glass substrates (Solems TEC 7, sheet resistance 7Ω/□) for the hydrogen production experiments or round indium tin oxide (ITO)-coated glass substrates (Solems ITO SOL 30, 1 mm thickness) for the operando UV-vis experiments and transient absorption measurements were cleaned by sonication in isopropanol, distilled water, and ethanol for 10 min each, followed by ozone-cleaning for 15 min. The F108 precursor solution was then spin-coated on the substrates (5000 rpm, 60 s), followed by sintering in an oven in air (30 min ramp to 450 °C, 30 min at 450 °C). Spin-coating and sintering were repeated for a total of four layers. The film thickness was measured by scanning electron microscopy (SEM) with a scanning electron microscope Zeiss Ultra 55 operating at 4 kV.

NiO electrodes were soaked in methanolic solutions (0.2 mM) of the different dyes and dyads (acidic form) at room temperature for 24 h under orbital stirring. For the time-correlated single-photon-counting (TCSPC) measurements, sensitizing solutions with 10 mM chenodeoxycholic acid (CDCA) added were used for sensitization. After sensitization, films were then rinsed with methanol and dried with pressurized air. After sensitization, NiO films were cut in half. One half of the sample was used to determine grafting densities pre operando, while the other half was used for photoelectrochemical experiments and afterward desorbed to determine grafting densities and possible degradation post operando.

**Dyad Loading Quantification.** Sensitized NiO films were soaked in a 1 M methanolic phenylphosphonic acid solution for 3 h to desorb grafted compounds. Afterward, the UV-vis spectra of the desorption solutions were then measured and dyad (or dye) loading was determined using the molar extinction coefficient at the π-π\* band (Figure S3) and the film surface areas. Cobalt quantification was

performed by inductively coupled plasma mass spectrometry (ICP-MS) using an iCAP RQ quadrupole mass instrument (Thermo Fisher Scientific GmbH, Germany). The samples were prepared by soaking each film in 1 mL of aq HNO<sub>3</sub> (65% w/v) for 1 min, rinsing with 1 mL of Milli-Q water, hydrolyzing again with 1 mL of HNO<sub>3</sub>, and rinsing with 1 mL of H<sub>2</sub>O and then 2.5 mL of H<sub>2</sub>O. The resulting solution (6.5 mL at 20% w/v HNO<sub>3</sub>) was diluted 20 times to yield a solution at 1% w/v HNO<sub>3</sub>, which was used for the measurement.

**Steady-State Spectroscopy.** Steady-state absorption spectra were recorded on an Agilent Cary 60 or a Jasco V780 spectrophotometer in 1 cm cuvettes. All solvents used for spectroscopy were of spectroscopic grade.

**Time-Correlated Single-Photon-Counting (TCSPC) Measurements.** The emission decay profiles were measured by time-correlated single photon counting (TCSPC) in a time window of 20 ns. After excitation of the sample with the frequency-doubled output of a Ti-sapphire laser (Tsunami, Newport Spectra-Physics GmbH) at λ<sub>ex</sub> = 365 nm at a pulse-to-pulse repetition rate of 400 kHz after passing a pulse selector (model 3980, Newport Spectra-Physics GmbH), the luminescence of the sample was collected in a 90° arrangement and detected using a Becker & Hickl PMC-100-4 photon-counting module. The lifetime values were obtained from mono- or biexponential fits convoluted with the instrument response function (IRF). Sample solutions were prepared to yield an optical density of 0.05–0.1 at the excitation wavelength in a 1.0 cm quartz cuvette using air-equilibrated, spectroscopic-grade solvents.

**Electrochemical and Photoelectrochemical Experiments.** Electrochemical and photoelectrochemical experiments were recorded using a BioLogic VSP 300, BioLogic SP 50, or Ivium CompactStat potentiostat. A three-electrode setup was used for all experiments. For electrochemical experiments, Merck SeccoSolv dry DMF was used as the solvent and tetrabutylammonium tetrafluoroborate was recrystallized from ethanol/water prior to use. The working electrode was a glassy carbon disk electrode, the auxiliary electrode was a Pt wire, and the reference electrode was a miniature leakless Ag/AgCl electrode (EDAQ). The supporting electrolyte was 0.1 M TBABF<sub>4</sub> in dry DMF, degassed by passing argon through the solution for 20 min before measuring. During the measurements, the argon flow was removed from the solution but left in the headspace of the cell. The scan rate during cyclic voltammetry was 50 mV·s<sup>-1</sup>, and the sample concentration was 1 mM. The potential of the reference electrode was calibrated after each measurement by adding ferrocene as a reference to the solution and recording the potential of the Fc<sup>+/0</sup> couple.

The photoelectrochemical measurements were carried out in a home-made three-electrode cell with a sensitized NiO film as the working electrode, a titanium wire as the auxiliary electrode, and a Ag/AgCl reference electrode made of a Ag/AgCl wire dipped into a 3 M aqueous KCl solution, separated from the electrolyte by a Vycor frit. The auxiliary electrode was separated from the main compartment of the cell by a Vycor frit. Irradiation was performed using a Newport 300 W ozone-free Xe lamp at either 280 or 130 W equipped with a water-filled Spectra-Physics 6123NS liquid filter to eliminate infrared radiation (λ > 800 nm) and a 400 nm long-pass filter (Spectra-Physics 59472). The power density was measured using a Newport PM1918-R power meter and adjusted to 65

mW·cm<sup>-2</sup> (equivalent to 1 sun irradiation) using appropriate neutral-density filters. The aqueous supporting electrolyte was either 0.1 M 2-(*N*-morpholino)ethanesulfonic acid (MES)/0.1 M NaCl buffer at pH 5.5. The electrolyte solution was degassed with nitrogen for 30 min prior to use. The amount of hydrogen evolved during the long-term chronoamperometric measurements was measured in the headspace by sampling aliquots in a Perkin Elmer Clarus 580 gas chromatograph equipped with a molecular sieve 5 Å column (30 m to 0.53 mm) and a thermal conductivity (TCD) detector. Additionally, the amount of hydrogen dissolved in solution was determined by a Unisense H<sub>2</sub> microsensor in a needle. The zero value for the microsensor was measured in the assembled cell prior to irradiation. Potentials are given as converted to potentials vs the reversible hydrogen electrode (RHE) using the formula

$$E_{\text{RHE}} = E_{\text{Ag/AgCl}} + 0.425 \text{ V} - E_{\text{Fe(III)/Fe(II)}} + 0.059 \times \text{pH}$$

where 0.425 V is the potential of the potassium ferrocyanide Fe(III)/Fe(II) couple vs normal hydrogen electrode (NHE) at 0.1 M potassium phosphate buffer at pH 7<sup>110</sup> and  $E_{\text{Fe(III)/Fe(II)}}$  is the potential of the potassium ferrocyanide Fe<sup>III/II</sup> couple measured vs the Ag/AgCl reference electrode.

For the photoelectrochemical degradation experiment, a home-made spectroelectrochemistry cell specifically designed for measurements on transparent semiconductor films was used with dye-sensitized NiO films on the ITO/glass substrate (Solems, ITO SOL 30, 1 mm thickness) as the working electrode, Pt wire as the auxiliary electrode, and a miniature leakless Ag/AgCl (EDAQ) as the reference electrode. The supporting electrolyte was 0.1 M 2-(*N*-morpholino)ethanesulfonic acid (MES)/0.1 M NaCl buffer at pH 5.5. The solution was degassed for 20 min prior to measuring. At an applied potential of -0.35 V vs Ag/AgCl (0.21 V vs RHE), the film was irradiated as in the photoelectrochemical experiments and UV-vis spectra were recorded in intervals.

**Transient Absorption Spectroelectrochemistry (TA-SEC) Measurements.** The setup for femtosecond transient absorption measurements has been previously described.<sup>111</sup> An amplified Ti:sapphire laser (Legend, Coherent Inc.) produced the 800 nm fundamental beam, which was split into two beams. One of the beams was used to pump an optical-parametric amplifier (TOPAS-C), whose output was spectrally centered at 480 nm and used as pump pulses for the pump-probe experiments. The pump pulses were typically set to 0.4 μJ per pulse, which was lowered to 0.2 μJ per pulse for measurements at -1.15 V vs Fc<sup>+0</sup> to avoid photodegradation. To achieve the pump-probe delay of 2 ns, the pump beam was directed over a delay line. The supercontinuum used as the probe pulse was generated by passing the second beam of the fundamental 800 nm through a CaF<sub>2</sub> window, with probe intensities falling into the range of hundreds of nanojoule. The probe light was split into two beams, one of which was focused through the sample, while the other served as the reference. A 488 nm notch filter was placed between the sample and the detector to remove scattered pump light. The probe and reference beams were detected by a double-stripe diode array and converted into differential absorption signals using a commercially available detection system (Pascher Instruments AB, Sweden). The recorded data was corrected for chirp and globally fitted using a sum of three exponentials. During the fitting, the pulse overlap region of ±200 fs was excluded to avoid contributions from coherent artifacts.<sup>112</sup>

The setup for nanosecond transient absorption measurements has been previously described elsewhere.<sup>113</sup> The pump pulse was generated by a Continuum Surelite OPO Plus (pumped by a Nd:YAG laser, ≈20 ns pulse duration, 10 Hz repetition rate). The probe light was generated by a 75 W xenon arc lamp, focused through the sample, and detected by a Hamamatsu R928 photomultiplier. The signal was amplified and processed by a commercially available detection system (Pascher Instruments AB, Sweden). The pump pulse energy was set to 0.13 mJ. To remove pump scatter, a 475 nm short-pass and a 500 nm long-pass edge filter were used for short and long wavelengths, respectively.

TA-SEC experiments were performed using a home-built spectroelectrochemical cell, designed to work in a three-electrode setup under inert conditions and to optimize time resolution in the femtosecond measurements, with a minimized path length (ca. 4 mm). The sensitized NiO film was used as the working electrode, a miniature leakless Ag/AgCl electrode (EDAQ) was used as the reference electrode, and a Pt wire was used as the auxiliary electrode. The cell was assembled in a glovebox and filled with 0.1 M TBABF<sub>4</sub> in ACN. Transient absorption measurements were performed at open-circuit potential and different applied potentials on the same film, moving the film in the plane periodically to prevent photodegradation. Prior to each experiment, the reference electrode was calibrated using ferrocene.

## ■ ASSOCIATED CONTENT

### Supporting Information

The Supporting Information is available free of charge at <https://pubs.acs.org/doi/10.1021/acscatal.0c05033>.

Detailed synthetic procedures and additional electrochemical, spectroscopic and photoelectrochemical data (PDF)

## ■ AUTHOR INFORMATION

### Corresponding Authors

**Benjamin Dietzek** – *Institute of Physical Chemistry and Abbe Center of Photonics, Friedrich Schiller University Jena, 07743 Jena, Germany; Department Functional Interfaces, Leibniz Institute of Photonic Technology Jena (Leibniz-IPHT), 07745 Jena, Germany; Center for Energy and Environmental Chemistry Jena (CEEC Jena), Friedrich Schiller University Jena, 07743 Jena, Germany;*

● [orcid.org/0000-0002-2842-3537](https://orcid.org/0000-0002-2842-3537);

Email: [benjamin.dietzek@leibniz-ipht.de](mailto:benjamin.dietzek@leibniz-ipht.de)

**Murielle Chavarot-Kerlidou** – *Laboratoire de Chimie et Biologie des Métaux, Univ. Grenoble Alpes, CNRS, CEA, IRIG, F-38000 Grenoble, France;* ● [orcid.org/0000-0003-2709-3772](https://orcid.org/0000-0003-2709-3772); Email: [murielle.chavarot-kerlidou@cea.fr](mailto:murielle.chavarot-kerlidou@cea.fr)

### Authors

**Sebastian Bold** – *Laboratoire de Chimie et Biologie des Métaux, Univ. Grenoble Alpes, CNRS, CEA, IRIG, F-38000 Grenoble, France; Institute of Physical Chemistry and Abbe Center of Photonics, Friedrich Schiller University Jena, 07743 Jena, Germany; Department Functional Interfaces, Leibniz Institute of Photonic Technology Jena (Leibniz-IPHT), 07745 Jena, Germany*

**Julien Massin** – *Laboratoire de Chimie et Biologie des Métaux, Univ. Grenoble Alpes, CNRS, CEA, IRIG, F-38000 Grenoble, France*



Emmanouil Giannoudis – Laboratoire de Chimie et Biologie des Métaux, Univ. Grenoble Alpes, CNRS, CEA, IRIG, F-38000 Grenoble, France

Matthieu Koepf – Laboratoire de Chimie et Biologie des Métaux, Univ. Grenoble Alpes, CNRS, CEA, IRIG, F-38000 Grenoble, France

Vincent Artero – Laboratoire de Chimie et Biologie des Métaux, Univ. Grenoble Alpes, CNRS, CEA, IRIG, F-38000 Grenoble, France; [orcid.org/0000-0002-6148-8471](https://orcid.org/0000-0002-6148-8471)

Complete contact information is available at:  
<https://pubs.acs.org/10.1021/acscatal.0c05033>

#### Author Contributions

The manuscript was written through contributions of all authors. All authors have given approval to the final version of the manuscript.

#### Funding

This work was supported by the European Commission's Seventh Framework Program (FP7/2007-2013) under grant agreement no. 306398 (FP7-IDEAS-ERC, Project PhotocatH<sub>2</sub>ode), the French National Research Agency in the framework of the "Investissements d'avenir" program (ANR-15-IDEX-02, Labex ARCANE, and CBH-EUR-GS, ANR-17-EURE-0003), and the Franco-German University.

#### Notes

The authors declare no competing financial interest.

#### ACKNOWLEDGMENTS

Quentin Vacher, Tatiana Straistari, and Adina Morozan are acknowledged for their help in the synthesis and purification of the compounds and for the SEM measurements. Jacques Pecaut (CEA/DRF/IRIG/DIESE/SyMMES) and Pierre-Alain Bayle (CEA/DRF/IRIG/DEPHY/MEM) are acknowledged for the ESI-MS and the 500 MHz NMR measurements, respectively. Stéphane Ravel from CEA/DRF/IRIG/DBSCI/PCV is acknowledged for the ICP-MS analysis. This work was supported by the European Commission's Seventh Framework Program (FP7/2007-2013) under grant agreement no. 306398 (FP7-IDEAS-ERC, Project PhotocatH<sub>2</sub>ode) and the French National Research Agency in the framework of the "Investissements d'avenir" program (ANR-15-IDEX-02, Labex ARCANE, and CBH-EUR-GS, ANR-17-EURE-0003). S.B. thanks the Franco-German University for the cotutelle thesis funding support. The authors thank the workshop of IPHT Jena for their help in building the spectroscopy cell.

#### REFERENCES

- (1) Nocera, D. G. Solar Fuels and Solar Chemicals Industry. *Acc. Chem. Res.* **2017**, *50*, 616–619.
- (2) Zhang, B.; Sun, L. Artificial Photosynthesis: Opportunities and Challenges of Molecular Catalysts. *Chem. Soc. Rev.* **2019**, *48*, 2216–2264.
- (3) House, R. L.; Iha, N. Y. M.; Coppo, R. L.; Alibabaei, L.; Sherman, B. D.; Kang, P.; Brennaman, M. K.; Hoertz, P. G.; Meyer, T. J. Artificial Photosynthesis: Where Are We Now? Where Can We Go? *J. Photochem. Photobiol., C* **2015**, *25*, 32–45.
- (4) Berardi, S.; Drouet, S.; Francàs, L.; Gimbert-Suriñach, C.; Guttentag, M.; Richmond, C.; Stoll, T.; Llobet, A. Molecular Artificial Photosynthesis. *Chem. Soc. Rev.* **2014**, *43*, 7501–7519.
- (5) Brennaman, M. K.; Dillon, R. J.; Alibabaei, L.; Gish, M. K.; Dares, C. J.; Ashford, D. L.; House, R. L.; Meyer, G. J.; Papanikolas, J. M.; Meyer, T. J. Finding the Way to Solar Fuels with Dye-Sensitized Photoelectrosynthesis Cells. *J. Am. Chem. Soc.* **2016**, *138*, 13085–13102.
- (6) Yu, Z.; Li, F.; Sun, L. Recent Advances in Dye-Sensitized Photoelectrochemical Cells for Solar Hydrogen Production Based on Molecular Components. *Energy Environ. Sci.* **2015**, *8*, 760–775.
- (7) Windle, C. D.; Kumagai, H.; Higashi, M.; Brisse, R.; Bold, S.; Joussetme, B.; Chavarot-Kerlidou, M.; Maeda, K.; Abe, R.; Ishitani, O.; Artero, V. Earth-Abundant Molecular Z-Scheme Photoelectrochemical Cell for Overall Water-Splitting. *J. Am. Chem. Soc.* **2019**, *141*, 9593–9602.
- (8) Fan, K.; Li, F.; Wang, L.; Daniel, Q.; Gabrielsson, E.; Sun, L. Pt-Free Tandem Molecular Photoelectrochemical Cells for Water Splitting Driven by Visible Light. *Phys. Chem. Chem. Phys.* **2014**, *16*, 25234–25240.
- (9) Li, F.; Fan, K.; Xu, B.; Gabrielsson, E.; Daniel, Q.; Li, L.; Sun, L. Organic Dye-Sensitized Tandem Photoelectrochemical Cell for Light Driven Total Water Splitting. *J. Am. Chem. Soc.* **2015**, *137*, 9153–9159.
- (10) Ji, Z.; He, M.; Huang, Z.; Ozkan, U.; Wu, Y. Photostable P-Type Dye-Sensitized Photoelectrochemical Cells for Water Reduction. *J. Am. Chem. Soc.* **2013**, *135*, 11696–11699.
- (11) Li, L.; Duan, L.; Wen, F.; Li, C.; Wang, M.; Hagfeldt, A.; Sun, L. Visible Light Driven Hydrogen Production from a Photo-Active Cathode Based on a Molecular Catalyst and Organic Dye-Sensitized p-Type Nanostructured NiO. *Chem. Commun.* **2012**, *48*, 988–990.
- (12) Meng, P.; Wang, M.; Yang, Y.; Zhang, S.; Sun, L. CdSe Quantum Dots/Molecular Cobalt Catalyst Co-Grafted Open Porous NiO Film as a Photocathode for Visible Light Driven H<sub>2</sub> Evolution from Neutral Water. *J. Mater. Chem. A* **2015**, *3*, 18852–18859.
- (13) Kamire, R. J.; Majewski, M. B.; Hoffeditz, W. L.; Phelan, B. T.; Farha, O. K.; Hupp, J. T.; Wasielewski, M. R. Photodriven Hydrogen Evolution by Molecular Catalysts Using Al<sub>2</sub>O<sub>3</sub>-Protected Perylene-3,4-Dicarboximide on NiO Electrodes. *Chem. Sci.* **2017**, *8*, 541–549.
- (14) Windle, C. D.; Massin, J.; Chavarot-Kerlidou, M.; Artero, V. A Protocol for Quantifying Hydrogen Evolution by Dye-Sensitized Molecular Photocathodes and Its Implementation for Evaluating a New Covalent Architecture Based on an Optimized Dye-Catalyst Dyad. *Dalton Trans.* **2018**, *47*, 10509–10516.
- (15) Pati, P. B.; Zhang, L.; Philippe, B.; Fernández-Terán, R.; Ahmadi, S.; Tian, L.; Rensmo, H.; Hammarström, L.; Tian, H. Insights into the Mechanism of a Covalently Linked Organic Dye–Cobaloxime Catalyst System for Dye-Sensitized Solar Fuel Devices. *ChemSusChem* **2017**, *10*, 2480–2495.
- (16) Kaeffer, N.; Massin, J.; Lebrun, C.; Renault, O.; Chavarot-Kerlidou, M.; Artero, V. Covalent Design for Dye-Sensitized H<sub>2</sub>-Evolving Photocathodes Based on a Cobalt Diimine–Dioxime Catalyst. *J. Am. Chem. Soc.* **2016**, *138*, 12308–12311.
- (17) Kaeffer, N.; Windle, C. D.; Brisse, R.; Gablin, C.; Leonard, D.; Joussetme, B.; Chavarot-Kerlidou, M.; Artero, V. Insights into the Mechanism and Aging of a Noble-Metal Free H<sub>2</sub>-Evolving Dye-Sensitized Photocathode. *Chem. Sci.* **2018**, *9*, 6721–6738.
- (18) Li, F.; Xu, R.; Nie, C.; Wu, X.; Zhang, P.; Duan, L.; Sun, L. Dye-Sensitized LaFeO<sub>3</sub> Photocathode for Solar-Driven H<sub>2</sub> Generation. *Chem. Commun.* **2019**, *55*, 12940–12943.
- (19) Creissen, C. E.; Warnan, J.; Antón-García, D.; Farré, Y.; Odobel, F.; Reiser, E. Inverse Opal CuCrO<sub>2</sub> Photocathodes for H<sub>2</sub> Production Using Organic Dyes and a Molecular Ni Catalyst. *ACS Catal.* **2019**, *9*, 9530–9538.
- (20) Wang, D.; Sheridan, M.; Shan, B.; Farnum, B. H.; Marquard, S. L.; Sherman, B. D.; Eberhart, M. S.; Nayak, A.; Dares, C. J.; Das, A. K.; Bullock, R. M.; Meyer, T. J. Layer-by-Layer Molecular Assemblies for Dye-Sensitized Photoelectrosynthesis Cells Prepared by Atomic Layer Deposition. *J. Am. Chem. Soc.* **2017**, *139*, 14518–14525.
- (21) Gross, M. A.; Creissen, C. E.; Orchard, K. L.; Reiser, E. Photoelectrochemical Hydrogen Production in Water Using a Layer-by-Layer Assembly of a Ru Dye and Ni Catalyst on NiO. *Chem. Sci.* **2016**, *7*, 5537–5546.



- (22) Shan, B.; Sherman, B. D.; Klug, C. M.; Nayak, A.; Marquard, S. L.; Liu, Q.; Bullock, R. M.; Meyer, T. J. Modulating Hole Transport in Multilayered Photocathodes with Derivatized P-Type Nickel Oxide and Molecular Assemblies for Solar-Driven Water Splitting. *J. Phys. Chem. Lett.* **2017**, *8*, 4374–4379.
- (23) Shan, B.; Das, A. K.; Marquard, S.; Farnum, B. H.; Wang, D.; Bullock, R. M.; Meyer, T. J. Photogeneration of Hydrogen from Water by a Robust Dye-Sensitized Photocathode. *Energy Environ. Sci.* **2016**, *9*, 3693–3697.
- (24) Creissen, C. E.; Warnan, J.; Reiser, E. Solar H<sub>2</sub> Generation in Water with a CuCrO<sub>2</sub> Photocathode Modified with an Organic Dye and Molecular Ni Catalyst. *Chem. Sci.* **2018**, *9*, 1439–1447.
- (25) Antila, L. J.; Ghamgosar, P.; Maji, S.; Tian, H.; Ott, S.; Hammarström, L. Dynamics and Photochemical H<sub>2</sub> Evolution of Dye–NiO Photocathodes with a Biomimetic FeFe-Catalyst. *ACS Energy Lett.* **2016**, *1*, 1106–1111.
- (26) Lyu, S.; Massin, J.; Pavone, M.; Muñoz-García, A. B.; Labrugère, C.; Toupance, T.; Chavarot-Kerlidou, M.; Artero, V.; Olivier, C. H<sub>2</sub>-Evolving Dye-Sensitized Photocathode Based on a Ruthenium–Diacetylide/Cobaloxime Supramolecular Assembly. *ACS Appl. Energy Mater.* **2019**, *2*, 4971–4980.
- (27) Shan, B.; Brennaman, M. K.; Troian-Gautier, L.; Liu, Y.; Nayak, A.; Klug, C. M.; Li, T. T.; Bullock, R. M.; Meyer, T. J. A Silicon-Based Heterojunction Integrated with a Molecular Excited State in a Water-Splitting Tandem Cell. *J. Am. Chem. Soc.* **2019**, *141*, 10390–10398.
- (28) Nie, C.; Ni, W.; Gong, L.; Jiang, J.; Wang, J.; Wang, M. Charge Transfer Dynamics and Catalytic Performance of a Covalently Linked Hybrid Assembly Comprising a Functionalized Cobalt Tetraazamacrocyclic Catalyst and CuInS<sub>2</sub>/ZnS Quantum Dots for Photochemical Hydrogen Production. *J. Mater. Chem. A* **2019**, *7*, 27432–27440.
- (29) Grau, S.; Schilling, M.; Moonshiram, D.; Benet-Buchholz, J.; Lubner, S.; Llobet, A.; Gimbert-Suriñach, C. Electrochemically and Photochemically Induced Hydrogen Evolution Catalysis with Cobalt Tetraazamacrocycles Occurs Through Different Pathways. *ChemSusChem* **2020**, *13*, 2745–2752.
- (30) Leung, C.; Chen, Y.; Yu, H.; Yiu, S.; Ko, C.; Lau, T.-C. Electro- and Photocatalytic Hydrogen Generation in Acetonitrile and Aqueous Solutions by a Cobalt Macrocyclic Schiff-Base Complex. *Int. J. Hydrogen Energy* **2011**, *36*, 11640–11645.
- (31) Gueret, R.; Poulard, L.; Oshinowo, M.; Chauvin, J.; Dahmane, M.; Dupeyre, G.; Lainé, P. P.; Fortage, J.; Collomb, M.-N. Challenging the [Ru(Bpy)<sub>3</sub>]<sup>2+</sup> Photosensitizer with a Triazatriangulenium Robust Organic Dye for Visible-Light-Driven Hydrogen Production in Water. *ACS Catal.* **2018**, *8*, 3792–3802.
- (32) Sandroni, M.; Gueret, R.; Wegner, K. D.; Reiss, P.; Fortage, J.; Aldakov, D.; Collomb, M.-N. Cadmium-Free CuInS<sub>2</sub>/ZnS Quantum Dots as Efficient and Robust Photosensitizers in Combination with a Molecular Catalyst for Visible Light-Driven H<sub>2</sub> Production in Water. *Energy Environ. Sci.* **2018**, *11*, 1752–1761.
- (33) Varma, S.; Castillo, C. E.; Stoll, T.; Fortage, J.; Blackman, A. G.; Molton, F.; Deronzier, A.; Collomb, M.-N. Efficient Photocatalytic Hydrogen Production in Water Using a Cobalt(III) Tetraaza-Macrocyclic Catalyst: Electrochemical Generation of the Low-Valent Co(I) Species and Its Reactivity toward Proton Reduction. *Phys. Chem. Chem. Phys.* **2013**, *15*, 17544.
- (34) Gimbert-Suriñach, C.; Alberio, J.; Stoll, T.; Fortage, J.; Collomb, M.-N.; Deronzier, A.; Palomares, E.; Llobet, A. Efficient and Limiting Reactions in Aqueous Light-Induced Hydrogen Evolution Systems Using Molecular Catalysts and Quantum Dots. *J. Am. Chem. Soc.* **2014**, *136*, 7655–7661.
- (35) Roy, S.; Bacchi, M.; Berggren, G.; Artero, V. A Systematic Comparative Study of Hydrogen-Evolving Molecular Catalysts in Aqueous Solutions. *ChemSusChem* **2015**, *8*, 3632–3638.
- (36) Yen, Y.-S.; Chen, W.-T.; Hsu, C.-Y.; Chou, H.-H.; Lin, J. T.; Yeh, M.-C. P. Arylamine-Based Dyes for p-Type Dye-Sensitized Solar Cells. *Org. Lett.* **2011**, *13*, 4930–4933.
- (37) Li, R.; Liu, J.; Cai, N.; Zhang, M.; Wang, P. Synchronously Reduced Surface States, Charge Recombination, and Light Absorption Length for High-Performance Organic Dye-Sensitized Solar Cells. *J. Phys. Chem. B* **2010**, *114*, 4461–4464.
- (38) Click, K. A.; Beauchamp, D. R.; Huang, Z.; Chen, W.; Wu, Y. Membrane-Inspired Acidically Stable Dye-Sensitized Photocathode for Solar Fuel Production. *J. Am. Chem. Soc.* **2016**, *138*, 1174–1179.
- (39) Yu, Y.; Click, K. A.; Chien, S.-C.; Sun, J.; Curtze, A.; Lin, L.-C.; Wu, Y. Decoupling pH Dependence of Flat Band Potential in Aqueous Dye-Sensitized Electrodes. *J. Phys. Chem. C* **2019**, *123*, 8681–8687.
- (40) Bold, S.; Zedler, L.; Zhang, Y.; Massin, J.; Artero, V.; Chavarot-Kerlidou, M.; Dietzek, B. Electron Transfer in a Covalent Dye–Cobalt Catalyst Assembly – a Transient Absorption Spectroelectrochemistry Perspective. *Chem. Commun.* **2018**, *54*, 10594–10597.
- (41) Zedler, L.; Mengele, A. K.; Ziemer, K. M.; Zhang, Y.; Wächtler, M.; Gräfe, S.; Pascher, T.; Rau, S.; Kupfer, S.; Dietzek, B. Unraveling the Light-Activated Reaction Mechanism in a Catalytically Competent Key Intermediate of a Multifunctional Molecular Catalyst for Artificial Photosynthesis. *Angew. Chem., Int. Ed.* **2019**, *58*, 13140–13148.
- (42) Zhang, Y.; Zedler, L.; Karnahl, M.; Dietzek, B. Excited-State Dynamics of Heteroleptic Copper(I) Photosensitizers and Their Electrochemically Reduced Forms Containing a Dipyrrophenazine Moiety – a Spectroelectrochemical Transient Absorption Study. *Phys. Chem. Chem. Phys.* **2019**, *21*, 10716–10725.
- (43) Dillon, R. J.; Alibabaei, L.; Meyer, T. J.; Papanikolas, J. M. Enabling Efficient Creation of Long-Lived Charge-Separation on Dye-Sensitized NiO Photocathodes. *ACS Appl. Mater. Interfaces* **2017**, *9*, 26786–26796.
- (44) D’Amario, L.; Antila, L. J.; Pettersson Ringard, B.; Boschloo, G.; Hammarström, L. Kinetic Evidence of Two Pathways for Charge Recombination in NiO-Based Dye-Sensitized Solar Cells. *J. Phys. Chem. Lett.* **2015**, *6*, 779–783.
- (45) McCrory, C. C. L.; Uyeda, C.; Peters, J. C. Electrocatalytic Hydrogen Evolution in Acidic Water with Molecular Cobalt Tetraazamacrocycles. *J. Am. Chem. Soc.* **2012**, *134*, 3164–3170.
- (46) Nie, C.; Liu, C.; Gong, L.; Wang, M. Boosting the Performance of a Silicon Photocathode for Photoelectrochemical Hydrogen Production by Immobilization of a Cobalt Tetraazamacrocyclic Catalyst. *J. Mater. Chem. A* **2021**, *9*, 234–238.
- (47) Cheng, X.; Sun, S.; Liang, M.; Shi, Y.; Sun, Z.; Xue, S. Organic Dyes Incorporating the Cyclopentadithiophene Moiety for Efficient Dye-Sensitized Solar Cells. *Dyes Pigm.* **2012**, *92*, 1292–1299.
- (48) Massin, J.; Bräutigam, M.; Kaeffer, N.; Queyriaux, N.; Field, M. J.; Schacher, F. H.; Popp, J.; Chavarot-Kerlidou, M.; Dietzek, B.; Artero, V. Dye-Sensitized PS-b-P2VP-Templated Nickel Oxide Films for Photoelectrochemical Applications. *Interface Focus* **2015**, *5*, No. 20140083.
- (49) Ji, Z.; Natu, G.; Huang, Z.; Wu, Y. Linker Effect in Organic Donor-Acceptor Dyes for p-Type NiO Dye Sensitized Solar Cells. *Energy Environ. Sci.* **2011**, *4*, 2818–2821.
- (50) Ishow, E.; Clavier, G.; Miomandre, F.; Rebarz, M.; Buntinx, G.; Poizat, O. Comprehensive Investigation of the Excited-State Dynamics of Push–Pull Triphenylamine Dyes as Models for Photonic Applications. *Phys. Chem. Chem. Phys.* **2013**, *15*, 13922.
- (51) Zieschang, F.; Schreck, M. H.; Schmiedel, A.; Holzapfel, M.; Klein, J. H.; Walter, C.; Engels, B.; Lambert, C. Photoinduced Electron Transfer Dynamics in Triarylamine-Naphthalene Diimide Cascades. *J. Phys. Chem. C* **2014**, *118*, 27698–27714.
- (52) de Miguel, G.; Wielopolski, M.; Schuster, D. I.; Fazio, M. A.; Lee, O. P.; Haley, C. K.; Ortiz, A. L.; Echegoyen, L.; Clark, T.; Guldi, D. M. Triazole Bridges as Versatile Linkers in Electron Donor–Acceptor Conjugates. *J. Am. Chem. Soc.* **2011**, *133*, 13036–13054.
- (53) Sheth, S.; Baron, A.; Herrero, C.; Vauzeilles, B.; Aukauloo, A.; Leibl, W. Light-Induced Tryptophan Radical Generation in a Click Modular Assembly of a Sensitizer-Tryptophan Residue. *Photochem. Photobiol. Sci.* **2013**, *12*, 1074.

- (54) Baron, A.; Herrero, C.; Quaranta, A.; Charlot, M.-F.; Leibl, W.; Vauzeilles, B.; Aukauloo, A. Click Chemistry on a Ruthenium Polypyridine Complex. An Efficient and Versatile Synthetic Route for the Synthesis of Photoactive Modular Assemblies. *Inorg. Chem.* **2012**, *51*, 5985–5987.
- (55) Baron, A.; Herrero, C.; Quaranta, A.; Charlot, M.-F.; Leibl, W.; Vauzeilles, B.; Aukauloo, A. Efficient Electron Transfer through a Triazole Link in Ruthenium(II) Polypyridine Type Complexes. *Chem. Commun.* **2011**, *47*, 11011.
- (56) Queyriaux, N.; Andreiadis, E. S.; Torelli, S.; Pecaut, J.; Veldkamp, B. S.; Margulies, E. A.; Wasielewski, M. R.; Chavarot-Kerlidou, M.; Artero, V. CuAAC-Based Assembly and Characterization of a Ruthenium–Copper Dyad Containing a Diimine–Dioxime Ligand Framework. *Faraday Discuss.* **2017**, *198*, 251–261.
- (57) Li, L.; Gibson, E. A.; Qin, P.; Boschloo, G.; Gorlov, M.; Hagfeldt, A.; Sun, L. Double-Layered NiO Photocathodes for p-Type DSSCs with Record IPCE. *Adv. Mater.* **2010**, *22*, 1759–1762.
- (58) Sumikura, S.; Mori, S.; Shimizu, S.; Usami, H.; Suzuki, E. Syntheses of NiO Nanoporous Films Using Nonionic Triblock Copolymer Templates and Their Application to Photo-Cathodes of p-Type Dye-Sensitized Solar Cells. *J. Photochem. Photobiol., A* **2008**, *199*, 1–7.
- (59) Ameline, D.; Diring, S.; Farre, Y.; Pellegrin, Y.; Naponiello, G.; Blart, E.; Charrier, B.; Dini, D.; Jacquemin, D.; Odobel, F. Isoindigo Derivatives for Application in P-Type Dye Sensitized Solar Cells. *RSC Adv.* **2015**, *5*, 85530–85539.
- (60) Boschloo, G.; Hagfeldt, A. Spectroelectrochemistry of Nanostructured NiO. *J. Phys. Chem. B* **2001**, *105*, 3039–3044.
- (61) Kirner, J. T.; Stracke, J. J.; Gregg, B. A.; Finke, R. G. Visible-Light-Assisted Photoelectrochemical Water Oxidation by Thin Films of a Phosphonate-Functionalized Perylene Diimide Plus CoOx Cocatalyst. *ACS Appl. Mater. Interfaces* **2014**, *6*, 13367–13377.
- (62) Sonavane, A. C.; Inamdar, A. I.; Shinde, P. S.; Deshmukh, H. P.; Patil, R. S.; Patil, P. S. Efficient Electrochromic Nickel Oxide Thin Films by Electrodeposition. *J. Alloys Compd.* **2010**, *489*, 667–673.
- (63) Xia, X. H.; Tu, J. P.; Zhang, J.; Wang, X. L.; Zhang, W. K.; Huang, H. Electrochromic Properties of Porous NiO Thin Films Prepared by a Chemical Bath Deposition. *Sol. Energy Mater. Sol. Cells* **2008**, *92*, 628–633.
- (64) Zietz, B.; Gabriellsson, E.; Johansson, V.; El-Zohry, A. M.; Sun, L.; Kloob, L. Photoisomerization of the Cyanoacrylic Acid Acceptor Group – a Potential Problem for Organic Dyes in Solar Cells. *Phys. Chem. Chem. Phys.* **2014**, *16*, 2251.
- (65) Queyriaux, N.; Wahyuno, R. A.; Fize, J.; Gablin, C.; Wächtler, M.; Martinez, E.; Léonard, D.; Dietzek, B.; Artero, V.; Chavarot-Kerlidou, M. Aqueous Photocurrent Measurements Correlated to Ultrafast Electron Transfer Dynamics at Ruthenium Tris Diimine Sensitized NiO Photocathodes. *J. Phys. Chem. C* **2017**, *121*, 5891–5904.
- (66) Bräutigam, M.; Kübel, J.; Schulz, M.; Vos, J. G.; Dietzek, B. Hole Injection Dynamics from Two Structurally Related Ru–Bipyridine Complexes into NiO Is Determined by the Substitution Pattern of the Ligands. *Phys. Chem. Chem. Phys.* **2015**, *17*, 7823–7830.
- (67) Han, Y.; Dillon, R. J.; Flynn, C. J.; Rountree, E. S.; Alibabaei, L.; Cahoon, J. F.; Papanikolas, J. M.; Dempsey, J. L. Interfacial Electron Transfer Yields in Dye-Sensitized NiO Photocathodes Correlated to Excited-State Dipole Orientation of Ruthenium Chromophores. *Can. J. Chem.* **2018**, *96*, 865–874.
- (68) Kou, Y.; Nakatani, S.; Sunagawa, G.; Tachikawa, Y.; Masui, D.; Shimada, T.; Takagi, S.; Tryk, D. A.; Nabetani, Y.; Tachibana, H.; Inoue, H. Visible Light-Induced Reduction of Carbon Dioxide Sensitized by a Porphyrin–Rhenium Dyad Metal Complex on p-Type Semiconducting NiO as the Reduction Terminal End of an Artificial Photosynthetic System. *J. Catal.* **2014**, *310*, 57–66.
- (69) Daeneke, T.; Yu, Z.; Lee, G. P.; Fu, D.; Duffy, N. W.; Makuta, S.; Tachibana, Y.; Spiccia, L.; Mishra, A.; Bäuerle, P.; Bach, U. Dominating Energy Losses in NiO P-Type Dye-Sensitized Solar Cells. *Adv. Energy Mater.* **2015**, *5*, No. 1401387.
- (70) Bold, S.; Straistari, T.; Muñoz-García, A. B.; Pavone, M.; Artero, V.; Chavarot-Kerlidou, M.; Dietzek, B. Investigating Light-Induced Processes in Covalent Dye-Catalyst Assemblies for Hydrogen Production. *Catalysts* **2020**, *10*, No. 1340.
- (71) Massin, J.; Bräutigam, M.; Bold, S.; Wächtler, M.; Pavone, M.; Muñoz-García, A. B.; Dietzek, B.; Artero, V.; Chavarot-Kerlidou, M. Investigating Light-Driven Hole Injection and Hydrogen Evolution Catalysis at Dye-Sensitized NiO Photocathodes: A Combined Experimental–Theoretical Study. *J. Phys. Chem. C* **2019**, *123*, 17176–17184.
- (72) Black, F. A.; Clark, C. A.; Summers, G. H.; Clark, I. P.; Towrie, M.; Penfold, T.; George, M. W.; Gibson, E. A. Investigating Interfacial Electron Transfer in Dye-Sensitized NiO Using Vibrational Spectroscopy. *Phys. Chem. Chem. Phys.* **2017**, *19*, 7877–7885.
- (73) Morandeira, A.; Boschloo, G.; Hagfeldt, A.; Hammarström, L. Coumarin 343-NiO Films as Nanostructured Photocathodes in Dye-Sensitized Solar Cells: Ultrafast Electron Transfer, Effect of the I3/I<sup>-</sup> Redox Couple and Mechanism of Photocurrent Generation. *J. Phys. Chem. C* **2008**, *112*, 9530–9537.
- (74) Morandeira, A.; Boschloo, G.; Hagfeldt, A.; Hammarström, L. Photoinduced Ultrafast Dynamics of Coumarin 343 Sensitized P-Type-Nanostructured NiO Films. *J. Phys. Chem. B* **2005**, *109*, 19403–19410.
- (75) Sheibani, E.; Zhang, L.; Liu, P.; Xu, B.; Mijangos, E.; Boschloo, G.; Hagfeldt, A.; Hammarström, L.; Kloob, L.; Tian, H. A Study of Oligothiophene–Acceptor Dyes in p-Type Dye-Sensitized Solar Cells. *RSC Adv.* **2016**, *6*, 18165–18177.
- (76) Smeigh, A. L.; le Pleux, L.; Fortage, J.; Pellegrin, Y.; Blart, E.; Odobel, F.; Hammarström, L. Ultrafast Recombination for NiO Sensitized with a Series of Perylene Imide Sensitizers Exhibiting Marcus Normal Behaviour. *Chem. Commun.* **2012**, *48*, 678–680.
- (77) Gibson, E. A.; Smeigh, A. L.; le Pleux, L.; Fortage, J.; Boschloo, G.; Blart, E.; Pellegrin, Y.; Odobel, F.; Hagfeldt, A.; Hammarström, L. A P-Type NiO-Based Dye-Sensitized Solar Cell with an Open-Circuit Voltage of 0.35 V. *Angew. Chem., Int. Ed.* **2009**, *48*, 4402–4405.
- (78) le Pleux, L.; Smeigh, A. L.; Gibson, E.; Pellegrin, Y.; Blart, E.; Boschloo, G.; Hagfeldt, A.; Hammarström, L.; Odobel, F. Synthesis, Photophysical and Photovoltaic Investigations of Acceptor-Functionalized Perylene Monoimide Dyes for Nickel Oxide p-Type Dye-Sensitized Solar Cells. *Energy Environ. Sci.* **2011**, *4*, 2075–2084.
- (79) Yu, Y.; Click, K. A.; Polen, S. M.; He, M.; Hadad, C. M.; Wu, Y. Electron Transfer Kinetics of a Series of Bilayer Triphenylamine-Oligothiophene-Perylenemonoimide Sensitizers for Dye-Sensitized NiO. *J. Phys. Chem. C* **2017**, *121*, 20720–20728.
- (80) Flender, O.; Scholz, M.; Klein, J. R.; Oum, K.; Lenzer, T. Excited-State Relaxation of the Solar Cell Dye D49 in Organic Solvents and on Mesoporous Al<sub>2</sub>O<sub>3</sub> and TiO<sub>2</sub> Thin Films. *Phys. Chem. Chem. Phys.* **2016**, *18*, 26010–26019.
- (81) Zhu, H.; Wang, X.; Ma, R.; Kuang, Z.; Guo, Q.; Xia, A. Intramolecular Charge Transfer and Solvation of Photoactive Molecules with Conjugated Push–Pull Structures. *ChemPhysChem* **2016**, *17*, 3245–3251.
- (82) Ishow, E.; Guillot, R.; Buntinx, G.; Poizat, O. Photoinduced Intramolecular Charge-Transfer Dynamics of a Red-Emitting Dicyanovinyl-Based Triarylamine Dye in Solution. *J. Photochem. Photobiol., A* **2012**, *234*, 27–36.
- (83) Gatty, M. G.; Pullen, S.; Sheibani, E.; Tian, H.; Ott, S.; Hammarström, L. Direct Evidence of Catalyst Reduction on Dye and Catalyst Co-Sensitized NiO Photocathodes by Mid-Infrared Transient Absorption Spectroscopy. *Chem. Sci.* **2018**, *9*, 4983–4991.
- (84) Morandeira, A.; Fortage, J.; Edvinsson, T.; Pleux, L. le.; Blart, E.; Boschloo, G.; Hagfeldt, A.; Hammarström, L.; Odobel, F. Improved Photon-to-Current Conversion Efficiency with a Nanoporous p-Type NiO Electrode by the Use of a Sensitizer-Acceptor Dyad. *J. Phys. Chem. C* **2008**, *112*, 1721–1728.
- (85) Qin, P.; Wiberg, J.; Gibson, E. A.; Linder, M.; Li, L.; Brinck, T.; Hagfeldt, A.; Albinsson, B.; Sun, L. Synthesis and Mechanistic Studies of Organic Chromophores with Different Energy Levels for



- P-Type Dye-Sensitized Solar Cells. *J. Phys. Chem. C* **2010**, *114*, 4738–4748.
- (86) Pöldme, N.; O'Reilly, L.; Fletcher, I.; Portoles, J.; Sazanovich, I.; Towrie, M.; Long, C.; Vos, J. G.; Pryce, M. T.; Gibson, E. A. Photoelectrocatalytic H<sub>2</sub> Evolution from Integrated Photocatalysts Adsorbed on NiO. *Chem. Sci.* **2019**, *10*, 99–112.
- (87) Gardner, J. M.; Beyler, M.; Karnahl, M.; Tschierlei, S.; Ott, S.; Hammarström, L. Light-Driven Electron Transfer between a Photosensitizer and a Proton-Reducing Catalyst Co-Adsorbed to NiO. *J. Am. Chem. Soc.* **2012**, *134*, 19322–19325.
- (88) Queyriaux, N.; Sun, D.; Fize, J.; Pécaut, J.; Field, M. J.; Chavarot-Kerlidou, M.; Artero, V. Electrocatalytic Hydrogen Evolution with a Cobalt Complex Bearing Pendant Proton Relays: Acid Strength and Applied Potential Govern Mechanism and Stability. *J. Am. Chem. Soc.* **2020**, *142*, 274–282.
- (89) Queyriaux, N.; Jane, R. T.; Massin, J.; Artero, V.; Chavarot-Kerlidou, M. Recent Developments in Hydrogen Evolving Molecular Cobalt(II)-Polypyridyl Catalysts. *Coord. Chem. Rev.* **2015**, *304*–305, 3–19.
- (90) Queyriaux, N.; Giannoudis, E.; Windle, C. D.; Roy, S.; Pécaut, J.; Coutsolelos, A. G.; Artero, V.; Chavarot-Kerlidou, M. A Noble Metal-Free Photocatalytic System Based on a Novel Cobalt Tetrapyrrolyl Catalyst for Hydrogen Production in Fully Aqueous Medium. *Sustainable Energy Fuels* **2018**, *2*, 553–557.
- (91) Zee, D. Z.; Chantarojsiri, T.; Long, J. R.; Chang, C. J. Metal-Polypyridyl Catalysts for Electro- and Photochemical Reduction of Water to Hydrogen. *Acc. Chem. Res.* **2015**, *48*, 2027–2036.
- (92) Materna, K. L.; Beiler, A. M.; Thapper, A.; Ott, S.; Tian, H.; Hammarström, L. Understanding the Performance of NiO Photocathodes with Alkyl-Derivatized Cobalt Catalysts and a Push–Pull Dye. *ACS Appl. Mater. Interfaces* **2020**, *12*, 31372–31381.
- (93) Kaeffer, N.; Chavarot-Kerlidou, M.; Artero, V. Hydrogen Evolution Catalyzed by Cobalt Diimine-Dioxime Complexes. *Acc. Chem. Res.* **2015**, *48*, 1286–1295.
- (94) Kaeffer, N.; Morozan, A.; Fize, J.; Martinez, E.; Guetaz, L.; Artero, V. The Dark Side of Molecular Catalysis: Diimine–Dioxime Cobalt Complexes Are Not the Actual Hydrogen Evolution Electrocatalyst in Acidic Aqueous Solutions. *ACS Catal.* **2016**, *6*, 3727–3737.
- (95) Anxolabéhère-Mallart, E.; Costentin, C.; Fournier, M.; Nowak, S.; Robert, M.; Savéant, J.-M. Boron-Capped Tris(Glyoximate) Cobalt Clathrochelate as a Precursor for the Electrodeposition of Nanoparticles Catalyzing H<sub>2</sub> Evolution in Water. *J. Am. Chem. Soc.* **2012**, *134*, 6104–6107.
- (96) Cobo, S.; Heidkamp, J.; Jacques, P.-A.; Fize, J.; Fourmond, V.; Guetaz, L.; Jousset, B.; Ivanova, V.; Dau, H.; Palacin, S.; Fontecave, M.; Artero, V. A Janus Cobalt-Based Catalytic Material for Electro-Splitting of Water. *Nat. Mater.* **2012**, *11*, 802–807.
- (97) Andreiadis, E. S.; Jacques, P.-A.; Tran, P. D.; Leyris, A.; Chavarot-Kerlidou, M.; Jousset, B.; Matheron, M.; Pécaut, J.; Palacin, S.; Fontecave, M.; Artero, V. Molecular Engineering of a Cobalt-Based Electrocatalytic Nanomaterial for H<sub>2</sub> Evolution under Fully Aqueous Conditions. *Nat. Chem.* **2013**, *5*, 48–53.
- (98) Lee, D. K.; Lee, D.; Lumley, M. A.; Choi, K. S. Progress on Ternary Oxide-Based Photoanodes for Use in Photoelectrochemical Cells for Solar Water Splitting. *Chem. Soc. Rev.* **2019**, *48*, 2126–2157.
- (99) Sahara, G.; Kumagai, H.; Maeda, K.; Kaeffer, N.; Artero, V.; Higashi, M.; Abe, R.; Ishitani, O. Photoelectrochemical Reduction of CO<sub>2</sub> Coupled to Water Oxidation Using a Photocathode with a Ru(II)–Re(I) Complex Photocatalyst and a CoOx/TaON Photoanode. *J. Am. Chem. Soc.* **2016**, *138*, 14152–14158.
- (100) Li, T. T.; Shan, B.; Meyer, T. J. Stable Molecular Photocathode for Solar-Driven CO<sub>2</sub> Reduction in Aqueous Solutions. *ACS Energy Lett.* **2019**, *4*, 629–636.
- (101) Cheshire, T. P.; Brennaman, M. K.; Giokas, P. G.; Zigler, D. F.; Moran, A. M.; Papanikolas, J. M.; Meyer, G. J.; Meyer, T. J.; Houle, F. A. Ultrafast Relaxations in Ruthenium Polypyridyl Chromophores Determined by Stochastic Kinetics Simulations. *J. Phys. Chem. B* **2020**, *124*, 5971–5985.
- (102) Tebo, A. G.; Quaranta, A.; Herrero, C.; Pecoraro, V. L.; Aukauloo, A. Intramolecular Photogeneration of a Tyrosine Radical in a Designed Protein. *ChemPhotoChem* **2017**, *1*, 89–92.
- (103) Herrero, C.; Quaranta, A.; el Ghachtouli, S.; Vauzeilles, B.; Leibl, W.; Aukauloo, A. Carbon Dioxide Reduction via Light Activation of a Ruthenium-Ni(Cyclam) Complex. *Phys. Chem. Chem. Phys.* **2014**, *16*, 12067–12072.
- (104) Herrero, C.; Quaranta, A.; Sircoglou, M.; Sénéchal-David, K.; Baron, A.; Marín, I. M.; Buron, C.; Baltaze, J.-P.; Leibl, W.; Aukauloo, A.; Banse, F. Successive Light-Induced Two Electron Transfers in a Ru–Fe Supramolecular Assembly: From Ru–Fe(II)–OH<sub>2</sub> to Ru–Fe(IV)–Oxo. *Chem. Sci.* **2015**, *6*, 2323–2327.
- (105) Herrero, C.; Batchelor, L.; Baron, A.; el Ghachtouli, S.; Sheth, S.; Guillot, R.; Vauzeilles, B.; Sircoglou, M.; Mallah, T.; Leibl, W.; Aukauloo, A. Click Chemistry as a Convenient Tool for the Incorporation of a Ruthenium Chromophore and a Nickel-Salen Monomer into a Visible-Light-Active Assembly. *Eur. J. Inorg. Chem.* **2013**, *2013*, 494–499.
- (106) Brown, A. M.; Antila, L. J.; Mirmohades, M.; Pullen, S.; Ott, S.; Hammarström, L. Ultrafast Electron Transfer Between Dye and Catalyst on a Mesoporous NiO Surface. *J. Am. Chem. Soc.* **2016**, *138*, 8060–8063.
- (107) Dalle, K. E.; Warnan, J.; Leung, J. J.; Reuillard, B.; Karmel, I. S.; Reiser, E. Electro- and Solar-Driven Fuel Synthesis with First Row Transition Metal Complexes. *Chem. Rev.* **2019**, *119*, 2752–2875.
- (108) Xu, P.; McCool, N. S.; Mallouk, T. E. Water Splitting Dye-Sensitized Solar Cells. *Nano Today* **2017**, *14*, 42–58.
- (109) Tong, L.; Duan, L.; Zhou, A.; Thummel, R. P. First-Row Transition Metal Polypyridine Complexes That Catalyze Proton to Hydrogen Reduction. *Coord. Chem. Rev.* **2020**, *402*, No. 213079.
- (110) O'Reilly, J. E. Oxidation-Reduction Potential of the Ferro-Ferricyanide System in Buffer Solutions. *Biochim. Biophys. Acta, Bioenerg.* **1973**, *292*, 509–515.
- (111) Karnahl, M.; Kuhnt, C.; Ma, F.; Yartsev, A.; Schmitt, M.; Dietzek, B.; Rau, S.; Popp, J. Tuning of Photocatalytic Hydrogen Production and Photoinduced Intramolecular Electron Transfer Rates by Regioselective Bridging Ligand Substitution. *ChemPhysChem* **2011**, *12*, 2101–2109.
- (112) Dietzek, B.; Pascher, T.; Sundström, V.; Yartsev, A. Appearance of Coherent Artifact Signals in Femtosecond Transient Absorption Spectroscopy in Dependence on Detector Design. *Laser Phys. Lett.* **2007**, *4*, 38–43.
- (113) Sittig, M.; Schmidt, B.; Görls, H.; Bocklitz, T.; Wächtler, M.; Zechel, S.; Hager, M. D.; Dietzek, B. Fluorescence Upconversion by Triplet–Triplet Annihilation in All-Organic Poly(Methacrylate)-Terpolymers. *Phys. Chem. Chem. Phys.* **2020**, *22*, 4072–4079.

## Supporting Information

# Spectroscopic investigations provide a rationale for the hydrogen-evolving activity of dye-sensitized photocathodes based on a cobalt tetraazamacrocyclic catalyst

Sebastian Bold,<sup>a,b,c</sup> Julien Massin,<sup>a</sup> Emmanouil Giannoudis,<sup>a</sup> Matthieu Koepf,<sup>a</sup> Vincent Artero,<sup>a</sup> Benjamin Dietzek<sup>\*b,c,d</sup> and Murielle Chavarot-Kerlidou<sup>\*a</sup>

a. Univ. Grenoble Alpes, CNRS, CEA, IRIG, Laboratoire de Chimie et Biologie des Métaux, 17 rue des Martyrs, F-38000 Grenoble, France.

b. Institute of Physical Chemistry and Abbe Center of Photonics, Friedrich Schiller University Jena, Helmholtzweg 4, 07743 Jena, Germany.

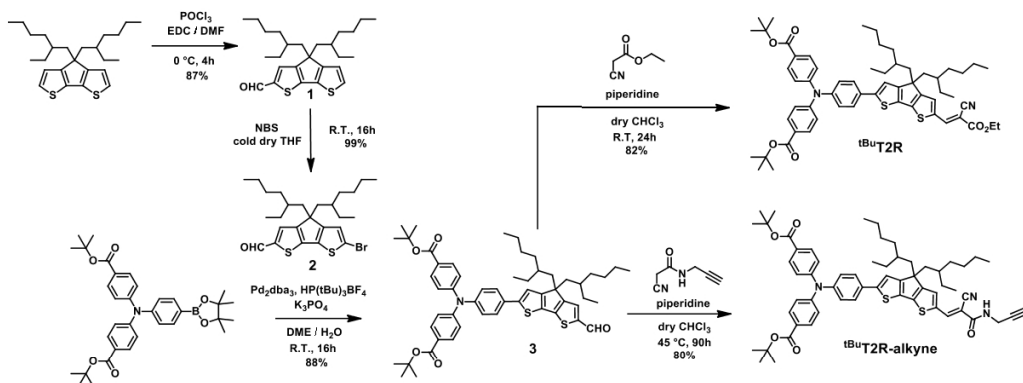
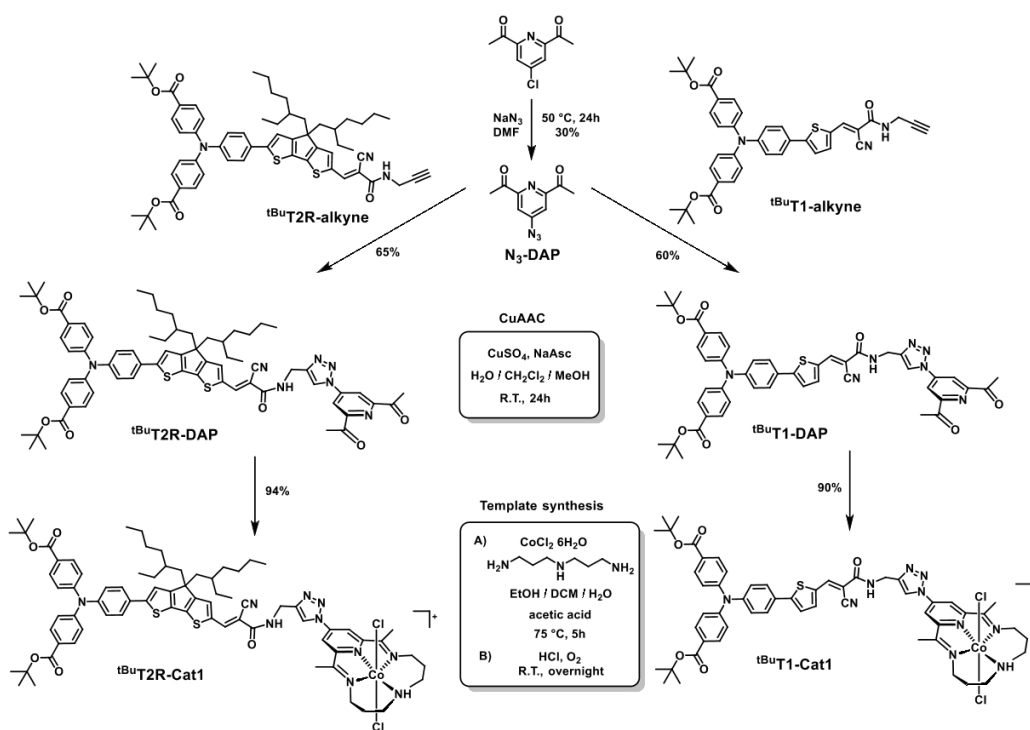
c. Department Functional Interfaces, Leibniz Institute of Photonic Technology Jena (IPHT), Albert-Einstein-Straße 9, 07745 Jena, Germany.

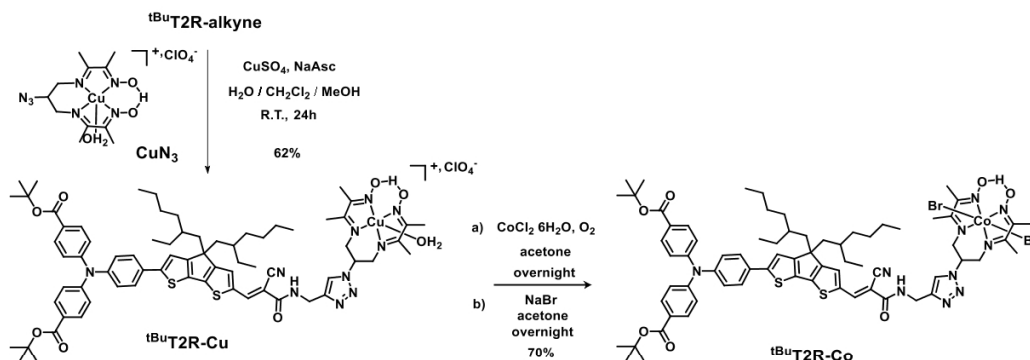
d. Center for Energy and Environmental Chemistry (CEEC Jena), Friedrich Schiller University Jena, Philosophenweg 8, 07743 Jena, Germany.

### Corresponding Author

\* Benjamin Dietzek; E-mail: [benjamin.dietzek@leibniz-ipht.de](mailto:benjamin.dietzek@leibniz-ipht.de)

\* Murielle Chavarot-Kerlidou; E-mail: [murielle.chavarot-kerlidou@cea.fr](mailto:murielle.chavarot-kerlidou@cea.fr)

Scheme S1. Synthetic route to **tBuT2R** and **tBuT2R-alkyne**.Scheme S2. Synthetic route to **tBuT1-Cat1** and **tBuT2R-Cat1**.



**Scheme S3.** Synthetic route to **tBuT2R-Co**.

**4,4-bis(2-ethylhexyl)-4H-cyclopenta[2,1-b:3,4-b']dithiophene-2-carbaldehyde (1).** To a cold solution of commercially available 4,4-bis(2-ethylhexyl)-4H-cyclopenta[2,1-b:3,4-b']dithiophene (5 g, 12.4 mmol) and *N,N*-dimethylformamide (1.2 equiv., 1.09 g, 14.9 mmol) in 1,2-dichloroethane (32 mL) was added at 0 °C phosphorus chloride oxide (1.2 equiv., 2.29 g, 14.9 mmol) under argon and the reaction solution was stirred at 0 °C for 4 hours. The color turned to yellow and a saturated sodium acetate aqueous solution (66 mL) was added. The mixture was stirred at room temperature for 2 hours. The crude product was extracted with  $\text{CH}_2\text{Cl}_2$ , and the organic layer was washed with brine solution and water, dried over sodium sulfate and filtered. After removal of the solvent under reduced pressure, the residue was purified on silica gel column using 30%  $\text{CH}_2\text{Cl}_2$  in petroleum ether as eluent to give a yellow oil (4.65 g, 10.8 mmol, 87%).  $^1\text{H}$  NMR (300 MHz,  $\text{CDCl}_3$ ):  $\delta$  in ppm 9.82 (s, 1H), 7.56 (s(br), 1H), 7.37 (d,  $J = 4.9$  Hz, 1H), 6.99 (m, 1H), 2-1.85 (m, 4H), 0.99-0.82 (m, 16H), 0.80-0.73 (m, 6H), 0.61-0.57 (m, 8H);  $^{13}\text{C}$  NMR (75 MHz,  $\text{CDCl}_3$ ):  $\delta$  in ppm 182.6, 162.0, 157.7, 148.0, 142.8, 135.9, 130.9, 129.2, 122.5, 53.7, 43.1, 35.1, 34.0, 28.5, 27.3, 22.7, 14.0, 10.5. HRMS (ESI<sup>+</sup>): calcd for  $\text{C}_{26}\text{H}_{39}\text{OS}_2$  ( $[\text{M}+\text{H}]^+$ ):  $m/z$  431.2437; found 431.2446. E.A.: calcd for  $\text{C}_{26}\text{H}_{38}\text{OS}_2$ : C, 72.50; H, 8.89; found: C, 72.68; H, 9.05.

**6-bromo-4,4-bis(2-ethylhexyl)-4H-cyclopenta[2,1-b:3,4-b']dithiophene-2-carbaldehyde (2).** **1** (2.58 g, 5.99 mmol) and NBS (1.1 equiv., 1.17 g, 6.59 mmol) were mixed in dry THF (165 mL) at 0°C under argon, and stirred at room temperature for 16 hours. The color turned to orange. The mixture was quenched with water (170 mL), extracted with  $\text{CHCl}_3$  (3 x 150 mL), washed with brine solution (150 mL), dried over  $\text{Na}_2\text{SO}_4$ , and filtered. The crude product was purified on silica gel column using  $\text{CHCl}_3$  as eluent and dried under vacuum to give a greenish oil (3.17 g, 5.99 mmol, 99%).  $^1\text{H}$  NMR (300 MHz,  $\text{CDCl}_3$ ):  $\delta$  in ppm 9.83 (s, 1H), 7.55 (s, 1H), 7.02 (s, 1H), 1.97-1.81 (m, 4H), 0.99-0.89 (m, 16H), 0.81-0.73 (m, 6H), 0.65-0.58 (m, 8H);  $^{13}\text{C}$  NMR (75 MHz,  $\text{CDCl}_3$ ):  $\delta$  in ppm 182.5, 160.7, 156.8, 146.9, 143.3, 136.3, 130.6, 125.6, 54.6, 43.0, 35.2, 34.1, 28.5, 27.3, 24.9,

22.7, 14.0, 10.6. HR-MS (ESI+): calcd for  $C_{26}H_{38}BrOS_2$  ( $[M+H]^+$ ):  $m/z$  509.1542; found 509.1548. E.A.: calcd for  $C_{26}H_{37}BrOS_2$ : C, 61.28; H, 7.32; found: C, 61.37; H, 7.45.

***Tert*-butyl-4,4'-((4-(6-formyl-4,4-bis(2-ethylhexyl)-4H-cyclopenta[2,1-b:3,4-b'] dithiophen-2-yl)phenyl)azanediyl)dibenzoate (3).** *Tert*-butyl 4,4'-((4-(4,4,5,5-tetramethyl-1,3,2-dioxaborolan-2-yl)phenyl)azanediyl)dibenzoate<sup>1</sup> (1.34 g, 2.34 mmol), **2** (1 equiv., 1.19 g, 2.34 mmol), Pd<sub>2</sub>dba<sub>3</sub> (0.05 equiv., 73 mg, 0.11 mmol) and HP(tBu)<sub>3</sub>BF<sub>4</sub> (0.1 equiv., 73 mg, 0.23 mmol) were dissolved in dry DME (23 mL) under argon. K<sub>3</sub>PO<sub>4</sub> (6 mL, 1 M) was added and the reaction mixture was stirred at room temperature for 16 hours. The color turned rapidly to orange. After pouring in 200 mL H<sub>2</sub>O, the mixture was extracted with CHCl<sub>3</sub> (3 x 200 mL), washed with brine solution (200 mL), dried with anhydrous Na<sub>2</sub>SO<sub>4</sub>, filtered and the solvent was evaporated. The crude product was purified on silica gel column using 10% CHCl<sub>3</sub> in toluene as eluent and was dried under vacuum to give an orange solid (1.80 g, 2.06 mmol, 88%). <sup>1</sup>H NMR (300 MHz, CDCl<sub>3</sub>): δ in ppm 9.84 (s, 1H), 7.89 (d, J = 8.4 Hz, 4H), 7.53 (m, 3H), 7.16-7.10 (m, 7H), 2.01-1.89 (m, 4H), 1.59 (s, 18H), 0.99-0.94 (m, 16H), 0.77-0.60 (m, 14H); <sup>13</sup>C NMR (75 MHz, CDCl<sub>3</sub>): δ in ppm 206.8, 182.4, 165.3, 163.1, 157.2, 150.3, 148.2, 146.1, 143.0, 135.1, 130.9, 130.6, 126.7, 125.9, 122.9, 118.3, 80.8, 54.1, 43.2, 35.3, 34.1, 32.1, 28.4, 27.4, 22.8, 14.0, 10.6. HRMS (ESI+): calcd for  $C_{54}H_{68}NO_5S_2$  ( $[M+H]^+$ ):  $m/z$  874.4533; found 874.4538. E.A.: calcd for  $C_{54}H_{67}NO_5S_2 + 0.3 H_2O$ : C, 73.73; H, 7.75; N, 1.59; found: C, 73.68; H, 7.85; N, 1.59.

**<sup>t</sup>BuT2R. 3** (200 mg, 0.23 mmol) and ethyl 2-cyanoacetate (1.2 equiv., 31 mg, 0.27 mmol) were mixed in CHCl<sub>3</sub> (12 mL). Piperidine (5 equiv., 98 mg, 1.15 mmol) was added and the reaction mixture was stirred at room temperature for 24 hours. The color turned to red. The reaction was quenched by addition of HCl 1M (100 mL). The mixture was extracted with CHCl<sub>3</sub> (3 x 70 mL), washed with brine solution (70 mL), dried over Na<sub>2</sub>SO<sub>4</sub>, filtered and the solvent was evaporated. The crude product was purified over silica gel column using 20% CHCl<sub>3</sub> in toluene as eluent to give **<sup>t</sup>BuT2R** as a red powder (180 mg, 0.19 mmol, 82%). This compound was further purified to eliminate some remaining aldehyde precursor using 7% of ethyl acetate in hexane as eluent. <sup>1</sup>H NMR (300 MHz, CDCl<sub>3</sub>): δ in ppm 8.27 (s, 1H), 7.89 (d, J = 8.7 Hz, 4H), 7.60-7.51 (m, 3H), 7.18 (s, 1H), 7.14-7.10 (m, 6H), 4.35 (q, J = 7.2 Hz, 2H), 1.95 (s(br), 4H), 1.59 (s, 18H), 1.38 (t, J = 7.0 Hz, 3H), 1.00-0.92 (m, 16H), 0.76-0.59 (m, 14H). <sup>13</sup>C NMR (75 MHz, CDCl<sub>3</sub>): δ in ppm 165.3, 163.7, 150.3, 146.3, 130.9, 130.6, 126.9, 126.7, 125.9, 125.8, 123.0, 80.9, 77.3, 62.2, 54.2, 43.1, 35.3, 34.1, 28.6, 28.5, 28.3, 27.4, 27.3, 22.8, 14.3, 14.1, 10.7. HR-MS (ESI+): calcd for  $C_{59}H_{73}N_2O_6S_2$  ( $[M+H]^+$ ):  $m/z$  969.4905, found 969.4906. E.A.: calcd for  $C_{59}H_{72}N_2O_6S_2$ : C, 73.11; H, 7.49; N, 2.89; found: C, 72.88; H, 7.58; N, 2.88.

**<sup>t</sup>BuT2R-alkyne. 3** (481 mg, 0.55 mmol) and 2-cyano-*N*-(prop-2-yn-1-yl)acetamide (3 equiv., 202 mg, 1.65 mmol) were mixed in dry CHCl<sub>3</sub> (30 mL). Piperidine (5 equiv., 234 mg, 2.75 mmol) was added and the reaction mixture was stirred at 45 °C for 90 hours. The color turned to red. The reaction was quenched by HCl 1M (250 mL) and extracted with CH<sub>2</sub>Cl<sub>2</sub> (3 x 150 mL), washed with brine solution (100 mL), dried over Na<sub>2</sub>SO<sub>4</sub> and filtered. The crude product was purified on silica gel column using CH<sub>2</sub>Cl<sub>2</sub> as eluent and dried under vacuum to give **<sup>t</sup>BuT2R-alkyne** as a red powder (427 mg, 0.44 mmol, 80%). <sup>1</sup>H NMR (300 MHz, CDCl<sub>3</sub>): δ in ppm 8.36 (s, 1H), 7.89 (d, J = 8.6 Hz, 4H), 7.57-7.51 (m, 3H), 7.18-7.10 (m, 7H), 6.35 (s(br), 1H), 4.20 (s(br), 2H), 2.30 (s, 1H), 2.00-1.87 (m, 4H), 1.53 (s, 18H), 0.99-0.93 (m, 16H), 0.77-0.59 (m, 14H). <sup>13</sup>C NMR (75 MHz, CDCl<sub>3</sub>): δ in ppm 165.5, 163.6, 161.4, 158.1, 150.5, 149.1, 148.9, 146.4, 145.7, 136.2, 135.2, 131.0, 130.9, 126.9, 126.0, 123.1, 118.4, 94.9, 81.0, 78.9, 72.4, 54.4, 43.4, 35.6, 34.4, 30.2, 28.7, 27.5, 22.9, 14.1, 10.8. HR-MS (ESI+): calcd for C<sub>60</sub>H<sub>72</sub>N<sub>3</sub>O<sub>5</sub>S<sub>2</sub> ([M+H]<sup>+</sup>): m/z 978.4908; found 978.4906. E.A.: calcd for C<sub>60</sub>H<sub>71</sub>N<sub>3</sub>O<sub>5</sub>S<sub>2</sub>: C, 73.66; H, 7.31; N, 4.29; found: C, 73.52; H, 7.40; N, 4.29.

**4-azido-2,6-diacetylpyridine (N<sub>3</sub>-DAP;** synthesis adapted from a previously reported procedure.<sup>2</sup> 4-chloro-2,6-diacetylpyridine<sup>3</sup> (250 mg, 1.25 mmol) and NaN<sub>3</sub> (20 equiv., 1.62 g, 25 mmol) were mixed in DMF (4 mL) and then heated to 50 °C. After 24 hours, the DMF was evaporated under reduced pressure. The crude product was purified on silica gel column using 50% pentane in CH<sub>2</sub>Cl<sub>2</sub> as eluent to give a white solid (75 mg, 0.4 mmol, 30%). <sup>1</sup>H NMR (300 MHz, CDCl<sub>3</sub>): δ in ppm 7.83 (s, 2H), 2.78 (s, 6H); <sup>13</sup>C NMR (75 MHz, CDCl<sub>3</sub>): δ in ppm 198.6, 154.5, 151.5, 114.7, 25.6; ESI-MS: m/z 227.0 ([M+Na]<sup>+</sup>), 205.0 ([M+H]<sup>+</sup>).

**<sup>t</sup>BuT1-diacetylpyridine:** **<sup>t</sup>BuT1-alkyne** (500 mg, 0.58 mmol) and **N<sub>3</sub>-DAP** (1 equiv., 118 mg, 0.58 mmol) were dissolved in 20.8 mL of degassed CH<sub>2</sub>Cl<sub>2</sub>. Sodium ascorbate (101 mg, 0.52 mmol) and CuSO<sub>4</sub>·5H<sub>2</sub>O (43 mg, 0.17 mmol) were dissolved in 10.4 mL of degassed H<sub>2</sub>O and then added to the reaction mixture. 34.6 mL of degassed MeOH were added until a single phase was obtained. The reaction mixture was stirred at room temperature for 18 hours. After removal of the volatile solvents, the mixture was extracted with CH<sub>2</sub>Cl<sub>2</sub> (3 x 75 mL), washed with brine solution (75 mL), dried over Na<sub>2</sub>SO<sub>4</sub> and filtered. The crude product was purified on silica gel column using CH<sub>2</sub>Cl<sub>2</sub>/AcOEt (7:3) as eluent and dried under vacuum to give a red solid (390 mg, 0.45 mmol, 60%). <sup>1</sup>H NMR (300 MHz, CDCl<sub>3</sub>): δ in ppm 8.61 (s, 2H), 8.39 (s, 1H), 8.28 (s, 1H), 7.90 (d, J = 8.5 Hz, 4H), 7.71 (d, J = 3.7 Hz, 1H), 7.60 (d, J = 8.5 Hz, 2H), 7.35 (d, J = 4.2 Hz, 1H), 7.15-7.09 (m, 6H), 6.92 (s(br), 1H), 4.79 (d, J = 5.8 Hz, 2H), 2.84 (s, 6H), 1.59 (s, 18H). HR-MS (ESI+): calcd for C<sub>48</sub>H<sub>46</sub>N<sub>7</sub>O<sub>7</sub>S ([M+H]<sup>+</sup>): m/z 864.3174; found: 864.3173. E.A.: calcd for C<sub>48</sub>H<sub>45</sub>N<sub>7</sub>O<sub>7</sub>S + 1 H<sub>2</sub>O: C, 65.37 ; H, 5.37; N, 11.12; found: C, 65.35 ; H, 5.31; N, 10.99.



**<sup>t</sup>BuT1-Cat1.** **<sup>t</sup>BuT1-diacetylpyridine** (50 mg, 0.058 mmol) was dissolved in EtOH (1 mL) and CH<sub>2</sub>Cl<sub>2</sub> (0.5 mL), and kept at 40 °C under argon. CoCl<sub>2</sub>·6H<sub>2</sub>O (1 equiv., 14 mg, 0.058 mmol) and water (0.56 mL) were added and the mixture was stirred at 55 °C to dissolve the salt. The reaction mixture was warmed at 75 °C and 3,3'-diaminodipropylamine (1 equiv., 8 μL, 0.058 mmol) and glacial acetic acid (5 μL) were added. The solution was stirred at 75 °C for 5 hours under argon. After cooling down to room temperature, 10 μL of concentrated HCl was added and the mixture was stirred at room temperature for 16 hours. After evaporation of the solvents, precipitation was carried out with addition of cold saturated aqueous solution of KCl. The red precipitate was purified on silica gel using CH<sub>2</sub>Cl<sub>2</sub>/AcOEt (6:4) then acetone/H<sub>2</sub>O/saturated aqueous KCl (90:9:1) as eluents to yield **<sup>t</sup>BuT1-Cat1** as a red solid (45 mg, 0.040 mmol, 70%). <sup>1</sup>H NMR (300 MHz, (CD<sub>3</sub>)<sub>3</sub>CO) δ in ppm 9.25 (s, 2H), 9.11 (s, 1H), 8.46 (s, 1H), 8.25 (s(br), 1H), 7.93 (d, J = 7.9 Hz, 4H), 7.82 (d, J = 8.3 Hz, 2H), 7.67 (s(br), 1H), 7.28-7.18 (m, 6H), 6.30 (s(br), 1H), 4.82 (s(br), 2H), 4.40 (d, J = 16.0 Hz, 2H), 3.78-3.68 (m, 2H), 3.50-3.40 (m, 2H), 3.36-3.31 (m, 2H), 3.18 (s, 6H), 2.43 (s(br), 2H), 2.31-2.28 (m, 2H), 1.58 (s, 18H). HR-MS (ESI+): calcd for C<sub>54</sub>H<sub>58</sub>CoN<sub>10</sub>O<sub>5</sub>SCl<sub>2</sub> ([M-Cl]<sup>+</sup>): *m/z* 1087.3016, found 1087.3014. E.A.: calcd for C<sub>54</sub>H<sub>58</sub>CoN<sub>10</sub>O<sub>5</sub>SCl<sub>3</sub> + 5 KCl + H<sub>2</sub>O: C, 42.80; H, 3.99; N, 9.24; found: C, 42.83; H, 4.60; N, 7.73.

**<sup>t</sup>BuT2R-diacetylpyridine.** **<sup>t</sup>BuT2R-alkyne** (570 mg, 0.58 mmol) and **N<sub>3</sub>-DAP** (1 equiv., 118 mg, 0.58 mmol) were dissolved in 20.8 mL of degassed CH<sub>2</sub>Cl<sub>2</sub>. Sodium ascorbate (101 mg, 0.52 mmol) and CuSO<sub>4</sub>·5H<sub>2</sub>O (43 mg, 0.17 mmol) were dissolved in 10.4 mL of degassed H<sub>2</sub>O and then added to the reaction mixture. 34.6 mL of degassed MeOH was added until a single phase was obtained. The reaction mixture was stirred at room temperature for 18 hours. After removal of the volatile solvents, the mixture was extracted with CH<sub>2</sub>Cl<sub>2</sub> (3 x 75 mL), washed with brine solution (75 mL), dried over Na<sub>2</sub>SO<sub>4</sub> and filtered. The crude product was purified on silica gel column using CH<sub>2</sub>Cl<sub>2</sub>/AcOEt (7:3) as eluent and dried under vacuum to give a red solid (447 mg, 0.38 mmol, 65%). <sup>1</sup>H NMR (300 MHz, CDCl<sub>3</sub>): δ in ppm 8.61 (s, 2H), 8.37 (s, 1H), 8.29 (s, 1H), 7.89 (d, J = 8.0 Hz, 4H), 7.57-7.52 (m, 3H), 7.17 (s, 1H), 7.14-7.09 (m, 6H), 6.86 (s(br), 1H), 4.80 (s(br), 2H), 2.84 (s, 6H), 1.93 (s(br), 4H), 1.59 (s, 18H), 1.00-0.93 (m, 16H), 0.77-0.59 (m, 14H). <sup>13</sup>C NMR (75 MHz, CDCl<sub>3</sub>): δ in ppm 198.0, 165.4, 163.7, 158.2, 155.2, 150.5, 149.2, 149.0, 146.5, 145.5, 136.2, 135.3, 131.1, 130.9, 127.0, 126.0, 123.1, 114.4, 105.9, 81.0, 54.4, 43.4, 35.6, 34.4, 28.8, 28.4, 27.5, 25.7, 22.9, 14.1, 10.8. HR-MS (ESI+): calcd for C<sub>69</sub>H<sub>80</sub>N<sub>7</sub>O<sub>7</sub>S<sub>2</sub> ([M+H]<sup>+</sup>): *m/z* 1182.5555; found 1182.5550. E.A.: calcd for C<sub>69</sub>H<sub>79</sub>N<sub>7</sub>O<sub>7</sub>S<sub>2</sub> + 0.9 H<sub>2</sub>O: C, 69.13; H, 6.79; N, 8.18; found: C, 69.14; H, 6.76; N, 8.07.

**<sup>t</sup>BuT2R-Cat1.** **<sup>t</sup>BuT2R-diacetylpyridine** (424 mg, 0.36 mmol) was dissolved in EtOH (2 mL) and CH<sub>2</sub>Cl<sub>2</sub> (1 mL), and kept at 40 °C under argon. CoCl<sub>2</sub>·6H<sub>2</sub>O (1 equiv., 90 mg, 0.37 mmol) and water (0.36 mL) were added and the solution was stirred at 55 °C to dissolve the salt. The reaction mixture

was warmed to 75 °C and 3,3'-diaminodipropylamine (1 equiv., 0.05 mL, 0.37 mmol) and glacial acetic acid (0.03 mL) were added and stirred at 75 °C for 5 hours under argon. After cooling down to room temperature, 0.1 mL of concentrated HCl was added and the reaction mixture was stirred at room temperature for 16 hours, kept for 2 hours at -15 °C and centrifuged. The crude product was purified on silica gel column using CH<sub>2</sub>Cl<sub>2</sub>/AcOEt (6:4), then acetone/H<sub>2</sub>O/saturated aqueous KCl (90:9:1) as eluents and dried under vacuum to give a red solid (360 mg, 0.25 mmol, 69%). <sup>1</sup>H NMR (500 MHz, CD<sub>3</sub>CN/CDCl<sub>3</sub> (5:1)) δ in ppm 9.00 (s, 1H), 8.92 (s, 2H), 8.38 (s, 1H), 7.85 (d, J = 8.5 Hz, 4H), 7.70-7.68-7.67 (3s, 1H), 7.58 (d, J = 8.5 Hz, 2H), 7.36 (s, 1H), 7.14-7.09 (m, 6H), 5.97 (s(br), 1H), 4.76 (s(br), 2H), 3.99 (d(br), J = 16.2 Hz, 2H), 3.58 (t(br), J = 15.3 Hz, 2H), 3.33 (q, J = 12.5 Hz, 2H), 2.93 (s(br), 2H), 2.89 (s, 6H), 2.29 (d(br), J = 13.8 Hz, 2H), 2.14 (s(br), 2H), 2.02-1.98 (m, 4H), 1.56 (s, 18H), 0.98-0.92 (m, 16H), 0.75-0.58 (m, 14H). HR-MS (ESI+): calcd for C<sub>75</sub>H<sub>92</sub>CoN<sub>10</sub>O<sub>5</sub>S<sub>2</sub>Cl<sub>2</sub> ([M-Cl]<sup>+</sup>): *m/z* 1405.5397; found 1405.5405; calcd for C<sub>75</sub>H<sub>92</sub>CoN<sub>10</sub>O<sub>5</sub>S<sub>2</sub>Cl ([M-2Cl]<sup>2+</sup>): *m/z* 685.2852; found 685.2855. E.A.: calcd for C<sub>75</sub>H<sub>92</sub>CoN<sub>10</sub>O<sub>5</sub>S<sub>2</sub>Cl<sub>3</sub> + 5 KCl + 1 H<sub>2</sub>O: C, 49.12; H, 5.17; N, 7.64; found: C, 48.99; H, 5.37; N, 7.07.

**<sup>t</sup>BuT2R-Cu. 9** (600 mg, 0.61 mmol) and **15** (1 equiv., 300 mg, 0.61 mmol) were dissolved in 21.9 mL of degassed CH<sub>2</sub>Cl<sub>2</sub>. Sodium ascorbate (0.9 equiv., 109 mg, 0.55 mmol) and CuSO<sub>4</sub>·5H<sub>2</sub>O (0.3 equiv., 45 mg, 0.18 mmol) were dissolved in 11.1 mL of degassed H<sub>2</sub>O and then added to the reaction mixture. 36.9 mL of degassed MeOH was added until a single phase was obtained. The reaction mixture was stirred at room temperature for 18 hours. After removal of the volatile solvents, the mixture was extracted with CH<sub>2</sub>Cl<sub>2</sub> (3 x 75 mL), washed with brine solution (75 mL), dried over Na<sub>2</sub>SO<sub>4</sub> and filtered. The crude product was purified on silica gel column using CH<sub>2</sub>Cl<sub>2</sub> 7/3 AcOEt as eluent and dried under vacuum to give a brownish red solid (506 mg, 0.38 mmol, 62%). HRMS (ESI+): calcd for C<sub>71</sub>H<sub>89</sub>N<sub>10</sub>O<sub>7</sub>CuS<sub>2</sub> ([M-H<sub>2</sub>O-ClO<sub>4</sub>]<sup>+</sup>): *m/z* 1320.5648; found 1320.5653.

**<sup>t</sup>BuT2R-Co. <sup>t</sup>BuT2R-Cu** (474 mg, 0.33 mmol) and CoCl<sub>2</sub>·6H<sub>2</sub>O (7 equiv., 532 mg, 2.24 mmol) were solubilized in 50 ml of acetone and stirred under air bubbling using an air pump overnight. The solution was evaporated under vacuum and the solid was purified by flash chromatography on silica gel using as eluent a mixture of CH<sub>3</sub>CN and KNO<sub>3</sub> aqueous solution at 10% of the saturating solution. The organic solvents were evaporated and the solution was extracted with dichloromethane. After evaporation, the solid was solubilized in 10 ml of acetone and 3 ml of NaBr-saturated aqueous solution was added. The reaction mixture was left stirring overnight. The precipitate was filtered, rinsed with water and dried under vacuum to give a red solid (336 mg, 0.23 mmol, 70%). <sup>1</sup>H NMR (300 MHz, CDCl<sub>3</sub>): δ in ppm 19.48 (s, 1H), 8.46 (s, 1H), 8.10 (s(br), 1H), 7.98 (d, J = 8.0 Hz, 4H), 7.86 (t, 1H), 7.75 (d, 2H), 7.60 (s, 1H), 7.41 (s(br), 1H), 7.24 (m, 6H), 5.88 (t, 1H), 4.83-4.59 (m, 6H), 2.65 (s, 12H), 1.67 (s, 18H), 1.07-1.02 (m, 16H), 0.84-0.70 (m, 14H). <sup>13</sup>C NMR (75 MHz,

CDCl<sub>3</sub>): δ in ppm 175.8, 165.4, 163.7, 162.2, 158.2, 157.1, 156.3, 150.5, 146.5, 136.1, 135.2, 131.1, 130.8, 127.0, 126.0, 123.2, 122.9, 118.3, 81.0, 55.7, 54.4, 43.4, 35.6, 34.4, 31.0, 28.8, 28.7, 28.4, 27.6, 27.4, 22.9, 18.3, 14.2, 10.8. HRMS (ESI<sup>+</sup>): *m/z* calcd for C<sub>71</sub>H<sub>89</sub>N<sub>10</sub>O<sub>7</sub>CoS<sub>2</sub> ([M-2Br]<sup>2+</sup>): *m/z* 658.2839; found 658.2848. E.A.: calcd for C<sub>71</sub>H<sub>89</sub>N<sub>10</sub>O<sub>7</sub>CoS<sub>2</sub>Br<sub>2</sub> + 0.5 NaBr: C, 55.78 ; H, 5.87; N, 9.16; found: C, 55.91; H, 6.00; N, 9.07.

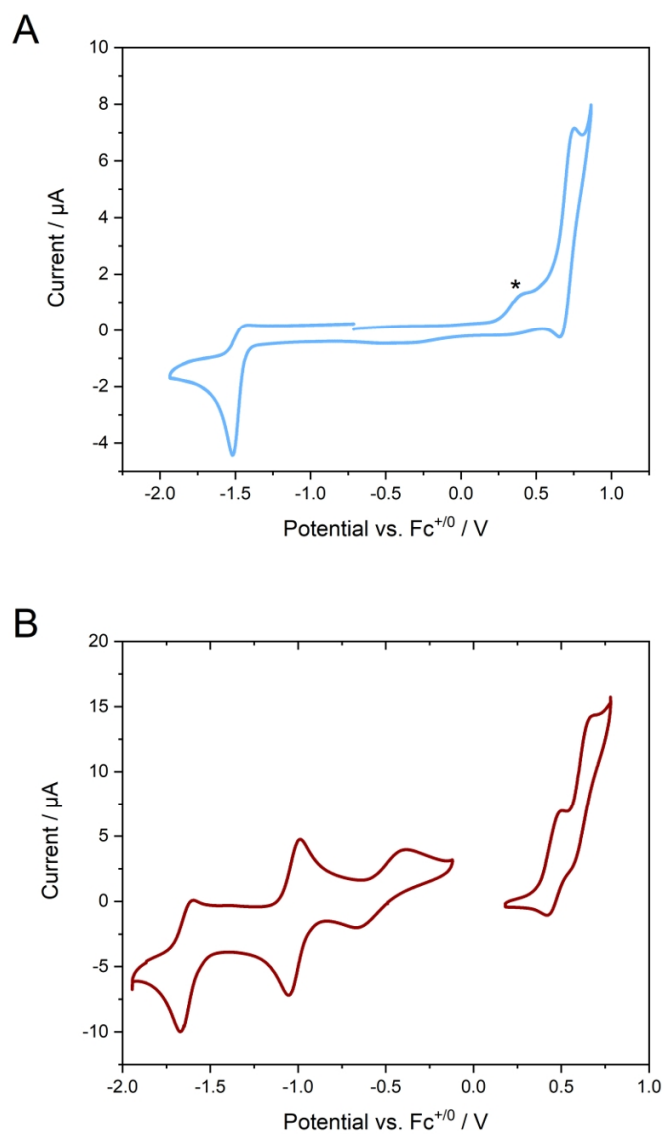


**Figure S1:** Cyclic voltammograms of A)  $t\text{BuT1}$  and B)  $t\text{BuT2R-Co}$ . CVs were recorded at  $50 \text{ mV}\cdot\text{s}^{-1}$  scan rate in  $0.1 \text{ M TBABF}_4$  in dry DMF. Measurements were carried out at a glassy carbon working electrode with a Pt wire auxiliary electrode and a Ag/AgCl reference electrode and converted to potentials vs.  $\text{Fc}^{+/0}$ .

\*The peak at  $0.4 \text{ V vs. Fc}^{+/0}$  is already present in the CV of the blank electrolyte solution without  $t\text{BuT1}$ .

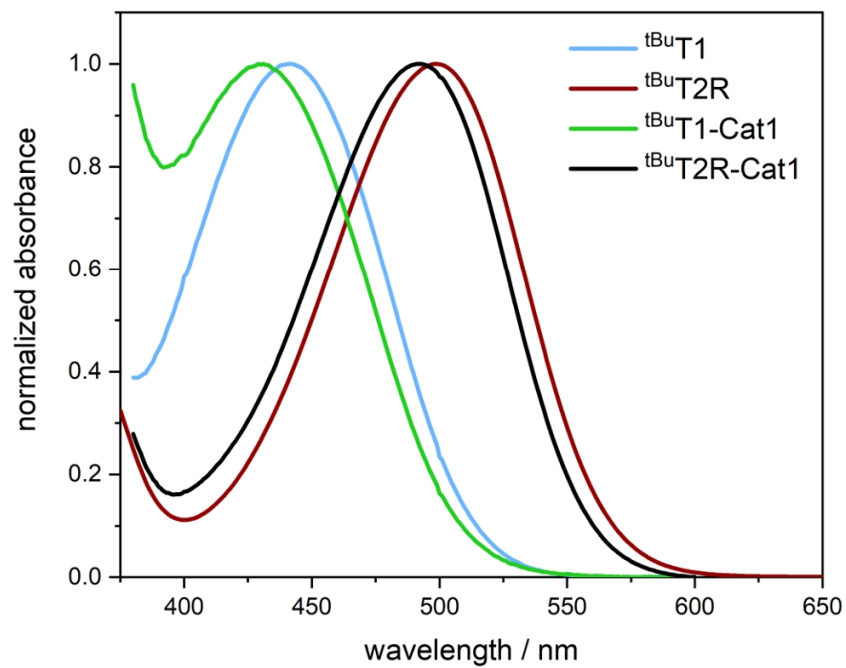


**Figure S2:** UV-Vis absorption spectra in ACN, normalized at the absorption maximum of the ICT band.

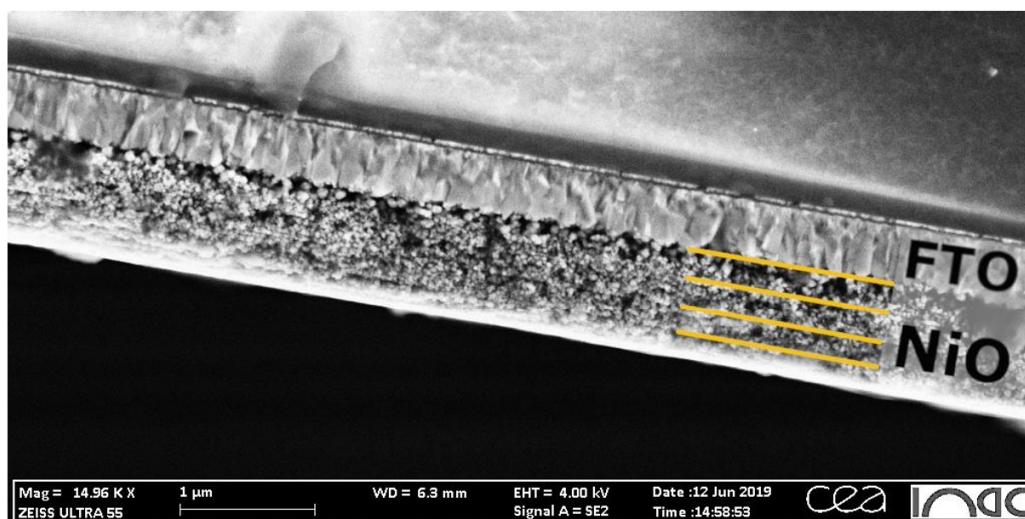


**Figure S3:** Scanning electron microscopy (SEM) image of a typical four-layer NiO film with a thickness of 847 nm. The average film thickness across three batches of NiO films was  $877 \pm 167$  nm (Table S2).

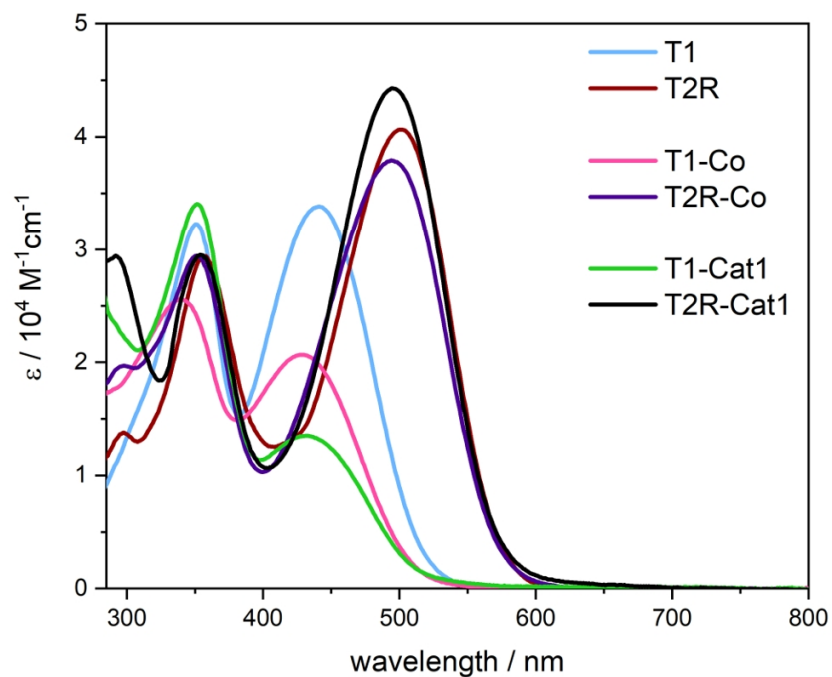


**Figure S4.** Extinction coefficients of **T1**, **T2R**, **T1-Co**, **T2R-Co** and **T2R-Cat1** in a 1M methanolic phenylphosphonic acid solution, as well as of **T1-Cat1** in a 1M DMF phenylphosphonic acid solution employed to determine the dyad and dye loadings for fresh and post-operando films.

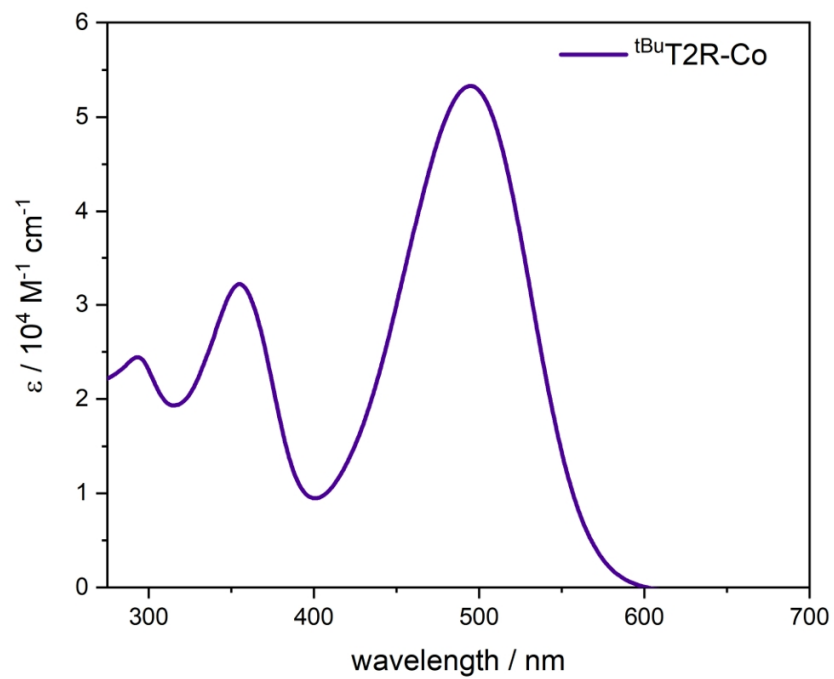


**Figure S5:** UV-Vis absorption spectrum of  $t\text{BuT2R-Co}$  in MeOH.



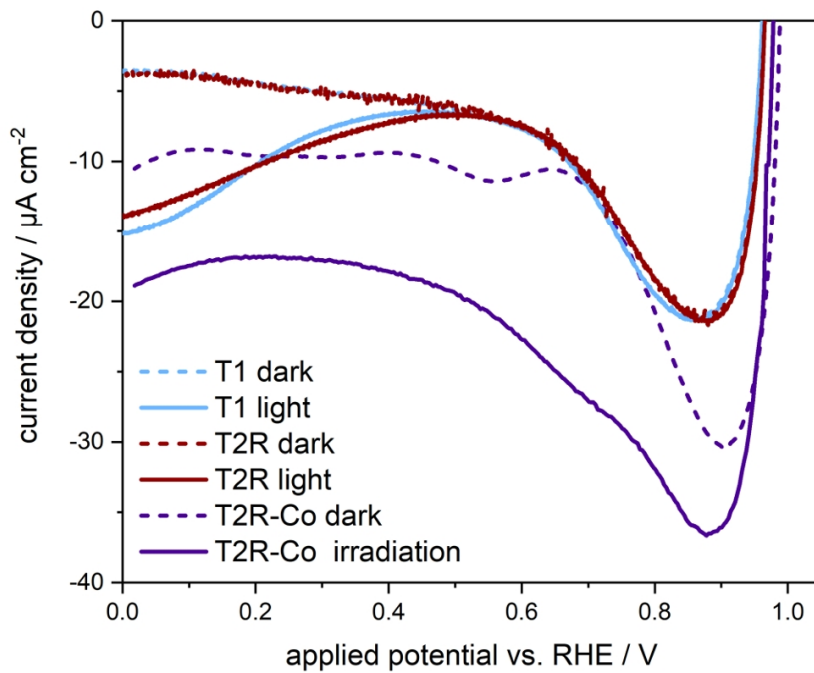


**Figure S6.** Linear scan voltammograms (LSV) of NiO films sensitized with **T1**, **T2R** and **T2R-Co** in 0.1 M MES buffer at pH 5.5 + 0.1 M NaCl aqueous buffer solutions in the dark (dashed) and under  $65 \text{ mW} \cdot \text{cm}^{-2}$  irradiation (solid).

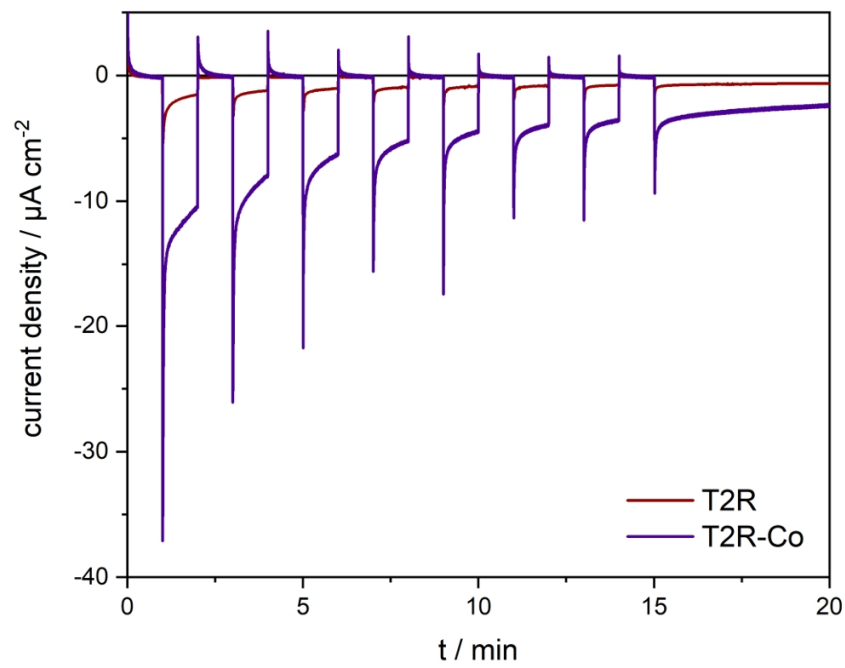


**Figure S7:** Chopped light chronoamperometry of NiO films sensitized with **T2R** (red) and the **T2R-Co** (violet) dyad in 0.1 M MES buffer at pH 5.5 + 0.1 M NaCl aqueous buffer solution. The applied potential was +0.14 V vs. RHE.

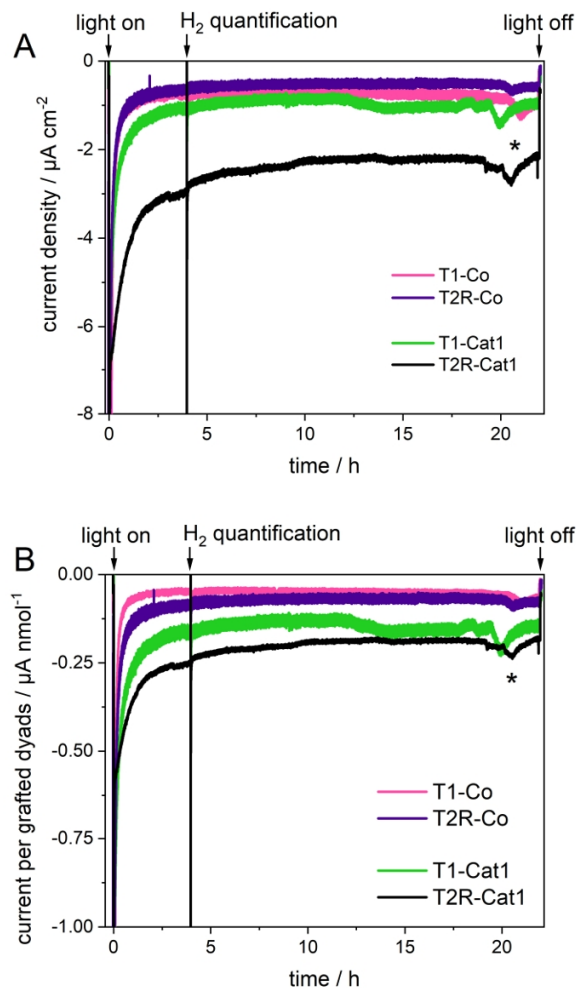


**Figure S8.** Chronoamperometric measurements under irradiation in aqueous 0.1 M pH 5.5 MES buffer at an applied potential of -0.4 V vs. Ag/AgCl (+0.11 V vs. RHE) of **T1-Co** (pink), **T2R-Co** (violet), **T1-Cat1** (green) and **T2R-Cat1** (black). Given are (a) current densities based on the geometric surface of the films and (b) the current normalized to the amount of grafted dyads.

The spike observed at 4 h is caused by the measurement of hydrogen produced. The spikes observed at around 20 h seem to be caused by environmental factors in the laboratory as they all appear around the same time in the morning.

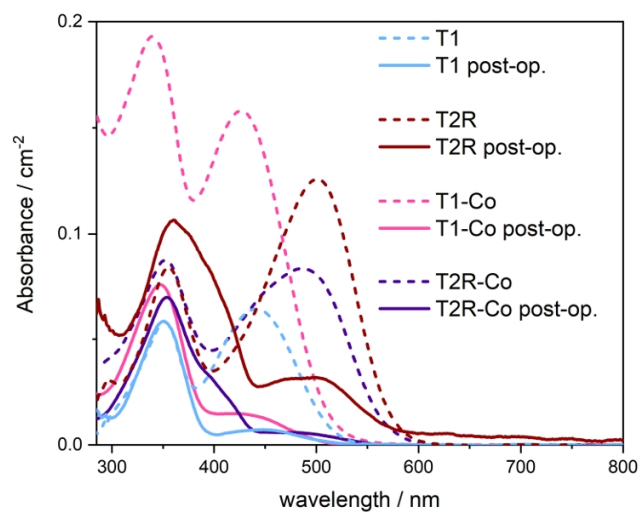


**Figure S9.** UV-Vis spectra of solutions obtained by desorbing **T1**- and **T2R**-sensitized NiO films with 1 M phenylphosphonic acid solution in methanol. Both freshly-sensitized films (dashed lines) as well as films employed for 22 hours photoelectrochemical experiments (solid lines) were desorbed.

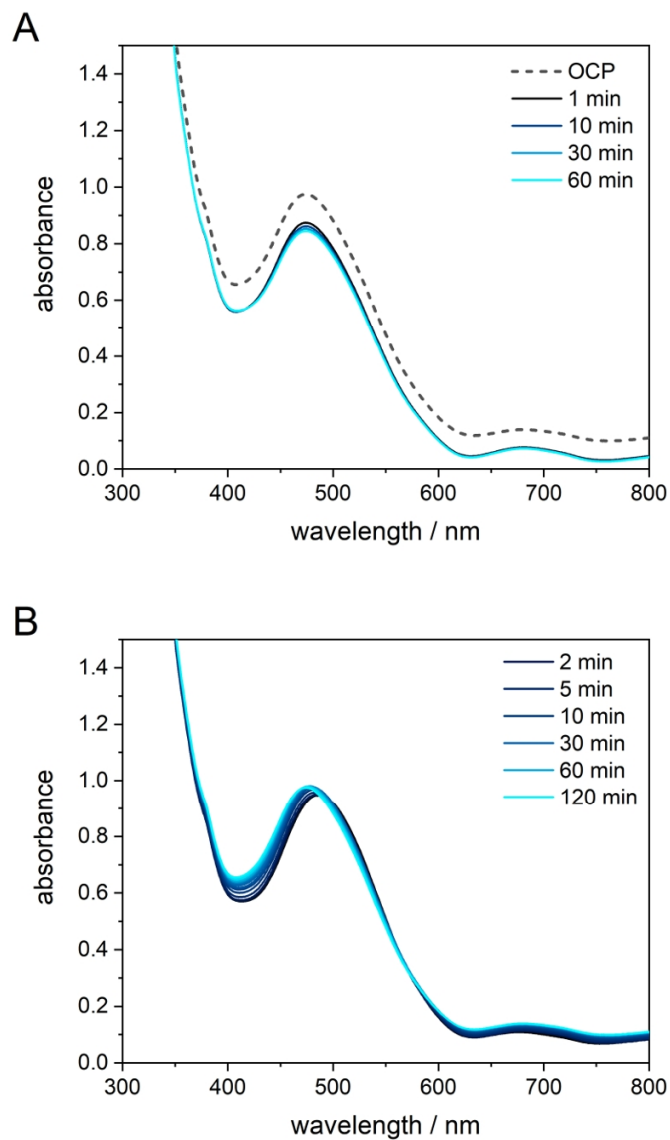


**Figure S10:** UV-Vis absorption spectra of **T2R-Cat1**-sensitized NiO films in contact with 0.1 M MES buffer at pH 5.5 while (a) applying a potential of -0.35 V vs. Ag/AgCl (+0.21 V vs. RHE) or (b) irradiating.

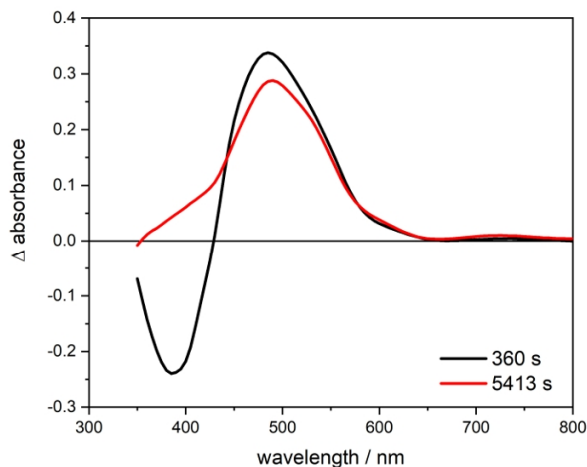


**Figure S11.** Decay-associated spectra (DAS) obtained by globally fitting the differential spectra obtained by measuring UV-Vis absorption spectra of **T2R-Cat1**-sensitized NiO films under operando photoelectrochemical conditions with a two-component exponential function of the form:

$$\Delta A(\lambda) = A_1(\lambda) * e^{-\frac{t}{\tau_1}} + A_2(\lambda) * e^{-\frac{t}{\tau_2}}$$

Where  $A_n$  are the wavelength-dependent amplitudes and  $\tau_n$  are the characteristic lifetimes of the two processes. The DAS are obtained by plotting the  $A_n(\lambda)$  as a function of  $\lambda$ .

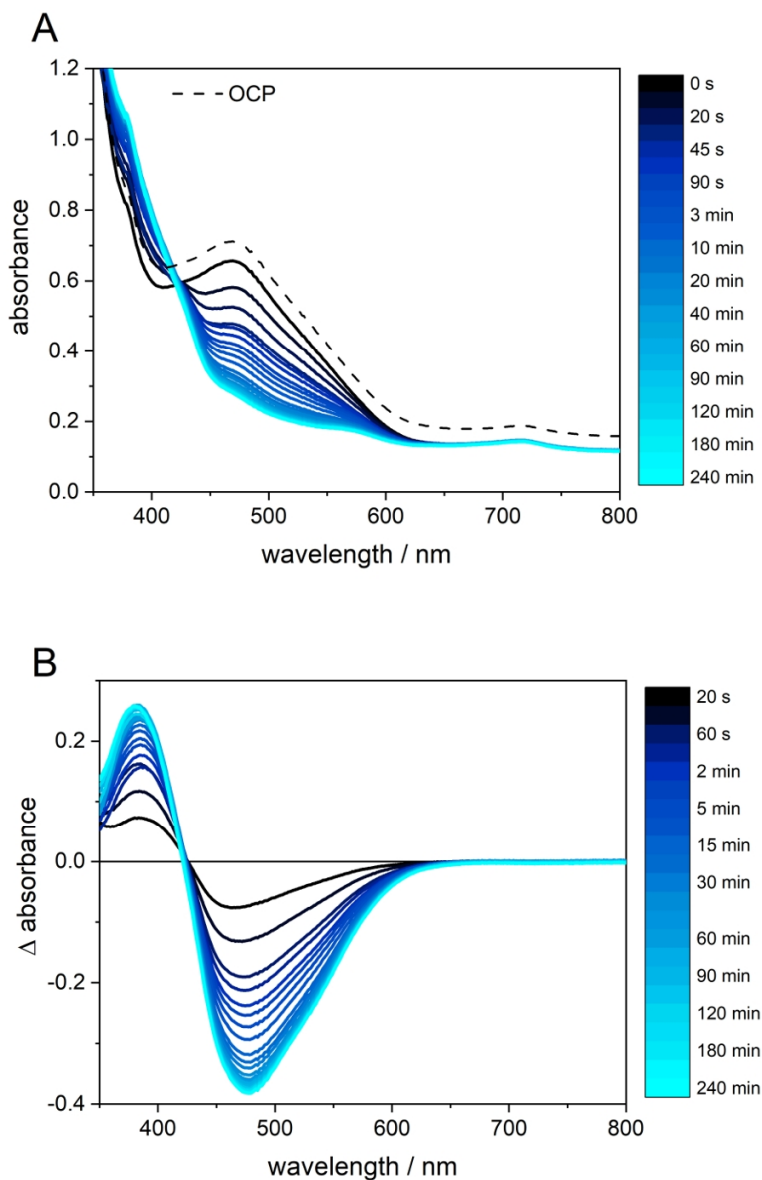


**Figure S12.** UV-vis absorption monitoring of **T2R**-sensitized NiO films under operando photoelectrochemical conditions (0.1 M MES buffer at pH 5.5 under irradiation and with an applied potential of -0.35 V vs. Ag/AgCl corresponding to +0.21 V vs. RHE). Top: UV-Vis spectra; bottom: differential spectra obtained by subtracting the spectrum obtained with applied potential before irradiation (0s).

The initial jump in absorbance upon applying a potential (between OCP and 0 s) is caused by the electrochromic nature of the NiO: Ni<sup>3+</sup> defects formed at the NiO surface show a broad absorption which disappears upon reducing these defects to Ni<sup>2+</sup> by applying a potential.<sup>4,5</sup>

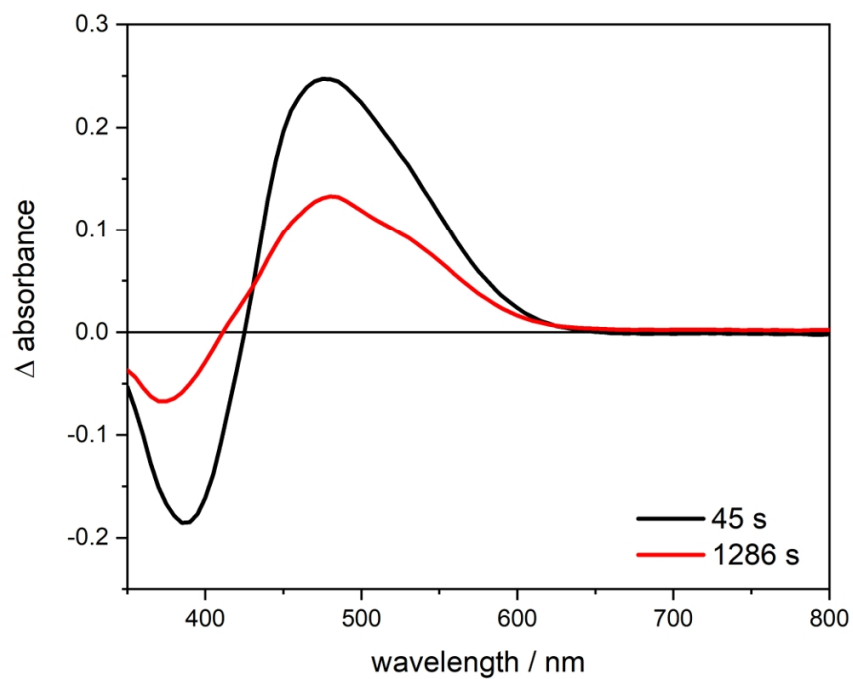


**Figure S13:** Decay-associated spectra (DAS) obtained by globally fitting the differential spectra obtained by measuring UV-Vis absorption spectra of **T2R**-sensitized NiO films under operando photoelectrochemical conditions with a two-component exponential function.



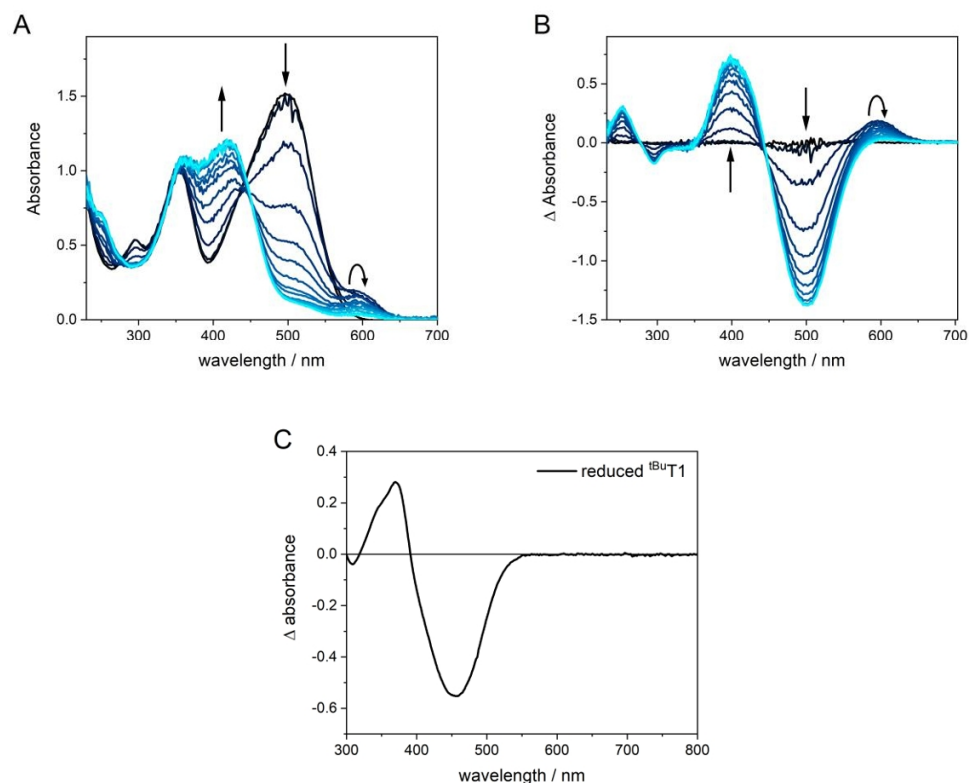


**Figure S14.** a) UV-Vis absorption spectra and b) differential spectra of **T2R** in 0.1 M TBABF<sub>4</sub> in ACN recorded while reducing the compound during a reductive LSV. c) UV-Vis absorption differential spectrum of **tBuT1** while reducing the compound in a reductive chronoamperometry.

The measurement was started at a potential more positive than the dye<sup>0/-</sup> redox potential and then the potential was swepted towards more negative potentials at a rate of 10 mV/s. Spectra were taken every 7 s, corresponding to a potential difference of 70 mV between each spectra. The differential spectra were obtained by subtracting the absorption spectrum prior to reduction of the dye. The pronounced bleach at 500 nm and the positive band at 400 nm are caused by the degradation of **T2R** in its reduced state (i.e., produced by the degradation product), while the transient band at 600 nm is the band characteristic of the reduced state of the dye. Since the degradation of **T2R** in its reduced state occurs very quickly, the exact ratio of bleach to the band at 600 nm for the reduced dye itself cannot be determined by this steady state measurement.

To obtain the absorbance for the comparison with the photocurrent presented in Figure 7, several steps of data treatment were performed to determine and subtract the signal caused by the bare NiO film: using the ratio of signal at the absorption maximum at  $t = 0$  and  $t = 22$  h from the desorption of films and assuming a completed degradation process at the end of the operando UV-Vis experiment, the initial absorbance of **T2R-Cat1** on the film was determined. The absorption spectrum of **T2R-Cat1** was then normalized to this value and subtracted from the operando UV-Vis spectrum at  $t = 0$  to obtain the spectrum of bare NiO. This spectrum was then subtracted from all operando UV-Vis spectra to obtain the spectra of the grafted species at each time  $t$ , which were then integrated from 400-800 nm. Finally, the values were normalized to the current at  $t = 50$  s.

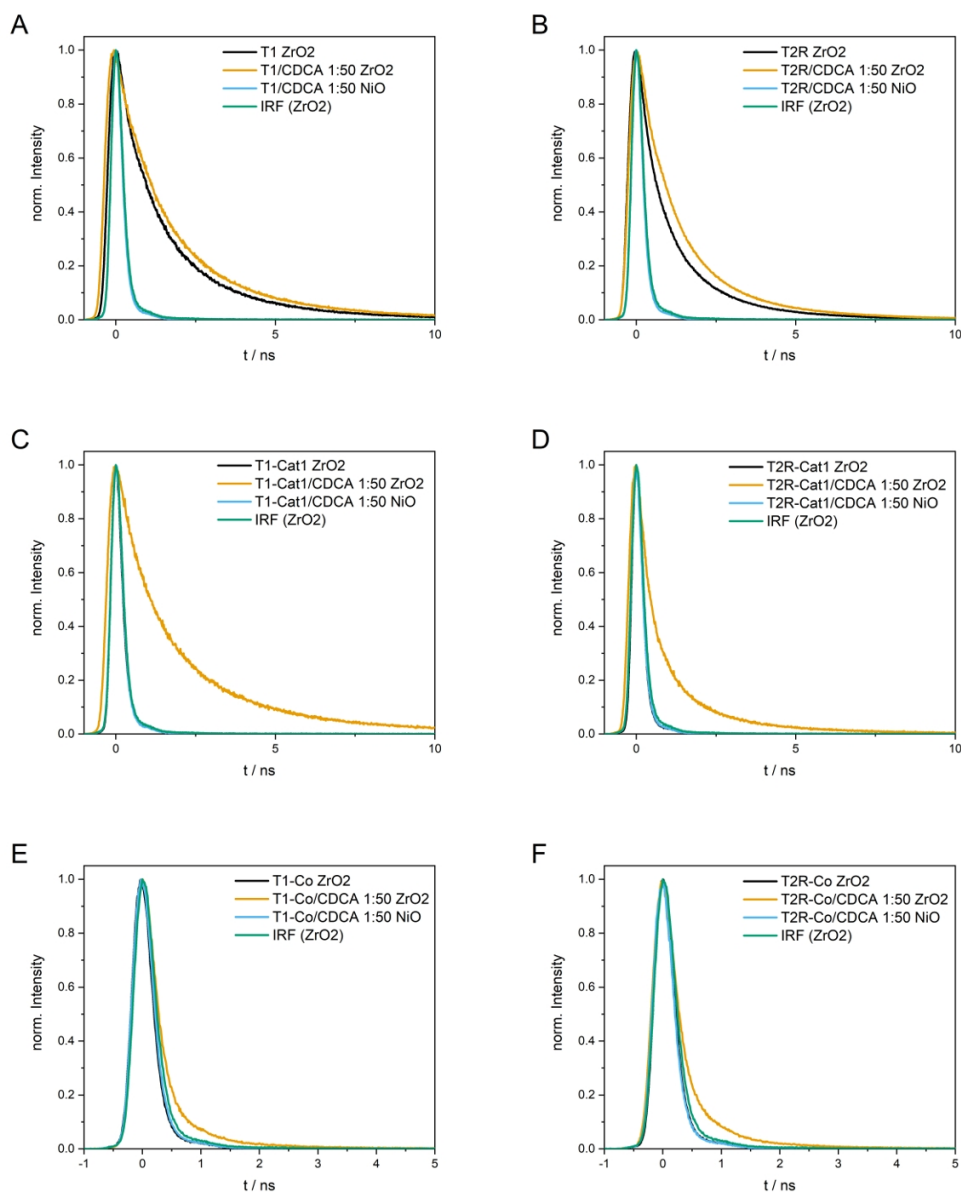


**Figure S15:** Emission decays of compounds **T1** (a), **T2R** (b), **T1-Cat1** (c), **T2R-Cat1** (d), **T1-Co** (e) and **T2R-Co** (f) on ZrO<sub>2</sub> (black), co-sensitized with CDCA in a 1:50 ratio on ZrO<sub>2</sub> (ochre) and on NiO (blue) as well as the instrument response function (green).

NiO and ZrO<sub>2</sub> films were prepared by doctor-blading Solaronix nickel oxide and zirconium dioxide paste, respectively, on microscopic slides and sintering them at 450 °C for 30 min. ZrO<sub>2</sub> is a metal oxide with a bandgap of 5 eV<sup>6</sup> into which no hole injection from the excited state of the dye is possible. Thus, sensitized ZrO<sub>2</sub> films serve as redox inert standards to highlight the effect of dye immobilisation. The compounds were co-grafted with chenodeoxycholic acid (CDCA), a widely used co-grafting agent which prevents dye aggregation on film surfaces.<sup>7,8</sup>

The dyes grafted on ZrO<sub>2</sub> show a biexponential decay with excited state lifetimes  $\tau_1 \approx 400$  ps and  $\tau_2 \approx 2$  ns, with **T2R** having a slightly longer lifetime (Table S7). When linked to the cobalt complex in the dye-catalyst assemblies, quenching of the excited state is observed, to the point where it becomes faster than the instrumental response function of our setup (FWHM = 430 ps). Although such quenching could be related to electron transfer, we showed previously by transient absorption spectroelectrochemistry (TA-SEC) that for **T1-Co**, no electron transfer occurs in solution, suggesting other deactivation pathways such as energy transfer to cobalt states.<sup>9</sup> When co-sensitized with CDCA, the emission quenching is reduced to yield lifetimes in the hundreds of ps to ns region, indicating that the largest contribution to excited state quenching on ZrO<sub>2</sub> is due to intermolecular interactions. This effect is strongest for the **Cat1** dyads, while the **Co** dyads still display short lifetimes with the main component of around 100 ps. By contrast, NiO films co-sensitized with the dyads and CDCA show the same degree of quenching as non-co-grafted ZrO<sub>2</sub>, proving that hole injection takes place on a timescale of shorter than tens of picoseconds.

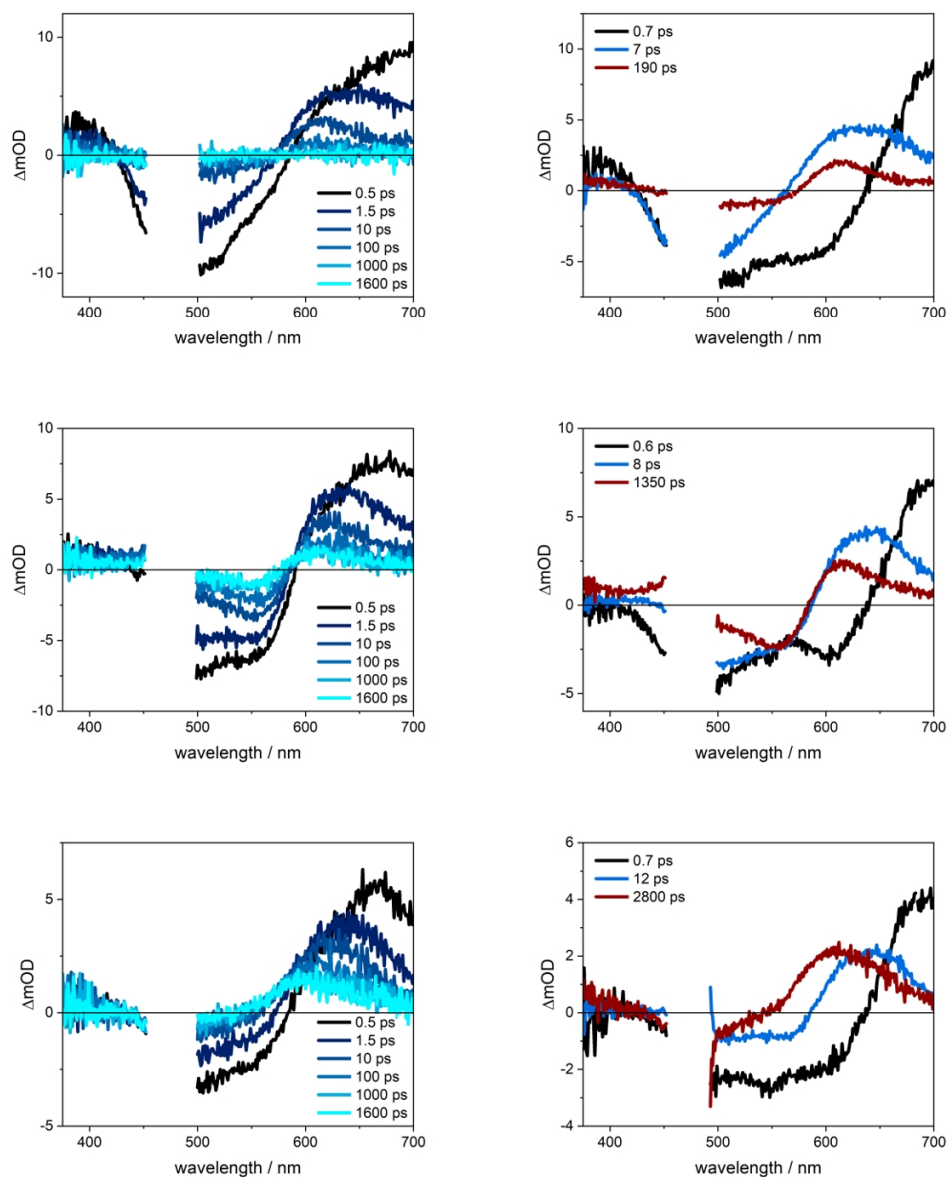


**Figure S16.** fs-TASEC data of a **T2R**-sensitized NiO film at OCP (top),  $-0.74$  V (middle) and  $-1.15$  V (bottom). Left: Transient absorption spectra at different pump-probe delays. Right: Decay-associated spectra obtained by sequential 3-component exponential fits.

At OCP (no applied potential), the fs-TA spectra initially show a ground-state bleach (GSB) between 425 and 575 nm and a broad excited state absorption (ESA) above 575 nm, resembling those recorded for the dye **T2R** in ACN (Figure S18). ESA above 650 nm and GSB decays in about 10 ps, leading to a transient spectrum with a maximum at 620 nm which decays in the accessible time window of 1.6 ns. In contrast to the situation in solution, where the excited-state lifetime is 2.3 ns, all excited-state processes on the film are completed within about 1 ns. In view of the favourable thermodynamics for hole injection and the very fast emission quenching observed, it seems reasonable to assume the fast excited state deactivation is due to hole injection followed by fast charge recombination. When

applying a three-component exponential fit to the data, the fastest component  $\tau_1$  (0.7 ps) shows loss of GSB and build-up of a positive band at 600 nm. This band can be assigned to the one-electron reduced state of the **T2R** dye (Figure S19), leading to the assignment of fast hole injection from the excited state of the dye to form  $\text{NiO}^+|\text{T2R}^-$ , in line with studies performed on **T1** and a related dye.<sup>10-13</sup> Note that the dye in solution shows a spectrally similar fast component without the loss of GSB, which is ascribed to thermalization of the initial excited state and can also be expected for the dye on the film. Thus, the first component on the film is most likely a mixture of hole injection and thermalization of the excited electron. The intermediate component  $\tau_2$  (7 ps) shows the spectral characteristics of deactivation of the excited state of the dye, albeit on a much faster scale than in solution. This fast deactivation can either occur via intermolecular interactions on the film surface or via hole injection coupled to fast recombination. Since the excited state decay of **T2R** on  $\text{ZrO}_2$  was only accelerated to 305 ps (Table S7), in line with literature reports of similar dyes,<sup>14,15</sup> it seems more likely that fast charge recombination is in fact responsible for the excited state decay. The decay of the  $\text{NiO}^+|\text{T2R}^-$  spectrum formed after completion of these processes, corresponding to charge recombination between the reduced dye and holes in NiO, takes place with a characteristic time constant of 188 ps, similar to that found for NiO films sensitized with the related **P1** dye.<sup>12,13</sup> When applying a reductive potential to the film, the spectral features as well as the initial kinetics remain essentially unchanged. The spectrum of the charge-separated state with the positive band at 600 nm, however, is much more long-lived than at OCP, reflected in a large increase in  $\tau_3$  as a function of applied reductive potential (1.3 and 2.8 ns at -0.74 and -1.15 V vs.  $\text{Fc}^{+/0}$ , respectively).

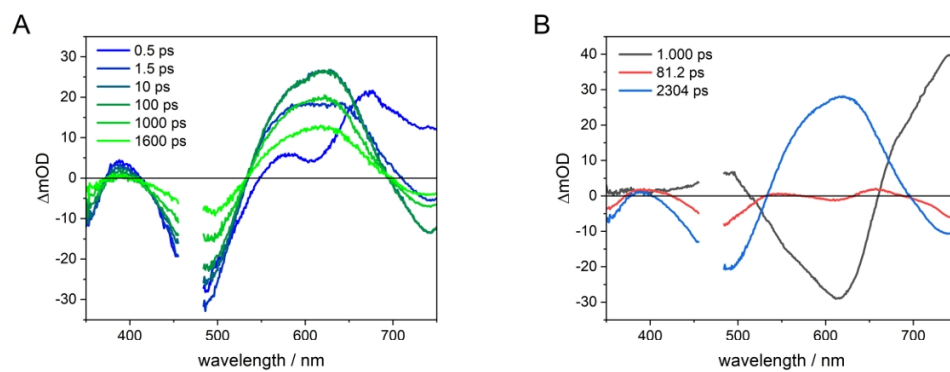


**Figure S17.** a) TA spectra of **T2R** in acetonitrile at different time delays up to 1.6 ns and b) the decay-associated spectra obtained with a sequential 3-component exponential fit.

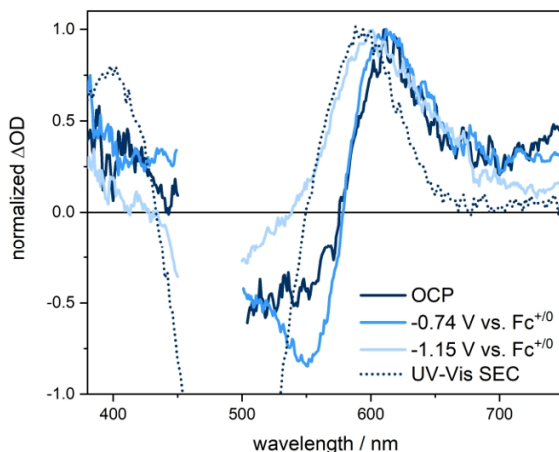


**Figure S18.** Transient absorption spectra of a **T2R**-sensitized film at OCP and at cathodic applied potentials as well as the UV-Vis absorption spectrum of the one-electron reduced dye **T2R** (from UV-Vis spectroelectrochemical measurements in solution, Figure S15).

The spectra were normalized to their absorption maximum around 600 nm. The TA-SEC spectra are the ones taken at 100 ps for the OCP and 1400 ps for the other measurements. The bleach of the charge-transfer band (at 493 nm) of **T2R** in the UV-Vis SEC experiment is more pronounced since the compound is unstable in its reduced form and undergoes a quick degradation reaction leading to loss of absorbance. This bleach therefore does not represent the spectral shape expected in the TA-SEC experiment, rather, the band at 620 nm is the characteristic band for their reduced dye that appears in the TA-SEC experiments.

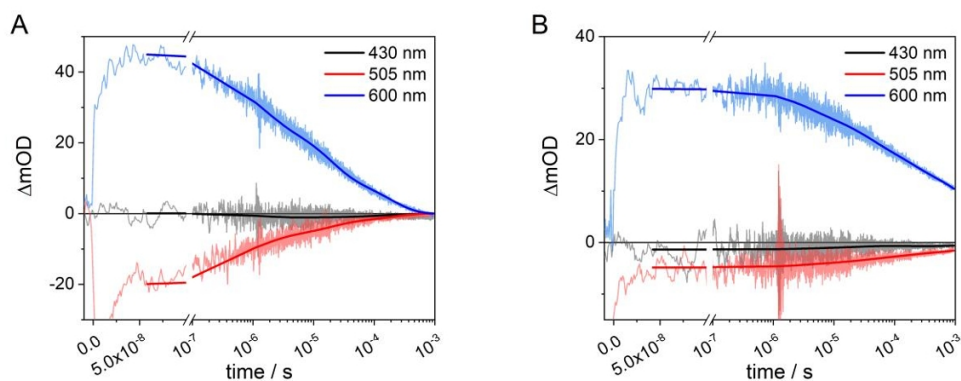


**Figure S19.** ns-TASEC data of **T2R**-sensitized films at a)  $-0.74$  V vs  $\text{Fc}^{+/0}$  and b)  $-1.15$  V vs  $\text{Fc}^{+/0}$ , at characteristic wavelengths: 430 nm (black), 505 nm (red) and 600 nm (blue).

Kinetic traces in the ns- $\mu$ s scale were measured at the characteristic wavelengths of the charge-separated state at 600 and 505 nm at identical applied potentials. A long-lived signal was observed which decayed in a non-exponential fashion, as observed before for charge recombination in dye-sensitized NiO films.<sup>16–20</sup> At  $-0.74$  V vs.  $\text{Fc}^{+/0}$ , the signal completely decays within 1 ms, while it becomes significantly longer lived at  $-1.15$  V vs.  $\text{Fc}^{+/0}$ .

The lower signal intensity at more negative applied potential is likely due to degradation of the dye in its reduced state during the experiment: As the charge-separated state has a longer lifetime at more negative applied potential, this damage is expected to be more severe, even though the duration of the experiment was reduced as much as possible to avoid this.



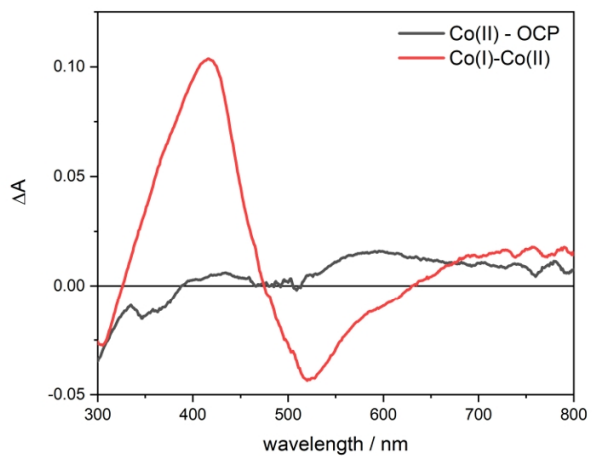


**Figure S20.** Differential UV-Vis SEC spectra of **T2R-Cat1** in 0.1M TBABF<sub>4</sub> in dry ACN upon reduction to the Co<sup>II</sup> and Co<sup>I</sup> state.

The spectra shown are the differential spectra for each reduction step, reflecting the spectral change that is expected upon photoinduced electron transfer in the TA-SEC experiments.

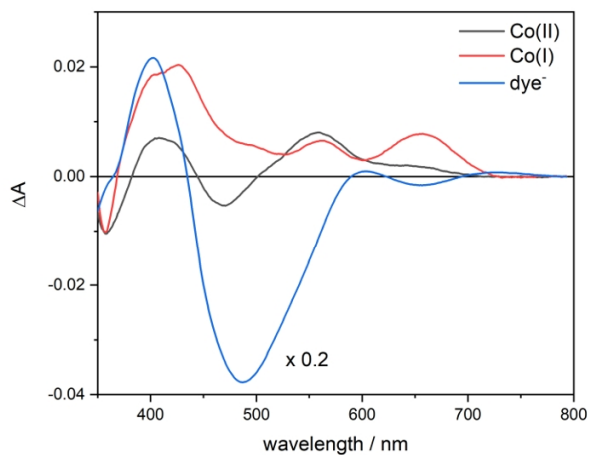


**Figure S21.** Differential UV-Vis SEC spectra of **T2R-Cat1**-sensitized NiO films in 0.1M TBABF<sub>4</sub> in dry ACN applying consecutively more reductive potentials sufficient to first reduce the cobalt catalyst to its Co<sup>II</sup> (black, -0.74 V vs Fc<sup>+0</sup>) and Co<sup>I</sup> (red, -1.15 V vs. Fc<sup>+0</sup>) state and then the dye to the one-electron reduced state (blue, -1.63 V vs. Fc<sup>+0</sup>).

The spectra shown are the differential spectra for each reduction step, reflecting the spectral change that is expected upon photoinduced electron transfer in the TA-SEC experiments. This does not hold true for reduction of the dye as the spectral response is produced by modification of the reduced dye rather than the reduced species itself.

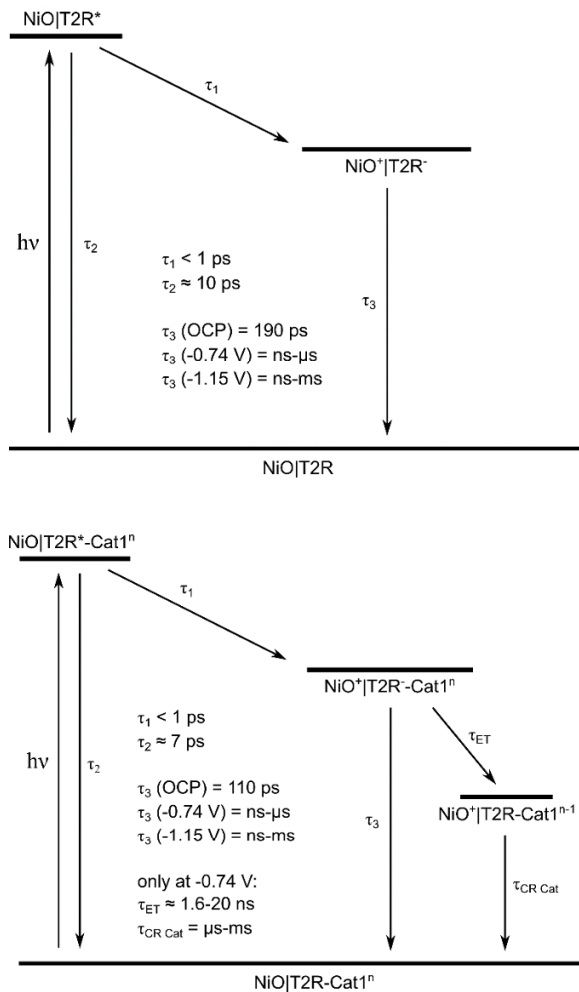


**Figure S22.** Jablonski scheme summarizing the light-induced processes in **T2R-** (top) and **T2R-Cat1**-sensitized (bottom) NiO films at different applied potentials.

Table S1. Photophysical and redox properties of Cat1, Co, <sup>t</sup>BuT1, <sup>t</sup>BuT2R, <sup>t</sup>BuT1-Cat1, <sup>t</sup>BuT1-Co, <sup>t</sup>BuT2R-Cat1 and <sup>t</sup>BuT2R-Co.

	$\lambda_{Abs}$ ( $\pi-\pi^*$ ) <sup>a</sup>	$\epsilon$ ( $\pi-\pi^*$ ) / $M^{-1}\cdot cm^{-1}$	$\lambda_{Abs}$ (ICT) <sup>a</sup>	$\epsilon$ (ICT) / $M^{-1}\cdot cm^{-1}$	$\lambda_{Em}$ <sup>a</sup>	$E_{ox1}^b$ (Dye <sup>+•/0</sup> )	$E_{ox2}^b$ (Dye <sup>2+/•+</sup> )	$E_{red1}^b$ (Co <sup>III/II</sup> )	$E_{red2}^b$ (Co <sup>II/I</sup> )	$E_{red3}^b$ (Dye <sup>0•-/•-</sup> )	$E_{0-0}^c$	$\Delta G_{inj}^d$	$\Delta G_1^e$	$\Delta G_2^f$
Cat1								-0.01	-0.51	-1.27				
Co								-0.04 <sup>22g</sup>	-0.58 <sup>22g</sup>					
<sup>t</sup> BuT1	354	29882	448	27666	649	1.25				-1.04	2.31	-0.81		
<sup>t</sup> BuT2R	355	31060	499	57374	674	1.05	1.23			-1.00	2.15	-0.61		
<sup>t</sup> BuT1-Cat1	354	32131	431	16707	615	1.21		0.04	-0.46	-1.08	2.45	-0.91	-1.12	-0.62
<sup>t</sup> BuT2R-Cat1	355	36900	493	57435	660	1.00	1.15	0.03	-0.40	-1.08	2.17	-0.63	-1.09	-0.66
<sup>t</sup> BuT1-Co	353	35451	433	30884	615	1.25 <sup>23</sup>		0.02 <sup>23</sup>	-0.45 <sup>23</sup>	-1.07 <sup>23</sup>	2.40	-0.87	-1.09	-0.62
<sup>t</sup> BuT2R-Co	355	32196	495	53287	662	1.02	1.19	0.04	-0.45	-1.10	2.17	-0.61	-1.13	-0.64

a) Maximum absorption and emission wavelengths in nm recorded in DMF for all **TI** systems and in MeOH for all **T2R** systems – see Figure 2.

b) In V vs NHE.  $1/2(E_{pc} + E_{pd})$  for Ered<sub>1</sub> and Ered<sub>2</sub>;  $E_{pc}$  for Ered<sub>3</sub>. The redox potentials were converted from Fc<sup>+0</sup> (Figure 1, S1) to NHE, obtained from the reduction potential considering  $E^\circ(\text{Fc}^{+/0}) = 0.53$  V vs. NHE in ACN,  $E^\circ(\text{Fc}^{+/0}) = 0.57$  V vs. NHE in DMF. Unless otherwise indicated, the data was recorded in DMF.

c) 0–0 transition energy,  $E_{0-0}$ , in eV, estimated from the intercept of the normalized absorption and emission spectra.

d) in eV, at pH = 5.5. The Gibbs free energy for the hole injection reaction was calculated according to  $\Delta G_{inj} = e[E_{FB}(\text{NiO}) - E(\text{Dye}^{•-})]$ ; with  $E_{FB}(\text{NiO}) = +0.46$  V vs NHE (see below) and  $E(\text{Dye}^{•-}) = E(\text{Dye}^{0•-}) + E_{0-0}$ .

e) The Gibbs free energy in eV for the electron transfer from the reduced dye to the Co(III) catalyst was calculated according to  $\Delta G_1 = e[E(\text{Dye}^{0•-}) - E(\text{Co}^{\text{III/II}})]$

f) The Gibbs free energy in eV for the electron transfer from the reduced dye to the Co(II) catalyst was calculated according to  $\Delta G_2 = e[E(\text{Dye}^{0•-}) - E(\text{Co}^{\text{II/I}})]$

The flat band potential of NiO at pH 5.5 was calculated according to the following formula taken from <sup>24</sup>:

$$E_{FB \text{ vs. NHE}} = 0.37 \text{ V} + 0.059 (7 - pH)$$

**Table S2.** Film thickness measured of three batches of NiO films by Scanning Electron Microscopy (SEM).

Batch	Thickness / nm
NiO9	690
NiO13	1094
NiO14	847
Average	$877 \pm 167$

**Table S3.** Extinction coefficient maxima positions and values for the  $\pi$ - $\pi^*$  and ICT bands in the studied dyes and dyads in 1M PPA solutions.

Sample	$\lambda_{\max}$ ( $\pi$ - $\pi^*$ ) / nm	$\epsilon_{\max}$ ( $\pi$ - $\pi^*$ ) / M <sup>-1</sup> cm <sup>-1</sup>	$\lambda_{\max}$ (ICT) / nm	$\epsilon_{\max}$ (ICT) / M <sup>-1</sup> cm <sup>-1</sup>	Solvent
<b>T1</b>	351	32269	441	33837	1M PPA in MeOH
<b>T2R</b>	356	29402	500	40649	1M PPA in MeOH
<b>T1-Cat2</b>	339	25605	428	20661	1M PPA in MeOH
<b>T1-Cat1</b>	352	34057	433	13505	1M PPA in DMF
<b>T2R-Cat2</b>	352	29435	494	37914	1M PPA in MeOH
<b>T2R-Cat1</b>	354	29518	495	44298	1M PPA in MeOH

**Table S4.** H<sub>2</sub> measurements during the course and at the end of the chronoamperometric measurements (MES buffer, pH 5.5, continuous visible light irradiation, applied potential: +0.14 V vs RHE)

	Time	Surface Area / cm <sup>2</sup>	Dyad (or dye) loading / nmol·cm <sup>-2</sup>	H <sub>2</sub> in the headspace / nmol	H <sub>2</sub> in solution / nmol	Total amount H <sub>2</sub> / nmol	Total amount H <sub>2</sub> / nmol·cm <sup>-2</sup>	Charge passed / mC·cm <sup>-2</sup>	FE / %	TON <sup>(a)</sup>
NiO	2h	3.3		0	2.9	2.9	0.9	2.3	7.2	
	2h	3.0		0	1.2	1.2	0.4	2.7	3.0	
	<b>average</b>	<b>3.1 ± 0.2</b>		<b>0 ± 0</b>	<b>2.1 ± 1.2</b>	<b>2.1 ± 1.2</b>	<b>0.6 ± 0.3</b>	<b>2.5 ± 0.3</b>	<b>5.1 ± 3</b>	
NiO/T1	4h	2.9	6.2	18.3	19.8	38.1	13.1	10.0	25.5	2.1
	4h	3.1	4.9	11.1	13.4	24.6	7.9	5.2	29.0	1.6
	4h	2.7	5.5	3.6	12.4	16.1	5.9	8.9	12.8	1.1
	<b>average</b>	<b>2.9 ± 0.2</b>	<b>5.5 ± 0.7</b>	<b>11 ± 7.3</b>	<b>15.2 ± 4</b>	<b>26.3 ± 11.1</b>	<b>9 ± 3.8</b>	<b>8 ± 2.5</b>	<b>22 ± 9</b>	<b>1.6 ± 0.5</b>
NiO/T2R	22h	2.9	6.2	32.6	14.4	47.0	16.2	40.4	7.8	2.6
	22h	3.1	4.9	23.8	7.0	30.8	9.9	30.3	6.3	2.0
	22h	2.7	5.5	10.2	6.5	16.8	6.1	48.4	2.4	1.1
	<b>average</b>	<b>2.9 ± 0.2</b>	<b>5.5 ± 0.7</b>	<b>22.2 ± 11.3</b>	<b>9.3 ± 4.4</b>	<b>31.5 ± 15.2</b>	<b>10.7 ± 5.1</b>	<b>39.7 ± 9</b>	<b>5 ± 3</b>	<b>1.9 ± 0.8</b>
NiO/T1-Cat1	4h	2.6	7.9	32.4	29.5	62.0	23.8	18.2	25.3	3.0
	4h	3.0	5.4	6.1	12.0	18.1	6.0	12.1	9.6	1.1
	4h	2.9	7.7	22.6	15.0	37.6	12.8	10.5	23.5	1.7
	<b>average</b>	<b>2.9 ± 0.2</b>	<b>7 ± 1.4</b>	<b>20.4 ± 13.3</b>	<b>18.8 ± 9.4</b>	<b>39.2 ± 22</b>	<b>14.2 ± 9</b>	<b>13.6 ± 4.1</b>	<b>19 ± 9</b>	<b>1.9 ± 1</b>
NiO/T1-Cat1	22h	2.6	7.9	36.9	17.7	54.6	20.9	102.7	3.9	2.7
	22h	3.0	5.4	12.7	8.1	20.8	6.9	60.9	2.2	1.3
	22h	2.9	7.7	44.1	6.4	50.5	17.1	51.5	6.4	2.2
	<b>average</b>	<b>2.9 ± 0.2</b>	<b>7 ± 1.4</b>	<b>31.2 ± 16.5</b>	<b>10.7 ± 6.1</b>	<b>41.9 ± 18.4</b>	<b>15 ± 7.3</b>	<b>71.7 ± 27.3</b>	<b>4 ± 2</b>	<b>2.1 ± 0.7</b>
NiO/T1-Cat1	4h	3.4	6.6	204.1	133.5	337.7	99.0	24.6	77.7	15.0
	4h	3.1	8.4	205.7	127.8	333.5	107.9	29.0	71.7	12.8
	4h	3.1	6.5*	183.7	61.1	244.8	79.6	33.0	46.6	12.3
	<b>average</b>	<b>3.2 ± 0.2</b>	<b>7.2 ± 1.1</b>	<b>198 ± 12</b>	<b>107 ± 40</b>	<b>305 ± 52</b>	<b>96 ± 14</b>	<b>29 ± 4</b>	<b>65 ± 17</b>	<b>13.4 ± 1.4</b>
	22h	3.4	6.6	495.8	49.4	545.2	159.9	88.2	35.0	24.2

	22h	3.1	8.4	494.9	69.3	564.2	182.6	118.7	29.7	21.7
	22h	3.1	6.5 <sup>b)</sup>	403.8	35.9	439.7	143.0	101.7	27.1	22.1
	<b>average</b>	<b>3.2 ± 0.2</b>	<b>7.2 ± 1.1</b>	<b>465 ± 53</b>	<b>52 ± 17</b>	<b>516 ± 67</b>	<b>162 ± 20</b>	<b>103 ± 15</b>	<b>31 ± 4</b>	<b>22.7 ± 1.4</b>
NiO T2R-Cat1	4h	3.3	11.8	395.7	275.4	671.1	206.5	55.1	72.3	17.5
	4h	3.3	13.5	420.7	306.8	727.5	220.5	57.0	74.7	16.3
	4h	3.1	6.6	337.2	169.3	506.5	162.7	55.0	57.1	24.7
	4h	3.1	5.9	394.9	165.8	560.8	180.4	52.9	65.9	30.6
	4h	3.0	9.2	393.2	196.0	589.2	196.4	62.4	60.7	21.4
	4h	3.0	10.8	325.9	148.4	474.3	156.2	47.8	63.0	14.4
	<b>average</b>	<b>3.1 ± 0.1</b>	<b>9.6 ± 3.0</b>	<b>378 ± 38</b>	<b>210 ± 65</b>	<b>588 ± 97</b>	<b>187 ± 25</b>	<b>55 ± 5</b>	<b>66 ± 7</b>	<b>20.8 ± 6.0</b>
	22h	3.3	11.8	1017.8	75.4	1093.2	336.4	207.1	31.3	28.5
	22h	3.3	13.5	1749.3	216.5	1965.8	595.7	226.1	50.8	44.1
	22h	3.1	6.6	730.5	64.6	795.2	255.4	162.3	30.4	38.7
	22h	3.1	5.9	876.7	68.4	945.2	304.1	129.0	45.5	51.5
	22h	2.9	11.7	1017.0	123.2	1140.1	397.0	196.0	39.1	33.9
	22h	2.8	8.2	752.2	77.8	830.0	301.4	162.9	35.7	36.7
	<b>average</b>	<b>3.1 ± 0.2</b>	<b>9.6 ± 3.1</b>	<b>1024 ± 376</b>	<b>104 ± 59</b>	<b>1128 ± 433</b>	<b>365 ± 122</b>	<b>181 ± 36</b>	<b>39 ± 8</b>	<b>38.9 ± 8.1</b>
NiO T1-Co	4h	3.2	14.2	18.7	16.5	35.1	11.2	26.5	8.1	0.8
	4h	3.3	15.1	16.5	17.5	34.0	10.3	22.9	9.1	0.7
	<b>average</b>	<b>3.2 ± 0.1</b>	<b>14.7 ± 0.6</b>	<b>18 ± 2</b>	<b>17 ± 1</b>	<b>35 ± 1</b>	<b>11 ± 1</b>	<b>25 ± 3</b>	<b>9 ± 1</b>	<b>0.7 ± 0.1</b>
	22h	3.2	14.2	25.8	22.5	48.3	15.3	100.8	2.9	1.1
	22h	3.3	15.1	25.3	7.8	33.1	10.0	74.5	2.7	0.7
	<b>average</b>	<b>3.2 ± 0.1</b>	<b>14.7 ± 0.6</b>	<b>26 ± 0</b>	<b>15 ± 10</b>	<b>41 ± 11</b>	<b>13 ± 4</b>	<b>88 ± 19</b>	<b>3 ± 0</b>	<b>0.9 ± 0.3</b>
NiO T2R-Co	4h	3.0	7.5	20.7	12.9	33.6	11.0	17.9	11.9	1.5
	4h	3.3	6	17.1	11.4	28.5	8.6	17.4	9.6	1.4
	<b>average</b>	<b>3.2 ± 0.2</b>	<b>6.8 ± 1.1</b>	<b>19 ± 3</b>	<b>12 ± 1</b>	<b>31 ± 4</b>	<b>10 ± 2</b>	<b>18 ± 0</b>	<b>11 ± 2</b>	<b>1.5 ± 0</b>
	22h	3.0	7.5	37.8	0.0	37.8	12.4	52.4	4.6	1.7
	22h	3.3	6	22.5	4.4	26.8	8.1	82.0	1.9	1.4



	<b>average</b>	<b>3.2 ± 0.2</b>	<b>6.8 ± 1.1</b>	<b>30 ± 11</b>	<b>2 ± 3</b>	<b>32 ± 8</b>	<b>10 ± 3</b>	<b>67 ± 21</b>	<b>3 ± 2</b>	<b>1.5 ± 0.2</b>
--	----------------	------------------	------------------	----------------	--------------	---------------	---------------	----------------	--------------	------------------

a) The TON given for NiO films sensitized with the dyes **T1** and **T2R** are normalized to the amount of dye grafted on the film. As there is no catalyst, the TON does not reflect a catalytic process but is rather given to ease comparison with dyad-sensitized NiO films.

b) We failed to measure the dye loading of this film and therefore used the average dye loading of **T1-Cat1**-sensitized films.

**Table S5:** Co surface concentration as determined by ICP-MS for **T2R-Cat1**-sensitized films after 0, 4 and 22 h of PEC experiment. For comparison between the two techniques, the grafting densities determined of the same films by UV-Vis absorption are given.

	Grafting density / nmol·cm <sup>-2</sup>				Co loss / %
	0 h (UV-Vis)	0 h (ICP)	4 h (ICP)	22 h (ICP)	
4 h PEC experiment	9.1	6.0	1.0		84
22 h PEC experiment	11.6	13.3		1.0	93

**Table S6:** Average grafting density of active **T2R-Cat1** dyads over the first 4 hours of PEC experiments, calculated based on the integral of the photocurrent and the initial surface concentration, and turn-over numbers for the active dyads.

PEC experiment	Average active dyad surface concentration / nmol·cm <sup>-2</sup>	TON of active dyads
1	2.5	82.6
2	2.5	87.8
3	1.5	111.4
4	1.6	112.1
5	2.1	95.3
6	2.2	72.6
<b>Average</b>	<b>2.0 ± 0.4</b>	<b>93.6 ± 15.9</b>

**Table S7:** Emission lifetimes obtained by fitting the time-resolved emission data of all dyes and dyads grafted on ZrO<sub>2</sub> as well as co-grafted with chenodeoxycholic acid (CDCA) in a 1:50 ratio on ZrO<sub>2</sub> and on NiO. The data was fitted with a mono- or biexponential fit. In case of the biexponential fits,  $\alpha$  gives the amplitude of the first component.

		ZrO <sub>2</sub>		ZrO <sub>2</sub> CDCA 50:1		NiO CDCA 50:1
		t / ps	$\alpha$	t / ps	$\alpha$	t / ps
<b>T1</b>	$\tau_1$	523	0.68	790	0.68	51
	$\tau_2$	2314		2819		
<b>T2R</b>	$\tau_1$	305	0.76	555	0.72	52
	$\tau_2$	1680		2064		
<b>T1-Cat1</b>	$\tau_1$	40		756	0.73	42
	$\tau_2$			3328		
<b>T2R-Cat1</b>	$\tau_1$	37		274	0.88	43
	$\tau_2$			2013		
<b>T1-Co</b>	$\tau_1$	42		117	0.98	47
	$\tau_2$			893		
<b>T2R-Co</b>	$\tau_1$	43		47	0.97	42
	$\tau_2$			682		

**Table S8.** Characteristic time constants obtained by applying multiexponential fits of the form

$$\Delta A(\lambda, t) = \sum_1^n A_i(\lambda) * e^{-\frac{t}{\tau_i}}$$

to the fs- and ns-TASEC data (global fit for the fs-TASEC data, ns-TASEC data as indicated), where  $n$  is the number of components,  $A_i$  are the wavelength-dependent amplitudes and  $\tau_i$  are the characteristic lifetimes of the processes.

The average lifetimes were calculated of the ns-TA data using the formula:

$$\tau_{ave} = \frac{\sum A_i \tau_i}{\sum A_i}$$

Where there was a need to fit an infinite component, the relative amplitudes of the average lifetime and the infinite component is given in parentheses.

System	Applied potential vs. $\text{Fc}^{+/0}$	fs-TASEC data			Wavelength	$\tau_1 / \mu\text{s}$	$\tau_2 / \mu\text{s}$	$\tau_3 / \mu\text{s}$	$\tau_4 / \mu\text{s}$	$\tau_{ave} / \mu\text{s}$
		$\tau_1 / \text{ps}$	$\tau_2 / \text{ps}$	$\tau_3 / \text{ps}$						
<b>T2R</b>	OCP	0.7	7	190						
	-0.74 V	0.6	8	1350	global	0.13	1.7	20	194	28
	-1.15 V	0.7	12	2800	global	3.5	37	383	Infinite (33 %)	184 (67 %)
<b>T2R-Cat1</b>	OCP	0.5	5	110						
	-0.74 V	0.6	8	2300	430	1.2	13	123	Infinite (16 %)	30 (84 %)
					505, 620	0.13	1.7	22	295	6.8
-1.15 V	0.5	9	3300	global	1.4	22	294	Infinite (27 %)	131 (73 %)	

**References.**

- (1) Yen, Y.-S.; Chen, W.-T.; Hsu, C.-Y.; Chou, H.-H.; Lin, J. T.; Yeh, M.-C. P. Arylamine-Based Dyes for p-Type Dye-Sensitized Solar Cells. *Organic Letters* **2011**, *13* (18), 4930–4933. <https://doi.org/10.1021/ol202014x>.
- (2) Huang, B.; Prantil, M. A.; Gustafson, T. L.; Parquette, J. R. The Effect of Global Compaction on the Local Secondary Structure of Folded Dendrimers. *Journal of the American Chemical Society* **2003**, *125* (47), 14518–14530. <https://doi.org/10.1021/ja037895a>.
- (3) Dumont, A.; Jacques, V.; Desreux, J. F. New Synthons for the Synthesis of Lanthanide Containing Macrocyclic Schiff Bases Featuring Substituents Available for Tethering. *Tetrahedron* **2000**, *56* (14), 2043–2052. [https://doi.org/10.1016/S0040-4020\(00\)00104-6](https://doi.org/10.1016/S0040-4020(00)00104-6).
- (4) Boschloo, G.; Hagfeldt, A. Spectroelectrochemistry of Nanostructured NiO. *Journal of Physical Chemistry B* **2001**, *105* (15), 3039–3044. <https://doi.org/10.1021/jp003499s>.
- (5) Xia, X. H.; Tu, J. P.; Zhang, J.; Wang, X. L.; Zhang, W. K.; Huang, H. Morphology Effect on the Electrochromic and Electrochemical Performances of NiO Thin Films. *Electrochimica Acta* **2008**, *53* (18), 5721–5724. <https://doi.org/10.1016/j.electacta.2008.03.047>.
- (6) Xu, Y.; Schoonen, M. A. A. The Absolute Energy Positions of Conduction and Valence Bands of Selected Semiconducting Minerals. *American Mineralogist* **2000**, *85* (3–4), 543–556. <https://doi.org/10.2138/am-2000-0416>.
- (7) Ito, S.; Miura, H.; Uchida, S.; Takata, M.; Sumioka, K.; Liska, P.; Comte, P.; Péchy, P.; Grätzel, M. High-Conversion-Efficiency Organic Dye-Sensitized Solar Cells with a Novel Indoline Dye. *Chemical Communications* **2008**, No. 41, 5194. <https://doi.org/10.1039/b809093a>.
- (8) Favereau, L.; Warnan, J.; Pellegrin, Y.; Blart, E.; Boujtita, M.; Jacquemin, D.; Odobel, F. Diketopyrrolopyrrole Derivatives for Efficient NiO-Based Dye-Sensitized Solar Cells. *Chemical Communications* **2013**, *49* (73), 8018. <https://doi.org/10.1039/c3cc44232b>.
- (9) Bold, S.; Zedler, L.; Zhang, Y.; Massin, J.; Artero, V.; Chavarot-Kerlidou, M.; Dietzek, B. Electron Transfer in a Covalent Dye–Cobalt Catalyst Assembly – a Transient Absorption Spectroelectrochemistry Perspective. *Chemical Communications* **2018**, *54* (75), 10594–10597. <https://doi.org/10.1039/C8CC05556D>.
- (10) Pati, P. B.; Zhang, L.; Philippe, B.; Fernández-Terán, R.; Ahmadi, S.; Tian, L.; Rensmo, H.; Hammarström, L.; Tian, H. Insights into the Mechanism of a Covalently Linked Organic Dye–Cobaloxime Catalyst System for Dye-Sensitized Solar Fuel Devices. *ChemSusChem* **2017**, *10* (11), 2480–2495. <https://doi.org/10.1002/cssc.201700285>.
- (11) Massin, J.; Bräutigam, M.; Bold, S.; Wächtler, M.; Pavone, M.; Muñoz-García, A. B.; Dietzek, B.; Artero, V.; Chavarot-Kerlidou, M. Investigating Light-Driven Hole Injection and Hydrogen Evolution Catalysis at Dye-Sensitized NiO Photocathodes: A Combined Experimental–Theoretical Study. *The Journal of Physical Chemistry C* **2019**, *123* (28), 17176–17184. <https://doi.org/10.1021/acs.jpcc.9b04715>.
- (12) Qin, P.; Wiberg, J.; Gibson, E. A.; Linder, M.; Li, L.; Brinck, T.; Hagfeldt, A.; Albinsson, B.; Sun, L. Synthesis and Mechanistic Studies of Organic Chromophores with Different Energy Levels for P-Type Dye-Sensitized Solar Cells. *The Journal of Physical Chemistry C* **2010**, *114* (10), 4738–4748. <https://doi.org/10.1021/jp911091n>.
- (13) Black, F. A.; Clark, C. A.; Summers, G. H.; Clark, I. P.; Towrie, M.; Penfold, T.; George, M. W.; Gibson, E. A. Investigating Interfacial Electron Transfer in Dye-Sensitized NiO Using Vibrational Spectroscopy.

- Physical Chemistry Chemical Physics* **2017**, *19* (11), 7877–7885.  
<https://doi.org/10.1039/C6CP05712H>.
- (14) Oum, K.; Lohse, P. W.; Klein, J. R.; Flender, O.; Scholz, M.; Hagfeldt, A.; Boschloo, G.; Lenzer, T. Photoinduced Ultrafast Dynamics of the Triphenylamine-Based Organic Sensitizer D35 on TiO<sub>2</sub>, ZrO<sub>2</sub> and in Acetonitrile. *Physical Chemistry Chemical Physics* **2013**, *15* (11), 3906.  
<https://doi.org/10.1039/c3cp44095h>.
- (15) Dryza, V.; Bieske, E. J. Does the Triphenylamine-Based D35 Dye Sensitizer Form Aggregates on Metal-Oxide Surfaces? *Journal of Photochemistry and Photobiology A: Chemistry* **2015**, *302*, 35–41.  
<https://doi.org/10.1016/j.jphotochem.2015.01.007>.
- (16) D'Amario, L.; Antila, L. J.; Pettersson Rimgard, B.; Boschloo, G.; Hammarström, L. Kinetic Evidence of Two Pathways for Charge Recombination in NiO-Based Dye-Sensitized Solar Cells. *The Journal of Physical Chemistry Letters* **2015**, *6* (5), 779–783. <https://doi.org/10.1021/acs.jpcclett.5b00048>.
- (17) Dillon, R. J.; Alibabaei, L.; Meyer, T. J.; Papanikolas, J. M. Enabling Efficient Creation of Long-Lived Charge-Separation on Dye-Sensitized NiO Photocathodes. *ACS Applied Materials & Interfaces* **2017**, *9* (32), 26786–26796. <https://doi.org/10.1021/acsami.7b05856>.
- (18) Lindquist, R. J.; Majewski, M. B.; Hoffeditz, W. L.; Phelan, B. T.; Farha, O. K.; Hupp, J. T.; Wasielewski, M. R. Photodriven Hydrogen Evolution by Molecular Catalysts Using Al<sub>2</sub>O<sub>3</sub>-Protected Perylene-3,4-Dicarboximide on NiO Electrodes. *Chem. Sci.* **2017**, *8* (1), 541–549.  
<https://doi.org/10.1039/C6SC02477G>.
- (19) Antila, L. J.; Ghamgosar, P.; Maji, S.; Tian, H.; Ott, S.; Hammarström, L. Dynamics and Photochemical H<sub>2</sub> Evolution of Dye–NiO Photocathodes with a Biomimetic FeFe-Catalyst. *ACS Energy Letters* **2016**, *1* (6), 1106–1111. <https://doi.org/10.1021/acsenergylett.6b00506>.
- (20) Gardner, J. M.; Beyler, M.; Karnahl, M.; Tschierlei, S.; Ott, S.; Hammarström, L. Light-Driven Electron Transfer between a Photosensitizer and a Proton-Reducing Catalyst Co-Adsorbed to NiO. *Journal of the American Chemical Society* **2012**, *134* (47), 19322–19325. <https://doi.org/10.1021/ja3082268>.
- (21) Varma, S.; Castillo, C. E.; Stoll, T.; Fortage, J.; Blackman, A. G.; Molton, F.; Deronzier, A.; Collomb, M.-N. Efficient Photocatalytic Hydrogen Production in Water Using a Cobalt(III) Tetraaza-Macrocyclic Catalyst: Electrochemical Generation of the Low-Valent Co(I) Species and Its Reactivity toward Proton Reduction. *Physical Chemistry Chemical Physics* **2013**, *15* (40), 17544.  
<https://doi.org/10.1039/c3cp52641k>.
- (22) Jacques, P.-A.; Artero, V.; Pecaut, J.; Fontecave, M. Cobalt and Nickel Diimine-Dioxime Complexes as Molecular Electrocatalysts for Hydrogen Evolution with Low Overvoltages. *Proceedings of the National Academy of Sciences* **2009**, *106* (49), 20627–20632.  
<https://doi.org/10.1073/pnas.0907775106>.
- (23) Kaeffer, N.; Massin, J.; Lebrun, C.; Renault, O.; Chavarot-Kerlidou, M.; Artero, V. Covalent Design for Dye-Sensitized H<sub>2</sub>-Evolving Photocathodes Based on a Cobalt Diimine–Dioxime Catalyst. *Journal of the American Chemical Society* **2016**, *138* (38), 12308–12311. <https://doi.org/10.1021/jacs.6b05865>.
- (24) Yu, Y.; Click, K. A.; Chien, S.-C.; Sun, J.; Curtze, A.; Lin, L.-C.; Wu, Y. Decoupling pH Dependence of Flat Band Potential in Aqueous Dye-Sensitized Electrodes. *The Journal of Physical Chemistry C* **2019**, *123* (14), 8681–8687. <https://doi.org/10.1021/acs.jpcc.9b00710>.





# Hydrogen Production at a NiO Photocathode Based on a Ruthenium Dye–Cobalt Diimine Dioxime Catalyst Assembly: Insights from Advanced Spectroscopy and Post-operando Characterization

Emmanouil Giannoudis,<sup>▽</sup> Sebastian Bold,<sup>▽</sup> Carolin Müller, Alexander Schwab, Jakob Bruhnke, Nicolas Queyriaux, Corinne Gablin, Didier Leonard, Christine Saint-Pierre, Didier Gasparutto, Dmitry Aldakov, Stephan Kupfer, Vincent Artero, Benjamin Dietzek, and Murielle Chavarot-Kerlidou\*



Cite This: *ACS Appl. Mater. Interfaces* 2021, 13, 49802–49815



Read Online

ACCESS |

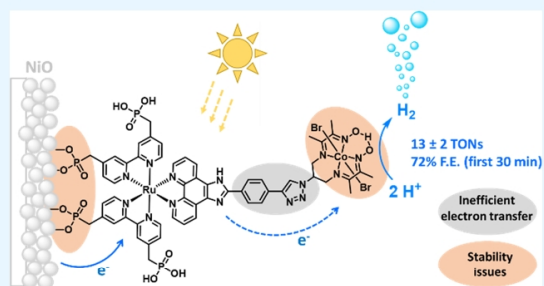
Metrics & More

Article Recommendations

Supporting Information

**ABSTRACT:** The production of hydrogen by efficient, low-cost, and integrated photoelectrochemical water splitting processes represents an important target for the ecological transition. This challenge can be addressed thanks to bioinspired chemistry and artificial photosynthesis approaches by designing dye-sensitized photocathodes for hydrogen production, incorporating bioinspired first-row transition metal-based catalysts. The present work describes the preparation and photoelectrochemical characterization of a NiO photocathode sensitized with a phosphonate-derivatized ruthenium tris-diimine photosensitizer covalently linked to a cobalt diimine dioxime hydrogen-evolving catalyst. Under simulated AM 1.5G irradiation, hydrogen is produced with photocurrent densities reaching  $84 \pm 7 \mu\text{A}\cdot\text{cm}^{-2}$ , which is among the highest values reported so far for dye-sensitized photocathodes with surface-immobilized catalysts. Thanks to the unique combination of advanced spectroscopy and surface characterization techniques, the fast desorption of the dyad from the NiO electrode and the low yield of electron transfer to the catalyst, resulting in the Co demetallation from the diimine dioxime framework, were identified as the main barriers limiting the performances and the stability of the system. This work therefore paves the way for a more rational design of molecular photocathodes for solar fuel production and represents a further step toward the development of sustainable processes for the production of hydrogen from sunlight and water.

**KEYWORDS:** solar fuels, hydrogen, photoelectrochemistry, dye-sensitized, cobalt catalyst



## INTRODUCTION

Production of hydrogen (H<sub>2</sub>) through sunlight-driven water splitting is one relevant strategy to meet the challenges of a carbon-neutral economy. Among the various technological approaches proposed to date, water splitting photoelectrochemical cells are appealing as integrated, low-cost, and scalable devices.<sup>1–3</sup> Dye-sensitized photoelectrochemical cells (DS-PECs) can more specifically elaborate on the well-established dye-sensitized solar cell (DSSC) technology to build active photoelectrodes via the immobilization of molecular components, *i.e.*, light-harvesting units and catalysts, on the surface of transparent conducting oxide films.<sup>4–7</sup> In addition, they benefit from the recent achievements in the field of bioinspired catalysis for energy-relevant applications to integrate appropriate first-row transition metal-based catalysts for hydrogen production.<sup>8–10</sup> A proof of concept for this approach was recently provided with the first DS-PECs based on such bioinspired catalysts and built in a tandem

configuration, reproducing the Z scheme of photosynthesis.<sup>11–13</sup>

Various electrode architectures have been successfully described to assemble molecular H<sub>2</sub>-evolving catalysts (cobalt, nickel, or iron complexes, typically) with light-harvesting units (organic dyes and porphyrin or ruthenium tris-diimine complexes) on the surface of a suitable mesoporous semiconducting oxide film.<sup>14–16</sup> They typically rely on the anchoring of supramolecular or covalent dye-catalyst assemblies,<sup>17–22</sup> the co-immobilization of both components,<sup>11–13,23–27</sup> or alternatively, a layer-by-layer assembly strategy.<sup>28–32</sup> In addition to this structural diversity, a wide

Received: June 28, 2021

Accepted: September 28, 2021

Published: October 12, 2021



range of activity conditions (nature and pH of the electrolyte, applied potential, light source and intensity, etc.) were reported, preventing the establishment of clear structure–activity relationships, although the latter would be highly beneficial to rationally improve the photocathode molecular design. Yet, all examples of functional H<sub>2</sub>-evolving dye-sensitized photocathodes reported so far display overall low performances in terms of photocurrent densities, turnover numbers (TONs), and in some cases, faradaic efficiencies (F.E.).

NiO is the main p-type semiconductor employed in these studies, and various procedures have been employed to prepare mesoporous nanostructured films with thicknesses varying from a few hundreds of nanometers to a few micrometers.<sup>33</sup> One important limitation with these NiO electrodes relates to the fast primary charge recombination processes reported to occur on the picosecond timescale, being thus competitive with charge accumulation and catalysis.<sup>15,25,30,32</sup> These investigations rely, however, on ultrafast spectroscopic measurements made on dry sensitized films, which questions the relevance of these kinetic data to rationalize the low photoelectrochemical activity. Indeed, the groups of Papanikolas and Hammarström independently reported bias-dependent charge recombination kinetics for Ru tris-diimine-sensitized NiO electrodes.<sup>34,35</sup> Applying a cathodic potential to the film was shown to fill the intrabandgap states at the origin of the fast recombination processes, with a subsequent increase in the charge separation state lifetime from the ps to  $\mu$ s timescale.

In addition to these kinetic limitations, photocurrents rapidly decrease within a few hours of activity, raising important questions about the stability of previously reported molecular photocathodes.<sup>11–13,17–32</sup> Comprehensive studies providing a deep understanding of the deactivation pathways at work with the photocatalytic systems remain scarce; however, in the literature, techniques allowing one to provide mass-related molecular information about the species present on the surface of the film, such as ToF-SIMS, have in particular not been employed in that context, apart by the groups of Price and Gibson<sup>18</sup> and by our group.<sup>25,36</sup> Deciphering, thanks to a combination of advanced techniques, the structural and electronic factors limiting the activity and affecting the stability of these photocathodes is thus of paramount importance to develop dye-sensitized water splitting devices that are able to meet robustness and efficiency.

We previously reported a series of hydrogen-evolving NiO photocathodes featuring covalent dye–cobalt catalyst assemblies prepared by a modular click chemistry coupling strategy.<sup>19,20,37,38</sup> A standardized protocol was established to assess the photoelectrochemical performances under identical conditions, thus allowing a rational comparison of the activity of the different dyads. In these studies, we exploited in particular the well-known properties of push–pull organic dyes to achieve a unidirectional electron transfer cascade from the electrode to the catalytic center; their degradation under reductive conditions was however identified as a main issue for stability.<sup>38</sup> This was further supported by transient absorption spectroelectrochemistry (TA-SEC) measurements recorded on the sensitized films at the operando potential, which allowed one to detect the formation of the Co<sup>I</sup> catalytically active species, albeit in very low yield, thus leading to the accumulation and degradation of the reduced dye on the surface of the film.<sup>38</sup> Here, we report on the synthesis and

characterization of a novel dyad, **RuP<sub>4</sub>-Co**, featuring a ruthenium tris-diimine photosensitizer substituted by four methylphosphonate anchoring groups,<sup>39</sup> covalently linked to the cobalt diimine dioxime H<sub>2</sub>-evolving catalyst.<sup>40</sup> Compared to the previous systems relying on the same catalyst,<sup>19,20,22,37,38</sup> significant improvements in the photocurrent density (4- to 6-fold increase) and F.E. (7-fold increase) for hydrogen production were achieved with the corresponding NiO-based **RuP<sub>4</sub>-Co**-sensitized photocathode (Figure 1). Moreover, the

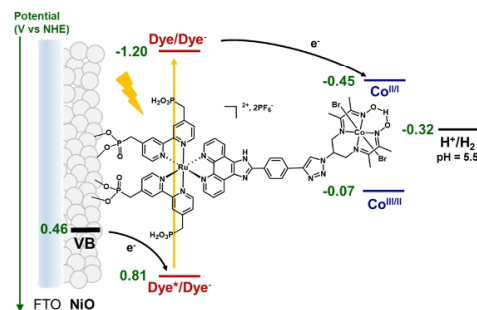


**Figure 1.** Energy diagram and working principle of the **RuP<sub>4</sub>-Co**-sensitized NiO photocathode at pH 5.5 (arbitrary representation of the phosphonate anchoring mode onto NiO). The NiO valence band edge potential was estimated from the 0.37 V vs NHE value previously reported at pH 7.<sup>41</sup>

main parameters affecting the performance of our system were identified thanks to a comprehensive analysis of the photoelectrochemical activity combined with TA-SEC measurements and quantum chemical simulations on the one hand and in-depth post-operando characterizations based on a combination of XPS, UV–vis, and mass spectrometry-related techniques on the other hand.

## RESULTS AND DISCUSSION

**Synthesis of RuP<sub>4</sub><sup>OEt</sup>-Co and Characterization in Solution.** **RuP<sub>4</sub><sup>OEt</sup>-Co** was synthesized by a copper-catalyzed azide-alkyne cycloaddition (CuAAC) coupling between the alkyne-substituted dye precursor **RuP<sub>4</sub><sup>OEt</sup>-EPIP**<sup>39</sup> and the azido-functionalized copper diimine dioxime complex,<sup>42</sup> followed by a transmetalation step from Cu to Co, according to our previously reported procedures.<sup>19,20</sup> Acid–base titrations revealed that the dye precursor and the dyad were isolated under their imidazole-protonated form (Figure S2). Full synthetic details and characterizations are provided in the Supporting Information.

The electronic and redox properties of **RuP<sub>4</sub><sup>OEt</sup>-Co** were first investigated in solution and were compared to the ones individually determined for the two components **RuP<sub>4</sub><sup>OEt</sup>-EPIP** and [Co(DO)(DOH)N<sub>3</sub>pNBr<sub>2</sub>]<sup>43</sup> (**CoN<sub>3</sub>**). Its UV–vis absorption spectrum recorded in acetonitrile (Figure S3) is characteristic for a ruthenium tris-diimine complex, with a broad absorption band centered at 460 nm and attributed to the metal-to-ligand charge transfer (<sup>1</sup>MLCT) transition. Quantum chemical simulations on the structurally closely related **RuP<sub>4</sub><sup>OMe</sup>-Co** assign three <sup>1</sup>MLCT transitions to this absorption feature, *i.e.*, into the S<sub>6</sub>, S<sub>8</sub>, and S<sub>10</sub> states, with mixed contributions from ruthenium to the bipyridine ligands as well as to the phenanthroline-based ligand (see Quantum Chemical Simulations). In the UV region, intense ligand-



**Table 1.** Redox Properties<sup>a</sup> of Co-N<sub>3</sub>, RuP<sub>4</sub><sup>OEt</sup>-EPIP, and RuP<sub>4</sub><sup>OEt</sup>-Co Recorded in Acetonitrile

	$E_{\text{ox}}^b$ Ru <sup>III</sup> /Ru <sup>II</sup>	$E_{\text{red}_1}^c$ Co <sup>III/II</sup>	$E_{\text{red}_2}^b$ Co <sup>II/I</sup>	$E_{\text{red}_3}^b$ Ru <sup>II</sup> /Ru <sup>II-L</sup> -	$\Delta G_{\text{inj}}^d$	$\Delta G_1^e$	$\Delta G_2^f$
Co-N <sub>3</sub>		-0.60 (-0.07)	-1.01 (-0.48)				
RuP <sub>4</sub> <sup>OEt</sup> -EPIP	+0.92 (+1.45)			-1.71 (-1.18)	-0.36		
RuP <sub>4</sub> <sup>OEt</sup> -Co	+0.89 (+1.42)	-0.60 (-0.07)	-0.98 (-0.45)	-1.73 (-1.20)	-0.34	-1.13	-0.75

<sup>a</sup>In V vs Fc<sup>+0</sup> and in V vs NHE (values in brackets). Redox potentials converted from Fc<sup>+0</sup> to NHE, considering  $E^\circ(\text{Fc}^{+0}) = +0.53$  V vs NHE in acetonitrile. <sup>b</sup> $1/2(E_{\text{pc}} + E_{\text{pa}})$ . <sup>c</sup> $E_{\text{pc}}$ . <sup>d</sup>In eV. Gibbs free energy for hole injection  $\Delta G_{\text{inj}} = e[E_{\text{VB}}(\text{NiO}) - E(\text{PS}^*/\text{PS}^-)]$ ; with  $E_{\text{VB}}(\text{NiO}) = +0.46$  V vs NHE at pH 5.5<sup>20</sup> and  $E(\text{PS}^*/\text{PS}^-) = E(\text{PS}/\text{PS}^-) + E_{00}$  (see Table S1 for  $E_{00}$  values). <sup>e</sup>In eV. Gibbs free energy for electron transfer from the reduced dye to the Co<sup>III</sup> catalyst  $\Delta G_1 = e[E(\text{Ru}^{\text{II}}/\text{Ru}^{\text{II-L}}-) - E(\text{Co}^{\text{III}}/\text{Co}^{\text{II}})]$ . <sup>f</sup>In eV. Gibbs free energy for electron transfer from the reduced dye to the Co<sup>I</sup> catalyst  $\Delta G_2 = e[E(\text{Ru}^{\text{II}}/\text{Ru}^{\text{II-L}}-) - E(\text{Co}^{\text{II}}/\text{Co}^{\text{I}})]$ .

**Table 2.** Figures of Merit Determined from the 2 h Chronoamperometric Measurements (Full Set of Experimental Data in Table S4)

irradiation	photocathode	$n(\text{H}_2)^a$ (nmol·cm <sup>-2</sup> )	charge <sup>b</sup> (mC·cm <sup>-2</sup> )	F.E. <sup>c</sup> (%)	TON <sub>Co</sub> <sup>d</sup>
400–800 nm	NiO	1 ± 1	3 ± 1	5 ± 2	
	NiO/Ru-EPIP	4 ± 1	9 ± 1	9 ± 1	
	NiO/RuCo	28 ± 2	24 ± 6	24 ± 5	5 ± 1
simulated AM 1.5G	NiO	5 ± 0	8 ± 1	13 ± 1	
	NiO/Ru-EPIP	10 ± 4	10 ± 4	22 ± 2	
	NiO/RuCo	60 ± 9	45 ± 6	26 ± 7	13 ± 2

<sup>a</sup>Total amount of H<sub>2</sub> produced, quantified in solution and in the headspace (detailed values in Table S4), divided by the geometric surface area (measured for each single film). <sup>b</sup>Charge passed during the course of the 2 h chronoamperometric measurement divided by the geometric surface area (measured for each single film). <sup>c</sup>Faradaic efficiency for hydrogen production. <sup>d</sup>Turnover number (calculated with the dyad loading determined for each single film).

centered  $\pi$ - $\pi^*$  absorption bands are observed between 270 and 350 nm, together with a small contribution from the cobalt center at 300 nm, by comparison with the spectrum recorded for CoN<sub>3</sub>. The redox properties are summarized in Table 1, and the cyclic voltammograms are displayed in Figure S4. On the anodic scan, RuP<sub>4</sub><sup>OEt</sup>-Co exhibits a reversible Ru<sup>III</sup>/Ru<sup>II</sup> process at +0.89 V vs Fc<sup>+0</sup>, which is not significantly affected by the coupling. On the cathodic scan, five reduction processes take place between -0.60 and -2.45 V vs Fc<sup>+0</sup>, corresponding to the two successive reductions of the cobalt center, Co<sup>III</sup>/Co<sup>II</sup> ( $E_{\text{pc}} = -0.60$  V vs Fc<sup>+0</sup>) and Co<sup>I</sup>/Co<sup>0</sup> ( $E_{1/2} = -0.98$  V vs Fc<sup>+0</sup>), and then the reduction of the three diimine ligands in the Ru<sup>II</sup> coordination sphere. Overall, the electronic and redox properties of RuP<sub>4</sub><sup>OEt</sup>-Co can be simply described as the superimposition of those of its individual RuP<sub>4</sub><sup>OEt</sup> and Co components, thus underlining the fact that the dye and the catalyst moieties are electronically decoupled in the ground state. Similar observations were previously made for ruthenium-copper<sup>42</sup> and the push-pull organic dye-based T1-Co dyad,<sup>20</sup> and they are frequently reported in the literature for triazole-based assemblies.<sup>44–46</sup>

Furthermore, the dye and dyad excited-state dynamics were investigated by nanosecond (ns) time-resolved absorption and emission spectroscopies on the as-synthesized complexes as well as on their neutral imidazole form (generated in situ by the addition of 1 equiv of triethylamine). Emission lifetimes of 170 and 160 ns were determined for RuP<sub>4</sub><sup>OEt</sup>-EPIP and RuP<sub>4</sub><sup>OEt</sup>-Co, respectively (Table S1 and Figure S5). In addition, upon excitation at 410 nm, very similar transient absorption spectra were recorded for both complexes, irrespective of the protonation state of the imidazole ring (Figures S6 and S7): a ground-state bleach is observed at 460 nm, together with broad and structureless absorption above 500 nm, assigned to the absorption of the <sup>3</sup>MLCT excited state. The latter decays concomitantly with the ground-state recovery over a few hundreds of nanoseconds, supporting the absence of any additional process, *i.e.*, no intramolecular

electron transfer process from the ruthenium excited state to the Co<sup>III</sup> center occurs in RuP<sub>4</sub><sup>OEt</sup>-Co, as previously reported for T1-Co.<sup>47</sup>

**NiO Film Sensitization and Dyad Loading Quantification.** Homemade F108-templated NiO films<sup>20</sup> were soaked for 24 h in a methanolic solution of the RuP<sub>4</sub>-Co dyad (or the RuP<sub>4</sub>-EPIP dye) after deprotection of the phosphonate anchoring groups (see the Supporting Information for experimental details). The amount of dyad loaded on the film was determined by UV-vis absorption spectroscopy after desorption of the freshly sensitized NiO film in a 1 M phenylphosphonic acid methanolic solution<sup>17,48</sup> using the molar extinction coefficient of the MLCT band at 460 nm (Figure S8). An average dyad loading of  $5.2 \pm 0.8$  nmol·cm<sup>-2</sup> was obtained (12 independent samples; Table S2), which is slightly lower than the ones we previously reported for related ruthenium tetrakisphosphonate dyes<sup>36</sup> but is in agreement with the lower thickness of the spin-coated films employed here (700 nm to 1  $\mu\text{m}$ , Figure S9). The dyad loading was systematically quantified on one half of a freshly sensitized NiO film, with the other half being employed for the photoelectrochemical experiments. Hence, the amount of dyad grafted on the electrode was precisely known for each sample and was used to calculate the TONs for hydrogen production activity (see below).

**Photoelectrochemical Performances of RuP<sub>4</sub>-Co-Sensitized NiO Photocathodes.** Photoelectrochemical measurements were conducted in aqueous conditions at pH 5.5 (0.1 M 2-(*N*-morpholino)ethanesulfonic acid (MES)/0.1 M NaCl buffer)<sup>19,20</sup> using a RuP<sub>4</sub>-Co-sensitized NiO film as a working electrode in a three-electrode setup. We previously showed that the activity of the cobalt diimine dioxime catalyst is optimal at mildly acidic pH values,<sup>49</sup> and no H<sub>2</sub> evolution could be detected at pH 7 for this catalyst anchored onto multiwalled carbon nanotubes.<sup>43</sup> Linear sweep voltammograms recorded under dark, light, and chopped light irradiation (filtered xenon lamp, 400–800 nm, 65 mW·cm<sup>-2</sup> equivalent to

1 sun) revealed the generation of cathodic photocurrents, steadily increasing from +0.9 V to 0 V *vs* RHE (Figure S10 and Table S3). To correlate them to some photoelectrocatalytic hydrogen production activity, 2 h chronoamperometric measurements (Figure S11) were performed under continuous light irradiation at an applied potential of +0.14 V *vs* RHE (−0.4 V *vs* Ag/AgCl); at the end of the experiment, the amount of hydrogen was quantified both in the headspace and in solution, according to our previously reported procedure.<sup>19</sup> Under these conditions,  $28 \pm 2 \text{ nmol}\cdot\text{cm}^{-2}$  ( $5 \pm 1 \text{ TONs}$ ) hydrogen was produced with  $24 \pm 5\%$  faradaic efficiency (F.E.) for the NiO/RuCo photocathode (Table 2).

Replacing the 400 nm cut-off filter by an AM 1.5G one, which better simulates solar irradiation, proved to be highly beneficial for the photoelectrochemical performances of RuP<sub>4</sub>-Co. A significant increase in the photocurrent density is observed (Figure 2, top), reaching up to  $97 \mu\text{A}\cdot\text{cm}^{-2}$  (Table

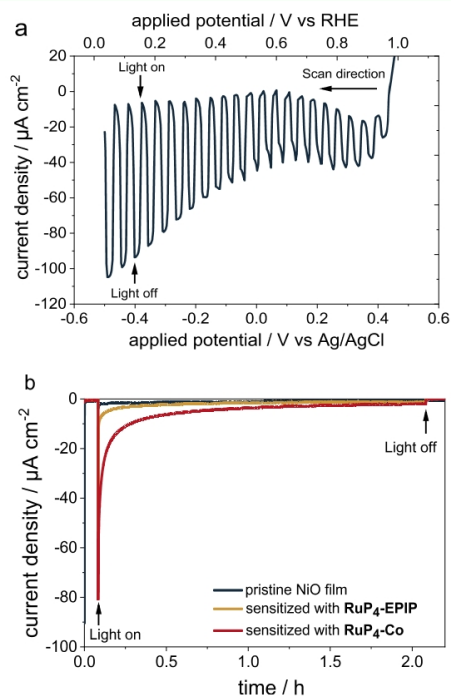


**Figure 2.** (a) Linear sweep voltammogram recorded on a RuP<sub>4</sub>-Co-sensitized NiO electrode under chopped light irradiation (simulated AM 1.5G, IR-filtered) in 0.1 M MES/0.1 M NaCl supporting electrolyte at pH 5.5. (b) Photocurrent densities recorded during the course of a 2 h chronoamperometric measurement under continuous light irradiation (simulated AM 1.5G, IR-filtered) at an applied potential of +0.14 V *vs* RHE.

S3). This is due to a beneficial contribution from the absorption in the UV part of the spectrum, as previously reported for homogeneous photocatalytic hydrogen production based on ruthenium tris-diimine photosensitizers.<sup>50,51</sup> Hence,  $60 \pm 9 \text{ nmol}\cdot\text{cm}^{-2}$  hydrogen ( $26 \pm 7\%$  F.E.) was produced during the course of a 2 h chronoamperometric measurement under these optimized irradiation conditions (Figure 2 and Figure S12), corresponding to  $13 \pm 2 \text{ TONs}$  (Table 2).

Regardless of the irradiation setup, control experiments using either nonsensitized NiO films or RuP<sub>4</sub>-EPIP-sensitized ones display significantly lower photocurrents compared to the RuP<sub>4</sub>-Co photocathode (Figure 2, bottom, and Figures S11 and S12). Moreover, in the absence of the Co catalyst on the surface of the film, the amount of hydrogen produced by the dye-sensitized photocathode is 6 to 7 times lower for similar dye loadings (Tables 2 and S4). These results clearly support a cobalt-based mechanism for the observed H<sub>2</sub>-evolving activity.

The performances of the RuP<sub>4</sub>-Co photocathode proved to be superior to the ones we previously reported for the T1-Co photocathode based on an organic push-pull dye, which displayed a TON of less than 5 and a 10% F.E. for hydrogen production, under identical conditions.<sup>19,20,38</sup> To further investigate the role played by the light-harvesting unit and its electronic nature, UV-vis-monitored photolysis experiments were performed on RuP<sub>4</sub><sup>OEt</sup>-Co and T1<sup>OEt</sup>-Co at  $4.5 \times 10^{-5} \text{ M}$  in a ACN/TEOA (90:10) solution (Figure S13).<sup>52</sup> Upon visible light irradiation, the characteristic two-band spectrum of the Co<sup>I</sup> species<sup>53</sup> builds up between 500 and 800 nm, albeit with a final absorption 2 to 3 times higher for RuP<sub>4</sub><sup>OEt</sup>-Co (reached after 30 min) compared to T1<sup>OEt</sup>-Co (reached after 60 min of irradiation). These observations thus suggest that the photoinduced generation of the Co<sup>I</sup> state, an entry point to the cobalt-centered H<sub>2</sub>-evolving catalytic cycle,<sup>40</sup> might be more efficient with RuP<sub>4</sub><sup>OEt</sup>-Co than with T1<sup>OEt</sup>-Co. Yet, the TON achieved by the cobalt diimine dioxime catalyst under the photoelectrochemical conditions reported here is very low compared to the TON of 300 previously obtained under homogeneous photocatalytic conditions<sup>54</sup> or the TON of 7000 achieved by the Co(DO)(DOH)pn-based electrocatalytic nanomaterial under close aqueous conditions.<sup>43</sup>

With TONs being affected by both the kinetics and stability over time of the system, we re-examined the LSV measurements to extract initial turnover frequency (TOF) values of activity. From the photocurrent densities at +0.14 V *vs* RHE under visible light irradiation (Table 3), a TOF of  $0.11 \text{ nmol}_{\text{e}^-}\cdot\text{nmol}_{\text{RuCo}}^{-1}\cdot\text{s}^{-1}$  was determined for the RuP<sub>4</sub>-Co-sensitized film (*i.e.*, each grafted RuP<sub>4</sub>-Co dyad efficiently relays one electron every 9 s), which is five times higher than for the T1-Co-sensitized film ( $0.02 \text{ nmol}_{\text{e}^-}\cdot\text{nmol}_{\text{T1Co}}^{-1}\cdot\text{s}^{-1}$ ). Including UV irradiation provides a track for improvement by increasing the Ru dye light absorption efficiency via its upper excited-state levels. This results in a slightly increased TOF, reaching  $0.18 \text{ nmol}_{\text{e}^-}\cdot\text{nmol}_{\text{RuCo}}^{-1}\cdot\text{s}^{-1}$  (Table 3), and in turn, a more than doubled TON (TON<sub>Co</sub>: 13 *vs* 5; see Table 2) over 2 h irradiation when simulated AM 1.5G irradiation conditions are employed compared to visible light irradiation. We could thus increase the initial TOF by varying either the nature of the light-harvesting unit or the irradiation conditions (all other conditions being strictly equal). This demonstrates that at the beginning of the 2 h chronoamperometric measurement, the cobalt-centered catalytic activity is not the limiting parameter of the system. This is further supported by the TOF value of  $1.3 \text{ s}^{-1}$  (equal to  $2.6 \text{ nmol}_{\text{e}^-}\cdot\text{nmol}_{\text{Co}}^{-1}\cdot\text{s}^{-1}$ ) determined from the specific rate of H<sub>2</sub> evolution previously measured for Co anchored onto multiwalled carbon nanotubes (MWCNTs).<sup>43</sup>

Conclusively, these observations strongly suggest that the RuP<sub>4</sub>-Co photocathode suffers from (i) kinetic issues, *i.e.*, the catalytic center is not correctly supplied with electrons to achieve fast catalysis, and (ii) stability issues, which are further supported by the very fast photocurrent decrease observed during the course of the chronoamperometric measurements



**Table 3.** Kinetic Data at +0.14 V vs RHE from the LSV Measurements (See the Full Set of Experimental Data in Table S3) and Comparison with the Activity of the Previously Reported MWCNT-Based Cathode Material Functionalized with Co

irradiation	(photo)cathode	photocurrent density ( $j$ ; $\mu\text{A}\cdot\text{cm}^{-2}$ ) <sup>a</sup>	TOF (electrons) ( $\text{nmol}_{\text{e-}}\cdot\text{nmol}_{\text{dye}}^{-1}\cdot\text{s}^{-1}$ ) <sup>b</sup>	TOF ( $\text{H}_2$ ) ( $\text{TON}\cdot\text{s}^{-1}$ )
400–800 nm	NiO/TiCo <sup>c</sup>	15 <sup>c</sup>	0.02	0.01 <sup>d</sup>
	NiO/RuP <sub>4</sub> -Co	58 ± 11	0.11 ± 0.03	0.055 <sup>d</sup>
simulated AM 1.5G	NiO/RuP <sub>4</sub> -Co	84 ± 7	0.18 ± 0.03	0.09 <sup>d</sup>
	MWCNT/Co <sup>e</sup>			1.3 <sup>f</sup>

<sup>a</sup>Dark current subtracted. <sup>b</sup>Converted from  $j$  using  $\text{TOF} = j/n\cdot F\cdot\Gamma$ , with  $j$  in  $\text{A}\cdot\text{cm}^{-2}$  ( $1\text{ A} = 1\text{ C}\cdot\text{s}^{-1}$ ),  $\Gamma$  in  $\text{mol}\cdot\text{cm}^{-2}$ ,  $n = 1$  electron transferred, and  $F = 96,485\text{ C}\cdot\text{mol}^{-1}$ . <sup>c</sup>Data taken from our previous study.<sup>20</sup> <sup>d</sup>Expected TOF( $\text{H}_2$ ) if  $\text{H}_2$  is produced with an F.E. of 100%. <sup>e</sup>Data taken from our previous study.<sup>43</sup> <sup>f</sup>Obtained by dividing the specific rate of  $\text{H}_2$  evolution at  $-0.6\text{ V}$  vs RHE ( $6\text{ nmol}_{\text{H}_2}\cdot\text{s}^{-1}\cdot\text{cm}^{-2}$ ) by the catalyst loading ( $4.5\text{ nmol}\cdot\text{cm}^{-2}$ ).

(>90% loss within the first hour of activity, Figure 2). These two points are addressed below in-depth, thanks to time-resolved spectroscopic studies on the sensitized films, quantum chemical simulations and post-operando characterization.

**Investigation of the Ultrafast Electron Transfer Processes.** The kinetics of the light-induced processes occurring at the dye-sensitized photocathode interface were investigated by transient absorption spectroelectrochemistry (TA-SEC). The TA spectra were recorded in a home-built spectroelectrochemical cell (see details in the Supporting Information) at different cathodic potentials applied to the film to determine the influence of the applied potential on the hole injection and charge recombination dynamics. Previous studies by the groups of Papanikolas<sup>34</sup> and Hammarström<sup>35</sup> indeed highlighted the pronounced dependence of the charge-separated state lifetime on the potential applied to NiO films sensitized by model Ru dyes, while our own preliminary work focused on the effect of potential on the excited-state reactivity in organic dye-catalyst dyads.<sup>38,47</sup> Measurements were carried out in a dry acetonitrile electrolyte to get rid of any catalytic turnover in order to accumulate and detect the  $\text{Co}^{\text{I}}$  species. The TA spectra were recorded at the open-circuit potential (OCP) and at  $-0.74\text{ V}$  vs  $\text{Fc}^{+/0}$ , which corresponds to the operando potential in the photoelectrochemical activity tests ( $-0.4\text{ V}$  vs  $\text{Ag}/\text{AgCl}$ ); a previous study showed that this potential is sufficient to generate the  $\text{Co}^{\text{II}}$  state of the cobalt catalyst on the surface of the film.<sup>23</sup> In addition, control experiments were also carried out (i) at  $-1.15\text{ V}$  vs  $\text{Fc}^{+/0}$ , where the cobalt catalyst is already in its  $\text{Co}^{\text{I}}$  state and, as a consequence, electron transfer is no longer thermodynamically possible, and (ii) on films sensitized with RuP<sub>4</sub>-EPIP instead of RuP<sub>4</sub>-Co at all of the aforementioned potentials.

The TA spectra of NiO films sensitized with RuP<sub>4</sub>-EPIP and RuP<sub>4</sub>-Co show the same general features: At early times, a spectrum with ground-state bleach (GSB) at 480 nm and excited-state absorption (ESA) around 590 nm is observed, corresponding to the MLCT state (Figure 3 and Figures S14–S17). At OCP, this spectrum decays almost completely within the time window of the experiment (7 ns), except for a weak positive band centered at 520 nm. At negative applied potentials, however, this minor feature develops into a broad and long-lived signal (between 540 and 480 nm), completely overwriting the GSB. The band at 540 nm is characteristic for the one-electron reduced Ru dye (dashed-dotted lines in Figure 3 and Figure S18). The band at 480 nm is tentatively assigned to oxidized Ni centers produced by hole injection (HI),<sup>55,56</sup> leading to the assignment of this spectrum to the primary charge-separated state produced by HI from the excited dye into the NiO film ( $\text{NiO}^{\text{I}}\text{Ru}^{\text{I}}$ ). A tri-exponential fit of the experimental data yields the time constants for HI

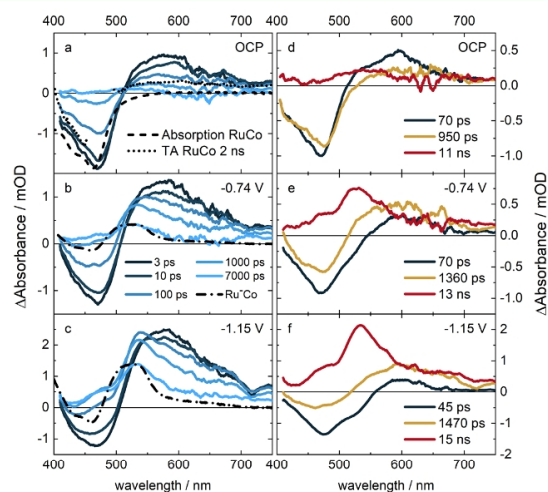


**Figure 3.** TA-SEC spectra (a–c) and decay-associated spectra (d–f) obtained with a three-component exponential fit of RuP<sub>4</sub>-Co-sensitized NiO films at early delays up to 7 ns at (a, d) OCP, (b, e)  $-0.74\text{ V}$ , and (c, f)  $-1.15\text{ V}$  vs  $\text{Fc}^{+/0}$  applied potential. For clarity, the spectra were integrated over  $\pm 10\%$  of the given times and smoothed by a 10-point adjacent averaging. The raw data without smoothing are depicted in Figure S21. The inverted absorption spectrum of RuP<sub>4</sub><sup>ox</sup>-Co in ACN (dashed line), the TA spectrum of RuP<sub>4</sub><sup>ox</sup>-Co in ACN at 2 ns time delay (dotted line), and the scaled differential absorption spectrum upon one-electron reduction of the Ru complex in RuP<sub>4</sub><sup>ox</sup>-Co (dashed-dotted line) are given for comparison.

ranging from 67 ps (at OCP) to 31 ps (at  $-1.15\text{ V}$  vs  $\text{Fc}^{+/0}$ ) for RuP<sub>4</sub>-EPIP and from 67 ps (at OCP) to 45 ps (at  $-1.15\text{ V}$  vs  $\text{Fc}^{+/0}$ ) for RuP<sub>4</sub>-Co (Table S5), *i.e.*, becoming faster and more pronounced at more negative potentials applied (Figure 3d–f). In addition, the initial GSB signal at 480 nm becomes weaker, while the initial reduced dye absorption signal at 540 nm is increased (Figure S19); this suggests that an additional ultrafast (<2 ps) HI process occurs when a cathodic potential is applied to the film. HI is ultimately followed by charge recombination (CR), which is also strongly affected by the applied potential: at OCP, CR is characterized by a time constant of tens of picoseconds, while at cathodic potentials, the charge-separated state lives for more than 7 ns, as previously observed for a ruthenium dye-sensitized NiO photocathode.<sup>34</sup>

In parallel to HI, there is a process with a characteristic time constant of about 1 ns, *i.e.*,  $\tau_2 = 950\text{--}1470\text{ ps}$ , which shows the spectral signature of a MLCT decay to the ground state

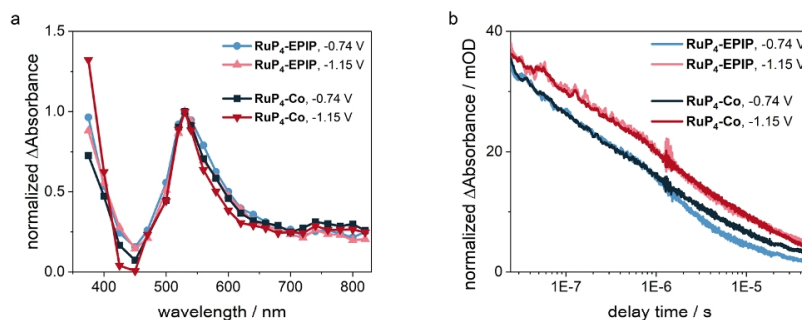


**Figure 4.** (a) TA spectra of RuP<sub>4</sub>-EPIP- and RuP<sub>4</sub>-Co-sensitized NiO films at  $-0.74$  V and  $-1.15$  V vs Fc<sup>+/0</sup> applied potential at 100 ns time delay, normalized to the signal at 530 nm. (b) Kinetic traces at 530 nm of the same data, averaged from 520 to 540 nm and normalized at 30 ns to the signal of RuP<sub>4</sub>-Co at the respective potential.

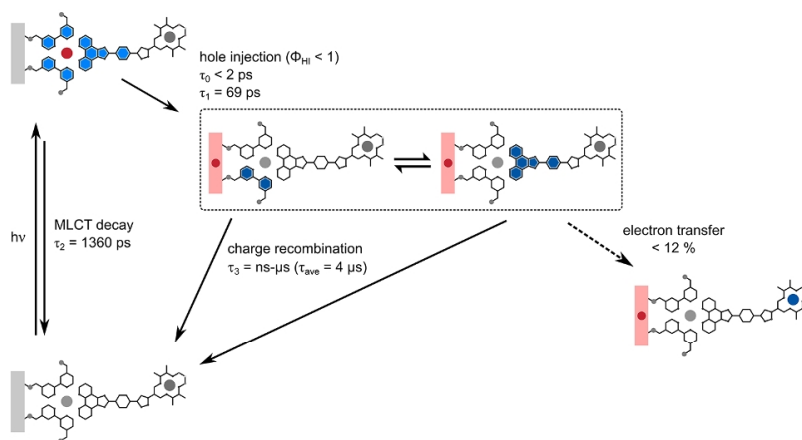


**Figure 5.** Jablonski diagram summarizing the light-induced processes occurring for RuP<sub>4</sub>-Co-sensitized NiO films at  $-0.74$  V vs Fc<sup>+/0</sup> (equivalent to  $-0.4$  V vs Ag/AgCl used in the photoelectrochemical experiments). Electron density is depicted in blue, while holes are depicted in red. Dashed arrows indicate the processes that have not been detected.

(concerted loss of GSB and ESA). This decay reflects a direct deactivation of excited molecules, which do not undergo HI. This process might be associated with self-quenching of tightly packed dyads on the NiO surface.<sup>57</sup> Alternatively, a combination of rate-limiting HI and rapid CR can account for the same spectral features. The lower amplitude and slower rate for this component at more negative applied potentials support this assignment: HI is faster, decreasing the amount of long-lived <sup>3</sup>MLCT states, and CR is slowed down by the lower concentration of holes on the NiO surface.

Most importantly, in the time window up to 7 ns, the TA spectra of RuP<sub>4</sub>-Co do not show any spectral indication of charge transfer to the cobalt catalyst unit. Such a charge transfer would be observable as an increasing absorption band between 550 and 750 nm produced by the Co<sup>I</sup> state (Figure S18), which is not present in the fs-TA-SEC spectra recorded for RuP<sub>4</sub>-Co at  $-0.74$  V vs Fc<sup>+/0</sup>. Since thermal electron transfer in triazole-bridged dyads has been shown to occur on the ns- $\mu\text{s}$  timescale,<sup>58–62</sup> especially for a related H<sub>2</sub>-evolving photocathode sensitized with a push-pull organic dye-cobalt catalyst covalent assembly,<sup>38</sup> we performed TA experiments under identical conditions in the ns- $\mu\text{s}$  timescale. The data recorded in this time range are spectrally identical to the last

spectra recorded in the fs-TA-SEC experiment and decay without any spectral changes, with 15% of the initial signal still left after 45  $\mu\text{s}$  (Figure 4 and Figures S20 and S21). The decay occurs in a non-exponential fashion as typical for charge recombination reactions in molecularly functionalized NiO photoelectrodes.<sup>34–36,63,64</sup> Quantitative kinetic analysis of the ns-TA data using a three-component exponential fit yields similar lifetimes at  $-0.74$  V and at  $-1.15$  V vs Fc<sup>+/0</sup> ( $\tau_{3,1} \approx 90$  ns,  $\tau_{3,2} \approx 1.4$   $\mu\text{s}$ , and  $\tau_{3,3} \approx 14$   $\mu\text{s}$  with an average lifetime of  $\tau_{\text{ave}} = 4$   $\mu\text{s}$  for RuP<sub>4</sub>-Co at  $-0.74$  V vs Fc<sup>+/0</sup>, Figures S20 and S21 and Table S5).

Applying a cathodic potential to the film thus leads to an increase of up to 5 orders of magnitude of the lifetime of the charge-separated state (up to 14  $\mu\text{s}$ ) compared to the situation without applied potential (OCP, a few hundreds of picoseconds). However, in spite of this long-lived charge-separated state, no direct evidence for electron transfer to the cobalt catalyst<sup>38</sup> could be observed on the ns to  $\mu\text{s}$  time window: indeed, within the experimental signal-to-noise ratio, the expected spectral signature of the Co<sup>I</sup> state between 550 and 750 nm was not detected on the TA spectra of RuP<sub>4</sub>-Co-sensitized NiO films at  $-0.74$  V vs Fc<sup>+/0</sup> (Figure 4), and the decay kinetics of the reduced Ru moiety were not accelerated

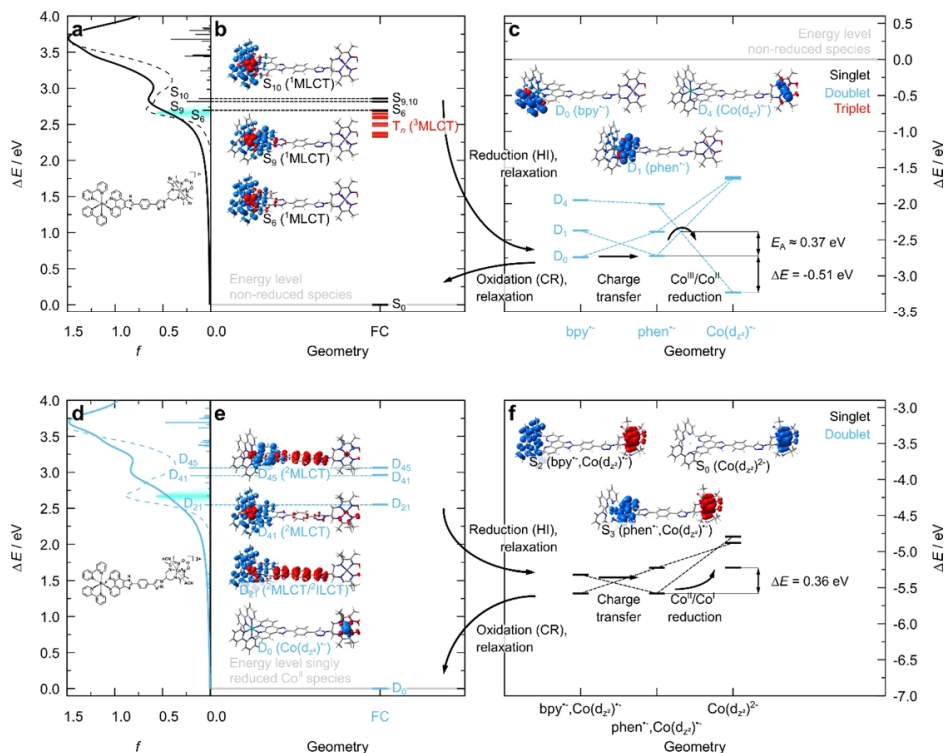


**Figure 6.** (a) Singlet UV-vis absorption spectrum of **Ru-Co** (experimental data: dashed line; simulated data: solid line) and (b) energy levels of prominent singlet and triplet excitations in the Franck-Condon geometry (FC, singlet ground-state equilibrium). (c) Singly reduced states with excess charge localized on one bpy ligand ( $\text{bpy}^-$ ), on the phen ligand ( $\text{phen}^-$ ), and at the catalytic center, leading to the partially charged  $\text{Co}^{\text{II}}$  species with a semi-occupied  $d_z^2(\text{Co})$  orbital. All states are shown in their respective equilibrium structures. (d) Spin-allowed doublet excitations contributing to the UV-vis absorption spectrum of **Ru-Co(ACN)<sub>2</sub>** (both Br-dissociated and two ACN-coordinated; simulated data: solid line). (e) Energy levels of prominent doublet excitations in the Franck-Condon geometry (doublet ground-state equilibrium of  $\text{Co}^{\text{II}}$  species shown in (c)). (f) Doubly reduced states with one excess charge localized at Co, *i.e.*,  $\text{Co}^{\text{I}}$  species, and the other excess charge on one bpy ligand ( $\text{bpy}^-$ ), on the phen ligand ( $\text{phen}^-$ ), and at the catalytic center, leading to the fully charged  $\text{Co}^{\text{I}}$  species with a doubly occupied  $d_z^2(\text{Co})$  orbital. All states are shown in their respective equilibrium structures. Quantum chemical results were obtained at the (time-dependent) density functional level of theory (B3LYP/def2-svp) including D3BJ dispersion correction and solvent effects (ACN) by a polarizable continuum model. The electronic nature of prominent transitions is shown by charge density differences, and charge localization in the respective electronic ground state of open-shell species is illustrated by the spin density. The highest-occupied molecular orbital of Co is shown in panel (f). Singlet, doublet, and triplet states are shown in black, blue, and red, respectively.

in comparison to **RuP<sub>4</sub>-EPIP**-sensitized films (Figure 4). Based on the ratio of the extinction coefficients of the reduced dye and of the  $\text{Co}^{\text{I}}$  state from the UV-vis SEC experiment (Figure S18), the growth of a signal with a 9.0 mOD intensity is expected if  $\text{Co}^{\text{I}}$  is formed with 100% yield from the primary charge-separated state already formed at the beginning of the ns-TA-SEC experiment. Considering the experimental noise of 0.5 mOD, the limit of detection at a signal-to-noise ratio of 2:1 is estimated to be 1 mOD, corresponding to a yield of formation of the  $\text{Co}^{\text{I}}$  species of 12%. The absence of any spectral evidence supporting the formation of  $\text{Co}^{\text{I}}$  thus clearly indicates that the electron transfer efficiency from the reduced dye to the catalytic center lies below this detection limit. In consequence, the TOF for hydrogen production is rather low as the active  $\text{Co}^{\text{I}}$  species is not formed efficiently. The light-induced processes occurring for the **RuCo**-sensitized film at the operando potential are summarized in Figure 5.

**Quantum Chemical Simulations.** To further investigate the photoinduced electron transfer processes at a molecular

level, we performed a series of quantum chemical simulations at the density functional (DFT) and time-dependent DFT level of theory for **Ru-Co** as well as for **RuP<sub>4</sub><sup>OMe</sup>-Co**. These simulations aim to elucidate the excited states populated upon photoexcitation, the subsequent reduction of the excited intermediate (*i.e.*, hole injection upon NiO immobilization of **RuP<sub>4</sub>-Co**), the sequential intramolecular electron transfer steps, and finally, the catalytic active species. Although the singly reduced  $\text{Co}^{\text{II}}$  is already obtained at the applied operando potential, the performed (TD)DFT simulations involve a potential light-driven  $\text{Co}^{\text{III}}/\text{Co}^{\text{II}}$  reduction as well as the second  $\text{Co}^{\text{II}}/\text{Co}^{\text{I}}$  reduction, investigated in-depth by the TA-SEC experiments.

Initially, the nature of the electronic transitions underlying the absorption spectrum of **Ru-Co** as well as of **RuP<sub>4</sub><sup>OMe</sup>-Co** was assessed using TDDFT, while the structural and electronic properties of **RuP<sub>4</sub><sup>OMe</sup>-Co** were obtained for the computationally less demanding **RuP<sub>4</sub><sup>OMe</sup>-Co** complex. Both complexes feature a broad absorption band between 500 and 400 nm,



which stems mainly from the excitation into three <sup>1</sup>MLCT states: Both lower energy MLCT transitions, predicted at roughly 460 nm (2.7 eV; **RuP<sub>4</sub><sup>OEt</sup>-Co**: S<sub>7</sub>; **Ru-Co**: S<sub>6</sub>) and 445 nm (2.8 eV; **RuP<sub>4</sub><sup>OEt</sup>-Co**; **Ru-Co**: S<sub>9</sub>), are of mixed electronic character and feature excitations from the Ru atom to the bpy as well as to the phen ligand spheres. In contrast, the higher energy transition at ca. 435 nm (2.85 eV; **RuP<sub>4</sub><sup>OEt</sup>-Co** and **Ru-Co**: S<sub>10</sub>) is of pure MLCT<sub>bpy</sub> nature; for details, see Figure 6a and Figure S22 as well as Tables S6 and S7 in the Supporting Information. The following computational analysis will be focused exclusively on **Ru-Co**. As highlighted above, the singly reduced **Ru-Co** species (*i.e.*, Co<sup>II</sup>) is already obtained at the applied operando potential. However, such species may be obtained as well in a light-driven fashion, which will be evaluated in the following based on computational modeling. Therefore, 480 nm excitation into the MLCT band of the nonreduced **Ru-Co**, into the S<sub>6</sub>, S<sub>9</sub>, and S<sub>10</sub> <sup>1</sup>MLCT states, may lead subsequently to an ultrafast intersystem crossing and the population of various close-lying <sup>3</sup>MLCT states (see Figure 6a and Tables S6 and S7). Consequently, electrochemical reduction may yield the singly reduced doublet Ru<sup>II</sup> species of **Ru-Co**, while the accessory charge is either localized on one bpy ligand or on the phen moiety, *i.e.*, in the lowest π<sub>bpy</sub><sup>\*</sup> or π<sub>phen</sub><sup>\*</sup> molecular orbital, respectively. Energetically, bpy-based reduction, as illustrated by the spin densities of D<sub>0</sub> (bpy reduction) in Figure 6c, is slightly more favorable with respect to the reduction of the phen moiety (see the spin density of D<sub>1</sub>). However, thermally induced distortions, *i.e.*, elongation of the Co–Br bond lengths, may stabilize the initially unfavorable Co-centered reduction (D<sub>4</sub> in Figure 6c, Co<sup>II</sup>), leading to the semicharged catalytic center. DFT predicts a driving force (ΔE) of –0.51 eV for this intramolecular electron transfer, while an activation energy (E<sub>A</sub>) of approximately 0.37 eV was predicted along a linear-interpolated internal coordinate connecting the equilibrium geometries of the phen-based and Co-based reductions using pysisyphus,<sup>65</sup> an efficient external optimizer written in Python, which is also aware of excited states. In line with previous computational studies, in which dissociation of the halide ligands becomes favorable upon reduction,<sup>66,67</sup> we observe a considerable elongation of the Co–Br bonds from 2.418 and 2.421 Å (phen-based reduction state) to 2.539 and 2.572 Å (Co-based reduction state; Table S8). Therefore, three different Co<sup>II</sup> structures were used in the quantum chemical simulations related to the photoinduced electron transfer, leading eventually to the catalytically active Co<sup>I</sup> species: the first one with two Br<sup>–</sup> ligands, the Co<sup>II</sup>-based catalyst structure proposed by Artero and co-workers,<sup>66</sup> with the two Br<sup>–</sup> ligands being dissociated and one ACN (solvent) molecule-coordinated ligand, and the Co<sup>II</sup> structure with two ACN-coordinated ligands as calculated by Hammes-Shiffer and co-workers.<sup>67</sup> In the following, only the computational results obtained for the Co<sup>II</sup> structure with two ACN molecules (**Ru-Co(ACN)<sub>2</sub>**) are described; results obtained for the Co<sup>II</sup> structure with one solvent molecule (**Ru-Co(ACN)**) as well as for the catalyst with two bromide ligands (**Ru-Co**) are discussed in the Supporting Information. Excitation of this singly reduced <sup>2</sup>[**Ru-Co(ACN)<sub>2</sub>**], as shown in Figure 6d, yields very similar mixed <sup>2</sup>MLCT<sub>bpy</sub> and <sup>2</sup>MLCT<sub>phen</sub> transitions (see D<sub>21</sub>, D<sub>41</sub>, and D<sub>45</sub> in Figure 6d as well as D<sub>36</sub> and D<sub>38</sub> in Tables S6 and S7) in the visible region, which was to be expected as the initial electronic configuration of the Ru<sup>II</sup> photosensitizer is recovered. However, a partial contribution of the bridging ligand is predicted by TDDFT (see D<sub>21</sub> and D<sub>45</sub> in Figure 6d).

In the case of the doubly reduced photocatalyst, <sup>1</sup>[**Ru-Co(ACN)<sub>2</sub>**], exclusively singlet species were considered as the fully charged Co<sup>I</sup> formally features a low-spin d<sup>8</sup> configuration. Figure 6f illustrates the intramolecular electron transfer pathways and the accessory charge localization, *i.e.*, with the second reduction centered on one bpy ligand (S<sub>2</sub>), on the phen-moiety (S<sub>3</sub>), and on the Co catalyst (S<sub>0</sub>), the fully charged and catalytic active Co<sup>I</sup> species. Analogous to the first electron transfer (Figure 6c), bpy- and phen-based reductions are isoenergetic, while a pronounced mixing of bpy and phen contributions hampered the identification and optimization of charge-separated Co<sup>II</sup> species (see the Supporting Information for details). However, the second reduction (Co<sup>II</sup>/Co<sup>I</sup>) proceeds with a thermodynamically unfavorable driving force of approximately +0.36 eV, thus hampering the formation of the catalytic active Co<sup>I</sup> species. However, the population of the Co<sup>I</sup> redox state leads, in consequence, to the dissociation of one ACN ligand (Table S8; d(CoACN<sub>1</sub>) = 3.821 Å), leading to **Ru-Co(ACN)** and thus substantially stabilizing the catalytic active species (Figure S23i).<sup>66</sup> It is worth noting that the driving force for the Co<sup>II</sup>/Co<sup>I</sup> reduction was found to be highly sensitive to Co<sup>II</sup>'s coordination sphere. An increased electron density at the Co<sup>II</sup> site, as given by two coordinated bromide ligands, yields an even more unfavorable driving force of +0.39 eV, while a decreased electron density, as given by the pentacoordinated Co<sup>II</sup> species (one ACN), yields a strong driving force of –1.15 eV for the Co<sup>I</sup> formation. Experimentally, a driving force of –0.75 eV was determined for the Co<sup>II</sup>/Co<sup>I</sup> reduction (recall Table 1). Presumably, this discrepancy reflects a coordination environment at the cobalt center with one coordinated and one loosely bound solvent molecule, which cannot be fully described based on the present computational approach. Metadynamic simulations are the method of choice to describe such a scenario; unfortunately, the computational demand prevents an application in the present case. Further details with respect to computational results and the impact of the cobalt coordination sphere on its redox properties are collected in the Supporting Information.

The reasons why the formation of the catalytically competent Co<sup>I</sup> state is not experimentally observed, whereas electron transfer from the reduced dye is predicted to occur with a high driving force, are still unclear at that stage. A possible explanation might involve a small electronic coupling between the redox states involved in the formation of the Co<sup>I</sup> species, *e.g.*, as shown previously for triazole-based linkers.<sup>68</sup> We recently made a similar observation for a related dyad based on a cobalt tetraazamacrocyclic catalyst covalently linked to a push–pull organic dye: the formation of the Co<sup>I</sup> state of the catalyst could be detected within 20 ns after laser pulse excitation but with a yield far from unity, a lot of reduced dye remaining present on the surface of the film on the μs time window.<sup>38</sup> This therefore raises questions regarding (i) the choice of a covalent dye-catalyst assembly based on a CuAAC coupling, the role played by the triazole unit in the photoinduced electron transfer processes presenting some controversy in the literature,<sup>69</sup> and (ii) the influence of the dyad anchoring within the pores of the NiO film, which might strongly affect the parameters controlling the thermal electron process to the catalytic center due to some conformational or topological constraints, thus leaving only a small fraction of dyads active for hydrogen production. Future joint synthetic–spectroscopic–theoretical studies of the consortium will focus on the impact of the electronic coupling on the electron



transfer kinetics in detail as shown recently by semiclassical Marcus theory and quantum dynamics for a ruthenium-cobalt photocatalyst model.<sup>70</sup>

**Post-operando Characterization.** X-ray photoelectron spectroscopy (XPS) and time-of-flight secondary ion mass spectrometry (ToF-SIMS) were first employed to characterize the structural modifications undergone by the photocathode during the course of the 2 h chronoamperometric experiment. The survey XPS spectrum of a post-operando **RuP<sub>4</sub>-Co**-sensitized NiO film is shown in Figure 7a, together with the

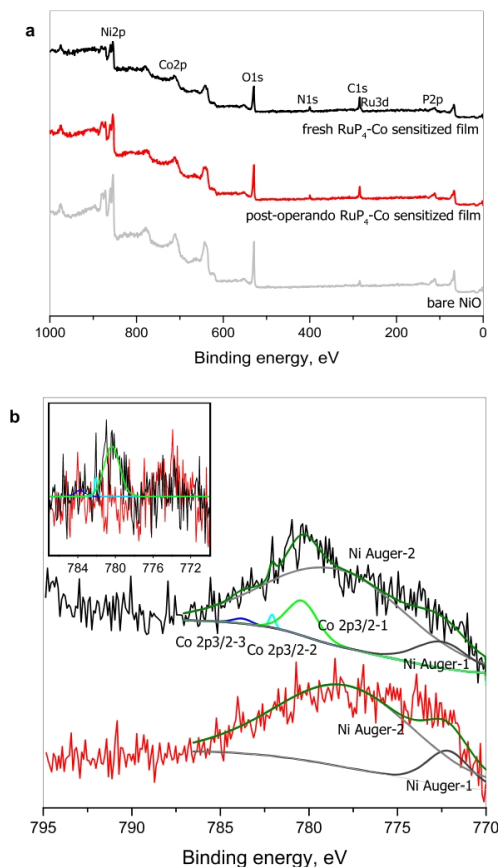


**Figure 7.** (a) Survey XPS spectra recorded on a pristine NiO film (gray), a fresh **RuP<sub>4</sub>-Co**-sensitized film (black), and the same film post-operando (red). (b) XPS core-level spectra of the Co 2p<sub>3/2</sub> region and corresponding deconvolution of the signals (inset: overlap of the spectra corrected for the Ni Auger background).

ones recorded on the same freshly sensitized film and on a bare NiO film, for comparison purposes. Surface modification by **RuP<sub>4</sub>-Co** is confirmed by the appearance of new peaks at 132.4, 280.6, and 400.1 eV, characteristic for the P 2p, Ru 3d, and N 1s core levels, respectively (Figure 7 and Figure S24). The chemical state of Ni is not modified upon sensitization nor post-operando (Figure S25); in particular, the formation of Ni<sup>0</sup> (typically observed at 852.6 eV) is not detected here. The relative concentration of these elements is decreased post-operando (Table S9), indicating that 30 to 50% of the dyad is

released in solution during the course of the photoelectrochemical activity measurement. The Co<sup>III</sup> catalyst is detected at 780.4 eV (Co 2p<sub>3/2</sub> core level) for the freshly sensitized film (Figure 7b): even though this signal is masked by the overlapping Ni Auger background, complicating its quantification, upon the deconvolution, it is possible to observe the Co signal (see the inset in Figure 7b). The latter is in perfect agreement with the XPS analyses previously reported for the same catalyst co-immobilized onto NiO with a push–pull organic dye<sup>23</sup> or anchored onto MWCNTs.<sup>43</sup> Furthermore, this signal is absent (or lies below the detection limit) in the spectrum recorded post-operando, suggesting that the loss of Co is more important compared to Ru. Desorption of the dyad from the surface of the NiO film is also evidenced by ToF-SIMS analysis. Comparison of the positive mode spectra recorded on a freshly sensitized film and the same one post-operando (Figure S26) clearly show that while some peaks attributed to the dyad are still significantly present (Ru-containing signatures such as the peak detected at  $m/z = 616.01$ ), others can hardly be detected at the end of the 2 h photoelectrocatalytic experiment (typically, the Co-containing signatures such as the peak detected at  $m/z = 659.17$ ). In the negative mode spectra, the detection of various Ni<sub>x</sub>P<sub>y</sub>O<sub>c</sub>H<sub>d</sub><sup>-</sup> fragments (Figure S27) provides evidence for the covalent attachment of the dyad on the surface of the NiO electrode through the formation of inorganic ester bonds, as previously observed for related systems.<sup>36</sup> These peaks are also detected post-operando.

In parallel to these two techniques directly probing the sensitized film at the end of the chronoamperometric measurements, desorption of the remaining molecular species from the surface of the film was also undertaken and the desorption solution was analyzed by UV–vis absorption spectroscopy. For all analyzed samples, the post-operando UV–vis spectra revealed an important decrease in absorption compared to those recorded for the other half of the freshly desorbed film (Figure 8), giving an average percentage of dyad desorption of 80% (independent of the irradiation conditions; see Table S4). Thus, the presence of the four phosphonate anchors failed to stabilize the grafting onto the NiO film surface. Working at pH 5.5 for an optimal H<sub>2</sub>-evolving activity, whereas phosphonate grafting is reported to be stable below pH 5,<sup>71,72</sup> might rationalize this behavior. In addition to UV–vis spectroscopy, MALDI-ToF mass spectrometry was employed to provide further information regarding the fate of the molecular dyad. The spectrum recorded after desorption of a freshly sensitized film (Figure S28) is quasi-superimposable to the **RuP<sub>4</sub>-Co** reference spectrum, with a main peak at  $m/z = 1448$  attributed to the [M-2PF<sub>6</sub>-2Br]<sup>4+</sup> ion, together with additional fragmentation peaks such as the loss of one oxygen atom at  $m/z = 1432$ . By contrast, at the end of the 2 h PEC experiment, these characteristic peaks have disappeared and the spectrum displays a single peak at  $m/z = 1224$  (Figure 8). Its isotopic pattern is in agreement with the one calculated for the diamino derivative of the dyad (structure presented in Figure 8), which could be formed via a degradation pathway involving the hydrolysis of the cobalt diimine dioxime catalytic core during the course of the PEC experiment.

To verify how these stability issues affect the faradaic efficiency of the system, a chronoamperometric test was run over half an hour instead of 2 h, with 59 nmol·cm<sup>-2</sup> hydrogen being produced with a 72% F.E. (Table S4). This clearly

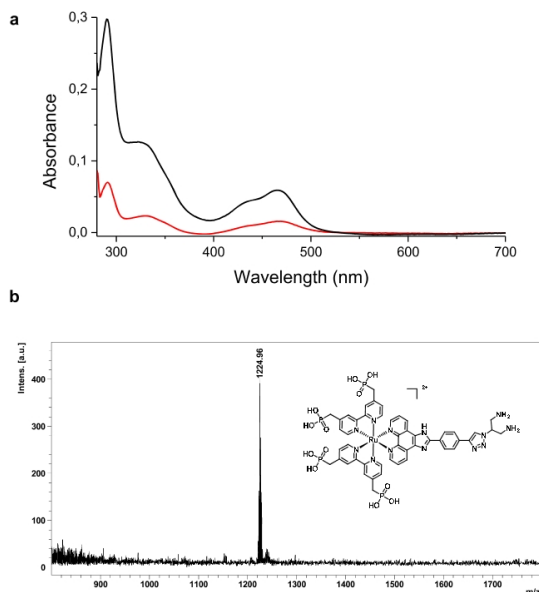


**Figure 8.** (a) UV-vis absorption spectra of desorption solutions (1 M phenylphosphonic acid in methanol) of a fresh  $\text{RuP}_4\text{-Co}$ -sensitized NiO film (black) and the same film post-operando (red). (b) MALDI-ToF mass spectrum recorded on the post-operando desorption solution and structure of the molecular assembly corresponding to the peak at 1224.

highlights the finding that during the first minutes of activity under continuous irradiation, the charges are selectively used to produce  $\text{H}_2$ , although this selectivity rapidly decreases over time to yield the 25% F.E. recorded after 2 h. The performances of the  $\text{RuP}_4\text{-Co}$  photocathode are thus strongly limited by the relatively fast dyad desorption from the surface of the NiO film, together with the lack of stability of the diimine dioxime coordination sphere under the photoelectrochemical conditions of activity, *i.e.*, in an aqueous electrolyte at pH 5.5. The latter point sharply contrasts with the previously reported activity for Co covalently anchored onto a nanostructured carbon-based electrode, continuously producing  $\text{H}_2$  for 4 h with a near-quantitative F.E. under very close aqueous conditions (acetate buffer, pH 4.5).<sup>43</sup> We believe that such a difference in stability is related to the supply of electrons to the catalytic center, which is optimized in the MWCNT/Co electrocatalytic material in contrast to the NiO/ $\text{RuCo}$  photocathode. The consequence of the low electron transfer efficiency identified above is a slow charge accumulation process at the cobalt center; this might leave enough time for the degradation of some catalytic intermediates through cobalt demetallation and subsequent hydrolysis of the diimine bonds of the ligand. Cobalt demetallation was previously reported to be the dominating deactivation pathway for a related cobaloxime-based photocathode, preventing any catalytic activity.<sup>32</sup>

## CONCLUSIONS

In conclusion, the preparation and characterization of a novel NiO photocathode integrating the cobalt diimine dioxime  $\text{H}_2$ -evolving catalyst covalently linked by CuAAC coupling to a

ruthenium tris-diimine light-harvesting unit is described. Photocurrent densities of  $84 \pm 7 \mu\text{A}\cdot\text{cm}^{-2}$  were recorded under simulated AM 1.5G irradiation, which is among the highest values reported so far for dye-sensitized photocathodes with surface-immobilized catalysts. Hydrogen was produced with an unprecedented 72% F.E. during the first 30 min of the chronoamperometric measurements, but this activity declined rapidly over 2 h. A comprehensive analysis of the photoelectrochemical data established that catalysis at the cobalt center is not the kinetically limiting process, with the initial TOF being increased when varying either the irradiation conditions or the nature of the light-harvesting unit, *i.e.*, it is five times higher herein compared to the one previously reported with the push-pull organic dye **TI**, with all other conditions being strictly equal. The interfacial electron transfer dynamics were further investigated by transient absorption measurements recorded with the operando potential applied to the film (TA-SEC) as well as by quantum chemical simulations addressing the stepwise intramolecular electron transfer processes among the various redox intermediates, eventually leading to the formation of the catalytic active species. The low yield of the thermally activated electron transfer from the reduced dye to the catalyst was identified as the main kinetic bottleneck and not the primary recombination between the reduced dye and the hole in NiO as often called on to explain the low performances reported so far for  $\text{H}_2$ -evolving dye-sensitized NiO photocathodes. In addition, a combination of post-operando characterization techniques, namely, XPS, ToF-SIMS, and UV-vis spectroscopy combined with MALDI-ToF mass spectrometry, allowed one to identify the hydrolytic degradation of the catalytic center and an important percentage of dyad released in solution as the two main stability issues. This study thus paves the way toward the construction of higher performing  $\text{H}_2$ -evolving dye-sensitized photocathodes in view of their integration in tandem water-splitting PECs. Work should focus in particular on the design of molecular assemblies, allowing one to more efficiently shuttle electrons from the dye to the catalytic center. The integration of robust molecular catalysts, typically the cobalt-polypyridyl<sup>73–76</sup> or cobalt tetraazamacrocyclic<sup>38,77</sup> complexes, will also be instrumental to increase the long-term stability. Finally, various surface chemistry strategies can be applied to stabilize the molecular grafting onto the electrode, such as the ALD deposition of a thin layer of alumina<sup>78</sup> or the use of silatrane anchors that are hydrolytically stable over a wide range of pH values.<sup>79,80</sup>

## ASSOCIATED CONTENT

### Supporting Information

The Supporting Information is available free of charge at <https://pubs.acs.org/doi/10.1021/acsami.1c12138>.

Experimental details regarding the synthesis and characterization in solution of the  $\text{RuP}_4^{\text{OEt-Co}}$  dyad and additional (photo)electrochemical, spectroscopic, and simulation data (PDF)

## AUTHOR INFORMATION

### Corresponding Author

Murielle Chavarot-Kerlidou – Univ. Grenoble Alpes, CNRS, CEA, IRIG, Laboratoire de Chimie et Biologie des Métaux, Université Grenoble Alpes, F-38000 Grenoble, France;



● [orcid.org/0000-0003-2709-3772](https://orcid.org/0000-0003-2709-3772);  
Email: [murielle.chavarot-kerlidou@cea.fr](mailto:murielle.chavarot-kerlidou@cea.fr)

### Authors

- Emmanouil Giannoudis** – Univ. Grenoble Alpes, CNRS, CEA, IRIG, Laboratoire de Chimie et Biologie des Métaux, Université Grenoble Alpes, F-38000 Grenoble, France
- Sebastian Bold** – Univ. Grenoble Alpes, CNRS, CEA, IRIG, Laboratoire de Chimie et Biologie des Métaux, Université Grenoble Alpes, F-38000 Grenoble, France; Institute of Physical Chemistry and Abbe Center of Photonics, Friedrich Schiller University Jena, 07743 Jena, Germany; Department Functional Interfaces, Leibniz Institute of Photonic Technology Jena (IPHT), 07745 Jena, Germany; Center for Energy and Environmental Chemistry Jena (CEEC Jena), Friedrich Schiller University Jena, 07743 Jena, Germany
- Carolin Müller** – Institute of Physical Chemistry and Abbe Center of Photonics, Friedrich Schiller University Jena, 07743 Jena, Germany; Department Functional Interfaces, Leibniz Institute of Photonic Technology Jena (IPHT), 07745 Jena, Germany; Center for Energy and Environmental Chemistry Jena (CEEC Jena), Friedrich Schiller University Jena, 07743 Jena, Germany
- Alexander Schwab** – Institute of Physical Chemistry and Abbe Center of Photonics, Friedrich Schiller University Jena, 07743 Jena, Germany
- Jakob Bruhnke** – Institute of Physical Chemistry and Abbe Center of Photonics, Friedrich Schiller University Jena, 07743 Jena, Germany
- Nicolas Queyriaux** – Univ. Grenoble Alpes, CNRS, CEA, IRIG, Laboratoire de Chimie et Biologie des Métaux, Université Grenoble Alpes, F-38000 Grenoble, France; ● [orcid.org/0000-0002-8525-280X](https://orcid.org/0000-0002-8525-280X)
- Corinne Gablin** – Univ Lyon, CNRS, Université Claude Bernard Lyon 1, Institut des Sciences Analytiques, F-69100 Villeurbanne, France
- Didier Leonard** – Univ Lyon, CNRS, Université Claude Bernard Lyon 1, Institut des Sciences Analytiques, F-69100 Villeurbanne, France; ● [orcid.org/0000-0002-7307-8947](https://orcid.org/0000-0002-7307-8947)
- Christine Saint-Pierre** – Univ. Grenoble Alpes, CNRS, CEA IRIG, SyMMES, F-38000 Grenoble, France
- Didier Gasparutto** – Univ. Grenoble Alpes, CNRS, CEA IRIG, SyMMES, F-38000 Grenoble, France; ● [orcid.org/0000-0002-7984-6177](https://orcid.org/0000-0002-7984-6177)
- Dmitry Aldakov** – Univ. Grenoble Alpes, CNRS, CEA IRIG, SyMMES, F-38000 Grenoble, France; ● [orcid.org/0000-0002-4581-2462](https://orcid.org/0000-0002-4581-2462)
- Stephan Kupfer** – Institute of Physical Chemistry and Abbe Center of Photonics, Friedrich Schiller University Jena, 07743 Jena, Germany; ● [orcid.org/0000-0002-6428-7528](https://orcid.org/0000-0002-6428-7528)
- Vincent Artero** – Univ. Grenoble Alpes, CNRS, CEA, IRIG, Laboratoire de Chimie et Biologie des Métaux, Université Grenoble Alpes, F-38000 Grenoble, France; ● [orcid.org/0000-0002-6148-8471](https://orcid.org/0000-0002-6148-8471)
- Benjamin Dietzek** – Institute of Physical Chemistry and Abbe Center of Photonics, Friedrich Schiller University Jena, 07743 Jena, Germany; Department Functional Interfaces, Leibniz Institute of Photonic Technology Jena (IPHT), 07745 Jena, Germany; Center for Energy and Environmental Chemistry Jena (CEEC Jena), Friedrich Schiller University Jena, 07743 Jena, Germany; ● [orcid.org/0000-0002-2842-3537](https://orcid.org/0000-0002-2842-3537)

Complete contact information is available at:  
<https://pubs.acs.org/10.1021/acsami.1c12138>

### Author Contributions

<sup>V</sup>E.G. and S.B. contributed equally to this work. The manuscript was written through contributions of all authors. All authors have given approval to the final version of the manuscript.

### Funding

This work was supported by the European Commission's Seventh Framework Program (FP7/2007-2013) under grant agreement no. 306398 (FP7-IDEAS-ERC, Project PhotocatH<sub>2</sub>ode), the Deutsche Forschungsgemeinschaft (German Science Foundation, PHOTOACC project, grant no. KU 3933/2-1), and the French National Research Agency in the framework of the "Investissements d'avenir" program (ANR-15-IDEX-02, Labex ARCANE and CBH-EURGS, ANR-17-EURE-0003) and the Franco-German University.

### Notes

The authors declare no competing financial interest.

### ACKNOWLEDGMENTS

Adina Morozan is acknowledged for the SEM measurements. Jacques Pecaut (CEA/DRF/IRIG/DIESE/SyMMES) is acknowledged for the ESI-MS measurements. S.B. wants to thank the Franco-German University for the cotutelle thesis funding support. We want to thank the workshop of the IPHT Jena for their help in building the spectroscopy cell.

### REFERENCES

- (1) Li, F.; Yang, H.; Li, W.; Sun, L. Device Fabrication for Water Oxidation, Hydrogen Generation, and CO<sub>2</sub> Reduction via Molecular Engineering. *Joule* **2018**, *2*, 36–60.
- (2) McKone, J. R.; Lewis, N. S.; Gray, H. B. Will Solar-Driven Water-Splitting Devices See the Light of Day? *Chem. Mater.* **2014**, *26*, 407–414.
- (3) Walter, M. G.; Warren, E. L.; McKone, J. R.; Boettcher, S. W.; Mi, Q.; Santori, E. A.; Lewis, N. S. Solar Water Splitting Cells. *Chem. Rev.* **2010**, *110*, 6446–6473.
- (4) Yun, S.; Vlachopoulos, N.; Qurashi, A.; Ahmad, S.; Hagfeldt, A. Dye Sensitized Photoelectrolysis Cells. *Chem. Soc. Rev.* **2019**, *48*, 3705–3722.
- (5) Zhang, S.; Ye, H.; Hua, J.; Tian, H. Recent Advances in Dye-Sensitized Photoelectrochemical Cells for Water Splitting. *EnergyChem* **2019**, *1*, 100015.
- (6) Xu, P.; McCool, N. S.; Mallouk, T. E. Water Splitting Dye-Sensitized Solar Cells. *Nano Today* **2017**, *14*, 42–58.
- (7) Brennaman, M. K.; Dillon, R. J.; Alibabaei, L.; Gish, M. K.; Dares, C. J.; Ashford, D. L.; House, R. L.; Meyer, G. J.; Papanikolas, J. M.; Meyer, T. J. Finding the Way to Solar Fuels with Dye-Sensitized Photoelectrosynthesis Cells. *J. Am. Chem. Soc.* **2016**, *138*, 13085–13102.
- (8) Dalle, K. E.; Warnan, J.; Leung, J. J.; Reuillard, B.; Karmel, I. S.; Reisner, E. Electro- and Solar-Driven Fuel Synthesis with First Row Transition Metal Complexes. *Chem. Rev.* **2019**, *119*, 2752–2875.
- (9) Artero, V. Bioinspired Catalytic Materials for Energy-Relevant Conversions. *Nat. Energy* **2017**, *2*, 17131.
- (10) Berardi, S.; Drouet, S.; Francàs, L.; Gimbert-Suriñach, C.; Guttentag, M.; Richmond, C.; Stoll, T.; Llobet, A. Molecular Artificial Photosynthesis. *Chem. Soc. Rev.* **2014**, *43*, 7501–7519.
- (11) Windle, C. D.; Kumagai, H.; Higashi, M.; Brisse, R.; Bold, S.; Jousset, B.; Chavarot-Kerlidou, M.; Maeda, K.; Abe, R.; Ishitani, O.; Artero, V. Earth-Abundant Molecular Z-Scheme Photoelectrochemical Cell for Overall Water-Splitting. *J. Am. Chem. Soc.* **2019**, *141*, 9593–9602.
- (12) Li, F.; Fan, K.; Xu, B.; Gabrielsson, E.; Daniel, Q.; Li, L.; Sun, L. Organic Dye-Sensitized Tandem Photoelectrochemical Cell for Light Driven Total Water Splitting. *J. Am. Chem. Soc.* **2015**, *137*, 9153–9159.

- (13) Fan, K.; Li, F.; Wang, L.; Daniel, Q.; Gabrielsson, E.; Sun, L. Pt-free Tandem Molecular Photoelectrochemical Cells for Water Splitting Driven by Visible Light. *Phys. Chem. Chem. Phys.* **2014**, *16*, 25234–25240.
- (14) Wu, H.-L.; Li, X.-B.; Tung, C.-H.; Wu, L.-Z. Sensitized Photocathodes: Recent Advances in Sensitized Photocathodes: From Molecular Dyes to Semiconducting Quantum Dots (Adv. Sci. 4/2018). *Adv. Sci.* **2018**, *5*, 1870023.
- (15) Gibson, E. A. Dye-Sensitized Photocathodes for H<sub>2</sub> Evolution. *Chem. Soc. Rev.* **2017**, *46*, 6194–6209.
- (16) Nikolaou, V.; Charisiadis, A.; Charalambidis, G.; Coutsolelos, A. G.; Odobel, F. Recent Advances and Insights in Dye-Sensitized NiO Photocathodes for Photovoltaic Devices. *J. Mater. Chem. A* **2017**, *5*, 21077–21113.
- (17) Lyu, S.; Massin, J.; Pavone, M.; Muñoz-García, A. B.; Labrugère, C.; Toupance, T.; Chavarot-Kerlidou, M.; Artero, V.; Olivier, C. H<sub>2</sub>-Evolving Dye-Sensitized Photocathode Based on a Ruthenium–Diacylide/Cobaloxime Supramolecular Assembly. *ACS Appl. Energy Matter* **2019**, *2*, 4971–4980.
- (18) Pöldme, N.; O'Reilly, L.; Fletcher, I.; Portoles, J.; Sazanovich, I. V.; Towrie, M.; Long, C.; Vos, J. G.; Pryce, M. T.; Gibson, E. A. Photoelectrocatalytic H<sub>2</sub> Evolution from Integrated Photocatalysts Adsorbed on NiO. *Chem. Sci.* **2019**, *10*, 99–112.
- (19) Windle, C. D.; Massin, J.; Chavarot-Kerlidou, M.; Artero, V. A Protocol for Quantifying Hydrogen Evolution by Dye-Sensitized Molecular Photocathodes and its Implementation for Evaluating a New Covalent Architecture Based on an Optimized Dye-Catalyst Dyad. *Dalton Trans.* **2018**, *47*, 10509–10516.
- (20) Kaeffer, N.; Massin, J.; Lebrun, C.; Renault, O.; Chavarot-Kerlidou, M.; Artero, V. Covalent Design for Dye-Sensitized H<sub>2</sub>-Evolving Photocathodes Based on a Cobalt Diimine–Dioxime Catalyst. *J. Am. Chem. Soc.* **2016**, *138*, 12308–12311.
- (21) Ji, Z.; He, M.; Huang, Z.; Ozkan, U.; Wu, Y. Photostable p-Type Dye-Sensitized Photoelectrochemical Cells for Water Reduction. *J. Am. Chem. Soc.* **2013**, *135*, 11696–11699.
- (22) Pati, P. B.; Zhang, L.; Philippe, B.; Fernández-Terán, R.; Ahmadi, S.; Tian, L.; Rensmo, H.; Hammarström, L.; Tian, H. Insights into the Mechanism of a Covalently Linked Organic Dye–Cobaloxime Catalyst System for Dye-Sensitized Solar Fuel Devices. *ChemSusChem* **2017**, *10*, 2480–2495.
- (23) Kaeffer, N.; Windle, C. D.; Brisse, R.; Gablin, C.; Leonard, D.; Jousselme, B.; Chavarot-Kerlidou, M.; Artero, V. Insights into the Mechanism and Aging of a Noble-Metal Free H<sub>2</sub>-Evolving Dye-Sensitized Photocathode. *Chem. Sci.* **2018**, *9*, 6721–6738.
- (24) Creissen, C. E.; Warnan, J.; Reisner, E. Solar H<sub>2</sub> Generation in Water with a CuCrO<sub>2</sub> Photocathode Modified with an Organic Dye and Molecular Ni Catalyst. *Chem. Sci.* **2018**, *9*, 1439–1447.
- (25) Antila, L. J.; Ghangosar, P.; Maji, S.; Tian, H.; Ott, S.; Hammarström, L. Dynamics and Photochemical H<sub>2</sub> Evolution of Dye–NiO Photocathodes with a Biomimetic FeFe-Catalyst. *ACS Energy Lett.* **2016**, *1*, 1106–1111.
- (26) Li, F.; Xu, R.; Nie, C.; Wu, X.; Zhang, P.; Duan, L.; Sun, L. Dye-Sensitized LaFeO<sub>3</sub> Photocathode for Solar-Driven H<sub>2</sub> Generation. *Chem. Commun.* **2019**, *55*, 12940–12943.
- (27) Creissen, C. E.; Warnan, J.; Antón-García, D.; Farré, Y.; Odobel, F.; Reisner, E. Inverse Opal CuCrO<sub>2</sub> Photocathodes for H<sub>2</sub> Production Using Organic Dyes and a Molecular Ni Catalyst. *ACS Catal.* **2019**, *9*, 9530–9538.
- (28) Gross, M. A.; Creissen, C. E.; Orchard, K. L.; Reisner, E. Photoelectrochemical Hydrogen Production in Water using a Layer-by-Layer Assembly of a Ru Dye and Ni Catalyst on NiO. *Chem. Sci.* **2016**, *7*, 5537–5546.
- (29) Shan, B.; Das, A. K.; Marquard, S.; Farnum, B. H.; Wang, D.; Bullock, R. M.; Meyer, T. J. Photogeneration of Hydrogen from Water by a Robust Dye-Sensitized Photocathode. *Energy Environ. Sci.* **2016**, *9*, 3693–3697.
- (30) Shan, B.; Sherman, B. D.; Klug, C. M.; Nayak, A.; Marquard, S. L.; Liu, Q.; Bullock, R. M.; Meyer, T. J. Modulating Hole Transport in Multilayered Photocathodes with Derivatized p-Type Nickel Oxide and Molecular Assemblies for Solar-Driven Water Splitting. *J. Phys. Chem. Lett.* **2017**, *8*, 4374–4379.
- (31) Wang, D.; Sheridan, M. V.; Shan, B.; Farnum, B. H.; Marquard, S. L.; Sherman, B. D.; Eberhart, M. S.; Nayak, A.; Dares, C. J.; Das, A. K.; Bullock, R. M.; Meyer, T. J. Layer-by-Layer Molecular Assemblies for Dye-Sensitized Photoelectrosynthesis Cells Prepared by Atomic Layer Deposition. *J. Am. Chem. Soc.* **2017**, *139*, 14518–14525.
- (32) Materna, K. L.; Beiler, A. M.; Thapper, A.; Ott, S.; Tian, H.; Hammarström, L. Understanding the Performance of NiO Photocathodes with Alkyl-Derivatized Cobalt Catalysts and a Push–Pull Dye. *ACS Appl. Mater. Interfaces* **2020**, *12*, 31372–31381.
- (33) Wood, C. J.; Summers, G. H.; Clark, C. A.; Kaeffer, N.; Braeutigam, M.; Carbone, L. R.; D'Amario, L.; Fan, K.; Farré, Y.; Narbey, S.; Oswald, F.; Stevens, L. A.; Parmenter, C. D. J.; Fay, M. W.; La Torre, A.; Snape, C. E.; Dietzek, B.; Dini, D.; Hammarström, L.; Pellegrin, Y.; Odobel, F.; Sun, L.; Artero, V.; Gibson, E. A. A Comprehensive Comparison of Dye-Sensitized NiO Photocathodes for Solar Energy Conversion. *Phys. Chem. Chem. Phys.* **2016**, *18*, 10727–10738.
- (34) Dillon, R. J.; Alibabaei, L.; Meyer, T. J.; Papanikolas, J. M. Enabling Efficient Creation of Long-Lived Charge-Separation on Dye-Sensitized NiO Photocathodes. *ACS Appl. Mater. Interfaces* **2017**, *9*, 26786–26796.
- (35) D'Amario, L.; Antila, L. J.; Pettersson Rimgard, B.; Boschloo, G.; Hammarström, L. Kinetic Evidence of Two Pathways for Charge Recombination in NiO-Based Dye-Sensitized Solar Cells. *J. Phys. Chem. Lett.* **2015**, *6*, 779–783.
- (36) Queyriaux, N.; Wahyuno, R. A.; Fize, J.; Gablin, C.; Wächtler, M.; Martinez, E.; Léonard, D.; Dietzek, B.; Artero, V.; Chavarot-Kerlidou, M. Aqueous Photocurrent Measurements Correlated to Ultrafast Electron Transfer Dynamics at Ruthenium Tris Diimine Sensitized NiO Photocathodes. *J. Phys. Chem. C* **2017**, *121*, 5891–5904.
- (37) Charisiadis, A.; Giannoudis, E.; Pournara, Z.; Kosma, A.; Nikolaou, V.; Charalambidis, G.; Artero, V.; Chavarot-Kerlidou, M.; Coutsolelos, A. G. Synthesis and Characterization of a Covalent Porphyrin-Cobalt Diimine-Dioxime Dyad for Photoelectrochemical H<sub>2</sub> Evolution. *Eur. J. Inorg. Chem.* **2021**, *2021*, 1122–1129.
- (38) Bold, S.; Massin, J.; Giannoudis, E.; Koepf, M.; Artero, V.; Dietzek, B.; Chavarot-Kerlidou, M. Spectroscopic Investigations Provide a Rationale for the Hydrogen-Evolving Activity of Dye-Sensitized Photocathodes Based on a Cobalt Tetraazamacrocyclic Catalyst. *ACS Catal.* **2021**, *11*, 3662–3678.
- (39) Queyriaux, N.; Giannoudis, E.; Lefebvre, J.-F.; Artero, V.; Chavarot-Kerlidou, M. Synthesis of Ruthenium Tris-Diimine Photosensitizers Substituted by Four Methylphosphonate Anchoring Groups for Dye-Sensitized Photoelectrochemical Cell Applications. *Eur. J. Inorg. Chem.* **2019**, *2019*, 2154–2161.
- (40) Kaeffer, N.; Chavarot-Kerlidou, M.; Artero, V. Hydrogen Evolution Catalyzed by Cobalt Diimine–Dioxime Complexes. *Acc. Chem. Res.* **2015**, *48*, 1286–1295.
- (41) Natu, G.; Hasin, P.; Huang, Z.; Ji, Z.; He, M.; Wu, Y. Valence Band-Edge Engineering of Nickel Oxide Nanoparticles via Cobalt Doping for Application in p-Type Dye-Sensitized Solar Cells. *ACS Appl. Mater. Interfaces* **2012**, *4*, 5922–5929.
- (42) Queyriaux, N.; Andreiadis, E. S.; Torelli, S.; Pécaut, J.; Veldkamp, B. S.; Margulies, E. A.; Wasielewski, M. R.; Chavarot-Kerlidou, M.; Artero, V. CuAAC-Based Assembly and Characterization of a Ruthenium–Copper Dyad Containing a Diimine–Dioxime Ligand Framework. *Faraday Discuss.* **2017**, *198*, 251–261.
- (43) Andreiadis, E. S.; Jacques, P.-A.; Tran, P. D.; Leyris, A.; Chavarot-Kerlidou, M.; Jousselme, B.; Matheron, M.; Pécaut, J.; Palacin, S.; Fontecave, M.; Artero, V. Molecular Engineering of a Cobalt-Based Electrocatalytic Nanomaterial for H<sub>2</sub> Evolution under Fully Aqueous Conditions. *Nat. Chem.* **2013**, *5*, 48–53.
- (44) Baron, A.; Herrero, C.; Quaranta, A.; Charlot, M.-F.; Leibl, W.; Vauzeilles, B.; Aukauloo, A. Click Chemistry on a Ruthenium Polypyridine Complex. An Efficient and Versatile Synthetic Route for



- the Synthesis of Photoactive Modular Assemblies. *Inorg. Chem.* **2012**, *51*, 5985–5987.
- (45) de Miguel, G.; Wielopolski, M.; Schuster, D. I.; Fazio, M. A.; Lee, O. P.; Haley, C. K.; Ortiz, A. L.; Echegoyen, L.; Clark, T.; Guldi, D. M. Triazole Bridges as Versatile Linkers in Electron Donor–Acceptor Conjugates. *J. Am. Chem. Soc.* **2011**, *133*, 13036–13054.
- (46) Zieschang, F.; Schreck, M. H.; Schmiedel, A.; Holzapfel, M.; Klein, J. H.; Walter, C.; Engels, B.; Lambert, C. Photoinduced Electron Transfer Dynamics in Triarylamine–Naphthalene Diimide Cascades. *J. Phys. Chem. C* **2014**, *118*, 27698–27714.
- (47) Bold, S.; Zedler, L.; Zhang, Y.; Massin, J.; Artero, V.; Chavarot-Kerlidou, M.; Dietzek, B. Electron Transfer in a Covalent Dye–Cobalt Catalyst Assembly – a Transient Absorption Spectroelectrochemistry Perspective. *Chem. Commun.* **2018**, *54*, 10594–10597.
- (48) Ameline, D.; Diring, S.; Farre, Y.; Pellegrin, Y.; Naponiello, G.; Blart, E.; Charrier, B.; Dini, D.; Jacquemin, D.; Odobel, F. Isoindigo Derivatives for Application in p-Type Dye Sensitized Solar Cells. *RSC Adv.* **2015**, *5*, 85530–85539.
- (49) Roy, S.; Bacchi, M.; Berggren, G.; Artero, V. A Systematic Comparative Study of Hydrogen-Evolving Molecular Catalysts in Aqueous Solutions. *ChemSusChem* **2015**, *8*, 3632–3638.
- (50) Hawecker, J.; Lehn, J. M.; Ziesel, R. Efficient Homogeneous Photochemical Hydrogen Generation and Water Reduction Mediated by Cobaloxime or Macrocyclic Cobalt Complexes. *New J. Chem.* **1983**, *7*, 271–277.
- (51) Fihri, A.; Artero, V.; Razavet, M.; Baffert, C.; Leibl, W.; Fontecave, M. Cobaloxime-Based Photocatalytic Devices for Hydrogen Production. *Angew. Chem., Int. Ed.* **2008**, *47*, 564–567.
- (52) Notably, under these conditions, TEOA is employed as a sacrificial electron donor to generate the reduced dye via the reductive quenching of its excited state.
- (53) Smolentsev, G.; Ceconi, B.; Guda, A.; Chavarot-Kerlidou, M.; van Bokhoven, J. A.; Nachtegaal, M.; Artero, V. Microsecond X-ray Absorption Spectroscopy Identification of Co<sup>I</sup> Intermediates in Cobaloxime-Catalyzed Hydrogen Evolution. *Chem. – Eur. J.* **2015**, *21*, 15158–15162.
- (54) Zhang, P.; Jacques, P.-A.; Chavarot-Kerlidou, M.; Wang, M.; Sun, L.; Fontecave, M.; Artero, V. Phosphine Coordination to a Cobalt Diimine-Dioxime Catalyst Increases Stability during Light-Driven H<sub>2</sub> Production. *Inorg. Chem.* **2012**, *51*, 2115–2120.
- (55) Adler, D.; Feinleib, J. Electrical and Optical Properties of Narrow-Band Materials. *Phys. Rev. B* **1970**, *2*, 3112–3134.
- (56) Boschloo, G.; Hagfeldt, A. Spectroelectrochemistry of Nanostructured NiO. *J. Phys. Chem. B* **2001**, *105*, 3039–3044.
- (57) Föhlinger, J.; Maji, S.; Brown, A.; Mijangos, E.; Ott, S.; Hammarström, L. Self-Quenching and Slow Hole Injection May Limit the Efficiency in NiO-Based Dye-Sensitized Solar Cells. *J. Phys. Chem. C* **2018**, *122*, 13902–13910.
- (58) Herrero, C.; Batchelor, L.; Baron, A.; El Ghachtouli, S.; Sheth, S.; Guillot, R.; Vauzeilles, B.; Sircoglou, M.; Mallah, T.; Leibl, W.; Aukauloo, A. Click Chemistry as a Convenient Tool for the Incorporation of a Ruthenium Chromophore and a Nickel–Salen Monomer into a Visible-Light-Active Assembly. *Eur. J. Inorg. Chem.* **2013**, *2013*, 494–499.
- (59) Sheth, S.; Baron, A.; Herrero, C.; Vauzeilles, B.; Aukauloo, A.; Leibl, W. Light-Induced Tryptophan Radical Generation in a Click Modular Assembly of a Sensitizer-Tryptophan Residue. *Photochem. Photobiol. Sci.* **2013**, *12*, 1074–1078.
- (60) Herrero, C.; Quaranta, A.; El Ghachtouli, S.; Vauzeilles, B.; Leibl, W.; Aukauloo, A. Carbon Dioxide Reduction via Light Activation of a Ruthenium–Ni(Cyclam) Complex. *Phys. Chem. Chem. Phys.* **2014**, *16*, 12067–12072.
- (61) Herrero, C.; Quaranta, A.; Sircoglou, M.; Sénéchal-David, K.; Baron, A.; Marín, I. M.; Buron, C.; Baltaze, J.-P.; Leibl, W.; Aukauloo, A.; Banse, F. Successive Light-Induced Two Electron Transfers in a Ru–Fe Supramolecular Assembly: From Ru–Fe(II)–OH<sub>2</sub> to Ru–Fe(IV)–oxo. *Chem. Sci.* **2015**, *6*, 2323–2327.
- (62) Tebo, A. G.; Quaranta, A.; Herrero, C.; Pecoraro, V. L.; Aukauloo, A. Intramolecular Photogeneration of a Tyrosine Radical in a Designed Protein. *ChemPhotoChem* **2017**, *1*, 89–92.
- (63) Gardner, J. M.; Beyler, M.; Karnahl, M.; Tschierle, S.; Ott, S.; Hammarström, L. Light-Driven Electron Transfer between a Photosensitizer and a Proton-Reducing Catalyst Co-adsorbed to NiO. *J. Am. Chem. Soc.* **2012**, *134*, 19322–19325.
- (64) Kamire, R. J.; Majewski, M. B.; Hoffeditz, W. L.; Phelan, B. T.; Farha, O. K.; Hupp, J. T.; Wasielewski, M. R. Photodriven Hydrogen Evolution by Molecular Catalysts using Al<sub>2</sub>O<sub>3</sub>-protected perylene-3,4-dicarboximide on NiO electrodes. *Chem. Sci.* **2017**, *8*, 541–549.
- (65) Steinmetzer, J.; Kupfer, S.; Gräfe, S. p-sisypheus: Exploring Potential Energy Surfaces in Ground and Excited States. *Int. J. Quantum Chem.* **2021**, *121*, No. e26390.
- (66) Bhattacharjee, A.; Andreadis, E. S.; Chavarot-Kerlidou, M.; Fontecave, M.; Field, M. J.; Artero, V. A Computational Study of the Mechanism of Hydrogen Evolution by Cobalt(Diimine-Dioxime) Catalysts. *Chem. – Eur. J.* **2013**, *19*, 15166–15174.
- (67) Solis, B. H.; Yu, Y.; Hammes-Schiffer, S. Effects of Ligand Modification and Protonation on Metal Oxime Hydrogen Evolution Electrocatalysts. *Inorg. Chem.* **2013**, *52*, 6994–6999.
- (68) Fang, D.; Zhang, Z.-Y.; Shangquan, Z.; He, Y.; Yu, C.; Li, T. (Hetero)aryloxy-1,2,3-triazoles: “Clicked” Photoswitches for Versatile Functionalization and Electronic Decoupling. *J. Am. Chem. Soc.* **2021**, *143*, 14502–14510.
- (69) Natali, M.; Campagna, S.; Scandola, F. Photoinduced Electron Transfer across Molecular Bridges: Electron- and Hole-Transfer Superexchange Pathways. *Chem. Soc. Rev.* **2014**, *43*, 4005–4018.
- (70) Koch, A.; Kinzel, D.; Dröge, F.; Gräfe, S.; Kupfer, S. Photochemistry and Electron Transfer Kinetics in a Photocatalyst Model Assessed by Marcus Theory and Quantum Dynamics. *J. Phys. Chem. C* **2017**, *121*, 16066–16078.
- (71) Gillaizeau-Gauthier, I.; Odobel, F.; Alebbi, M.; Argazzi, R.; Costa, E.; Bignozzi, C. A.; Qu, P.; Meyer, G. J. Phosphonate-Based Bipyridine Dyes for Stable Photovoltaic Devices. *Inorg. Chem.* **2001**, *40*, 6073–6079.
- (72) Hanson, K.; Brennaman, M. K.; Luo, H.; Glasson, C. R. K.; Concepcion, J. J.; Song, W.; Meyer, T. J. Photostability of Phosphonate-Derivatized, Ru<sup>II</sup> Polypyridyl Complexes on Metal Oxide Surfaces. *ACS Appl. Mater. Interfaces* **2012**, *4*, 1462–1469.
- (73) Queyriaux, N.; Jane, R. T.; Massin, J.; Artero, V.; Chavarot-Kerlidou, M. Recent Developments in Hydrogen Evolving Molecular Cobalt(II)–Polypyridyl Catalysts. *Coord. Chem. Rev.* **2015**, *304*–305, 3–19.
- (74) Queyriaux, N.; Giannoudis, E.; Windle, C. D.; Roy, S.; Pécaut, J.; Coutsolelos, A. G.; Artero, V.; Chavarot-Kerlidou, M. A Noble Metal-Free Photocatalytic System Based on a Novel Cobalt Tetrapyrrolyl Catalyst for Hydrogen Production in Fully Aqueous Medium. *Sustainable Energy Fuels* **2018**, *2*, 553–557.
- (75) Tong, L.; Duan, L.; Zhou, A.; Thummel, R. P. First-Row Transition Metal Polypyridine Complexes that Catalyze Proton to Hydrogen Reduction. *Coord. Chem. Rev.* **2020**, *402*, 213079.
- (76) Queyriaux, N.; Sun, D.; Fize, J.; Pécaut, J.; Field, M. J.; Chavarot-Kerlidou, M.; Artero, V. Electrocatalytic Hydrogen Evolution with a Cobalt Complex Bearing Pendant Proton Relays: Acid Strength and Applied Potential Govern Mechanism and Stability. *J. Am. Chem. Soc.* **2020**, *142*, 274–282.
- (77) Nie, C.; Liu, C.; Gong, L.; Wang, M. Boosting the Performance of a Silicon Photocathode for Photoelectrochemical Hydrogen Production by Immobilization of a Cobalt Tetraazamacrocyclic Catalyst. *J. Mater. Chem. A* **2021**, *9*, 234–238.
- (78) Hanson, K.; Losego, M. D.; Kalanyan, B.; Parsons, G. N.; Meyer, T. J. Stabilizing Small Molecules on Metal Oxide Surfaces Using Atomic Layer Deposition. *Nano Lett.* **2013**, *13*, 4802–4809.
- (79) Materina, K. L.; Jiang, J.; Crabtree, R. H.; Brudvig, G. W. Silatrane Anchors for Metal Oxide Surfaces: Optimization for Potential Photocatalytic and Electrocatalytic Applications. *ACS Appl. Mater. Interfaces* **2019**, *11*, 5602–5609.

(80) Materna, K. L.; Lalaoui, N.; Laureanti, J. A.; Walsh, A. P.; Ringard, B. P.; Lomoth, R.; Thapper, A.; Ott, S.; Shaw, W. J.; Tian, H.; Hammarström, L. Using Surface Amide Couplings to Assemble Photocathodes for Solar Fuel Production Applications. *ACS Appl. Mater. Interfaces* **2020**, *12*, 4501–4509.

**Supporting information**  
**for**  
Hydrogen production at a NiO photocathode based  
on a ruthenium dye – cobalt diimine dioxime  
catalyst assembly: insights from advanced  
spectroscopy and post-operando characterization

E. Giannoudis,<sup>\*a</sup> S. Bold,<sup>\*a,b,c,d</sup> C. Müller,<sup>b,c,d</sup> A. Schwab,<sup>b</sup> J. Bruhnke,<sup>b</sup> N. Queyriaux,<sup>a</sup> C. Gablin,<sup>c</sup> D. Leonard,<sup>c</sup> C. Saint-Pierre,<sup>f</sup> D. Gasparutto,<sup>f</sup> D. Aldakov,<sup>f</sup> S. Kupfer,<sup>b</sup> V. Artero,<sup>a</sup> B. Dietzek,<sup>b,c,d</sup> M. Chavarot-Kerlidou<sup>\*a</sup>

<sup>\*</sup>These authors contributed equally to this work.

[murielle.chavarot-kerlidou@cea.fr](mailto:murielle.chavarot-kerlidou@cea.fr)

a. Univ. Grenoble Alpes, CNRS, CEA, IRIG, Laboratoire de Chimie et Biologie des Métaux, Université Grenoble Alpes, 17 rue des Martyrs, F-38000 Grenoble, France.

b. Institute of Physical Chemistry and Abbe Center of Photonics, Friedrich Schiller University Jena, Helmholtzweg 4, 07743 Jena, Germany.

c. Department Functional Interfaces, Leibniz Institute of Photonic Technology Jena (IPHT), Albert-Einstein-Straße 9, 07745 Jena, Germany.

d. Center for Energy and Environmental Chemistry Jena (CEEC Jena), Friedrich Schiller University Jena, Philosophenweg 8, 07743 Jena, Germany.

e. Univ Lyon, CNRS, Université Claude Bernard Lyon 1, Institut des Sciences Analytiques, UMR 5280, 5, rue de la Doua, F-69100 Villeurbanne, France.

f. Univ. Grenoble Alpes, CNRS, CEA IRIG, SyMMES, F-38000 Grenoble, France.

All reagents were purchased from Sigma Aldrich or Strem and used as obtained unless otherwise stated. Reagent-grade solvents were used without further purification. The 4,4'-bis(diethylphosphonomethyl)-2,2'-bipyridine ( $(4,4'-(\text{CH}_2\text{PO}_3\text{Et}_2)_2\text{-bpy})^1$  and  $N2,N2'$ -2-azidopropanediylbis(2,3-butadione-2-imine-3-oxime)<sup>2</sup> ligands were custom-synthesized by the companies Oribase Pharma and Provence Technologies, respectively. The 2-(4-ethynylphenyl)-1H-imidazo[4,5-f][1,10]phenanthroline (EPIP) ligand,<sup>3</sup>  $[\text{Ru}(4,4'-(\text{CH}_2\text{PO}_3\text{Et}_2)_2\text{-bpy})_2(\text{EPIP})](\text{PF}_6)_2$  ( $\text{RuP}_4^{\text{OEt-EPIP}}$ ),<sup>4</sup>  $[\text{Cu}(\text{DO})(\text{DOH})\text{N}_3\text{pn}(\text{OH}_2)](\text{ClO}_4)$  ( $\text{CuN}_3$ )<sup>3</sup> and  $[\text{Co}(\text{DO})(\text{DOH})\text{N}_3\text{pnBr}_2]^2$  ( $\text{CoN}_3$ )<sup>2</sup> complexes were prepared according to our previously reported procedures. <sup>1</sup>H and <sup>13</sup>C NMR spectra were recorded at 298 K on a Bruker Avance 300 MHz spectrometer and the resulting spectra are referenced to the residual solvent peak and reported in relative to tetramethylsilane reference ( $\delta = 0$  ppm). UV-vis absorption spectra were recorded either on a Shimadzu UV-1800 spectrometer or on an Agilent Cary 60 UV-vis spectrometer. Electrospray ionization mass spectrometric (ESI-MS) measurements were carried out on a Thermoquest Finnigan LCQ spectrometer. Accurate mass measurements (HRMS) were performed on a Bruker maXis mass spectrometer by the "Fédération de Recherche" ICOA/CBM (FR 2708) platform and elemental analysis on a Thermofisher Scientific "Flash 2000" by the "Plateforme d'analyse pour la chimie" (GDS 3648, Strasbourg).

**Photolysis experiments.** A  $3.6 \times 10^{-5}$  M solution of the dye-catalyst assembly (either  $\text{RuP}_4^{\text{OEt-Co}}$  or  $\text{T1-Co}$ ) in dry, degassed  $\text{CH}_3\text{CN}/\text{TEOA}$  (90:10 v/v) mixture was prepared in a  $\text{H}_2\text{O}/\text{O}_2$ -free glovebox and transferred in a quartz cuvette (1 mm optical light path). Irradiation of the samples was carried out outside the glovebox and UV-Vis absorption spectra were recorded at time intervals of 1 min from 0 to 10 min, then every 5 min, 10 min and 15 min until no absorption change was observed.

**Electrochemistry in solution.** Electrochemical analysis was performed using a BioLogic SP300 potentiostat controlled via EC-Lab V10 software. Electrochemical experiments were recorded in a three-electrode cell combining a glassy carbon working electrode, a platinum wire auxiliary electrode, and a custom-made Ag/AgCl reference electrode (separated from the solution by a Vycor frit). Typical measurements were carried out in argon-purged acetonitrile solution (0.1 M *n*-Bu<sub>4</sub>NBF<sub>4</sub> as supporting electrolyte) of 1 mM complex. Ferrocene was added at the end of each measurement as an internal reference, hence every value is referenced versus the  $\text{Fc}^{+/0}$  redox couple.



**Spectro-electrochemistry.** UV-Vis-SEC measurements were performed in a three-electrode setup in a H<sub>2</sub>O/O<sub>2</sub>-free glovebox, using a 1 mm cell equipped with a Pt mesh working electrode, a Pt wire auxiliary electrode and a Ag wire as reference electrode. A BioLogic VSP-300 potentiostat connected to the glovebox was used. The spectra were recorded with an optical fiber external-sampler connected to the UV-Vis spectrometer. 0.1 M tetrabutylammonium tetrafluoroborate (TBABF<sub>4</sub>) in dry acetonitrile was used as electrolyte solution. Initially, a cyclic voltammetry (CV) was carried out to determine the redox potentials. Then, potentials were applied in a chronoamperometry (CA) and UV-Vis spectra were recorded until equilibrium was reached.

**Photoelectrochemical measurements.** For a typical photoelectrocatalytic experiment, irradiation was carried out with a 300W ozone-free Xe lamp operated at 280 W equipped with a water-filled filter for elimination of IR irradiation (Spectra-Physics 6123NS) and either a UV cut-off filter (Spectra-Physics 59472,  $\lambda > 400$  nm) or a AM 1.5G filter (Spectra-Physics 81094). The power density was calibrated to 65 mW·cm<sup>-2</sup> (0.65 sun; corresponding to the 400-800 nm range of the full spectrum) using a 60% optical density filter for the set-up with the UV cut-off filter and to 1 sun for the AM 1.5G filter (0.7 sun after adding the water filter eliminating IR irradiation), using a Newport PM1918-R power-meter. The experiments were performed in a three-electrode cell, using the NiO-sensitized film as working electrode (2.5 to 3.3 cm<sup>2</sup>, accurately measured for each experiment), Ag/AgCl as the reference electrode and a Pt wire as the auxiliary electrode. Calibration of the reference electrode was realized with [K<sub>4</sub>Fe(CN)<sub>6</sub>] in 0.1 M potassium phosphate buffer at pH 7 and the potentials were converted to RHE using the equation  $E(\text{V vs RHE}) = E(\text{V vs Ag/AgCl}) + 0.059 \times \text{pH} + 0.2 \text{ V}$ . The supporting electrolyte was 0.1 M 2-(*N*-morpholino)ethanesulfonic acid (MES) / 0.1 M NaCl buffer at pH 5.5. The volume of supporting electrolyte (around 5 ml) and the headspace volume (around 2 ml) were accurately measured for each single experiment. The different compartments of the cell and the electrolyte were degassed for 30 minutes before the PEC experiments. The amounts of evolved hydrogen were determined after two hours of chronoamperometry run by sampling 50  $\mu\text{l}$  of the headspace in Perkin Elmer Clarus 580 gas chromatograph equipped with a molecular sieve 5 A column (30m – 0.53 mm) and by micro-clark electrode in the electrolyte solution.<sup>5</sup>

**Linear sweep voltammograms (LSV).** Prior to the long-term chronoamperometric experiments, linear sweep voltammograms were recorded for each sensitized NiO film under

dark conditions (lamp off), then continuous irradiation (lamp on), then chopped light irradiation (lamp on-off), screening from + 0.5 V to - 0.5 V vs Ag/AgCl with a scan rate of 10 mV.s<sup>-1</sup>.

**X-ray Photoelectron Spectrometry (XPS).** XPS analyses were carried out with a Versa Probe II spectrometer (ULVAC-PHI) equipped with a monochromated Al K $\alpha$  source ( $h\nu = 1486.6$  eV). The core level peaks were recorded with a constant pass energy of 23.3 eV. The XPS spectra were fitted with CasaXPS 2.3.15 software using Shirley background and a combination of Gaussian (70%) and Lorentzian (30%) distributions. Binding energies were referenced with respect to the adventitious carbon (C 1s BE = 284.6 eV).

**Time-of-flight secondary ion mass spectrometry (ToF-SIMS).** ToF-SIMS measurements were recorded on a TRIFT III ToF-SIMS instrument from Physical Electronics operated with a pulsed 22 keV Au<sup>+</sup> ion gun (ion current of 2 nA) rastered over a 300  $\mu\text{m} \times 300 \mu\text{m}$  area. An electron gun was operated in pulsed mode at low electron energy for charge compensation. The ion dose was kept below the static conditions limit. Data were analyzed using the WinCadence<sup>TM</sup> software. Mass calibration was performed on hydrocarbon secondary ions.

**MALDI-ToF mass spectrometry.** The mass spectra were acquired in positive ion mode on a Bruker Microflex LRF mass spectrometer equipped with a 337 nm nitrogen laser and pulse delay extraction. The resolution was increased by using the reflector mode which allows to obtain the isotopic profile. The matrix was prepared as saturated solution of  $\alpha$ -cyano-4-hydroxycinnamic acid (HCCA) in 7:3 acetonitrile/water (v/v). Sample (1  $\mu\text{L}$ ) was added to 1  $\mu\text{L}$  of the matrix solution and spotted on a polished stainless target plate using the dried droplet method. Mass spectra were calibrated using reference peptides mixture of known masses.

**Transient absorption spectroscopy and spectroelectrochemistry.**

*fs-TA spectroscopy.* A custom-built setup was utilized to acquire fs-TA data. The TA setup is described in detail elsewhere.<sup>6</sup> A white-light supercontinuum probe pulse at 1 kHz repetition rate was used to analyze the excited state dynamics. The supercontinuum was generated by focusing a minor part of the output of the Ti:Sapphire amplifier onto a CaF<sub>2</sub> plate mounted on a rotating stage and after generation, it was split into a probe and reference beam. Using a concave mirror, the probe pulse was focused onto the sample. The spectra of probe and reference were detected by a Czerny-Turner spectrograph of 150 mm focal length (SP2150, Princeton Instruments) equipped with a diode array detector (Pascher Instruments AB,

Sweden). The pump pulses used were of 400 nm wavelength and a pulse duration of approximately 100 fs. The repetition rate of the pump pulses was reduced to 0.5 kHz by a mechanical chopper and the polarization adjusted to the magic angle of  $54.7^\circ$  by a Berek compensator and a polarizer. The data was analyzed using a customized data analysis software written by Jens Uhlig (Lund University). First, the data was corrected for the chirp and subsequently, a sum of exponential functions was fitted to the data. The artifact region of  $\pm 1$  ps was removed from the data during the fitting process to exclude the coherent artefacts present in this temporal region.

*ns-TA spectroscopy.* The setup for ns transient absorption measurements was previously described.<sup>7</sup> The pump pulse was generated by a Continuum Surelite OPO Plus (pumped by a Nd:YAG laser,  $\approx 20$  ns pulse duration, 10 Hz repetition rate). The probe light was generated by a 75 W Xenon arc lamp and focussed through the sample and detected by a Hamamatsu R928 photomultiplier. The signal was amplified and processed by a commercially available detection system (Pascher Instruments AB, Sweden). The measurements were performed upon 410~nm (2.0 W) at sample (**RuP<sub>4</sub><sup>OEt</sup>-EPIP** and **RuP<sub>4</sub>-Co**) concentrations of 15  $\mu\text{M}$  (OD at  $\lambda_{\text{exc}} \approx 0.25$ ) in acetonitrile and upon addition of 1 molar equivalent of triethylamine (TEA).

*Preparation of NiO films for spectroelectrochemistry.* NiO films were prepared using a F108 precursor solution prepared by mixing 2 g of NiCl<sub>2</sub>, 2 g of F108 triblock copolymer in a mixture of ethanol (15 mL) and Milli-Q water (6 mL), according to our previously reported procedure.<sup>8</sup> The mixture was sonicated for 6 h, centrifuged and passed through a 45  $\mu\text{m}$  pore size polyethersulfone syringe filter. Round ITO-coated glass substrates (Solems ITO SOL 30, 1 mm thickness) were cleaned by sonication in isopropanol, distilled water and ethanol for 10 min each. The F108 precursor solution was then spin-coated on the substrates (5000 rpm, 60 s) followed by sintering in an oven in air (30 min ramp to 450  $^\circ\text{C}$ , 30 min at 450  $^\circ\text{C}$ ). Spin-coating and sintering was repeated for a total of four layers. The NiO films were then soaked in methanolic solutions (0.2 mM) of **RuP<sub>4</sub>-EPIP** and **RuP<sub>4</sub>-Co** at room temperature for 24 h. After sensitization, films were rinsed with methanol and dried with pressured air. To deprotonate the initially protonated species that results from the synthesis, the films were then soaked in distilled water for 5 minutes and rinsed with dry acetonitrile.

*TA-SEC measurements.* TA-SEC experiments on films were performed using a home-built spectroelectrochemical cell, designed to work in a three-electrode setup under inert conditions and to optimize time resolution in the fs measurements, with a minimized path length (ca. 4 mm). The sensitized NiO film was used as the working electrode, a miniature leakless Ag/AgCl

electrode (EDAQ) as reference electrode and a Pt wire as auxiliary electrode. The cell was assembled in a glove box and filled with 0.1 M TBABF<sub>4</sub> in ACN. Transient absorption measurements were performed at open circuit potential and different applied potentials on the same film, moving the film in the plane periodically to prevent photodegradation. Prior to each experiment, the reference electrode was calibrated using ferrocene. In the ns-TASEC experiments, the pump pulse ( $\lambda = 485$  nm) power was set to 0.2 mJ. To remove pump scatter, a 475 nm short pass and a 500 nm long pass edge filters were used for short and long wavelengths, respectively.

### Quantum chemical calculations.

All quantum chemical calculations determining structural and electronic properties of the present dyads comprising a ruthenium-based photosensitizer and cobalt-based hydrogen evolving photocatalyst were the Gaussian 16 program.<sup>9</sup>

Initially, the **RuP<sub>4</sub><sup>OMe</sup>-Co** dyad was investigated. This dyad is structurally closely related to **RuP<sub>4</sub><sup>OEt</sup>-Co** while the ethyl groups of the phosphoric acid ethyl esters were replaced by methyl groups to reduce the computational demand without affecting its photophysical properties. Fully relaxed equilibrium geometry of **RuP<sub>4</sub><sup>OMe</sup>-Co** was obtained within the singlet ground state at the density functional level of theory (DFT) by means of the B3LYP XC functional.<sup>10-11</sup> The def2-SVP basis<sup>12-13</sup> as well as the respective core potentials were applied for all atoms. A vibrational analysis was carried out to verify that a minimum on the potential energy (hyper-)surface (PES) was obtained.

Subsequently, excited state properties such as excitation energies, oscillator strengths and electronic characters were calculated within the Frack-Condon structure at the time-dependent DFT (TDDFT) level of theory. Therefore, the 100 lowest singlet excited states were calculated. Thereby, the same XC functional, basis set and core potentials were applied as for the preceding ground state calculations. Several joint spectroscopic-theoretical studies on structurally related complexes proved that this computational protocol enables an accurate prediction of ground and excited states properties with respect to experimental data, *e.g.* UV-vis absorption, resonance Raman spectra, (spectro-)electrochemical and electron transfer properties.<sup>14-21</sup> A balanced description of excited states featuring, *i.e.*, metal-to-ligand charge transfer (MLCT), ligand-to-metal charge transfer (LMCT), ligand-to-ligand charge transfer (LLCT), intra-ligand charge transfer (ILCT), intra-ligand (IL) and metal-centered (MC) character, as provided by the present computational setup, is essential to assess the photophysics of transition metal

complexes. Effects of interaction with a solvent (acetonitrile, ACN:  $\epsilon = 35.688$ ,  $n = 1.344$ ) were taken into account on the ground and excited states properties by the solute electron density (SMD) variant of the integral equation formalism of the polarizable continuum model.<sup>22-23</sup> The non-equilibrium procedure of solvation was used for the calculation of the excitation energies within the Franck-Condon point, which is well adapted for processes where only the fast reorganization of the electronic distribution of the solvent is important. All calculations were performed including D3 dispersion correction with Becke-Johnson damping.<sup>24</sup>

Furthermore, DFT and TDDFT simulations were performed in order to address the photoinduced electron transfer processes, eventually leading to the formation of the catalytic active species of **Ru-Co**, *i.e.* **RuP<sub>4</sub><sup>OMe</sup>-Co** without anchoring groups. Therefore, the equilibrium structure of **Ru-Co** was obtained at the DFT level of theory (using the same computational protocol as described for **RuP<sub>4</sub><sup>OMe</sup>-Co**) within several redox states, namely within the non-reduced singlet ground state  $^1[\text{Ru-Co}]^{2+}$ , as well as within the singly reduced doublet  $^2[\text{Ru-Co}]^+$ , and the doubly reduced singlet  $^1[\text{Ru-Co}]^0$  ground state.

In case of  $^1[\text{Ru-Co}]^{2+}$ , the excited state properties of the 100 lowest energy singlet excited states and the 100 lowest triplet states were determined at the TDDFT level of theory. These simulations allow to elucidate the nature of the spin-allowed singlet-singlet transitions underlying the absorption features of **Ru-Co** within the visible region as well as of the triplet states accessible upon ultra-fast intersystem crossing, *i.e.* upon 480-nm (2.58 eV) excitation. TDDFT reveals mainly three singlet excitations of metal-to-ligand charge transfer character ( $^1\text{MLCT}$ , into  $S_6$ ,  $S_9$  and  $S_{10}$ ), while the electron density is excited on surrounding coordination sphere of the Ru centre, *i.e.* into the lowest  $\pi^*$  orbitals of the bipyridine (bpy) ligands and the phenanthroline (phen)-based bridging ligand.

Reduction of  $^1[\text{Ru-Co}]^{2+}$  or its excited species ( $^1\text{MLCT}$  or  $^3\text{MLCT}$ ) yields  $^2[\text{Ru-Co}]^+$ . The fully relaxed doublet ground state, directly accessible from the equilibrium structure of  $^1[\text{Ru-Co}]^{2+}$ , localizes the ancillary electron in the former lowest unoccupied molecular orbital of one bpy ligand ( $\pi_{\text{bpy}}^*$ ,  $\text{bpy}^*$ ). TDDFT calculation on the lowest ten doublet states within this structure reveal two further states of interest, namely excitation into  $D_1$ , a formal ligand-to-ligand charge transfer (LLCT) mainly described by a transition  $\pi_{\text{bpy}}^*/\pi_{\text{phen}}^*$  as well as excitation into the  $D_4$  state. Excitation into  $D_4$  yields the singly reduced  $\text{Co}^{\text{II}}$  species by transferring the additional electron from the  $\pi_{\text{bpy}}^*$  into the  $d_z^2(\text{Co})$  orbital, or rather into  $\sigma_{\text{CoBr}}^*$ , thus lowering the bond order between the cobalt and the coordinated bromide ligands. These two excited states were fully relaxed by TDDFT using the external python-based optimizer pysisyphus<sup>25</sup> – interfaced

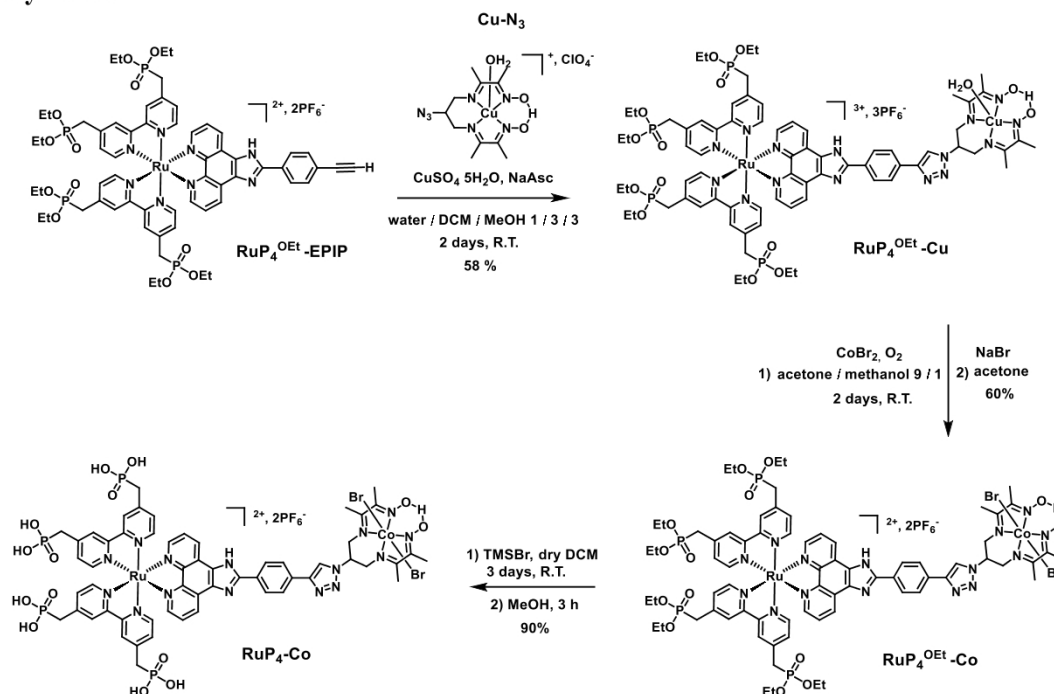
to Gaussian 16 – and equilibrate to ground state minima within their respective equilibria. The activation energy related to the thermally induced  $\pi_{\text{phen}}^*/\sigma_{\text{CoBr}}^*$  charge transfer – proceeding in the doublet ground state – was estimated along a linear-interpolated internal coordinate connecting the equilibrium structures of the respective donor and acceptor state.

As shown in the literature,  $\text{Co}^{\text{III}}/\text{Co}^{\text{II}}$  reduction leads to the dissociation of the two bromide ligands from the cobalt centre.<sup>26-27</sup> This finding is in agreement with our predictions as the population of a  $\sigma_{\text{CoBr}}^*$  orbital leads in consequence to an increase of the Co-Br bond length from 2.422 Å (and 2.418 Å) in  $^1[\text{Ru-Co}]^{2+}$  to 2.572 Å (and 2.539 Å) in the  $\text{Co}^{\text{II}}$  species of  $^2[\text{Ru-Co}]^+$ . Therefore, the  $\text{Co}^{\text{II}}$ -based catalyst structure as proposed by Artero and co-workers,<sup>26</sup> with the two  $\text{Br}^-$  ligands being dissociated and one ACN (solvent) molecule coordinated ( $^2[\text{Ru-Co(ACN)}]^{3+}$ ), as well as the structure proposed by Hammes-Schiffer and co-workers,<sup>27</sup> with two ACN (solvent) molecule coordinated ( $^2[\text{Ru-Co(ACN)}_2]^{3+}$ ), were used in the quantum chemical simulations related to the photoinduced electron transfer leading eventually to the catalytically active  $\text{Co}^{\text{I}}$  species. In a similar fashion as shown above on the first light-driven electron transfer yielding the  $\text{Co}^{\text{II}}$  species, the photophysics, reduction and subsequent electron transfer pathways potentially yielding the  $\text{Co}^{\text{I}}$  species were addressed. Therefore, the singly reduced  $\text{Co}^{\text{II}}$  species formed upon dissociation of the bromide ligands and coordination of one and two ACN molecule(s), *i.e.*  $^2[\text{Ru-Co(ACN)}]^{3+}$  and  $^2[\text{Ru-Co(ACN)}_2]^{3+}$ , were optimized at the DFT level of theory. Subsequently, the performed TDDFT calculations on the 500 lowest excited states allowed to assign the absorption features. The electronic transitions in resonance with the 480-nm laser excitation were found to be mainly in resonance with  $^2\text{MLCT}$  transitions from the  $\text{Ru}^{\text{II}}$  centre to the adjacent bpy and phen ligand spheres. The simulated electronic absorption spectra of  $^2[\text{Ru-Co(ACN)}_2]^{3+}$ ,  $^2[\text{Ru-Co}]^{+2}$  and  $[\text{Ru-Co(ACN)}]^{3+}$ , as shown in Figure 6d as well as in Figure S23d and S23g, yield very similar mixed  $^{(2)}\text{MLCT}_{\text{bpy}}$  and  $^{(2)}\text{MLCT}_{\text{phen}}$  transitions (see Tables S6 and S7) in the visible region in comparison to the non-reduced  $^1[\text{Ru-Co}]^{+2}$ , which was to be expected as the initial electronic configuration of the  $\text{Ru}^{\text{II}}$  photosensitizer is recovered upon reduction. However, in case of  $[\text{Ru-Co(ACN)}_2]^{3+}$  a partial contribution of the bridging ligand is predicted by TDDFT ( $D_{26}$  in Tables S6 and S7).

Reduction of  $^2[\text{Ru-Co(ACN)}_2]^{3+}$  or its optical accessible excited states ( $^2\text{MLCT}$ ) leads to the formation of a doubly reduced opened-shell singlet species ( $^1[\text{Ru-Co(ACN)}_2]^{2+}$ ) with one unpaired electron localized on one bpy ligand ( $\pi_{\text{bpy}}^*$ ,  $\text{bpy}^{\cdot-}$ ) and the other unpaired electron at the cobalt, *i.e.*  $\text{Co}^{\text{II}}$ . In a similar fashion as shown above for the first reduction step, three reduction sites ( $\text{bpy}^{\cdot-}$ ,  $\text{phen}^{\cdot-}$  and  $\text{Co}^{\text{I}}$ ) were identified and optimized at the (opened-shell) DFT and TDDFT levels using pysisyphus.<sup>25</sup> Noteworthy, a pronounced mixing of bpy and phen

contributions was observed in case of  $^1[\text{Ru-Co(ACN)}_2]^{2+}$ ; in consequence, only two reduction sites (bpy $^{\cdot-}$ /phen $^{\cdot-}$  and Co $^{\text{I}}$ ) were identified and optimized. The thermodynamics with respect to Co $^{\text{I}}$  formation via intramolecular electron transfer for are discussed in the manuscript in detail for  $^1[\text{Ru-Co(ACN)}_2]^{2+}$ . In case of  $^1[\text{Ru-Co(ACN)}]^{2+}$ , bpy and phen-based reductions are almost isoenergetic, while the reduction of the phenanthroline is slightly favoured - analogous as for the first electron transfer (Figures 6c/S23c). However, and in strong contradiction to the initial Co $^{\text{III}}$ /Co $^{\text{II}}$  reduction, the second reduction (Co $^{\text{II}}$ /Co $^{\text{I}}$ ) proceeds without a barrier, as the singlet ground state is always given by the closed-shell Co $^{\text{I}}$  species. In consequence, the driving force for the intramolecular electron transfer from the phen to the Co is with -1.15 eV more than two times higher in comparison to the first Co reduction.

## Synthesis

Scheme S1. Synthetic route to the RuP<sub>4</sub>-Co dyad.

**Synthesis of RuP<sub>4</sub><sup>OEt</sup>-Cu.** In an argon-purged round bottom flask, RuP<sub>4</sub><sup>OEt</sup>-EPiP (150 mg, 0.09 mmol) and CuN<sub>3</sub> (86 mg, 0.18 mmol) were dissolved in a 15 mL of a degassed homogeneous 3:3:1 MeOH/CH<sub>2</sub>Cl<sub>2</sub>/H<sub>2</sub>O solvent mixture. Sodium ascorbate (93 mg, 0.46 mmol) and copper sulfate (11 mg, 0.05 mmol) were added under argon and the reaction mixture was stirred at room temperature under argon in the dark over the weekend. After evaporation of the organic solvents and dropwise addition of 5ml saturated KPF<sub>6</sub> aqueous solution, the orange solution was extracted with dichloromethane and dried under vacuum. The crude product was purified by column chromatography on silica gel (MeCN/0.4 M aqueous KNO<sub>3</sub>, 80:20). The organic solvents were evaporated and the product was extracted with dichloromethane after the dropwise addition of 5 ml of saturated KPF<sub>6</sub> aqueous solution. After evaporation of dichloromethane and drying under vacuum, RuP<sub>4</sub><sup>OEt</sup>-Cu was isolated as a dark orange powder. Yield: 58 % (110 mg). ESI-MS: m/z 559.3 [M-H<sub>2</sub>O-3PF<sub>6</sub>]<sup>3+</sup>, 838.3 [M-H<sub>2</sub>O-3PF<sub>6</sub>]<sup>2+</sup>, 911.0 [M-H<sub>2</sub>O-2PF<sub>6</sub>]<sup>2+</sup>. HR-MS (ESI+): m/z calcd for C<sub>72</sub>H<sub>90</sub>CuN<sub>15</sub>O<sub>14</sub>P<sub>4</sub>Ru 559.1355; found 559.1356 [M-3PF<sub>6</sub>]<sup>3+</sup>. E.A.: calcd for C<sub>72</sub>H<sub>93</sub>CuN<sub>15</sub>O<sub>15</sub>P<sub>8</sub>F<sub>24</sub>Ru: C, 37.98; H, 4.12; N, 9.23; found: C, 39.01; H, 4.53; N, 8.74.



**Synthesis of RuP<sub>4</sub><sup>OEt</sup>-Co. RuP<sub>4</sub><sup>OEt</sup>-Cu** (110 mg, 0.05 mmol) and CoBr<sub>2</sub> hydrate (100 mg, 0.45 mmol, 9 eq) were solubilized in a mixture of acetone/methanol 9 / 1 (15 ml) and stirred under air bubbling overnight. The organic solvents were evaporated and the crude product was purified by column chromatography on silica gel using a 90:9:1 acetone/H<sub>2</sub>O/KBr (sat. aq. solution) eluent mixture. The organic solvents were evaporated and the product was extracted with dichloromethane after the dropwise addition of a saturated KPF<sub>6</sub> aqueous solution. After evaporation of dichloromethane and drying under vacuum, **RuP<sub>4</sub><sup>OEt</sup>-Co** was isolated as an orange powder. Yield: 60 % (70 mg). <sup>1</sup>H NMR (300 MHz, CD<sub>3</sub>CN): δ (ppm) 19.35 (s, 1H), 9.67 (d, *J* = 8.1 Hz, 1H), 9.10 (d, *J* = 8.73 Hz, 1H), 8.66 (d, *J* = 8.7, 2H), 8.53 (s, 1H), 8.43 (d, *J* = 14.4, 4H), 8.12 (t, *J* = 8.28 Hz, 2H), 7.98 (d, *J* = 6.8 Hz, 2H), 7.81 – 7.76 (m, 4H), 7.52 (t, *J* = 4.6, 2H), 7.40 (d, *J* = 5.6, 2H), 7.16 (d, *J* = 6.2, 2H), 5.89 (t, *J* = 11.2, 1H), 4.78 – 4.57 (m, 4H), 4.1 – 3.88 (m, 16H), 3.46 – 3.29 (m, 8H), 2.64 – 2.57 (m, 12H), 1.22 – 1.1 (m, 24H). ESI-MS: *m/z* 584.8 [M-Br-2PF<sub>6</sub>]<sup>3+</sup>, 916.6 [M-2PF<sub>6</sub>]<sup>2+</sup>. HR-MS (ESI+): *m/z* calcd for C<sub>72</sub>H<sub>90</sub>Br<sub>2</sub>CoN<sub>15</sub>O<sub>14</sub>P<sub>4</sub>Ru 916.6239; found 916.6227 [M-2PF<sub>6</sub>]<sup>2+</sup>. E.A.: calcd for C<sub>72</sub>H<sub>91</sub>Br<sub>2</sub>CoN<sub>15</sub>O<sub>14</sub>F<sub>18</sub>P<sub>7</sub>Ru: C, 38.11; H, 4.04; N, 9.26; found: C, 39.21; H, 4.44; N, 8.93.

At the end of the synthesis, we observed that **RuP<sub>4</sub><sup>OEt</sup>-Co** was isolated under a protonated imidazole (ImH<sub>2</sub><sup>+</sup>) form (see acido-basic titration Figure S2). A similar observation was made for the Ru-imidazole precursor **RuP<sub>4</sub><sup>OEt</sup>-EPIP**. For a related Ru-imidazole complex, Aukauloo and coworkers determined pK<sub>a</sub> values of 3.1 for the first protonation (ImH<sub>2</sub><sup>+</sup> ↔ ImH) and of 8.7 for the second protonation (ImH ↔ Im<sup>+</sup>) of the imidazole group in aqueous solution.<sup>28</sup> *This supports that RuP<sub>4</sub><sup>OEt</sup>-Co is under its neutral Im form under our operating photoelectrochemical conditions (pH 5.5).* However, as the imidazole-protonation state might affect intramolecular electron transfer efficiencies (either photoinduced or thermal electron transfer processes), spectroscopic data were recorded in acetonitrile solution both in the absence and in the presence of 1 equivalent of base (triethylamine) and transient absorption – spectroelectrochemical (TA-SEC) measurements were recorded on sensitized films that have been washed with distilled water beforehand.

**Synthesis of RuP<sub>4</sub>-Co. RuP<sub>4</sub><sup>OEt</sup>-Co** (16 mg, 0.007 mmol) was added in an oven-dried schlenk under argon and was solubilized in 2 ml of dry dichloromethane. Under argon, TMSBr (21 μl, 0.17 mmol) was added and the reaction mixture was stirred at room temperature, under argon for 3 days. After evaporation of the solvent, 5 ml of methanol was added and the solution was stirred for 3 hours. The organic solvent was evaporated and the orange powder was dried under

vacuum. Yield: 90 % (13 mg). The deprotected dyad was then immediately employed for the NiO film sensitization.

The same procedure was used to prepare **RuP<sub>4</sub>-EPIP** from **RuP<sub>4</sub><sup>OEt</sup>-EPIP**.

**Film sensitization.** F108-templated NiO films were prepared according to our previously reported procedure.<sup>8</sup> Sensitization was achieved by soaking them for 24h in 0.1 mM **RuP<sub>4</sub>-Co** or **RuP<sub>4</sub>-EPIP** methanolic solutions. Keeping the NiO films in the grafting solution for 2 days or more did not increase the amount of grafted compound on the surface. Finally, the films were soaked in pure methanol to remove physisorbed compounds from the surface and dried under air flow.

**Determination of the surface concentration in RuP<sub>4</sub>-Co (or RuP<sub>4</sub>-EPIP).** Every film was cut in half after sensitization. One half was used to determine the surface concentration and the other half was used for the assessment of the PEC activity. The freshly grafted half of the film was dipped for 4 hours in 5 mL of 1 M phenylphosphonic acid methanolic solution in order to desorb the dyad from the surface, according to a previously reported procedure.<sup>29-30</sup> The UV-Visible absorption spectrum of the desorption solution was then recorded to determine the amount of grafted complex from the molar extinction coefficient at the MLCT band. It should be noted that  $\epsilon$  values were determined for **RuP<sub>4</sub>-Co** and **RuP<sub>4</sub>-EPIP** (Figure S4) in 1 M phenylphosphonic acid methanolic solution. Knowing the surface concentrations in **RuP<sub>4</sub>-Co** allowed us to calculate turn-over numbers (TON) based on the amount of catalyst present at the surface of the film.

A similar desorption procedure was applied to the other half of the film after the PEC measurements for post-operando analysis.

**Table S1.** Photophysical properties (recorded in acetonitrile, w/o 1 equivalent of triethylamine (TEA)) of  $\text{RuP}_4^{\text{OEt-EPIP}}$  and  $\text{RuP}_4^{\text{OEt-Co}}$ .

Complex	TEA	$\lambda_{\text{abs}}$ in nm ( $\epsilon$ in $\text{M}^{-1} \cdot \text{cm}^{-1}$ )	$\lambda_{\text{em}}$ in nm	$E^{00}$ in eV <sup>a</sup>	$\tau_{\text{em}}$ in ns <sup>b</sup>
$\text{RuP}_4^{\text{OEt-EPIP}}$	0 eq	290 (114 978), 462 (19 245)	621	2.00	170
	1 eq	290 (101289), 465 (19 222)	620	2.00	150
$\text{RuP}_4^{\text{OEt-Co}}$	0 eq	291 (121 535), 462 (20 612)	618	2.01	160
	1 eq	291 (103121), 463 (17 684)	620	2.00	150

a-  $E^{00}$  calculated from the maximum emission wavelength  $\lambda_{\text{em}}$  at room temperature.

b- Aerated conditions.

**Table S2.** Dyad loading in  $\text{RuP}_4\text{-Co}$  (in  $\text{nmol} \cdot \text{cm}^{-2}$ ) determined by the desorption procedure for 12 freshly grafted films; this corresponds to an average surface concentration of  $5.2 \pm 0.8 \text{ nmol} \cdot \text{cm}^{-2}$ .

F1	F2	F3	F4	F5	F6	F7	F8	F9	F10	F11	F12
5.5	5.1	5.8	4.2	5.3	6.4	5.6	4.7	3.3	6.1	5.5	5.2

**Table S3.** Photocurrent data analysis (photocurrent densities at +0.4 V vs RHE from LSV measurements recorded under chopped light irradiation for different sensitized NiO films).

		Dyad loading ( $\Gamma$ ; $\text{nmol} \cdot \text{cm}^{-2}$ )	Photocurrent density <sup>a</sup> ( $j$ ; $\mu\text{A} \cdot \text{cm}^{-2}$ )	TOF ( $\text{s}^{-1}$ ) <sup>b</sup>
<b>400-800 nm</b>	NiO  $\text{RuP}_4\text{-Co}$	6.4	42	0.07
		5.6	66	0.12
		4.7	65	0.14
	average		<b><math>58 \pm 11</math></b>	<b><math>0.11 \pm 0.03</math></b>
	NiO T1-Co <sup>c</sup>	8.2 <sup>c</sup>	<b>15<sup>c</sup></b>	<b>0.02</b>
<b>AM 1.5 Irradiation (IR filtered)</b>	NiO  $\text{RuP}_4\text{-Co}$	5,5	79	0.15
		4,2	88	0.22
		5,3	97	0.19
		3,3	78	0.24
		5,2	80	0.16
	average		<b><math>84 \pm 7</math></b>	<b><math>0.19 \pm 0.03</math></b>

a- Dark current subtracted.

b- Calculated using the formula:  $\text{TOF} = j / n.F.\Gamma$ , with  $j$  in  $\text{A} \cdot \text{cm}^{-2}$  ( $1 \text{ A} = 1 \text{ C} \cdot \text{s}^{-1}$ ),  $\Gamma$  in  $\text{mol} \cdot \text{cm}^{-2}$ ,  $n = 1$  electron transferred,  $F = 96\,485 \text{ C} \cdot \text{mol}^{-1}$ .

c- Data taken from our previous study.<sup>8</sup>

**Table S4.** Figures of merit determined from the photoelectrochemical (PEC) measurements (continuous irradiation for 2 hours; MES buffer, pH 5.5; applied potential: +0.14 V vs RHE): amount of H<sub>2</sub> produced, charge passed, faradaic efficiency (F.E.), turnover numbers (TONCo) and % of dyad/dye desorption from the post-operando characterisations.

Irradiation	Film	Surface Area (cm <sup>2</sup> )	Dyad (or dye) loading (nmol · cm <sup>-2</sup> )	H <sub>2</sub> in the headspace <sup>a</sup> (nmol)	H <sub>2</sub> in solution <sup>a</sup> (nmol)	Total H <sub>2</sub> (nmol)	Total H <sub>2</sub> (nmol · cm <sup>-2</sup> )	Charge passed (mC · cm <sup>-2</sup> )	F.E. (%)	TON	% desorp.
400-800 nm	NiO	3.3	—	0	3	3	1	2	7	—	—
	<i>average</i>	3.0	—	0	1	1	<1	3	3	—	—
	NiO RuP <sub>4</sub> -EPIP	3.2	3.7	2	13	15	5	9	10	—	79
	<i>average</i>	3.3	1.9	0	11	11	3	8	8	—	73
	NiO RuP <sub>4</sub> -Co	3.3	6.4	70	33	102	31	32	19	5	69
	<i>average</i>	3	5.6	57	21	78	26	22	23	4	85
Simulated AM 1.5G irradiation (IR filtered)	NiO	2.8	—	6	6	13	5	7	13	—	—
	<i>average</i>	2.6	—	4	9	13	5	8	12	—	—
	NiO RuP <sub>4</sub> -EPIP	2.6	4.2	6	30	36	14	13	20	—	—
	<i>average</i>	3.2	2.1	3	16	19	6	6	23	—	—
	NiO RuP <sub>4</sub> -Co	3.2	5.5	78	154	232	72	38	37	13	87
	<i>average</i>	2.5	3.3	74.1	53	127	51	42	23	15	—
	NiO RuP <sub>4</sub> -Co <sup>b</sup>	3.0	5.2	25 <sup>b</sup>	153 <sup>b</sup>	178 <sup>b</sup>	60 ± 9	45 ± 6	26 ± 7	13 ± 2	80 ± 6
	<i>average</i>					59 <sup>b</sup>		16 <sup>b</sup>	72 <sup>b</sup>	11 <sup>b</sup>	73 <sup>b</sup>

a- Measured by gas chromatography in the headspace and with a micro-Clark electrode in solution (See ref. 5). Of note, the respective concentrations strongly depend on the equilibration between the gas and the solution phases; this equilibration process will not be the same from one experiment to another due to subtle differences such as the equilibration time before the measurement or the amount of H<sub>2</sub> produced (which varies with the dyad loading).

b- After 30 min instead of two hours.

**Table S5.** Data obtained in the TA-SEC measurements including the initial ratio of the signal at 540 and 480 nm, the zero crossing time at 480 nm and the characteristic time constants obtained by fitting the data with multiexponential fits.

	Applied potential	$\left(\frac{\Delta mOD_{540nm}}{\Delta mOD_{480nm}}\right)_{t=2.5 ps}$	$t(\Delta mOD_{480nm} = 0) / ps$	$\tau_1 / ps$	$\tau_2 / ps$	$\tau_3$	$\tau_1 / \mu s$	$\tau_2 / \mu s$	$\tau_3 / \mu s$	Normalized integral DAS	$\tau_{ave} / \mu s$
<b>RuP4-EPIP</b>	OCP	0.39	3292	67	1074						
	-0.74 V vs. Fc <sup>+0</sup>	0.60	785	52	735		0.1	1.6	15	1	0.48
	-1.15 V vs. Fc <sup>+0</sup>	0.83	143	31	655	> 7	0.1	1.5	16	1	0.93
<b>RuP4-Co</b>	OCP	0.44	3091	67	952	ns					
	-0.74 V vs. Fc <sup>+0</sup>	0.97	588	69	1357		0.08	1.2	13	1	0.66
	-1.15 V vs. Fc <sup>+0</sup>	1.83	59	45	1470		0.08	1.2	13	1	0.77

**Table S6.** Excited state properties, such as electronic character, excitation energy, wavelength and oscillator strength, of the bright singlet excitations contributing to the UV/vis absorption of **RuP<sub>4</sub>OMe-Co** and **Ru-Co** in its non-reduced singlet ( $^1[\text{Ru-Co}]^{2+}$ ) and singly reduced doublet ( $^2[\text{Ru-Co}]^+$ ,  $^2[\text{Ru-Co}(\text{ACN})]^{3+}$  and  $^2[\text{Ru-Co}(\text{ACN})_2]^{3+}$ ) species obtained at the time-dependent density functional level of theory (B3LYP/def2-svp) including D3BJ dispersion correction and solvent effects (ACN) by a polarizable continuum model. Additionally, the energies of spin-forbidden singlet-to-triplet transitions are given for  $^3\text{MLCT}$  states accessible upon inter-system crossing within the Franck-Condon point (optimized singlet ground state) of  $^1[\text{Ru-Co}]^{2+}$ . Electronic characters of selected transitions are visualized by charge density differences (CDDs) in Table S2.

<b>RuP<sub>4</sub>OMe-Co</b>						
State	Character	$E / \text{eV}$	$\lambda / \text{nm}$	$f$	$\lambda_{\text{exp}} / \text{nm}$	$\langle s^2 \rangle$
S <sub>7</sub>	MLCT <sub>bpy/phen</sub>	2.68	462	0.0988	460	0.00
S <sub>9</sub>	MLCT <sub>phen/bpy</sub>	2.78	447	0.1544	460	0.00
S <sub>10</sub>	MLCT <sub>bpy</sub>	2.84	437	0.2090	435	0.00
<b><math>^1[\text{Ru-Co}]^{2+}</math></b>						
State	Character	$E / \text{eV}$	$\lambda / \text{nm}$	$f$	$\lambda_{\text{exp}} / \text{nm}$	$\langle s^2 \rangle$
S <sub>6</sub>	MLCT <sub>bpy/phen</sub>	2.69	460	0.0853	460	0.00
S <sub>9</sub>	MLCT <sub>phen/bpy</sub>	2.82	440	0.2504	460	0.00
S <sub>10</sub>	MLCT <sub>bpy</sub>	2.86	434	0.1225	435	0.00
T <sub>7</sub>	MLCT <sub>phen</sub>	2.33	532	-	-	2.00
T <sub>9</sub>	MLCT <sub>bpy</sub>	2.34	530	-	-	2.00
T <sub>11</sub>	MLCT <sub>bpy</sub>	2.37	523	-	-	2.00
T <sub>12</sub>	MLCT <sub>phen/bpy</sub>	2.38	520	-	-	2.00
T <sub>13</sub>	MLCT <sub>bpy/phen</sub>	2.48	500	-	-	2.00
T <sub>14</sub>	MLCT <sub>bpy</sub>	2.51	493	-	-	2.00
T <sub>15</sub>	MLCT <sub>phen</sub>	2.58	480	-	-	2.00
T <sub>16</sub>	MLCT <sub>bpy</sub>	2.61	476	-	-	2.00
T <sub>17</sub>	MLCT <sub>bpy</sub>	2.64	469	-	-	2.00
T <sub>18</sub>	MLCT <sub>phen</sub>	2.68	463	-	-	2.00
<b><math>^2[\text{Ru-Co}]^+</math></b>						
State	Character	$E / \text{eV}$	$\lambda / \text{nm}$	$f$	$\lambda_{\text{exp}} / \text{nm}$	$\langle s^2 \rangle$
D <sub>75</sub>	MLCT <sub>bpy</sub>	2.64	470	0.0865	-	0.76
D <sub>89</sub>	MLCT <sub>bpy</sub>	2.77	448	0.2389	-	0.81
D <sub>96</sub>	MLCT <sub>bpy</sub>	2.82	440	0.1232	-	0.76
<b><math>^2[\text{Ru-Co}(\text{ACN})]^{3+}</math></b>						
State	Character	$E / \text{eV}$	$\lambda / \text{nm}$	$f$	$\lambda_{\text{exp}} / \text{nm}$	$\langle s^2 \rangle$
D <sub>26</sub>	MLCT <sub>phen/ILCT</sub>	2.68	462	0.0543	460	0.76
D <sub>38</sub>	MLCT <sub>bpy</sub>	2.93	423	0.0666	435	0.76
D <sub>41</sub>	MLCT <sub>bpy</sub>	2.96	419	0.2138	435	0.76
D <sub>43</sub>	ILCT/MLCT <sub>phen</sub>	3.08	402	0.2158	435	0.78
<b><math>^2[\text{Ru-Co}(\text{ACN})_2]^{3+}</math></b>						
State	Character	$E / \text{eV}$	$\lambda / \text{nm}$	$f$	$\lambda_{\text{exp}} / \text{nm}$	$\langle s^2 \rangle$
D <sub>21</sub>	MLCT <sub>phen/ILCT</sub>	2.55	486	0.0605	460	0.76
D <sub>36</sub>	MLCT <sub>phen/bpy</sub>	2.86	433	0.0496	435	0.76
D <sub>38</sub>	MLCT <sub>phen/bpy</sub>	2.93	423	0.0481	435	0.76
D <sub>41</sub>	MLCT <sub>bpy/phen</sub>	2.96	419	0.2108	435	0.82
D <sub>45</sub>	ILCT/MLCT <sub>phen</sub>	3.07	404	0.2232	435	0.84



**Table S7.** Charge density differences (CDDs) of the bright excitations contributing to the UV/vis absorption of  $\text{RuP}_4^{\text{OMe}}\text{-Co}$  and  $\text{Ru-Co}$  in its non-reduced singlet ( $^1[\text{Ru-Co}]^{2+}$ ) and singly reduced doublet ( $^2[\text{Ru-Co}]^+$ ,  $^2[\text{Ru-Co}(\text{ACN})]^{3+}$  and  $^2[\text{Ru-Co}(\text{ACN})_2]^{3+}$ ) species obtained at the time-dependent density functional level of theory (B3LYP/def2-svp) including D3BJ dispersion correction and solvent effects (ACN) by a polarizable continuum model. Additionally, the energies of spin-forbidden singlet-to-triplet transitions are given for  $^3\text{MLCT}$  states accessible upon inter-system crossing within the Frack-Condon point (optimized singlet ground state) of  $^1[\text{Ru-Co}]^{2+}$ . Charge transfer takes place from red to blue.

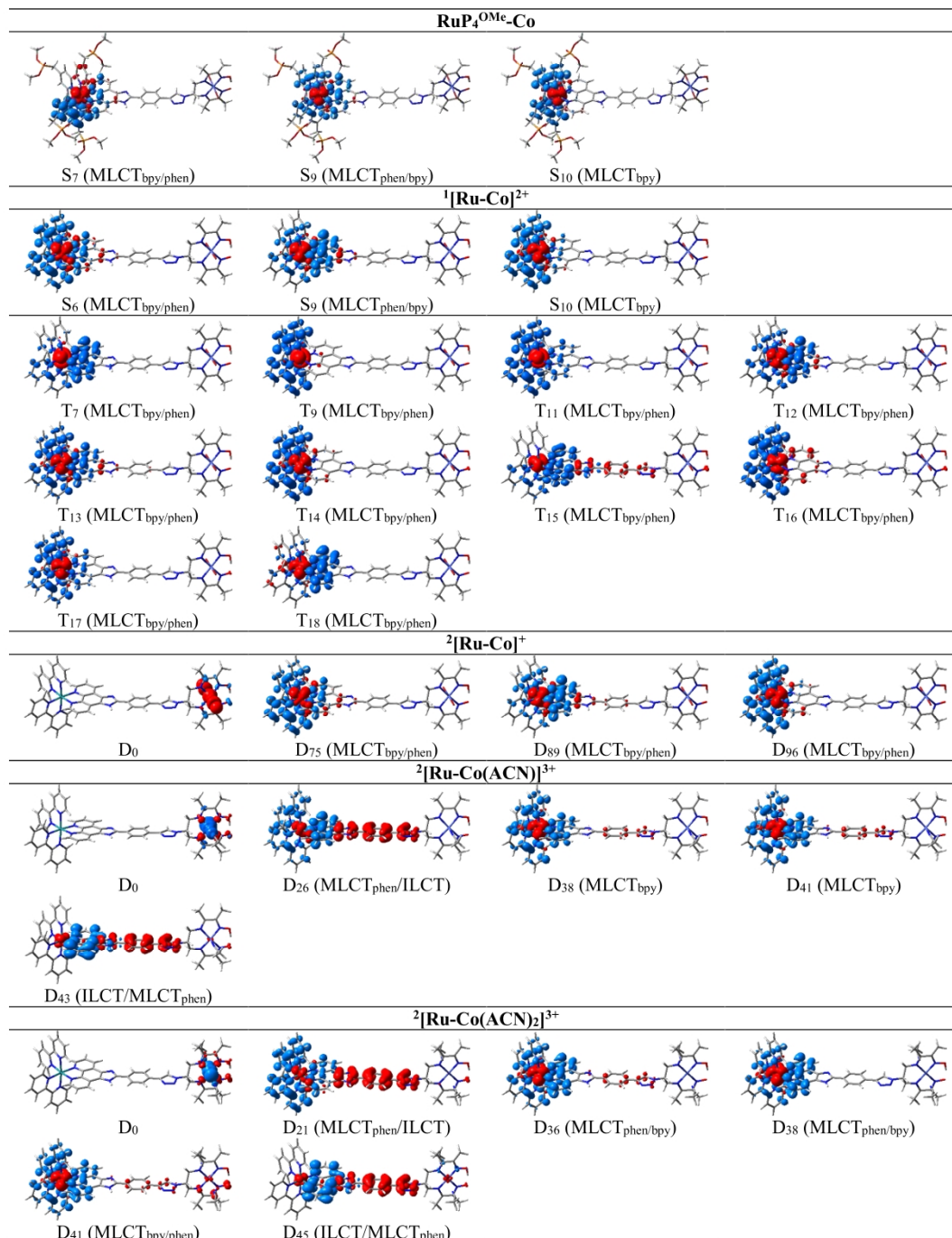


**Table S8.** Calculated bond lengths between the Co atom and the ancillary ligands (bromide vs. acetonitrile) given for the fully relaxed equilibrium structure of the respective intermediate.

	<b>Co<sup>III</sup></b> <b>(non-reduced singlet)</b>		<b>Co<sup>II</sup></b> <b>(singly reduced doublet)</b>		<b>Co<sup>I</sup></b> <b>(doubly reduced singlet)</b>	
	$d(\text{CoL}_1) / \text{\AA}$	$d(\text{CoL}_2) / \text{\AA}$	$d(\text{CoL}_1) / \text{\AA}$	$d(\text{CoL}_2) / \text{\AA}$	$d(\text{CoL}_1) / \text{\AA}$	$d(\text{CoL}_2) / \text{\AA}$
<b>RuP<sub>4</sub><sup>OMe</sup>-Co</b>	2.4218	2.4175	-	-	-	-
<b>Ru-Co</b>	2.4217	2.4178	2.5718	2.5389	dissociated (5.9649)	2.4785
<b>Ru-CoACN</b>	-	-	2.0609	-	1.9321	-
<b>Ru-CoACN<sub>2</sub></b>	-	-	3.3250	3.2218	3.8209	1.9218

**Table S9.** Relative concentrations of the different elements present in **RuP<sub>4</sub>-Co** vs Ni determined by XPS measurements recorded on freshly sensitized films and post-operando PEC measurements (second half of the same sensitized film).

	<b>Fresh</b>	<b>Post-operando</b>	<b>% loss</b>
<b>[Ni]<sub>at</sub>/[Ru]<sub>at</sub></b>	10.7	18.6	42 %
<b>[Ni]<sub>at</sub>/[P]<sub>at</sub></b>	4.1	6.1	33 %
<b>[Ni]<sub>at</sub>/[N]<sub>at</sub></b>	1.9	3.5	47 %





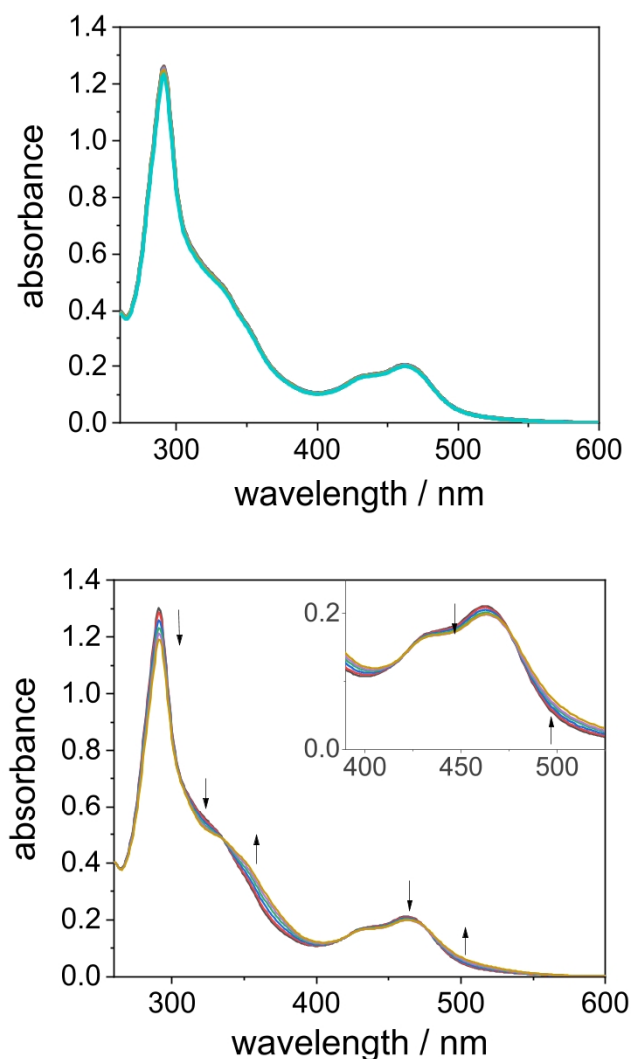


**Figure S2.** UV-visible absorption-monitored acid-base titration of **RuP<sub>4</sub><sup>OEt</sup>-Co** ( $1.1 \times 10^{-5}$  M in acetonitrile). Top: addition of 0 to 1 eq. of TFA (aliquots of 4.4  $\mu$ L from of a TFA stock solution  $10^{-3}$  M in acetonitrile; spectra corrected for dilution). Bottom: addition of 0 to 1 eq. of TEA (aliquots of 4.4  $\mu$ L from of a TEA stock solution  $10^{-3}$  M in acetonitrile; spectra corrected for dilution).

The absorption spectrum of **RuP<sub>4</sub><sup>OEt</sup>-Co** is not modified by addition of tetrafluoroacetic acid (TFA), suggesting that the imidazole ring is fully protonated (ImH<sub>2</sub><sup>+</sup> form) in the as-synthesized complex. In addition, the main absorption bands slightly decrease in intensity upon addition of triethylamine (TEA), while the shoulder at 350 nm and the tail at 500 nm increase. This behaviour is in full agreement with a previous study from A. Aukauloo and coworkers,<sup>28</sup> and is attributed to the deprotonation of the imidazole ring (ImH<sub>2</sub><sup>+</sup>  $\rightarrow$  ImH). Similar results were obtained with **RuP<sub>4</sub><sup>OEt</sup>-EPIP**.

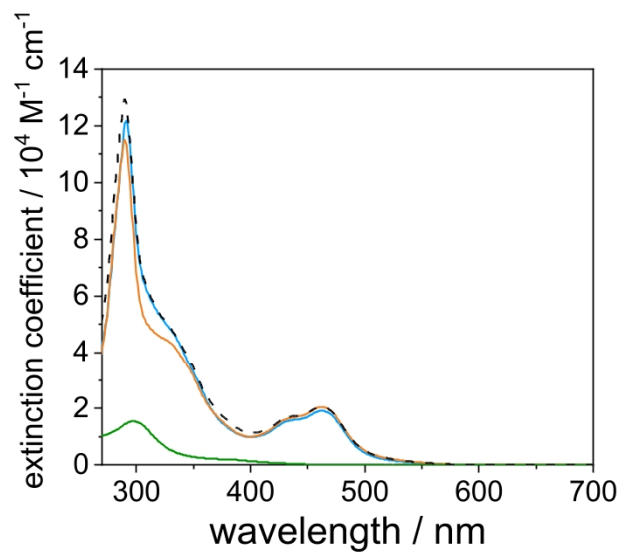


**Figure S3.** UV-vis absorption spectra of **RuP<sub>4</sub><sup>OEt</sup>-Co** (imidazole-protonated form, blue line), **RuP<sub>4</sub><sup>OEt</sup>-EPIP** (imidazole-protonated form, orange line), **CoN<sub>3</sub>** (green line) recorded in CH<sub>3</sub>CN; the sum of the absorption of **RuP<sub>4</sub><sup>OEt</sup>-Co** and **RuP<sub>4</sub><sup>OEt</sup>-EPIP** is presented as the dotted line.

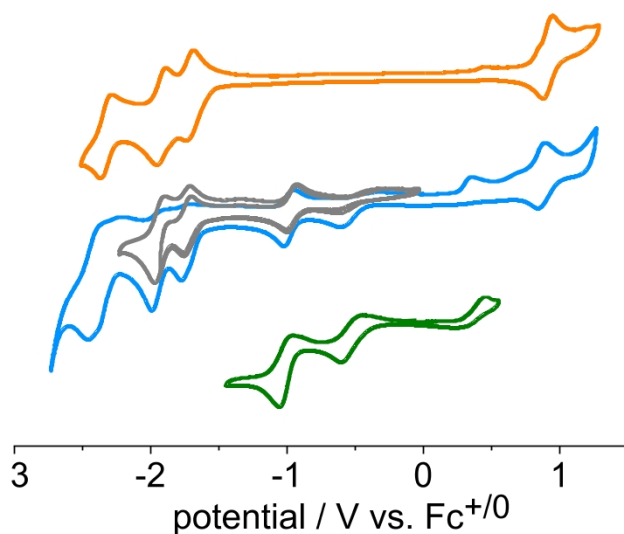


**Figure S4.** Cyclic voltammograms of **RuP<sub>4</sub><sup>OEt</sup>-Co** (imidazole-protonated form, blue and grey lines), **RuP<sub>4</sub><sup>OEt</sup>-EPIP** (imidazole-protonated form, orange line) and **CoN<sub>3</sub>** (green line). Measurements were carried out at 100 mV·s<sup>-1</sup> at a glassy carbon electrode in acetonitrile (0.1 M *n*Bu<sub>4</sub>NPF<sub>6</sub>).

According to the study by Aukauloo and coworkers,<sup>28</sup> the redox potentials of the Ru<sup>III/II</sup> couple and of the ligand-based reduction processes are almost unaltered upon remote protonation or deprotonation of the imidazole unit (see Table 2 in the quoted reference).

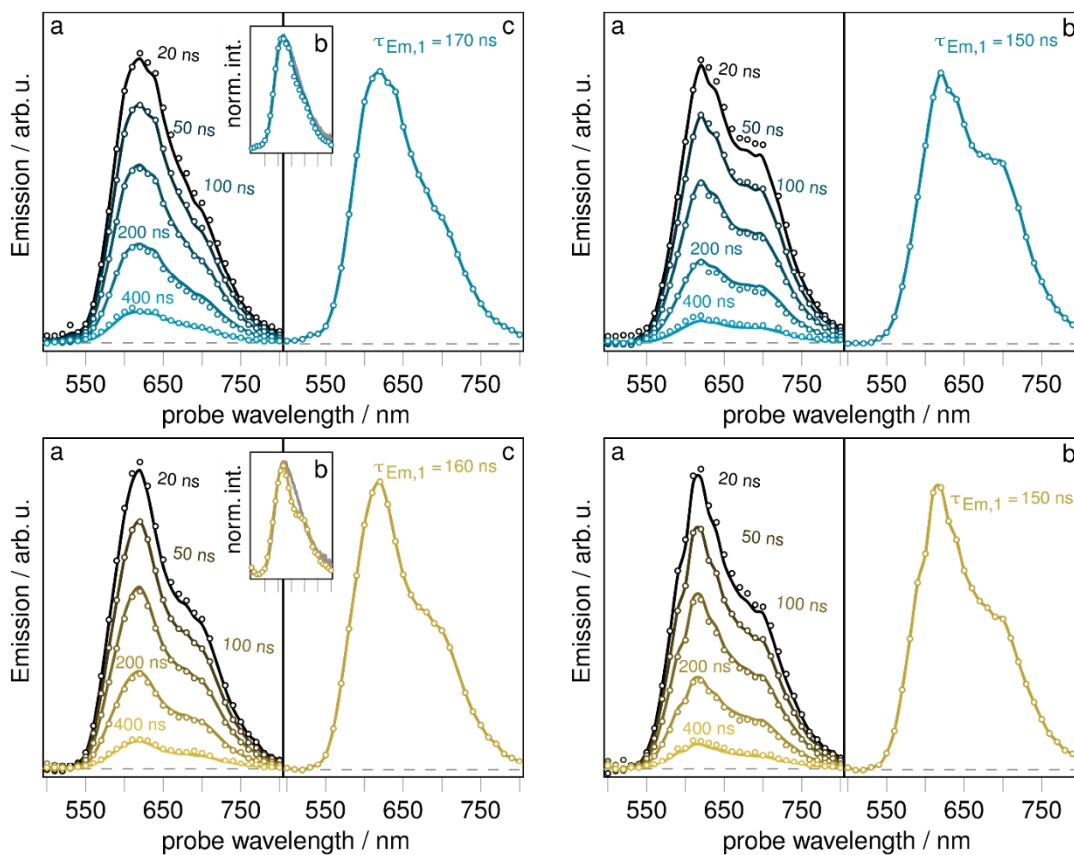


**Figure S5.** Nanosecond time-resolved emission spectra of  $\text{RuP}_4^{\text{OEt-ETIP}}$  (top) and  $\text{RuP}_4^{\text{OEt-Co}}$  (bottom) recorded in acetonitrile in the absence (left) and in the presence (right) of 1 equivalent of TEA. The spectra are collected upon excitation at 410 nm (2.0 mW).

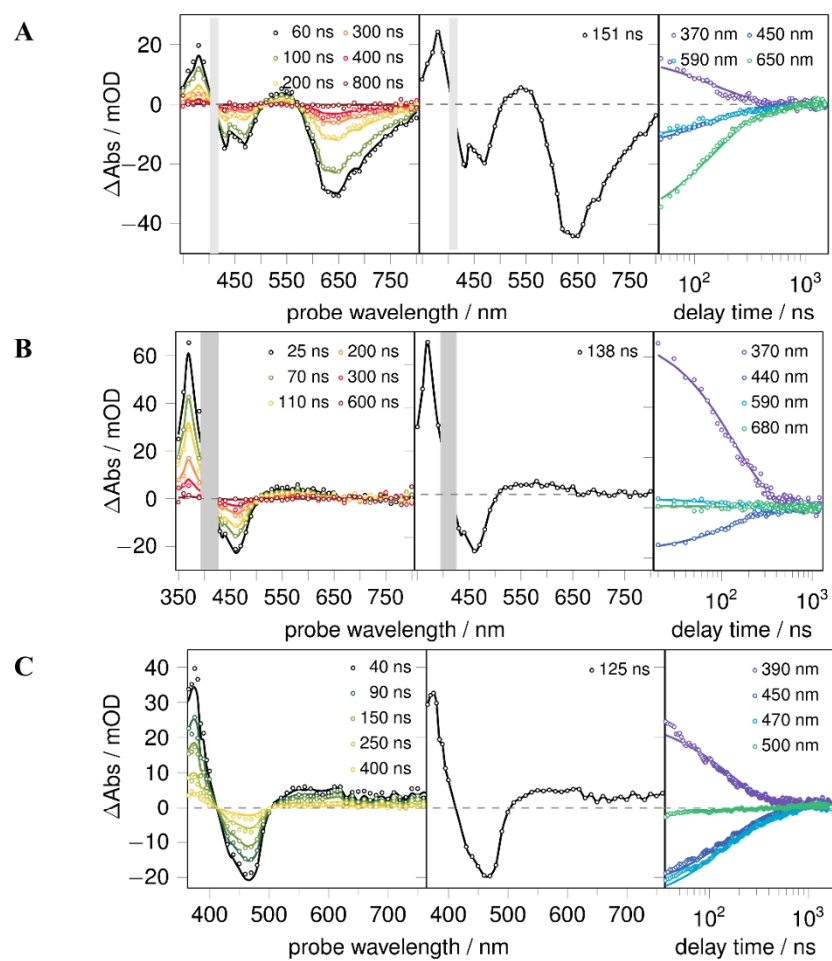


**Figure S6.** Nanosecond transient absorption spectra (left), decay associated spectra (middle) and kinetic traces at some selected probe wavelengths (right) of  $\text{RuP}_4^{\text{OEt}}\text{-EPiP}$  recorded in acetonitrile (top row, **A**), with correction for the stimulated emission (middle row, **B**), and in acetonitrile in the presence of 1 equivalent of TEA, with correction for the stimulated emission (bottom row, **C**). The spectra are collected upon excitation at 410 nm (2.0 mW).

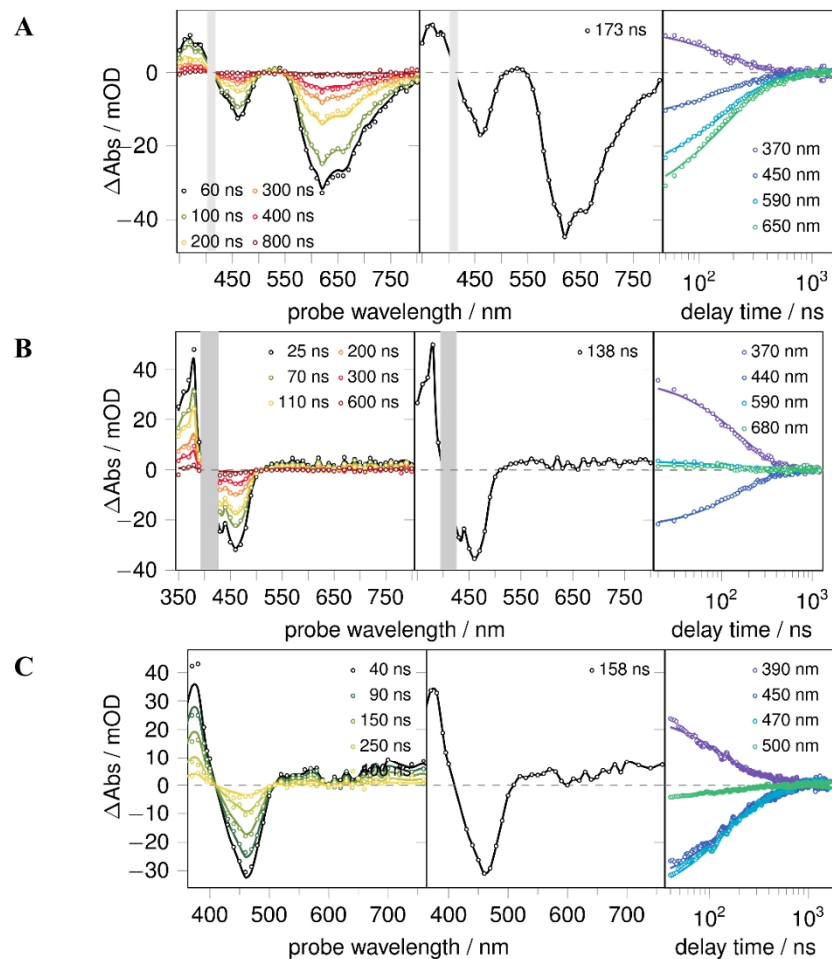


**Figure S7.** Nanosecond transient absorption spectra (left), decay associated spectra (middle) and kinetic traces at some selected probe wavelengths (right) of  $\text{RuP}_4^{\text{OEt-Co}}$  recorded in acetonitrile (top row, **A**), with correction for the stimulated emission (middle row, **B**), and in acetonitrile in the presence of 1 equivalent of TEA, with correction for the stimulated emission (bottom row, **C**). The spectra are collected upon excitation at 410 nm (2.0 mW).

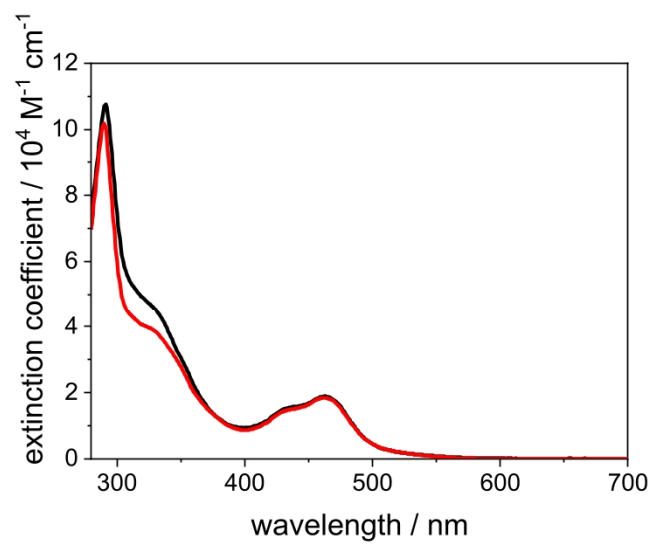


**Figure S8.** UV-vis absorption spectrum (epsilon curve) of **RuP<sub>4</sub>-Co** (black line) and **RuP<sub>4</sub>-EPIP** (red line) in 1 M phenylphosphonic acid methanolic solution.



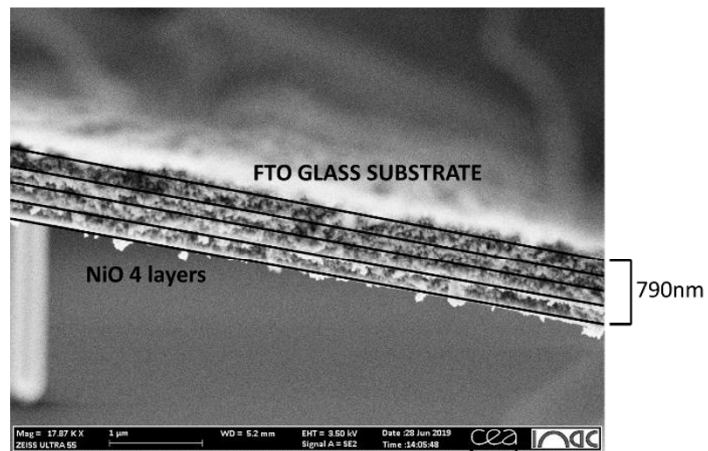


**Figure S9.** Scanning electron microscopy (SEM) image showing the four spin-coated layers of a mesoporous NiO film onto a FTO glass substrate with thickness of 790 nm. Depending on the NiO batches, thicknesses vary between 700 nm and 1  $\mu\text{m}$ .

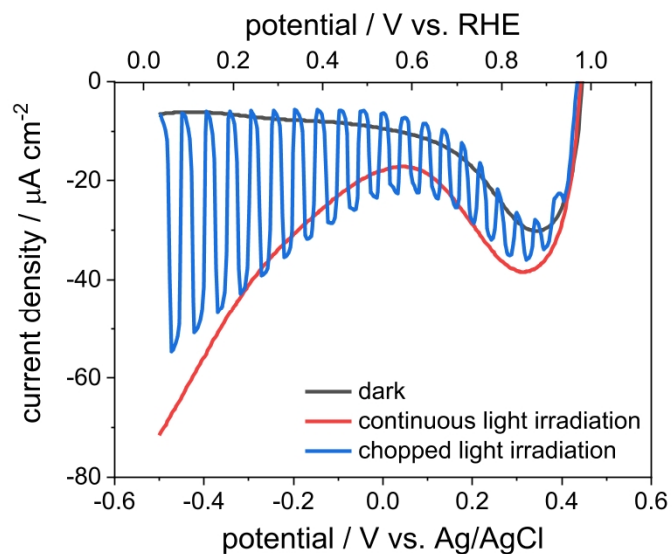


**Figure S10.** Linear sweep voltammogram recorded on a **RuP<sub>4</sub>-Co**-sensitized NiO electrode under dark conditions (black line), continuous irradiation (red line) and chopped light irradiation (blue line) in MES 0.1 M/NaCl 0.1M supporting electrolyte at pH 5.5. Irradiation conditions: visible light (400 – 800 nm).

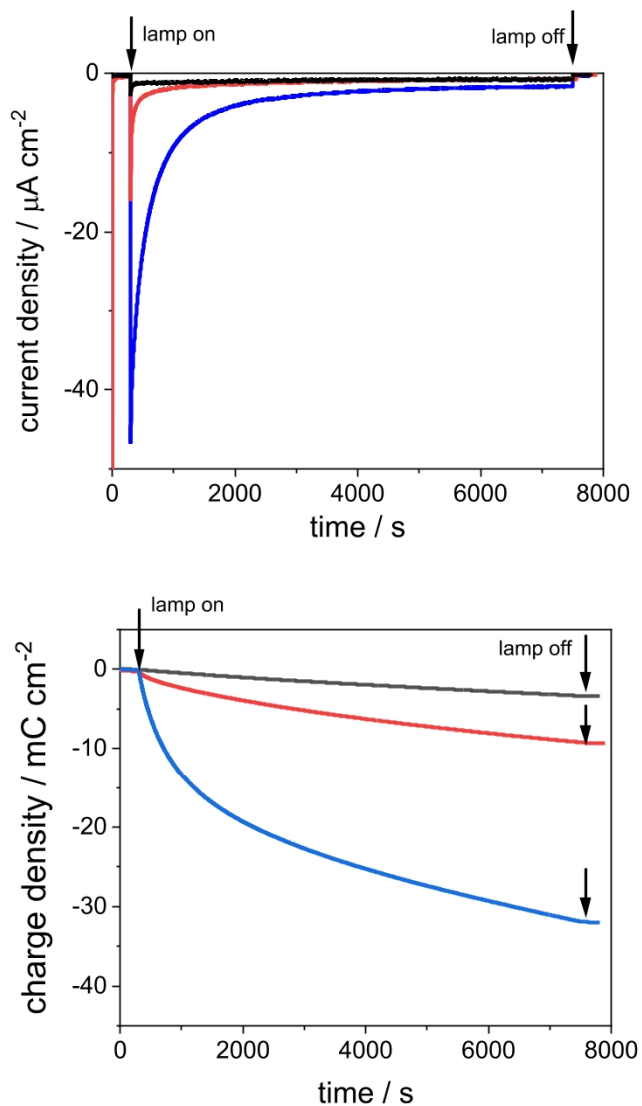


**Figure S11.** Photocurrent densities (top) and corresponding charges (bottom) recorded during the course of two-hour chronoamperometric measurements under continuous light irradiation at an applied potential of + 0.14 V vs RHE on a **RuP<sub>4</sub>-Co**-sensitized NiO electrode (blue line), a **RuP<sub>4</sub>-EPIP**-sensitized NiO electrode (red line) and a pristine NiO electrode (black line). *Irradiation conditions: visible light (400 – 800 nm).*

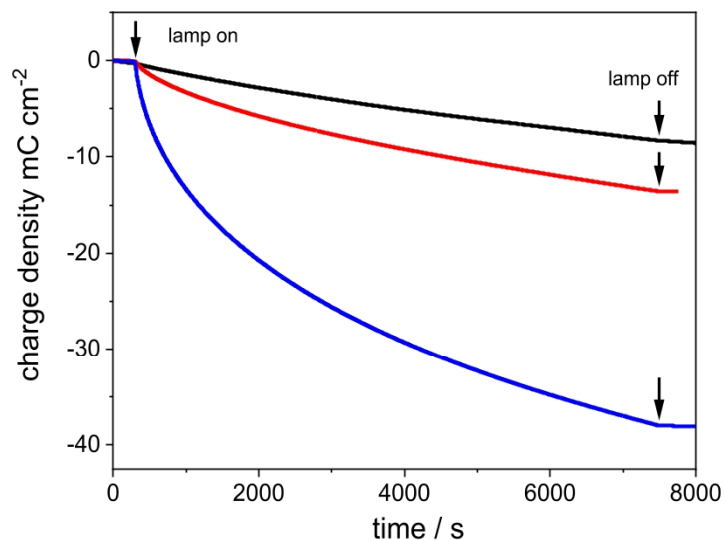


**Figure S12.** Charges recorded during the course of two-hour chronoamperometric measurements under continuous light at an applied potential of + 0.14 V vs RHE on a **RuP<sub>4</sub>-Co**-sensitized NiO electrode (blue line), a **RuP<sub>4</sub>-EPIP**-sensitized NiO electrode (red line) and a pristine NiO electrode (black line). *Irradiation conditions: simulated AM 1.5G (IR filtered).*

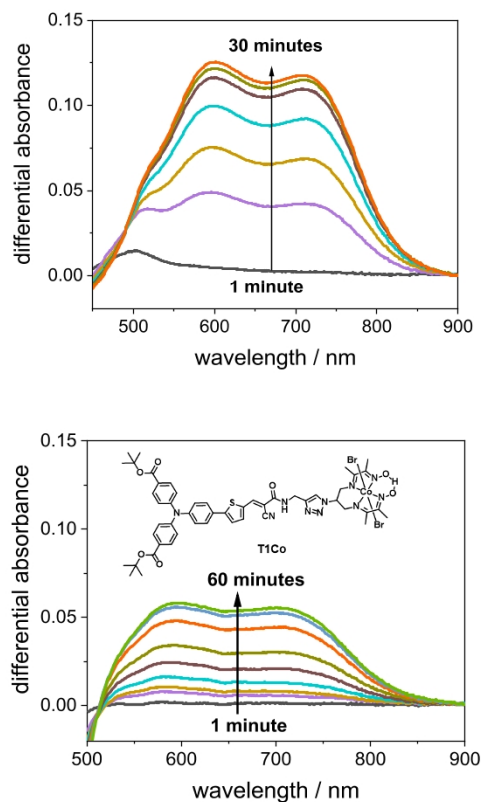


**Figure S13.** UV-vis monitoring (differential absorbance) of the formation of the  $\text{Co}^{\text{I}}$  derivative for **RuP<sub>4</sub><sup>OEt</sup>-Co** (left) and for our previously-reported covalent dyad **T1-Co**, both at  $4.5 \times 10^{-5}$  M in  $\text{CH}_3\text{CN}/\text{TEOA}$  (90:10 v/v) upon visible-light irradiation (400 – 800 nm).

Of note, under these conditions, TEOA is employed as a sacrificial electron donor to generate the reduced dye via the reductive quenching of its excited state.

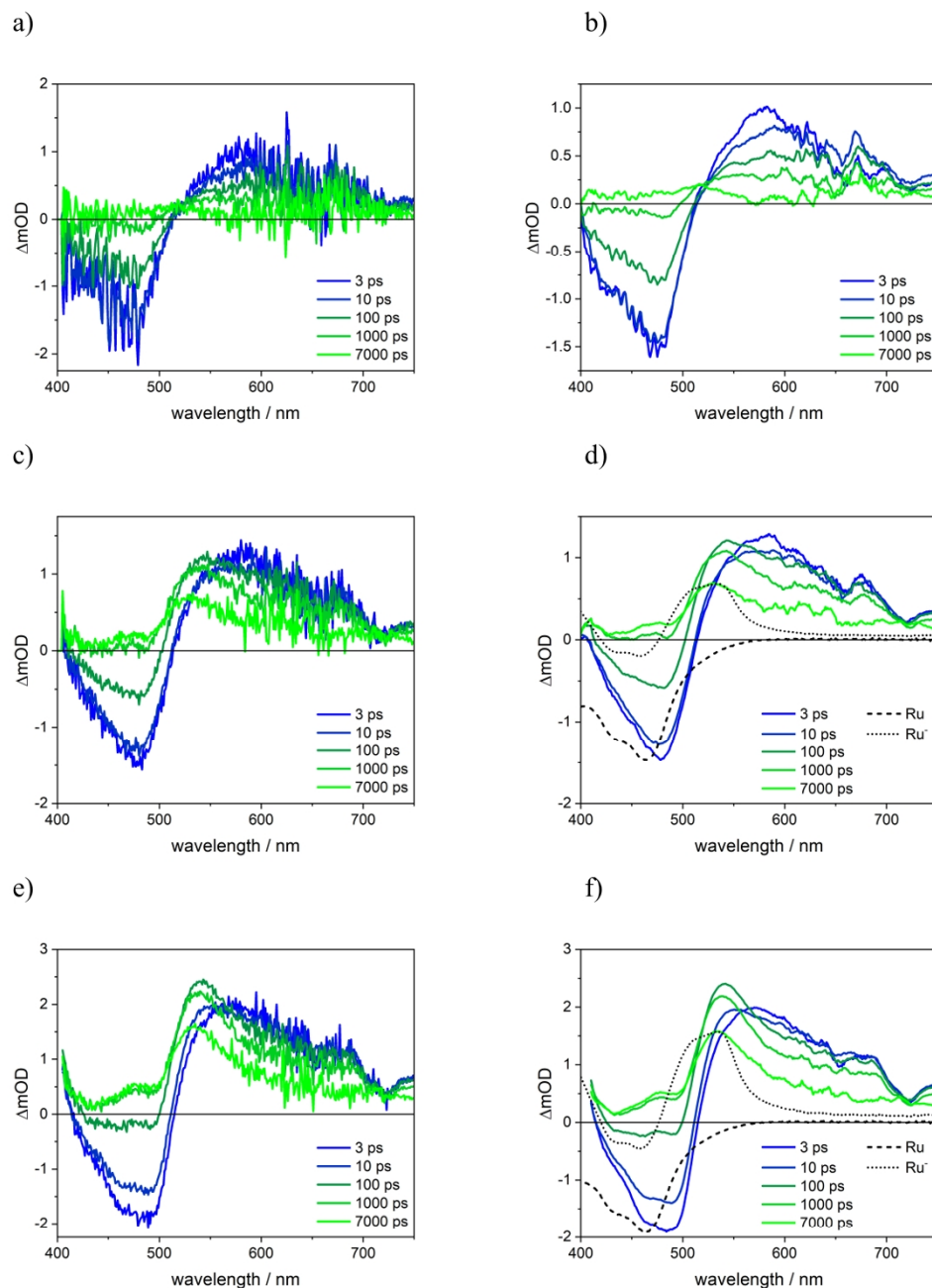


**Figure S14.** TA-SEC spectra of **RuP<sub>4</sub>-EPiP**-sensitized NiO films at early delays up to 7 ns at OCP (a-b),  $-0.74$  V vs.  $\text{Fc}^{+/0}$  (c-d) and  $-1.15$  V vs.  $\text{Fc}^{+/0}$  (e-f) applied potential. a,c,e show the raw data integrated over  $\pm 10\%$  of the given times while b,d,f show 10 point adjacent average smoothed versions of the former. The dashed lines show the inverted scaled absorption spectrum of **RuP<sub>4</sub><sup>OEt</sup>-EPiP** and the dotted lines show the scaled differential spectrum of one-electron reduced **RuP<sub>4</sub><sup>OEt</sup>-EPiP**.

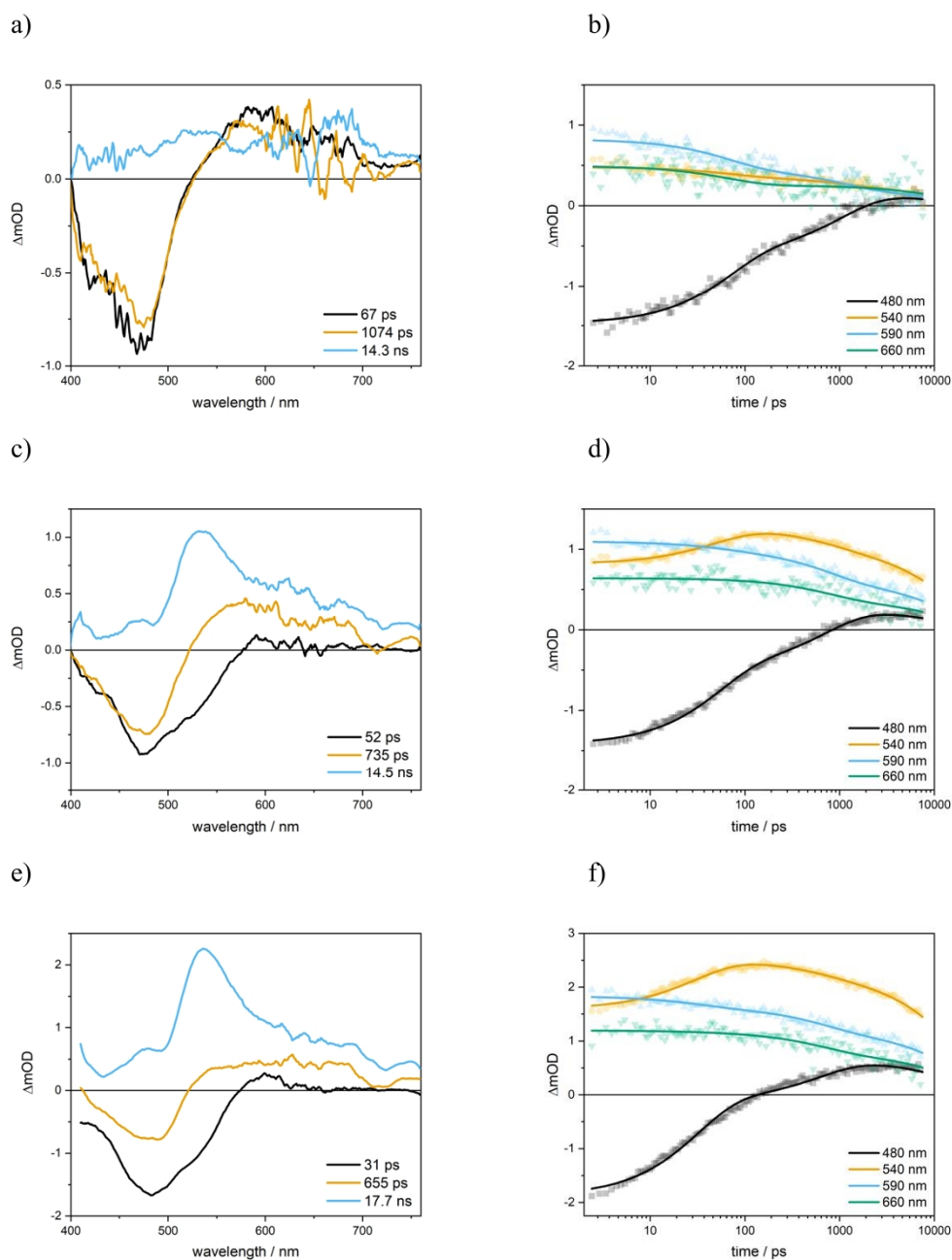


**Figure S15.** Decay-associated spectra (a,c,e) obtained via a three-component exponential fit to the transient absorption data of **RuP<sub>4</sub>-EPiP**-sensitized NiO films at early delays up to 7 ns and smoothed with a 10 point adjacent average smoothing. b,d,f show the kinetics traces at characteristic wavelengths (scatter) with the obtained fit (line), both of which were integrated over  $\pm 10$  nm. The data correspond to the situation at OCP (a-b),  $-0.74$  V vs.  $\text{Fc}^{+/0}$  (c-d) and  $-1.15$  V vs.  $\text{Fc}^{+/0}$  (e-f) applied potential.

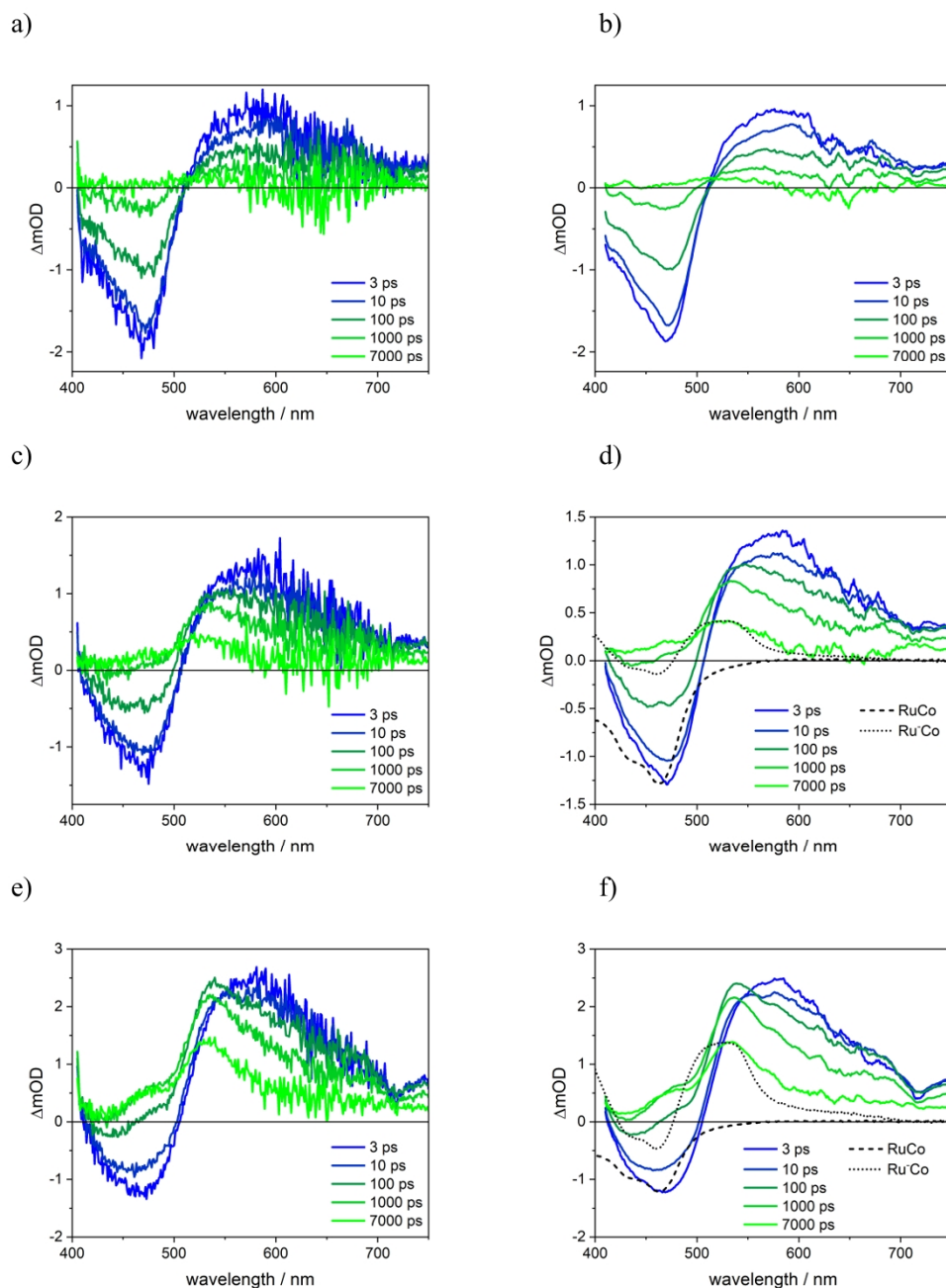


**Figure S16.** TA-SEC spectra of **RuP<sub>4</sub>-Co**-sensitized NiO films at early delays up to 7 ns at OCP (a-b),  $-0.74$  V vs.  $\text{Fc}^{+/0}$  (c-d) and  $-1.15$  V vs.  $\text{Fc}^{+/0}$  (e-f) applied potential. a,c,e show the raw data integrated over  $\pm 10\%$  of the given times while b,d,f show 10 point adjacent average smoothed versions of the former. The dashed lines show the inverted scaled absorption spectrum of **RuP<sub>4</sub>-Co** and the dotted lines show the scaled differential spectrum upon one-electron reduction of the dye unit of **RuP<sub>4</sub>-Co**.



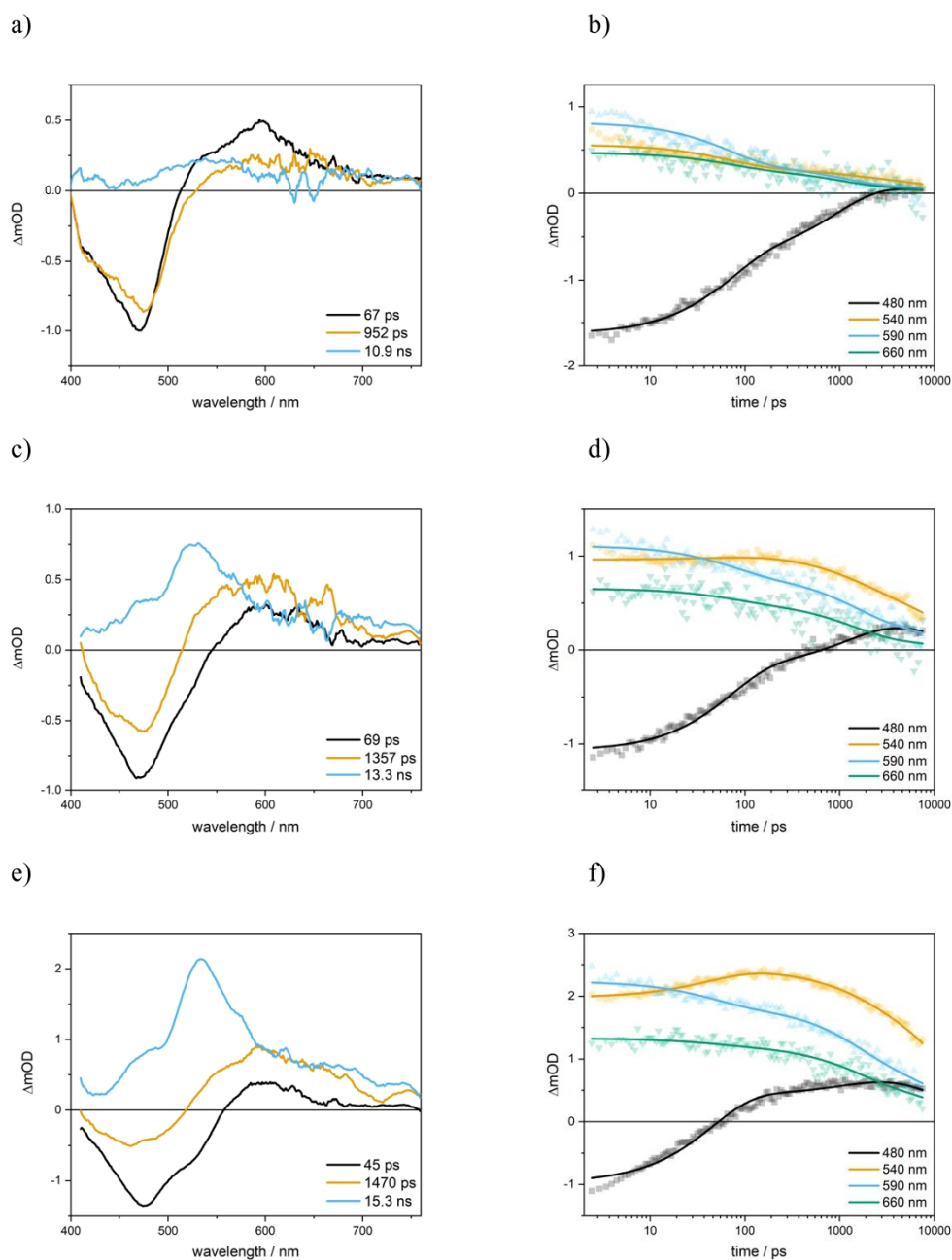


**Figure S17.** Decay-associated spectra (a,c,e) obtained via a three-component exponential fit to the transient absorption data of **RuP<sub>4</sub>-Co**-sensitized NiO films at early delays up to 7 ns and smoothed with a 10 point adjacent average smoothing. b,d,f show the kinetics traces at characteristic wavelengths (scatter) with the obtained fit (line), both of which were integrated over  $\pm 10$  nm. The data correspond to the situation at OCP (a-b),  $-0.74$  V vs.  $\text{Fc}^{+/0}$  (c-d) and  $-1.15$  V vs.  $\text{Fc}^{+/0}$  (e-f) applied potential.

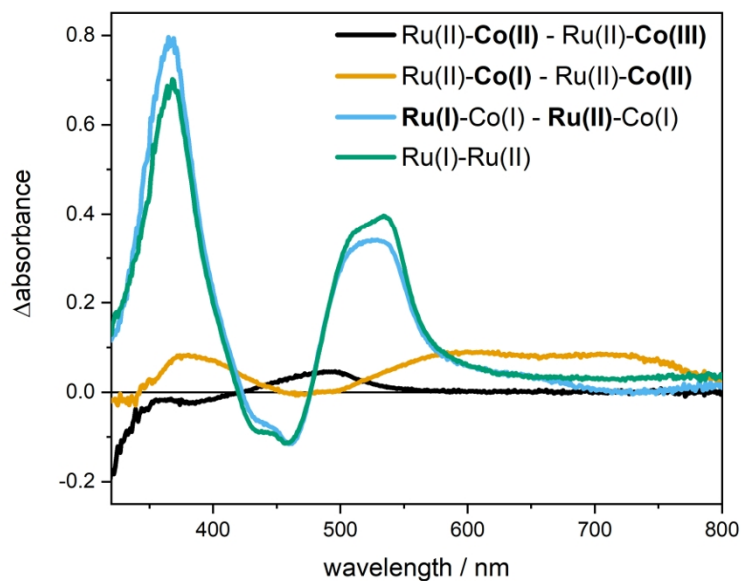


**Figure S18.** Differential UV-Vis spectra obtained by stepwise reduction of **RuP<sub>4</sub><sup>OEt</sup>-EPiP** and **RuP<sub>4</sub><sup>OEt</sup>-Co**. The spectra were obtained by subtracting the spectra obtained directly before reduction from the spectra obtained upon reduction to isolate the spectral changes upon each reduction step.

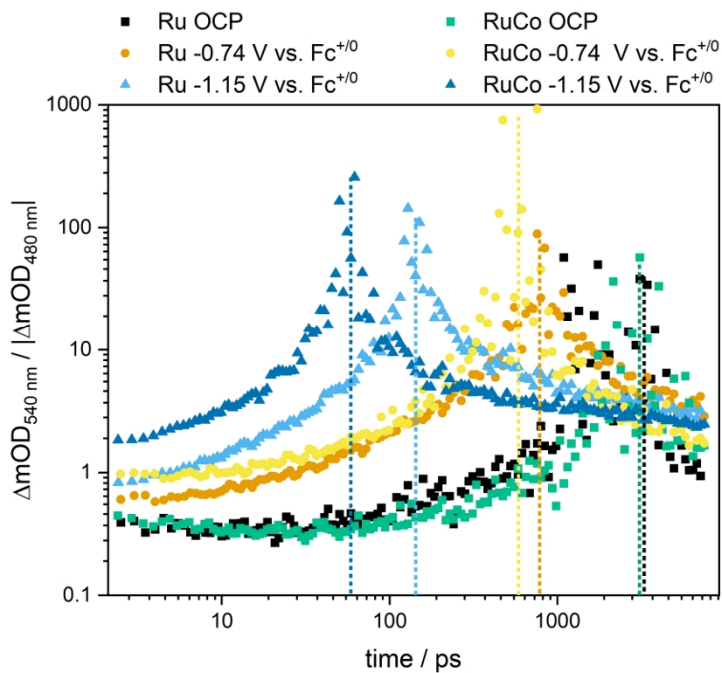


**Figure S19.** Ratio of transient absorption kinetics traces at 540 nm and 480 nm of **RuP<sub>4</sub>-EPIP-** and **RuP<sub>4</sub>-Co-**sensitized NiO films at different applied potentials. The vertical dotted lines mark the zero crossing of the 480 nm trace.

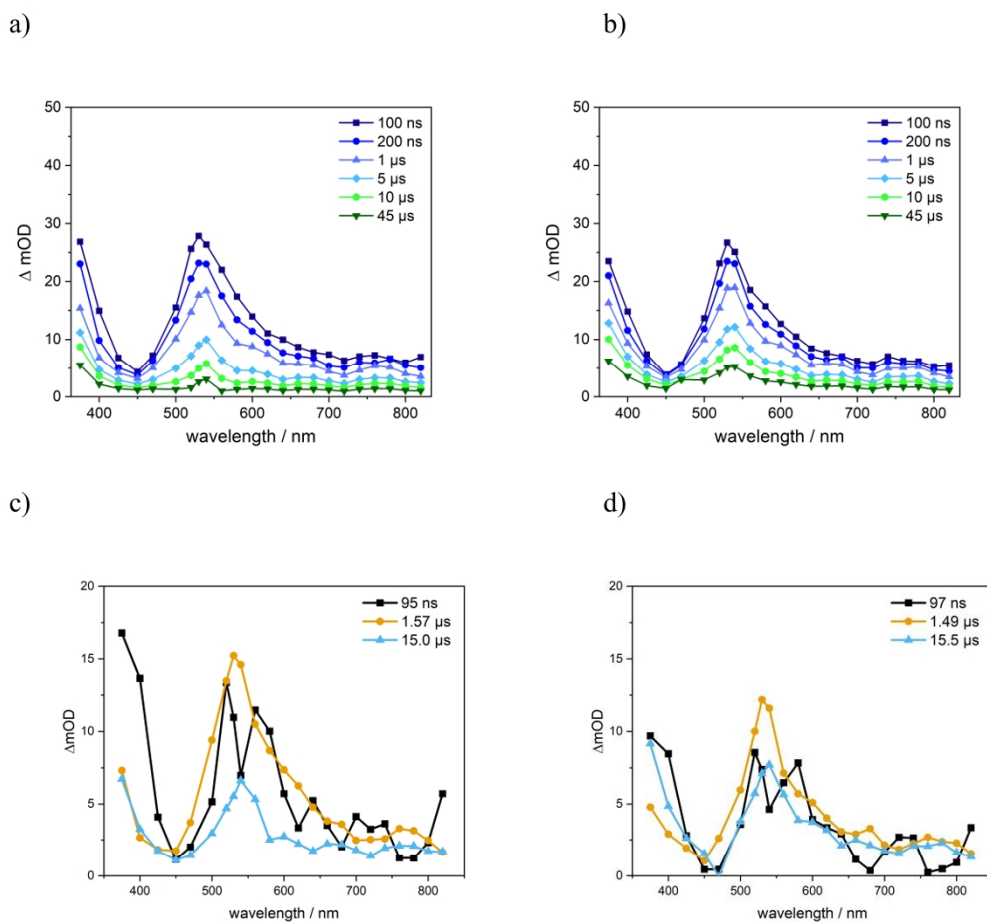


**Figure S20.** TA spectra (a-b) recorded in the ns- $\mu$ s range for **RuP<sub>4</sub>-EPIP**-sensitized Nio films and DAS obtained by a three-component exponential fit (c-d) at  $-0.74$  V (a,c) and  $-1.15$  V vs.  $\text{Fc}^{+/0}$  (b,d). To reduce noise, the data in the TA spectra was integrated over time between two time delays (such that the 200 ns spectrum is the integral from 100 to 200 ns etc).

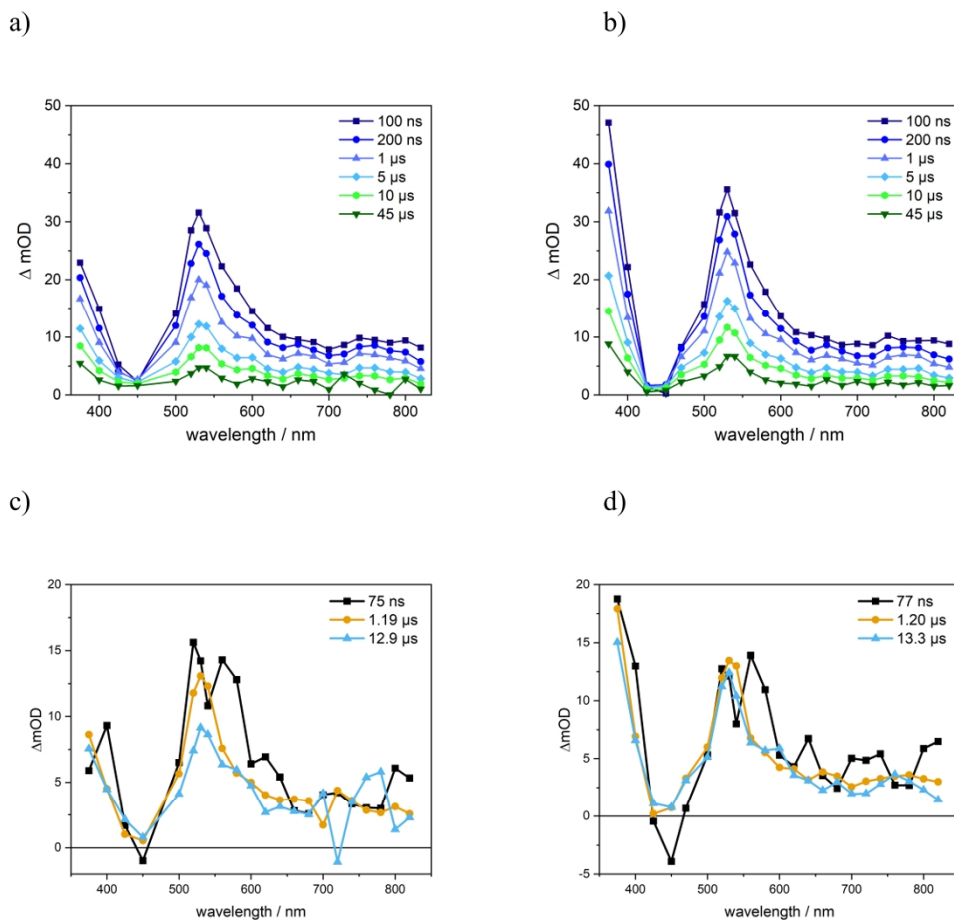


**Figure S21.** Transient absorption spectra (a-b) recorded in the ns- $\mu s$  range for RuP<sub>4</sub>-Co-sensitized NiO films and DAS obtained by a three-component exponential fit (c-d) at  $-0.74$  V (a,c) and  $-1.15$  V vs. Fc<sup>+0</sup> (b,d). To reduce noise, the data in the TA spectra were integrated over time between two time delays (such that the 200 ns spectrum is the integral from 100 to 200 ns, etc...).

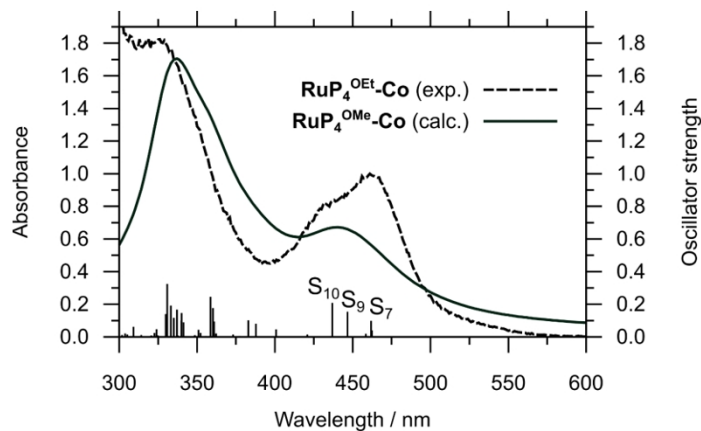


**Figure S22.** Experimental ( $\text{RuP}_4^{\text{OEt}}\text{-Co}$ ) and simulated ( $\text{RuP}_4^{\text{OMe}}\text{-Co}$ , black lines) UV/vis absorption spectrum. Quantum chemical results were obtained at the time-dependent density functional level of theory (B3LYP/def2-svp) including D3BJ dispersion correction and solvent effects (ACN) by a polarizable continuum model.

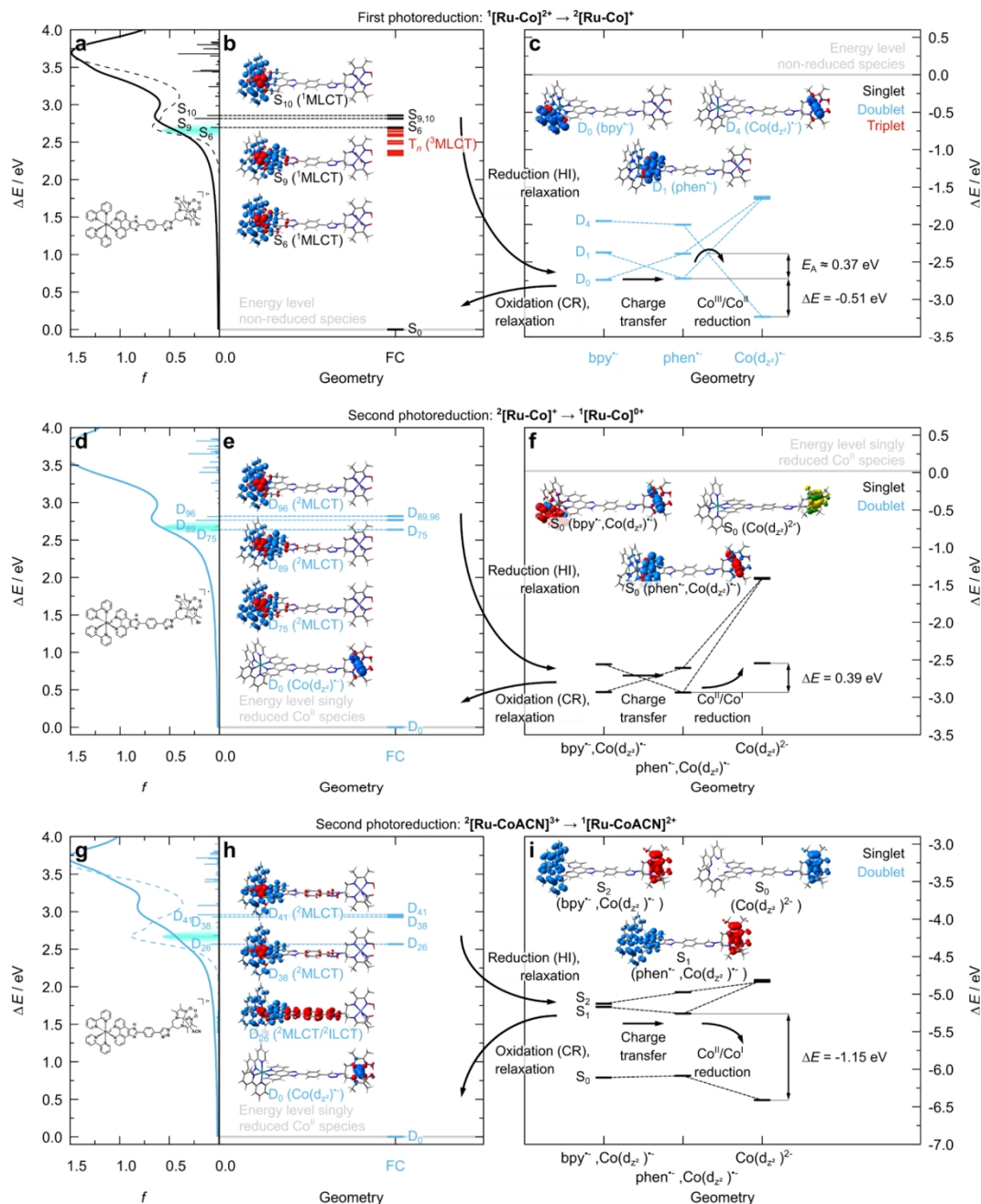


**Figure S23.** a) Singlet UV-vis absorption spectrum of **Ru-Co** (experimental data: dashed line, simulated data: solid line) and, b), energy levels of prominent singlet and triplet excitations in the Franck-Condon geometry (FC, singlet ground state equilibrium). c) Singly reduced states with excess charge localized on one bpy ligand ( $\text{bpy}^*$ ), on the phen ligand ( $\text{phen}^*$ ) and at the catalytic centre – leading to the partially charged  $\text{Co}^{\text{II}}$  species with semi-occupied  $d_z^2(\text{Co})$  orbital. All states are shown in their respective equilibrium structures. d) Spin-allowed doublet excitations contributing to the UV-vis absorption spectrum of **Ru-Co** (simulated data: solid line). e) Energy levels of prominent doublet excitations in the Franck-Condon geometry (doublet ground state equilibrium of  $\text{Co}^{\text{II}}$  species shown in c)). f) Doubly reduced states with one excess charge localized at the Co, *i.e.*  $\text{Co}^{\text{II}}$  species, and the other excess charge on one bpy ligand ( $\text{bpy}^*$ ), on the phen ligand ( $\text{phen}^*$ ) and at the catalytic centre

– leading to the fully charged  $\text{Co}^{\text{I}}$  species with doubly occupied  $d_{z^2}(\text{Co})$  orbital. The highest-occupied molecular orbital of the  $\text{Co}^{\text{I}}$  is shown in f). Singlet, doublet, and triplet states are shown in black, blue, and red, respectively. g) Spin-allowed doublet excitations contributing to the UV-vis absorption spectrum of  ${}^2[\text{Ru-CoACN}]^{3+}$  (simulated data: solid line). h) Energy levels of prominent doublet excitations in the Franck-Condon geometry (doublet ground state equilibrium of  $\text{Co}^{\text{II}}$  species shown in c)). i) Doubly reduced states with one excess charge localized at the Co, *i.e.* C species, and the other excess charge on one bpy ligand ( $\text{bpy}^{\bullet}$ ), on the phen ligand ( $\text{phen}^{\bullet}$ ) and at the catalytic centre. Electronic nature of prominent transitions is shown by charge density differences, charge localization in the respective electronic ground state of opened-shell species is illustrated by the spin density. The highest-occupied molecular orbital of  $\text{Co}^{\text{I}}$  is shown in f). Singlet, doublet, and triplet states are shown in black, blue, and red, respectively.



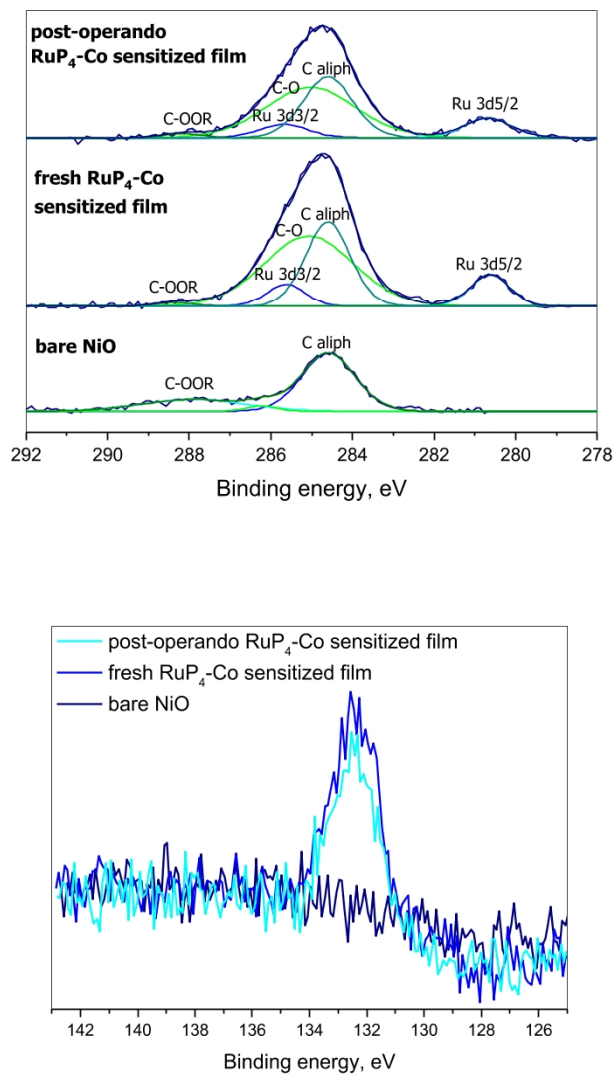


**Figure S24.** XPS core-level spectra of the C 1s + Ru 3d region (top) and P 2p region (bottom) recorded on fresh **RuP<sub>4</sub>-Co**-sensitized and post-operando **RuP<sub>4</sub>-Co**-sensitized films.

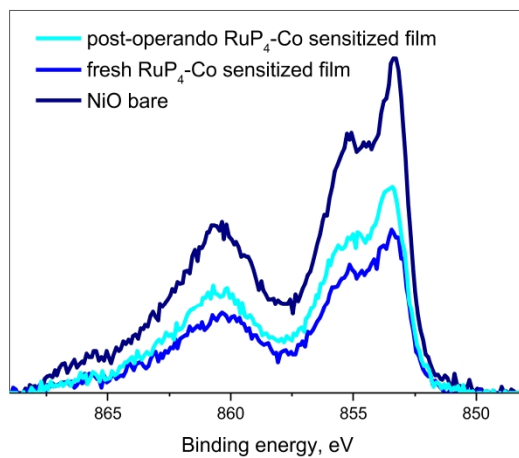
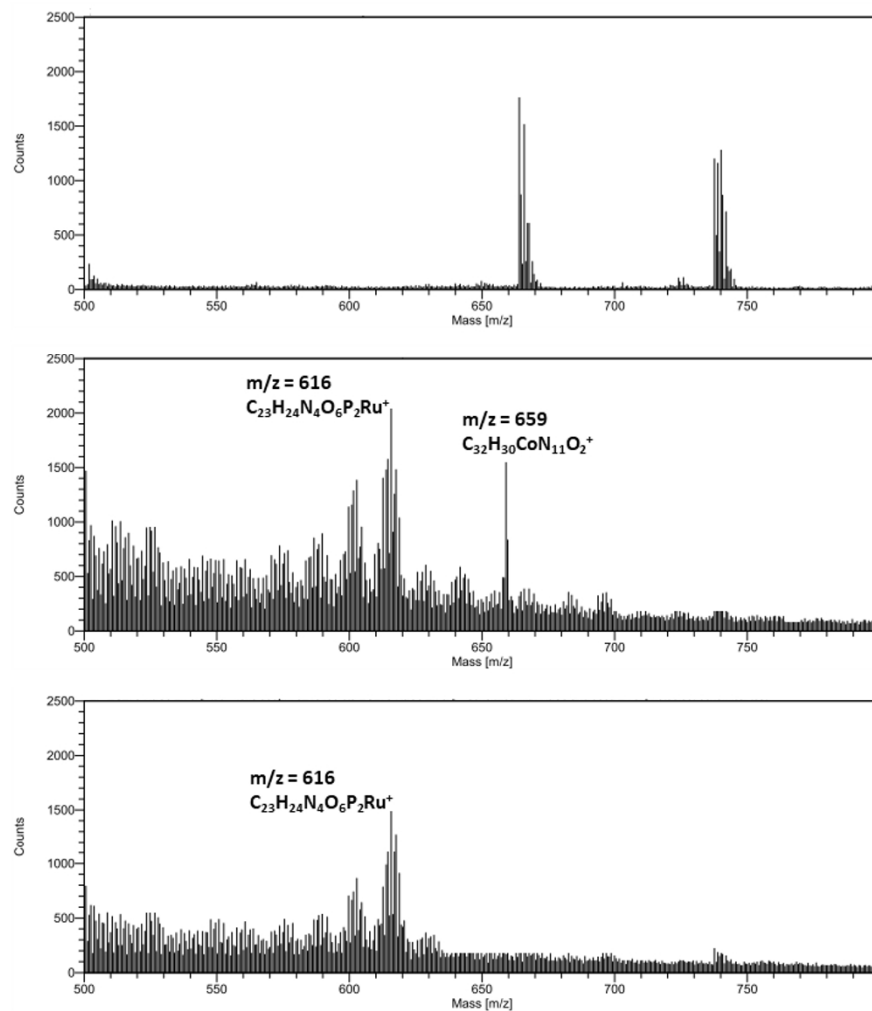
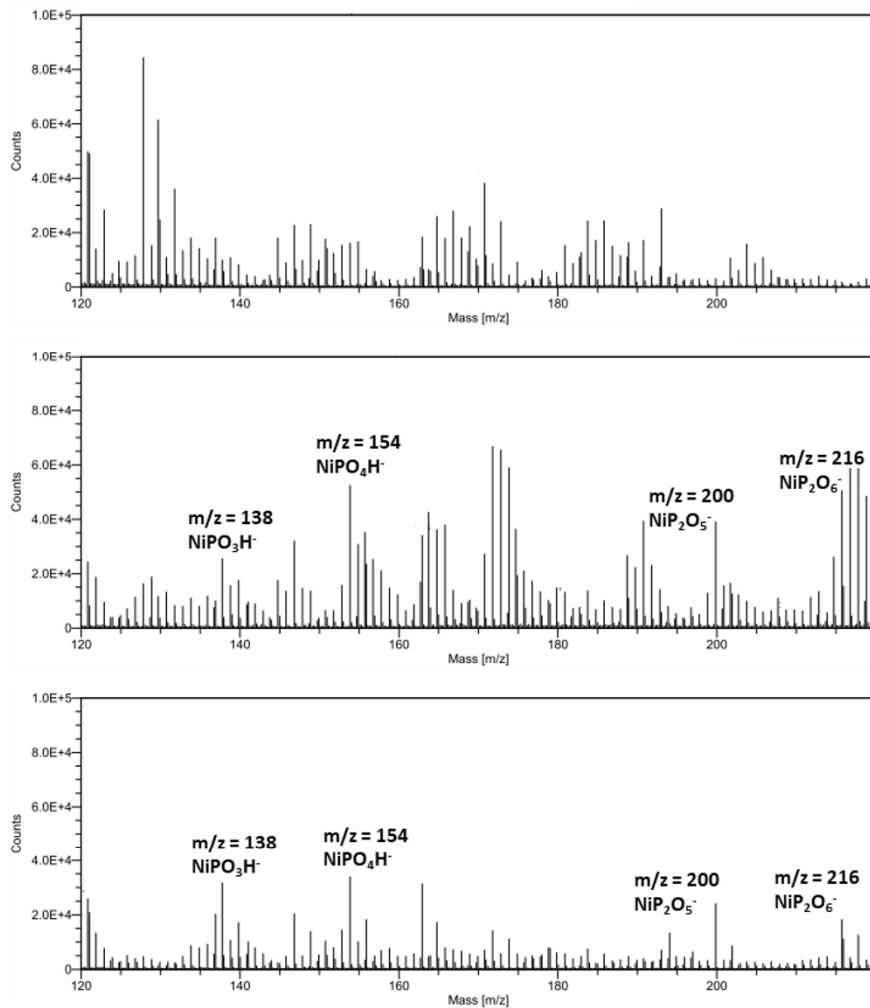


Figure S25. Overlay of the XPS core-level spectra of the Ni 2p region recorded on bare NiO (dark blue), on fresh **RuP<sub>4</sub>-Co**-sensitized (blue) and post-operando **RuP<sub>4</sub>-Co**-sensitized (cyan) films.



**Figure S26.** Positive mode ToF-SIMS spectra of bare NiO (top), fresh (middle) and post-operando (bottom)  $RuP_4^{OH}$ -Co-sensitized electrodes in the  $500 < m/z < 800$  range.

Of note, all ions are detected as singly-charged species, something previously observed in the literature for other ruthenium complexes;<sup>31-32</sup> we attribute it to the formation of protonated fully reduced complexes under the ToF-SIMS conditions of analysis.



**Figure S27.** Negative mode ToF-SIMS spectra of bare NiO (top), fresh (middle) and post-operando (bottom)  $\text{RuP}_4^{\text{OH}}$ -Co-sensitized electrodes in the  $120 < m/z < 220$  range.

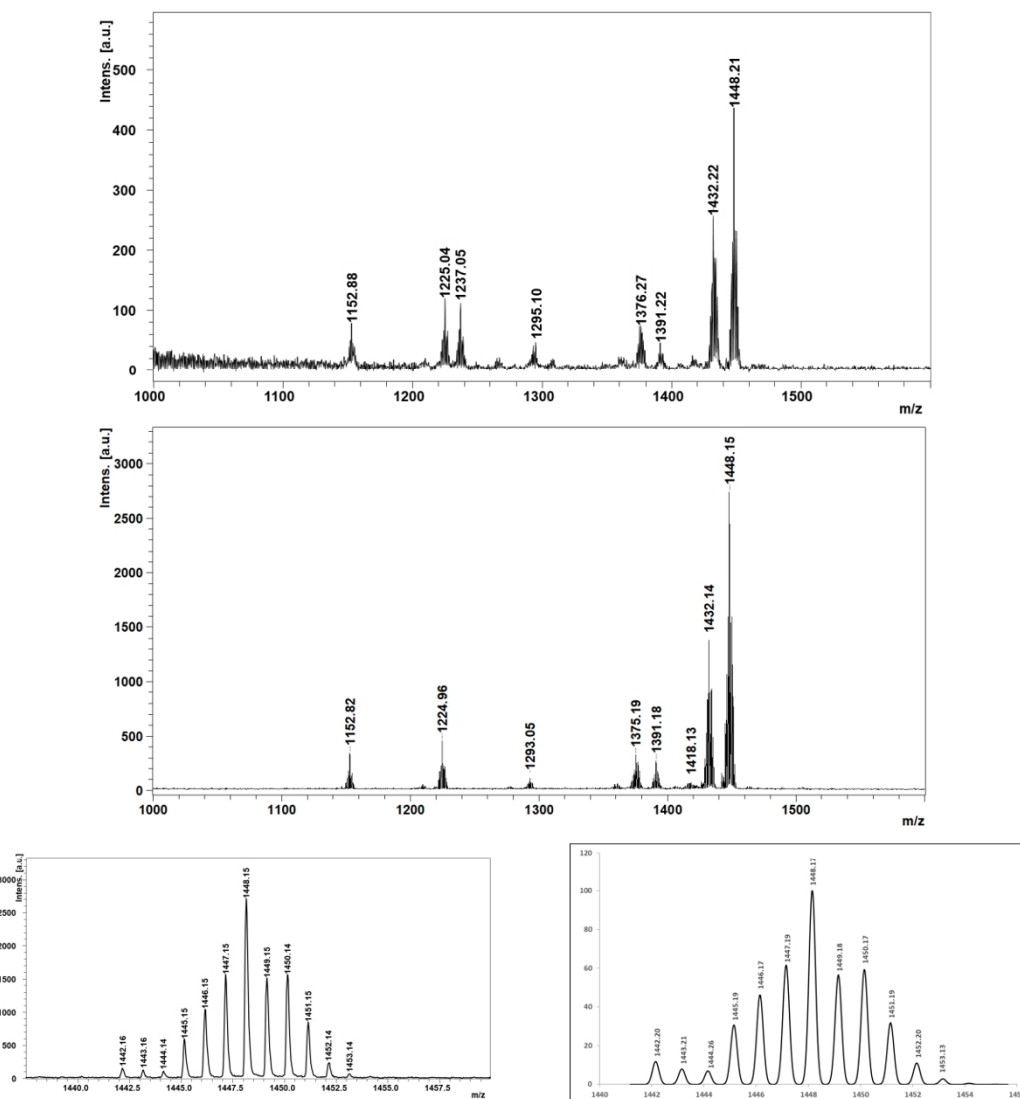


**Figure S28.** MALDI-ToF mass spectra obtained from a 1M phenylphosphonic acid methanolic solution of **RuP<sub>4</sub>-Co** recorded as reference (top) and after desorption of a fresh **RuP<sub>4</sub>-Co**-sensitized film (middle). Experimental isotopic pattern for the main fragment at 1448.15 and calculated one for  $C_{48}H_{49}N_{13}O_{12}P_4Ru (MH^+)$  (bottom right), corresponding to  $[M-2PF_6-2Br]^+$ .

Of note, all ions are detected as singly-charged species, something previously observed in the literature for other ruthenium complexes and attributed to the formation of protonated fully reduced complexes ( $MH^+$ ) under these conditions of analysis.<sup>33-34</sup>

**References.**

- (1) Gillaizeau-Gauthier, I.; Odobel, F.; Alebbi, M.; Argazzi, R.; Costa, E.; Bignozzi, C. A.; Qu, P.; Meyer, G. J. Phosphonate-Based Bipyridine Dyes for Stable Photovoltaic Devices. *Inorg. Chem.* **2001**, *40* (23), 6073-6079, DOI: 10.1021/ic010192e.
- (2) Andreiadis, E. S.; Jacques, P.-A.; Tran, P. D.; Leyris, A.; Chavarot-Kerlidou, M.; Jusselme, B.; Matheron, M.; Pécaut, J.; Palacin, S.; Fontecave, M.; Artero, V. Molecular engineering of a cobalt-based electrocatalytic nanomaterial for H<sub>2</sub> evolution under fully aqueous conditions. *Nature Chem.* **2013**, *5* (1), 48-53.
- (3) Queyriaux, N.; Andreiadis, E. S.; Torelli, S.; Pecaut, J.; Veldkamp, B. S.; Margulies, E. A.; Wasielewski, M. R.; Chavarot-Kerlidou, M.; Artero, V. CuAAC-based assembly and characterization of a ruthenium-copper dyad containing a diimine-dioxime ligand framework. *Faraday Discuss.* **2017**, *198* (0), 251-261, DOI: 10.1039/C6FD00204H.
- (4) Queyriaux, N.; Giannoudis, E.; Lefebvre, J.-F.; Artero, V.; Chavarot-Kerlidou, M. Synthesis of Ruthenium Tris-Diimine Photosensitizers Substituted by Four Methylphosphonate Anchoring Groups for Dye-Sensitized Photoelectrochemical Cell Applications. *Eur. J. Inorg. Chem.* **2019**, *2019* (15), 2154-2161, DOI: 10.1002/ejic.201900151.
- (5) Windle, C. D.; Massin, J.; Chavarot-Kerlidou, M.; Artero, V. A protocol for quantifying hydrogen evolution by dye-sensitized molecular photocathodes and its implementation for evaluating a new covalent architecture based on an optimized dye-catalyst dyad. *Dalton Trans.* **2018**, *47* (31), 10509-10516, DOI: 10.1039/C8DT01210E.
- (6) Siebert, R.; Akimov, D.; Schmitt, M.; Winter, A.; Schubert, U. S.; Dietzek, B.; Popp, J. Spectroscopic Investigation of the Ultrafast Photoinduced Dynamics in  $\pi$ -Conjugated Terpyridines. *ChemPhysChem* **2009**, *10* (6), 910-919, DOI: <https://doi.org/10.1002/cphc.200800847>.
- (7) Sittig, M.; Schmidt, B.; Görls, H.; Bocklitz, T.; Wächtler, M.; Zechel, S.; Hager, M. D.; Dietzek, B. Fluorescence upconversion by triplet-triplet annihilation in all-organic poly(methacrylate)-terpolymers. *Phys. Chem. Chem. Phys.* **2020**, *22* (7), 4072-4079, DOI: 10.1039/D0CP00232A.
- (8) Kaeffler, N.; Massin, J.; Lebrun, C.; Renault, O.; Chavarot-Kerlidou, M.; Artero, V. Covalent Design for Dye-Sensitized H<sub>2</sub>-Evolving Photocathodes Based on a Cobalt Diimine-Dioxime Catalyst. *J. Am. Chem. Soc.* **2016**, *138* (38), 12308-12311, DOI: 10.1021/jacs.6b05865.
- (9) Frisch, M. J.; Trucks, G. W.; Schlegel, H. B.; Scuseria, G. E.; Robb, M. A.; Cheeseman, J. R.; Scalmani, G.; Barone, V.; Petersson, G. A.; Nakatsuji, H.; Li, X.; Caricato, M.; Marenich, A. V.; Bloino, J.; Janesko, B. G.; Gomperts, R.; Mennucci, B.; Hratchian, H. P.; Ortiz, J. V.; Izmaylov, A. F.; Sonnenberg, J. L.; Williams, F.; Ding, F.; Lipparini, F.; Egidi, F.; Goings, J.; Peng, B.; Petrone, A.; Henderson, T.; Ranasinghe, D.; Zakrzewski, V. G.; Gao, J.; Rega, N.; Zheng, G.; Liang, W.; Hada, M.; Ehara, M.; Toyota, K.; Fukuda, R.; Hasegawa, J.; Ishida, M.; Nakajima, T.; Honda, Y.; Kitao, O.; Nakai, H.; Vreven, T.; Throssell, K.; Montgomery Jr., J. A.; Peralta, J. E.; Ogliaro, F.; Bearpark, M. J.; Heyd, J. J.; Brothers, E. N.; Kudin, K. N.; Staroverov, V. N.; Keith, T. A.; Kobayashi, R.; Normand, J.; Raghavachari, K.; Rendell, A. P.; Burant, J. C.; Iyengar, S. S.; Tomasi, J.; Cossi, M.; Millam, J. M.; Klene, M.; Adamo, C.; Cammi, R.; Ochterski, J. W.; Martin, R. L.; Morokuma, K.; Farkas, O.; Foresman, J. B.; Fox, D. J. *Gaussian 16 Rev. B.01*, Wallingford, CT, 2016.
- (10) Becke, A. D. Density-functional thermochemistry. III. The role of exact exchange. *J. Chem. Phys.* **1993**, *98* (7), 5648-5652, DOI: 10.1063/1.464913.
- (11) Lee, C.; Yang, W.; Parr, R. G. Development of the Colle-Salvetti correlation-energy formula into a functional of the electron density. *Phys. Rev. B* **1988**, *37* (2), 785-789, DOI: 10.1103/PhysRevB.37.785.
- (12) Weigend, F.; Ahlrichs, R. Balanced basis sets of split valence, triple zeta valence and quadruple zeta valence quality for H to Rn: Design and assessment of accuracy. *Phys. Chem. Chem. Phys.* **2005**, *7* (18), 3297-3305, DOI: 10.1039/B508541A.
- (13) Weigend, F. Accurate Coulomb-fitting basis sets for H to Rn. *Phys. Chem. Chem. Phys.* **2006**, *8* (9), 1057-1065, DOI: 10.1039/B515623H.
- (14) Guthmuller, J.; González, L. Simulation of the resonance Raman intensities of a ruthenium-palladium photocatalyst by time dependent density functional theory. *Phys. Chem. Chem. Phys.* **2010**, *12* (44), 14812-14821, DOI: 10.1039/C0CP00942C.
- (15) Pfeffer, M. G.; Zedler, L.; Kupfer, S.; Paul, M.; Schwalbe, M.; Peuntinger, K.; Guldi, D. M.; Guthmuller, J.; Popp, J.; Gräfe, S.; Dietzek, B.; Rau, S. Tuning of photocatalytic activity by creating a tridentate coordination sphere for palladium. *Dalton Trans.* **2014**, *43* (30), 11676-11686, DOI: 10.1039/C4DT01034E.

- (16) Zedler, L.; Guthmuller, J.; Rabelo de Moraes, I.; Kupfer, S.; Kriek, S.; Schmitt, M.; Popp, J.; Rau, S.; Dietzek, B. Resonance-Raman spectro-electrochemistry of intermediates in molecular artificial photosynthesis of bimetallic complexes. *Chem. Commun.* **2014**, *50* (40), 5227-5229, DOI: 10.1039/C3CC47487A.
- (17) Kupfer, S. Extended charge accumulation in ruthenium-4H-imidazole-based black absorbers: a theoretical design concept. *Phys. Chem. Chem. Phys.* **2016**, *18* (19), 13357-13367, DOI: 10.1039/C6CP00911E.
- (18) Kupfer, S.; Wächtler, M.; Guthmuller, J.; Popp, J.; Dietzek, B.; González, L. A Novel Ru(II) Polypyridine Black Dye Investigated by Resonance Raman Spectroscopy and TDDFT Calculations. *J. Phys. Chem. C* **2012**, *116* (37), 19968-19977, DOI: 10.1021/jp3067958.
- (19) Latouche, C.; Skouteris, D.; Palazzetti, F.; Barone, V. TD-DFT Benchmark on Inorganic Pt(II) and Ir(III) Complexes. *J. Chem. Theory Comput.* **2015**, *11* (7), 3281-3289, DOI: 10.1021/acs.jctc.5b00257.
- (20) Escudero, D. Photodeactivation Channels of Transition Metal Complexes: A Computational Chemistry Perspective. In *Transition Metals in Coordination Environments: Computational Chemistry and Catalysis Viewpoints*; Broclawik, E.; Borowski, T.; Radoń, M., Eds.; Springer International Publishing: Cham, 2019; pp 259-287.
- (21) González, L.; Escudero, D.; Serrano-Andrés, L. Progress and Challenges in the Calculation of Electronic Excited States. *ChemPhysChem* **2012**, *13* (1), 28-51, DOI: <https://doi.org/10.1002/cphc.201100200>.
- (22) Mennucci, B.; Cappelli, C.; Guido, C. A.; Cammi, R.; Tomasi, J. Structures and Properties of Electronically Excited Chromophores in Solution from the Polarizable Continuum Model Coupled to the Time-Dependent Density Functional Theory. *J. Phys. Chem. A* **2009**, *113* (13), 3009-3020, DOI: 10.1021/jp8094853.
- (23) Marenich, A. V.; Cramer, C. J.; Truhlar, D. G. Universal Solvation Model Based on Solute Electron Density and on a Continuum Model of the Solvent Defined by the Bulk Dielectric Constant and Atomic Surface Tensions. *J. Phys. Chem. B* **2009**, *113* (18), 6378-6396, DOI: 10.1021/jp810292n.
- (24) Grimme, S.; Ehrlich, S.; Goerigk, L. Effect of the damping function in dispersion corrected density functional theory. *J. Comput. Chem.* **2011**, *32* (7), 1456-1465, DOI: <https://doi.org/10.1002/jcc.21759>.
- (25) Steinmetzer, J.; Kupfer, S.; Gräfe, S. pysisyphus: Exploring potential energy surfaces in ground and excited states. *Int. J. Quantum Chem.* **2021**, *121* (3), e26390, DOI: <https://doi.org/10.1002/qua.26390>.
- (26) Bhattacharjee, A.; Andreiadis, E. S.; Chavarot-Kerlidou, M.; Fontecave, M.; Field, M. J.; Artero, V. A Computational Study of the Mechanism of Hydrogen Evolution by Cobalt(Diimine-Dioxime) Catalysts. *Chem. Eur. J.* **2013**, *19* (45), 15166-15174, DOI: 10.1002/chem.201301860.
- (27) Solis, B. H.; Yu, Y.; Hammes-Schiffer, S. Effects of Ligand Modification and Protonation on Metal Oxide Hydrogen Evolution Electrocatalysts. *Inorg. Chem.* **2013**, *52* (12), 6994-6999, DOI: 10.1021/ic400490y.
- (28) Quaranta, A.; Lachaud, F.; Herrero, C.; Guillot, R.; Charlot, M.-F.; Leibl, W.; Aukauloo, A. Influence of the Protonic State of an Imidazole-Containing Ligand on the Electrochemical and Photophysical Properties of a Ruthenium(II)-Polypyridine-Type Complex. *Chemistry – A European Journal* **2007**, *13* (29), 8201-8211, DOI: 10.1002/chem.200700185.
- (29) Ameline, D.; Diring, S.; Farre, Y.; Pellegrin, Y.; Naponiello, G.; Blart, E.; Charrier, B.; Dini, D.; Jacquemin, D.; Odobel, F. Isoindigo derivatives for application in p-type dye sensitized solar cells. *RSC Advances* **2015**, *5* (104), 85530-85539, DOI: 10.1039/C5RA11744E.
- (30) Lyu, S.; Massin, J.; Pavone, M.; Muñoz-García, A. B.; Labrugère, C.; Toupance, T.; Chavarot-Kerlidou, M.; Artero, V.; Olivier, C. H<sub>2</sub>-Evolving Dye-Sensitized Photocathode Based on a Ruthenium-Diacetylde/Cobaloxime Supramolecular Assembly. *H<sub>2</sub>-Evolving Dye-Sensitized Photocathode Based on a Ruthenium-Diacetylde/Cobaloxime Supramolecular Assembly* **2019**, *2* (7), 4971-4980, DOI: 10.1021/acsaem.9b00652.
- (31) Queyriaux, N.; Wahyuono, R. A.; Fize, J.; Gablin, C.; Wächtler, M.; Martinez, E.; Léonard, D.; Dietzek, B.; Artero, V.; Chavarot-Kerlidou, M. Aqueous Photocurrent Measurements Correlated to Ultrafast Electron Transfer Dynamics at Ruthenium Tris Diimine Sensitized NiO Photocathodes. *J. Phys. Chem. C* **2017**, *121* (11), 5891-5904, DOI: 10.1021/acs.jpcc.6b12536.
- (32) Pöldme, N.; O'Reilly, L.; Fletcher, I.; Portoles, J.; Sazanovich, I. V.; Towrie, M.; Long, C.; Vos, J. G.; Pryce, M. T.; Gibson, E. A. Photoelectrocatalytic H<sub>2</sub> evolution from integrated photocatalysts adsorbed on NiO. *Chem. Sci.* **2019**, *10* (1), 99-112, DOI: 10.1039/C8SC02575D.
- (33) Bodige, S.; Torres, A. S.; Maloney, D. J.; Tate, D.; Kinsel, G. R.; Walker, A. K.; MacDonnell, F. M. First-Generation Chiral Metallodendrimers: Stereoselective Synthesis of Rigid D<sub>3</sub>-Symmetric Tetranuclear Ruthenium Complexes. *J. Am. Chem. Soc.* **1997**, *119* (43), 10364-10369, DOI: 10.1021/ja9720467.

- (34) Hunsucker, S. W.; Watson, R. C.; Tissue, B. M. Characterization of inorganic coordination complexes by matrix-assisted laser desorption/ionization mass spectrometry. *Rapid Commun. Mass Spectrom.* **2001**, *15* (15), 1334-1340, DOI: <https://doi.org/10.1002/rcm.377>.